Aerospace and Mechanical Engineering

Edited by
Qi Luo

TRANS TECH PUBLICATIONS

Aerospace and Mechanical Engineering

Edited by
Qi Luo

Aerospace and Mechanical Engineering

Selected, peer reviewed papers from the
2014 Conference on
Aerospace and Mechanical Engineering
(AME 2014),
April 13-14, 2014, Bangkok, Thailand

Edited by

Qi Luo

Trans Tech Publications Ltd
Kreuzstrasse 10
CH-8635 Durnten-Zurich
Switzerland
http://www.ttp.net

Volume 565 of
Applied Mechanics and Materials
ISSN print 1660-9336
ISSN cd 1660-9336
ISSN web 1662-7482

Full text available online at *http://www.scientific.net*

***Distributed** worldwide by*

Trans Tech Publications Ltd
Kreuzstrasse 10
CH-8635 Durnten-Zurich
Switzerland

Fax: +41 (44) 922 10 33
e-mail: sales@ttp.net

and in the Americas by

Trans Tech Publications Inc.
PO Box 699, May Street
Enfield, NH 03748
USA

Phone: +1 (603) 632-7377
Fax: +1 (603) 632-5611
e-mail: sales-usa@ttp.net

Preface

2014 International Conference on Aerospace and Mechanical Engineering (AME 2014) will be held on April 13-14, 2014, Bangkok, Thailand.

The book is aimed at readers falling between two ends of a broad spectrum: at one end are aerospace or mechanical engineers with basic knowledge in control systems; at the other are control engineers with little or no knowledge about gas turbines (the typical electrical engineer may fit this category). Of course, any “interpolated” engineer will also benefit from this book, since it includes detailed information on turbine engine systems and introduces advanced control topics.

AME 2014 focus on three topics: (I) Materials Science and Materials Processing Technology; (II) Aerospace and Mechanical Engineering, Applied Mechanics; (III) Computation Methods and Information Technologies. Some papers were highly evaluated by the scientific committees and the reviewers. For example, the “A Development of Human Machine Interface in a Miniature 3-Axis Milling Machine Prototyping” by Pornjit Pratumsuwan, Anan Suebsomram; the “Modeling of atmospheric processes based on the averaged Navier-Stokes equations” by Bakytzhan Zhumagulov, Dauren Zhakebaev and Aigerim Abdibekova was highly evaluated. We expect that the conference and its publications will be a trigger for further related research and technology improvements in these importance subjects.

AME 2014 was both stimulating and informative with an interesting array of keynote and invited speakers from all over the world. Delegates had a wide range of sessions to choose. The program consisted of invited sessions, technical workshops and discussions with eminent speakers covering a wide range of topics. This rich program provided all attendees with the opportunity to meet and interact with one another.

We would like to thank the organization staff, the members of the program committees and reviewers. They have worked very hard in reviewing papers and making valuable suggestions for the authors to improve their work. We also would like to express our gratitude to the external reviewers, for providing extra helps in the review process, and the authors for contributing their research result to the conference.

We hope that AME 2014 will be successful and enjoyable to all participants. We look forward to seeing all of you next year at the AME.

QI Luo

Conference Committees

Honorary Chair

Yuan Lee, Northestern University, USA

General Chairs

Jun Zhang, Huazhong University of Science and Technology, China
Minli Dai, Suzhou University, China

Organizing Chairs

Khine Soe Thaung , Maldives College of Higher Education, Maldives
Biswanath Vokkarane, Society on Social Implications of Technology and Engineering , Maldives

Program Chairs

Hong Zhang, Wuhan University, China
Dehuai Yang , Huazhong Normal University, China

Program Chairs

Qi Luo, Singapore Management and Sports Science Institute, Singapore

International Committee

Minli Dai, Suzhou University, China
Ying Zhang, Wuhan Uniersity, China
Zhenghong Wu, East China Normal University
Tatsuya Akutsu, ACM NUS Singapore Chapter, Singapore
Aijun An, National University of Singapore,Singapore
Yuanzhi Wang, Anqing Teachers' University, China
Yiyi Zhouzhou,Azerbaijan State Oil Academy,Azerbaijan
Khine Soe Thaung , Maldives College of Higher Education, Maldives
Biswanath Vokkarane, Society on Social Implications of Technology and Engineering
Jessica Zhang, Information Engineering Research Institute, USA
David Meng, Information Engineering Research Institute, USA
Kath David, Information Engineering Research Institute, USA

Table of Contents

Chapter 3: Computation Methods and Information Technologies

CHAPTER 1:

Materials Science and Materials Processing Technology

Applied Mechanics and Materials Vol. 565 (2014) pp 3-8

doi:10.4028/www.scientific.net/AMM.565.3

Improvement of TA Cloning Method to Facilitate Direct Directional Cloning of PCR Products

Jigang Li[a], Guoying Han[b], Xiumin Li[c], Jiaojiao Sun[d], Kejing Song[e] and Ting Zhang[f]

College of Life Sciences, Key Laboratory of Microbial Diversity Research and Application of Hebei Province, Hebei University, Baoding, People's Republic of China

[a]lijigang@hbu.edu.cn, [b]hanguoying_1@126.com, [c]lixiumin@hbu.edu.cn, [d]522399118@qq.com, [e]kejingsong_1@126.com, [f]874004118@qq.com

Keywords: polymerase chain reaction, expression plasmid vector construction, thermostable DNA polymerase, terminal transferase, direct directional cloning

Abstract Directional cloning is a prerequisite for the construction of expression vectors in molecular biology laboratories. Although TA cloning is widely used to clone unmodified PCR (polymerase chain reaction) products, a major disadvantage of this technique is that cloning is not directional. Here we reported a novel PCR products cloning vector with one deoxythymidine overhang and one deoxycytidine overhang at two 3'-ends respectively. With the choice of nucleotides of 5'-ends of PCR primers, PCR products can be cloned to this vector both directly and directionally. The feasibility and efficacy of this cloning method were confirmed by using a pET-17b derivative vector and a green fluorescent protein gene (*EGFP*) and a red fluorescent protein reporter (*Ds-Red*) gene. This cloning strategy may be useful in the high-throughput construction of expression vectors and could be viewed as an interesting improvement of existing TA cloning method.

Introduction

TA cloning has been used in direct cloning of PCR products in molecular biology laboratories for over twenty years [1]. This cloning method does not require restriction enzyme digestion of target DNA fragments and usually allows blue-white screening of recombinant plasmids. Addition of an extra adenosine residue by the terminal transferase activity of thermo-stable DNA polymerases (e. g., Taq DNA polymerase) is the basis of TA cloning method [2, 3, 4]. Although TA cloning still remains popular for its performance in efficiency, convenience and cost saving, it is not suitable for construction of expression vector due to randomness of direction of inserted DNA fragments.

In this report, we devised a novel cloning method that facilitates directional cloning of PCR products directly. The key of the method is the design of a cloning vector with a deoxythymidine overhang and a deoxycytidine overhang at two 3' ends respectively. According to previous observations [3, 5], 3'-terminal deoxyguanosine overhang of PCR products occurs only when the corresponding primer has a 5'-terminal deoxycytidine residue if the PCR reaction is catalyzed by Taq DNA polymerase. Therefore, to enable the ligation of PCR products to such a linearized vector, one PCR primer is designed to possess a 5'-terminal deoxycytidine residue and the other to possess a 5'-terminal non-deoxycytidine residue. Theoretically, PCR product with a deoxyadenosine overhang at one 3' end and a deoxyguanosine overhang at the other 3' end will be present in PCR products generated with such primer pair and Taq DNA polymerase. Obviously, only PCR product of this kind can be ligated to a linear vector with a 3'-T overhang and a 3'-C overhang in the mode of TA cloning at one end and GC cloning at the other, generating recombinant plasmids with unidirectional inserts (Fig. 1).

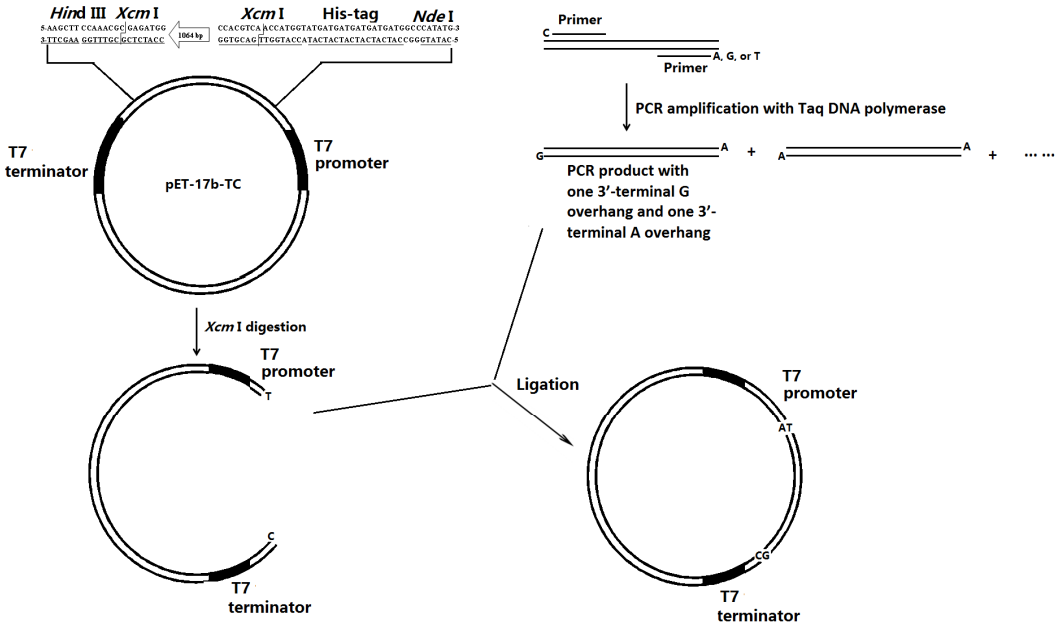

Fig. 1 Schematic representation of directional cloning *via* a hybrid strategy of TA and GC cloning.

The key of this strategy is the choice of base of the 5'-termini of PCR primers to control the base type of the 3'-terminal overhang of the PCR products. Sequence above plasmid pET-17b-TC was designed to introduce one start codon, one histidine-tag encoding sequence (underlined), two *Xcm* I sites (underlined). Linearized pET-17b-TC was obtained through *Xcm* I digestion. Primed by a forward primer with a 5' end A and a reverse primer with a 5' end C, a Taq DNA polymerase-catalyzed DNA sequence can be introduced between the 3'-terminal overhang T and C of the linearized pET-17b-TC, whereby a single glycine residue and six histidine residues are added to the expressed polypeptide at the N-terminal upon translation.

Material and methods

Modification of pET-17b vector

We first synthesized a pair of PCR primers NXAF and HXAR (Table 1) to modify an *Escherichia coli* expression pET-17b vector pET-17b. Primer NXAF contains an *Nde* I and an *Xcm* I sites. The start codon ATG in *Nde* I site of Primer NXAF is followed by one glycine and six histidine codons. Primer HXAR contains a *Hin*d III site and an *Xcm* I site. This primer pair was designed to amplify an insect arginine kinase gene, or *ark* (GenBank accession: EF600057) harbored in a pUC-19 derivative plasmid. The *ark* fragment of 1000 bp (base pair) long was used as stuffer in this modification process. PCR reaction was performed according to conventional PCR protocol. PCR product was separated by agarose gel electrophoresis, followed by gel recovery with a spin-column kit (CWbio, Beijing, China), digestion with *Nde* I and *Hin*d III (Takara, Dalian, China) and ligation to vector pET-17b linearized with *Nde* I and *Hin*d III. The identity of the final plasmid was confirmed by dideoxy sequencing.

Table 1 Primers used during this study

Primer	Sequence (5' to 3')
NXAF	CGGATCGCATATGGGCCATCATCATCATCATCATACCATGGTTGACGTGGCAACAATCG
HXAR	AAAAAGCTTCCAAACGCGAGATGGTTAACCGA
AgfpF	ATGGTGAGCAAGGGCGA
CgfpR	CCGGCCGCTTTACTTGT
ArfpF	ATGACCATGATTACGCCA
CrfpR	CTACAGGAACAGGTGGT
T7	TAATACGACTCACTATAGGG

Directional cloning efficacy test

In order to test the cloning efficacy of the linearized pET-17b-TC, EGFP (Enhanced Green Fluorescent Protein) encoding gene of plasmid pEGFP-N2 and Ds-Red (red fluorescent protein) encoding gene of pDsRed-Express (Clontech Lab, CA, USA) were amplified with two pairs of PCR primers. The two primer pairs were designed to start with a deoxyadenosine nucleotide at the 5'-end of forward primers (AgfpF and ArfpF, Table 1) and a deoxycytidine nucleotide at 5' ends of reverse primers (CrfpR and CrfpR, Table 1). PCR reactions were performed in a volume of 40 μl containing 2 U of Taq polymerase (ExTaq, Takara, Dalian, China) and other reagents. Purified *EGFP* or *Ds-Red* PCR product (100 ng) and pET-17b-TC (100 ng) were added to the ligation mixture in a total volume of 10 μl. Ligation reactions were proceeded at 16℃ for 16 hours. Then ligation mixtures were introduced into DH5α competent cells by electroporation method. Bacterial culture was spread on agar plates containing 50 μg ml^{-1} ampicilin.

Three pairs of PCR primers were used for screening of *EGFP* or *Ds-Red* expression plasmid respectively, Primer pair a (including Primer AgfpF and CgfpR, or Primer ArfpF and CrfpR), b (including T7 promoter primer and Primer CgfpR, or T7 promoter primer and Primer CrfpR) and c (including Primer AgfpF and T7 promoter primer, or Primer ArfpF and T7 promoter primer). A positive colony of each transformation was picked for sequencing. Extracted plasmids of both transformations were transformed into expression host BL21(DE3)separately. Liquid culture of each expression colony was grown on agar plates supplemented with 50 μg ml^{-1} ampicilin and 14 μl IPTG (**β**-D-1-thiogalactopyranoside, 0.8 mol L^{-1}).

Results

Modification of pET-17b vector

In order to modify pET-17b vector, Primer NHAX and HXAR were so designed that the final modified plasmid (pET-17b-TC) possesses a 3'-terminal deoxythymidine overhang residue at the promoter side and a 3'-terminal deoxycytidine overhang residue at the terminator side after digestion with *Xcm* I (New England Biolabs) (Fig. 1). The two *Xcm* I-cassettes and other elements introduced were confirmed by sequencing with T7 terminator primer (Fig. 2A) and T7 promoter primer (Fig. 2B).

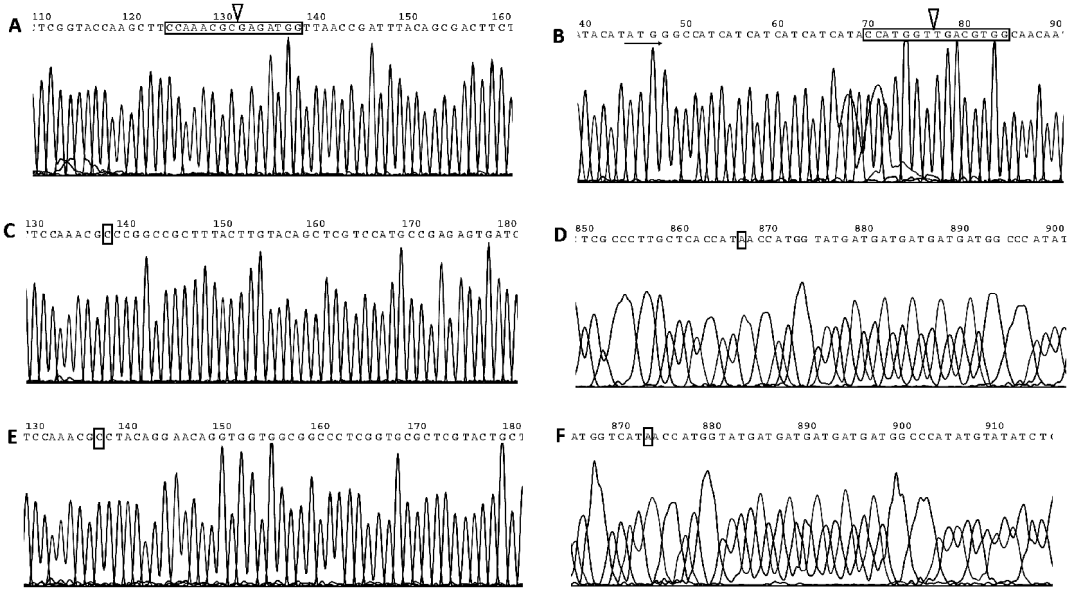

Fig. 2 Sequencing chromatogram of pET-17b-TC plasmid (A and B), *EGFP* expression plasmid (C and D), and *Ds-Red* expression plasmid (E and F). *Xcm* I sites (framed) at the terminator side and promoter side were confirmed by sequencing with T7 terminator primer (A) and T7 promoter primer (B). The cleavage sites were indicated with open arrows (A and B). *EGFP* and *Ds-Red* expression plasmids were sequenced with T7 terminator primer (C- F). Bases involved in GC cloning (C and E) and AT cloning (D and F) were indicated (framed).

Directional cloning efficacy test

Transformation of ligation mixtures of *EGFP* and *Ds-Red* PCR product resulted in thirty-three and fifty transformant colonies repectively. Ten colonies of each transformation were picked for plasmid extraction and PCR analysis (Fig. 3). Three primer pairs were used for screening of recombinants of each transformation, including Primer pair a, Primer pair b, and Primer pair c. Primer pair a is gene specific and can amplify recombinant colonies. Primer pair b and c can amplify recombinant colony with insert of direct and reverse direction respectively. If recombinant plasmids containing inserts of direct direction were amplified, Primer pair b should produce specific band of slightly larger size than Primer pair a. PCR amplification of *EGFP* showed that nine of the ten plasmids are recombinants with direct inserts (Fig. 3A). Only one plasmid (Fig. 3A, Plasmid 10) was identified to be the product of self-ligation of pET-17b-TC. The directional cloning ratio (number of directional colonies/ number of recombinants) reached 100%. Meanwhile, as shown in Figure 3B, PCR amplification of *Ds-Red* showed that all the ten plasmids are recombinant plasmids with direct inserts (Fig. 3B). The directional cloning ratio also reached 100%.

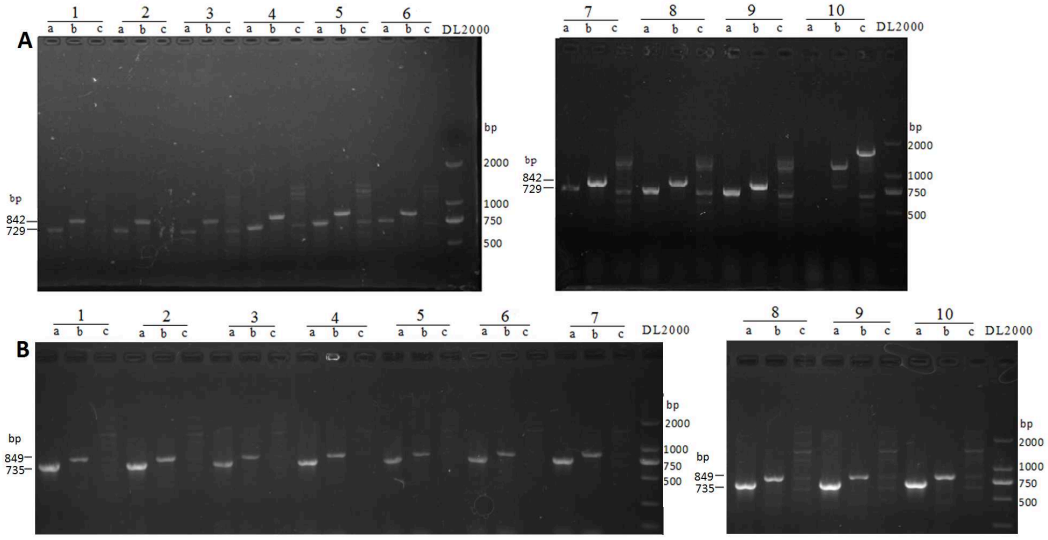

Fig. 3 Amplification of recombinant plasmids by PCR. (A and B) Plasmid 1 to 10 of each transformation were amplified by using 3 pairs of PCR primers including Primer pair a (gene specific primer), Primer pair b (T7 promoter primer and reverse primer) and Primer pair c (forward primer and T7 promoter primer). DL2000 is a DNA marker purchased from Takara Company (Dalian, China).

The ten plasmids of each transformation were retransformed into expression host BL21/DE3 respectively. Green or red fluorescence of all the correct expression colonies as identified by PCR is visible after the overnight plates were placed under 4℃ for another 7 days, suggesting the successful expression of green or red fluorescence protein (data not shown). *EGFP* and *Ds-Red* expression plasmids were sequenced with T7 terminator primer (Fig. 2C, 2D, 2E and 2F) separately. Sequencing data revealed that the ligation occurred in TA cloning mode at the T7 promoter side (Fig. 2D and 2F) and in GC cloning mode at the T7 terminator side (Fig. 2C and 2E) as expected.

Discussions

In construction of expression vectors following traditional protocols, tedious work in DNA manipulation is always necessary. These manipulations usually include selection of restriction enzyme sites, addition of restriction enzyme sites to DNA sequence of the target genes by PCR, plasmid digestion with restriction enzymes and gel recovery of DNA fragments. Gateway cloning technology developed by Invitrogen Company circumvents most of these steps, becoming wide-spread in molecular laboratories [6]. But expensive and special enzymes are required in Gateway cloning process.

Various strategies have been developed to enable directional cloning with traditional TA cloning method [7, 8]. Usually, indicative features are designed and added to T-vectors to make screening of recombinant plasmid with insert of desired direction more convenient in these strategies. In contrast, the method we just described allows insert of only one orientation. It can be viewed as a hybrid method of TA cloning and GC cloning, which require terminal transferase activity of thermo-stable DNA polymerase used in PCR reactions. As we have demonstrated with a GFP and a Ds-Red reporter genes, this novel method can guarantees the desired direction of inserted DNA fragments very well. In this study, only ExTaq (Takara, Dalian, China), a thermo-stable DNA polymerase with terminal transferase activity and high sequence fidelity DNA polymerase was used. Nevertheless, other commercially available thermo-stable DNA polymerases with terminal transferase activity and better sequence fidelity may also be suitable for this purpose. Target DNA of larger size, such as an insect dsRNAase encoding gene (1300 bp), an insect chitin deacetylase encoding gene (1600 bp) and an insect laccase encoding gene (2200 bp), have also been successfully ligated to pET-17b-TC directionally with similar performance (data unpublished). According to [9], TA cloning efficiency is greatly affected by the type of base of 5' ultimate and penultimate end of the primers and adenosine added on the 5' end of primers improved TA cloning efficiency of PCR products. Therefore, it will be beneficial to carry out further experiments to reveal the relationship of between cloning efficiency and the type of nucleotide of the 5' ultimate and penultimate ends of the PCR primers.

Conclusions

In summary, with the choice of nucleotides of 5'-ends of PCR primers, it was possible to clone PCR products to a linear cloning vector with one deoxythymidine overhang and one deoxycytidine overhang at respective two 3'-ends both directly and directionally. Besides its convenience, this method is also cost-effective. If frequently-used destination expression vectors, such as yeast, plant, or mammal expression vectors, have been modified properly as described in this study, subsequent construction of expression vector will be as simple as TA cloning.

Acknowledgments

This work was financially supported by the Open Project Funds for Young Scientists of Key Laboratory of Microbial Diversity Research and Application of Hebei Province, China (Grant No. 09265631D-11) and Student Innovation and Entrepreneurship Training Program (Grant No. 201310075026).

References

[1] D.A. Mead, N.K. Pey, C. Herrnstadt, R.A. Marcil, L.M. Smith, A universal method for the direct cloning of PCR amplified nucleic acid. *Biotechnology (N Y)*, 9 (7): 657-663, (1991).

[2] J.M. Clark, Novel non-templated nucleotide addition reactions catalyzed by procaryotic and eucaryotic DNA polymerases. *Nucleic Acids Research*, 16 (20): 9677-9686, (1988).

[3] G. Hu, DNA polymerase-catalyzed addition of nontemplated extra nucleotides to the 3' end of a DNA fragment. *DNA Cell Biology*, 12 (8): 763-770, (1993).

[4] V.L. Magnuson, D.S. Ally, S.J. Nylund, Z.E. Karanjawala, J.B. Rayman, J.I. Knapp, A.L. Lowe, S. Ghosh, F.S. Collins, Substrate nucleotide-determined non-templated addition of adenine by Taq DNA polymerase: implications for PCR-based genotyping and cloning. *Biotechniques*, 21 (4): 700-709, (1996).

[5] M.J. Brownstein, J.D. Carpten, J.R. Smith, Modulation of non-templated nucleotide addition by Taq DNA polymerase: primer modifications that facilitate genotyping. *Biotechniques*, 20 (6): 1004-1006, 1008-1010, (1996).

[6] D. Esposito, L.A. Garvey, C.S. Chakiath, Gateway cloning for protein expression. *Methods in molecular biology*, 498: 31-54, (2009).

[7] D. Horn, Directional enrichment of directly cloned PCR products. *Biotechniques*, 39 (1): 40, 42, 44, 46, (2005).

[8] Q. Wu, X. Zhong, C. Zhai, J. Yang, X. Chen, L. Chen, W. Wang, L. Ma, A series of novel directional cloning and expression vectors for blunt-end ligation of PCR products. *Biotechnology letters*, 32 (3): 439-443, (2010).

[9] R.H. Peng, A.S. Xiong, J.G. Liu, F. Xu, C. Bin, H. Zhu, Q.H. Yao, Adenosine added on the primer 5' end improved TA cloning efficiency of polymerase chain reaction products. *Analytical Biochemistry*, 363 (1): 163-165, (2007).

Applied Mechanics and Materials Vol. 565 (2014) pp 9-13

doi:10.4028/www.scientific.net/AMM.565.9

High-Temperature Antioxidant Screening for Silicone Oil

Haijun Yang[1, a], Huizhen Wang[1,b], Li Zhong[1,c], Junqing Zhang[1,d], and Yuejia Liu[1,e]

[1] School of materials science and engineering, Southwest University of Science and Technology, Sichuan Province nonmetal composite and Functional Materials Lab, Mianyang 621010, Sichuan, China

[a]yanghaijun@swust.edu.cn

Keywords: silicone oil, antioxidant, screening

Abstract. In order to prevent silicone oils from suffering oxidative deterioration and prolong its service life at high-temperature, an effective way is adding an appropriate antioxidant package in the base oil. Antioxidants can not only inhibit oil oxidation that produces acidic substances but also prevent the viscosity of oil from increasing. In this work, 1,3-dioctyl-1,1,3,3-tetraphenyl-disiloxane (OPDS) was used as silicone base oil, and several commercially available antioxidants were screened. Data show that TNPP, phenyl sulfide, 2088, and KY01 were effective at 300 ^{o}C, which could be further used as candidates for the antioxidant formulations of silicone base oils used as high temperature lubricants or hydraulic oils.

Introduction

Silicone oil with outstanding thermal endurance could be used as high temperature aerospace lubricating material. Because of the favorable anti-shear performance, silicone oil has become one of the widely used hydraulic oil. Silicone oil may suffer oxidative deterioration which can induce obvious change of the acid value and viscosity in high temperature working environment, therefore the performance and life of silicone oil will be influenced [1].

Currently, in order to prevent the silicone oil from suffering oxidative deterioration, two main techniques are adopted[2]: one is optimization of the oil's molecular structure, and another is the using of effective antioxidants. As an economical and effective method, addition of antioxidants which can break the chain reaction between hydrocarbon and oxygen can improve oil's antioxidant properties without adverse effects [3-5].

In this study, 1,3-dioctyl-1,1,3,3-tetraphenyl-disiloxane (OPDS) was used as silicone base oil (Fig. 1), which was prepared previously in our research group, and has a boiling point over 580 ^{o}C, a flash point over 280 ^{o}C, as well as a fire point over 300 ^{o}C. Its excellent physical properties allow it to be a good high-temperature aerospace lubricant or hydraulic oil. However, OPDS will become dark and viscous after being used under 300 ^{o}C because of oxidation. In order to improve the working performance and life at high-temperature, antioxidant formulations for the silicone base oil need to be studied.

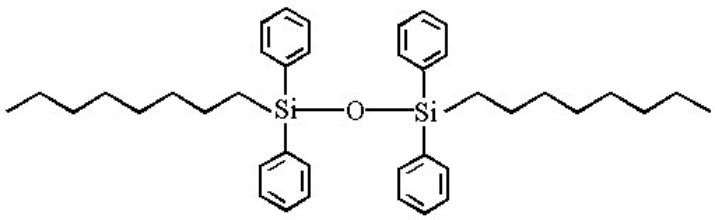

Fig. 1 Structure of 1,3-dioctyl-1,1,3,3-tetraphenyl-disiloxane (OPDS)

Actually, it has been largely reported that a lot of antioxidants have been applied in different base oils. However, few commercially available antioxidants are suitable to the OPDS oil because of low thermo-stability, and/or poor compatibility. Especially, few antioxidants reported could stand a

temperature higher than 250 °C[6]. Screening of antioxidants should be carried out to obtain suitable antioxidant candidates for the antioxidant formulations of the OPDS oil used in high-temperature conditions.[7,8]

Experiment

Materials

1,3-Dioctyl-1,1,3,3-tetraphenyl-disiloxane (OPDS), synthesized in our Lab; Antioxidant T557, A.R., Guangzhou Zhengtong Chemical Technolody Co., LTD.; Antioxidant 1520, A.R., Zibo Hanbo Chemical Co., LTD.; Antioxidant T502A, A.R., Nanjing Datang Chemical Co., LTD.; Antioxidant RH505, A.R., Jinzhou Xinxing Petroleum Additive Co., LTD.; Antioxidant 1024,A.R., Nanjing Milan Chemicals; Antioxidant TNPP, A.R, Jilin Jiuxin Industry Group Chemical Co., LTD.; Antioxidant 2088,A.R., Jilin Jiuxin Industry Group Chemical Co., LTD.; Phenyl sulfide, A.R., Xiya Reagent; 1,10-phenanthroline, A.R., Xiya Reagent; Antioxidant DNPP, A.R, Jilin Jiuxin Industry Group Chemical Co., LTD.; Tricresyl Phosphate (TCP), A.R., Xiya Reagent; Antioxidant KY01, A.R., Jiangsu Feiya Chemical Industry Group; Antioxidant KY531, A.R., Jiangsu Feiya Chemical Industry Group; Silica gel (200-300 mesh), Qingdao Haiyang Chemical Co., LTD.

Instruments

SHZ-III Circulating Water Pump, Shanghai Yarong Biochemical Instrument Plant; RE52CS rotatory evaporator, Shanghai Yarong Biochemical Instrument Plant; B-220 Constant temperature water bath, Shanghai Yarong Biochemical Instrument Plant; DFY-20/120 Constant Temperature Reactor, Gongyi Yuhua Instrument Group Co. Ltd; SHT-Digital Thermostat Magnetic Stirring Electric Heating Jacket, Shandong Zhengcheng Hualu Electric Instrument Group Co. Ltd; 2XZ-4 Rotary-vane Vaccum Pump, Haimen Shenming Rotary-vane Vacuum Pump Factory; NDJ-5S Rotational Type Viscometer, Guangzhou Huarui Chemical Instrument Co., Ltd..

Experimental procedures

Purification of silicone base oil

OPDS base oil (50 g) dissolved in petroleum ether (100 mL) was filtered through a silica gel column using petroleum ether as eluent. After filtration, petroleum ether was evaporated in vacuum, and the residual trace petroleum ether was further removed by an oil pump.

Screening of antioxidants

To an OPDS base oil was added a certain amount of antioxidant. The mixture was stirred and then heated to 300 °C. Experimental phenomena were recorded at regular intervals (Table 1). The acid value and dynamic viscosity at 40 °C of the mixture were determined after being heated at 300 °C for 54 h (Table 2).

Results and discussion

Purification of silicone base oil

The OPDS oil was prepared previously in our laboratory. Impurities such as inorganic salts with strong polarity existing in the OPDS oil may facilitate the oxidation of silicone oil at a high temperature, and thus deactivate the antioxidants added. Therefore, it is necessary to purify the silicone base oil before using. Comparing with inorganic salts, the polarity of silicone oil is comparatively weak. Complete separation of OPDS and inorganic salts could be acquired by silica gel filtration using petroleum ether as eluent.

Screening of antioxidants

Based on the data reported in documents, 13 antioxidants were obtained commercially (Table 1). Silicone oils containing 2% wt of antioxidants were heated at 300 °C for 54 h, and the corresponding experimental phenomena were recorded in Table 1.

Table 1 Experimental phenomena of silicone oil heated at 300 °C for 54 h.

Samples	Temperature	Phenomena
Silicone oil +2%TNPP	300 °C	wine-red, transparent, and with good flowability after 54h
Silicone oil +2% phenyl sulfide	300 °C	wine-red, transparent, and with good flowability after 54h
Silicone oil +2%2088	300 °C	wine-red, transparent, and with good flowability after 54h
Silicone oil +2%DNBP	300 °C	black and opaque after 3h; with poor flowability after 54h
Silicone oil + 2% 1,10-phenanthroline	300 °C	black and opaque after 3h; carbonized after15h; with poor flowability after 20h
Silicone oil +2%KY-531	300 °C	black and opaque after 5h; with poor flowability after 54h
Silicone oil +2%KY-01	300 °C	black and opaque after 5h; with poor flowability after 54h
Silicone oil +2%T557	300 °C	black and opaque after 25h; with poor flowability after 54h
Silicone oil +2%1520	300 °C	blacken after 20h; deep-brown after 54h; with poor flowability and transparency after 54h
Silicone oil +2%T502A	300 °C	black and opaque after 9h; carbonized after 30h
Silicone oil +2%RH505	300 °C	solidified after 5h
Silicone oil +2%1024	300 °C	black and opaque after 9h; carbonized after 40h
Silicone oil +2%TCP	300 °C	black and opaque after 12h; with poor flowability after 54h
Reference silicone oil	300 °C	deep-brown after 54h; with middle flowability after 54h

From Table 1, we can find that carbonization was observed when 1, 10-phenanthroline, T502A, or 1024 were added, and agglomeration occurred when RH505 was added. Interestingly, the OPDS oils including DNBP, T557, 1520, or tricresyl phosphate (TCP) etc. show a good flowability after heated at 300 °C for 54 h. Besides, oils containing KY01 or KY531 also show a good flowability after heated at 300 °C for 54 h though a black color was observed. Therefore, antioxidants such as DNBP, T557, 1520, KY01, KY531, and/or tricresyl phosphate (TCP) could be potential candidates for the antioxidant formulations of OPDS base oil.

Acid value and viscosity are key parameters for evaluating oil oxidation resistance. If antioxidants could obviously lower the acid value and viscosity than those of the reference base oil after heating at 300 °C for 54h, it could be concluded that the antioxidants are effective for high temperature oxidation resistance. Based on the Chinese standard GB/T264–1983 for the acid value measurement of oil products, the formula of acid value is as follows:

$$X = VT / G;$$

$$T = 56.1 \times N$$

V–the volume of a KOH ethanol solution consumed in titration, mL; G–quality of the sample, g; T–titer of KOH ethanol solution, mg KOH/g; N–molar concentration of KOH ethanol solution, mol/L.

The acid values and viscosities of OPDS oils after being heated at 300 °C for 54 h are shown in Table 2.

Table 2 Acid values and viscosities of silicone oils under 300 °C for 54h

Samples	Acid values (mgKOH/g)	Average value (mgKOH/g)	dynamic viscosities (mpa·s)	Average value (mpa·s)
Silicone oil+ 2%TNPP	1.06	0.87	155	145
	0.78		144	
	0.77		138	
Silicone oil+ 2% phenyl sulfide	1.47	1.29	199	200
	1.21		193	
	1.19		210	
Silicone oil + 2% 2088	1.44	0.77	227	223
	1.10		245	
	1.20		229	
Reference silicone oil	1.63	1.43	305	279
	1.30		254	
	1.35		277	

Data in Table 2 show that the adding of TNPP, phenyl sulfide, or 2088 could decrease the acid values of OPDS oils by 39.2%, 9.8%, and 46.2%. At the same time, the dynamic viscosities could be decreased by 48.0%, 28.3%, and 20.1%, respectively. It could be concluded that oxidants such as TNPP, phenyl sulfide, and 2088 are effective for the high temperature oxidation resistance of silicone oils. The oxidants obtained above have different structures and different anti-oxidant mechanisms, which could be further used synergistically for the formulations of silicone base oils used at high temperature.

Summary

In this work, OPDS silicone oil was used as base oil, and 13 commercially available antioxidants were screened for their antioxidation properties for the OPDS base oil used at high temperature. Data show that antioxidants such as TNPP, phenyl sulfide, 2088, and KY01 have good thermo-stabilities and are effective in antioxidation for the OPDS base oil. The antioxidants obtained in this work could inhibit obviously the high temperature oxidation of silicone oils, which could be used as candidates for the formulations of silicone base oils used at high temperature.

References

[1] Liu W Y. The application and market demands of hydraulic oil [J]. *Lubricating Oil* (in Chinese), 2004, 19(2): 1-5.

[2] Cao K, Zhao X Y. Investigation of silicone oil thermal-oxidative stabilizer [J]. *Synthetic Lubricants* (in Chinese), 2011, 38(4): 12-14.

[3] Bai S C, Chen R Z. Overview of silicone oil thermal oxidation stability agent [J]. *Synthetic Lubricants* (in Chinese), 1991, 18(1): 28-31.

[4] Chang T C, Yu P Y, Hong Y S *etal*. Effect of phenolic phosphite antioxidant on the thermo-oxidative degradation of PMMA [J]. Polymer Degradation and Stability, 2002, 77(3): 29-34.

[5] Frank, Wang C Y. Polymer additive analysis by pyrolysis-gas chromatography IV. antioxidants [J]. *Journal of Chromatography A*, 2000, 891: 325-336.

[6] Li S Y, Wang B, Chen D L. Necessity of T501 antioxidant addition in mineral oil [J]. *Jilin Electric Power* (in Chinese), 2007, 35(3): 29-30.

[7] Yao J B, Gaston A, Steven G D. Study on the synergistic effects of the antioxidants for lubricant [J]. *Lubricating Oil* (in Chinese), 2009, 24(4): 38-44.

[8] Bauer I, Habicher W D, Korner S, Al-Malaika S. Antioxidant interaction between organic phosphites and hindered amine light stabilizers: effects during photoxidation of polypropylene-II [J]. *Polymer Degradation and Stability*, 1997, 55: 214-244.

[9] Zhang E K. The cause and preventive measures of oil acid value increaseing [J]. *Electric Safety Technology* (in Chinese), 2003, 11(5): 11-12.

[10] Tang J J. The hydraulic oil viscosity characteristics and product selection [J]. *Petroleum Products Application Research* (in Chinese), 2006, 4: 35-40.

[11] Rudnick L R. Lubricant additives chemistry and applications [M]. CRC Press, 2009, pp: 5-16.

[12] Wan J X. Study on the preparation and characterization of anti-oxidizing polyphenylene Sulfide [D]. Zhejiang: *Zhejiang Science and Technology University* (in Chinese), 2012: 1-55.

[13] Bai Y H. Influence of the hydraulic oil's quality on hydraulically operated equipment [J]. *Sci/tech Information Development & Economy* (in Chinese), 2004, 14(5): 249.

Applied Mechanics and Materials Vol. 565 (2014) pp 14-19

doi:10.4028/www.scientific.net/AMM.565.14

Transverse Stiffness Prediction of Fibrous Metal Matrix Composites

Gergis W. William[1, a], Samir N. Shoukry[1,b] and Jacky C. PruczOthers[1,c]

[1]West Virginia University, P.O. Box 6106, Morgantown, WV 26506, USA

[a]gwwilliam@mail.wvu.edu, [b]snshoukry@mail.wvu.edu, [c]jcprucz@mail.wvu.edu

Keywords: Metal matrix composites, Transverse stiffness, Unit cell models, Residual stresses, Finite element Analysis.

Abstract. This paper presents two new 3D finite element Multi Fiber Models (MFM) that account for the effects of neighboring fibers on the stress distribution over fiber-matrix interface. One model assumes a hexagonal packing pattern of the neighboring fibers whereas the other assumes that the neighboring fibers are packed in a square pattern. Two scenarios regarding the contact surface between the fiber and the matrix are considered: the first one assumes no bond over the interface while in the other one the interface is perfectly bonded. The cooling process of the composite was simulated and then a transverse loading is applied to the composite. The results indicate that packing system and the characteristics of the fiber-matrix interface greatly influence the magnitude of the residual stresses developed in the matrix.

Introduction

Transverse stiffness represents an important aspect of the structural properties of unidirectional fibrous lamina. Inverse rule of mixture [1] and Halpin-Tsai [2] formula have been used for predicting of transverse stiffness of lamina; however comparison with the experimental data indicated the results obtained using both methods represent the lower and upper estimates for the transverse stiffness values respectively for glass-epoxy composites [1]. Additional problems are encountered when applying these models on metal matrix composites due to the residual stresses that arise during the manufacturing process and affect the stiffness and strength properties of the composites [3,4]. Moreover, the assumption of the perfect bond between the fibers and matrix may not be practically achieved. Therefore, complicated situations such as fiber-matrix separations due to transverse or shear loads applied to a weakly bonded composite are not accounted for by micromechanical models. Thus, transverse properties estimated by using such models may deviate considerably from reality.

Micromechanical Finite Element Models (FEM) were used to accurately predict the transverse properties of continuously reinforced fiber composites. Using FEM, it is possible to simulate a perfectly bonded interface as well as an unbonded interface between the matrix and fiber. Two types of Unit Cell Models (UCM) were used for predicting the composite properties: one contains a single complete fiber fully embedded in the matrix surrounding it, whereas the second containing only a quarter-fiber embedded in matrix surrounding it [5,6]. The boundary conditions are imposed such that compatibility with surrounding cells is achieved. Symmetry conditions are applied on three mutually perpendicular faces of the model. The remaining three faces are constrained to uniform displacement conditions such that their movement is parallel to the corresponding planes. The actual displacement of the nodes near the boundaries is not expected to be uniform, due to the non-uniform distribution of the stress within the matrix and the fiber. Thus, the imposed boundary conditions will result in the development of stress states near the interface region. This makes the accuracy of the UCM questionable.

Multi-Fiber Model

A new unit cell model was developed to predict more accurately the residual stresses developed in CFMMCs during their fabrication processes [7]. The model is applicable for any system of

continuous fiber reinforced composites, both for predicting processing-induced residual stresses and material properties in the transverse direction. The primary characteristic of this Multi Fiber Model (MFM) is that the cell boundaries are moved away from the fiber-matrix interface so as to eliminate the effects of idealized boundary conditions on the predicted values of stress and strain at the interface. Two kinds of packing geometries are considered in the MFM model:

1. Square Array Packing shown in Figure 1-a.
2. Hexagonal Array Packing shown in Figure 1-b

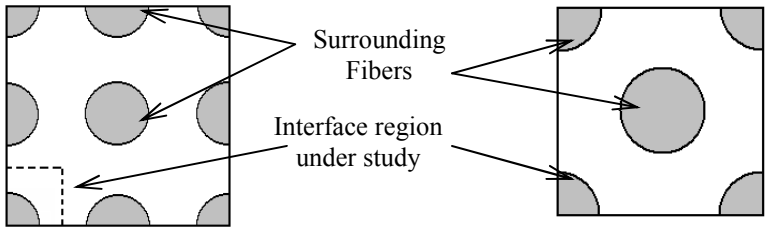

a Square Array Packing b. Hexagonal Array Packing

Figure 1 Muti-Fiber Unit Cell Models.

The conventional UCM and the MFM representative volumes are modeled using LS-DYNA. Since the cooling down process induces matrix contraction not only in the transverse, but also in the longitudinal direction, a tri-axial state of stress is created in the unit cell, consequently eight-node solid brick elements, with 24 degrees of freedom, are used in order to account for axial or shear stresses and the possibility of relative displacements along weak or debonded interfaces. Sliding interfaces are modeled between the matrix and the fiber. The characteristics of the interface depend mainly on the adhesion agent used and fiber irregularities. The shear limit of the interface can also be specified in the FE model, if such information is available. In this study, two scenarios are investigated with respect to the interface condition:

1. A perfectly bonded interface between fiber and matrix provides a worst case scenario of residual stresses in the composite and upper bound for transverse stiffness.
2. An unbonded interface predicts a minimum level of processing induced residual stresses and lower estimate for transverse stiffness.

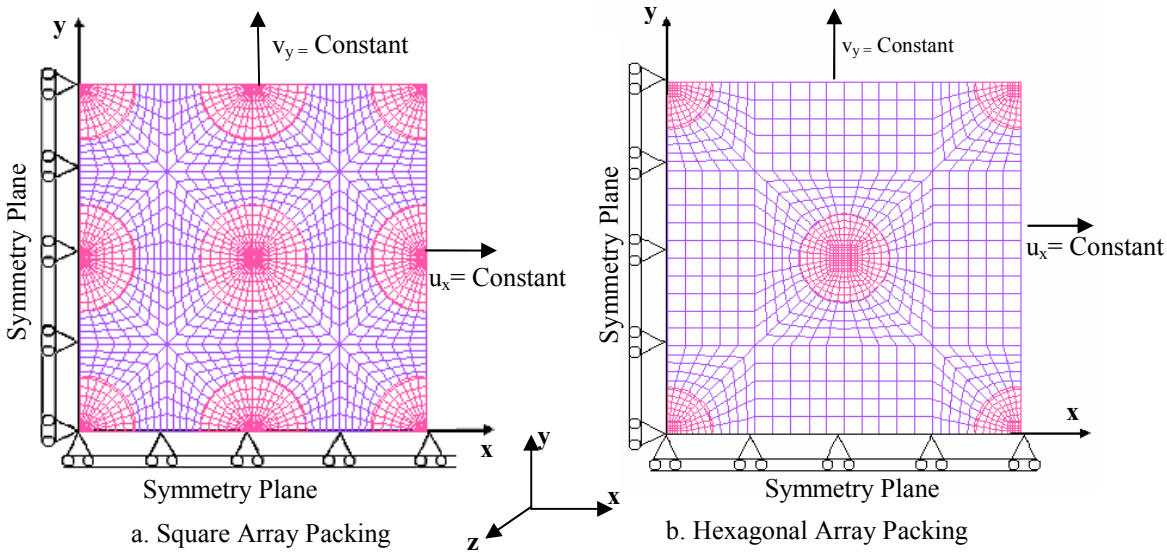

Figure 2 Finite Element Mesh for MFM.

As shown in Figure 2, idealized symmetry boundary conditions are applied on the various finite element models to ensure displacement compatibility between the MFM and the surrounding composite system. Symmetry conditions require that the displacement u_x is constrained in the x-direction for the left face while the displacement component v_y is constrained in the y-direction

along the lower face. Uniform displacement u_x is imposed in the x-direction on the right face and uniform displacement v_y is imposed in the y-direction on the top face. The front face is constrained in the z-direction, i.e $w_z = 0$ and the rear face is constrained such that it displaces parallel to the front face, i.e. all the points on this face undergo uniform displacement w_z = constant. The accuracy of the results predicted by the above FE models has been verified through correlation with both theoretical and experimental data [7].

Model Loading

The 3D finite element equation solver allows the initialization of the model to any state of deformation and stresses that may simulate residual stresses generated in the composite during the cooling process. This is done by specifying a thermal load that was applied to simulate the cooling of the composite from the processing temperature of 927 °C to the room temperature of 21 °C. This temperature change induces residual stresses due to the mismatch between the CTEs of the fiber and the matrix. The cooling is carried out in several steps and the induced stresses are recorded at the end of each step in order to detect the yielding of the matrix during the cooling process. Then the model is processed in a dynamic relaxation mode that builds up the static stresses and displacements at the specified parts of the model. Upon full dynamic relaxation, the model becomes deformed and loaded with stresses that simulate the state of residual stresses in the composite. A data file containing the deformed model becomes the starting file to which any magnitudes and configurations of transverse mechanical loading is applied prior to its reprocessing in a static or dynamic mode. In this study, the initialization feature was used to examine the state of processing-induced residual stresses in the CFMMC materials.

After cooling, a transverse tensile load is applied on the right face of the model in the form of a uniformly distributed stress. The load is increased incrementally and the displacement of the right face for each increment of load is recorded. The transverse strain is calculated for each incremental displacement value. Using these incremental values of stress and strain, the stress-strain relationship can be generated for various representative volume elements.

Mechanical Response to Transverse Loading

One of the advantages of the finite element equation solver used in this study is the capability of handling loads that vary with time. Use is made of such feature to investigate the effect of loading rate on the behavior of the composite and the determined transverse stiffness of such composites. The composite model is subjected for this purpose to transverse loads that all have the same magnitude of

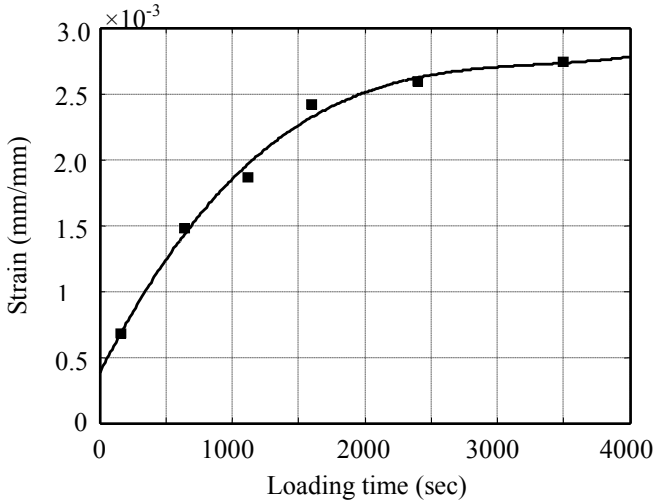

Figure 3 Strain variations with loading time for a constant strain of 200 MPa

275 MPa, and are applied at the cell edge with different time durations. A range of time intervals varying from 160 to 3500 seconds has been selected for this study. As the loading time increases, the composite constituents have more time to respond, which resulted in larger transverse strains at the same applied load magnitude of 200 MPa as shown in Figure 3. Such increase in the strain results in lower stiffness values. This reduction of stiffness with longer loading times can be observed from the stress-strain relations that were obtained for various loading intervals and plotted together on a single graph, as shown in the Figure 4.

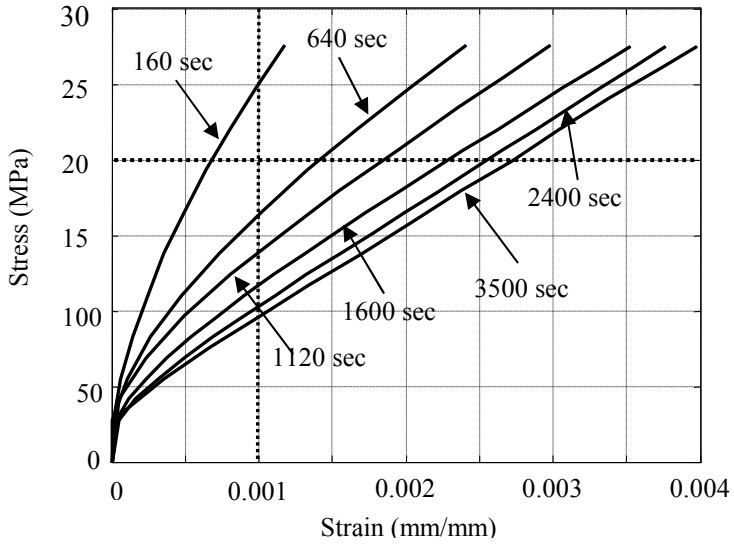

Figure 4 Stress-strain relations for Square array packing and different durations of loading times

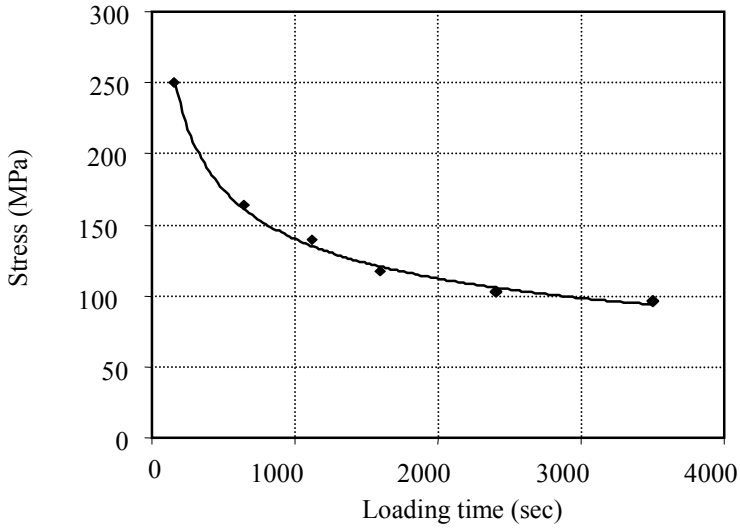

Figure 5 Convergence of the stress-strain relation at loading durations of 3500 sec

It can be seen that convergence of the curves is observed from increasing load time since the curves become closer as the duration of loading increases. A convergence plot is drawn with the above stress values and loading durations as shown in Figure 5. It can be observed that as the loading duration increases, the variations in the stress values are drastically reduced. Finally, minimal variation in the stresses is observed with further increase in the duration of loading, which means a good convergence is reached at this level of loading duration. The stress-strain curves are then predicted for square and hexagonal packing by using the converged loading duration of 3500 seconds as shown in Figure 6.

Bilinear approximation is assumed for the predicted stress-strain curves shown in Figures 6-a and 6-b. This approximation facilitates the stiffness predictions of the composite before and after the separation of fiber-matrix interface when subjected to transverse tensile loads. Such predicted stiffness values of the composite with unbonded interfaces are obtained for both packing systems as

shown in Table 1. Under identical conditions like fiber volume fraction, temperature drop and mechanical loading, the composite modeled with square array packing displayed higher initial stiffness (i.e. stiffness before separation) than the composite modeled with hexagonal array packing. This difference is attributed to the compressive residual stresses developed in the composite during cool-down process. From the Table 2, it can be seen that for 30 percent of volume fraction of fiber, the compressive hoop residual stresses developed in the composite modeled with square array packing (-44.5 MPa) are greater than the compressive stresses (-15.7 MPa) developed in hexagonal array packing which translates into higher clamping force of the matrix around the fibers. Greater transverse stiffening of the square array packing is due to this state of higher residual compressive stresses. Separation of the fiber-matrix interface starts as soon as the residual compressive stresses are overcome by the transverse tensile load. This is followed by an abrupt drop in the transverse strength of the composite. As can be seen in Figures 6-a and 6-b, the slope of the stress-strain curves changes for both packing systems after the corresponding residual stress values are no longer sufficiently high to prevent debonding under the action of the applied tensile transverse load.

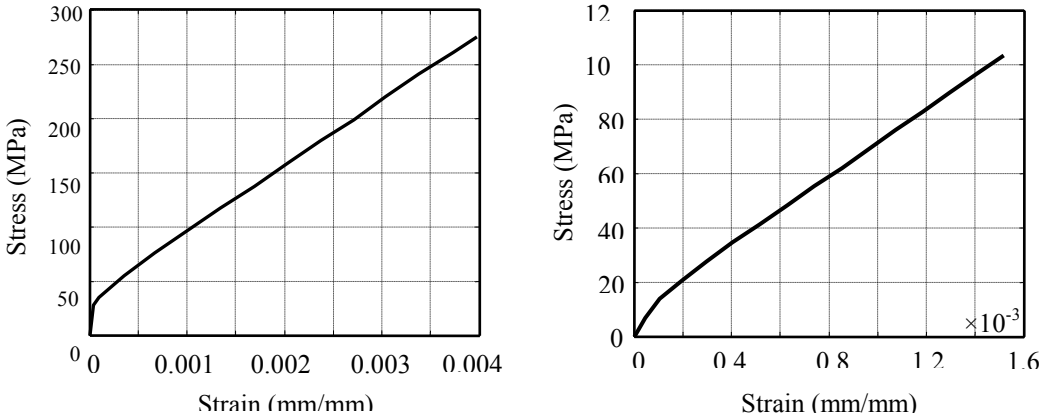

a. Square Array Packing **System** b. Hexagonal Packing System

Figure 6 Stress-Strain Relations.

TABLE 1 Bilinear Transverse Stiffness Values of Ti-6Al-4Va/Al_2O_3

	Square Packing	Hexagonal Packing
Initial Stiffness	153 GPa	139 GPa
Secondary Stiffness	60.3 GPa	63.789 GPa

TABLE 2 Predicted Hoop Stresses (MPa) for Two Packing Types

	Square Packing		Hexagonal Packing	
	Unbonded Interface	Bonded Interface	Unbonded Interface	Bonded Interface
Vf=10%	6.3	-120	104.7	-32.8
Vf=20%	-0.8	-86.8	19.08	-29.31
Vf=30%	-44.5	37.2	-15.7	117.2

Conclusions

To overcome the deficiencies of the conventional UCM, a new representative volume element called as Multi-Fiber Model has been developed to predict the behavior of fiber reinforced MMCs using FEM. The characteristic feature of this model is that it incorporates several fibers and thus takes into account the neighboring fiber interaction and eliminates unrealistic boundary conditions used in

traditional UCMs. The predictions of this model were compared to the predictions of traditional UCMs and also with published experimental results. It has been shown that the predictions of residual stresses and transverse stiffness from the MFM agree better with the experimental results. The following conclusions can be drawn:The traditional UCMs impose unrealistic boundary conditions on the models, and consequently are unable to accurately represent the behavior of the composites

- The predictions of residual stresses by MFM for SCS6/Ti-24Al-11Nb composite having unbonded interface correlates better with the experimental results, owing to the fiber-matrix separation which occurs in real-life.
- Predictions of transverse stiffness using models having unbonded interfaces agree better with the experimental data than predictions with bonded interfaces.
- The packing system and the characteristics of the fiber-matrix interface greatly influence the magnitude of the residual stresses developed in the matrix. Hexagonal packing system develops higher residual stresses than square packing system.
- Increasing fiber-volume fraction from 10% to 30% reduces the residual stresses, as predicted by MFM for bonded interfaces by 49% and 41% for square and hexagonal packing system respectively.

References

[1] E.J. Barbero. *Introduction to Composite Materials Design*, 2nd Edition (CRC Press, USA 2011).

[2] Halpin,J., and Tsai, S.W. *Effects of Environmental Factors on Composite Materials*. Air Force Materials Lab-Technical Report 67-423, Department of Defense, USA (1969).

[3] Mall, S., Fecke, T., Foringer, M.A, Titanium Matrix Composites: Mechanical Behavior, S. Mall, and T. Nicholas, Lancaster, PA: Technomic Publishing Co., pp. 1-22 (1998).

[4] Rangaswamy, P., Jayaraman, N. Issues Related to Prediction of Residual Stresses in Titanium Alloy Matrix Composites. *ASTM STP 1253* (1996) p. 66.

[5] Biglow, C. A., Bahei-El-Din, Y.A., and Mirdamadi, M. Time–Dependent Deformation of Titanium Metal Matrix Composites. ASTM STP 1253 (1996) p. 278.

[6] Nimmer, R. P., Bankert, R. J., Russell, E. S., Smith, G. A., Wright, P. K. Micromechanical Modeling of Fiber/Matrix Interface Effects in Transversely Loaded Sic/Ti-6-4 Metal Matrix Composites. *Journal of Composites Technology & Research*, Vol. 13 (1991), p. 3-13.

[7] Shoukry, S.N., William, G.W., Prucz, J.C., Shankaranaryana, P., Eluripati, R. Multi-Fiber Unit Cell for Prediction of Residual Stresses of Continuous Fiber Composites. *Mechanics of Advanced Materials and Structures* Vol. 14, (2007), p. 531.

Applied Mechanics and Materials Vol. 565 (2014) pp 20-24

doi:10.4028/www.scientific.net/AMM.565.20

Gold Ball Wire Bonding Energy Transfer Mechanism and Experimental Studies

Qianqian Wu[1,2,3, a], Liguo Chen[1,2,3,b], Mingqiang Pan[1,2,3,c], Linsen Chen[4,d]

[1] Mechanical and Electrical engineering College of Soochow University, China

[2] College of Mechatronics Engineering &Collaborative Innovation Center of Suzhou Nano Science and Technology, Soochow University, Suzhou 215123, China

[3] Robot and micro system research center of Soochow University, China

[4] Institute of Information Optical Engineering, Soochow University, Suzhou 215123, China

[a]wuqianqian77@163.com, [b]clg@hit.edu.cn, [c]pmqwl@126.com (Corresponding author), [d]lschen@suda.edu.cn

Keywords: Wire bonding, Mechanism analysis, Process parameters test

Abstract: Because of the complexity of bonding process, the mechanism of bonding has been unable to agree. Accoding to previous research, a new bond energy transfer model is established: bond energy equals to energy caused by temperature rising and the friction energy.Then do experiment on bonding time, bonding stress and ultrasonic energy.Experimental results show that as the increase of process parameters, the bonding strength first increases then decrease, which consistent with the hypothesis.

Introduction

Microelectronics technology development has the vital significance to the national economy and semiconductor manufacturing technology is the basis of microelectronics. The connection between the connected electrode of semiconductor chip and external lead terminal of encapsulation is realized by welding process. Because the wire bonding has the advantages of lower cost during equipment manufacturing, more mature technology and more flexible programmability. Now more than 90% of the connections between semiconductor chips use the wire bonding technology[1]. With the fast development of MEMS and micro-electronic technology, wire bonding turns to fine pitch, fine quantitative control and non-regular, so conventional process method can't adapt to developing needs.

Although the wire bonding technology already has several decades of development history, but because of its large number of process parameters, complexity of bonding process, so there is not a unified conclusion for bonding mechanism research. First, reachers think that metal becomes melting bacause of the temperature rise and then bonding happens[2]. But Jeng Y.R calculated that the highest temperature of bonding interface is around 300℃[3] which can't make the metal melted. Then, scholars think that during the bonding process lateral plastic deformation occured in the wire which make the pollutants move and exposed the fresh surface of bonding which promote bonding[4], but for easy oxidation interface such as Al and Cu, the content of oxide is less than 4%[5], and as a more stable metal Au, the content of surface oxide should be lower. Studies have found that the surface always has the trace of the friction and wear after hot pressing ultrasonic wire bonding[6], which means microslip phenomenon, this is concluded by observing microstructure of the surface of bonding.

Synthesis of the existing research, research of bonding mechanism still stay on the analysis from the viewpoint of organizational structure, and most theories tend to qualitative explanation, this is not a complete bonding mechanism. Therefore, this article will put forward our theory on the basis of the predecessors, and establish bonding model , through the experiments of process parameters quantitative analysis the effects of each process parameters made on the bonding process, which supporting our conjecture about the bonding mechanism.

Bonding energy transfer mechanism analysis

As we know, temperature rise, plastic deformation and micro-sliding wear theory all can't explain wire bonding mechanism perfectly. Now, a new bond energy transfer model has to be established.

According to the law of conservation of energy, bond energy E equals to heating energy Q caused by temperature rise and the friction energy W caused by the bonding pressure and the tangential force produced by ultrasound. So,

$$E=Q+W \tag{Eq.1}$$

The heating energy Q is concerned with the temperature rise ΔT before and after bonding. Assuming impact factor is k, which is concerned with the materials. According to thermodynamic equation,

$$Q=\mathrm{k}\Delta T^2 \tag{Eq.2}$$

The friction energy W is concerned with the bonding pressure P and ultrasonic energy. Ultrasonic energy is determinded by ultrasonic frequency f and ultrasonic vibration amplitude A. Assuming the friction coefficient of the bonding interface is u and bonding time is t. According to tribology equation,

$$W=\mathrm{uPAft} \tag{Eq.3}$$

At last,

$$E=\mathrm{k}\Delta T^2+\mathrm{uPAft} \tag{Eq.4}$$

According to the equation, bonding energy transfer mechanism is concerned with the following four factors.

bonding temperature. Bonding temperature is very important to wire bonding because wire bonding may failed when it is too low or too high. With temperature rise, metal surface becomes activity and metal atoms take strenuous exercise. According to the TEM pictures of bonding interface is like polycrystaline metal boundry and with no melting phenomenon[7]. But if temperature continues rising, the metal will become softer, it may reduce bonding strength. ΔT comes from two parts. One is the setting bonding temperature of the wire bonding experimental platform. It is often set as a fixed value. The other is caused by ultrasonic vibration.

bonding pressure. When loading the bonding pressure, gold ball happpens plastic deformation while it contacts the bonding pad. If the pressure is too small, the contaction area is too small and tension strength will decrease. Otherwise, too much pressure will impact the bonding pad and even make it broken. So bonding pressure control is very important and process parameter test will help.

ultrasonic energy. Ultrasonic can remove pollutant of bonding interface, which will improve the bonding quality. When ultrasonic energy increases, vibrational friction will rise the temperature to active metal atoms movement. But if it gets higher, the bonding pad of low-melting-point may occurs deformation and the workpiece will broken. What's more, the ultrasonic energy should be connect with the bonding set temperature and pressure. They can't be increased together.

bonding time. Wire bonding is a quick reaction process, so the bonding time setting should be concerned. It affects on the absorption of heat, pressure and ultrasonic. If the time is too short, the boding energy won't be enough for stable connection. On contrary, absorbing too much energy will soft the metal leading to strength decrease or even make the bonding failed. If ultrasonic energy and bonding pressure are set as a big value, then bonding time should be lower.

Process parameters test

Experimental programes

To analyze the bonding mechanism, the changes of strength in the bonding pad will be tested under different process parameters. Different process parameters will be quantified to research the quality

of the bonding pad. According to the analysis of the bonding model, the temperature in the processing will be set in 140℃. In the experiment, the bonding time, ultrasonic power and the pressure which are the main parameters in the bonding processing will be set in different magnitude to measure the strength of the bonding pad.

The experiment will be done in the bonding platform called gold wire ball bonding equipment (Figure 1).The positioning accuracy of this platform is 5um and visual recognition accuracy is 10um. The quality of bonding pad will be valued by the bond pulling test (BPT) and shear stress test (BST)[8]. The DS2/ZP digital tension tester will be used to test the strength of the bonding pad. The maximum of the tester is 2N and the measurement precision is 0.001N. Many factors affect the test results of bonding force, such as pull point position, length of lead and lag angle, the results are very random. In every parameter setting, test will be done many times trying to eliminate the adverse effects of the experimental results. The material in the experiment will adopt 25um wire made of gold.

Fig.1 Wire bonding experiment platform

Only change one parameter such as the bonding time, ultrasonic power, bonding pressure to finish the single factor comparison experiments while keeping the other parameters as constant set following the selected reference value. In the experiment, the strength of the bonding pad will be measured to value the influence of different parameters during the bonding process. Considering the previous research experience and results, the experiment will use the following standard values (Table 1, note: the setting values in the table is corresponded to the numbers in the platform panel).

Table 1 Parameters of standard setting

Temperature	Bonding time	Ultrasonic power	Bonding pressure	Bonding time	Bonding current
140℃	5	7	6	6	5

Experiment results

The experiment will be done by adjusting the bonding time (or ultrasonic power, bonding pressure), keeping the other parameters and the preset reference value unchanged, and the range of each parameters is 1-10. In the state of each parameter, the strength of the bonding was measured many times to get the equal value. Table 2 shows the strength of bonding pad, figure 2 shows the trend of the strength changing.

Table 2 Bonding tension strength under different parameters value

Parameter value	Bonding strength N		
	Bonding time	Ultrasonic energy	Bonding pressure
1	0	0	0
2	0.024	0	0.029
3	0.03	0.024	0.032
4	0.045	0.026	0.04
5	0.073	0.031	0.05
6	0.06	0.044	0.063
7	0.058	0.068	0.044
8	0.046	0.061	0.042
9	0.037	0.05	0.031
10	0.022	0.04	0

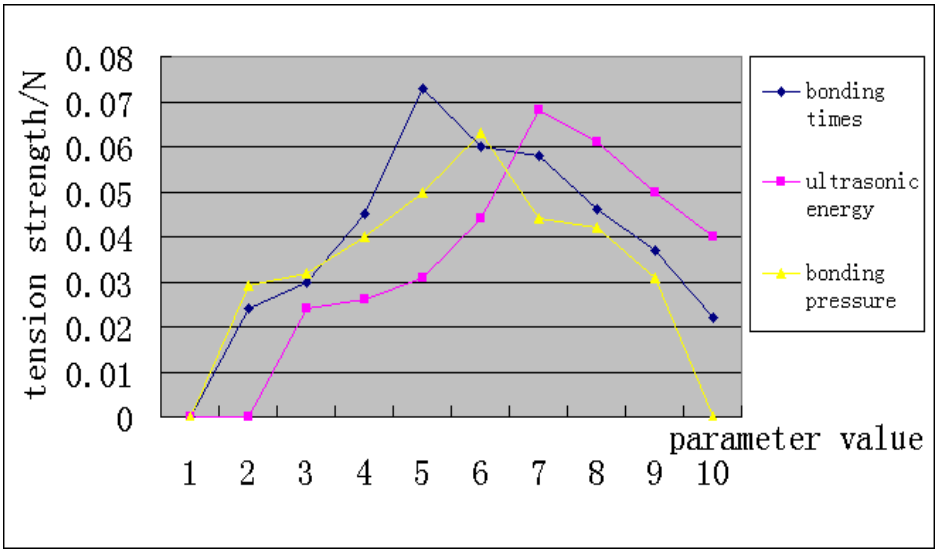

Fig. 2 Changing trend of bonding tension strength

Data analysis

The experimental data show how process parameters affect on the bonding process.
bonding time: with the increase of bonding time, the more energy absorbed in golden ball, the larger of the diameter of the bonding point, the greater of the contact with the bonding pad area , which will not only result in bonding strength increased, but also results in the decrease of strength of the neck. Bond if stay too long at one time, the diameter of the bonding point will continues to increase, which is more likely free welding plate boundary and cause the bonding failure. Therefore, to ensure that the bonding strength the bonding time should be set to about 5.

ultrasonic power: studies have shown that ultrasonic plays a leading role in the plastic deformation during the process of bonding. Ultrasonic power is too small, especially below 2, the plastic deformation produced is too small, the heat energy produced by friction is aford the power of combining metal atoms, which will result in failure or tail cock. With the increase of ultrasonic power, bonding tensile strength also started to increase, but the ultrasonic power is too big, which will lead to the fracture of the root of bond ,and even cause the plate which on the edge of solder fracture. Therefore, to guarantee the bonding strength, ultrasonic power should be set around 7.

bonding pressure: when the bonding pressure acting on the bonding point's normal direction is too small, it will produce friction, and make the contaction between golden ball and the bonding interface insufficiently, which lead to bond is not successful. With the increase of bonding

pressure, golden and bonding pad contact area increases, the bonding point of tensile strength also increases, but lead to the larger bonding pressure , so the impact force made to the bonding pad surface will be too large, at last cause the bonding solder joint fracture. Therefore, to guarantee the bonding strength, ultrasonic power should be set around 6.

Summary

Experimental results show that as the increase of process parameters like bonding time, bonding stress and ultrasonic energy, the bonding tension strength first increases then decrease, which consistent with the hypothesis.On the basis of the experiment, wire bonding is essentially under the action of stress, heat and ultrasonic. First, the bonding interface occurred plastic deformation, then expose clean surface. With the temperature increasing, metal surface becomes activity and metal atoms take strenuous exercise. At last, the bonding pressure and the tangential force produced by ultrasound work together to cause micro-sliding wear between gold ball and bonding pad. Utill now, the formation of connection strength has been finished.

Acknowledgment

This work is supported by the National Project (the Grant Number 2012AA040404), the National Science Foundation for Post-doctoral Scientists of China (the Grant Number 2012M511316), and the Jiangsu Postdoctoral Sustentation Fund (the Grant Number 1102162C).

Reference

[1] Wu Huixian，Xu Yangjian，Liu Yong，Process parameters design of wire bonding in microelectronics packaging[J] , Mechanical strength, 2012, 34(4):516-521

[2] Yu Zhai，Technology reseach to improve hot-pressing ultrasonic ball bonding strength，Southwest Jiaotong Univesity master's thesis，2010

[3] Jeng Y R, Horng J H. A microcontact approach for ultrasonic wire bonding in microelectronics. ASME J. of Tribology. 2001, 123: 725-731.

[4] Zhang Heng，Copper ball wire bonding heating device and experimental studies，Guangdong Univesity of Technology master's thesis，2013

[5] Klaus Dittmer, Suresh Kumar, Frank Wulff. Influence of Bonding Conditions on Degradation of Small Ball Bonds due to Intermetallic Phase (IP) Growth IMAPS, Denver, April, 1999.

[6] Tian Yanhong，Wang Chunqing，Liu Wei, etc translation，Micro connection with nano connection[M]，China Machine Press，P174-177

[7] James E. Krzanowski. A Transmission Electron Microscopy Study of Ultrasonic Wire Bonding. IEEE Trans. On Components, Hybrids and Manufacturing Technology. 1990, 13(1):176-181.

[8] Medding J, Mayer M, In situ ball bond shear measurement using wire bonder head[A], IEEE/CPMT/SEMI 28th Int Electronics Manufacturing Technology Symp[C], San Jose, USA, 2003, 59—63

Applied Mechanics and Materials Vol. 565 (2014) pp 25-30

doi:10.4028/www.scientific.net/AMM.565.25

A Preliminary Study on the Sound Absorption of Self-facing Date Palm Fibers

Elwaleed A. Khidir[1,a], N. Nikabdullah[2,b], M.J.M. Nor[3,c], M.F.M. Tahir[3,d] and M.Z. Nuawi[3,e]

[1]Space Science Center, InstitutPerubahanIklim, UniversitiKebangsaan Malaysia

[2]German Academic & Career Centre, Universiti Malaysia Pahang

[3]Department of Mechanical and Materials Engineering, UniversitiKebangsaan Malaysia

[a]elwaleed@ukm.my, [b]enikkeister.2@gmail.com, [c]jailani@eng.ukm.my, [d]faizalmt@eng.ukm.my, [e]zaki@eng.ukm.my

Keywords: Sound absorption, Self-facing, Date palm fiber, Impedance tube.

Abstract. Sound absorption of self-facing natural date palm fibershas been investigated.A single layer sample of the fibers was tested for its sound absorption properties. The sample was then faced with the originally date palm fiber netted structure. Experimental measurements were conducted on the impedance tube at the acoustic lab, Faculty of Engineering, UniversitiKebangsaan Malaysia, to determine the sound absorption coefficient.The single layer was also tested using an aluminum perforated plate, as facing, for comparison purposes.The results show a good improvement in the sound absorption for the self-facing panel for the whole frequency range. However, when using the aluminum perforated panel an improvement in the sound absorption was observed only above 2500 Hz. The effect of introducing air gap thickness was studied. The results show improvement for the sound absorption the low frequency.

Introduction

Vegetable fiber is one of the varieties of natural fibersobtained from stems, leaves, roots, fruits and seeds ofplants. However, fromcommercial and technological points of view, cotton, kenaf,sisal, flax, palm, coir, arecanut and banana fibersacquire utmost significance, since reinforced plastics,strings, cords, cables, ropes, mats, brushes, hats, baskets and fancy articles such as bags are manufactured with those fibers[1].

The date palm (*Phoenix dactylifera*) is one of the most cultivated palms around the world. It geographically covers the deserts from the Atlantic coastline of Mauritania to India and from the Mediterranean Sea to about 15^{o} in Africa. The main date-producing countries of the world are Iraq, Saudi Arabia, Egypt, Iran, Algeria, Pakistan and the Sudan. The date palm in Sudan is common in the Northern Sudan along the Nile [2]. Date palms have a fibrous structure, with four types of fibers: leaf fibers in the peduncle, baste fibers in the stem, wood fibers in the trunk and surface fibers around the trunk [3]. The application of the date palm fibers have been investigated by different researchers for various applications[4, 5].

Most practical sound absorbing products used in the building construction industry consistof glass- or mineral-fiber materials.However, the growing concern about the potential health risks popularly seen as being associated with glass- or mineral-fiber materials provides an opportunity to develop for sound absorption panels made of natural fibers. Many researches have conducted in developing particle composite boards using agricultural wastes [6-8].

Yang et al. produced rice straw-wood particle composite boards which properties are to absorb noise, preserve the temperature of indoor living spaces and to be able to partially or completely substitute for wood particleboard and insulation board in wooden construction. They reported that the sound absorption coefficient of rice straw-wood particle composite boards are higher than other wood-based materials in the 500-8000 Hz frequency range, which is caused by the low specific gravity of composite boards, which are more porous than other wood-based materials [7].

From the view of environmental protection, natural bamboo fibers were used for sound absorbing purposes. Impedance tube measurement of the bamboo fiber samples, reveal similar properties to that of glass wool. Bamboo material formed into a fiber board, yields a superior sound absorption property when compared to plywood material of similar density [9].

Ersoy and Kucuk[10] experimentally investigated the sound absorption feature of tea leaf fiber as an industrial waste material. The good acoustic absorption aspect of that fiber with respect to other absorbers was noticed. Coconut is one of the most important harvests in Malaysia. Coir fiber from coconut husk is one of the hardest natural fibers having high amount of lignin. The sound absorption attribute of coir fiber was investigated previously in Automotive Research Group laboratories, UniversitiKebangsaan Malaysia. Those studies covered experimental observations in reverberation room [11]. and using impedance tube [12].

The aim of this research is to study the potential use of date palm fiber for sound absorption applications.

Materials and Methods

Date Palm Fiber

The fiber is collected from the sheathingleaf base, which surrounds the stem. The leaf base has a netted instructure, which is covered by soft tissues (Fig. 1).It is collected from the tree and dried to remove the excess moisturecontent.The pulp aroundfiber is removed by combing.The average diameter of the fiber is 0.408 mm and the average density is 919 kg/m^3.

Fig. 1 The sheathing leaf base netted structure and the fiber

The samples to be tested were prepared using two plastic molds. The molds are of 100 mm and 28 mm internal diameters, which are equivalent to equivalent to the diameters of the impedance tubes to cover the low and high frequency range of measurements. Fig. 2 shows the plastic molds and samples of date palm fibers. The thickness and the density of the prepared samples are 30 mm and 77kg/m^3, respectively.

Fig. 2 Plastic molds and date palm fiber samples

Experimental Measurement in Impedance Tube

In this research the experiments to determine the sound absorption properties of the samples were conducted using two impedance tubes of 28 mm and 100 mm diameters, noise generator, two channel data acquisition system 01 dB, two ¼ in microphones type GRAS-40BP in each tube, software package SCS8100.The measurements were made based on ISO 10534-2 standard [13]. The microphones' sensitivity was calibrated using calibrator type GRAS-42AB (114 dB at 1 kHz). Photo of the system is shown in Fig. 3. Noise generator transmitted a random noise into the tubes. Interior sound pressure spectrum was measured by the two microphones and transfer functions between them were calculated. The acoustical absorption coefficient was calculated from these transfer functions and distances between the microphones and date palm fiber sample. The frequency span of experiment was 100–5000 Hz with 3 Hz resolution. The frequency range for the 100 mm diameter tube is up to 1000 Hz and for the 28 mm diameter tube is above 1000 Hz. Before running the experiment the two impedance tube microphones were calibrated relatively to each other using the standard switching technique. This was based on mounting the sample in the sample holder and conducting the measurement to make sure that the sound field inside the tube is well defined.

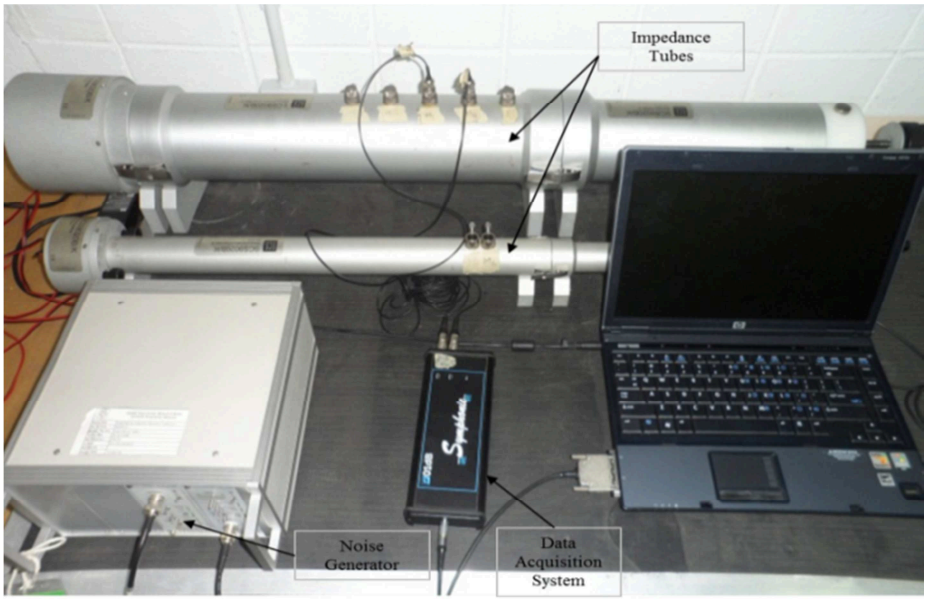

Fig. 3 Sound absorption experimental set-up

The experiment was conducted for the sample without facing. The sample was then tested with facing using the date palm netted structure. To compare the results a perforated plate (PP) made of aluminum was used as a facing. The self-facing netted structure and the aluminium PP are shown in Fig. 4. For further improvements of the self-facing panel, experiments were conducted using air gap thicknesses of 10 mm, 20 mm and 30 mm were used between the date palm fiber sample and the rigid backing of the impedance tube. Fig. 5 shows a sketch of the set-up used for the measurement of the sound absorption of the sampleinside the impedance tube.

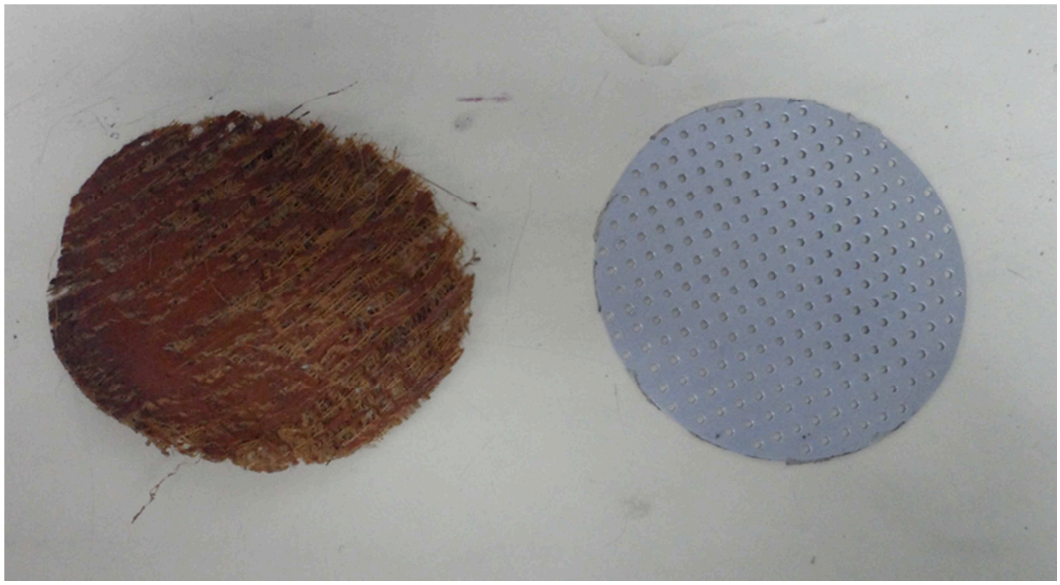

Fig. 4 The netted structure used for self-facing and the aluminum perforated panel

Fig. 5 Sketch of the palm date fibers sample and the PP inside the impedance tube

Results and Discussion

Sound absorption of the uncovered sample (UC), self-facing natural date palm fibers and facing using PP aluminum plate has been investigated. The experimental results for the three cases are shown in Fig. 6. The results show a good improvement in the sound absorption for the self-facing panel for the whole frequency range. However, when using the aluminum PP panel an improvement in the sound absorption was observed only above 2500 Hz. This indicates that the improvement obtained in case of self-facing is not due to the role of the perforation of the sample but also to the contribution of the self-facing structure in absorbing part of the sound.

For further improvement of the sound absorption at the lower frequency range, air-gap between the sample and the rigid backing of the impedance tube was introduced. Fig. 7 illustrates the effect of varying the airgap distance on sound absorption coefficient for the self-facing panel. The results show that the introduction of air-gap enhanced the low frequency absorption. It can be seen that increasing the air gap thickness can be useful for increasing the absorption coefficient at some lower frequencies range. The general indication is that air-gap shifts the resonance absorption towards the low frequency range. Below 2000 Hz frequency there is improvement in sound absorption coefficient for all air gap thicknesses. It can be observed that the increase in the air gap thickness moved the peaks toward lower frequencies and improved the low frequencies absorption and above the 4000 Hz. However, that increase coincided with reduction in medium frequency absorption. This increase is due to loss of acoustical wave energy of transmitted wave in the presence of sample-air passage and of reflected wave from rigid backing, through air-sample passage in the propagation of acoustical wave[14].

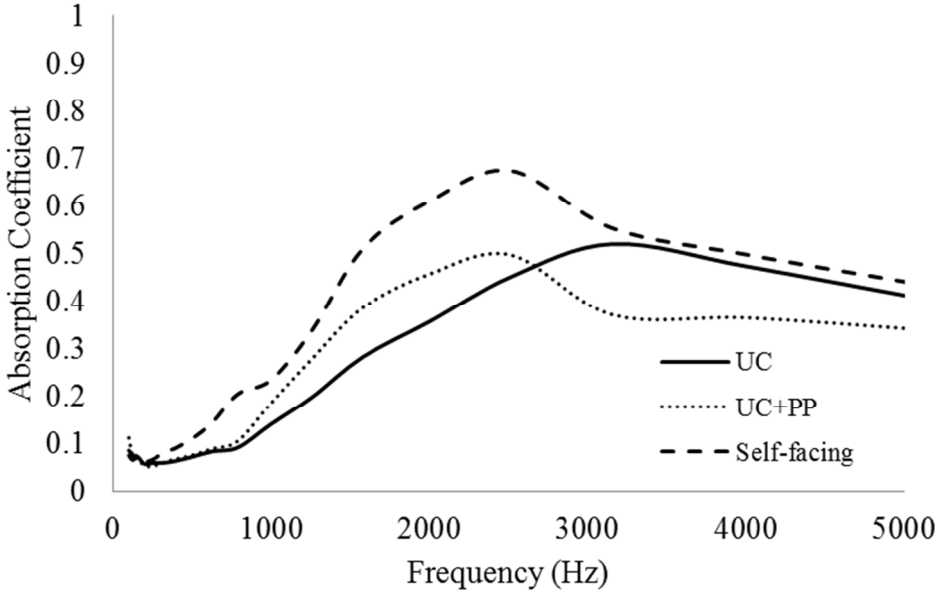

Fig. 6 Sound absorption of the uncovered sample (UC), self-facing natural date palm fibers and PP aluminum facing using

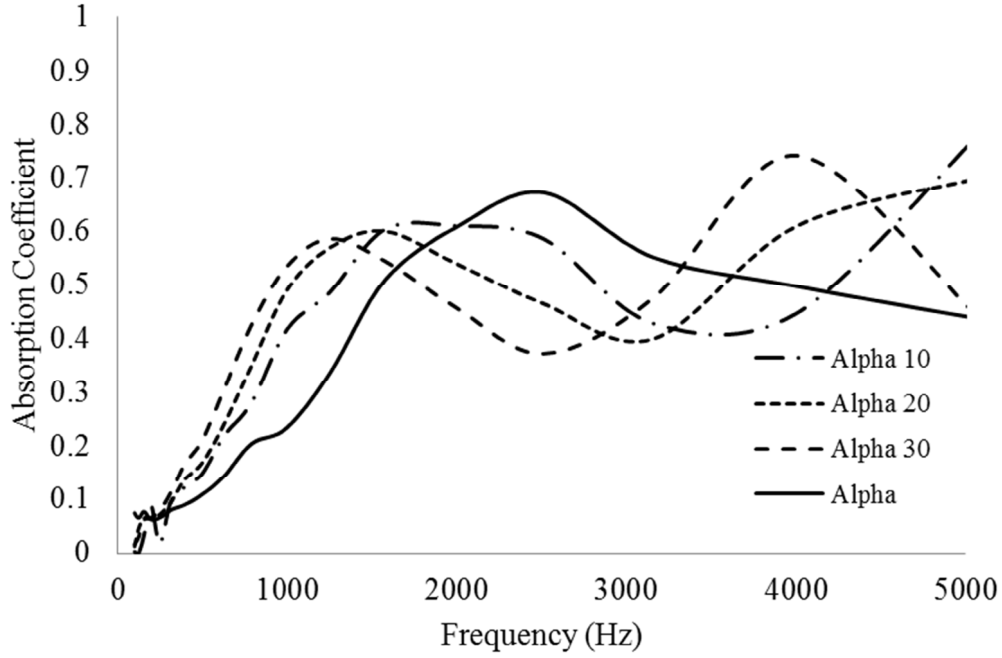

Fig. 7 Sound absorption (Alpha) of the self-facing panel for different air gap thicknesses (10 mm, 20 mm and 30 mm)

Conclusions

Sound absorption of self-facing natural date palm fibers has been investigated. A single layer sample of the fibers was tested for its sound absorption properties. The sample was then faced with the originally netted structure. The single layer was also tested using a aluminum perforated plate for comparison purposes. The results show a good improvement in the sound absorption for the self-facing panel for the whole frequency range. However, when using the aluminum perforated plate panel an improvement in the sound absorption was observed only above 2500 Hz. The effect

of introducing air gap thickness was studied. The results show improvement for the sound absorption the low frequency range.

References

[1] K. Murali Mohan Rao, K. Mohana Rao: Composite Structures Vol. 77 (2007),p. 288.

[2] P. Khristova ,O. Kordsachia,T. Khider:Bioresource TechnologyVol. 96 (2005), p. 79.

[3] A. Kriker,G. Debicki, A. Bali, M.M. Khenfer, M. Chabannet: Cement & Concrete Composites Vol. 27 (2005),p. 554.

[4] K.Riahi, A.B.Mammoub, B.B. Thayer: Journal of Hazardous Materials: Vol. 161 (2009), p. 608.

[5] F. Al-Sulaiman:Energy Conversion and ManagementVol. 43 (2002), p. 2267.

[6] J.Khedari, S.Charoenvai, J.Hirunlabh: Building and Environment Vol.38 (2003), p. 435.

[7] H.-S. Yang, D.-J.Kim, H.-J. Kim:Bioresource Technology Vol. 86 (2003), p. 117.

[8] J.Khedari, N.Nankongnab, J.Hirunlabh, S.Teekasap: Building and Environment Vol. 39 (2004), p. 59.

[9] T. Koizumi, N.Tsujiuchi, A. Adachi, in: The development of sound absorbing materials using natural bamboo fibres, edited byC.A. Brebbia, W.P. De Wilde, volume 4 of High performance structures and composites,Witpress(2002), p. 157..

[10] S. Ersoy, H. Kucuk:.ApplAcoustVol. 7 (2009), p. 215.

[11] R. Zulkifli, M.J.M. Nor, M.F.M. Tahir, A.R. Ismail, M.Z. Nuawi: J ApplSciVol. 8 (2008), p. 3709.

[12] M.H.Fouladi, Md. Ayub, M.J.M. Nor: Applied Acoustics Vol. 72 (2011), p. 35.

[13] ISO 10534-2. Determination of sound absorption coefficient and impedance in impedance tubes – part 2: transfer function method (1998).

[14] S. Fatima,A.R. Mohanty:Appl. Acoust. Vol. 72 (2011), p. 108.

Applied Mechanics and Materials Vol. 565 (2014) pp 31-35

doi:10.4028/www.scientific.net/AMM.565.31

Study of Thermal Analysis for Monitoring of Liquid Metal in Production of Aluminum Casting

Phatthaya Saohin[1], Julathep Kajornchaiyakul[2]

and Chaiyasit Banjongprasert[1, a]

[1]Department of Physics and Materials Science, Faculty of Science

Chiang Mai University, Chiang Mai, 50200, Thailand

[2]National Metal and Materials Technology Center (MTEC), National Science and Technology Development Agency, Klong Luang, Pathumthani 12120, Thailand

[a]chaiyasit.b@cmu.ac.th

Keywords: Casting, Aluminum-Silicon, Thermal Analysis, Grain Refiner

Abstract. The main objective of this study is to present the elementary path to develop applications of thermal analysis technique from the solidification in casting of hypoeutectic aluminum-silicon alloy. In order to successfully use the technique as a monitoring tool for an appropriate production of aluminum casting, all affecting process conditions must be taking into accounts when cooling curves are used as indicators. Although, the cooling curves can indicate the solidification characteristics, previous studies on casting trials designed by Taguchi method show that thermal analysis can be complex and sensitive. Also, there are many factors that influence the characteristics of cooling curves when grain refinement becomes more prominent. This study is to determine the effects of grain refiners and magnesium contents on the undercooling of nucleation of Alpha (α) aluminum phase. Different cooling rates and different magnesium contents were studied and the undercooling temperatures were measured. The cast samples were then subjected to the metallurgical analysis by macrostructure study to determine the average grain size. Under a controlled casting condition, it was found that grain refinement tended to decrease degrees of undercooling temperature. Also, higher magnesium content led to the suppression of the undercooling temperature.

Introduction

Aluminum-silicon alloy is one of the most important aluminum based foundry alloys because of its excellent castability, good mechanical and physical properties [1-2]. In case of aluminum casting alloys, the control of grain size has been also used to improve the feeding capability of the melt and to improve the mechanical properties [3]. In addition to the grain size, the eutectic silicon morphology and the dendrite arm spacing (DAS) of the primary α (Al) phase play a major role in the production of high quality aluminum casting [3]. Many researchers and technologists have attempted to monitor and improve the quality of liquid metal in production of aluminum casting such as cast aluminum alloy cylinder heads in gravity semi-permanent mold technology to determine the influence of process parameters upon DAS [4]. Another approach is to modify grain structure by semi-solid metal processing technique [5, 6]. Grain refinement by inoculation is accomplished by the addition of a master alloy, the most common master alloys are based on the Al - Ti - B system (Al - 5%Ti - 1%B being the most common composition - percentages are by weight unless stated), containing TiB_2 and Al_3Ti within α-aluminum matrix [7]. Thermal analysis technique can be used for evaluating the metallurgical quality of the liquid metal in which alloy A356 is one of the most studied alloys [8]. The influence of alloying elements such as Mg contents has been studied. Mg depresses the eutectic temperature and makes the eutectic Si structure more heterogeneous [9]. Several parameters associated with primary solidification of the aluminum rich solution have been suggested to assess grain refinement, such as under-cooling, recalescence or time related parameters [8] and other influence parameters for thermal analysis are pouring temperature, degassing and cooling rate [3].

This research aims to apply the thermal analysis on inspection of melt quality using degree of undercooling and cooling curves of an aluminum-silicon alloy, A356 as a representative alloy. The knowledge from this research will be then summarized.

Experimental procedures

The Al-Si alloy was prepared using A356 commercial alloy and the chemical composition of the alloy in this study is listed in the Table 1. The effects of grain refiner and magnesium contents on cooling curves and undercooling temperatures were studied. The experiment was divided into two parts: Experiment I-without degassing and Experiment II-with degassing. For Experiment I, magnesium was added in the alloy with five different contents: 0, 0.2, 0.4, 0.6 and 0.8 wt% under two different conditions: without grain refinement and with 1wt% of Al-5%Ti-1%B grain refiner. In a controlled condition on experiment II, three different magnesium contents were added (0, 0.1 and 0.2wt% of magnesium) with degassing by argon 4 litres/min (1 min).

Al-Si A356 alloy was melted by an induction furnace at 850 ℃. After degassing with argon, grain refiners and Al-Mg master alloy were added into the melt. The melt was stirred and poured at the temperature 800 ℃ into the cylindrical stainless steel cup. Then, cooling temperature at a different time was recorded by a data logger. The chemical composition of samples were analysed by emission spectrometer analysis. The samples were cut from the same positions and then grinding and polishing. After polishing, the samples were etched in a Keller's solution of 5% H_2O, 5% HF, 30% HNO_3 and 60% HCl in order to reveal the grain boundary, and the final average grain size was determined by linear intercept method.

Table 1 : Chemical composition of the A356 alloy.

Element	Cu	Mg	Si	Fe	Mn	Ni	Zn	Pb	Sn	Ti	Al
(wt.%)	0.06	0.33	7.17	0.50	0.05	0.01	0.06	-	-	0.06	91.74

Results and discussion

Figure 1 shows the Optical Macrographs of (a) without grain refinement and (b) with grain refinement. Thermal analysis of A356 hypoeutectic Al-Si alloys without grain refiner and with grain refiner (by adding 1wt% of Al-5%Ti-1%B) illustrated that undercooling temperatures of the alloy with grain refinement decreased from 2.24℃ to 2.00℃ and led to a decrease of the average grain size from 2038.80 μm to 949.20 μm and from 2062.97 μm to 909.44 μm from experiment I and experiment II respectively as seen in the Table 2 when the average cooling rate of the samples was at 0.17 ℃/s. The undercooling temperatures of samples (from the experiment I - without degassing) show no trend. A higher amount of magnesium content tended to slightly decrease the undercooling temperatures. The effects of degassing were also studied. It was clear that degassing had a strong influence on the thermal analysis i.e. degassing gave rise to an obvious trend of undercooling temperatures in both samples without grain refiner and those containing grain refiner. The level of gas content of samples from experiment II was showed in the Table 3 and the optical macrographs of the samples from both experiment were showed in Figure 4 that was compared the degassing conditions. The percent of porosity without degassing and after degassing was showed in the Table 4, the porosity of the samples from experiment II tended to decrease after degassing and lower than those without degassing from experiment I.

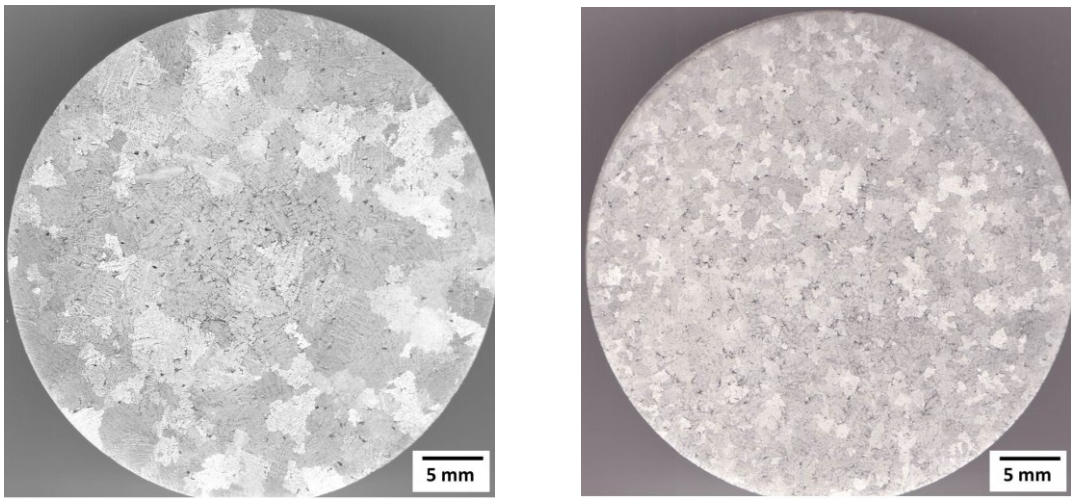

Figure 1 Optical Macrographs

(a) Without grain refinement (b) With grain refinement

Table 2: The Average grain size of A356 Alloys.

Experiment	Average grain size (μm)	
	Without grain refinement	With grain refinement
I	2038.80	949.20
II	2062.97	909.44

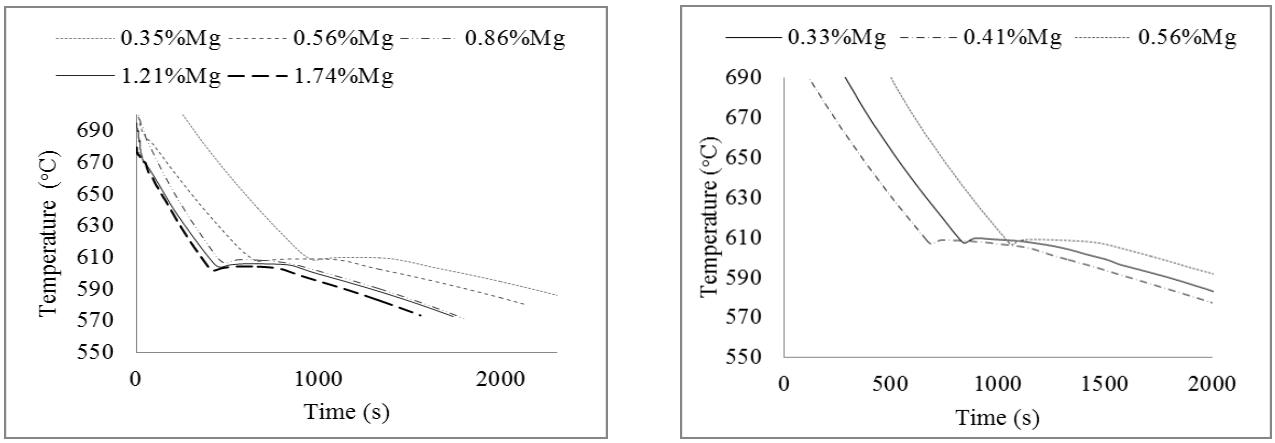

Figure 2 Cooling curves

(a) Expriment I : without degassing (b) Experiment II : with degassing

The cooling curves of two experiments were showed in the Figure 2. The undercooling temperatures derived from the cooling curves in the Figure 2 were illustrated in the Figure 3. No obvious trend can be seen for experiment I without degassing. For experiment II, when degassing was applied, the undercooling temperature tended to decrease with higher magnesium content.

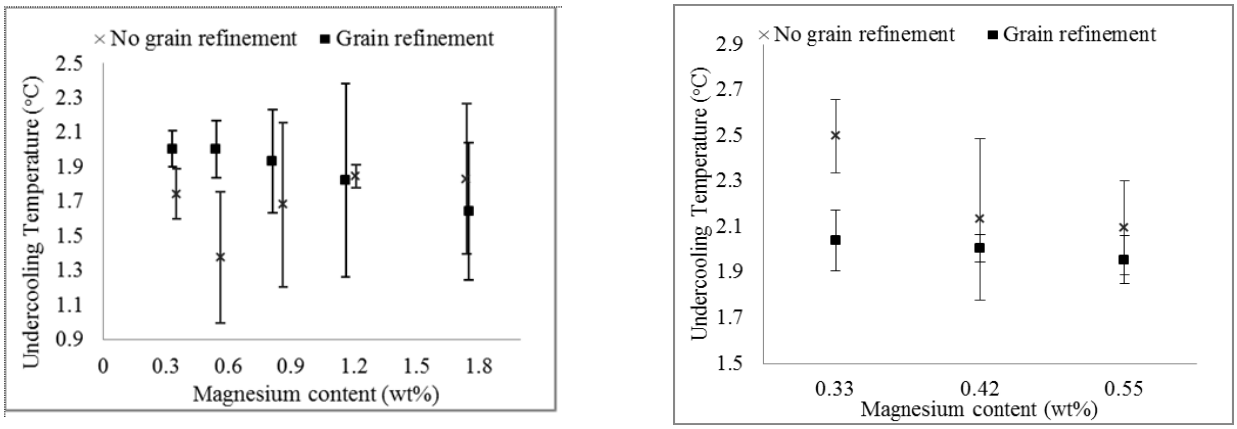

Figure 3 Undercooling temperature of A356 alloy

(a) Experiment I: without degassing (b) Experiment II: with degassing

Table 3: Level of gas content of samples.

Conditions		cc/100 g Al
Without grain refinement	1	0.43
	2	0.30
	3	0.27
With grain refinement	1	0.46
	2	0.38
	3	0.40

Table 4: Porosity of the samples.

Experiment	Mg content (wt%)	% Porosity (in volume %)	
		Without grain refinement	With grain refinement
I	0.35	1.28	1.16
	0.56	1.96	0.79
	0.86	1.09	1.22
	1.21	1.55	1.51
	1.74	1.35	1.68
II	0.33	0.58	0.94
	0.42	0.41	0.32
	0.55	0.26	0.17

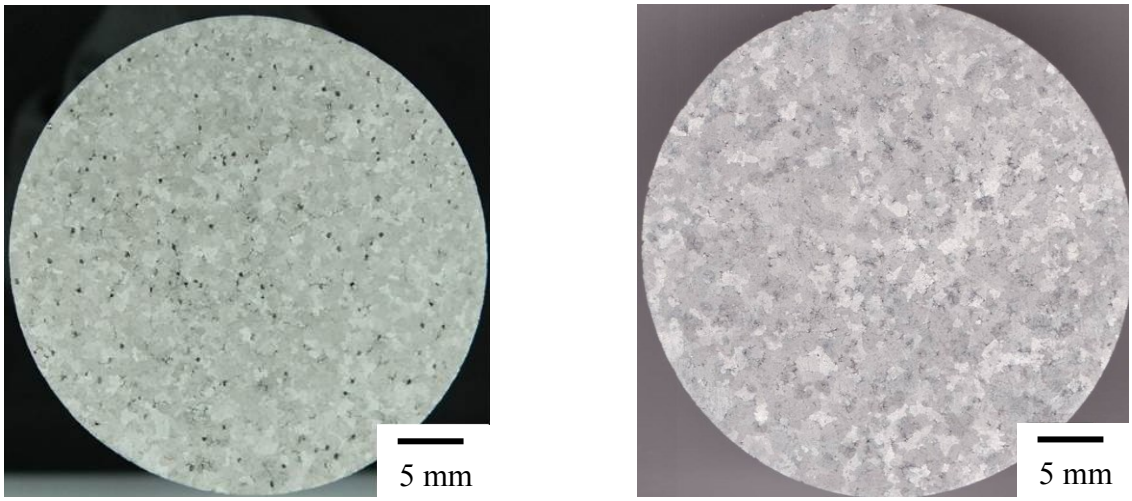

Figure 4 Optical macrographs

(a) Without degassing (b) With degassing

Summary

This study demonstrates the successful application of thermal analysis to monitor the melt quality of aluminum casting. It can be concluded that 3 main factors have strong effects on the undercooling temperature: (1) effects of Al-5%Ti-1%B grain refiner on the macrostructure and undercooling temperature. An addition of the grain refiner resulted in a decrease of average grain size and undercooling temperature. (2) Magnesium content, the undercooling temperature decreased as the level of magnesium increased. (3) Degassing had a strong effects on the cooling curve and undercooling temperature. Degassing is crucial when thermal analysis is used. To summarize, the above 3 main factors can be applied in monitoring and eventually in controlling melt quality in production of aluminum casting.

Acknowledgements

The authors would like to gratefully acknowledge the National Science and Technology Development Agency (NSTDA) through Young Scientist and Technologist Program (YSTP), 2012 for financial supports.

References

[1] P.S. Mohanty, J.E. Gruzleski: Acta Mater Vol. 45 (1996), p. 3749-3760.
[2] L. Heusler, W. Schneider: Light Metals Vol. 2 (2002), p. 17-26.
[3] D. Gloria, “Control of Grain Refinement of Al-Si Alloys by Thermal Analysis”: PhD Thesis, McGill University, Canada (1999).
[4] B. Zhang, M. Garro, C. Tagliano: Metall Sci Tech 21 (2003).
[5] S. Nafisi, R. Ghomashchi, J Mater Process Tech, Vol. 174 (2006) p. 371-383.
[6] J. Wannasin, S. Thanabumrungkul, Songklanakarin J. Sci. Technol, Vol. 30(2) (2008), p. 215-220.
[7] T. E. Quested, Mater Sci Tech Ser, Vol. 20 (2004), p. 1357-1369.
[8] A. Niklas, U. Abaunza, A.I. Fernández-Calvo, J. Lacaze, R. Suárez, the 69th World Foundry Congress (WFC), 16-20 October 2010, Hangzhou, China.
[9] C.H. Caceres, C.J. Davidson, J.R. Griffiths, Q.G. Wang, Metall Mater Trans A, Vol. 30A (1998), p. 1999-2611.

Applied Mechanics and Materials Vol. 565 (2014) pp 36-45

doi:10.4028/www.scientific.net/AMM.565.36

Tool Wear Monitoring of High Speed Milling Based on Vibratory Signal Processing

Hadjadj Abdechafik[1, a], Kious Mecheri[2, b] and Ameur Aissa[3, c]

[1]LACoSERE Laboratory, AMAR TELIDJI University of LAGHOUAT, ALGERIA

[2]Semiconductor and fonctionnel materials Laboratory, AMAR TELIDJI University of LAGHOUAT ALGERIA

[3]LeDMaSD Laboratory, AMAR TELIDJI University of LAGHOUAT ALGERIA

[a]ahadjadjdz@yahoo.fr,[b]kious2005@yahoo.fr,[c]amaissa1@yahoo.fr

Keywords: Flank wear; vibration, milling; signal processing; monitoring.

Abstract. The objective of this study is to develop a process of treatment of the vibratory signals generated during a horizontal high speed milling process without applying any coolant in order to establish a monitoring system able to improve the machining performance. Thus, many tests were carried out on the horizontal high speed centre (PCI Météor 10), in given cutting conditions, by using a milling cutter with only one insert and measured its frontal wear from its new state that is considered as a reference state until a worn state that is considered as unsuitable for the tool to be used. The results obtained show that the first harmonic follow well the evolution of frontal wear, on another hand a wavelet transform is used for signal processing and is found to be useful for observing the evolution of the wavelet approximations through the cutting tool life. The power and the root mean square (RMS) values of the wavelet transformed signal gave the best results and can be used for tool wear estimation. All this features can constitute the suitable indicators for an effective detection of tool wear and then used for the input parameters of an on-line monitoring system. Nevertheless we noted the remarkable influence of the machining cycle on the quality of measurements by the introduction of a bias on the signal; this phenomenon appears in particular in horizontal milling and in the majority of studies is ignored

Introduction

The monitoring of tool failure and tool wear has been the subject of active areas of research for quite some time. Tool wear is a complex phenomenon occurring in different metal cutting processes. Generally, worn tools adversely affect the finished surface of the workpiece and therefore there is a need to develop tool wear condition monitoring systems that alert the operator to the state of the tool and avoiding the undesirable consequences. Wear monitoring methods are generally classified as either direct or indirect methods. The direct methods are those that utilize the effects caused directly by tool wear. The direct methods usually performed by means of optical, radiometric, pneumatic, white light interferometer or contact sensors can be effectively applied to off-line measurements of wear. However, such direct means of measuring tool wear have not been easily adaptable for shop floor application. Unfortunately, these techniques are unable to assure a continuous monitoring of cutting tool state, where the need of on-line techniques is very important.

The indirect methods monitor parameters that change to some degree with tool wear. These include, temperature, finished surface, cutting forces and vibration. The indirect methods are usually easy to implement but have lower sensitivity. Due to an increased availability of computing power and increased reliability of modern electronics, the indirect methods are becoming more reliable.

In most approaches, proposed for the tool wear monitoring area, several parameters can be measured on-line during the machining process such as forces, spindle motor current, vibrations and acoustic emission which are directly correlated with tool wear. The main objective of these researches is to develop and select the appropriate parameters which are sensitive to the tool state change (breakage and wear).

Tansel et al. [1] use the acoustic emission monitoring for tool breakage detection. They observed high amplitude acoustic emissionbursts at tool breakage moment.

Elbestawi et al. [2] exploit the cutting force; they found that certain harmonics of the cutting force increase significantly with flank wear, the number of such sensitive harmonics being related to the number of inserts of the milling cutter and the immersion rate.

Altintas [3] has shown that the first-order autoregressive time series model AR1 can be used to distinguish the force signal during normal flank wear to that when tool failure occurs.

Based on ISO3685-1977, the criterion recommended for end of tool life is when the average width of the flank wear (V_b) exceeds 0.3 mm.

The use of force and vibration information in tracking tool wear has been proposed and shown to be viable by a large number of researchers. Unfortunately, the tool position and machining cycle, that affect measurement significantly, were not taken into account in particularly in horizontal milling. For this reason, this study was undertaken in order to highlight the influence of these parameters, So two signals are acquired from two sensors mounted at different places, the first one is fixed at the spindle and the second at the pallet (table) of the machine-tool.

Cutting tool wear

Standard NFE 66-505 presents the various manifestations of wear schematized by figure 1. Cutting tool is considered as worn when V_B exceeds 0.3mm [8].

Currently, the model of Taylor is sufficiently representative; it is usually used today for all materials of tools. In practice, and also theoretically, the flank wear V_B follows the pattern represented by the figure 2, and presents three wear phases: (1) Break in (2) Normal wear, (3) Severe wear. [9]

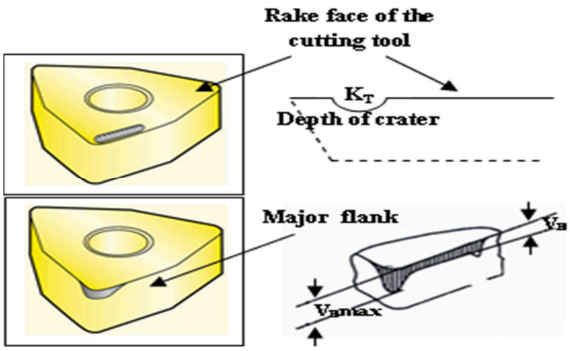

Fig. 1 Cutting tool wear Schematisations

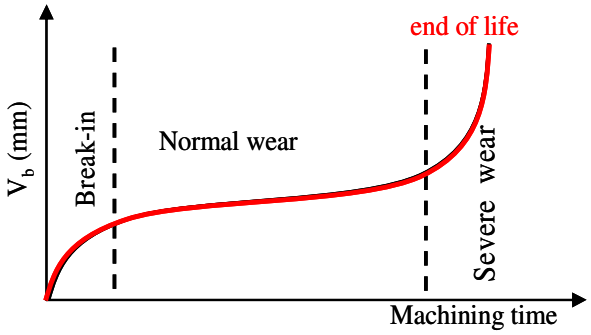

Fig. 2 Theoretical tool wear pattern

Experimental setup

An experimental setup was carried out on a horizontal high speed machining center (PCI Meteor 10). In our study we have used a single milling insert: RT130408R-31 with 25 mm of the cutter diameter and workpiece material type (hardened steel): 40CMD8+S. The milling operations were conducted without applying any coolant and all cutting tests were performed at the following cutting conditions (Table.1).

Table.1 Cutting condition

S_s	V_c	S_t	a
2293 rpm	180 m/min	0.25 mm/tooth	2 mm

Wear of the insert was measured with an optical microscope at intervals by stopping the machining operation. Twopiezo-accelerometers are mounted; the first one on the spindle quill and the second on the table of the machine tool. The vibratory signal is sampled at a frequency of 16384 Hz and stored in PC via Bruel&kjear pulse system.

The machining of the workpiece has been done up to down vertically and left to right across then when it reaches the bottom edge it starts machining again up from right to left until it reaches the top .

Results and discussions

Fig.3 shows the images of crater wear K_t and flank wear $V_b$taken at the start and the end of the milling process; it can be seen in figure 4 that the pattern trend of flank wear V_b follows the theoretical tool wear pattern, and presents the three main phases of wear.

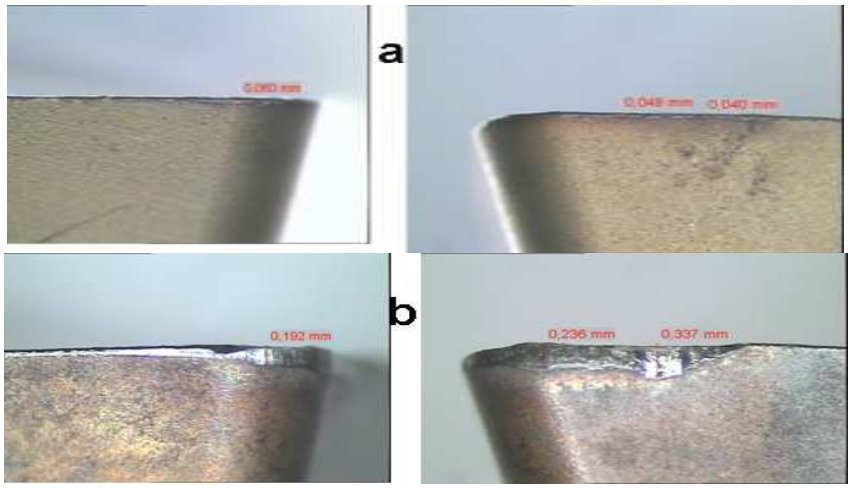

Fig.3 Flank wearV_b and crater wear $K_t$image

a) Taken at the beginning, b) Taken at the end of machining.

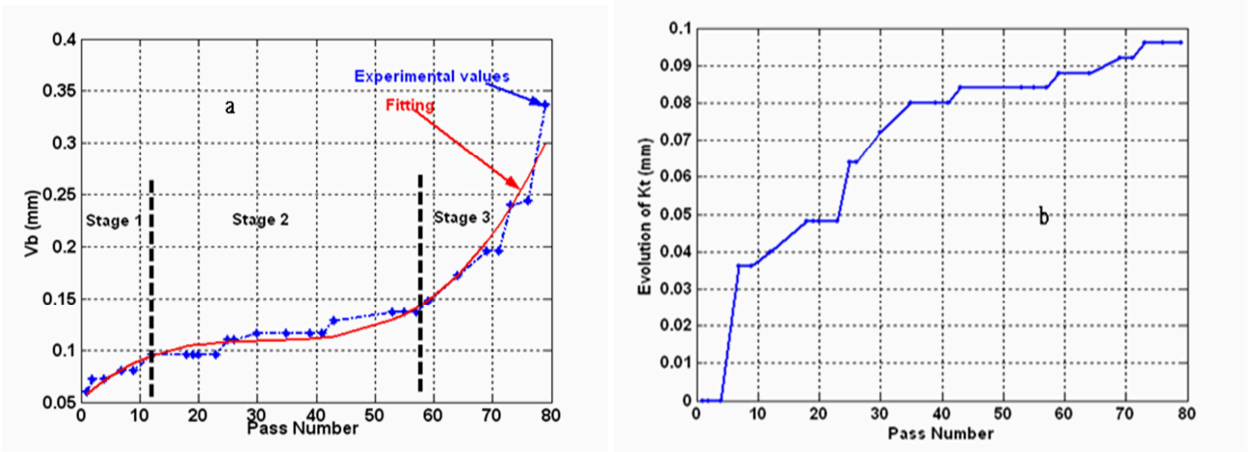

Fig. 4 Evolution of a) Flank wear V_b b) Crater wear K_t

Characterization of the Horizontal Milling by Time-Frequency Analysis

In horizontal milling the chips are evacuated by the gravity effect that represents a significant advantage. In order to characterize horizontal milling very well, it is necessary to make a general study of the machining process in time and frequency domains, with the aim to extract the relevant parameters sensitive to any change of the milling process.

To get the relevant information from the acquired signals, at the first time we have done a time-frequency analyses using the Wigner-ville Transformation.

Wigner-Ville Transform (or Distribution) is the method to represent data (signals) in the time-frequency domain, and provide a tool to define localized spectral density for the nonstationary processes.

The Wigner-Ville Distribution is defined as:

$$W_x(t,\upsilon)=\int_{-\infty}^{\infty} x(t+\frac{\tau}{2})\cdot x^*(t-\frac{\tau}{2})\cdot e^{-j2\pi\upsilon\tau}d\tau \quad (1)$$

The Wigner-Ville Distribution shows the best jointed frequency-time resolution, but unfortunately it is severely affected by the cross-term interference. One way to mitigate the effects of the cross-term interferences, consists in windowing the Wigner Ville Distribution in time or smoothing in frequency domains, obtaining the Pseudo Wigner-Ville Distribution, as it is shown the following equation:

$$PW_x(t,\upsilon)=\int_{-\infty}^{+\infty} h(t-\tau)W_x(\tau,\upsilon)d\tau \quad (2)$$

In our case; the Wigner-Ville representation can allow the localization of the significant frequencies which provide the useful information of milling process.

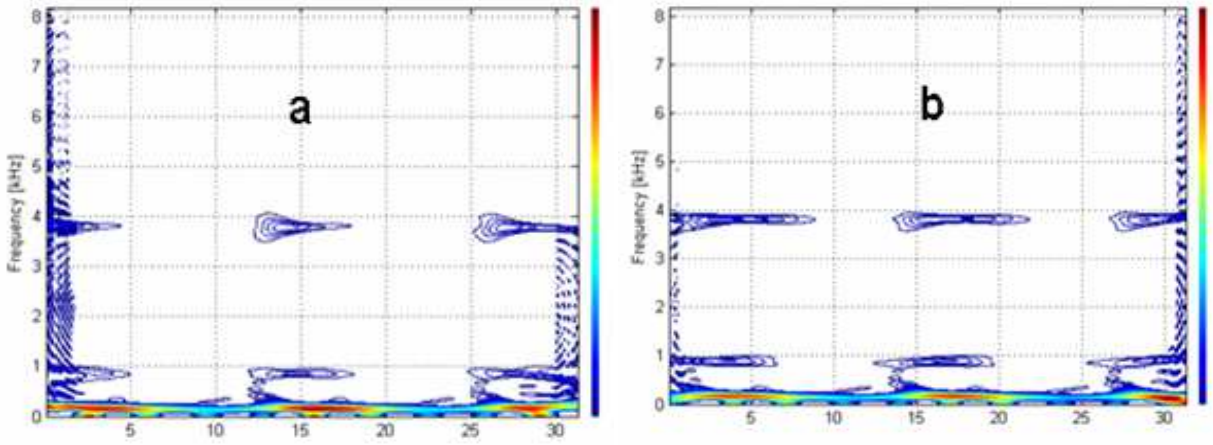

Fig.5Wigner-ville Distribution of vibratory signal at. a) First Pass, b) last Pass.

The results show that the low frequencies contain almost the useful information (Fig. 5). In addition to that we can see that other frequencies at the range of 1 KHz, and 4 kHz have also useful information, these frequencies seem to represent the natural frequencies of the system. The localisation and the fellow up of these frequencies can give a useful information on the evolution of cutting tool wear.

Another approach is proposed to determine the system characteristic frequencies; this approach is based on FFT spectrum analysis of the signal acquired with empty milling operation. As a consequence we have found the flowing frequencies:F_1=3200 Hz, F_2= 4000 Hz. F_3= 4783Hz. (Fig. 6)

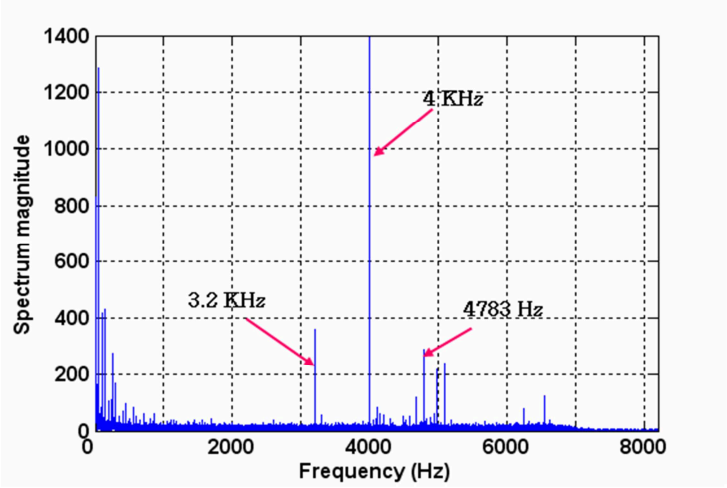

Fig.6 Determination of the system characteristics frequencies.

The kurtosis permits to evaluate the law of probability flatness compared to a normal distribution and it is the fourth statistical moment and the skewness characterizes the distribution symmetry; it is the third statistical moment.

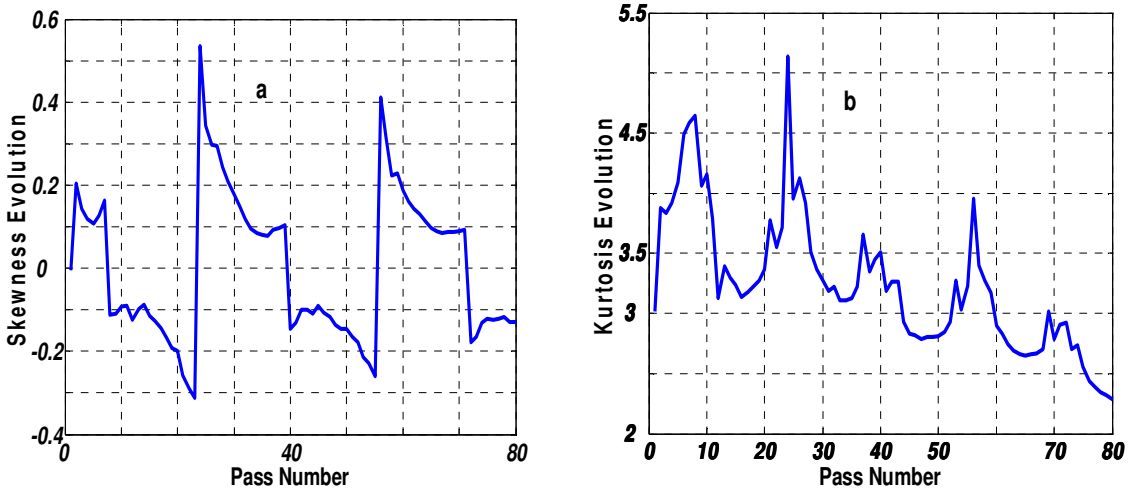

Fig.7 Vibratory signal (a) Skewness (b) Kurtosis

The graphs of the kurtosis and the skewness (Fig. 7) take a periodic form characterizing the machining cycle that shows the major influence of the tool position on the quality of measurements.

Spectral analysis

In the following section we analyze the vibratory signals resulting from two accelerometers the first fixed on the pallet and the second on the spindle.

The spectrum graph provided more information about machining process than the time waveform graph [11]. In this study, one period of cutting process, i.e. one revolution of the tool holder, lasts 26.1665ms, this corresponds to the tooth passing frequency (TPF) that equals 38.2167 Hz. (Fig.8)

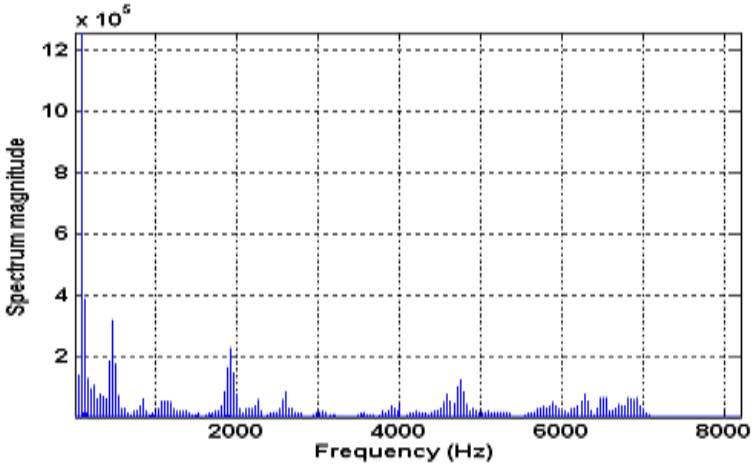

Fig. 8 Spectrum of vibratory signal at the third pass

The fellow-up of the harmonic at the frequency 4 KHz makes possible to predict the tool life as Fig. 9 shows it; the inflection point which represents the acceleration phase of wear can be detected by a notable change on spectral energy of this frequency as shown in the spectrum plot at the 56th pass number, which characterizes the beginning of the acceleration stage of tool wear. The graph of Fig. 13 presents two states,this is an important report that can be used such as a good detector of the transition: stabilizationphase / acceleration phase of wear and it will be easily implanted in an on-line monitoring system.

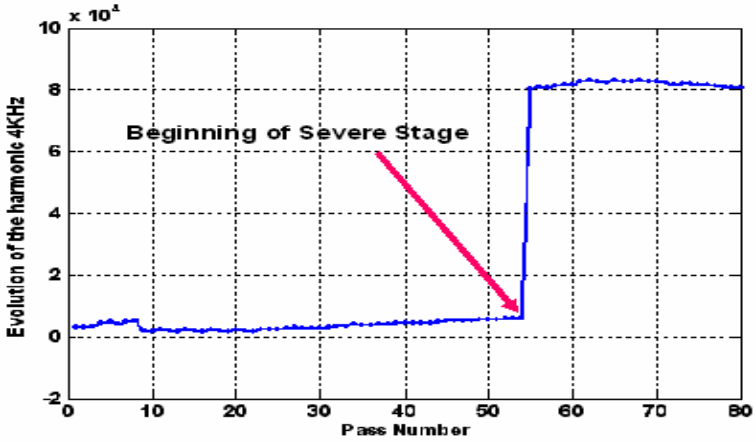

Fig. 9 Evolution of the harmonic at 4 KHz

The fellow-up of the first vibratory harmonic of the signal allows evaluating of the tool wear level as shown in Fig. 10-a &Fig.10-b. Any increase in the spectral energy of the first harmonic corresponds to an increase in the degree of wear; nevertheless we noticed the important influence of the tool position on the spectral energy of this harmonics.

The sensor which is fixed (Fig. 10-a) on the spindle provides the best results, it is less sensitive to the variations of the direction of machining because the position of the sensor compared to the point of contact tool-workpiece is constant. [10]

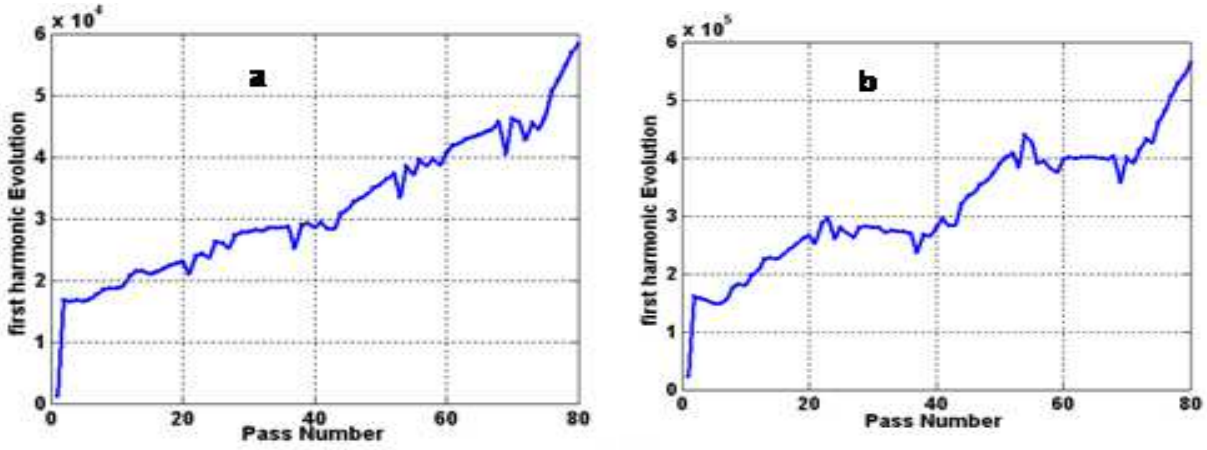

Fig.10 Evolutions of the first Harmonics

a) Accelerometer fixed at Spindle b) Accelerometer fixed at pallet

Discrete wavelet transform (dwt) analysis

DWT is a signal processing technique in the time–frequency domain. It gives signal decomposition with reasonable resolutions in both the time and the frequency domains and a better reconstruction of the original signal in terms of the decomposition results. Given a time-varying signal x[n], DWT consists of computing coefficients which are inner products of the signal and a family of scaling and wavelet functions. It is defined as :

$$h_j\left[n-2^j k\right]=2^{-j/2}\phi\left(\frac{t-2^j k}{2^j}\right). \tag{3}$$

With ϕ as the scaling function defined together with

$$c_{j,k}=\sum x[n]h_j\left[¨n-2^j k\right]. \tag{4}$$

C_{jk} are called the approximation coefficients, which are the low-frequency maps of the original discrete time signal x[n]. [10, 11, 12]

A multiresolution analysis approach is used in which a discrete wavelet (ψ) function is used to compute the details ($d_{j,k}$) coefficients, which are the sampled versions of the original signal and are the high frequency representations of it.

$$g_j\left[n-2^j k\right]=2^{-j/2}\psi\left(\frac{t-2^j k}{2^j}\right). \tag{5}$$

$$d_{j,k}=\sum x[n]g_j\left[n-2^j k\right] \tag{6}$$

The original vibratory signal is decomposed using the Daubechies wavelet function, into approximation and detail coefficients, for different levels of resolution.

The series reconstructed from the approximation coefficients, representing the lower frequency components of the signal, is taken as its filtered version. A level seven decomposition was found to give satisfactory results (Fig. 11). Beyond this level, the entry and exit transients are seen to get attenuated.

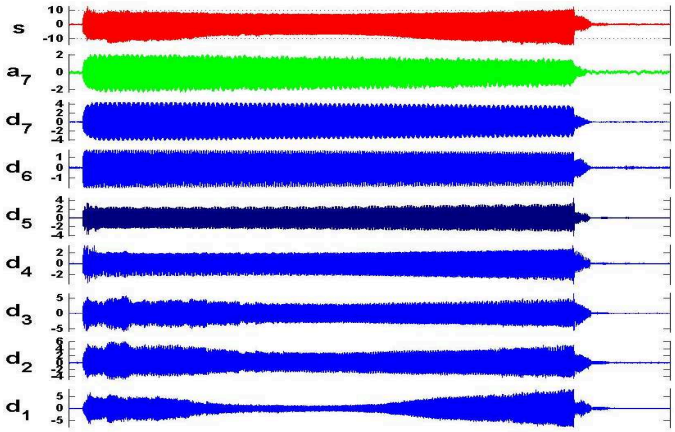

Fig.11 Wavelet Decomposition of vibratory signal

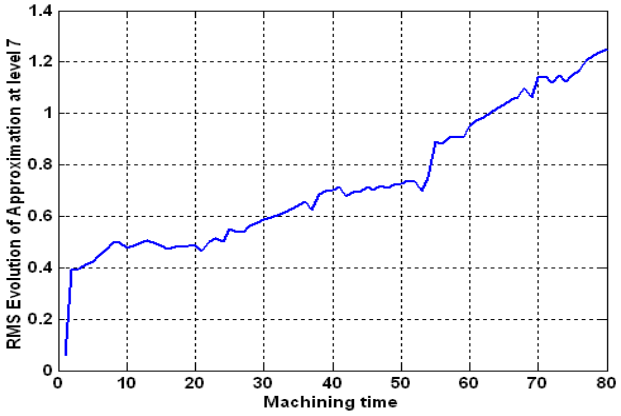

Fig.12 Evolution of the RMS of a_7

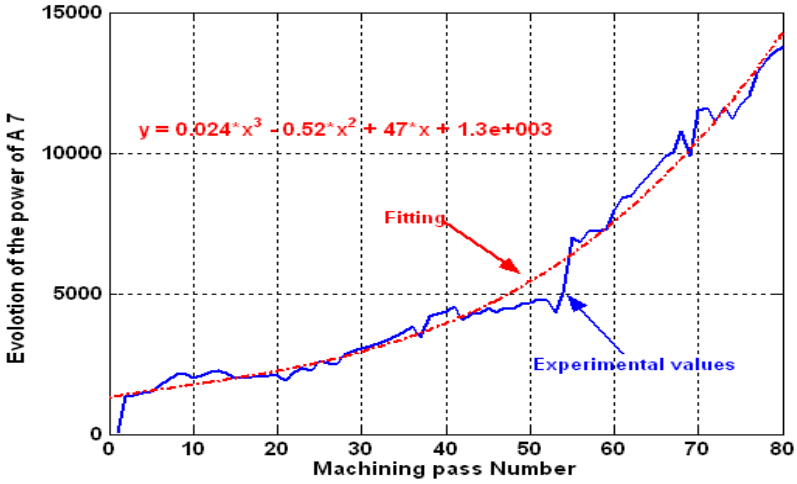

Fig.13 Evolution of the a_7 power

The RMS values (Fig. 12) and the power of the approximation at level 7 (Fig. 13) can be used to estimate the flank wear because they have the same pattern with the graph shown in Fig. 5; then it can be exploited such an appropriate indicator of wear for any tool wear monitoring system.

Conclusion

To monitor the milling process successfully, the selection of an appropriate signal and signal processing algorithm is very important. All approaches (AE, current driver, cutting forces) showed successful results on tool-breakage detection which represents the final phase of the tool life, but an instantaneous detection of the wear level remains a research field completely not yet exhausted, it is

from this point of view which our contribution intervenes.The analysis and correlation of the features of the vibration signal to cutting tool wear have been carried out. Time domain features were deemed to be more sensitive to cutting tool wear, whereas frequency based features correlated well with the tool wear. Based on the measurements of cutting tool wear form and the analysis of the vibration signatures, it has been possible to identify the trend of the sensor signals as the insert wear length increased.

The analysis of the vibratory signal of the accelerometer fixed on the spindle provides the best results; it is the less sensitive to the variations of the machining direction and the tool position.

The severe phase of wear can be easily detected by the notable change on the amplitude of the harmonics at frequency 4 KHz; this is a very important observationand a very useful parameter to estimate the tool life.

The characteristics showed that the measured wear values correlated well with the wavelet approximation trends at level seven. It has been possible to establish distinct differences in signal characteristics when cutting was performed with a new insert from that occurring with a worn insert The first harmonic evolution provides also best results; they increased significantly with flank wear. A threshold level can be drawn up to estimate the tool life

Acknowledgment

The authors wish to thank Mr: Stephen Huretand Mr. Bruno Quilin of Safety group for their assistance in data acquisition.

References

[1] I.Tansel, M. Trujillo, A. Nedbouyan, C. Velez, Wei-Yu Bao, T. T. Arkan and B. Tansel, Micro-end-milling-III Wear estimation and tool breakage detection using acoustic emission signals, International Journal of Machine Tools & Manufacture 38 (1998) 1449-1466.

[2] M. A. Elbestawi, T. A. Papazafiriou and R. X. Du, In-process monitoring of tool wear in milling using cutting force signature, International Journal of Machine Tools & Manufacture 31 (1991) 55-73.

[3] Y. Altintas, I. Yellowley, In-process detection of tool breakage in milling using cutting force models, Journal of Engineering for Industry 111 (1988) 149–157.

[4] D.E. Dimla Sr., Sensor signals for tool wear monitoring in metal cutting operations—review of methods, International Journal of Machine Tools & Manufacture 40 (2000) 1073–1098.

[5] C. Scheffer, P.S. Heyns, Wear monitoring in turning using vibration and strain measurements, Mechanical Systems and Signal Processing 15 (6) (2001) 1185–1202.

[6] P.W. Prickett, C. Johns, An overview of approaches to end milling tool monitoring, International Journal of Machine Tools & Manufacture 3 (1999) 105–122.

[7] E. Kuljanic, M. Sortino, TWEM, a method based on cutting forces—monitoring tool wear in face milling, International Journal of Machine Tools & Manufacture 45 (2005) 29–34.

[8] S.K. Choudhury, SubhashreeRath, In-process tool wear estimation in milling using cutting force model, Journal of Materials Processing Technology 99 (2000)113-119 .

[9] S.N. Huang, K.K. Tan, Y.S. Wong, C.W. de Silva, H.L. Goh, W.W. Tan, Tool wear detection and fault diagnosis based on cutting force monitoring, International Journal of Machine Tools & Manufacture 47 (2007) 444–451.

[10] Rodolfo E. Haber, Jose E. Jiménez, C. Ronei Peres, An investigation of tool-wear monitoring in a high-speed machining process, Sensors and Actuators A 116 (2004) 539–545.

[11] C.K. Toh, Vibration analysis in high speed rough and finish milling hardened steel, Journal of Sound and Vibration 278 (2004) 101–115.

[12] N. Kasashima, K. Mori, G.H. Ruiz, N. Taniguchi, Online failure detection in face milling using discrete wavelet transform, Annals of CIRP 44 (1) (1995) 483–487.

Applied Mechanics and Materials Vol. 565 (2014) pp 46-52

doi:10.4028/www.scientific.net/AMM.565.46

Neural Network Monitoring Strategy of Cutting Tool Wear of Horizontal High Speed Milling

Kious Mecheri[1, a], Benhorma Hadj Aissa[2, b], Ameur Aissa[3, c] and Hadjadj Abdechafik[4, d]

[1]Semiconductor and fonctionnel materials Laboratory "AMAR TELIDJI" University of LAGHOUAT, ALGERIA

[2]Mechanical laboratory "AMAR TELIDJI" University of LAGHOUAT, ALGERIA

[3]LeDMaSD Laboratory, "AMAR TELIDJI" University of LAGHOUAT, ALGERIA

[4]LACoERE Laboratory, "AMAR TELIDJI" University of LAGHOUAT, ALGERIA

[a]kious2005@yahoo.fr, [b]benhormaha@yahoo.com ,[c] amaissa1@yahoo.fr,[d] ahadjadjdz @yahoo.fr

Keywords: Flank wear, Cutting forces, High speed milling, Signal processing, Neural network.

Abstract. The wear of cutting tool degrades the quality of the product in the manufacturing processes. The on line monitoring of the cutting tool wear level is very necessary to prevent the deterioration of the quality of machining. Unfortunately there is not a direct manner to measure the cutting tool wear on line. Consequently we must adopt an indirect method where wear will be estimated from the measurement of one or more physical parameters appearing during the machining process such as the cutting force, the vibrations, or the acoustic emission etc…. In this work, a neural network system is elaborated in order to estimate the flank wear from the cutting force measurement and the cutting conditions

Introduction

Milling is one of the main methods in the manufacturing. Therefore, the detection of tool wear is essential to improve manufacturing quality and to increase productivity. A successful on-line monitoring system for machining operations has the potential to reduce cost, to guarantee consistency of product quality, to improve productivity and to provide a safer environment for the operator. Wear of the cutting tool in milling is a complicated process that requires a reliable technique for monitoring and control of the cutter performance [1, 2].

In most approaches, proposed for the tool wear monitoring area, several parameters can be measured, such as forces, vibrations and acoustic emission, which are directly correlated with tool wear [3-7]. Furthermore, these parameters are measured on-line during the machining process. Several studies have focused their effort on the detection of tool breakage. The effect of tool breakage is usually revealed through an abrupt change in the processed measurements showing a value which is in excess of a threshold value.

One of the more common indirect tool Wear monitoring methods is the use of cutting force measurements.

The cutting force signal is considered to be the most suitable signal for tool failure detection in milling operations because the cutting force signal can offer a clear feature for the detection of tool failure/wear.

Several researchers used the cutting force, to give model for the machining process, or of detect the defects (fracture or wear) of the cutting tool. For this last point the researchers try to find a correlation between the tool wear evolution and the variations of the cutting force parameters. For example, Altintas [2] has shown that the first-order autoregressive time series model AR1 can be used to distinguish the force signal during normal flank wear to that when tool failure occurs. Elbestawi et al. [3] They found that certain harmonics of the cutting force increase significantly with flank wear, the number of such sensitive harmonics being related to the number of inserts of the milling cutter and the immersion rate.

Sarhan et al [4] have shown that the magnitudes of the first harmonics of frequency spectrum increased significantly with increase in tool flank wear, feed per tooth and axial depth of cut.

Therefore, the extraction of the first harmonics from signal spectrum can be used as an indicator to detect the variations of the involved process parameters. Based on ISO 3685-1977, the criterion recommended for end of tool life is when the average width of the flank wear (V_b) exceeds 0.3 mm.

In this context the cutting forces were analyzed in order to determine the relevant parameters which characterize well the cutting tool wear. A series of experiments has been carried out at "Studies and Research Center for cutting Tools, CEROC, LMR, University of Tours, FRANCE" and which constituted the data base of this study.

Experimental Setup

An experimental setup was carried out on a horizontal high speed milling machine (PCI Meteor 10). The cutting force was measured by

a dynamometer (Kistler 9255B) and the measured force was amplified using a charge amplifier (Kistler 5011). The dynamometer was used to measure the cutting forces in three mutually perpendicular directions: X, Y and Z-axis. During the milling, the Z-axis cutting force component contained little information, but the X and Y-axis cutting forces allowed modelling of the process [5].

The dynamometer was clamped between the workpiece and the table (or pallet), as shown in figure 2. In this study, we have used cutter milling type RT130408R-31 with diameter of 25 mm and a workpiece material type 40CrMnMoS8.

The cutting force signal is sampled at frequency of 12 KHz. The milling operations were conducted without applying any coolant, and all cutting tests were performed at the following cutting conditions (table 1), with a single insert.

Table. 1 Cutting conditions

S_s	V_c	S_t	a
3647 rpm	280 m/min	0.15 mm/tooth	2 mm

Fig. 1 Illustration of experimental setup

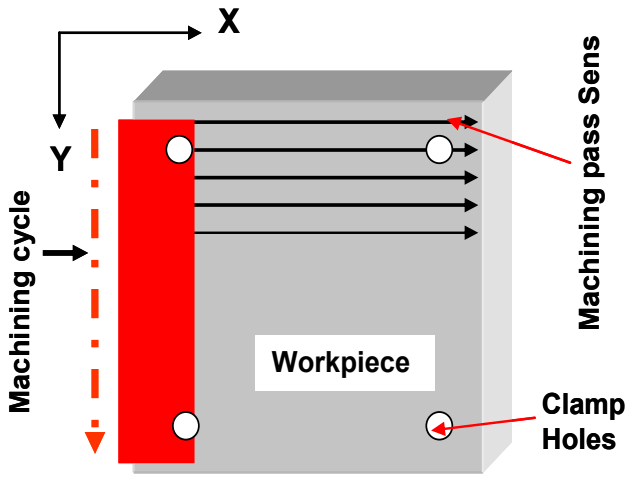

Fig.2 Machining procedure

The workpiece is machined on its length with catch of measurement at the beginning of race. Figure 2 illustrates the machining cycle.

Results and Discussion

In the first stage, to have extra-information about the cutting force, we focus on the "force signal part". Windowing the parts of the signal corresponding to the passing of the tool by clamp holes and the tool entry as illustrated in figure 3.

Thirty-nine recordings were collected during our experimental test that enabled us to follow the evolution of tool wear during machining time. Figure 4 show the evolution of flank wear Vb during the test.

The off-line measurement of Vb and Kt has been done by means of an electronic microscope which is specially conceived to this kind of tasks.

It can be seen in figure 4 that flank wear Vb follows the theoretical pattern and presents the three stages of wear, characterized by a change of slope.

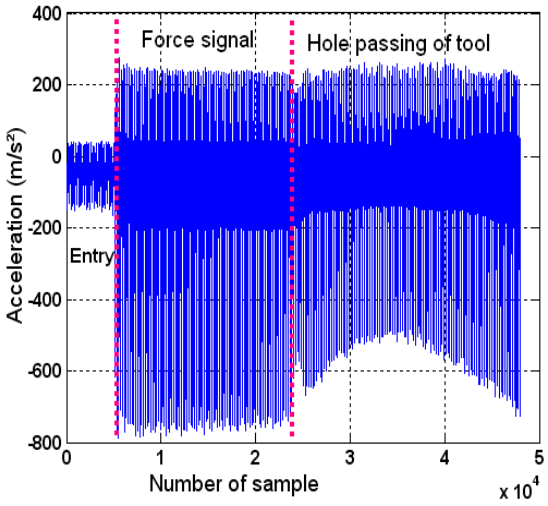

Fig.3 Temporal Cutting force signal

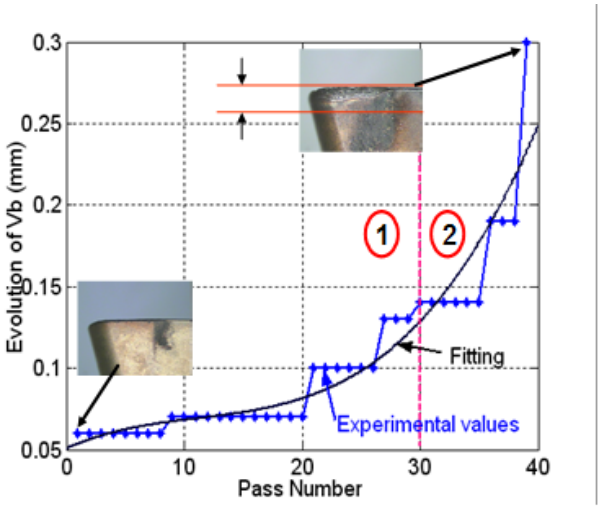

Fig.4 Evolutions of Flank wear Vb

Extraction Of Tool Wear Features By Temporal And Frequency Analysis

Temporal Analysis.

The temporal analysis of cutting force signal is presented in Fig.5 & Fig. 6. Using such statistical parameters as mean, Root Mean Square and variance, it can be observed that the variance values provided more relevant information on the evolution of the milling cutter wear than the values of other parameters.[5,6]

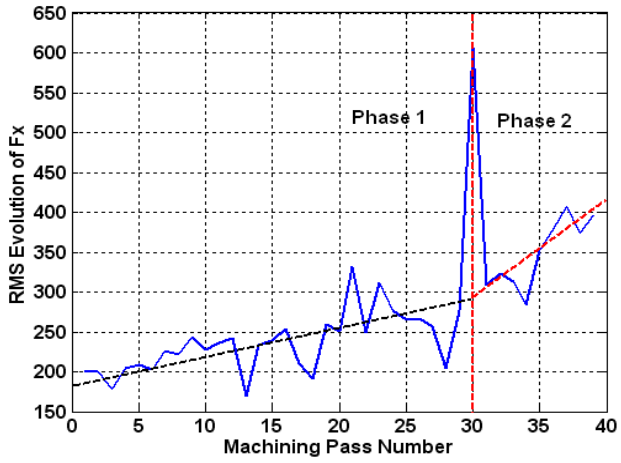

Fig.5 Evolution of the RMS of F_x

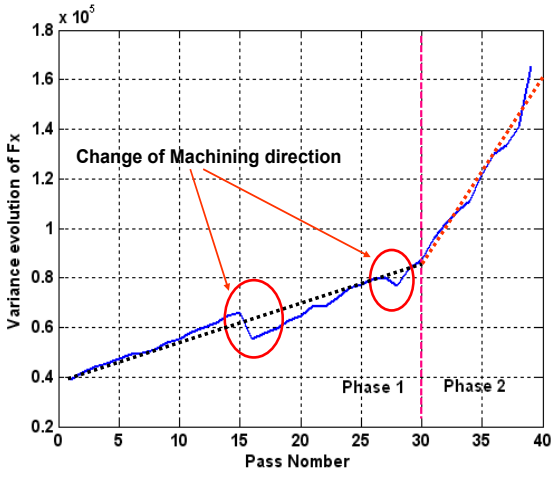

Fig.6 Evolution of the variance of F_x

The variance evolution (Fig.6) has certain characteristics on the fifteenth (t=300sec) and the thirtieth passes (t=600sec) which represent the change of the machining cycle of the workpiece.
On the other hand, the transition between the second phase (2) and the third phase (3) is characterized by a peak at the thirtieth pass (t=600 sec).

Frequencial Analysis

Our study is limited to the evolution of the first six harmonics corresponding to the three cutting forces (radial, axial and resultant) during the machining process, and we observed that the axial force Fx gives best results than the others.

Under a normal cutting condition in the milling process, the dominant frequency components in the spectrum graph are around the tooth passing frequency (TPF), the spindle rotating frequency and their harmonics (Fig.7). TPF is determined using the following equation:

$$TPF = (S_S.N)/60 \quad (Hz) \tag{1}$$

Where Ss is the spindle rotating velocity (rpm), N is the number of teeth of the cutter.
In this study TPF = 60.78 Hz.

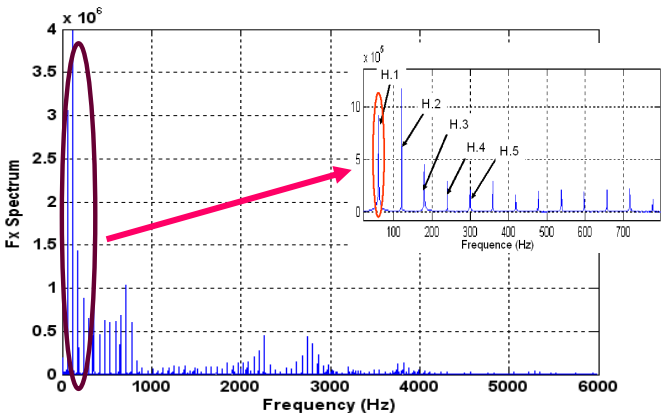

Fig.7 F_x Spectrum of F_x

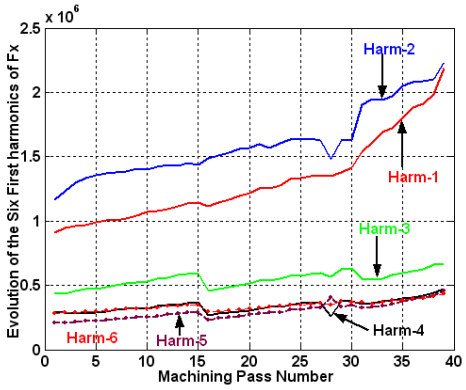

Fig.8 Evolution of the First Six harmonics

In Fig. 11, it can be seen that the magnitudes of certain cutting harmonics increased significantly with flank wear while other harmonics are unaffected.

Furthermore, we have remarked that the first harmonic of the axial force was the most sensitive to the variation of tool wear. In contrast to the variance plot, the harmonic's evolution has certain characteristics only on the fifteenth pass (t=300sec), representing the change of the machining cycle of the workpiece but not on the thirtieth one (t=600sec). Consequently, we deduce that any change of the cutting conditions or the tool performance leads to changes in the amounts of flank wear and then in the significant cutting forces harmonics.

Stimate of Flank Wear vb by Neural Network.

By definition a neural network is an assembly of elements or nodes “processors” where an under group makes an independent treatment and passes the result to the second under group. The processing capacities of the network are store in the forces (or the weights) of connected inter units which are obtained by an adjustment process (training process). These networks are a type of artificial intelligence which tries to imitate the operation of a human brain. Instead of using a model digital, in which all the operations handle of the zeros and the ones, a neural network proceeds by creating connection between nodes. The organization and the weights determine the outputs. The neural networks can be used to estimate an output from one or more input and a target output [8,9,10].

The generation stage of the NN gives the following results (Fig.9 & Fig10). We notice that the estimated output differs much from the measured output Vb, owing to the fact that this result is obtained before the training of the network. The error between Vb measured and the estimated output of the NN are expressed by:

$$\text{Error} = \left\| \text{Vb -real output} \right\| \quad (2)$$

The stage of training consists in minimizing this error; for that we fixed the iteration number at 1000, and the error at 0; that give us the results shown by Fig. 10. From this figure, we can notice that the error between the estimated output and the measured output (Vb experimental) is practically equal zero.

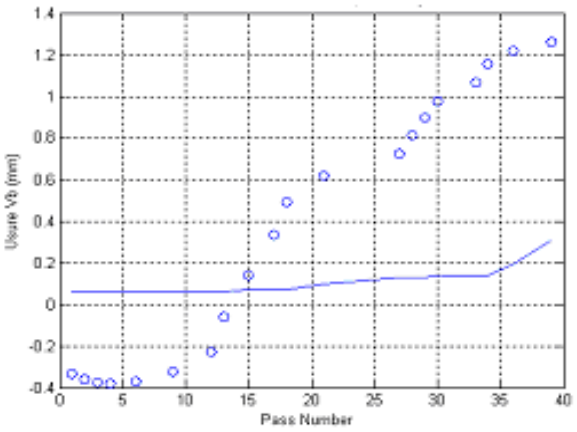

Fig.9 Output of the NN before the training

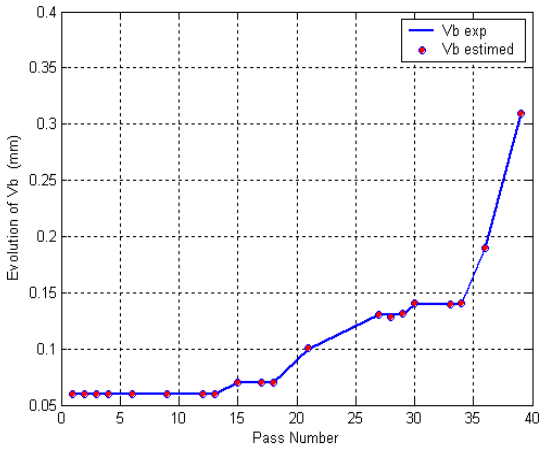

Fig.10 Output of the NN after the training step

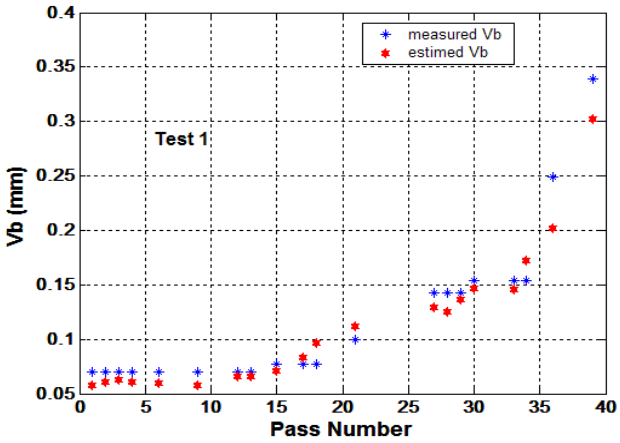

Fig.11 Test 1 of NN (validation)

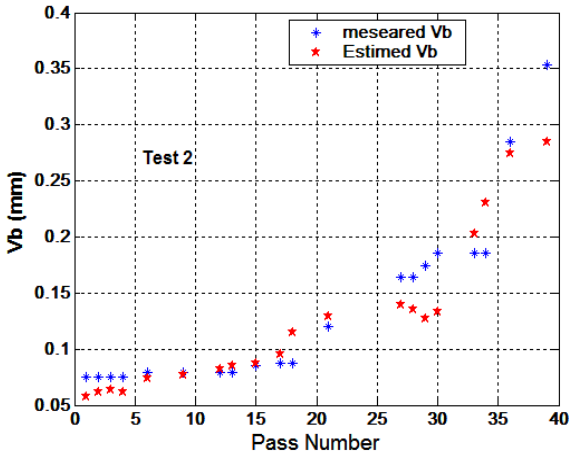

Fig.12 Test 2 of NN (validation)

The curves of Fig.11 & Fig.12 show that the output estimated by the NN tends towards the measured output, consequently, we can conclude that the training of the NN has been well carried out.

In our case, this method makes it possible to estimate wear V_b from the following inputs (K_s, a, C_w, D, V_c, S_t, z, the first harmonic, the variance and the RMS) with a NN (10 neural in input layer-5 neural in hidden layer and one neural in output layer). And if we want to make a classification of cutting tool wear we can draw up a threshold.

Conclusion

This study investigated the use of cutting force signal measurements to improve the on-line tool wear detection and monitoring of coated tools in milling process by developing a predictive method of their wear. To achieve this goal, we have used the cutting force analysis to establish a relationship between the wear evolution and the cutting force variations.

Indeed, we observed some values on the evolution curves of the variance and of the first harmonic that show a change in the nature of the efforts. This change becomes more significant and is characterized by an increase in slope of the evolution curve; it is also directly linked to the transition from the normal phase of the cutting tool wear to the severe phase. We stressed on the influence of the machining cycle on the quality of measurements. This phenomenon should be well taken into account during any measurement of the cutting forces, specially, in horizontal milling.

The first stage was to determine the appropriate indicator revealing of useful information about the cutting tool wear state, it appears that the variance and the first harmonic (spectral) of cutting force according to X-axis provide the relevant information.

An automatic monitoring system of tool wear based on neural networks has been implemented using the cutting condition, the insert type, the values of the variance, and the first harmonic of the cutting force as input vectors to estimate the tool wear. The results obtained are hopeful, it was shown that it is possible to repeat this study on a large scale, by dressing a data base of many inserts. This would make it possible to get knowledge about the tool life for each insert type under various cutting conditions and help to avoid the wasting of inserts because their use time would be optimized. The economic impact of this optimized use would be obviously very significant for industries which use a large quantity of this type of tools.

Nomenclature

a Depth of cut (mm).
Cw The edge force constant (N/mm2).
Fx Axial force (N).
Ks Specific cutting pressure of workpiece material (N/mm2).
St Feed rate per tooth (mm/tooth).
Vb The flank wear width (mm).
Kt The crater wear depth (mm).
Vf Feed speed (m/min).
Vc Cutting speed (m/min).
Ss Spindle speed (rpm).

References

[1] Bin Li, A review of tool wear estimation using theoretical analysis and numerical simulation technologies, Int Journal of Refractory Metals and Hard Materials, 35, (2012), 143-151.

[2] M. A. Elbestawi, T. A. Papazafiriou and R. X. Du, In-process monitoring of tool wear in milling using cutting force signature, International Journal of Machine Tools & Manufacture 31(1991) 55-73.

[2] Y. Altintas, I. Yellowley, In-process detection of tool breakage in milling using cutting force models, Journal of Engineering for Industry 111 (1988) 149–157.

[4] Sarhan, et al, Interrelationships between cutting force variation and tool wear in end-milling' Journal of Materials Processing Technology 109 (2001), 229-235.

[5] M. Kious, A. Ouahabi, M. Boudraa, R. Serra, Detection process approach of tool wear in high speed milling , Measurement, Volume 43, Issue 10, (2010),1439-1446.

[6] P. Bhattacharyya, D. Sengupta, S. Mukhopadhyay , Cutting force-based real-time estimation of tool wear in face milling using a combination of signal processing techniques,Mechanical Systems and Signal Processing, 21, (2007),2665-2683.

[7] J.A. Ghani, M. Rizal, M.Z. Nuawi, M.J. Ghazali, C.H.C. Haron, Monitoring online cutting tool wear using low-cost technique and user-friendly GUI, Wear, 271, (2011), 2619-2624.

[8] S.L Chen, Y.W. Jen ,Data fusion neural network for tool condition monitoring in CNC milling machining, Int. J. Machine Tools & Manufacture 40 (2000),, 381–400.

[9] H. Saglam, A. Unuvar, Tool condition monitoring in face milling based on cutting forces by a neural network, International Journal of Production Research 41 (2003), 1519–1532.

[10] N. Ghosh et al, Estimation of tool wear during CNC milling using neural network-based sensor fusion, Mechanical System and Signal Processing 21 (2007), 466–479.

Applied Mechanics and Materials Vol. 565 (2014) pp 53-58

doi:10.4028/www.scientific.net/AMM.565.53

Influence of Welding Speed over Dilution for Circular Grid plate Hardfaced with Colmonoy-5

Balaguru S[1], Deenadayalan K[2], Vela Murali[3], Chellapandi P[4]

[1, 2] Anna University, Chennai, India

[3] Head & Professor I/c, Engineering Design Division, Department of Mechanical Engineering, Anna University, Chennai, India

[4] Director, Nuclear & Safety Engineering Group, IGCAR, Kalpakkam, India

balaguru_iit@yahoo.co.in, aerodeena008@gmail.com

Keywords – PFBR, Colmonoy, PTAW, Dilution, Hardness, Microstructure, Positive Material Identification.

Abstract. Colmonoy is a nickel based alloy hardfaced with SS-316 used in Prototype Fast Breeder Reactors (PFBR) to avoid self welding and galling between nuclear reactor and grid plate. Colmonoy is coated on the base metal –SS 316 by Plasma transfer arc welding. Due to thermal cycling that exist in reactors de-bonding between colmonoy and base metal occurs which may lead to catastrophic failure of the Prototype fast breeder reactor. Hence, estimation of the fatigue life period of hardfaced colmonoy is mandatory. Before that, finding optimum parameters which influences fusion, weld strength, composition and dilution are mandatory. In order to evaluate the dilution characteristics with respect to welding speed, different specimens were prepared by holding other parameters constant. Prepared specimens were tested for hardness, microstructure and dilution to locate the difference between each specimen. Comparative studies were carried out on the specimen and their parameters like travelling speed, microscopic structure, Hardness and dilution percentage were tabulated. Based on the tabulated results, the best specimen is chosen with respect to its individual parameters.

Introduction

Hardfacing alloys like Colmonoy are overlaid on nuclear components to provide corrosion, wear and galling resistance under high temperature service conditions in PFBR (Prototype Fast Breeder Reactor). The liquid sodium coolant acts as a reducing agent and removes the protective oxide film present on the SS surface of the in-sodium components. Many of these components would be in contact with each other or would have relative motion during operation, and their exposure at high operating temperatures (typically 550°C) coupled with high contact stresses could result in self-welding of the clean metallic mating surfaces. In addition, the relative movement of mating surfaces could lead to galling, a form of high temperature wear, in which material-transfer occurs from one mating surface to another due to repeated self-welding and breaking at contact points of mating surfaces. Hardfacing of the mating surfaces has been widely used in components of water-cooled and liquid-sodium cooled FBRs to avoid self-welding and galling. Ni based hardfacing alloys, which have already been used in various fast breeder reactors worldwide was the alternate material although weldability of these alloys is poor compared to Co based alloys. Plasma Transferred Arc Welding process, which is highly amenable for automation was considered for Ni deposition. Further, significant variation in microstructure of the deposition with respect to different welding speeds which will cause different dilution of the base metal need to be observed.

Specimen preparation

316 LN SS was chosen because of its enhanced corrosion resistance, high temperature oxidation resistance or their strength. In order to evaluate the influence of welding speed on hardfaced

coatings, four specimens were prepared with four different welding speeds keeping other parameters constant. Using PTAW, 4mm height of colmonoy was deposited on base metal with dimension of 90mm diameter and 40mm thickness plate. The height of coating should be $1/10^{th}$ of that of base metal. (Thickness of base metal becomes height). The base metal was preheated to 400^0C to relieve stresses and then the colmonoy was coated over the surface. The travelling speeds of the welding nozzle are 1.5 mm/sec, 2 mm/sec, 2.5 mm/sec and 3 mm/sec. Fig.1 shows the specimen prepared at a speed of 3mm/sec. The cross sections of the specimens showing interface are shown in Fig. 2. (However, the specimen prepared at the speed of 3.5mm/sec was not considered as blow holes were induced from this higher speed onwards)

Fig.1 Specimen at 3 mm/sec

Fig. 2 Cross sections

Evaluation of hardness, microstructure and dilution

a. Hardness: Here hardness is measured using Micro Vickers hardness tester. Hardness survey has been taken for every 0.5 mm gap across the interface starting with deposited material (Colmonoy overlay) towards parent metal as shown in fig. 3. Below the interface, the locations are mentioned as negative and above the interface, they are positive. This survey helps to know the hardness values at all zones viz. Substrate, Interface, Heat affected Zone and filler material, which is more important to characterize the properties of different zones and their grain structures.

The comparative study of hardness values for different welding speeds is shown in Fig 4.

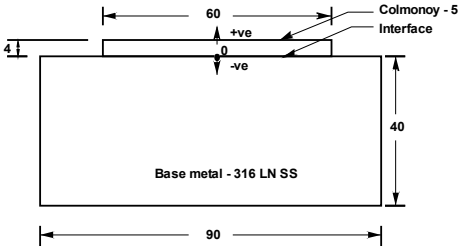

Fig. 3 Hardness survey points across interface

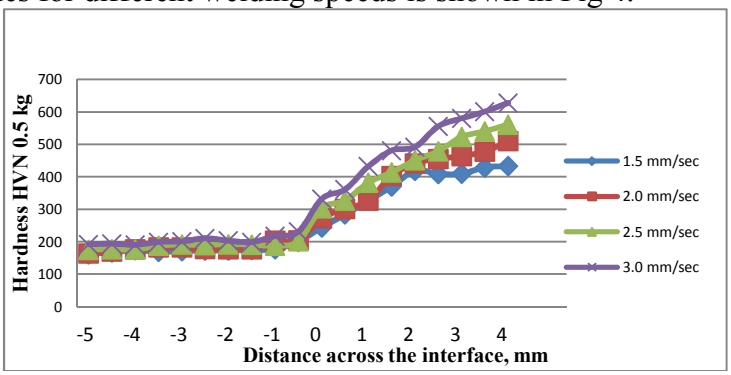

Fig 4 Comparative study of hardness for different welding speed

b. Microstructure: Micro structural tests were performed using conventional optical microscope named De-Wintor Inverted Trinocular Metallurgical Microscope. The microstructures of the test specimens were electrolytic etched using oxalic acid. Images of microstructure obtained using optical microscope at magnifications M 100X for test specimens of 1.5mm/sec and 3.0 mm/sec are shown in Fig 4 and Fig 5 respectively.

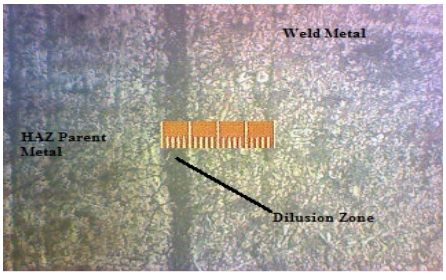

Fig. 5 Microstructure of Diffusion zone – 1.5 mm/sec

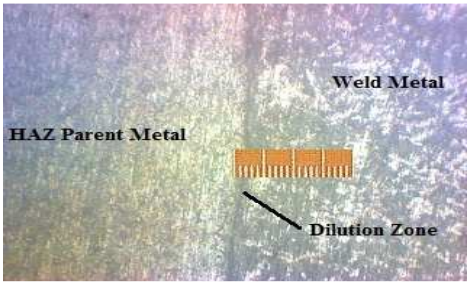

Fig. 6 Microstructure of Diffusion zone – 3.0 mm/sec

c. Dilution: Finding dilution percentage of welding process has significant role in finding the final weld composition and its elements weight percentage. Average dilution percentage can be found using the ratio between the area of melted parent metal and total welding region. This is the common method employed to find dilution, but there is a possibility for errors because it considers only area measurement. Moreover dilution is dependent upon base metal (substrate), filler material, elements constituents, preheating temperature, heat supplied during welding, solidification time etc. Hence, an alternative method was considered here to find the nominal dilution by comparing the weight percentage of individual elements present in the base metal (SS-316), Overlay (Colmonoy) and final weld composition. Using initial and final elements constituents, quadratic equations were formed and dilution percentage was found by solving it. The chemical composition of 316 LN SS and colmonoy are given in Tab 1 .

Tab 1 Chemical composition of 316 SS LN and colmonoy

Material	C	Mn	Si	P	S	Cr	Mo	Ni	N	Fe	B
316 SS LN	0.03	2.0	0.75	0.045	0.03	18	3.0	14	0.1	62.05	--
Colmonoy	0.6	0.1	3.8	--	--	11.5	--	77.5	--	4.4	2.6

Final weld composition is a combination of base metal and filler metal. Base metal dilution is nothing but the amount of base metal melted and contributed for final weld composition and filler metal dilution is the amount of filler metal melted and contributed to final weld composition. The readings taken by handheld XRF are shown in Tab 2.

Tab2. Weight percentage of various elements for different welding speeds by PMI (X-Ray fluorescence)

ELEMENTS	SYMBOLS	DIFFERENET WELDING SPEEDS							
		1.5 mm/sec				2 mm/sec			
		1	2	3	Average	1	2	3	Average
Chromium	**Cr**	13.2	13.5	13.88	13.52	13	12.95	13.45	13.1
Manganese	**Mn**	1.26	1.3	1.28	1.28	1.2	1.2	1	1.13
Iron	**Fe**	41.4	42.42	40.6	**41.47**	34.5	33.6	35.3	**35.54**
Cobalt	**Co**	0.4	0.45	0.45	0.43	0.24	0.28	0.25	0.26
Nickel	**Ni**	36.8	36.1	35	**35.9**	42.2	41.8	41.6	**41.9**
Copper	**Cu**	6.5	6.2	6.3	6.33	4.7	4.7	5.2	4.87
Molybdenum	**Mo**	1.5	1.3	1.1	1.3	1.55	1.6	1.4	1.51
Tantalum	**Ta**	0	0.01	0	0	0	0.07	0.01	0.027
Vanadium	**V**	0	0.02	0.02	0.013	0.01	0	0	0
Niobium	**Nb**	0.03	0.02	0.02	0.023	0.04	0.03	0	0.023
Tungsten	**W**	0.4	0.3	0.4	0.36	0.15	0.13	0.16	0.15

ELEMENTS	SYMBOLS	DIFFERENET WELDING SPEEDS							
		2.5 mm/sec				3 mm/sec			
		1	2	3	Average	1	2	3	Average
Chromium	**Cr**	11.35	11.28	11.3	11.3	11.8	11.1	11.9	11.6
Manganese	**Mn**	0.4	0.3	0.2	0.3	0.6	0.5	0.6	0.57
Iron	**Fe**	31	31	29.4	**30.4**	25.8	25	24	**24.9**
Cobalt	**Co**	0.3	0.5	0.4	0.4	0.3	0.28	0.3	0.29
Nickel	**Ni**	52	51.8	47	**50.26**	63.15	52	57.1	**57.4**
Copper	**Cu**	6	6	5.6	5.87	4	4	3.4	3.8
Molybdenum	**Mo**	1.1	0.95	0.8	0.95	0.9	1.2	1	1.05
Tantalum	**Ta**	0.01	0.01	0.01	0.01	0.01	0.02	0.01	0.013
Vanadium	**V**	0	0.08	0.04	0.04	0.06	0.02	0.02	0.033
Niobium	**Nb**	0.04	0	0.05	0.03	0.01	0.01	0.03	0.017
Tungsten	**W**	0.6	0.5	0.5	0.533	0.95	1.1	1	1

For 1.5 mm/sec speed, in the welding pool, 62.05 % Fe from SS 316 is added with 4.4% Fe in colmonoy and produces 41.47% Fe at the interface. Similarly, 14% Ni from base metal is added with 77.5%Ni in colmonoy and produces 35.9% Ni at the interface. Using these values, two equations for Fe and Ni are formed and by solving them base metal dilution and filler metal dilution are found. By comparing the numeric weight percentage Fe and Ni of original composition with interface compositions dilution percentage can be evaluated as follows. Generally dilution percentages are found only major elements, hence using PMI element percentages at the final weld composition are found and given in Table 3

Tab 3 Weight percentage Ni & Fe for different welding speeds (final weld composition)

Element	**1.5mm/s**	**2.0mm/s**	**2.5mm/s**	**3.0mm/s**
Iron	41.47	35.54	30.4	24.9
Nickel	35.9	41.9	50.26	57.4

For 1.5mm/sec

Elements	**Base metal**	**+ Overlay**	**→**	**Final weld composition**
Iron	62.05 %	+ 4.4 %	→	41.47%
Nickel	14 %	+ 77.5%	→	35.9%

Let X_1, X_2, X_3 & X_4 are dilution contribution from Colmonoy for the welding speeds of 1.5, 2.0, 2.5 & 3.0 mm/sec respectively whereas Y_1, Y_2, Y_3, & Y_4 are dilution contribution from base metal for the welding speeds of 1.5, 2.0, 2.5 & 3.0 mm/sec respectively.

An equation with X (denotes contribution of colmonoy) and Y (denotes contribution of base metal) has been arrived based on major element Fe present in base metal and colmonoy before weld as given in Table 4. equated to the Fe constituent present in the interface (after weld) which are given in Table 3 for different weld speeds. Similarly, another equation with same unknowns X & Y is formed with reference to element Ni. By solving two equations, dilution percentage of base metal and Colmonoy can be found as shown in Table 4. Since Fe dilution affects hardness, a graph showing the variation in Fe dilution with welding speed is shown in Fig 7

Tab 4 Dilution of base metal and weld metal

Welding speed	**Equations**	**Dilution**
1.5 mm/sec	$4.4\ X_{1+} 62.05 Y_1 = 41.47$ $77.5\ X_1 + 14\ Y_1 = 35.9$	$X_1 = 0.40$; 40% $Y_1 = 0.64$; 64 %
2.0 mm/sec	$4.4\ X_{2+} 62.05 Y_2 = 35.54$ $77.5\ X_2 + 14\ Y_2 = 41.9$	$X_2 = 0.38$; 38 % $Y_2 = 0.53$; 53 %
2.5 mm/sec	$4.4\ X_{3+} 62.05\ Y_3 = 30.4$ $77.5\ X_3 + 14\ Y_3 = 50.26$	$X_3 = 0.54$; 54% $Y_3 = 0.45$; 45 %
3.0 mm/sec	$4.4\ X_4 + 62.05\ Y_4 = 24.9$ $77.5\ X_4 + 14\ Y_4 = 57.4$	$X_4 = 0.72$; 72 % $Y_4 = 0.35$; 35%

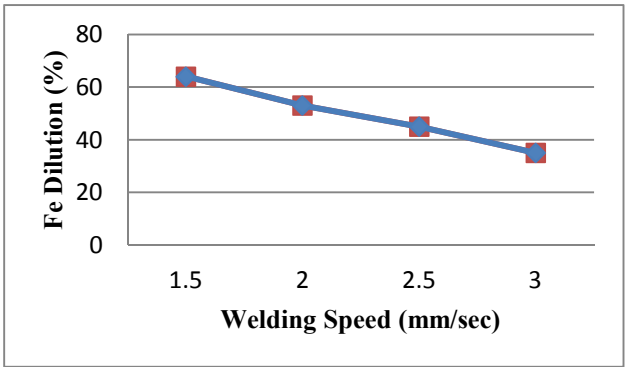

Fig 7 Fe dilution for different welding speeds.

Results and Discussion

From Fig 4 and Fig 7, the process with lower welding speed of 1.5 mm/sec has yielded higher hardness and higher base metal dilution. As the speed increases from 1.5mm/sec to 3mm/sec, Fe dilution decreases from 64% to 35%. The process with lower speed also resulted in higher heat affected zone and hence the interface line is wider (50 micron) and wavy in lower speed compared to higher speed in which it is thin (20 micron) and straight as shown in Fig 5 and Fig 6. Microstructure of specimens with speeds 2.5 mm/sec and 3.0 mm/sec shows higher dendritic pattern of austenite grains due to rapid solidification of liquid metal at weld pool while at lower speeds those patterns are low. Hardness of 316 LN SS is low (160 HVN) and constant until interface and then it increases gradually upto 2mm above the interface and remains almost constant (650 HVN) after that height for all speeds. Due to welding heat, Fe from base metal crosses interface and merges with colmonoy upto the height of 2mm. This region is known as dilution region. Due to this mixing of iron in colmonoy in the dilution region, the hardness of colmonoy is lower than its actual value. When we measure iron content in dilution region, it decreases as we go above the interface and hence hardness seem to increase. Beyond this dilution region, hardness is not affected.

Conclusions

The following conclusions have been arrived at:

The thickness of interface decreases by 60% from 50micron to 20micron as the welding speed increases by 100% from 1.5mm/sec to 3mm/sec. However, beyond the welding speed of 3mm/sec, blow holes start appearing. Hence, it is not recommended to increase welding speed beyond 3mm/sec.

PMI study shows that for every 0.5 mm/sec increment in welding speed, there is 15% reduction in dilution of base metal.

As speed increases, the amount of Fe from base metal merging with colmonoy decreases due to lower heat input as the result of rapid solidification. Hence hardness is always maximum at highest speed in all locations.

Since hardness of colmonoy is very important in application point of view, the welding speed of 3mm/sec is recommended. It is also recommended as future work to deposit colmonoy inside the groove cut on the surface of base metal such a way that atleast 1mm projection above the surface is attained so that de-bonding may be avoided.

References

[1] Balasubramanian. V, A. K. Lakshminarayanan, R Varahamoorthy, S, Babu, Application of Response Surface Methodolody to Prediction of Dilution in Plasma Transferred Arc Hardfacing of Stainless Steel on CarbonSteel Original Research Article, Journal of Iron and Steel Research, International, Volume 16, Issue 1, January 2009, Pages 44-53

[2] Bhaduri. A. K, R. Indira, S.K. Albert, B.P.S. Rao, S.C. Jain, S. Asok kumar, Selection of hardfacing material for components of the Indian Prototype Fast Breeder Reactor Original research Article journal of Nuclear Materials, Volume 334, Issues 23, 1 September 2004, Pages 109-114

[3] Chang. J. H, C.P. Chang, J.M. Chou, R.I. Hsieh, J.L. Lee , Microstructure and bonding behavior on the interface of an induction-melted Ni-based alloy coating and AISI 4140 steel substrate Original Research Article, Surface and Coatings Technology, Volume 204, Issue20, 15 July 2010, Pages 3173-3181.

[4] Cockeram. B. V, Fracture toughness testing and toughening mechanisms of some commercial cobalt-free hardfacing alloys, Original Research Article Surface and Coatings Technology, Volumes 108–109, 10 October 1998, Pages377-384.

[5] Gurumoorthy. K, M. Kamaraj, K. Prasad Rao, A. Sambasiva Rao, S. Venugopal , Microstructural aspects of plasma transferred arc surfaced Ni- based hardfaced alloy Original Research Article Materials Science and Engineering: A, Volume 456, Issues 1–2, 15 , May 2007, Pages 11-19.

[6] Kesavan. D, M. Kamaraj ,The microstructure and high temperature wear performance of a nickel base hardfaced coating, Original Research Article, Surface and Coatings Technology, Volume 204, Issue 24, 15 September 2010, Pages 4034-4043.

[7] Sudha. C, P. Shankar, R.V. Subba Rao, R. Thirumurugesan, M. Vijayalakshmi, Baldev Raj Microchemical and microstructural studies in a PTA weld overlay of Ni–Cr–Si–B alloy on AISI 304L stainless steel Original Research Article, Surface and coatings Technology, Volume 202, Issue 10, 15, February 2008, Pages 2103-2112

CHAPTER 2:

Aerospace and Mechanical Engineering, Applied Mechanics

Applied Mechanics and Materials Vol. 565 (2014) pp 61-66

doi:10.4028/www.scientific.net/AMM.565.61

Quasisolution of the Inverse 3D Aerohydrodynamics Problem

Pyotr N. Ivanshin[1, a]

[1]Russia, 420008, Kazan, Universitetskaya str., 18, Kazan Federal University

[a]pivanshin@gmail.com

Keywords: Aerohydrodynamics, analytic function, polyharmonic function, spline.

Abstract. In the article we generalize the quasisolution approach to the planar aerohydrodynamics problems to 3D case. We search for solution in the form of the spline.

Introduction

In the article we generalize the quasisolution approach to the planar aerohydrodynamics problems to the 3D case.

The first step in solution of the planar problems was made by Mangler [1]. Later Tumashev rediscovered this approach [2]. The main problem in the inverse solution construction is that there exist certain conditions of both mathematical and mechanical origin, i.e. the reconstructed contour must be a closed Jordan curve and the velocity at infinity must equal some specified value. In order to overcome these difficulties researchers introduced numerous quasisolutions [3, 4, 5].

Here we try to extend the planar constructions to the 3D case. We reduce the 3D problem to the set of planar ones similarly to the cases of the other 3D problems [6, 7]. So here we have something close but not identical to section-to-section analysis widely applied to the problem under consideration. The sections under consideration are not mutually independent since we consider the flow component transversal to the sections. We search for solution in the form of the spline linear on the transversal to section coordinate.

Main Results

Let us consider the set of equations:

$$\frac{\partial u}{\partial x}+\frac{\partial v}{\partial y}+\frac{\partial w}{\partial h}=0.$$

$$\frac{\partial u}{\partial y}=\frac{\partial v}{\partial x},\frac{\partial u}{\partial h}=\frac{\partial w}{\partial x},\frac{\partial w}{\partial y}=\frac{\partial v}{\partial h}.$$

We search for the solution in the form of the linear on h polynomial:

$$u(x,\ y,\ h)=u_0(x,\ y)+h\ u_1(x,\ y),$$
$$v(x,\ y,\ h)=v_0(x,\ y)+h\ v_1(x,\ y),$$
$$w(x,\ y,\ h)=w_0(x,\ y)+h\ w_1(x,\ y).$$

Then we have the following relations on $u_j, v_j, w_j,\ j=0,1$:

$$\frac{\partial u_1}{\partial x}=-\frac{\partial v_1}{\partial y},\frac{\partial u_1}{\partial y}=\frac{\partial v_1}{\partial x}. \quad (1)$$

$$\frac{\partial u_0}{\partial x}=-\frac{\partial v_0}{\partial y}-w_1,\frac{\partial u_0}{\partial y}=\frac{\partial v_0}{\partial x}. \quad (2)$$

$$\frac{\partial w_0}{\partial x}+h\frac{\partial w_1}{\partial x}=u_1,\frac{\partial w_0}{\partial y}+h\frac{\partial w_1}{\partial y}=v_1. \quad (3)$$

The last set of relations implies that $w_1 = const$. Thus we obtain

$$\frac{\partial w_0}{\partial x} = u_1, \frac{\partial w_0}{\partial y} = v_1. \quad (4)$$

System of equations (4) is correct due to the second equation of system (1). Let us introduce the usual complex variable z=x+i y. Thus we obtain the solution

$$w_0 = \frac{1}{2i}(\int v_1(z) + iu_1(z)dz - \overline{\int v_1(z) + iu_1(z)dz}).$$

So this function is up to some real constant defined by the velocities u_1 and v_1.

This linear spline allows us to obtain two adjacent airfoil profiles. So we have the unknown functions u_0, v_0, u_1, v_1 and w_0, and one unknown constant w_1. Assume that we fix the velocity values at these adjacent sections. Then for the functions u_1 and v_1 we have the usual plane problem. This allows us to reconstruct the analytic function $f_1(z,\bar{z}) = v_1(z) + iu_1(z)$. The harmonic function constructed by u_0 and v_0 we can find up to the summand depending on w_1 : $f_0(z,\bar{z}) = v_0(z) + iu_0(z) + i\bar{z}w_1$.

It seems natural for the air or fluid particles to travel along geodesic lines on the surface of the airfoil. Because of this we necessarily obtain the additional condition: the geodesic lines on the upper and lower surfaces of the airfoil must have the same start and end points. Also we naturally must have

$$w(x,y,h)\big|_B = 0. \quad (5)$$

Here B is the flow branch point.

We now have a system of 4 real-valued equations on the functions $hf_1 + f_0$ and f_0. These problems we solve as the standard inverse aerohydrodynamics problems. We note that modified system (2) is closely related to classical system (1). Even the functions f_0 and f_1 are both harmonic. The only difference in the solution is that the velocity potential ω_0 for the function f_0 equals $\phi_0(z) + i\psi_0(z) + iw_1|z|^2$. So for the cut we must have the following initial data: the tangent to the cut velocity V depending on the cut length coordinate, the transversal to the cut velocity w_1 and the velocities V and w_1|s| vector sum. The last notion is exactly what we apply to solve the classical problems. So we first obtain f_0 and f_1 then deduce from them $iw_1\bar{z}$ and find u_0, v_0, u_1 and v_1.

The last procedure is as follows: we solve the equations

$$\frac{\partial x}{\partial t} = u = g_1 - w_1 x, \frac{\partial y}{\partial t} = v = g_2 - w_1 y.$$

Under the ordinary initial conditions x(0)=y(0)=0. Here g_1 and g_2 are the solutions of the classical problem. All this allows us to reconstruct the contours.

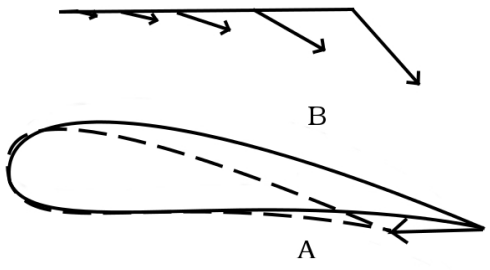

Fig. 1 A – Contour reconstructed from equations with the help of the analytic function, B – Contour reconstructed under w_1 shift.

The solutions of the system depend on parameter w_1. The simplest and most natural way to solve the equations is to determine the value of w_1 from the initial conditions. Then we construct w_0 with the help of condition (5) and boundary conditions.

The next step is to attach the adjacent section to the first one. In general the linear spline does not allow us to glue together values of u and v on the common section so we simply ignore this section and solve the problem only for the newly added third section.

Sections position

Let us now turn to the problem of the adjacent sections mutual positioning. Note first that in general even values of the velocity coordinates may not provide us with the directions of the planes tangent to the constructed surface. For example, in the case of $w_0 = w_1 = 0$ we have absolutely no information on this matter. Also these planes do not define an integrable distribution as the sector height tends to 0 since all the planes are transversal to the sections. Thus we need to introduce another way of this positioning.

Note that we have a wing section as a ruled surface with the lines connecting points on two boundary sections.

Hence the easiest method is the well-known least square method. We apply this method to the set of lengths between points on the contours. Since we obtain the contours as the set of points $C_1 : (x_1^1, y_1^1), \ldots, (x_1^n, y_1^n)$, $C_2 : (x_2^1, y_2^1), \ldots, (x_2^n, y_2^n)$ we are able to consider the function $f(x, y) = \sum_{j=1}^{n} ((x_j^1 - x_j^2 + a)^2 + (y_j^1 - y_j^2 + b)^2)$. Then we find the minimal point (a, b) of this function. Thus we minimize the mean distance between the contours.

Statement.

If the contours C_1 and C_2 are similar then the limit optimal point also minimizes the square of the ruled surface S between C_1 and C_2.

Proof.

Let us consider the triangulation of the surface S so that the triangles has either vertices $(x_1^j, y_1^j), (x_1^{j+1}, y_1^{j+1}), (x_2^j, y_2^j)$ or $(x_2^j, y_2^j), (x_2^{j+1}, y_2^{j+1}), (x_1^j, y_1^j)$. Let us denote the first triangle as Δ_1^j and the second as Δ_2^j.

Then the surface is the sum of the numbers $S_1 = \sum_{j=1}^{n} \Delta_1^j$ and $S_2 = \sum_{j=1}^{n} \Delta_2^j$ limits as $n \to \infty$.

Note that since the contours are similar we have $S(\Delta_2^j) = \alpha S(\Delta_1^j)$ for any $j = 1, \ldots, n$ and some $\alpha > 0$.

The first sum as $n \to \infty$ turns into the integral $\int_{C_1} \sqrt{(x^1(t) - x^2(t) + a)^2 + (y^1(t) - y^2(t) + b)^2}\, dt.$

The minimum of this integral happens at the same point as the minimum of the function f(x, y).

Example 1.

Let us consider the standard velocity distribution. We obtain the following contours:

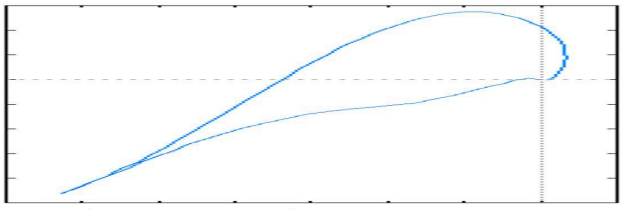

Fig. 2 The lower (longer) section

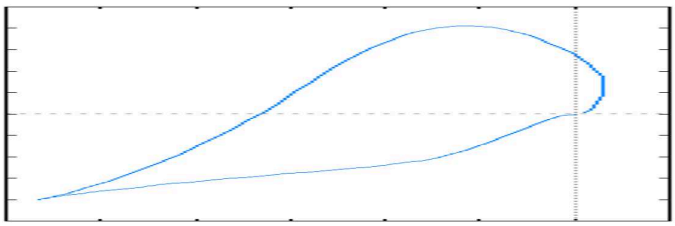

Fig. 3 The upper (shorter) section

Their mutual shift is given by numbers a=-0.089794872821941, being the shift along OX axis, and b=0.191236618879538, being the shift along OY axis. This means that the point with coordinates (0, 0) on the second graph has coordinates (a, b) in the coordinate system of the first graph.

Nonlinear spline and the adjacent sectors gluing

Let us search for the solution in the form of the polynomial quadratic on h:

$u(x,\ y,\ h) = u_0(x,\ y) + h\ u_1(x,\ y) + h^2\ u_2(x,\ y),$

$v(x,\ y,\ h) = v_0(x,\ y) + h\ v_1(x,\ y) + h^2\ \mathrm{v}_2(x,\ y),$

$w(x,\ y,\ h) = w_0(x,\ y) + h\ w_1(x,\ y) + h^2\ \mathrm{w}_2(x,\ y).$

Then similarly to the linear case we have the following relations on $u_j, v_j, w_j,\ j = 0,1,2$:

$$\frac{\partial u_2}{\partial x} = -\frac{\partial v_2}{\partial y}, \frac{\partial u_2}{\partial y} = \frac{\partial v_2}{\partial x}. \tag{6}$$

$$\frac{\partial u_1}{\partial x} = -\frac{\partial v_1}{\partial y} - 2w_2, \frac{\partial u_1}{\partial y} = \frac{\partial v_1}{\partial x}. \tag{7}$$

$$\frac{\partial u_0}{\partial x} = -\frac{\partial v_0}{\partial y} - w_1, \frac{\partial u_0}{\partial y} = \frac{\partial v_0}{\partial x}. \tag{8}$$

Hence the eldest coefficient $w_2 = const$. Also

$$\frac{\partial w_1}{\partial x} = 2u_2, \frac{\partial w_1}{\partial y} = 2v_2. \tag{9}$$

$$\frac{\partial w_0}{\partial x} = u_1, \frac{\partial w_0}{\partial y} = v_1. \tag{10}$$

Thus we have the harmonic functions $w_1(z,\bar{z}) = \frac{1}{2i}(\int (v_2 + iu_2)dz - \overline{\int (v_2 + iu_2)dz})$,

$w_0(z,\bar{z}) = \frac{1}{4i}(\int (v_1 + iu_1)dz - \overline{\int (v_1 + iu_1)dz})$.

Assume that we construct our solution only for two sections. Then we have only two boundary conditions on three functions f_0, f_1 and f_2. Note that w_0 is again defined by u_0 and v_0 and does not suffer any impact from the boundary data.

The construction steps are as follows:

1. For the first section we find w_1, construct the linear spline and obtain $f_0 + hf_1$.
2. For the second sector we fix w_1' and again construct the linear spline.

3. We add to the first solution the function $2hiw_2\overline{z}+h^2f_2=2hiw_2\overline{z}+v_2+iu_2$ so that $2hw_2+w_1=w_1'$. Thus $w_2=\frac{w_1'-w_1}{2h}$.

4. This transforms v_1+iu_1 into $v_1+iu_1-2iw_2\overline{z}$ and v_0+iu_0 changes by $\frac{1}{2i}(\int(v_2+iu_2)dz-\overline{\int(v_2+iu_2)dz})$. Thus we must choose v_2+iu_2 so that the expression $\overline{z}\frac{1}{2}(\int(v_2+iu_2)dz-\overline{\int(v_2+iu_2)dz})+h^2(v_2+iu_2)-2hiw_2\overline{z}$ on the contour is minimal possible.

Similarly we can construct the spline of any degree n.

Then we have n-1 additional anti-analytic summands being the integration constants for $i\int w_2d\overline{z}$ and n-1 analytic compensating functions being the summands of v_k+iu_k. Again the functions $f_k=v_k+iu_k+ik\int w_kd\overline{z}$ are analytic due to relations similar to (9) and (10). At the same time the summands v_k+iu_k and $ik\int w_kd\overline{z}$ are polyharmonic functions. Let us say that the images of v_k+iu_k in the summands w_{k-1} and subsequently $v_{k-2}+iu_{k-2}$ are iterations of v_k+iu_k.

Note that the coefficient with any degree of $z^l\overline{z}^m$ in the last iteration of v_n+iu_n is similar to $\frac{n!}{(n/2)!^2\,2^{n/2}}\approx 2^k$. This fact allows us to approximate the contours on the common section of the adjacent wing sectors.

The approximation is as follows:

We approximate the function $iw_1\overline{z}$ with the n/2-th iteration, i.e. the summand of v_0+iu_0 of the function constructed with the help of v_n+iu_n. The norms of this function iterations diminish as we move from level 0 up to the n-th one by 1/2. So the difference norm is majored by $\sum_{k=1}^{n/2}\frac{h^k}{2^k}\|w_1\overline{z}\|_\infty$ and does not exceed $h^2\|w_1\overline{z}\|_\infty$.

Then we approximate all the penultimate iteration of v_n+iu_n, i.e. the summand of v_2+iu_2, with the ultimate iteration of $v_{n-2}+iu_{n-2}$. Thus we make the difference norm strictly less than $h^4\|w_1\overline{z}\|_\infty$.

The next step is approximation of the third from the last iteration of v_n+iu_n and the penultimate iteration of $v_{n-2}+iu_{n-2}$ by the last iteration of $v_{n-4}+iu_{n-4}$. This makes the difference norm no greater than $h^6\|w_1\overline{z}\|_\infty$. And so on. Thus the greater degree on h we consider and the smaller is h the better is the approximation.

So the greater degree on h we consider and the less is the step the better is the correspondence between contours of the adjacent wing sections.

References

[1] W. Mangler: J. Deutschen Luftfahrtforschung, Vol. 1 (1938), p. 146

[2] M. T. Nuzhin and G. G. Tumashev: Trudy Sem. Kraev. Zadacham Vyp. Vol. 7 (1970), pp. 18—27

[3] A. M. Elizarov and N. B. Il'inskii: Soviet Mat. Vol. 10 (1984), pp. 50—59

[4] A.M. Elizarov and D.A. Fokin: ZAMM, Vol. 79 (1999), pp. 757—762

[5] P. N. Ivan'shin: Russian Math. Vol. 57 (2013), pp. 9—19

[6] P. Ivanshin and E. Shirokova: IMA Journal of Applied Mathematics, doi: 10.1093/imamat/hxs009

[7] E.A. Shirokova and P.N. Ivanshin: *Spline-Interpolation Solution of One Elasticity Theory Problem* (Bentham e-books, 2011)

Applied Mechanics and Materials Vol. 565 (2014) pp 67-73

doi:10.4028/www.scientific.net/AMM.565.67

Modeling and Simulation of Solar Array Drive Assembly Disturbance Driving a Flexible Load

Jiangpan Chen*[1, a], Wei Cheng[1,b] and Yunfeng Wang[1,c]

[1]School of Aeronautic Science and Engineering, Beijing University of Aeronautics and Astronautics, Beijing 100191, China

[a]chenjiangpan@hotmail.com, [b]cheng_wei@buaa.edu.cn, [c]wangyunfengdoc@126.com

Keywords: Solar Array Drive Assembly, disturbance model, flexible load, disturbance frequencies.

Abstract. SADA (Solar Array Drive Assembly) is used to drive solar array rotating in spacecraft in order to get the most solar energy. The disturbance generated by SADA driving its load will influence the imaging quality and pointing accuracy of spacecraft. This research focuses on the disturbance properties of SADA driving a flexible load. Firstly, the disturbance model of SADA driving no load is obtained by deducing and simplifying the electromagnetic model of SADA. Secondly, the disturbance model of SADA driving a flexible load (a three-degree of freedom inertia-spring-damping system) is achieved based on the disturbance model of SADA driving no load. Finally, the disturbance model of SADA driving a flexible load is simulated by using Matlab/Simulink toolbox. The simulation result shows that: the disturbance frequencies of SADA driving a flexible load are consisting of all the natural frequencies of the coupled mechanical system and the input frequency of the electrical pulse signal and its harmonic frequencies.

Introduction

The micro-vibrations of spacecraft have a significant influence on its imaging quality and pointing accuracy. There are many possible disturbance sources in spacecraft, such as Control Moment Gyroscopes, Reaction/Momentum Wheels and SADA [1]. SADA is a typical rotation moving part in spacecraft, and the contribution of the disturbance generated by SADA driving solar array rotating to spacecraft micro-vibrations cannot be ignored. As solar array is a flexible device, to study on the disturbance of SADA driving a flexible load is helpful for analyzing the disturbance properties of SADA driving solar array rotating.

The SADA discussed in this paper is a two-phase hybrid stepper motor, and its subdivision number is 32. Stepper motor is an actuator which transforms electrical pulse signal into angular displacement [2]. Because of its simple structure, high positioning accuracy and no accumulating error[3], stepper motor has been widely used in aerospace field. Both solar array and digital attena of spacecraft use stepper motor as the drive assembly.

Many articles have studied on SADA. Reference [3] presents the dynamic model of SADA, reference [4] studys on the reliability of SADA, reference [5] invents a new acutator of SADA, and reference [6,7] emphasise on the study of SADA control methods. However, references on SADA disturbance is poor. The purpose of this paper is to study on the disturbance properties of SADA driving a flexible load, and it laids a solid foundation for studying on the disturbance of SADA driving the real solar array working in space.

Disturbance Model of SADA Driving No Load

The output magnetic energy of SADA is presented as

$$W = \frac{1}{2}\mathbf{L}\mathbf{I}^2. \tag{1}$$

Where **L** is the symmetric and positive definite inductance matrix, **I** is the current vector. And they are given by

$$\mathbf{I}=\begin{bmatrix} I_A & I_B & I_f \end{bmatrix}^T;\mathbf{L}=\begin{bmatrix} L_{AA} & L_{AB} & L_{Af} \\ L_{AB} & L_{BB} & L_{Bf} \\ L_{Af} & L_{Bf} & L_{ff} \end{bmatrix}. \tag{2}$$

Where I_A and I_B is the current of phase A and phase B respectively, I_f is the equivalent current excited by rotor permanent magnet, L_{ii} (i=A, B) is the self-inductance of winding A and B, L_{ij} (i, j=A, B) is the mutual inductance between phases A and B, L_{ff} is the self-inductance of the fictitious rotor winding, L_{if}(i=A, B) is the mutual inductance between phases A, B and the fictitious rotor current I_f [8]. Ignoring the second and more harmonics of the cyclical permeance function [5], each component of the inductance matrix **L** is given by

$$\begin{aligned} &L_{AA}=L_{BB}=L_0;L_{AB}=0;L_{Af}=L_{m0}+L_{m1}\cos(z\theta); \\ &L_{Bf}=L_{m0}+L_{m1}\sin(z\theta);L_{ff}=L_{f0}+L_{f1}\cos(4z\theta). \end{aligned} \tag{3}$$

Where z is the rotor teeth number and θ is the angle of the rotor has turned.

The output torque of SADA is obtained by the derivative of magnetic energy on rotation angle.

$$T_e=\frac{\partial W}{\partial\theta}=\frac{1}{2}\mathbf{I}^T\frac{\partial\mathbf{L}}{\partial\theta}\mathbf{I}. \tag{4}$$

Substituting Eq.2 and Eq.3 into Eq.4, the output torque of SADA can be shown as

$$T_e=K_t\left[I_B\cos(z\theta)-I_A\sin(z\theta)\right]-D\sin(4z\theta). \tag{5}$$

Where K_t=zI_fL_{m1} is the electromagnetic torque coefficient, D=$2zI_f^2L_{fl}$ is the detent torque coefficient, and K_t and D are all constants. I_A and I_B are given by

$$I_A=I\cos(\gamma i);I_B=I\sin(\gamma i). \tag{6}$$

Where I is the amplitude of I_A and I_B, γ is the electrical angle of each micro-step after subdivision, i=1,2, ⋯. γ is given by

$$\gamma=\frac{2\pi}{pn}. \tag{7}$$

Where p is the beat number, n is the subdivision number.

Substituting Eq.6 into Eq.5, the output torque of SADA can be written as

$$T_e=K_tI\sin(\gamma i-z\theta)-D\sin(4z\theta). \tag{8}$$

In the right side of Eq.8, the first part is called electromagnetic torque, and the second part is called detent torque. Detent torque is far less than electromagnetic torque which can be ignored [8]. So Eq.8 can be simplified as

$$T_e=K_tI\sin\left[z\left(\frac{\gamma i}{z}-\theta\right)\right]. \tag{9}$$

In Eq.9, the physical meaning of ($\gamma i/z$-θ) is that: ($\gamma i/z$-θ) is the included angle between rotor's real position and theoretical equilibrium position during the time that after the input of electrical pulse signal i completed and before the input of electrical pulse signal (i+1), where $\gamma i/z$ is rotor's theoretical equilibrium position in this period and θ is rotor's real position. To ensure SADA rotating without losing step, the range of ($\gamma i/z$-θ) is given by

$$-\frac{\gamma}{z} \le \frac{\gamma i}{z} - \theta \le \frac{\gamma}{z}. \tag{10}$$

Where γ/z is the micro-step angle of SADA after subdivision. In this paper, the rotor teeth of SADA z is 50, the beat number p is 4 and the subdivision number n is 32. Substituting Eq.7 into Eq.10, it can be written as

$$-\frac{\pi}{64} \le z\left(\frac{\gamma i}{z} - \theta\right) \le \frac{\pi}{64}. \tag{11}$$

What can be obtained from Eq.11 is that: $z(\gamma i/z$-$\theta)$ is very small, so Eq.9 can be written as

$$T_e = K_t I \gamma i - K_t I z \theta. \tag{12}$$

The dynamic model of SADA is presented in reference [3], which is shown as

$$J_0 \ddot{\theta} = T_e - C_0 \dot{\theta}. \tag{13}$$

Where J_0 is the moment of inertia of SADA rotor, C_0 is the internal damping of SADA. Substituting Eq.12 into Eq.13, the disturbance model of SADA driving no load can be obtained as

$$J_0 \ddot{\theta} + C_0 \dot{\theta} + K_0 \theta = K_t I \gamma i. \tag{14}$$

Where K_0=$K_t Iz$ is the electromagnetic stiffness [8].

A significant conclusion can be achieved from Eq.14: when SADA rotates driving no load, it can be equivalent to an inertia-electromagnetic spring-damping system, in other words, the rotor of SADA vibrates with damping under the exciting force of stator. K_0 is the stiffness of electromagnetic spring, ($K_0\theta$) is the restoring force of electromagnetic spring, ($K_t I \gamma i$) is the exciting force of the stator which is a step wave.

Assuming that the stator of SADA is a rigid body, then the torque of the stator acting on the rotor equals to the torque of the stator acting on the spacecraft body. The torque of the stator acting on the rotor equals to the moment of inertia of the rotor times the rotor acceleration, therefore, the torque of the stator acting on the spacecraft body is obtainded as

$$T_d = J_0 \ddot{\theta} = K_t I \gamma i - C_0 \dot{\theta} - K_0 \theta. \tag{15}$$

Then T_d is the disturbance torque of SADA.

Most of the dynamic simulations of SADA use its dynamic model (Eq.13) so far. However, there is no explicit formulation of the electromagnetic stiffness in the dynamic model, the coupling effect of the electromagnetic spring and the flexible load is difficult to reflect when SADA rotates driving a flexible load. The disturbance model of SADA (Eq.14) can easily solve this problem.

Disturbance Model of SADA Driving a Flexible Load

In order to study the disturbance properties of SADA driving a flexible load, a three-degree of freedom inertia-spring-damping system is taken as the flexible load. The simplified dynamic model of SADA driving this flexible load is shown in Fig.1.

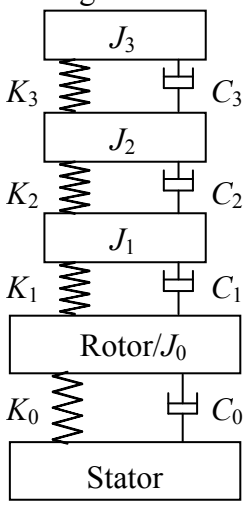

Fig.1 Simplified dynamic model of SADA driving the flexible load

The disturbance model of this mechanical system is shown as

$$\mathbf{J}\ddot{\boldsymbol{\theta}}+\mathbf{C}\dot{\boldsymbol{\theta}}+\mathbf{K}\boldsymbol{\theta}=\mathbf{T}. \tag{17}$$

Where $\mathbf{J}$, $\mathbf{C}$, $\mathbf{K}$, $\mathbf{T}$ and $\boldsymbol{\theta}$ are given by

$$\begin{aligned}
\mathbf{J}&=\begin{bmatrix} J_0 & 0 & 0 & 0 \\ 0 & J_1 & 0 & 0 \\ 0 & 0 & J_2 & 0 \\ 0 & 0 & 0 & J_3 \end{bmatrix};\mathbf{C}=\begin{bmatrix} C_0+C_1 & -C_1 & 0 & 0 \\ -C_1 & C_1+C_2 & -C_2 & 0 \\ 0 & -C_2 & C_2+C_3 & -C_3 \\ 0 & 0 & -C_3 & C_3 \end{bmatrix}; \\
\mathbf{K}&=\begin{bmatrix} K_0+K_1 & -K_1 & 0 & 0 \\ -K_1 & K_1+K_2 & -K_2 & 0 \\ 0 & -K_2 & K_2+K_3 & -K_3 \\ 0 & 0 & -K_3 & K_3 \end{bmatrix};\mathbf{T}=\begin{bmatrix} K_t I\gamma i \\ 0 \\ 0 \\ 0 \end{bmatrix};\boldsymbol{\theta}=\begin{bmatrix} \theta_0 \\ \theta_1 \\ \theta_2 \\ \theta_3 \end{bmatrix}.
\end{aligned} \tag{18}$$

The disturbance torque of SADA driving this flexible load is obtained as

$$T_d=K_t I\gamma i-C_0\dot{\theta}-K_0\theta. \tag{19}$$

Simulation

Matlab/Simulink toolbox is used to simulate the disturbance model of SADA driving a flexible load. The principle diagram of the simulation is shown in Fig.2.

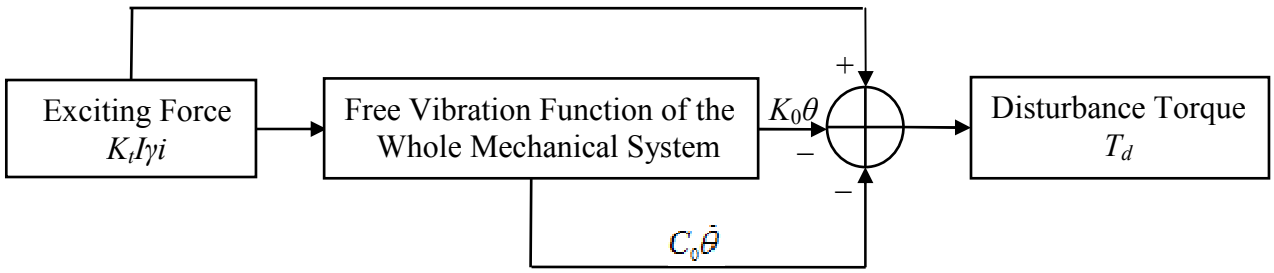

Fig.2 Principle diagram of the simulation

The simulation parameters are shown in Tab.1. The simulation result of the exciting force of the stator ($K_tI\gamma i$) in time domain is shown in Fig.3. The simulation result of the disturbance torque T_d in frequency domain is shown in Fig.4.

Tab.1 Simulation parameters

Parameter	Physical Meaning	Value	Units
z	Rotor Teeth	50	——
p	Beat Number	4	——
n	Subdivision Number	32	——
I	Current Amplitude	0.1	[A]
K_t	Electromagnetic Torque Coefficient	10	[N.m/A]
ω	Rotor Speed	π/432	[rad/s]
C_0	Internal Damping	0.005	[N.m.s/rad]
C_1	Damping of Load	0.005	[N.m.s/rad]
C_2	Damping of Load	0.005	[N.m.s/rad]
C_3	Damping of Load	0.005	[N.m.s/rad]
J_0	Moment of Inertia of Rotor	0.01	[kg.m^2]
J_1	Moment of Inertia of Load	0.19	[kg.m^2]
J_2	Moment of Inertia of Load	0.1	[kg.m^2]
J_3	Moment of Inertia of Load	0.2	[kg.m^2]
K_0	Electromagnetic Stiffness	50	[N.m/rad]
K_1	Stiffness of Load	100	[N.m/rad]
K_2	Stiffness of Load	150	[N.m/rad]
K_3	Stiffness of Load	200	[N.m/rad]

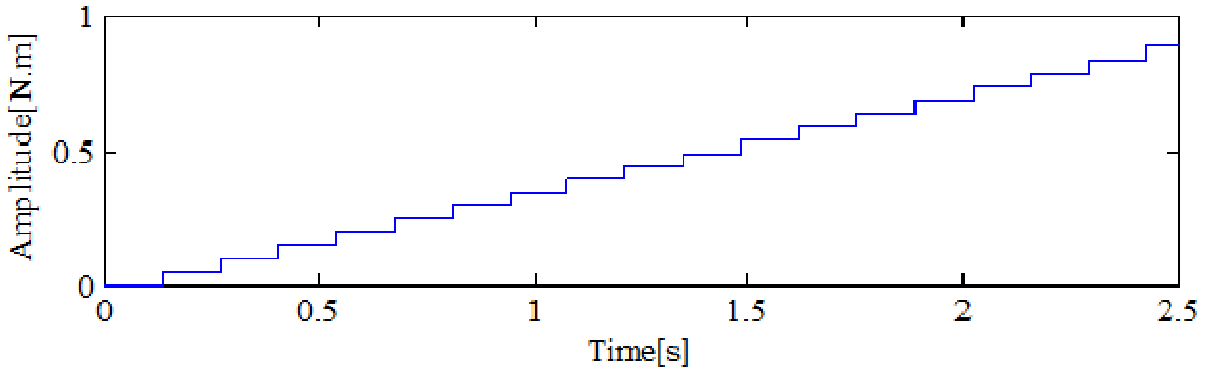

Fig.3 Simulation result of the exciting force in time domain

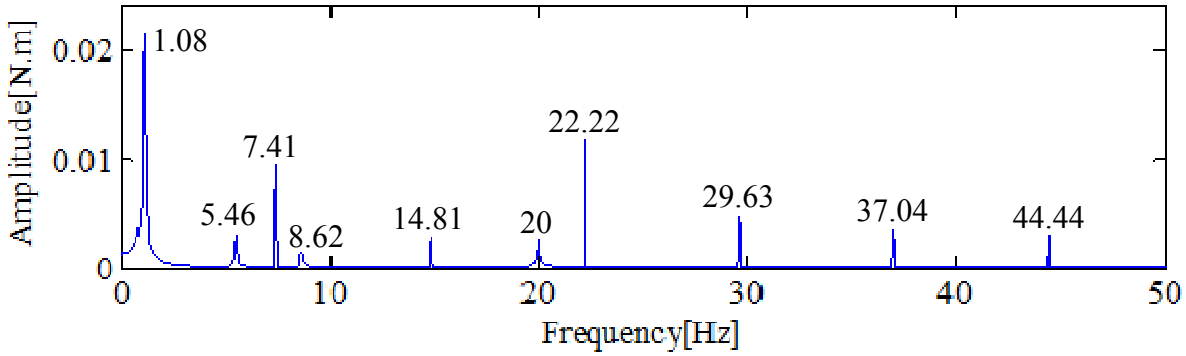

Fig.4 Simulation result of the disturbance torque in frequency domain

The free vibration function of the whole mechanical system is

$$\mathbf{J}\ddot{\boldsymbol{\theta}}+\mathbf{C}\dot{\boldsymbol{\theta}}+\mathbf{K}\boldsymbol{\theta}=\mathbf{0}. \tag{20}$$

Substituting Eq.18 and the simulation parameters in Tab.1 into Eq.20, the natural frequencies of the coupled mechanical system consisting of the electromagnetic spring and the flexible load can be obtained in Tab.2.

Tab.2 Natural frequencies

Frequency Order	1	2	3	4
Frequency[Hz]	1.08	5.46	8.62	20

The input frequency of electrical pulse signal of SADA is related to the rotor teeth number, beat number, subdivision number and rotor speed, which is shown as

$$f_1=\frac{zpnw}{2\pi}. \tag{21}$$

Substituting the parameters in Tab.1 into Eq.21, the value of f_1 can be obtained as

$$f_1=7.41\text{Hz}. \tag{22}$$

A significant result can be obtained from Fig.4, Tab.2 and Eq.22 that: the disturbance frequencies of SADA driving a flexible load are consisting of all the natural frequencies of the coupled mechanical system and the input frequency of the electrical pulse signal and its harmonic frequencies.

Summary

In this paper, the disturbance model of SADA driving a flexible load is obtained, and Matlab/Simulink toolbox is used to simulate this disturbance model. As the real solar array is a flexible device, all the conclusions obtained from this paper laid a solid foundation for studying on the disturbance properties of SADA driving the real solar array working in space.

References

[1] P.F. Zhang, W. Cheng, Y. Zhao. Measure of Reaction Wheels Disturbance Considering Coupling Effect, J. Journal of Beijing University of Aeronautics and Astronautics (2011)

[2] M.J. Li, B.D. Liu. Study on Electromagnetic Torque of Stepping Motor Subdivided Driving, J. Control Engineering of China (2013)

[3] Z.H. Si, Y.W. Liu, K. L. Research on Modeling and Design of Solar Array Drive Assembly, J. Aerospace Control and Application (2012)

[4] L. Shi. Reliability Analysis of Solar Array Drive Assembly, D. University of Electronic Science and Technology of China (2011)

[5] S.Y. He. Research of All Digital Two-phase Hybrid Stepper Motor Drivers, D. Central South University (2008)

[6] Elsodany N M, Rezeka S F, Maharem N A. Adaptive PID Control of a Stepper Motor Driving a Flexible Rotor, J. Alexandria Engineering Journal (2011)

[7] Qun Q F, Xue-Dong J, Shi-qing Z. Design of Stepping Motor Control System Based on AT89C51 Microcontroller, J. Procedia Engineering, (2011)

[8] Yang Y L, Cheng W, Wu S J, et al. Experiment and Simulation of Electromagnetic Stiffness for Stepper Motor, J. Applied Mechanics and Materials (2010)

[9] Bodson M, Sato J S, Silver S R. Spontaneous Speed Reversals in Stepper Motors, C. Decision and Control, 2003. Proceedings. 42nd IEEE Conference on. IEEE (2003)

Applied Mechanics and Materials Vol. 565 (2014) pp 74-79

doi:10.4028/www.scientific.net/AMM.565.74

Modeling of Atmospheric Processes Based on the Averaged Navier-Stokes Equations

Bakytzhan Zhumagulov, Dauren Zhakebaev, Aigerim Abdibekova

71, al-Farabi av., Almaty, Kazakhstan

dauren.zhakebaev@kaznu.kz , a.aigerim@gmail.com

Keywords: Atmospheric process, Dynamic process, Navier - Stokes equations, Large eddy simulation, Rayleigh-Taylor instability process.

Abstract. This work is devoted to the mathematical and numerical modeling of atmospheric processes based on the ensemble -averaged Navier-Stokes equations with the implementation of large eddy simulation. Within the real scientific research work are shown features of modeling atmospheric processes, the mathematical model of dynamic processes was developed in the average atmosphere, the numerical scheme and algorithm of the problem solution were developed, and realization of the problem characterized by instability of Rayleigh-Taylor about convective mass substances transfer with various densities was made.

Introduction

Study of the atmosphere is one of the actual problems of the modern science connected with the solving both fundamental problems of theoretical physics and applied physics, concerning various ranges radio waves distribution in atmospheric layers. Despite the huge amount of experimental data only a relatively small number of studies have been attempts from theoretical positions to explain the observed disturbances in the atmosphere from terrestrial and atmospheric sources. It should be noted that the works in this area played a significant role in the understanding the mechanism of connection in the system the lithosphere – the atmosphere - the ionosphere. In the last decade due to the computer performance increase and the emergence of powerful computing clusters, as well as the development of computational hydrodynamics a new direction in atmospheric physics – study the dynamics of the ionosphere by numerical solutions of nonlinear equations of geophysical fluid dynamics. The application of such numerical methods allows considering many factors in common. [1-3].

For the purpose of better conception the atmosphere is divided into layers - areas in which the maxima concentration of free electrons per unit volume are reached [4, 5]. Such separation allows scientists to examine atmospheric processes as Rayleigh-Taylor instability process. As the field of study the layers which are characterized by different properties, including different concentrations of substances, different densities, different temperatures and etc., are selected [6]. It is required to determine the unstable convective process as well as its impact on the atmospheric chaos, on the turbulence that occurs in the atmosphere. Here it is necessary to note about the so-called Rayleigh-Taylor instability problem, as well as Rayleigh-Benard problem, the implementation of which contributes the solution of the problem of modeling some atmospheric processes.

It is important to note, that in this case if the pulsing volume forces connected with the velocity of pulsation, have strong impact on nature turbulence. The simplest example is the gravity strong impact on a current with density pulsations. If the density pulsations caused by the fact that there is an average gradient of density in that direction, as an average gradient of velocity, or when the current occurs due to the difference of average densities, then between pulsations of density and velocity, a good correlation is available and buoyancy force impact can be very great. In the case where the density decreases upward faster than it is necessary to preserve environment hydrostatic balance, then the existing turbulent energy can be converted into potential energy which means that the turbulent mixing tends to reduce the density gradient, and thus to increase the volume of the center of gravity of the environment.

Within the real research, we consider cubic area, where in the cube there is an incompressible flow with different density - ρ_1 and ρ_2. (Fig. 1) and its streams are transferred in this area as a results of infringement of stability. The problem is to calculate and display convective transfer inside the cube based on the implementation of the method described herein. Modeling is carried out for various Rayleigh numbers: Ra=10^5, Ra=10^6, Ra=10^7.

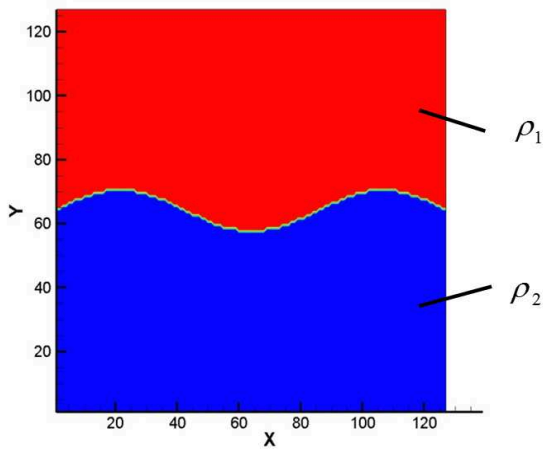

Fig. 1. The gradient of concentration changes at the initial time.

Statement of the Problem

In this work, we consider the case when the density increased in the vertical direction from the bottom to up, we have unstable flow, and the interrelation of density and velocity can lead to transformation of potential energy to turbulent kinetic energy. To estimate flow instability it is necessary numerically modeling all the physical parameters change in accordance with time at different Rayleigh numbers.

Numerical modeling of the problem is carried out based on Navier - Stokes non-stationary filtered equations solution, with the continuity equation and equation for concentration in the Cartesian coordinate system:

$$\begin{cases} \dfrac{\partial \overline{u}_i}{\partial t} + \dfrac{\partial}{\partial x_j}\left(\overline{u}_i \overline{u}_j\right) = -\dfrac{\partial \overline{p}}{\partial x_i} + \dfrac{1}{\mathrm{Re}} \dfrac{\partial^2 \overline{u}_i}{\partial x_j \partial x_j} - \dfrac{\partial \tau'_{ij}}{\partial x_j} + \dfrac{1}{Fr}, \\ \dfrac{\partial \overline{u}_j}{\partial x_j} = 0, \\ \dfrac{\partial \overline{C}}{\partial t} + \overline{u}_j \dfrac{\partial \overline{C}}{\partial x_j} = \dfrac{1}{Pe} \dfrac{\partial^2 \overline{C}}{\partial x_j^2} - \dfrac{\partial Q_j}{\partial x_j}, \\ where \quad \tau_{ij} = \overline{u_i u_j} - \overline{u}_i \overline{u}_j, \\ Q_j = \overline{u_j C} - \overline{u}_j \overline{C}. \end{cases} \tag{1}$$

Where $\overline{u}_i$ – velocity of components, $\overline{p}$ – pressure, t – time, C – medium concentration, $\rho(C) = \rho_1 C + \rho_2 (1 - C)$ – concentration density, $Ra = \dfrac{g\beta L^3 \Delta C}{\nu D}$ – the Rayleigh number, ν –

kinematic coefficient of viscosity, g – acceleration of gravity, η – dynamic viscosity coefficient, D – diffusion coefficient, β – temperature coefficient of the heat transfer volume expansion, $Sc = \frac{\eta}{D\rho(c)}$ – the Schmidt number, $Gr = \frac{Ra}{Sc}$ – the Grashof number, $Fr = \frac{\mathrm{Re}^2}{Gr}$ – the Froude number, $\mathrm{Re} = \sqrt{Gr}$ – the Reynolds's number, $Pe = Sc \cdot \mathrm{Re}$ – the Peclet number, L – characteristics length, $\tau_{i,j}$ – subgrid tensor which is responsible for small-scale structures, Q_j – scalar transfer of concentration.

Viscous model is used for modeling subgrid tensor, which is represented as $\tau_{ij} - \frac{\delta_{ij}}{3}\tau_{kk} = -2\nu_T \overline{S}_{ij}$, where $v_T = C_S \Delta^2 \left(2\overline{S}_{ij}\overline{S}_{ij}\right)^{1/2}$ - turbulent viscosity; $\delta_{ij} = \begin{cases} 1, i = j \\ 0, i \neq j \end{cases}$ - the Kronecker symbol; C_S - empirical coefficient; $\Delta = \left(\Delta_i \Delta_j \Delta_k\right)^{1/3}$ - the width of the grid filter; $\overline{S}_{ij} = \frac{1}{2}\left(\frac{\partial \overline{u}_i}{\partial x_j} + \frac{\partial \overline{u}_j}{\partial x_i}\right)$ - the value of the strain rate tensor [3, 4].

There is a closing model for scalar transfer of concentration. Other spatially compact filters including asymmetric filters give comparable results with changes in decomposition coefficients below. It is supposed that the filtering operation is performed with spatial derivatives, which is valid for spatially homogeneous filter [7].

Traditional procedure consists in using large-scale and physical parameters for modeling of non-closed terms in the Eq.1. The form of a diffusive gradient is often adopted where the scalar flow of subgrid filter model is connected with the gradient of the solution amounts: $Q_j = -k_{TC}\frac{\partial C_\alpha}{\partial x_j}$, where k_{TC} -is an eddy scalar diffusivity. Among large eddy models Smagorinsky's model using is whidespread which takes the following form: $k_{TC} = \frac{1}{\sigma_T}(C_s\Delta)^2\left(\overline{S}_{ij}\overline{S}_{ij}\right)^{1/2}\overline{S}_{ij}$ where σ_T - the Schmidt's turbulent number (gets out equal 1).

The initial conditions for concentration defined as follows:

$$C = \begin{cases} 1, \ z \geq A\sin(3\pi y) + \frac{1}{2}, \ 0 \leq y \leq L_2, \\ 0, \ z < A\sin(3\pi y) + \frac{1}{2}, \ 0 \leq y \leq L_2. \end{cases} \quad (2)$$

for the velocity components: $U_i = 0, \ i = 1, 2, 3.$ (3)

The boundary conditions for the above problem is selected value of C=0 on the top and bottom sides of the cube. For the other walls of the cube:

$$\frac{\partial C}{\partial x_i} = 0, \quad i = 1, 2, 3. \quad (4)$$

Boundary conditions for velocity:

$$U_i|_\Gamma = 0, \ i = 1, 2, 3. \quad (5)$$

Numerical method

To solve the Navier-Stokes equation Eq.1 the splitting scheme in physical parameters is used, which consists of three stages.

$$\text{I.}\quad \frac{\vec{u}^{*}-\vec{u}^{n}}{\tau}=-\left(\vec{u}^{n}\nabla\right)\vec{u}^{*}+\frac{1}{\mathrm{Re}}\Delta\vec{u}^{*}-\nabla\tau^{u}+\frac{1}{Fr}, \tag{6}$$

$$\text{II.}\quad \Delta p=\frac{\nabla\vec{u}^{*}}{\tau}, \tag{7}$$

$$\text{III.}\quad \frac{\vec{u}^{n+1}-\vec{u}^{*}}{\tau}=-\nabla p. \tag{8}$$

$$\text{IV.}\quad \frac{C^{n+1}-C^{n}}{\tau}=-\left(\vec{u}^{n}\nabla\right)C+\frac{1}{Pe}\Delta C-\nabla Q \tag{9}$$

At the first stage, the Navier-Stokes equation is solved without pressure. For the approximation of the convective and diffusive members of equation, the compact scheme of high accuracy is used [8]. During the second stage, Poisson equation is solved which is resulted from the continuity equation considering the first stage field of velocities. For solving the three-dimensional Poisson equation, the solution algorithm developed to the spectral transformation in combination with matrix factorization. The pressure field is used for computing the final field of velocities at the third stage. During the last stage, in the set area the concentration equation according to the founded velocities field considering the different densities of the flow is solved.

Results of modeling

To estimate the flow instability was carried out some calculations of three-dimensional non stationary problem (Eq. 1) in the L1 = L2 = L3 = 1 domain, for different Rayleigh numbers: Ra = 105, Ra = 106, Ra = 107, value of the Schmidt number is taken as Sc = 1. Calculations were made at the uniform rectangular staggered grids 128x128x128. The time step was set equal to 0.005.

The simulation results shown in Figures 2 - 4 illustrate the concentration gradient changes over time, for different Rayleigh numbers. Established that with increasing values of the Rayleigh number convective structures sizes increase, which leads to increase the turbulent kinetic energy. Determined that the rate accrue rapidly, the convective flow becomes unsteady.

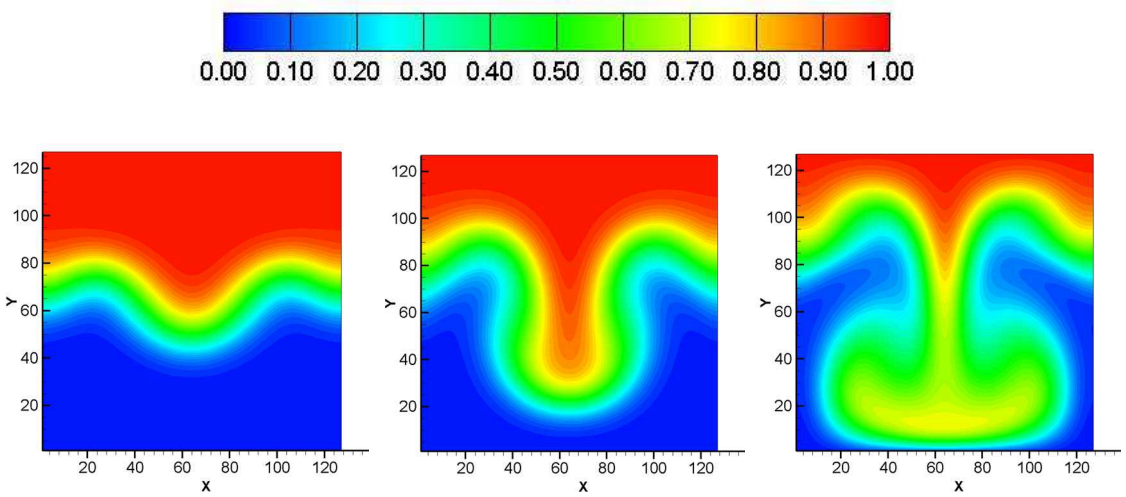

Fig. 2. The concentration gradient changes over time, with Ra=10^5:

(a) t=0.1; (b) t=0.4; (c) t=0.7;

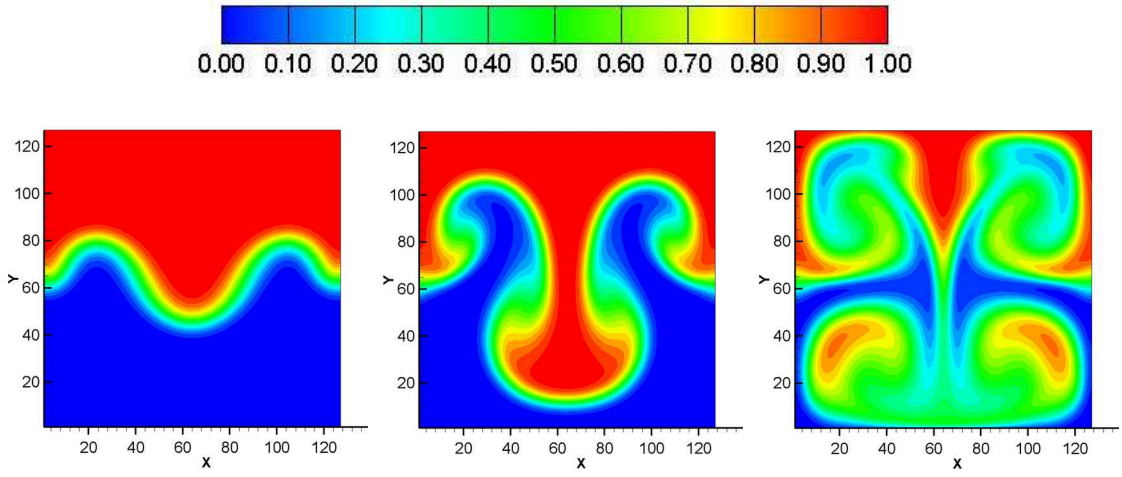

Fig. 3. The concentration gradient changes over time, with $Ra=10^6$:

(a) t=0.1; (b) t=0.4; (c) t=0.7;

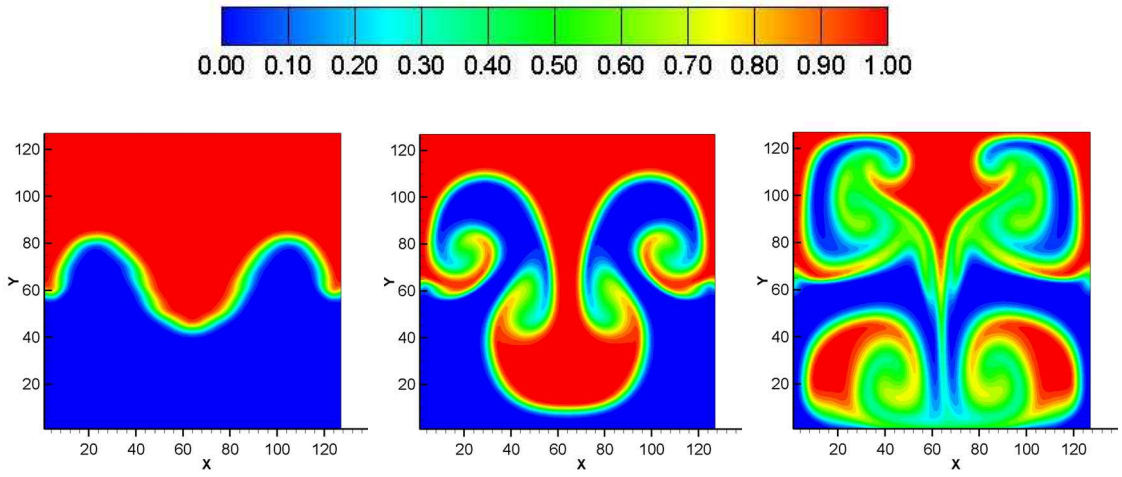

Fig. 4. The concentration gradient changes over time, with $Ra=10^7$:

(a) t=0.1; (b) t=0.4; (c) t=0.7;

Summary

Thus within the real work atmospheric processes modeling features are studied, mathematical model of dynamic processes in the average atmosphere is developed. The realization of problem was made, where at Rayleigh number variation, when the number reaches some critical value convective transfers of flow occurs in a liquid. Laminar flow observed at the Rayleigh small and large numbers, as shown in figures 2-4, upon termination of time laminar stream turns into turbulent flow, where in the flow spontaneously formed numerous vortexes of different sizes. The small-scale as well as the large-scale eddies, formed in turbulent slow contribute development the kinetic energy of the flow. With increasing the kinetic energy, there are observed chaotic moving of layers and increasing the rate of the mixing process.

Providing results of convective transfer of mass substances of different densities illustrate Rayleigh number impact on the flow stability.

References

[1] S.A. Kitaygorodsky: *Physics of atmosphere-ocean interaction*. L. Hydrometeopub (1970), p. 183

[2] A.C. Newell, T. Passot, and J. Lega: Order parameter equations for patterns. Annual Rev. Fluid Mechanics. Vol. 25, (1993) p. 399-453.

[3] J.P. Gollub and S.V. Benson: Many routes to turbulent convection. Journal of Fluid Mechanics, Vol.100, Issue 3, (1980), p. 449-470.

[4] B. Migulin: Ionosphere and its study. RADIO, (1987) number 11.

[5] M. Dubois, P. Bergi: Experimental evidence for the oscillations in a convective biperiodic regime. Phy. Letters A (1980), Vol.76, Issue 1, p. 53-56.

[6] Y. A. Kucherenko, O. E. Shestachenko, Y. A. Piskunov, E. V. Sviridov, V. M. Medvedev, and A.I.Baishev: Experimental investigation into the self-similar mode of mixing of different density gases in the Earth's gravitational field. Laser Part. Beams, Vol. 21, Issue 3, (2003), p.385-388.

[7] S. Ghosal and P. Moin: The basic equations for the large-eddy simulation of turbulent flows in complex geometry. J.Comp.Phys. Vol.118, (1995), p. 24- 37.

[8] U.S. Abdibekov, B. T. Zhumagulov, D. B. Zhakebaev, and K. J. Zhubat: Degeneration of isotropic turbulence modeling based on large eddies. Mathematical modeling, Vol. 25, Issue 1, (2013), p. 18-32.

Applied Mechanics and Materials Vol. 565 (2014) pp 80-84

doi:10.4028/www.scientific.net/AMM.565.80

Exploration of Navigation Simulator Applying in Maritime Trial

Jinlong Wu[a], Huiling Guo[b]

No. 8 Yashen Road, Haihe Education District, Tianjin, 300350, China

[a] email:wujinlong4000@163.com, [b]email: guoguo3425@126.com

Keywords: Navigation Simulator, Maritime Trial, Application

Abstract. Navigation simulator is a product of highly developed maritime technology, the STCW 78/95 Convention puts forward the corresponding requirements on the application of the navigation simulator. This paper analyzes the current applying status of navigation simulator, discusses the professional technical characteristics of maritime cases and limitations of traditional maritime trial, points out the relative hysteresis quality of the maritime trial in application of navigation technology, and makes a prospect for the application of navigation simulator in trial maritime, including assisting the judges to ascertain the facts of cases and fix the evidence to promote case hearing rapidly and improve the scientific judgment.

Introduction

Maritime trial work takes an important mission to provide high quality and efficient judicial guarantees for the development of the shipping industry and construction of shipping center, and plays an important role in maintaining of shipping order and promoting social stability. In the current context of rapid development of world shipping, shipping accidents occur frequently, that the maritime trial is also faced with unprecedented development opportunities and more challenges. With the development of maritime technology, maritime simulators play the major role in the crew education, training and evaluation, and with the improvement of technology innovation and requirements of the Convention, the function of maritime simulator is constantly improved, and its applications are also exploring gradually,the usage of navigation simulator in trial practice will become a new research field of its application, which will have a significant meaning for the effective identify of evidence, improvement of trial efficiency and the maintenance of justice.

The structure, function and application of navigation simulator

The basic structure and function of navigation simulator

Tianjin Maritime College adopts a set of navigation simulator from Norwegian in 2012, which has the world's advanced performance on the market today, it could provide the most realistic work environment in all aspects of ship maneuvering and collision prevention, crew training, examination and assessment, including the devices of radar and ARPA, ECDIS, steering instrument, GPS, depth sounder, the meter instrument, and etc. The functions of simulator covers AIS, VDR, sailing and watch, ship maneuvering, cargo stowage, GMDSS and internal and external communications, inter-ship sound signals, light communication, the emergency functions in a variety of states in order to meet the demands of new technologies.

The Sea Voyage Data Recorder (VDR), can automatically record the ship status and operating information and access to navigational data equipment, will plays a key role in investigating the accident, identifying the cause and fixing the responsibility. In the core of computer, the Electronic Chart Display and Information System (ECDIS) connects positioning, sounding, radar and other equipment, based on the electronic chart, comprehensively reflects of the state of the ship running, offering a variety of information query, calculation and the specialized tools for sailing records. Automatic Identification System (AIS), is a radio response system on ship operating in VHF marine band, that could send ship identification, position and signal to other ships and shore in certain update rate. The implement of functions of Marine simulator VDR, ECDIS, AIS makes it more integrity for the simulator, which could record the static and dynamic parameters of the training

process in real time, show the trace of each ship. Through the simulator, you can repeat the training process, display the realistic motion of ship, providing a real-time and more accurate dynamic information, to facilitate the analysis of the reasonableness of the key measures.

The application of navigation simulator under the requirement of the new Convention

Applications of navigation simulator and the "The International Convention on Standards on Seafarers' Training, Certification and Watch of 1978 "(STCW Convention) are inseparable.The 2010 Manila amendments of STCW78/95 put forwards the specific demands on navigation simulator application. The new Convention is divided into A, B parts. Part A is mandatory, part B for the proposed requirements and guidelines. The first A-Ⅰ/12 sets out the criteria for the use of simulators, and requirements on simulator training are raised for different departments on board and levels of the crew, in which there are 25 items of mandatory minimum requirements for the officer who is responsible for the ship's navigational watch on ship of 500 dwt or above; there are 15 items of certification guidance for captain and first officer who is responsible for the ship's navigational watch on ship of 500 dwt or above; there are 10 items of certification guidance for the officer who is responsible for the ship's navigational watch on ship of 500 dwt or above; there are 19 items of mandatory minimum requirements against oil tankers and chemical tankers for the master, officers and crew training and qualification; 1 item of mandatory minimum requirements against liquefied gas tanker for the captain, officers and crew training and qualification.

The provisions of the Convention is mainly for the standards and requirements of marine simulator training and evaluation, from the the required training and assessment projects, we can see many features can be achieved through navigation simulator. Although the provisions of the Convention stipulate that the navigation simulator is a mandatory requirements as partly operation in crew training and evaluation and some proposed requirements as guidelines, but it does not prohibit the simulator applied in other fields. On the contrary, the marine simulator used more widely in practice, which is more used in teaching, research, shipping companies, maritime authorities, salvage units, etc., and will also be applied in more fields.

The characteristics and limitations of maritime trial

Professional technical features of maritime cases

Maritime cases generally occurs at sea. The legal relationship contained is complex, usually involving the profession and technology of ship, crew, navigation, cargo transportation and management. On ships, it involves the structure, properties, equipment and safety conditions of the ship are related; On crew, it involves the qualification , training, watch and certification; On navigation, it involves steering, routes developing, radar observation, the usage of navigation publications, weather reports and engine operation; On the cargo transportation, it involves the characteristics of the goods, the cargo loading and unloading, custody and taking care thereof and so on. With the development of economic, trade and shipping industry, maritime cases raise increasingly, the proportion of such high technical professional maritime cases in the courts has gradually increased. According to statistics, the case heard in Shanghai Maritime Court involved an increasingly complex and extensive professional and technical problems. Including the maritime cases accepted by this court, the cases of ship collisions, marine insurance, charter parties, ship repair and other ship construction accounts for about 10% of total cases, which involve construction of ships, marine technical principles and other professional knowledge.

Limitations of Traditional Marine trial

Firstly, from the composition of trial team , the judges engaged in maritime work are judicial officers to exercise jurisdiction according to law, the Chapter IV of "PRC Law on Judges", "Conditions of judges" makes accurate stipulation of the qualifications and conditions of judges, it requires the judge graduated from university with legal profession, or graduated from college with a non-legal profession but having legal knowledges, passing the national unified judicial examination, appointed and removed in accordance with legal procedures. With the strict conditions of the judges, the judges are mostly the persons with legal profession, the proportion of non-legal professional judges with

legal expertise is very small, especially those with technical expertise and relevant experience are few in maritime court.

Secondly, from the trial procedures and methods of cases identification, usually the evidences exchanged by the parties submit before the court hearing, in exceptional circumstances may be investigated and collected by court provided applied by parties, then through the trial court investigation procedure and the parties cross-examination of evidence, and ultimately by the court debate, the judge may confirm the facts of the case and determine the parties' responsibility based on legal and valid evidences. The maritime cases generally occur in the ocean, it is difficult to fix the evidence, the trial judge mostly hear the cases based on the existing data of ship as evidence due to the lack of a factual record in the Marine trial, these data mainly including: logbooks, telegraph book, ship certificates, crew testimony, voyage data recorder, etc., judges prove the facts of the case through legal inference and make division of responsibility attribution, but the incident process reproduction can not be achieved clearly and completely by court hearing, it is very hard to achieve the desired results.

Thirdly, from the point of the evidence, the evidence is the basis of determining the cases and the core of litigation, all the litigation activities are in fact carried out surrounding the collection and usage of evidences. From the newly revised"Civil Procedure Law" implemented on January 1, 2013, there are eight kinds of evidence: (a) statements of the parties; (b) documentary evidence; (c) physical evidence; (d) audiovisual materials; (e) electronic data; (f) testimony of witnesses; (g) identification objection; (h) inquest record. The electronic data is a new kind of evidence, which is the result of science and technology development. For the concept of electronic data is currently no uniform identification, I believe that we can draw on the concept of "data message" in "Electronic Signature Law": "data message refers to the information generated, sent, received or stored by electronic, optical, magnetic or similar means. " Although this provision is applicable in the field of e-commerce law, electronic data also exists in navigation, so the electronic data also apply in the maritime evidence. In addition to the traditional forms of documentary evidence, physical evidence, witness testimony, etc., ship navigation data described by VDR and ECDIS is static electronic data, and dynamic evidence can be obtained assisted by simulation capabilities of simulator that a more realistic cases reduction process can be achieved, the provisions of "Civil Procedure Law" provides legal support for this kind of maritime evidence.

Status of nautical technology applying in maritime trial

Status analysis of nautical technology applications in the maritime trial

The professional technical characteristics of maritime cases enhance the complexity of the cases. If the cases heard at Court involving technical issues, it is necessary to identify the technical facts and the decision is rendered on the basis of applicable law, which makes the difficulty increasing in maritime trial. The judges in Maritime Court is limited by the professional background, they are lack of professional navigational and technical knowledge, and appeared to be inadequate in case encountering maritime cases with high professional and technical quality, which is not conducive to effective hearing of the case.

To solve this problem, many maritime court needs help of relevant professionals with specialized skills or experience to assist the party concerned to clarify their objection or the judge to make scientific judgment. But specialist's opinion only represents the personal views, which is not a legal form of evidence, it is a still question about the strength of evidence. In fact, Wuhan and Tianjin Maritime Court exercise a integrated utilization of network information, such as making use of shipping statistical analysis Website manner to predict the shipping market situation timely and effectively in order to determine the possible changes of the type and number of cases, and make effective plans in advance; making use of ship data query website to determine the exact information of shipowner to ensure the accuracy of cases handling to avoid the possibility of wrongful arrest; utilizing AIS information to master the real-time ship position and shipping movement, which makes it more active to deal with the cases involving ships.

These practices enhance the flexibility and initiative of maritime trials on a certain extent, which improve the quality and efficiency of court hearing. But it is necessary to be careful with the reliability of the network resource information, which can only provide a reference but not be taken as the basis to determine the responsibility directly. Today, maritime technology is highly developed, the advanced navigational equipments are already used in shipping, the navigation simulator also has had a more complete structure and functions and become mandatory training and assessment requirements of the Convention, but in the event of maritime accidents, the maritime trial body failed to reproduce the realism of the case during the incident with the help of the related devices to strengthen the evidence effect and obtain the dynamic evidence to support the trial hearing, to some extent, which indicates the lag of trials means.

Feasibility of navigation simulator used in maritime trial

Navigation simulator and network technology widely used makes it possible that today's maritime trial is developed by navigation technology, which using advanced simulator and accurate electronic data to restore the process of incident and obtain electronic data combined dynamic and static evidences. Some maritime courts have been trying in the trial practice with the help of navigational equipments and technology.

The court in Chongqing of Wuhan Maritime Court contacted Chongqing local Maritime Bureau in the case hearing, they overcome the technical difficulties and launched GPS ship water monitoring system on the court website. GPS ship water monitoring system is integrated water traffic safety management system including the GPS satellite positioning technology, GSM and CDMA1X (or GPRS) mobile communication technology, GIS geographic information technology, computer technology and Internet technology, it contains the functions of vessel monitoring, navigation aids, investigation and evidence collection, and information services and others. Nowadays, the number of all kinds of ships with Chongqing membership has been more than 1150, all of which installed GPS terminal and can be very easily found on computers of Chongqing courts. And it provide good convenient for the maritime courts trial.

With the development of technology, a lot of new technologies are operated in maritime, such as electronic charts and VDR are manifested in the form of electronic data, which record the detailed information of navigation data, these informations can be playback through the simulator to restore the more real process of accident and determine the static and dynamic evidences, which is the process of of evidence identifying on legal essence. The law stipulates that evidence must be verified according to the facts and can be as the basis of determining the facts. The function of high simulating of navigation simulator provides more real and effective verification methods to identify the evidence of maritime accident, and the evidences derived from which have a stronger persuasiveness, authenticity and power of proof.

Application Prospects and significance of navigation simulator in maritime Trial

If the evidence in the form of electronic data is widely applied in the Marine trial, it is not only enhances the species of marine evidence, but also substantively expand the evidence sources and materials, which will promote the maritime trial undoubtedly. This form of evidence will also be increasingly used in the maritime trial.

Based on the research on the characteristics of maritime trial and function of navigation simulator, the author believes that the maritime court could make use of the auxiliary functions of simulator and take the following measures to serve the maritime trial practice.

(A)Making fully use of marine simulator to achieve realistic dynamic reduction process of accident and strengthen the evidence certification and improve trial efficiency

When the cases of ship collision is heard, the facts identification is the basis of determining the responsibility. But the facts of the collision case in general usually occurred instantaneously, the parties often hold the opposite point of view, if the collision course could be restored in realistic will make it more authentic of evidence certification. We could enter the vessel’s name of accident and associated navigational data into navigation simulator system to achieve the dynamic playback of accident accurately and locate track, course, speed and other raw materials of the ship around the

collision accident occurred, thereby fixing the dynamic evidence and providing support for identification of accident process, the cause of the accident and the responsibility. This incident process reproduce is based on real data, which is of more convincing, and objectivity and fairness, it is more persuasive than the expert opinion.

(B) Introduction the inter-disciplinary talent who possesses both legal and experience of professional knowledge to join the Marine trial team, or giving technical training to the judges with a pure legal professional in order that the judicial officers can make use of their legal analysis capabilities and maritime professionals technology and appropriate equipment with advanced navigation simulator to make more rational and scientific legal analysis and evidence argumentation, confirm the legal responsibility, resolve maritime legal disputes quickly and effectively.

Summary

Maritime trial is an important part of Country's judicial work, it is important for responsibility division of parties concerned accurately and protection of the legitimate interests of the parties. The function of navigation simulator has been continuously improved under the support of scientific and technology as well as new requirements of the Convention. navigation simulator appropriately applied in trial practice will assist the judges to ascertain the facts of cases and fix the evidence, which will be conducive to promote case hearing rapidly, improve the scientific judgment and fairness of court hearing, protect the legitimate interests of the parties and escort the development of shipping industry.

References

[1] Si Yuzhuo, Maritime Law, Beijing: Law Press, March 2007 2nd Edition

[2] "1978 International Convention on Standards of Seafarers' Training, Certification and Watchkeeping" 2010, Manila amendments

[3] Tianjin Maritime Court Net http://tjfy.chinacourt.org/public/detail.php?id=17147 Making use of the Internet to boost maritime trial court

[4] Chinese Foreign Commercial Maritime Network http://www.sina.com.cn trial court in Chongqing of Wuhan Maritime Court to build high-tech information platform to improve the performance of maritime trial and legal services

[5] "PRC Maritime Procedure Law" in 2012 to amend section 63

Applied Mechanics and Materials Vol. 565 (2014) pp 85-91

doi:10.4028/www.scientific.net/AMM.565.85

Estimation of Critical Performance Parameters of the Thermocouple in a Bypass Device, Made of SME Alloy, Designed for LIABs on Spacecraft

Zh.M. Blednova[a], N.A. Protsenko[b]

Kuban State Technological University, Krasnodar, Russia

[a]blednova@mail.ru, [b]procenko_n@list.ru

Keywords: Lithium-ion storage batteries (LISB), Spacecraft, Bypass device (BD), Material with shape memory effect (SME), Thermocouple, Critical parameters, Modeling, Thermal problem.

Abstract. Critical parameters of the bypass device thermocouple made of SME alloy are optimized on the base of the developed thermal model of Lithium-Ion storage battery (LISB) for space applications. It is shown that the terminal is the most dangerous element within LIAB. To ensure LIAB reliability in case of one cell failure, a temperature limit in the vicinity of the terminal is set to 100°C, and the bypass device action time – to 2–3 s, which corresponds to phase transitions temperature range of the thermocouple spring made of SME alloy.

Introduction

Currently Lithium-ion storage batteries (LISB), providing the highest energy density as compared with other battery technologies, are used increasingly as secondary power supply sources for a spacecraft. Along with unconditional positive qualities, Lithium-ion cells (LICs) have some inherent drawbacks, the main of which is fire and explosion hazard due to high concentration of energy. In using LICs, those drawbacks need to be taken into account, especially in extreme conditions of outer space. In case of short circuit, overcharging, overheating or mechanical damages, colossal energy release is possible, causing cell destruction and spacecraft equipment damage [1]. To improve storage battery (SB) reliability, a large volume of fundamental and applied research [2-4] was carried out, which allowed to clarify the mechanisms responsible for those drawbacks, and develop a number of structural and technological solutions aimed at failure prevention [5,6].

For LIABs designed for spacecrafts with 10-15 years lifetime, the issue of LICs' state of health monitoring in operation, and their state investigation before installation is very important. Monitoring the state of each LIC within battery is an important technical-scientific challenge. Currently there are no reliable enough methods of LIC's state control and its performance prediction for the long-term operation. Enhancement of SB reliability and durability is achieved by installation of specially developed bypass devices (BDs), designed to remove potentially dangerous and unreliable LICs out of a circuit, prior to critical situation involving their possible destruction (Fig. 1). In recent years, BD design and technological solutions have been developed and implemented [6], among which the most promising ones for use in extreme conditions of outer space are BDs with the thermocouple spring made of SME material (Russian Federation patents № 2392494, 2415489, 127252).

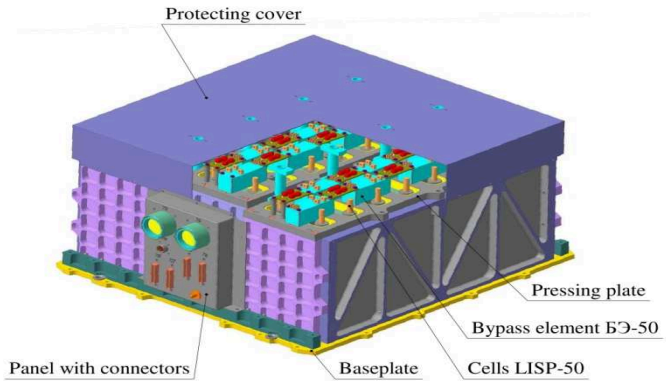

Fig. 1. Lithium-ion storage battery

One of the requirements for BD is to provide continuity of SB power circuit during BD action. And here a momentary short circuit occurs inevitably in a cell that is removed from the power circuit. The short circuit is accompanied by severe heat generation, which can cause cell heating to temperatures, at which the processes within the LIC are no more manageable, cell housing destruction, and electrode materials and electrolyte release into spacecraft atmosphere [7]. Intensity of cell and SB parts heating is estimated by parts' thermal links, heat capacities and heat generation power. In turn, thermal links are estimated by LIC and SB thermal and physical characteristics and design, and heat generation power – by LIC internal resistance.

Criterion of BD efficiency is its action time, during which the heat generation within LIC volume, caused by short-circuit, on the one hand, does not lead to the adjacent LICs' heating to critical temperature, at which performances are degraded; but on the other hand, it is higher than the temperature in the end of the reverse martensitic transformation of a SME spring in the thermocouple of the adjacent BDs. This is needed to avoid the possibility of false, spontaneous BD action. Temperature limitation is also needed for LIC hermeticity preservation and LIC failure isolation. Thus, explosion prevention in case of BD action is determined by the following critical parameters: speed of BD action (short circuit duration), and LICs optimal arrangement in a SB, corresponding to the optimal thermal links between LIC and SB parts. The purpose of this paper is to estimate the critical performance parameters of the BD thermocouple made of SME alloy, ensuring reliable operation of LIAB on spacecraft in case of one cell failure. This problem can be solved by modeling of thermal processes in LIAB.

Research methodology

Thermal processes are simulated as applied to SB 23LI-50, consisting of 23 cells LISP-50, arranged in three rows on a rectangular baseplate made of alloy MA2-1. Failed LIC is removed from the power circuit by a bypass device. Fragment of one of SB rows, comprising four LICs in serial on SB baseplate, is outlined in Figure 2. From the perspective of the maximum thermal action of LIC with short circuit on adjacent LICs, short circuit in the outermost cell is the most dangerous one.

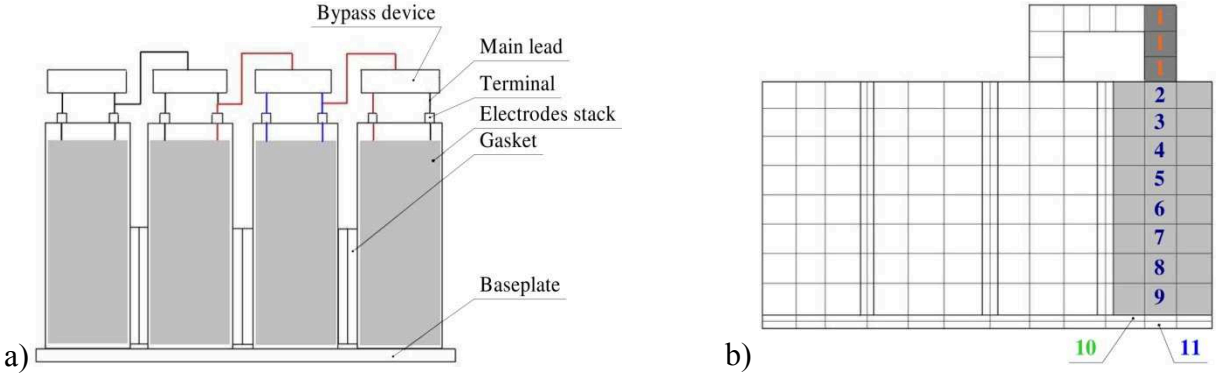

Fig. 2. LICs arrangement in SB - a); computational grid to solve the thermal conductivity equation - (b)

In thermal processes modeling in LISB the following assumptions are made:

The problem of temperature distribution in the system is solved in a two-dimensional region, considering SB fragment, consisting of one row of LIC, including the LIC with a short circuit (Fig. 2a) ;

LIC with short circuit is the outermost one, and heat from the failed LIC is transferred through the wire only to one adjacent cell;

According to LIC energy-balance model [8], volume-averaged LIC temperature for each time interval is used in the calculations;

Stack of electrodes occupies the entire internal volume of LIC; in the region of terminal and BD thermal characteristics of elements are determined only by mass and size characteristics of the main leads.

The mathematical formulation of heat generation process in LIC with short circuit is based on Fourier - Kirchhoff differential equation:

$$\rho c \frac{dT}{dt} = \frac{\partial}{\partial x}\left(\lambda \frac{dT}{dx}\right) + \frac{\partial}{\partial y}\left(\lambda \frac{dT}{dy}\right) + \frac{\partial}{\partial z}\left(\lambda \frac{dT}{dz}\right) + q_v, \quad (1)$$

Where ρ is density, kg/m^3; c - specific heat capacity, J/(kg·K); λ - thermal conductivity, W/(m·K); q_V - power of volumetric heat generation sources, W/m^3 , T - temperature, °C; t – process duration, s.

Equation (1) is solved by method of control volumes [9] on a rectangular grid. Figure 2b presents a schematic diagram of a grid for equation (1) solution, reflecting the principles of control volumes building. The scheme shows six specific regions of the calculated domain, including control volumes of grid partitioning for healthy LICs (they are lighter in Fig. 2b); SB baseplate; area between adjacent LICs in a row; failed LIC with uniform heat generation; copper wire in the circuit of short-circuit current (darker); copper wire involved in heat transfer from the failed LIC to the adjacent cell.

The following initial and boundary conditions were used in the solution of equation (1). SB initial temperature is T = 22°C, practically corresponding to the maximum possible temperature of SB in the end of charge for the design cycling modes within spacecraft. Boundary conditions include heat flow conditions for all boundary control volumes of the calculated domain. Heat flow for the lower boundary of SB baseplate is estimated by equation (2),

$$q = \sigma \cdot \varepsilon \cdot (T_2^4 - T_1^4), \quad (2)$$

Where: q is specific heat flow, W/m^2; $\varepsilon = 0{,}85$ – LIC surface emissivity; $\sigma = 5{,}67 \cdot 10^{-8}$ – Stefan-Boltzmann constant, W/(m^2·K^4); T_2 - temperature of the bottom surface of SB baseplate, K; $T_1 = 0$ for heat emission into outer space.

For all other boundaries of LIC spatial configuration

$$\lambda \frac{\partial T}{\partial n} = 0, \quad (3)$$

Where n is a vector of normal to the involved boundary in LIC spatial configuration.

To estimate LIC thermal parameters it is necessary to determine cell heat generation power during cycling, W_T, given that in charge the efficiency is 100%, and self-discharge current is negligible. Temperature profile over time was calculated from the heat balance equation using heat generation diagram R_{LIC}.

$$W_T = C_{LIC} \cdot \frac{dT}{d\tau} + \frac{(T - T_{TP})}{R_{LIC}}, \quad (4)$$

where R_{LIC} is thermal resistance, C_{LIC} – heating capacity, T_{TP} – thermal plate temperature, R_{LIC} – LIC internal charge and discharge resistance, which is temperature-dependent (Table 1).

Table 1. LIC internal resistance at different ambient temperature

Ambient temperature, C°				
-10	0	10	26	40
LIC resistance at charge, Ohm				
0.0284	0.0235	0.0221	0.0168	0.0151
LIC resistance at discharge, Ohm				
0.0266	0.0200	0.0175	0.0158	0.0125

Parameters of LIC thermal model were identified by test results selection in terms of a prototype battery 6LI-25. Fig. 3 shows the structure of SB 6LI-25 with installed temperature-sensing elements

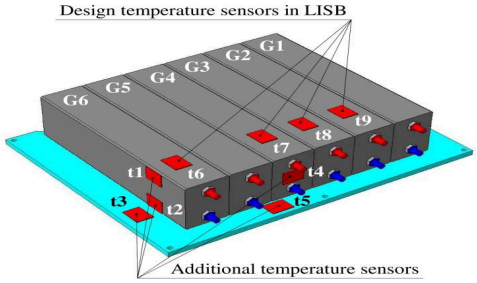

Fig. 3. Scheme of SB 6LI-25 with installed temperature-sensing elements

For testing SBs were placed in a charge-discharge stand with adjustable temperature of the thermal plate. Thermal resistance R_{LIC} for each specified LIC was estimated by integration over the last few "charge - discharge" cycles till the cut-off moment, i.e. SB temperature stabilization. Thermally neutral voltage values, U_{TN} and C_{LIC}, were determined by their values selection in the solution of equation (1) versus experimental curves.

Discussion

Figures 4 and 5 show simulation data for the thermal processes in LIAB in case of one cell failure, obtained using the developed model. Fig. 4 shows temperature distribution in the thermal model for the cross-sections parallel to SB baseplate (from the bottom - to the top of LIC) for time t = 315 s (time of end of discharge in LIC, and, respectively, time of attaining the peak temperature of the failed LIC in its most thermally stressed upper part), and time t = 2200 s (end of calculation). The x-axis (Fig. 4) shows serial number of the control volume for the horizontal cross-section. Here, the lines A, B and C correspond to control volumes of LIC side faces (A - face of a healthy LIC, B and C – side faces of the failed LIC). Lines 1-11 represent sequential (from LIC top to SB baseplate) temperature cross-sections; here, line 11 is the temperature of SB baseplate. Construction of the temperature profile for different elements of LISB allows to optimize bypass device location.

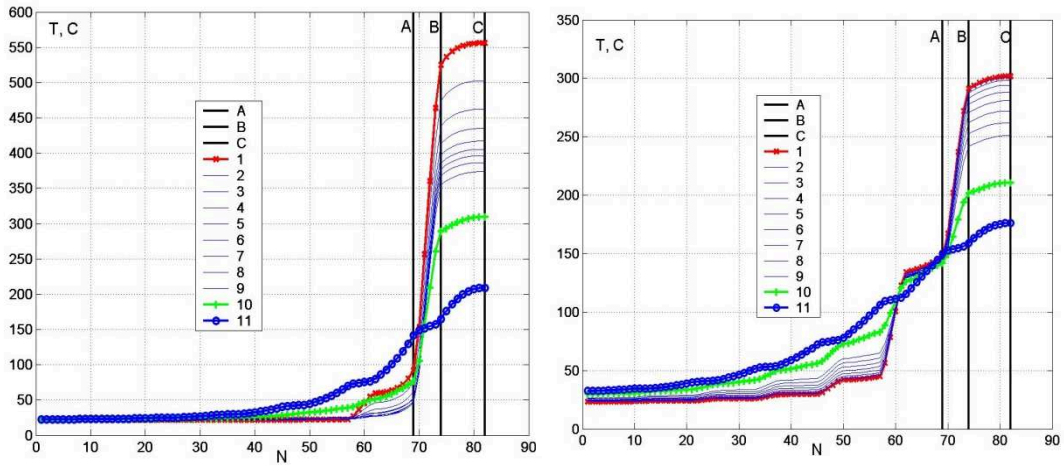

Fig. 4. Temperature distribution at t = 315 s and t = 2200 s ($t > t_{short\ circuit}$).

Analysis shows that heating of LIC, adjacent to the failed one, has high lag effect with respect to BD action time. When t_{BD} = 150, the temperature of LIC adjacent to the failed one, will not exceed 80-82°C during the subsequent hour. Fig. 5 (curve 1) shows the change in temperature in the hottest place of a healthy LIC. At the same time, due to such action time of BD, wire temperature in the region of the failed LIC terminal reaches very high values (Figure 5, curve 2). Experimental studies have confirmed the calculated temperatures. Thus, it is temperature and BD action time that are determinative factors in this problem solution. Maximum wire heating in the region of failed LIC terminal occurs in the end of BD action (Fig. 5), at t_{BD}=3sec. Therefore, the optimal value of BD safe operation criterion should be theaction time t_{BD} < 2-3 sec.

The described thermal model of LIC allows predicting accurately enough the heat generation power in different operating conditions of SB. The model is applicable to other types of cells, the design of which involves the same materials of electrochemical group and design philosophy of the base sample; it is also applicable to cells obtained by scaling the above one. Using the principle of similarity, one can construct a 3D-model of a storage battery with a specific mass, heat capacity, thermal conductivity and thermal links between its structural elements. This will allow determining the temperature in any point of SB for different operating conditions and initial temperatures.

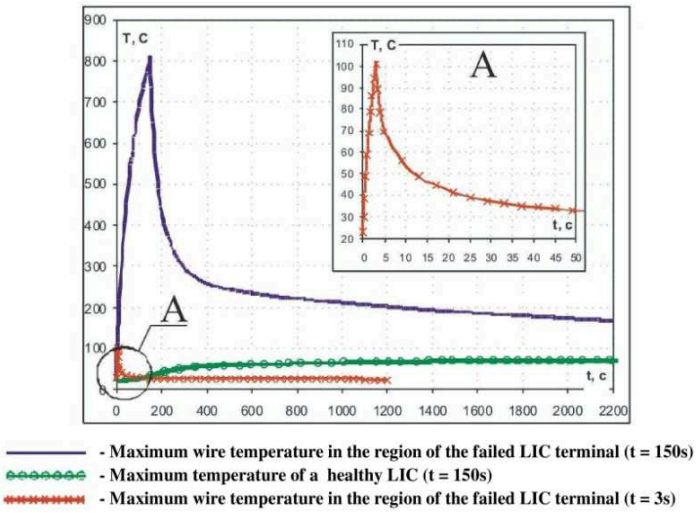

Fig. 5. Wire temperature in the region of terminal and healthy LIC temperature

As the thermocouple, containing temperature sensitive SME material, is a BD component, it is necessary to estimate the chosen material resistance to operating temperatures impact. SME material should preserve its functional properties after SB thermal cycling in the course of charge /discharge cycles, associated with solstice and eclipse periods of spacecraft orbit, as well as during storage, transportation, and SB testing. Ambient temperature values in such conditions of SB operation differ substantially. Thus, during SB storage and transportation, all its elements, including BD, should preserve their performances in the temperature range from -50°C to +50°C. During SB cycling aboard spacecraft in outer space, as a rule, temperature varies from -10°C to plus 40°C. In case of SB failure, (e.g. one cell failure), the temperature of its individual nodes can reach +60 ° C.

For all the variety of temperatures, BD, or rather its thermal sensing element made of SME material, should operate reliably and without false (spontaneous) action. To meet these requirements it is necessary to define the boundaries of SME material phase transformations. On the one hand, the temperature of reverse martensitic transition, during which the force of BD spring is generated, should exceed the maximum possible temperature of SB, even in case of failure, so that to eliminate the possibility of false action. On the other hand, this temperature cannot exceed the maximum allowable operating temperature for materials and coatings, BD structural elements are made of.

Thus, on the base of the detailed analysis of the SB and BD design, and experimental studies, the minimum temperature in the beginning of reverse martensitic transformation was estimated to be 80°C, and the maximum temperature in the end of phase transition – 120°C. Temperature of direct transition has less effect on BD performance capability. Its influence is reflected in conditions of

BD re-cocking. This temperature limits the conditions of checking actuations at the stage of technology development and acceptance testing. It is desirable that this temperature is slightly higher than normal room temperature, which will simplify the testing procedure and eliminate the need for BD additional cooling after its trial actuation. Our studies allowed to choose for thermocouple an alloy on the base of Ti-Ni, containing 50,0-50,2 atomical % of Ni. Interval of martensitic transformations for this alloy was regulated by thermo-mechanical treatment. The methodology developed for the control and management of structural (phase transformation temperatures, coefficient of restitution) and mechanical properties (actuation force) of BD thermocouple made of SME material ensured the required reliability level of 0.999 [10]. The investigations of operational factors' (temperature cycling, harmonic and random vibrations, single and multiple shocks) influence on the power components of BD thermocouple made of SME alloy confirmed preservation of deformations and strains of shape memory [11].

Summary

On the base of the developed thermal model for LISB, it was found out that in case of one cell failure the most critical structural component is LIC terminal; heat is generated in its volume due to short circuit. In order to avoid LIC unsealing and isolate the failure, the maximum allowable temperature of the copper wire in the region of terminal is set, T_{max} = 100°C. This criterion corresponds to BD action time 2–3 sec. Experimental validation of heat generation in LISB normal operation allowed to optimize BD location in each LIC within SB. Good convergence of mathematical modeling results on heat generation estimation with experimental values is observed. Data on BD action time and temperature distribution in case of one cell failure, obtained by modeling of thermal processes in LISB, allowed to choose SME material for BD spring, develop manufacturing technique, solve problem of optimal BD location within LISB, and ensure its reliable operation.

This work was financially supported by the Ministry of Education and Science of the Russian Federation within the project 1.2.1 / 6803 "Development of physical and technological bases for creating high-reliability electromechanical devices using SME materials to ensure efficient and reliable operation of lithium-ion batteries for space application".

References

[1] M.V. Luk'yanenko, V.S. Kudryashov/ Spacecrafts energy equipment and on-board power supplies // Bulletin of Siberian State Aero-space University named after M.F Reshetnev. 2008. № 1. P. 141-145. (in Russian). .

[2] Gang, Ning, Branko N. Popov. Capacity fade study of lithium-ion batteries cycled at high discharge rates. // Journal of Power Sources. – 2003. – № 117. – P. 160-169. doi:10.1016/S0378-7753(03)00029-6

[3] Meng Guo, Ralph E. White. Thermal Model for Lithium Ion Battery Pack with Mixed Parallel and Series Configuration. J. Electrochem. Soc. 2011, 158 (10), A1166-A1176.

[4] E.A. Nizhnikovskiy/ Sources of autonomous power supply for operation in extreme conditions //Russian Chemical Journal. 2006,T.1, № 5. P. 102-112. (in Russian).

[5] Blednova Zh.M., Galkin V.V., Makhutov N.A., Protsenko N.A. Ways of safety and lifetime insurance for Lithium-Ion storage batteries for space application // Problems of safety and emergency. 2010. №1. - P. 43-54. (in Russian).

[6] Zh.M. Blednova, N.A. Protsenko. Ensuring reliability of Lithium- ion batteries for space applications using functional shape memory materials. Advanced Materials Research, Vol. 772, Trans Tech Publications (2013) pp 693-698. Doi:10.4028/www.scientific.net/AMR.772.693

[7] Zh.M. Blednova, N.A. Makhutov, N.A. Protsenko. Ensuring reliability of Lithium-ion batteries for space applications using functional shape memory materials. // Problems of mechanical engineering and automatization, 2013 - № 12. – P. 3-13. (in Russian).

[8] Zh.M. Blednova, V.Yu. Lapshin, N.A. Protsenko/ Estimation of LISB thermo-physical parameters on the base of energy-balance model // Transactions of Academenergo, 2011 - № 2. – P. 117-127. (in Russian).

[9] S.V. Patankar. Numerical methods for solving problems of heat exchange and dynamics of liquid.- M.: Energoatomizdat, 1984. – 152 p. (in Russian).

[10] N.A. Protsenko, Zh.M. Blednova Structural-mechanical Control of Bypass Reactivity in LISB for Space Application using Shape Memory Alloys. Materials Science Forum Vols. 738-739 Trans Tech Publications, Switzerland (2013) pp 601-606. doi:10.4028/www.scientific.net/MSF.738-739.601

[11] V.V. Galkin, Zh.M. Blednova, N.A. Protsenko. Reliability and life time estimation of LISB bypass device with a spring made of SME materials for space application, taking into account technological and operational factors, Polyot, № 5 (2012) 20-27 (in Russian).

Applied Mechanics and Materials Vol. 565 (2014) pp 92-97

doi:10.4028/www.scientific.net/AMM.565.92

Sensitivity Analysis of Airdrop Condition Parameters Based on Response Surface Method

Jianyang Li[a], Hongyan Wang[b], Qiang Rui[c], and Huangjie Hong[d]

Department of Mechanical Engineering, Academy of Armored Force Engineering, Dujiakan 21, Fengtai District, Beijing 100072, China.

[a]yang_zgy@sina.cn, [b]why_cvt@263.net, [c]ruiqiang2006@163.com, [d]gundamwing5@163.com

Keywords: Airborne vehicle, Sensitivity analysis, Airdrop condition parameters, Response surface method

Abstract. The airborne vehicle would suffer from impact at landing. The magnitude of impact and stability of airborne vehicle are constraint parameters of successful landing. There was a lack of scientific explanation on the sensitivity of landing condition parameters. For overcoming the deficiency of classical sensitivity analysis, this paper describes the application of new technology for the sensitivity analysis. Based on the Finite Element and Response Surface method, the research on sensitivity analysis of landing condition parameters was proposed. The results have important significance in the design and optimization of airborne vehicle and airbags system. It can be also provide guidance for airdrop operation.

Introduction

As the development of airdrop technology and cushion equipment, airdrop technology was used in rescue and relief work, goods delivery work and so on. Because of the variety of wind, attitude of system, landing velocity and ground line gradient, there would be different condition when airborne vehicle was landing. Sensitivity analysis of landing condition parameters is needed for researching on the affect of landing responses. Traditional sensitivity analysis [1] provides local gradient information. It changes one of input variables a little with others invariant, the coefficient of sensitivity is defined as the ratio of variation of output to the input. The sensitivity analysis based on response surface method can replace the real structure as the response surface model, which can greatly reduce the finite element calculation. Computational efficiency is improved for the complex system such as airborne vehicle and airbags system especially. Based on the finite element and response surface method, the research on the affect of landing responses by landing condition parameters was proposed (Figure 1). The results have important significance in the design and optimization of airborne vehicle and airbags system. It can be also provide guidance for airdrop operation.

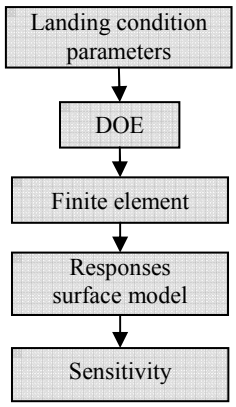

Fig.1 Flow chart for the sensitivity analysis

Sensitivity analysis based on response surface method

Response surface method

Response surface method [2] is a statistical technique to obtain a relationship between a number of independent variable and a system response based on results calculated at various points in the design space. The model used to describe the relationship between the response and the variables may be written in general as follows

$$f(x) = \widetilde{f}(x) + \varepsilon \tag{1}$$

Where $f(x)$ represents the actual value, $\widetilde{f}(x)$ is the approximate model, ε is the error which represents the difference between the actual response value and approximate response value.

To construct response surface approximations for an objective function and constraints, a large number of observations in the design space must be required. To use computational resources wisely, the designer must consider both the quantity and the distribution of the observation points in the design space. The selection of observation points in the design space where the response must be evaluated is commonly called design of experiments. There are many techniques for design of experiments. In this study, because of the uniform filling of the design space property, we applied Latin Hypercube design to select the design points for constructing response surface approximations.

Probabilistic sensitivity analysis

Sensitivity analysis is important for design optimization of structure. Traditional sensitivity analysis provides local gradient information merely. It changes one of input variables a little with others invariant. The coefficient of sensitivity is defined as the ratio of variation of output to input. The interactions among the variables are ignored, and so does the influence of the range of input variables. In fact, the ranges of variables are different. So it is necessary for considering the gradient information integrate with the scatter of input variables. Probabilistic sensitivity analysis gives consideration to the two problems. It can be written as

$$S_i = \left| \left. \frac{\partial \widetilde{y}}{\partial \widetilde{x}_i} \right|_{(\bar{x}_1, \bar{x}_2, \cdots, \bar{x}_n)} \cdot (x_i^+ - x_i^-) \right| \Bigg/ \sum_{i=1}^{n} \left| \left. \frac{\partial \widetilde{y}}{\partial \widetilde{x}_i} \right|_{(\bar{x}_1, \bar{x}_2, \cdots, \bar{x}_n)} \cdot (x_i^+ - x_i^-) \right| \tag{2}$$

Where $\bar{x}_1, \bar{x}_2, \cdots, \bar{x}_n$ are the average of variables, x_i^+, x_i^- are upper bound and lower bound of the ith variable, they are $\bar{x}_i \pm 3\sigma$ practically.

Statistical distribution for the parameters of landing condition

The parameters of landing condition, which concerned in this paper, included vertical velocity, horizontal velocity, pitch angle, heel angle and gradient. In this paper, a dynamics model of the parachute and airborne vehicle system had been built up. The whole airdrop process included extraction, deployment, inflation and stable falling processes [3]. The landing speed and attitude would be calculated by Monte Carlo method, and then probabilistic distribution analysis is performed.

Computing method for probabilistic distribution of landing condition parameters

The computing method for probabilistic distribution of landing condition parameters was summarized as follow [4].

(1) Established dynamics model of parachute system and airborne vehicle.

(2) Confirmed the probability density function of random factors, and supposed all of the factors were independent mutually.

(3) Each random factors created random numbers $F(x_{ij})$ in the interval of [0,1]

$$F(x_{ij}) = \int_{-\infty}^{x_{ij}} f(x_i) dx_i \tag{3}$$

Where i is the number of variables, $i = 1,2,\cdots,n$. j is the times of simulation, $j = 1,2,\cdots,m$.

(4) Substituted each random numbers to the dynamic equations of airdrop system and calculated circulative *m* times, the mean and variance were obtained by the *m* groups of landing speed and attitude.
(5) Graphed the bar chart and fit the distribution for landing speed and attitude.
(6) Hypothesis testing for landing speed and attitude.

Probabilistic distribution of landing condition parameters

In this paper, the horizontal velocity of airborne vehicle depended on the wind velocity mostly, so the horizontal velocity was considered to be equal to the wind velocity.

Programming the airdrop process in series (extraction, deployment, inflation, stable falling). Simulating the airdrop process 5000 times by Monte Carlo Method, and the frequency of vertical velocity and attitude were obtained. The regularities of distribution can be presented by fitting the probabilistic distribution function (Table 1).

Tab.1 The regularities of distribution of landing speed and attitude

Landing condition parameters	Regularities of distribution	Properties	
horizontal velocity W (m/s)	Weibull	β=2.9	η=6.3
vertical velocity V (m/s)	Normal	μ=7.1	σ=0.6
pitch angle α_x ( )	Normal	μ=0	σ=3.33°
heel angle α_z ( )	Normal	μ=0	σ=2.33°
gradient α_g ( )	Normal	μ=0	σ=1.67°

Response surface model building

As the development of computing and CAE technology, the fidelity of numerical model was improved. As a result, the simulation would consume more computing resource. The elements number of finite element model of airborne vehicle and airbags system is more than one hundred thousand. Such systems are characterized by highly non-linear behavior. However, the simulation of a cushion process of 300 millisecond duration typically requires tens of hours of CPU time [5], making it impractical to perform the large number of analysis runs necessary for the cushion process of varied landing conditions.

This paper presents a methodology for overcoming these problems with reference to sensitivity analysis. The approach utilizes the Response Surface method to build high quality response surface from a relatively small number of FE analysis runs. The response surface model was used to replace the finite element model of airborne vehicle and airbags systems and to perform sensitivity analysis of the landing condition parameters.

Design of experiment

The DOE method adopted was based on Latin Hypercube. It is the most typical DOE with reasonably uniform sampling point distribution property. For the response surface model building, a Latin Hypercube of 30 runs was performed. The range of landing condition parameters is shown in Table 2. The scheme of DOE is presented in Table 3.

Tab.2 The span of landing condition parameters

level \ parameters	horizontal velocity W (m/s)	vertical velocity V (m/s)	pitch angle α_x ( )	heel angle α_z ( )	gradient α_g ( )
lower bound	2	5.3	-10	-7	-5
upper bound	9	8.9	10	7	5

Tab.3 Scheme of DOE by Latin Hypercube

Serial number	horizontal velocity W (m/s)	vertical velocity V (m/s)	pitch angle α_x ( )	heel angle α_z ( )	gradient α_g ( )	peak vertical acceleration $a_{\max}$ (g)
1	2.59	-5.48	9.35	-1.72	4.17	15.73
2	7.39	-7.16	4.5	6.15	-1.17	8.07
3	5.33	-7.28	-0.35	0.25	-1.5	9.06
4	4.88	-8.24	-1.73	-3.69	1.17	14.4
5	8.76	-7.52	-3.12	4.67	-4.5	7.73
6	6.47	-7.04	-6.58	6.64	-3.5	13.36
7	6.25	-6.92	0.35	0.74	4.5	11.46
8	8.30	-7.64	1.04	-7.13	3.5	37.53
9	7.62	-7.76	7.97	-2.21	0.5	24.21
10	6.02	-5.36	5.89	-2.71	-4.83	5.80
11	4.19	-8.84	5.2	3.69	-1.83	21.93
12	4.42	-5.96	-3.81	-5.17	0.17	8.77
13	8.53	-5.60	6.58	1.72	2.17	7.60
14	2.36	-6.08	1.73	3.2	-2.83	6.35
15	5.10	-8.60	-4.5	-4.18	-3.83	12.27
16	3.96	-8.00	10.04	-6.15	-4.17	23.96
17	8.99	-7.88	8.66	-1.23	-0.17	22.02
18	6.93	-6.68	2.42	-0.74	2.5	14.36
19	5.56	-8.48	3.81	1.23	1.5	12.71
20	4.65	-6.32	3.12	2.71	0.83	8.29
21	3.05	-8.72	-7.27	-4.67	3.83	25.03
22	6.70	-6.80	-5.20	-3.2	-2.17	9.46
23	2.82	-7.40	-1.04	7.13	4.83	8.16
24	3.28	-6.20	-5.89	-6.64	-2.5	9.09
25	5.79	-6.44	7.27	5.66	1.83	7.49
26	3.51	-5.72	-8.66	5.17	-0.83	6.44
27	8.07	-5.84	-9.35	-0.25	-0.5	7.84
28	7.84	-8.12	-10.04	4.18	2.83	25.93
29	7.16	-6.56	-7.97	-5.66	3.17	19.34
30	3.73	-8.36	-2.42	2.21	-3.17	10.92

Response surface fitting

According to the scheme of DOE, the peak vertical acceleration solved by RADIOSS is presented in Table 3. The response surface fitting algorithm used was Least Squares Regression. The response surfaces of the peak vertical acceleration against landing condition parameters were shown in Figure 2.

It can be seen from Figure 2(a) that acceleration in proportion to vertical velocity, and it is less affected by horizontal velocity. Figure 2 (b) shown the response surface of acceleration against gradient and vertical velocity, the horizontal velocity is 5m/s. The vehicle landing upgrade when the gradient is positive, the acceleration is higher. As can be seen from the Figure 2(c), when the horizontal velocity is low, the acceleration is less affected by gradient. When the horizontal velocity is high, the impact acceleration when landing upgrade is much higher than landing downgrade.

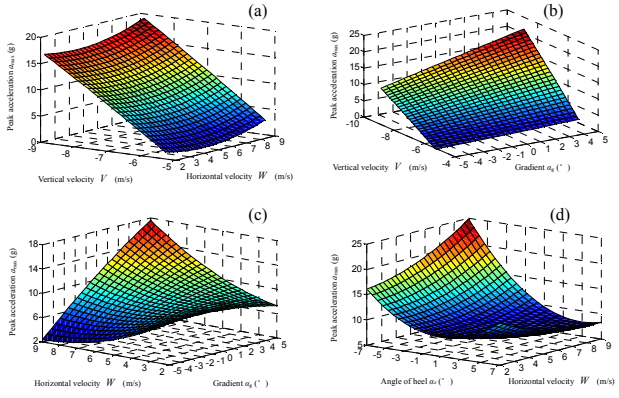

Fig.2 Response surfaces of the peak vertical acceleration against landing condition parameters

As it is shown in Figure 2 (d), the acceleration is in proportion to heel angle and horizontal velocity when heel angle is negative. Whereas, the acceleration in proportion to heel angle and in inverse proportion to horizontal velocity when heel angle is positive.

The response surfaces of the peak horizontal acceleration against landing condition parameters were gained in the same way. (Figure 3)

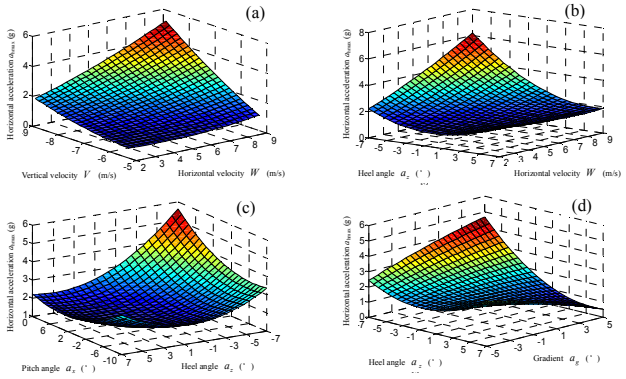

Fig.3 Response surfaces of the horizontal acceleration against landing condition parameters

Sensitivity analysis

Base on the response surfaces, the probabilistic sensitivity was obtained by the theory of sensitivity analysis. The result is shown in Figure 4.

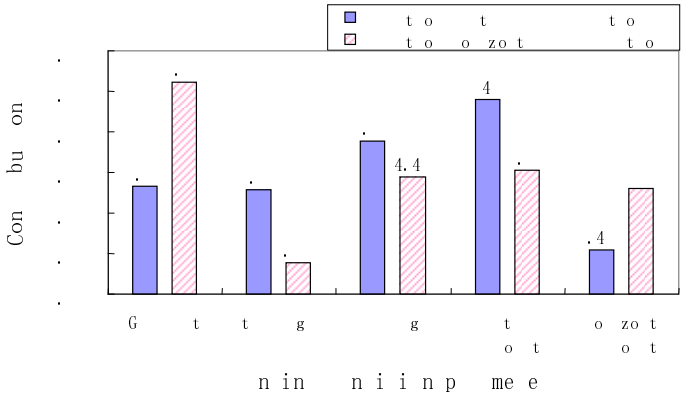

Fig.4 Results of probabilistic sensitivity analysis

As it is shown in Figure 4, the effect of vertical velocity on the vertical acceleration is the largest, heel angle takes second place, horizontal velocity is the least. The effect of gradient on the horizontal acceleration is the largest, vertical velocity and horizontal velocity are lesser, pitch angle is the least.

According to the results of sensitivity analysis, it is needed to control vertical velocity to avoid excessive vertical impact load. So parachute system is the key component for landing safely. The horizontal acceleration is the primary influence on landing stability of airdrop system. According to the sensitivity results, the gradient is the key for improving landing stability.

Conclusions

The methodology, which based on Finite Element and Response Surface method, was found to be a valuable tool that can be applied to execute sensitivity analysis. The ability to execute sensitivity analysis based on response surface built by 30 FE analysis runs was found to be particularly powerful. Such a capability is invaluable in this application where fully representative airdrop testing is difficult and expensive.

According to the sensitivity analysis results, it is found that
1) Vertical velocity effects the vertical acceleration most, so parachute system is the key component for avoiding excessive landing impact.
2) The gradient is the key for improving landing stability, so the landing terrain is important for the security of airborne vehicle.

References

[1] Xueqian CHEN, Shifu XIAO and Xin'en LIU: *An application of response surface method to structural parameter sensitivity and reliability analysis* (Mechanics in Engineering, Beijing 2012).

[2] C. M. Douglas: *Design and Analysis of Experiments*, (John Wiley & Sons 2005).

[3] E.G.Ewing, H.W.Bixby and T.W.Knacke: *Recovery systems design guide* (Report AFFDL-TR-78-151,Irvin Industries Inc,California,US 1978).

[4] Sibo NIU, Hongyan WANG and Baoshan CHI: *Cushioning characteristics of double-chamber airbag for heavy equipment recovery system* (Journal of Vibration and Shock., 2012).

[5] Hongyan WANG and Huangjie HONG: *Research on Simulation and Optimization of Cushion Characteristic of Airbags for Airborne Vehicle* (ACTA ARMAMENTARII.,2012).

Applied Mechanics and Materials Vol. 565 (2014) pp 98-106

doi:10.4028/www.scientific.net/AMM.565.98

Quadrotor Position Control Using Cascaded Adaptive Integral Backstepping Controllers

Younes Al Younes[1, a], Ahmad Drak[2, b], Hassan Noura[3, c], Abdelhamid Rabhi[4, d] and Ahmed El Hajjaji[5, e]

[1]Higher Colleges of Technology, Al Ain, United Arab Emirates

[2,3]United Arab Emirates University, Al Ain, United Arab Emirates

[4,5] University of Picardie Jules Verne, Amiens, France

[a]yalyounes@hct.ac.ae, [b]ahmad.drak@gmail.com,
[c]hnoura@uaeu.ac.ae,[d]abdelhamid.rabhi@u-picardie.fr, [e] ahmed.hajjaji@u-picardie.fr

Keywords: Quadrotor Vehicle, Nonlinear Control, Integral Backstepping Controller, Adaptive Law.

Abstract. This paper proposes a nonlinear control technique to control the position of the Qball-X4 quadrotor using a cascaded methodology of two Adaptive Integral Backstepping Controllers (AIBC). The nonlinear algorithm uses the principle of Lyapunov methodology in the backstepping technique to ensure the stability of the vehicle, and utilizes the integral action to eliminate the steady state error that caused by the disturbances and model uncertainties, as well as, the adaptation law will estimate the modeling errors caused by assumptions in simplifying the complexity of the quadrotor model. The algorithm goes through two stages of cascaded AIBCs; the first stage aims to stabilize the attitude and the altitude of the quadrotor, and the second stage feeds the first stage with the desired attitude values to control the position of the quadrotor.Flight test results show that the proposed algorithm is capable of controlling the position of the nonlinear quadrotor model.

Introduction

Nowadays, many research and studies are conducted on the area of the Vertical Take Off and Landing vehicles (VTOL). The high power to weight ratio and marvelous maneuverability gives the VTOL crafts the advantage over the other types of the Unmanned Arial Vehicles (UAV). Besides that, the cutting edge technology in electronics, sensor devices, and processing units encourage the researchers to design control methodologies that deals with the nonlinearities in such a system as the four rotors vehicle that called a quadrotor.

The first rotary-wing aircraft was built by Louis and Jacques Breguet in 1907. Since that time till now, the development that the world witnessed in the different aspects of technology and science, made from the quadrotor aircraft an attractive device for various research areas. The quite challenging dynamic nature of the quadrotor vehicle encouraged the researchers to apply their control methodologies on the vehicle, starting from the classical control theories, up to the complicated nonlinear control techniques.

The quadrotors are relatively cheap and easy to fly, thus making them the best choice when it comes to testing different control strategies on a UAV. Control strategies can be classified mainly into two different categories, linear and non-linear control. Different control strategies had been implemented in the quadrotor vehicle, some are explained thoroughly in [1-5].

The Linearization techniques of a nonlinear system degrades the controller performance, and in some cases, the linear controller fails to control the vehicle. Hence, lately the nonlinear control algorithms are gaining more interest than the linear control techniques.

The backstepping control technique is applied in [6] to stabilize the attitude of a micro quadrotor. The controller stabilizes the orientation angles in the presence of relatively high disturbances. [7] [8] and others used various nonlinear control techniques,such as: Hybrid Backstepping and Sliding-Mode control,to control the attitude and the altitude.

Controlling the position of the quadrotor is another challenging task. In this paper, the research is steered to control the position of the Qball-X4 quadrotor system that is assembled in the control

laboratory of the United Arab Emirates University (UAEU). The high performance onboard CPU, the reliable positioning camera system and the flexibility of deploying the control algorithm onboard through Matlab/Simulink made from this vehicle a suitable platform for research purposes.

Previous work from the author [9] has been considered by implementing the integral backstepping controller to stabilize the attitude and altitude of the quadrotor, and then augmenting the adaptation scheme on the control algorithm as represented in the work of [10]. The aim of this work is controlling the quadrotor position by cascading the translational subsystem controllers with the rotational subsystem controllers using AIBC technique.

In section II, the quadrotor nonlinear equations of motions will be provided. Section III will go through the derivation of the proposed control algorithm, and finally in section IV, real flight test results will be performed to validate the proposed algorithm.

Quadrotor Model

Fromthe literature, a set of nonlinear equations that represents the motion of the quadrotor is extracted and it will be used in this project, as shown below in (1). The derivation is based on the force/moment dynamics and kinematics. The work flow starts with defining the frames and notations used in the equations of motion, then the transformation between the different frames, and finally, the kinematics and dynamics of the quadrotor to extract the equations of motion.[4] [6][11] and [12]

$$\begin{bmatrix} \dot{\phi} \\ \dot{\theta} \\ \dot{\psi} \\ \dot{p} \\ \dot{q} \\ \dot{r} \\ \ddot{x}^e \\ \ddot{y}^e \\ \ddot{z}^e \end{bmatrix} = \begin{bmatrix} p + s(\phi)\, t(\theta)\, q + c(\phi)\, t(\theta)\, r \\ c(\phi)\, q - s(\phi)\, r \\ (s(\phi)/c(\theta))\, q + (c(\phi)/c(\theta))\, r \\ \left(-k_{dp}p^2 + \left(I_{yy} - I_{zz}\right) q\, r - J\omega_r q + \tau_{lift,x}\right)/I_{xx} \\ \left(-k_{dq}q^2 + (I_{zz} - I_{xx})\, p\, r + J\omega_r p + \tau_{lift,y}\right)/I_{yy} \\ \left(-k_{dr}r^2 + \left(I_{xx} - I_{yy}\right) p\, q + \tau_{drag}\right)/I_{zz} \\ \left(-k_{dx}\dot{x}^e + (c(\psi)\, s(\theta)\, c(\phi) + s(\psi)\, s(\phi)) \sum_{i=1}^{4} f_i\right)/m \\ \left(-k_{dy}\dot{y}^e + (s(\psi)\, s(\theta)\, c(\phi) - c(\psi)\, s(\phi)) \sum_{i=1}^{4} f_i\right)/m \\ \left(-k_{dz}\dot{z}^e - mg + (c(\theta)\, c(\phi)) \sum_{i=1}^{4} f_i\right)/m \end{bmatrix} \quad (1)$$

Where,

$c \equiv \text{cosine}$ and $s \equiv \text{sine}$

$(\phi, \theta, \psi)$are the rotational angles.

(p, q, r) represents the body angular rates vector about the body frame.

I_{xx} represents the inertia matrix of the quadrotor around the indicated axis.

$J$is the rotor's moment of inertia, and $(\omega_r = \omega_2 + \omega_4 - \omega_1 - \omega_3)$,

$k_{d(x,y,z)}$ represent the translational drag coefficients

$k_{d(p,q,r)}$ represent the rotational drag coefficients.

Quadrotor Control

The backstepping in nonlinear control is a technique that uses a recursive Lyapunov methodology to ensure the stability of the vehicle.

In this paper, a cascaded design of two integral backstepping controllers is proposed. The objective of the first controller is to stabilize the attitude and the altitude of the quadrotor and is called –Adaptive Integral Backstepping Controller for Attitude and Altitude Stabilization (AIBCAAS)-.

The second controller is feeding AIBCAAS with the desired attitude values to control the position in x and y axes. This controller will be known as, -Adaptive Integral Backstepping Controller for Position Control (AIBCPC)-.

In this section, the backstepping technique with integral action will be presented, and accordingly, the AIBCAAS and AIBCPC will be designed.

AdaptiveIntegral Backstepping Control Algorithm[11]

The general representation of the quadrotor nonlinear system is:

$$\dot{x} = f(x,u) + \alpha \tag{2}$$

Where vector **α** represents the time-dependent estimator of the modelling errors in the quadrotor dynamics. The modelling errors could be caused by assumptions in simplifying the complexity of the quadrotor model, manufacturing problems (asymmetry), variation in the quadrotor parameters at operation … etc. For any state variable in the system, the tracking error and its derivative could be written as follows:

$$e_1 = x_{1d} - x_1$$

$$\frac{de_1}{dt} = \dot{x}_{1d} - \dot{x}_1 \tag{3}$$

Where, x_{1d} is the desired value of the state variable, and x_1 is the state variable. This definition will systematically drive the tracking error to zero.

The Lyapunov function$V(e_1)$ is introduced, where it is positive definite around the desired position:

$$V(e_1) = \frac{1}{2}e_1^2$$

$$\dot{V}(e_1) = e_1(\dot{x}_{1d} - \dot{x}_1) \tag{4}$$

If the velocity $\dot{x}_1$ is the control input, it would be straightforward to choose $\dot{x}_1$ to have exponential convergence for the system:

$$\dot{x}_1 = \dot{x}_{1d} + c_1 e_1 \tag{5}$$

Where, c_1 is positive number that determines the convergence speed of the error. Consequently, the derivative of the Lyapunov function will be semi-negative definite and the error will converge exponentially to zero:

$$\dot{V}(e_1) = -c_1 e_1^2 \leq 0 \tag{6}$$

The integral action.The integral action will be introduced by choosing the virtual input as follows:

$$x_2 = c_1 e_1 + \dot{x}_{1d} + \lambda_1 \mathcal{X}_1 \tag{7}$$

Where,$\mathcal{X}_1 = \int_0^t e_1(\tau)d\tau$,$\lambda_1$ is the integral constant.

The integral action will eliminate the steady state error that is caused by many reasons, e.g. disturbances, modeling error and uncertainties, etc.

Since,x_2 is not our control input, there exists a dynamic error between it and its desired behaviorx_{2d}. Therefore, the dynamic error will be compensated by defining the velocity tracking error and its derivative as follows:

$$e_2 = x_2 - (c_1 e_1 + \dot{x}_{1d} + \lambda_1 \mathcal{X}_1)$$

$$\frac{de_2}{dt} = \dot{x}_2 - c_1(\dot{x}_{1d} - \dot{x}_1) - \ddot{x}_{1d} - \lambda_1 e_1 \tag{8}$$

We can re-write the derivative of the position and velocity tracking errors:

$$\frac{de_1}{dt} = -c_1 e_1 - e_2 - \lambda_1 \mathcal{X}_1$$

$$\frac{de_2}{dt} = \dot{x}_2 - \ddot{x}_{1d} + c_1(c_1 e_1 + e_2 + \lambda_1 \mathcal{X}_1) - \lambda_1 e_1 \tag{9}$$

The augmented Lyapunov function will be:

$$V(e_1, e_2, \mathcal{X}_1) = \frac{1}{2}e_1^2 + \frac{1}{2}e_2^2 + \frac{\lambda_1}{2}\mathcal{X}_1^2 \tag{10}$$

The derivative will satisfy the convergence of the velocity tracking error, if and only if:

$$\dot{V} = -c_1 e_1^2 - c_2 e_2^2 \leq 0 \tag{11}$$

Therefore, the state variable rate should be chosen:

$$\dot{x}_2 = (1 - c_1^2 + \lambda_1)e_1 + (c_1 + c_2)e_2 - c_1\lambda_1 \mathcal{X}_1 + \ddot{x}_{1d} - \alpha_1 \tag{12}$$

If we consider the nonlinear term in (2) is equal $f(x,u) = f^*(x) + Bu$, then the control input will be:

$$u_2 = \frac{1}{b_1}[(1 - c_1^2 + \lambda_1)e_1 + (c_1 + c_2)e_2 - c_1\lambda_1 \mathcal{X}_1 + \ddot{x}_{1d} - f_1^*(x) - \alpha_1] \tag{13}$$

The Adaptation Scheme. The main purpose of the adaptation law is the online anticipation of α_1. But the real value of α_1 is unknown, therefore it will be replaced by the estimated value $\hat{\alpha}_1$ and the adaptation law will be designed:

$$u_2 = \frac{1}{b_1}[(1 - c_1^2 + \lambda_1)e_1 + (c_1 + c_2)e_2 - c_1\lambda_1 \mathcal{X}_1 + \ddot{x}_{1d} - f_1^*(x) - \hat{\alpha}_1] \tag{14}$$

The update law for the estimated parameter α should be derived to achieve the estimation. For this purpose, the parameter estimation error signal in (14) will be defined as follows:

$$\tilde{\alpha}_1 = \hat{\alpha}_1 - \alpha_1 \tag{15}$$

By substituting (14) into (8) the velocity tracking error derivative will be:

$$\frac{de_2}{dt} = -c_2 e_2 - e_1 + \tilde{\alpha}_1 \tag{16}$$

The positive definite Lyapunov function should consider the estimated parameter error as follows:

$$V(e_1, e_2, \mathcal{X}_1, \tilde{\alpha}_1) = \frac{1}{2}e_1^2 + \frac{1}{2}e_2^2 + \frac{\lambda_1}{2}\mathcal{X}_1^2 + \frac{1}{2\gamma_1}\tilde{\alpha}_1^2 \tag{17}$$

Consequently the derivative of the Lyapunov function will be:

$$\dot{V} = \lambda_1 \mathcal{X}_1 \dot{\mathcal{X}}_1 + e_1\dot{e}_1 + e_2\dot{e}_2 + \frac{\tilde{\alpha}_1}{\gamma_1}\frac{d\hat{\alpha}_1}{dt}$$

$$\dot{V} = -c_1 e_1^2 - c_2 e_2^2 + \tilde{\alpha}_1\left\{e_2 + \frac{1}{\gamma_1}\frac{d\hat{\alpha}_1}{dt}\right\} \tag{18}$$

Where; γ_1 is a positive constant that determines the estimate convergence speed.

In order to render the non-positivity of the Lyapunov derivative in (18), the adaptation law for the estimated parameter $\hat{\alpha}_1$ will be chosen as follows:

$$\frac{d\hat{\alpha}_1}{dt} = -\gamma_1 e_2 \tag{19}$$

By integrating (38):

$$\hat{\alpha}_1 = -\gamma_1 \mathcal{X}_2 \tag{20}$$

Where; $\mathcal{X}_2 = \int_0^t e_2(\tau)d\tau$. This is will lead to satisfy the convergence conditions for both $\tilde{\alpha}_1$ and the derivative of Lyapunov function as in (11).

Finally, the control input that represents the adaptation law and the integral action is extracted as shown below:

$$u_2 = \frac{1}{b_1}[(1 - c_1^2 + \lambda_1)e_1 + (c_1 + c_2)e_2 - c_1\lambda_1 \mathcal{X}_1 + \gamma_1 \mathcal{X}_2 + \ddot{x}_{1d} - f_1^*(x)] \tag{21}$$

By the definition of Lyapunov function and its negative definite derivative, the position tracking error e_1, the velocity tracking error e_2, the integral term $\mathcal{X}_1$, and the estimated modelling error α_1, are bounded states. Hence, the boundness of all the states in the closed-loop control system is fulfilled. Therefore the derivatives of the error signals, $\dot{e}_1$ and $\dot{e}_2$, are bounded as well.

Control System Representation

To apply the integral backstepping algorithm on each of the equations of motion, the state variables vector and the control inputs vector will be defined first:

State variables.

$$\begin{aligned}
x_1 &= \phi & \dot{x}_1 &= x_2 \\
x_2 &= \dot{\phi} & \dot{x}_2 &= \ddot{\phi} \\
x_3 &= \theta & \dot{x}_3 &= x_4 \\
x_4 &= \dot{\theta} & \dot{x}_4 &= \ddot{\theta} \\
x_5 &= \psi & \dot{x}_5 &= x_6 \\
x_6 &= \dot{\psi} & \dot{x}_6 &= \ddot{\psi} \\
x_7 &= x^e & \dot{x}_7 &= x_8 \\
x_8 &= \dot{x}^e & \dot{x}_8 &= \ddot{x}^e \\
x_9 &= y^e & \dot{x}_9 &= x_{10} \\
x_{10} &= \dot{y}^e & \dot{x}_{10} &= \ddot{y}^e \\
x_{11} &= z^e & \dot{x}_{11} &= x_{12} \\
x_{12} &= \dot{z}^e & \dot{x}_{12} &= \ddot{z}^e
\end{aligned}$$

$$u_1 = \sum_{i=1}^{4} f_i = k.\sum_{i=1}^{4} \Omega_i^2$$

$$u_2 = \tau_{lift,x} = l(f_4 - f_2) = k.l(\Omega_4^2 - \Omega_2^2)$$

$$u_3 = \tau_{lift,y} = l(f_1 - f_3) = k.l(\Omega_1^2 - \Omega_3^2)$$

$$\begin{aligned}
u_4 = \tau_{drag} &= d(f_2 + f_4 - f_1 - f_3) \\
&= k.d(\Omega_2^2 + \Omega_4^2 - \Omega_1^2 - \Omega_3^2)
\end{aligned}$$

Where;
$k \equiv$ force-velocity constant
$l \equiv$ arm length
$d \equiv$ rotor's reaction torque constant

Control inputs.

Assumption- For attitude control, the assumption $\ddot{\boldsymbol{\Theta}} = \dot{\boldsymbol{\omega}}^{\mathbf{b}}$ is valid for small angles perturbation [6]. Thus, the nonlinear system (1) can be re-written as follows:

$$\begin{bmatrix} \dot{x}_1 \\ \dot{x}_2 \\ \dot{x}_3 \\ \dot{x}_4 \\ \dot{x}_5 \\ \dot{x}_6 \\ \dot{x}_7 \\ \dot{x}_8 \\ \dot{x}_9 \\ \dot{x}_{10} \\ \dot{x}_{11} \\ \dot{x}_{12} \end{bmatrix} = \begin{bmatrix} x_2 \\ \left(-k_{dp}{x_2}^2 + \left(I_{yy} - I_{zz}\right)x_4x_6 - J\omega_r x_4 + u_2\right)/I_{xx} \\ x_4 \\ \left(-k_{dq}{x_4}^2 + (I_{zz} - I_{xx})x_2x_6 + J\omega_r x_2 + u_3\right)/I_{yy} \\ x_6 \\ \left(-k_{dr}{x_6}^2 + \left(I_{xx} - I_{yy}\right)x_2x_4 + u_4\right)/I_{zz} \\ x_8 \\ [-k_{dx}x_8 + (c(x_5)\,\mathrm{s}(x_3)\,\mathrm{c}(x_1) + \mathrm{s}(x_5)\,\mathrm{s}(x_1))u_1]/m \\ x_{10} \\ [-k_{dy}\,x_{10} + (\mathrm{s}(x_5)\,\mathrm{s}(x_3)\,\mathrm{c}(x_1) - \mathrm{c}(x_5)\,\mathrm{s}(x_1))u_1]/m \\ x_{12} \\ [-k_{dz}\,x_{12} - mg + (\mathrm{c}(x_3)\,\mathrm{c}(x_1))\,u_1]/m \end{bmatrix} \quad (22)$$

Next, the first stage of the cascaded AIBCs will be implemented.

Adaptive Integral Backstepping Controller for Attitude and Altitude Stabilization (AIBCAAS).

The stabilization of the attitude and altitude will be achieved by substituting the equations of motion (roll, pitch, yaw, and altitude z) into equation (21). Consequently, the control inputs are going to be:

$$u_2 = I_{xx}[(1 - c_1^2 + \lambda_1)e_1 + (c_1 + c_2)e_2 - c_1\lambda_1\mathcal{X}_1 + \gamma_1\mathcal{X}_2 + \ddot{x}_{1d}] + k_{dp}{x_2}^2 - \left(I_{yy} - I_{zz}\right)x_4x_6 + J\omega_r x_4$$

Similarly, for pitch, yaw and z control:

$$u_3 = I_{yy}[(1 - c_3^2 + \lambda_3)e_3 + (c_3 + c_4)e_4 - c_3\lambda_3\mathcal{X}_3 + \gamma_2\mathcal{X}_4 + \ddot{x}_{3d}] + k_{dq}{x_4}^2 - (I_{zz} - I_{xx})x_2x_6 - J\omega_r x_2$$

$$\begin{aligned}
u_4 = I_{zz}[(1 - c_5^2 + \lambda_5)e_5 + (c_5 + c_6)e_6 - c_5\lambda_5\mathcal{X}_5 + \gamma_3\mathcal{X}_6 + \ddot{x}_{5d}] + k_{dr}{x_6}^2 \\
- \left(I_{xx} - I_{yy}\right)x_2x_4
\end{aligned}$$

$$u_1 = \frac{m}{\mathrm{c}(x_3)\,\mathrm{c}(x_1)}\left[(1 - c_{11}^2 + \lambda_{11})e_{11} + (c_{11} + c_{12})e_{12} - c_3\lambda_5\mathcal{X}_5 + \gamma_6\mathcal{X}_{12} + \ddot{x}_{11d} + \frac{k_{dz}}{m}\,x_{12} + g\right] \quad (23)$$

Adaptive Integral Backstepping Controller for Position Control (AIBCPC)

The coupling between the rotational and translational motions (as shown in the equations of motion (22)) leads to the idea of cascading AIBCAAS with another controller, which is AIBCPC, so that the position on *x-axis&y-axis* will be controlled by adjusting the desired angles $\boldsymbol{\theta_d}$and $\boldsymbol{\phi_d}$respectively. The AIBCPC uses the backstepping technique to ensure the stability of the system, the integral action to eliminate the steady state error in the position, and the adaptation scheme to estimate the modelling error. From equation (21) and the equations of motion (22), the control inputs of AIBCPC are:

$$x_{1d} = \sin^{-1}\left[\frac{1}{c(x_5)}\left(-\frac{m}{u_1}\left[(1-c_9^2+\lambda_9)e_9+(c_9+c_{10})e_{10}-c_9\lambda_9\chi_9+\gamma_5\chi_{10}+\ddot{x}_{9d}+\frac{k_{dy}}{m}\,x_{10}\right]\right)+s(x_5)\,s(x_3)\,c(x_1)\right]$$

$$x_{3d} = \sin^{-1}\left[\frac{1}{c(x_5)\,c(x_1)}\left(\frac{m}{u_1}\left[(1-c_7^2+\lambda_7)e_7+(c_7+c_8)e_8-c_7\lambda_7\chi_7+\gamma_4\chi_8+\ddot{x}_{7d}+\frac{k_{dx}}{m}\,x_8\right]\right)-s(x_5)\,s(x_1)\right] \quad (43)$$

The equations show the coupling between the different angles. Where, no assumptions are taken to reduce the complexity of the motion in x and y directions. As a result, AIBCPC shows reliability in controlling the position with different yaw angle.

The block diagram of the control architecture used in this project is depicted in Fig. 1:

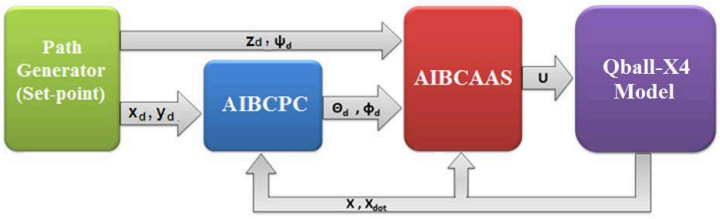

Fig. 1 Control Architecture.

The block diagram gives an overall view about the control structure for attitude, altitude, and position control of Qball-X4 quadrotor.

Flight Test Results

QUANSER platform is mainly consist of a quadrotor called Q-ballX4, ground station and six Optitrack cameras. A safety netis constructed to ensure the safety of the operator(s) and to avoid fatal crashes of the Qball-X4 (See Fig. 2). The control algorithm can be programmed using Matlab/Simulink environment and then uploaded wirelessly to the Q-ballX4 [8], [14]. The Optitrack cameras are usedto determine the position of the Qball-X4 in the workspace as shown in Fig. 2.

Fig. 2 Safety net outlining the Qball-X4 workspace.

TABLE I
QBALL-X4 QUADROTOR PARAMETERS [14]

Mass , *m*	1.4 kg
I_X	0.03 kg.m^2
I_Y	0.03 kg.m^2
I_Z	0.04 kg.m^2
Rotor inertia , *J*	1.04 x 10^{-4} kg.m^2
Arm length, *l*	0.2 m

A list of the Qball-X4 quadrotor parameters is presented in Table I:

The following considerations are taken to perform a safe flight test of the Qball-X4 quadrotor:

1. The integral backstepping controllers' parameters are tuned according to the limitation of the control inputs, which are the forces generated by the rotors of the Qball-X4 quadrotor.
2. The saturation blocks are implemented to ensure the work under the actual capabilities of the system.
3. For safety purposes, the desired outputs of AIBCPC (desired pitch and roll angles) are saturated in the range of ±5º.

In this flight tests the performance of the quadrotor is analyzed in following a pre-generated square path. The square path ranges from -0.5 m to +0.5 m (X-axis) and -0.5m to 0.5m (Y-axis). The Z-axis (altitude) is kept constant at 0.5m. The quadrotor flies for 10 sec on each side of the square path, and stays 5 sec on each corner.

Fig. 5 depicts the measured values of the roll, pitch and position (X, Y, Z) data:

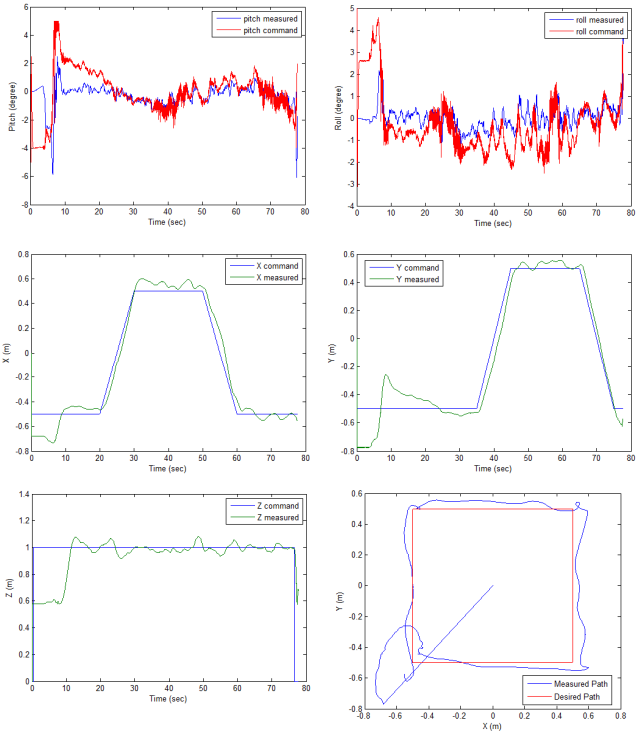

Fig. 3 System response using the CABIC

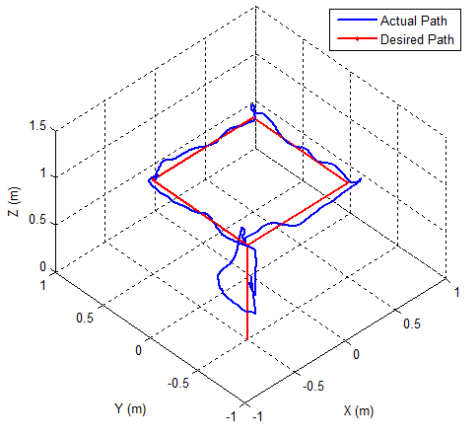

Fig. 4 Position response

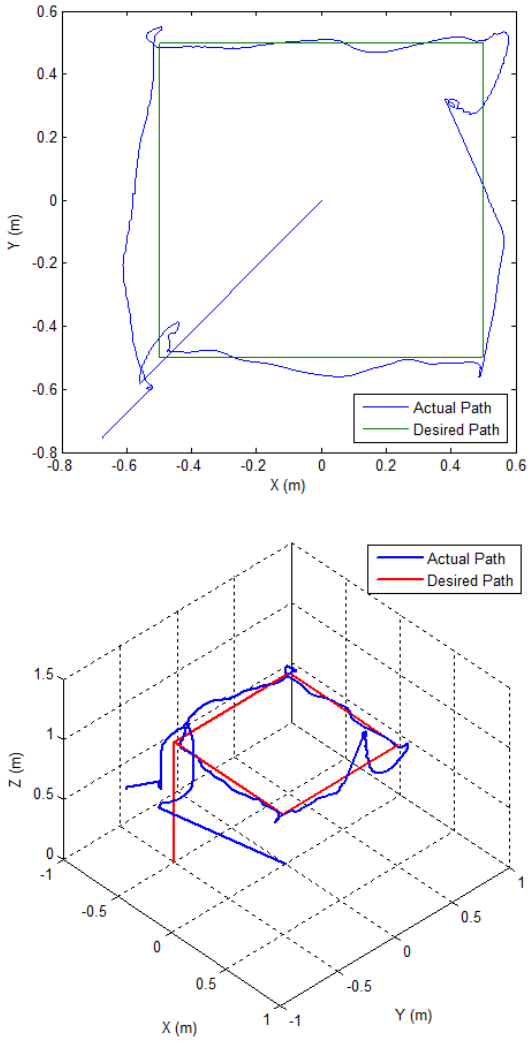

Fig. 5 Position response with faulty cameras reading

A 3D trajectory is shown in Fig. 4:

The position readings are taken according to the location of the markers on the quadrotor. The height reading starts from +0.5 m while the quadrotor still in the ground. This is because the markers are fixed half a meter above the ground level (on the quadrotor's cage). Therefore, +1 m altitude means that the quadrotor flies with a height of +0.5 m.

The results show that the controller is able to track the trajectory with a square-mean-error of about 6 cm in both X and Y axes.

One of the trails involved a faulty position reading because of the cameras calibration. The controller dealt with the fault and returned the quadrotor to the correct path as shown in Fig. 5.

In general, the results have validated the control algorithm capabilities in controlling the position of the quadrotor with and without faulty readings and disturbances.

Conclusion

In this paper, a nonlinear control approach is proposed based on CAIBC methodology. The technique employs the coupling between the rotational and translational systems to feed the AIBCAAS with the desired attitude values to control the position of the quadrotor. The adaptation scheme with the Integral action will overcome any disturbances and model uncertainties and the Lyapunov methodology will ensure the system stability. Altogether, the cascaded scheme of the AIBCAAS and AIBCPC are proposed to control the attitude and the position of Qball-X4 quadrotor, where the flight test results have validated the control algorithm and shown the system performance in controlling the position of the quadrotor.

Future work.The study of reconfiguring the controller is crucial in fault tolerant control, where the optimization and adaptation of the controller's parameters according to the present fault is an interesting research area to look at, beside the detection and isolation for sensor and actuator faults.

Acknowledgment

This work is supported by Higher Colleges of Technology (HCT) with the collaboration of United Arab Emirates University (UAEU).

References

[1] Fowers, G. Spencer "Stabilization and Control of a Quad-Rotor Micro-Uav Using Vision Sensors". Provo, UT : Brigham Young University, 2008. Master Thesis.

[2] G. Hoffmann, D.G.Rajnarayan, S.L. Waslander, D. Dostal, J.S. Jang, C.J. Tomlin, "The Stanford testbed of autonomous rotorcraft for multi agent control (STARMAC)," Digital Avionics Systems Conference, 2004. DASC 04. The 23rd , vol.2, pp. 12.E.4- 121-10 Vol.2, 24-28.

[3] C. Henrik, Stefen, Lars, Michael, "Autonomous Hovering with a Quadrotor Helicopter". Aalborg, Denmark : Aalborg University, 2008.

[4] T. Zhang, W. Li, M. Achtelik, K. Kuhnlenz and M. Buss, "Multi-sensory motion estimation and control of a mini-quadrotor in an air-ground multi-robot Sys" in *Robotics and Biomimetics*, 2009.

[5] F. Sharifi, M. Mirzaei, B. Gordon and Y. Zhang, "Fault tolerant control of a quadrotor UAV using sliding mode control," in *Control and Fault-Tolerant Systems (SysTol), 2010*, Nice, 2010.

[6] S. Bouabdallah, "Design and Control of Quadrotors with Application to Autonomous Flying". Algeria : University of AboubekrBelkaid, 2007. Master Thesis.

[7] J. Colorado, A. Barrientos, A. Martinez, B. Lafaverges, J. Valente, "Mini-quadrotor attitude control based on Hybrid Backstepping &Frenet-Serret theory," Robotics and Automation (ICRA), 2010 IEEE International Conference on , pp.1617-1622, 3-7 May 2010.

[8] H. Bouadi, M. Bouchoucha, M. Tadjine, "Sliding Mode Control based on BacksteppingApproach for an UAV Type-Quadrotor". World Academy of Science, Engineering and Technology, 2007.

[9] Y. Al Younes, "Establishing Autonomous AUS-Quadrotor," M.S. thesis, Dept. of Mechatronics. Eng., AUS Univ., Sharjah, UAE, 2009.

[10] Pettersen, Mustafic, and Fogh, "Nonlinear Control Approach to Helicopter Autonomy," M.S. thesis, Dept. Electronic. Sys., Aalborg Univ., Denmark, 2005.

[11] Beard, Randal W, "Quadrotor Dynamics and Control," M.S. thesis, Brigham Young Univ., Provo, UT, 2008.

[12] John J. Craig, *Introduction to Robotics Mechanics and Control*. Addison-Wesley Publishing Company, Inc, 2nd edition, 1989.

[13] Y. Al Younes, M. Jarrah and S. Sukkariah, “Adaptive Integral Backstepping Controller for an Autonomous Rotorcraft”, the 6th International Symposium on Mechatronics and its Applications (ISMA’09), Sharjah, UAE, March 23-26, 2009.

[14] Quanser, "QUARC® Real-Time Control Software," 13 January 2013. [Online]. Available: http://www.quanser.com/products/QUARC. [Accessed 10 December 2013].

Applied Mechanics and Materials Vol. 565 (2014) pp 107-112

doi:10.4028/www.scientific.net/AMM.565.107

Asymmetrical Lateral Jet Interaction on a Slender Body in Supersonic Flow

Shijie Luo[a]

China Academy of Aerospace Aerodynamics, Beijing, P.R.China, 100074

[a]lord.p@163.com

Keywords: Slender body, Supersonic, Lateral jet interaction, Asymmetrical lateral jet, Near-field interaction, Far-field interaction

Abstract. The lateral jet interaction on a slender body with rudders in supersonic flow had been investigated by numerical simulation, when the lateral jet is not in the longitudinal symmetry plane. It was called Asymmetrical lateral jet interaction in this paper. The flow features of jet interaction flowfield on the surface of the body or in the space far from the surface at different angles of attack and total pressure of jet was analyzed. As a result, the lateral jet interaction disturbed the pressure distributions of the slender body, and it was divided into near-field interaction near jet and far-field interaction aft-body on the basis of distance to jet. With the variety of the angle of attack and total pressure of jet, the pressure distributions at the aft-body change tempestuously, thereby the normal and lateral load will be from positive to negative, or reverse. The results also showed that the far-field interaction played a major role in the lateral jet interaction on a slender body in supersonic flow. The far-field interaction was caused by the changing of the outflow direction and intensity. Besides, the force/moment amplification factors presented highly nonlinear with the variety of angle of attack and total pressure of jet.

Introduction

The flowfield induced by a jet exhausting into a crossflow is a complex flow that has widespread applications in both military and civil industries., such as rocket motor thrust vector control systems, supersonic combustion, high speed flight vehicle reaction control system [1,2,3] The jet interaction is similar to protuberant obstacle interaction, such as column in plate, quadrate columniation in plate, rudder in revolution body. The interaction exhibits highly complicated flow phenomena, including shock/boundary layer interaction, shock/shock interaction, flow separation and reattachment as well as complex spatial vortices. Foretime, there are many studies devoted to the flowfield, jets in the flat plate and jets in a revolution body. For jet interaction on a revolution body, there are two major interactions of lateral jet interaction, which are near-field interaction near the jet and far-field interaction after-body [4]. The jet interaction on a revolution body of cone-cylinder-flare is investigated [5]. The jet/lifting surfaces interaction on a revolution body is investigated [6,7]. But, these studies are focused on jet in the longitudinal symmetry plane paralleling the freestream, the study of jet not in the longitudinal symmetry plane is very few, these tow kinds of lateral jet interaction are called symmetrical lateral jet interaction and Asymmetrical lateral jet interaction.

In this paper, a numerical investigation has been conducted to research the Asymmetrical lateral jet interaction, and the interaction characteristic at different angles of attack α and pressure ratio P_j/P_∞ is analyzed. Besides, the present paper also analyzes the near-field interaction, far-field interaction and jet interaction efficiency considered by force/moment amplification factors also.

Numerical Method and Calculating Conditions

Numerical method

The numerical study uses a finite-difference approach and multi-block patched grid to solve the 3-D Reynolds-Averaged Navier-Stokes equations, and the classical Spalart-Allmaras model for turbulence.

The no-slip, no-penetration and adiabatic wall conditions are adopted to deal with the body surface. The injection nozzle is considered as part of the computational domain.

Calculating model and conditions

The computational model is a cone-cylinder body with four rudders and a supersonic jet nozzle. The total model length is 832mm. The diameter of column is 50mm, and the center-point of circular supersonic nozzle is located 240mm from the nose tip of the body, and the nozzle has a nominal diameter of 4mm. The Mach number of jet (M_j) is 3.0. The angle of cone is 25°. The origin of body coordinates is located 450mm from the nose tip.

The configuration of model is shown in Fig. 1. Note that all of the rudders have the same exposed semi-span 30mm, and the leading edge sweep angle of 51°.The position of nozzle relative to rudders is shown in Fig. 2. The angle from nozzle to rudder2 is 45°. Fig. 3 shows the circumferential angle (φ) definition. Fig. 4(a) shows the multi-block grid structure for model. Fig. 4(b) shows the grid near the jet.

The calculation parameters based on test cases are listed in Table 1. The exhausting gas of jet is air. The total pressure and temperature of freestream are $P_{0\infty}$ and $T_{0\infty}$, respectively. The total pressure and temperature of jet are P_{0j} and T_{0j}, respectively. P_j/P_∞ is the ratio of nozzle exit static pressure P_j to static pressure P_∞ of freestream.

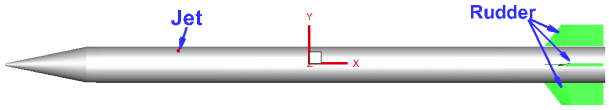

Fig. 1 Configurations of slender body/rudders

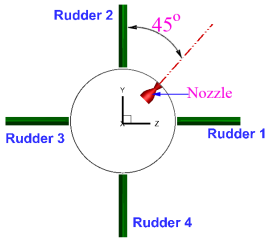

Fig. 2 The position of nozzle on slender body

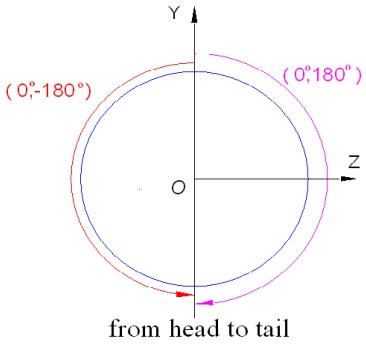

Fig. 3 The definition of circumferential angle(φ)

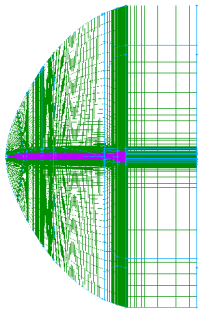

(a) Multi-block grid structure for model

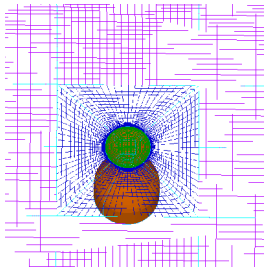

(b) Jet domain.

Fig. 4 Calculating grid

Table 1 Calculation parameters

Freestream parameters				Jet parameter		
M_∞	$P_{0\infty}$(MPa)	$T_{0\infty}$(K)	α(°)	M_j	P_{0j}(MPa)	T_{0j}(K)
3.0	0.3	293	10	3.0	4.0	293
2.0	0.2	293	-20~15	3.0	2.0, 4.0, 6.0, 8.0	293

Results and Discussions

Near-field interaction and far-field interaction

When jet is in the longitudinal symmetry plane, the interaction flowfield is symmetrical about the longitudinal symmetry plane. However, when the jet is not in the longitudinal symmetry plane, the interaction flowfield is not symmetrical about the longitudinal symmetry plane.

Fig. 5 shows the surface pressure contours and stream lines with and without jet interaction flowfield for α=10°, M_∞=3.0, P_{0j}=4.0. In Fig. 5, when a supersonic jet is injected into the supersonic free stream, the surface pressure distribution near jet was destroyed, the direction and intensity of outflow was changed on aft-body and rudders. The stream lines ahead of second rudder are asymmetrical about the longitudinal symmetry plane, then, the pressure distribution after body and rudders is asymmetrical. This not only caused a normal load, but also caused a lateral load, and the main region generated lateral load is after body and second rudder, the secondary region is near nozzle.

According to above, the jet interaction is divided into near-field interaction near jet and far-field interaction after body. In Fig. 6, the pressure (P/P_∞) with jet interaction is compared to pressure without jet interaction on the nozzle meridian. Fig. 6 also shows the near-field and far-field interaction region The pressure near-field interference region varies greatly, while the pressure far field interference region changes smoothing. However, the area of far-field interference region is much larger than the area of near-field interference region, which resulted the load in far-field interaction region will be greater than the load in near-field interaction region. Fig. 5 and Fig. 6 shows that the far-field interaction palyed a major role in the flowfield for jet not in the longitudinal symmetry plane.

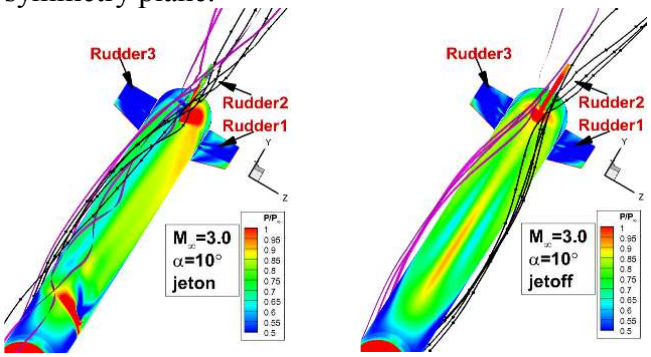

(a) With jet interaction (b) Without jet interaction

Fig. 5 The surface pressure (P/P_∞) contour and streamlines (M_∞=3.0, P_{0j}=4.0)

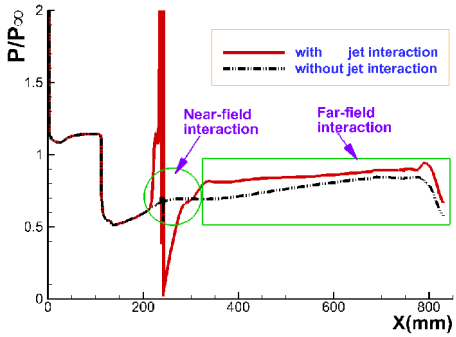

Fig. 6 Comparison pressure (P/P_∞) with jet interaction and pressure without jet interaction on the nozzle meridian (M_∞=3.0, P_{0j}=4.0)

Analysis of angle of attack influence

In order to analysis the supersonic flowfield, the parametric study was carried out for α= -10°, 0°, 10°, 15°, M_∞=2.0, P_{0j}=4.0. Fig. 7 shows the surface pressure contours and stream lines with and without jet interaction flow field of angles of attack. In Fig. 7, when supersonic jet exhausts into supersonic free stream, the surface pressure distribution near jet was destroyed. The surface pressure distribution aft-body and rudders were destroyed at α is 10°, 15°, but when α is -10°, or 0°, the surface pressure distribution aft-body and rudders are symmetrical about the longitudinal symmetry plane and same to surface pressure distribution without jet interaction.

In Fig. 7, the surface pressure contour and streamlines ahead of rudder2 were showed at α is -10°, 0°, 10°, 15°. From these figures, the freestream was interacted by jet, the streamlines aft-body are asymmetrical about the longitudinal symmetry plane α is 10°, 15°, but, the streamlines aft-body are symmetrical about the longitudinal symmetry plane α is -10°, 0°. When increasing the angle of attack, the asymmetrical range is increasing from near jet to rudder, then, the surface pressure distribution also changed from near jet to rudder, especially the positive angles of attack. Since lateral jet interfered, the direction and intensity of outflow varies greatly with angle of attack, which directly affects surface pressure after body and rudders. This not only caused a normal load, but also caused a lateral load, and the main region generated lateral load is after body and rudders, and, the secondary region is near nozzle.

In Fig. 7c-d, it can be seen the jet interaction produces a positive lateral load at angle of attack of 10°. otherwise produces a negative lateral load at 15°. In Fig. 5a-b, the lateral load at angle of attack of

-10°, 0° is far less than that at angle of attack of 10° or 15°. According to above, jet interaction presents highly nonlinear with angle of attack, the interaction effect showed favorable or unfavorable interaction.

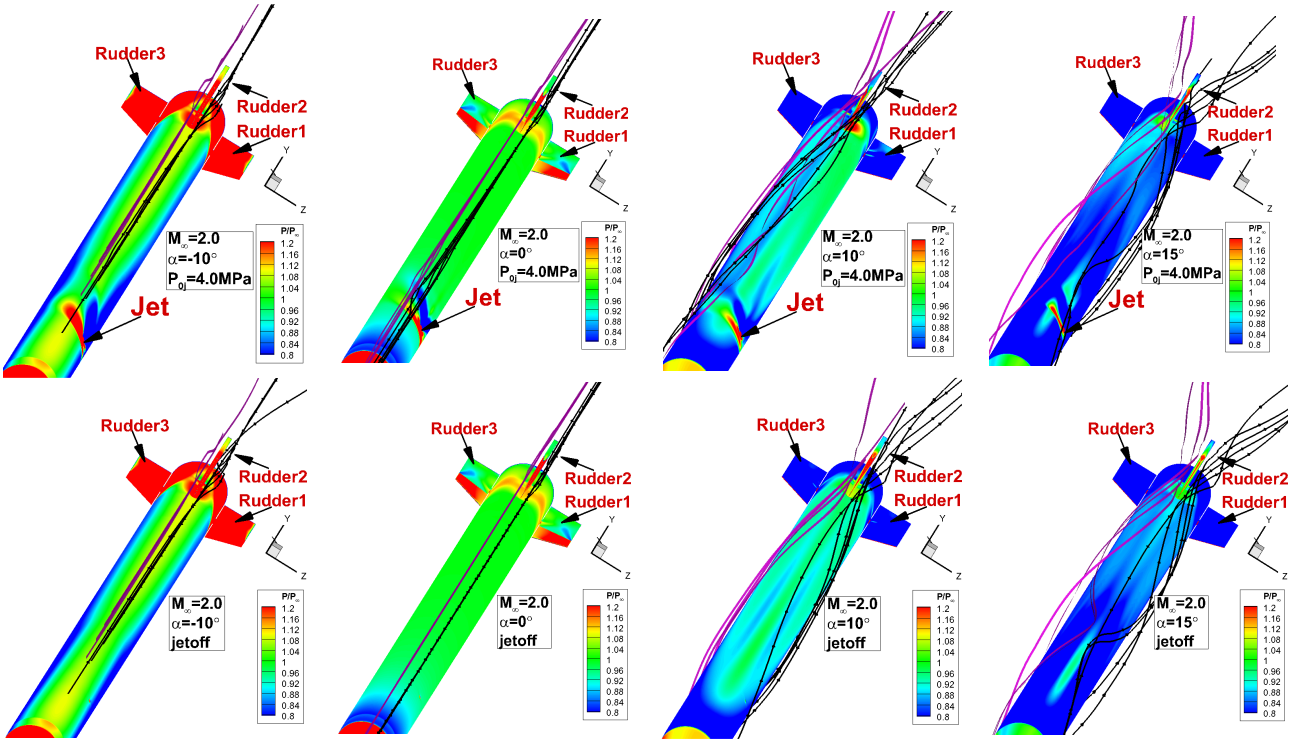

(a) α = -10° (b) α = 0° (c) α = 10° (d) α = 15°

Fig. 7 The surface Pressure (P/P_∞) contour and streamlines of different angles of attack (jetoff represents without jet interaction)

According to above, jet interaction is divided into near-field interaction near jet and far-field interaction after body. In Fig. 8, the pressure with jet interaction is compared to pressure without jet interaction on the nozzle meridian at different angles of attack. Fig. 6 also shows the pressure near-field interaction region varies greatly, while the pressure far field interaction region changes smoothing. However, the area of far-field interaction region is much larger than the area of near-field interaction region, which resulted the load in far-field interference region will be greater than the load in near-field interference region.

In order to illuminate the circumferential interaction characteristic , Fig. 9 compared pressure with jet interaction to pressure without jet interaction on the section located 745mm from the nose tip at α is -10°, 0°, 10°, 15°. The section produces a positive lateral load at angle of attack of 10°, produces a negative lateral load at 15°. Fig. 9 shows more clearly the phenomenon of the lateral load rapid change at positive angle of attack, and the leeward region is the main interaction region. From Fig. 7-9, it can be seen that the far-field interaction plays a major role for Asymmetrical lateral jet interaction. The jet interaction efficiency will be highly nonlinear changed with angle of attack.

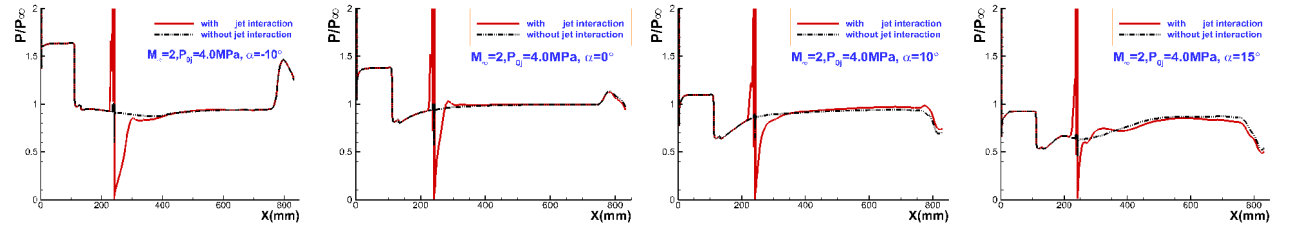

(a) α = -10° (b) α = 0° (c) α = 10° (d) α = 15°

Fig. 8 Comparison with pressure (P/P_∞) with jet interaction and pressure without jet interaction on the nozzle meridian at α is -10°, 0°, 10°, 15°.

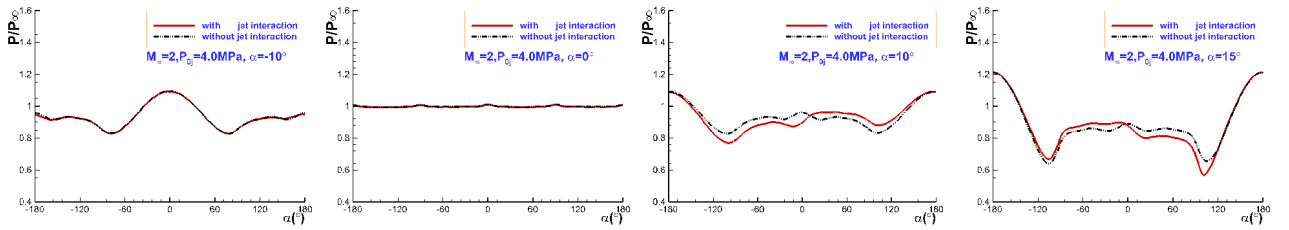

(a) α = -10° (b) α = 0° (c) α = 10° (d) α = 15°

Fig. 9 Comparison pressure (P/P_∞) with jet interaction to pressure without jet interaction on the secton located 745mm from the nose tip at α is -10°, 0°, 10°, 15°.

Analysis of total pressure of jet influence

According to above, surface pressure contour and streamlines ahead of rudder2 change tempestuously at positive angle of attack. In order to illuminate thoroughly positive angle of attack interaction characteristic, the pressure ratio study was carried out for P_{0j}=2.0, 4.0, 6.0MPa. Fig. 10 shows the surface Pressure (P/P_∞) contour and streamlines of different total pressure of jet. When increasing the total pressure of jet, the high pressure region and streamlines ahead of rudder2 are change tempestuously. The lateral jet interaction produces a positive lateral load at P_{0j} is 2.0MPa, produces a negative lateral load at P_{0j} is 4.0MPa, 6.0MPa, 8.0MPa. In addition, the lateral load for P_{0j}=4.0MPa is far less than the lateral load for P_{0j}=6.0, 8.0MPa.Namely, the influence of jet interacts freestream is changes tempestuously with pressure ratio. The jet interaction efficiency will be highly nonlinear changed with pressure ratio.

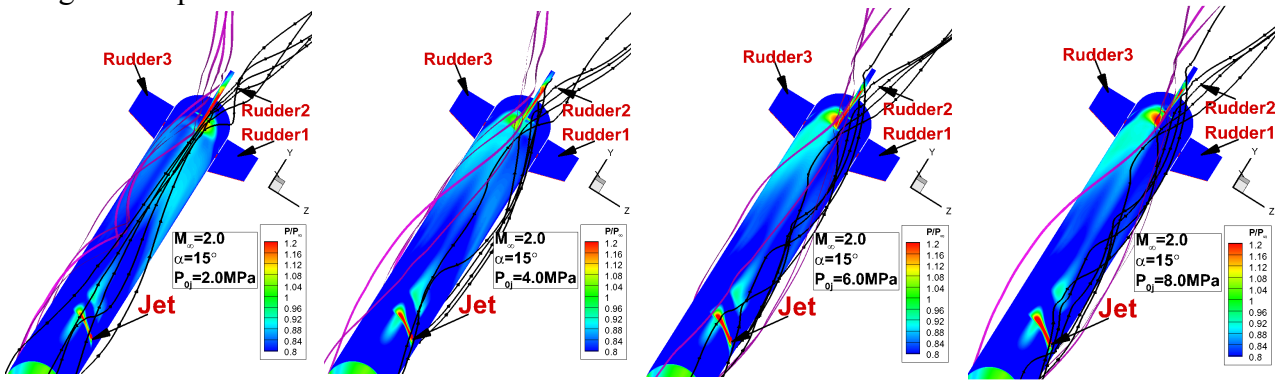

(a) P_{0j}=2.0MPa (b) P_{0j}=4.0 MPa (c) P_{0j}=6.0 MPa (d) P_{0j}=8.0 MPa

Fig. 10 The surface Pressure (P/P_∞) contour and streamlines of different total pressure of jet (P_{0j})

Analysis of Jet Efficiency

Jet interaction can simultaneously produce lateral and normal load, the efficiency of jet interaction can be considered as force/moment amplification factor refer with: Eq. 1

$$K_i = \left(F_{jeton\ i} - F_{jetoff\ i}\right)/T \tag{1}$$

where, K_i represents the force/moment amplification factor, F_{jeton} represents the force/moment with jet interaction, F_{jetoff} represents the force/moment without jet interaction, T represents the force/moment of lateral jet, i represents the loads in coordinate system, which can be z, y, mz, my.

In Fig. 11, force/moment amplification factors of three total pressure of jet are plotted as a function of angle of attack. The force/moment amplification factors are nonlinear changed with angle of attack. However, at the positive angle of attack, amplification factors present highly nonlinear versus angle of attack and total pressure of jet. Especially, Kz and Kmy sometimes is greater than zero and sometimes is less than 0, in other words, when a slight increase of α or P_{0j} at the positive angle of attack, the lateral jet interaction efficiency can vary from the favorable interaction to unfavorable interaction. In Fig. 7-10， force/moment amplification factors presented highly nonlinear are caused by far-field interaction. This brings difficulty to Reaction Control System design.

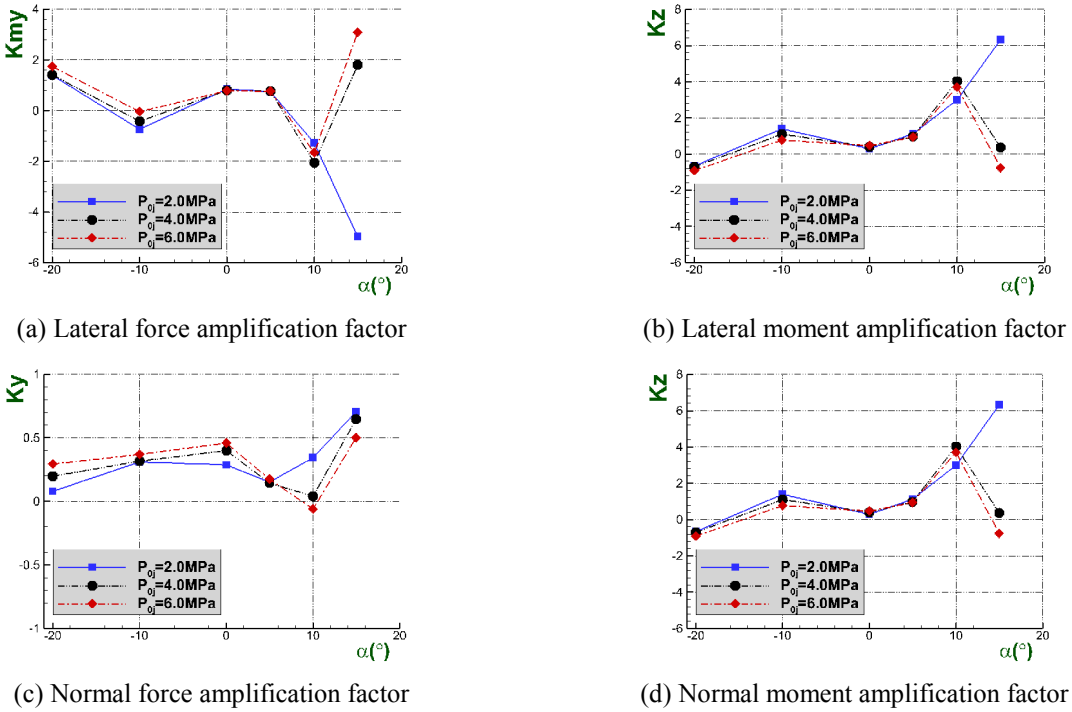

(a) Lateral force amplification factor

(b) Lateral moment amplification factor

(c) Normal force amplification factor

(d) Normal moment amplification factor

Fig. 11 Force/moment amplification factors of different total pressure of jet versus α

Conclusion

The Asymmetrical lateral jet interaction on a slender body in supersonic flow was investigated by numerical simulation, when the lateral jet nozzle is not in the longitudinal symmetry plane. The jet interaction is divided into near-field interaction near jet and far-field interaction after body. The results show that the far-field interaction played a major role in the Asymmetrical lateral jet interaction, and the leeward region is the main interaction region. Force/moment amplification factors are smoothing at negative angles of attack. However, force/moment amplification factors present highly nonlinear with angle of attack and pressure ratio, especially the lateral force/moment amplification factors. These provide a basis for reaction control system design.

References

[1] R.J. Margason, Fifty years of jet in cross flow research, In: AGARD-CP-534, Winchester, United Kingdom, 1993, p. 1-141.

[2] A.R. Karagozian, Transverse jets and their control, Progress in Energy and Combustion Science, Vol. 36, 2010, p. 531–553.

[3] K. Mahesh, The interaction of Jets with crossflow, Annu. Rev. Fluid Mech. Vol. 45, 2013, p. 379-407.

[4] S.X. Li, Complex flow dominated by shock wave and boundary layer. Science Press, Beijing, Chinese, 2007.

[5] G. Patrick, A. Reza, and L. José, Computational comparisons of the interaction of a lateral jet on a supersonic generic missile, AIAA-2008-6883.

[6] J. Brandeis, J. Gill, Experimental investigation of super- and hypersonic jet interaction on configurations with lifting surfaces, AIAA-1997-3723, p. 684-694.

[7] Z.Y. Ni, Y.W. Liu, and S.X. Li, Visualization of vortex Structures induced by lateral jet flow on a revolution body, 11th Asian Symposium on Visualization, Niigata, Japan, 2011.

Applied Mechanics and Materials Vol. 565 (2014) pp 113-119

doi:10.4028/www.scientific.net/AMM.565.113

Simulation and Testing Verification of Tracked Vehicle's Steering Process Considering Track Skidding

Hongyan Wang[1, a], Junkui Li[1, b], Haozhan Li[1, c], Qiang Rui[1, d]

[1]Department of Mechanical Engineering, Academy of Armored Force Engineering,

Dujiakan 21, Fengtai District of Beijing, 100072, China

[a]why_cvt@263.net, [b]549423820@qq.com, [c]haozhan8932@163.com, [d]ruiqiang2006@163.com

Keywords: Steering process; skidding; Testing verification

Abstract: A steering dynamics model considering track skidding is built, which the kinematical and dynamic characteristic about the track forces, turning resistance moment, turning radius, and angular speed are presented. The results show that the turning radius is about 1.5 times and the turning angular speed is 67% in skid-steer situation, which compared to the calculation results based on traditional theory. Experimental results show that steering model is creditable.

Introduction

The steering of tracked vehicles is one of the key factors which decide the maneuvering performance, but the results based on traditional steering theory and actual situation are different in turning radius, steering angular velocity and track-ground force [1], and this difference is mainly due to ignorance of the skid of track-ground. The earliest study about skid steering of tracked vehicles is owed to British Steeds W [2]. A productive work about the steering process had been made by Japanese Kitano [3], Canadian Wong J.Y [4] et al. Some meaningful research work has also been made by Chinese from 1980s [5-7]. A steering model considering the skid of track has been established in this paper, which credibility is verified by the vehicle test. The results show that the steering model is creditable.

Longitudinal Force, Lateral Force and Steering Torque of Track

Assumptions of Kinematics and Dynamic Analysis.

A ground coordinate system XOY and a vehicle coordinate system xoy are shown in Figure 1, where point O is the geometric center of vehicle and point CG is the mass center of vehicle.

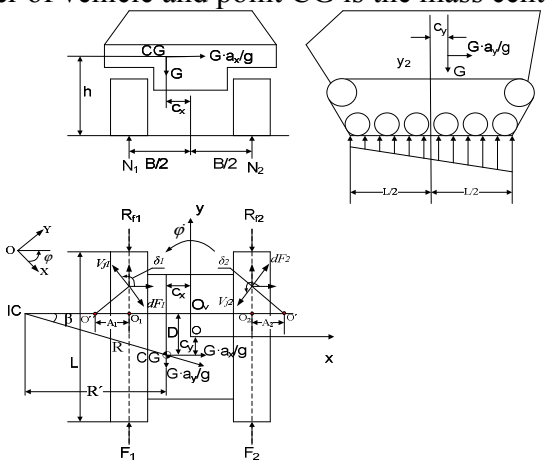

Fig.1 Kinematic relation and track-ground pressure of steering process

Some assumptions are made to analysis and calculate expediently, as follows:

1. Tracked vehicle is driving at a constant speed and on the ground where is horizontal and firm, besides, the shear force between the track and the ground is relate to shear displacement;

2. The sinkage of track, the bulldozing effect caused by lateral shearing of track is negligible;

3. The effect that the width of track have on tractive force and braking force is negligible, and track cannot be stretched;

4. The distribution of track-ground's pressure is continuous and linear.

Shear Displacement of Track-Ground

When the vehicle is turning around the instantaneous steering center IC at an angular velocity of $\dot{\varphi}$, the skidding velocity along longitudinal direction on track-ground is

$$V_{t_i j} = \pm\left[(R' \mp B/2 + c_x)\dot{\varphi} - r_z\omega_i\right] = A_i\dot{\varphi}, \quad i = 1,2 \tag{1}$$

When the vehicle is turning around the instantaneous steering center IC at an angular velocity of $\dot{\varphi}$, the skidding velocity along longitudinal direction on track-ground is

$$V_{t_i j} = \pm\left[(R' \mp B/2 + c_x)\dot{\varphi} - r_z\omega_i\right] = A_i\dot{\varphi}, \quad i = 1,2 \tag{2}$$

The track does composite movement which composes of transport motion and relative motion during steering, In the geodetic coordinate system, lateral component of sliding velocity at any point (x_i, y_i) of both side tracks is

$$V_{jX_i} = -\left[(R' \mp B/2 + c_x)\dot{\varphi} - r_z\omega_i\right]\sin\varphi - y_i\dot{\varphi}\cos\varphi = A_i\dot{\varphi}\sin\varphi - y_i\dot{\varphi}\cos\varphi \qquad i = 1,2 \tag{3}$$

The component of sliding velocity along longitudinal direction is

$$V_{jY_i} = \left[(R' \mp B/2 + c_x)\dot{\varphi} - r_z\omega_i\right]\cos\varphi - y_i\dot{\varphi}\sin\varphi = A_i\dot{\varphi}\cos\varphi - y_i\dot{\varphi}\sin\varphi \qquad i = 1,2 \tag{4}$$

Where φ is course angle; $\dot{\varphi}$ is angle velocity of vehicle steering, rad/s.

The shear deformation at any point (x_i, y_i) of track-ground is

$$j_i = \sqrt{j_{Xi}^2 + j_{Yi}^2}, i = 1,2 \tag{5}$$

Where j_{xi} and j_{yi} is the shear deformation component along X direction and Y direction at any point of both sides track-ground in the XOY coordinate system

$$\begin{cases} j_{xi} = \int_0^t V_{jXi}dt = (R' \mp B/2 + c_x)(\cos\varphi - 1) - y_i\sin\varphi \\ j_{yi} = \int_0^t V_{jYi}dt = (R' \mp B/2 + c_x)\sin\varphi - L/2 + y_i\cos\varphi \end{cases} \tag{6}$$

Model of Lateral Force, Longitudinal Force of Track and Track-Ground Pressure

When there is centrifugal force on point CG in steering process, the steering pole has longitudinal offset D, at the same time the pressure of two side of track-ground is

$$p_i(y_i) = \frac{N_i}{bL} - \frac{6G}{bL^3}\left(c_y + h\frac{V^2}{gR}\sin\beta\right)y_i, \qquad i = 1,2 \tag{7}$$

Where, R′-turning radius, which is the straight-line distance between the instantaneous center and the vertical line through the point CG, m; $y_{1,2}$- the vertical coordinates values of point on both side of the track-ground. N_i is the normal load of track-ground

$$N_i = G\left(\frac{1}{2} \mp \frac{h}{B}\frac{V^2}{gR}\cos\beta - \frac{c_x}{B}\right), \qquad i = 1,2 \tag{8}$$

The shear force of track-ground is related to the value of skidding, the shear force can be expressed by [4]

$$\tau = p\mu(1 - e^{-j/K}) \tag{9}$$

Where p is normal press of track-ground, K is shear modulus of ground, μ is a constant value of friction coefficient between track and ground.

The tangential force acted on unit area of the track-ground is

$$dF_i = \tau_i dA = p_i\mu(1 - e^{-j_i/K})dA, i = 1,2 \tag{10}$$

The longitudinal force acted on both sides of tracks is

$$F_{yi} = \int dF_i\sin(\pi + \delta_i) = -b\int_{-L/2}^{L/2} p_i(y_i)\mu(1 - e^{-j_i/K})\sin\delta_i dy, \qquad i = 1,2 \tag{11}$$

Where $\delta_{1,2}$ is the angle between x axle and sliding velocity on the side of high-speed and low-speed.

The lateral force acted on both sides of tracks is

$$F_{x_i} = \int dF_i\cos(\pi + \delta_i) = -b\int_{-L/2}^{L/2} p_i(y_i)\mu(1 - e^{-j_i/K})\cos\delta_i dy \tag{12}$$

Calculation Model of Steering Driving Moment and Steering Resistance Moment

The turning driving moment on both sides of tracks can be calculated using longitudinal force and its moment arm to O_v in figure 1

$$M_{D_i} = \int dF_i \sin(\pi + \delta_i) B = -\frac{1}{2} b \int_{-L/2}^{L/2} B p_i(y_i) \mu (1 - e^{-j_i/K}) \sin \delta_i dy \qquad i = 1,2 \tag{13}$$

The turning resistance moment can be calculated using the lateral force of tracks and its moment arm to O_2,O_1 on both sides of tracks respectively.

$$M_{\mu_i} = \int dF_i \cos(\pi + \delta_i) y_i = -b \int_{-L/2}^{L/2} y_i p_i(y_i) \mu (1 - e^{-j_i/K}) \cos \delta_i dy \qquad i = 1,2 \tag{14}$$

Sliding angle δ_2, δ_1 of track can be calculated according to the relation of movement in figure 1.

Dynamic Equations of Steering

According to the force balance on x axle and y axle direction, and the torque balance to point O_v, the dynamic equations of steering at a constant speed can be expressed by

$$\begin{aligned}
&\sum F_x = 0, \quad F_{x_2} + F_{x_1} - \frac{GV^2}{g\mathrm{R}} \cos\beta = 0 \\
&\sum F_y = 0, \quad F_{y_2} + F_{y_1} - \frac{GV^2}{gR} \sin\beta - \left(R_{f1} + R_{f2}\right) = 0 \\
&\sum M_{ov} = 0, \quad M_{D2} - M_{D1} - \frac{B}{2}\left(R_{f_2} - R_{f_1}\right) + \left(D\cos\beta + c_x \sin\beta\right)\frac{GV^2}{gR} = M_{\mu_2} + M_{\mu_1}
\end{aligned} \tag{15}$$

Where R_{f_2}, R_{f1} are the resistance force of both tracks, which are related to the normal load and the resistance coefficient of ground f_r.

$$R_{fi} = G\left[\frac{1}{2} \mp \left(\frac{h}{B}\frac{V^2}{gR}\cos\beta - \frac{c_x}{B}\right)\right] f_r \qquad i = 1,2 \tag{16}$$

In the equations of motion, the mainly unknown quantity is A_2, A_1 and D. when the vehicle structure parameters, ground parameters and turning kinematics parameters are given, the steering pole offsets a_1, a_2, a_3 under all kinds of vehicle velocities and turning radius, the force and torque on track can be calculated by iterative calculations of the above three equations

Correction Coefficient of Steering Kinematics Parameters

There is a large difference between actual radius, actual turning angle speed and their theoretical value due to the skid of track-ground, therefore, the correction coefficient of turning radius and turning angle speed must be given. In local coordinate system, theoretical velocity of track is velocity of the instantaneous steering center of track O′, O″ along y axle direction,

$$\dot{\varphi}\left(R' \mp B/2 + c_x \mp A_i\right) = V_i \qquad i = 1,2 \tag{17}$$

The equations of the actual relative turning radius and the actual turning angular speed are

$$\begin{aligned}
&\dot{\varphi} = \frac{V_2(1 - 1/K_V)}{B} \frac{1}{1 + \lambda/2(a_2 + a_1)} = f_\varphi \dot{\varphi}_t \\
&\rho = \frac{1}{2} \frac{\left[\left(1 + \triangle c_x + \lambda a_1\right) + K_V\left(\lambda a_2 + 1 + \triangle c_x\right)\right]}{1 - K_V} = f_\rho \rho_t \\
&f_\varphi = \frac{1}{1 + \lambda/2\left(a_2 + a_1\right)} \\
&f_\rho = \frac{\left[\left(1 + \triangle c_x + \lambda a_1\right) + K_V\left(\lambda a_2 + 1 + \triangle c_x\right)\right]}{1 + K_v}
\end{aligned} \tag{18}$$

Where, $\triangle c_x = 2c_x / B$, K_v=V_2/V_1 is the theoretical speed ratio of high-speed track and low-speed track; f_φ, f_ρ is correction coefficient of turning angle speed and turning radius respectively.

Turning Process Simulation and Test Verification

Using the former built model of steering, the change rules of steering parameters can be calculated. Driving resistance coefficient used in the calculation is obtained by real vehicle test, which range of variation is 0.049~0.055, so f =0.05 in the paper. The friction coefficient of track-ground μ=0.9 and the shear modulus of the soil K=0.015m. The calculated tractive force of both sides of tracks is shown in figure 2. The change rules of velocity, turning radius with tractive force, braking force are shown in the figure, these two become bigger as the turning radius become smaller. Because centrifugal force

plays a beneficial role of steering, when the velocity is high, the tractive force and braking force of track are smaller than the forces when the velocity is low. In the range of small radius, centrifugal force has a bigger effect on the steering, especially for the effect on low-speed track's braking force.

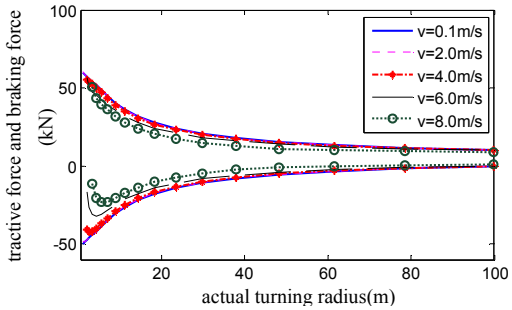

Fig 2 The changing relationship curve of tractive force and braking force with turning radius

The changing relationship curve of turning resistance moment is shown in figure 3. Turning resistance moment becomes smaller as turning radius become bigger. When turning radius is small, the velocity has a big effect on turning resistance torque.

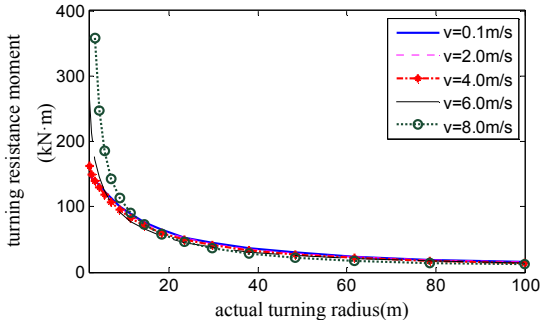

Fig 3 The changing relationship curve of turning resistance moment with turning radius and vehicle velocity

Testing Verification of Steering Model

To verify the credibility of the established model, an actual vehicle test has been taken on firm ground composed by sandy soil. Tracked vehicle is operated in first gear and working on hydraulic condition in the test, then the vehicle is made a clockwise turning with different radius. The rotate speed of both sides of sprockets, rotate speed and torque of transmission output shaft, the heading angle of vehicle, traveling track, velocity and so on are recorded synchronously. The composition of test system is shown in figure 4. The parameters of turning radius, velocity and heading angle are measured accurately by the GPS system, which has a function of second difference.

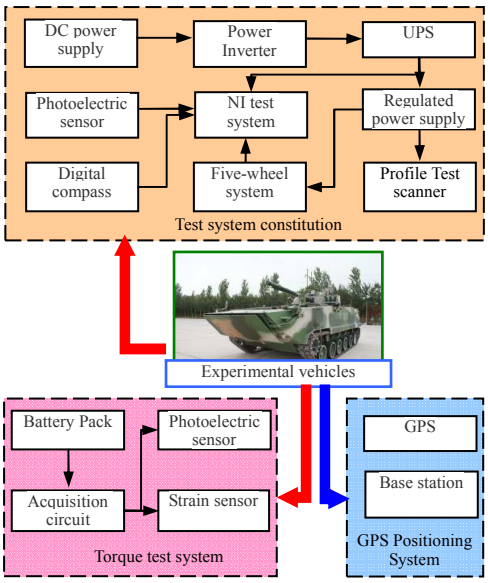

Fig 4 Experimental test system composition

The experimental and computational results comparison of correction coefficient of turning radius, correction coefficient of turning angle speed, are shown in figure 5~7 respectively. The results in figure 5~6 show that the turning radius is about 1.5 times and the turning angular speed is 67% in skid-steer situation, which compared to the calculation results based on traditional theory. Beside, the experimental results of the correction coefficient of turning radius have a good consistency with the computational results of correction coefficient of turning angle speed under different turning radius.

The range of tracked vehicle's velocity is 0.665m/s~1.025m/s in the test, the turning radius is obtained by fitting the measure results of traveling track, and the tractive force and braking force under different radius are shown in figure 7. The calculated velocity in figure is 1.0m/s, according to the comparison of experimental results and computational results, the variation trend and values of these two forces is consistent.

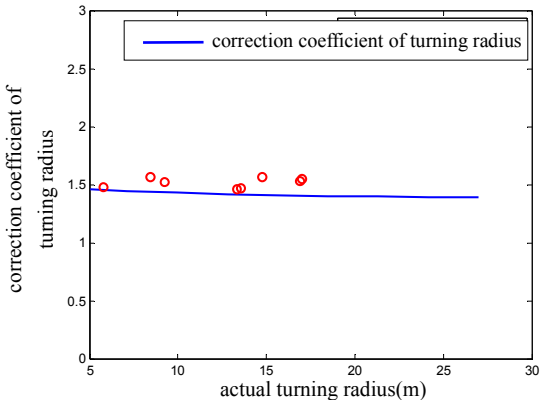

Fig 5 The experimental and computational results comparison of correction coefficient of turning radius

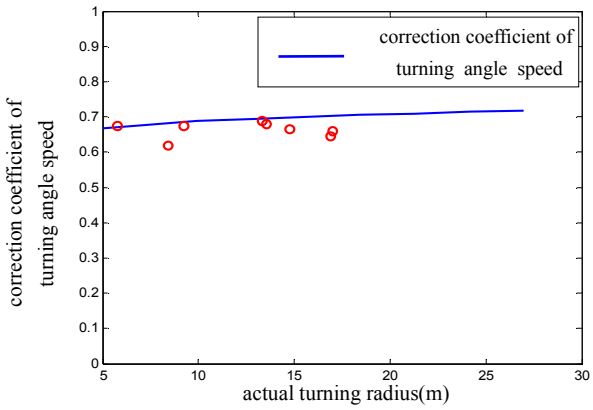

Fig 6 The experimental and computational results comparison of correction coefficient of turning angle speed

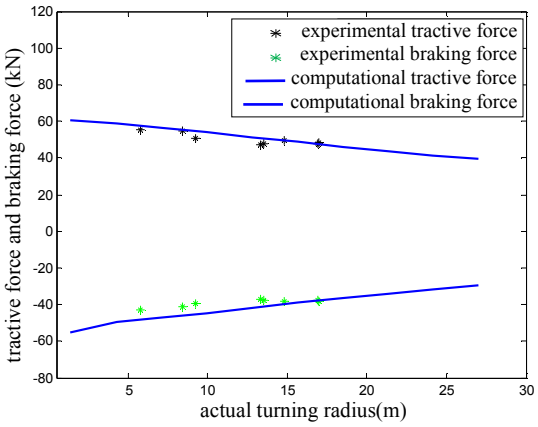

Fig 7 The experimental and computational results comparison of tractive force and braking force

In a word, the comparison of experimental results and computational results verified that the established model considering track skidding in paper is credible.

Conclusion

In this paper a model of vehicle steering considering the skid of track has been established, using which the change rule of tractive force, braking force, turning resistance moment, turning radius and turning angle speed can be calculated. The consistency between the comparison of experimental results and computational results shows that the established steering model is credible. The consistency between correction coefficient of turning radius, turning angle speed and experimental results shows that the correction coefficient model is credible, so this model can be used to calculate steering correction coefficient in engineering application.

References

[1] Cheng Junwei, Gao Lianhua, Wang Hongyan. Analysis of Tracked vehicles Steering Considered Tracks' Skid and Slip[J]. Journal of Mechanical Engineering, 2006(42); 192~195(in Chinese)

[2] W. Steeds. Tracked vehicles--an analysis of the factors involved in steering[J]. Automobile Engineer, April 1950: 143~148.

[3] Kitano, M. and Jyorzaki, H. A Theoretical Analysis of Steerability of Tracked Vehicles[J]. Journal of Terramechanics, Vol. 13, No. 4; 1976: 241-258.

[4] J. Y. Wong. Theory of ground vehicles [M]. 3rd edition. John Wiley & Sons Inc, 2001:390~420.

[5] Song Zhenjia. Theory of tracked vehicles steering on firm ground under uniform distribution load [J]. Teaching and Scientific research, Academy of Armored Force Technique. 1980(3):1~10 (in Chinese)

[6] Song Haijun, Li Jun. Simulation and Experiment Research of Tracked Vehicle Turning Course[J]. Journal of Academy of Armored Force Engineering. 2005,19(3):17~21. (in Chinese)

[7] Cheng Junwei, Gao Lianhua, Wang Hongyan. Analysis on the Steering of Tracked Vehicles[J]. ACTA ARMAMENTARIL. Vol. 28, No. 9; 2007:1110~1115. (in Chinese)

Applied Mechanics and Materials Vol. 565 (2014) pp 120-125

doi:10.4028/www.scientific.net/AMM.565.120

A Development of Human Machine Interface in a Miniature 3-Axis Milling Machine Prototyping

Pornjit Pratumsuwan[a] and Anan Suebsomram[b]

Department of Teacher Training in Mechanical Engineering

King Mongkut's University of Technology North Bangkok (KMUTNB), Thailand, 10800

[a]pornjitp@kmutnb.ac.th, [b]asr@kmutnb.ac.th

Keywords: human machine interface, 3-axis milling machine, virtual and physical prototype

Abstract. This paper presents a development of human machine interface (HMI) which was applied to a miniature 3-axis milling machine prototyping. The development began with the study and design of a milling machine. Then, virtual prototyping, this stage is the integration of aided design, programming design, and simulation design to demonstration the functionality of the virtual machine in a computer environment. After that, the virtual prototype which was verified and optimized to be used a physical prototyping. Finally, links the virtual and physical together. The experimental results show that a performance of proposed HMI in a machine prototyping was satisfactory**.**

Introduction

Milling is the machining process of using rotary cutters to remove material from a work piece advancing in a direction at an angle with the axis of tool. It is one of the most commonly used processes in industry and machine shops today for machining parts to precise sizes and shapes [1]. With the dramatic increase of the growing demand of miniature product, therefore, current industry practice tends to downsize the milling machine used to produce small volume objects, small machine for small products. However, the study of past research, which involved a miniature milling machine [2-5] that most often designed without simulation functionality to visualize and customize before creating the real machine. Moreover, such research is often used comercial motion controller which makes the lack of flexibility and the high cost in the design and development.

To enhance performance and efficiency in machine prototyping, therefore, this reseach aims to develop a HMI which was applied to a miniature 3-axis milling machine prototyping. For this project will be focus on the combination of SolidWorks with LabVIEW and the NI SoftMotion module that used for virtual and physical prototyping. The process of a 3-axis milling machine developing and the link between virtual and physical prototype to HMI is presented in Fig. 1. The development process consists of four main steps: design of machinary, configuration control, design and simulation of systems, make machine and test work. The whole process will work in harmony together which details are discussed in the following order.

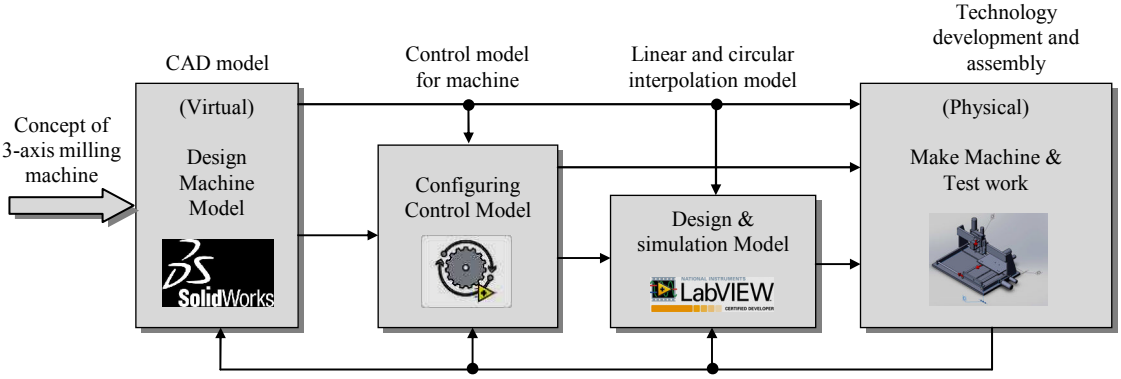

Fig. 1 The process of development of HMI in machine prototyping.

Design Machine Model

Milling machines typically consist of a table that moves in the X and Y axes, and a tool spindle that moves in the Z (depth). On commercial metalworking machine closed loop controls are standard and required in order to provide the accuracy, speed, and repeatability demanded. These machines working are commanded by G-code. G-code is a language in which people tell computerized machine tools what to make and how to make it. The "how" is defined by instructions on where to move to, how fast to move, and through what path to move [1]. In designing the mechanical structure of a miniature CNC milling machine will use the SolidWorks, the dimension of the work volume is 210 x 300 x 50 mm. Each axis will use a permanent magnet DC (PMDC) motor through a reduction gear box to driven ball screw. For detecting of position and speed of each axis be use an incremental encoder. In addition, there are others parts that are designed to assemble the machine. However, this design process must engineering calculations and considers the real parts and accessories that are used in the industry and can find devoid difficult. The result of the design is shown by Fig. 2.

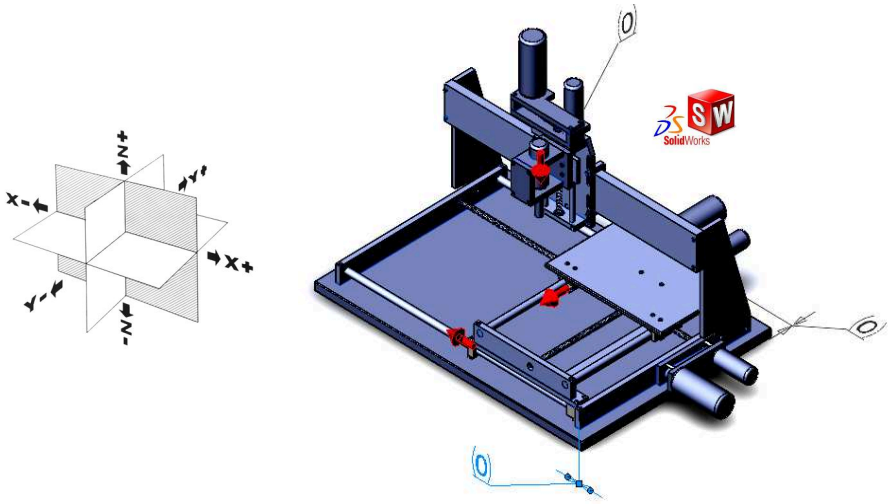

Fig. 2 A 3D-CAD of a miniature 3-axis milling machine.

Configuring Control Model

The concept of position and speed control of each axis of the machine is shown by Fig. 3. In this take on/off for position control and speed control using PID controller Signal from the on/off controller was sent to control the h-bridge driver to control the position of the PMDC motor according to the command signal. In the meantime, the signal from PID controller will be changed to PWM and then sent into the h-bridge driver to control the motor speed according to the desired command. To dectect both the position and speed of each axis of the machine to provide feedback on both controller will use incremental encoder.

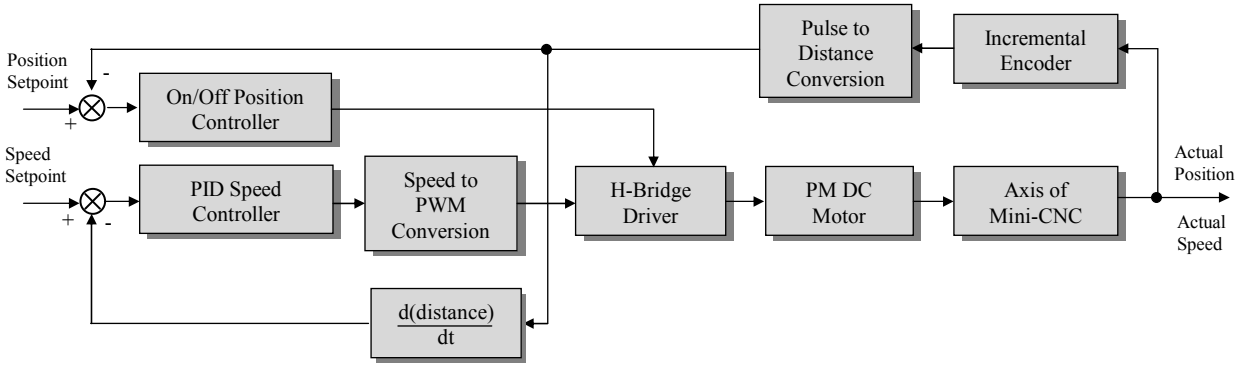

Fig. 3 Block diagram of position and speed control of each axis's the machine.

Design and Simulation of the Model

In the simulation of any systems, we need to know the mathematical model of those systems. As we have discussed in the past topic, the design of mechanical structure, we need to select and configure devices and accessories as fact and sometimes necessary to provide for use in testing of important parameters. For this project to be of calculating the size of motor is 24 watts, and select a 24 volts PMDC motor.

Transfer function of the position and speed control can be accomplished in several ways, but for this project will be used to analyze the transient response of second order system as shown by (1).

$$\frac{\omega(s)}{V_a(s)}=\frac{K\omega_0^2}{s^2+2\varsigma\omega_0 s+\omega_0^2} \tag{1}$$

Testing results of the axes x, y, and z represented by (2), (3), and (4), respectively.

$$\frac{\omega(s)}{V_a(s)}=\frac{1035.006056}{s^2+13.862961s+1035.006056} \tag{2}$$

$$\frac{\omega(s)}{V_a(s)}=\frac{1633.164595}{s^2+38.678645s+1360.970496} \tag{3}$$

$$\frac{\omega(s)}{V_a(s)}=\frac{624.633553}{s^2+34{,}495233s+624.633553} \tag{4}$$

Linear Interpolation. Creating a linear trajectory path to determine the motion of a tip of the tool milling machine, this project is based on the G-code standard. G00 and G01 instead ordered the tool moving along a straight line. When G00 is the command for moving a no-load, the G01 command moves the tool moving milling [6]. User commands to specify the values of the starting point (x_1,y_1), ending point (x_2,y_2), and the speed of movement of the milling tool (v_f). The relationship of milling speed and speed of x, y axes shown by Fig. 4, and can be expressed by (5), (6), respectively.

$$v_x=v_f\cos\theta=v_f\frac{x_2-x_1}{\sqrt{(x_2-x_1)^2+(y_2-y_1)^2}} \tag{5}$$

$$v_y=v_f\sin\theta=v_f\frac{y_2-y_1}{\sqrt{(x_2-x_1)^2+(y_2-y_1)^2}} \tag{6}$$

Where, v_x and v_y are the velocity of x, y axes, v_f is the velocity of the feed milling. However, the ability to move in a straight line at an angle (θ) in the horizontal plane is limited by the features of the machine. For this angles are in the approximately range 15° to 75° of each quadrant.

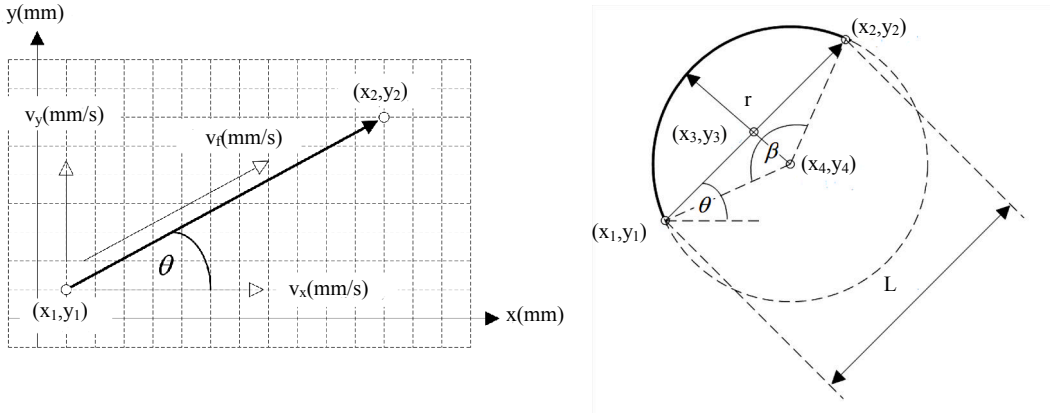

Fig. 4 Llnear and circular trajectory paths for determine the motion of machine.

Circular Interpolation. Creating a circular trajectory path to determine the motion of a tip of the tool milling machine, there are basically two types of motion, clockwise (G02) and counterclockwise (G03) [6]. User commands to specify the value of the starting point, ending point, and radius of a circle. Fig. 4 shows an example of circular path trajectory. Where (x_1,y_1) is starting point, (x_2,y_2) is

ending point, (x_3,y_3) is a half of L, L is the displacement from (x_1,y_1) to (x_2,y_2), (x_4,y_4) is the center, and r is the radius of circle. For calculating the angle (θ) as defined by the user can be divided into the 8 cases following.

case 1: $x_2>x_1, y_2>y_1$, $\theta=\tan^{-1}\left(\frac{y_2-y_1}{x_2-x_1}\right)$, case 2: $x_2>x_1, y_2<y_1$, $\theta=\tan^{-1}\left(\frac{y_2-y_1}{x_2-x_1}\right)$

case 3: $x_2<x_1, y_2>y_1$, $\theta=180+\tan^{-1}\left(\frac{y_2-y_1}{x_2-x_1}\right)$, case 4: $x_2<x_1, y_2<y_1$, $\theta=180+\tan^{-1}\left(\frac{y_2-y_1}{x_2-x_1}\right)$

case 5: $x_2>x_1, y_2=y_1$, $\theta=0°$, case 6: $x_2<x_1, y_2=y_1$, $\theta=180°$

case 7: $x_2=x_1, y_2>y_1$, $\theta=90°$, case 8: $x_2=x_1, y_2<y_1$, $\theta=270°$

When β is the angle that was used as a parameter for selecting the number of points on a circular path, in case the user wants to move the tip of the milling tool just some of the circle, which can be calculated from the cosine rule following.

$$L^2=r^2+r^2-2r^2\cos\beta=2r^2(1-\cos\beta)=\frac{L^2}{2r^2}=1-\cos\beta,\ \beta=\cos^{-1}\left[1-\left(\frac{L^2}{2r^2}\right)\right] \quad (7)$$

The sequence of any position calculating on the circular path can be represented by Fig. 5.

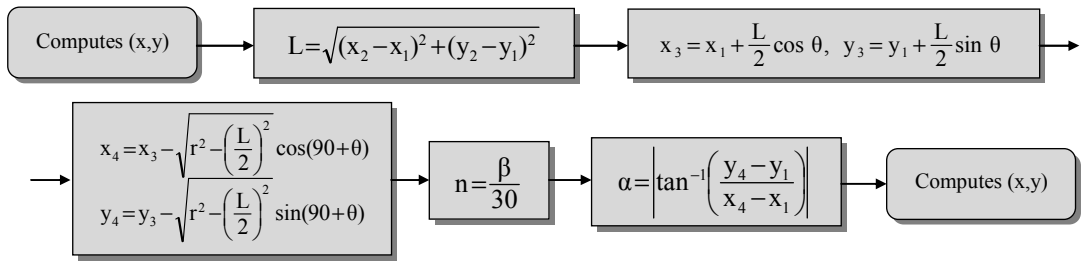

Fig. 5 Process for calculation of any position on the circular path.

Simulation. Models, methods, and algorithms that are discussed in the previous topic will be built and designed in the LabVIEW program. Existing SolidWorks 3D-CAD models can be connected to LabVIEW, which automatically links the motor actuators and position sensors defined in the model. Using the functions delivered in NI SoftMotion for SolidWorks, we can link algorithm designed to control a 3D-CAD model to visualize realistic machine behavior [7]. Fig. 6 is examples of linear and circular trajectory simulation results of the virtual prototype was designed.

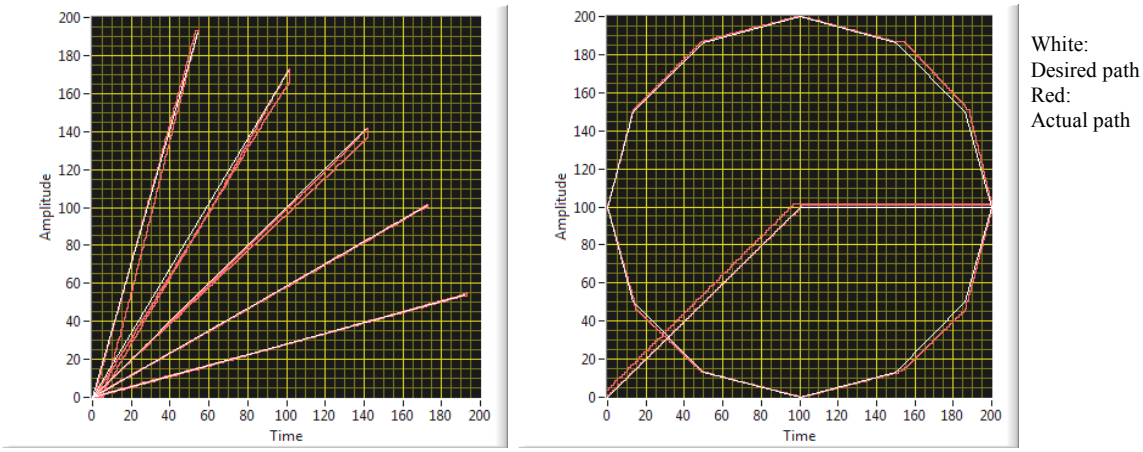

Fig. 6 Examples of linear and circular trajectory path.

Make Machine and Test Work

The actual devices being used in this project is shown by Fig. 7. Algorithm that was designed with LabVIEW (included embedded module) in computer will be sent to ARM7 microcontroller and the

output signal from processing will be sent to PWM driver board to drive the PMDC motor used to driven the axis. The incremental encoder detects the position and speed feedback into the microcontroller. The main component used in this machine is the selfsame all 3-axis.

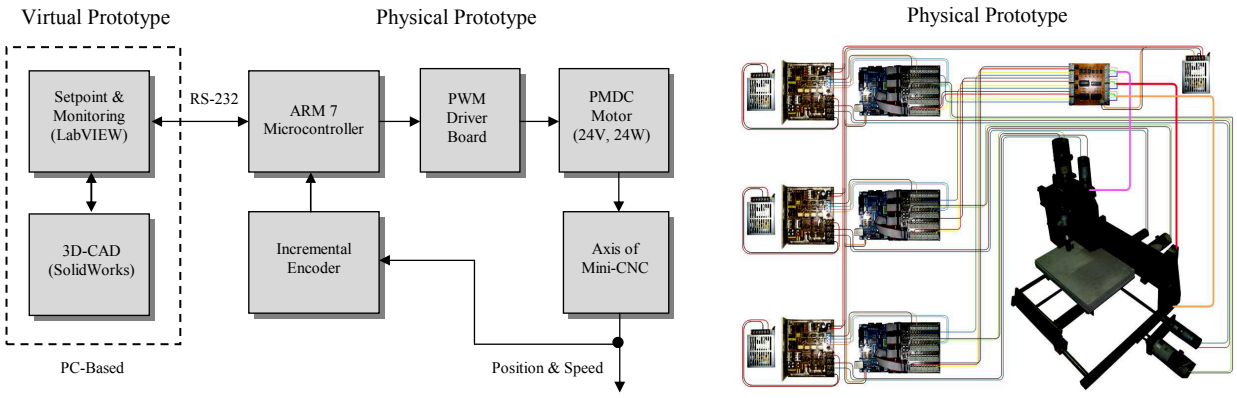

Fig. 7 The main components of the machine.

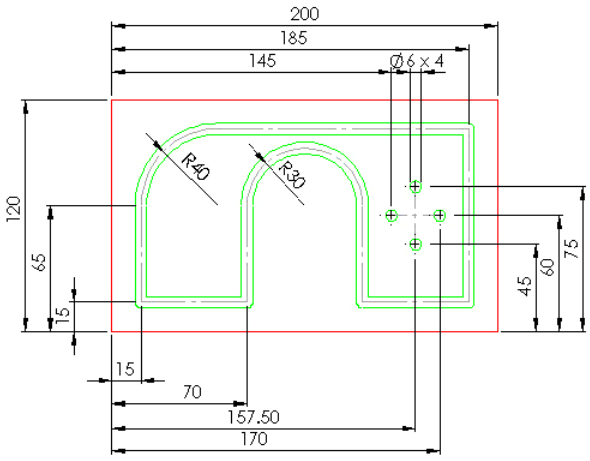

	G-Code	X (mm)	Y (mm)	Z (mm)	Radius (mm)	Feed (mm/s)
N01	G00	15	15	0	0	0
N02	G01	15	15	30	0	2
N03	G01	70	15	30	0	0.7
N04	G01	70	65	30	0	0.7
N05	G02	100	95	30	30	0.7
N06	G02	130	65	30	30	0.7
N07	G01	130	15	30	0	0.7
N08	G01	185	15	30	0	0.7
N09	G01	185	105	30	0	0.7
N10	G01	55	105	30	0	0.7
N11	G03	15	65	30	40	0.7
N12	G01	15	15	30	0	0.7
N13	G00	15	15	0	0	2
N14	G00	157.5	45	0	0	2
N15	G01	157.5	45	30	0	2
N16	G00	157.5	45	0	0	2
N17	G00	145	60	0	0	2
N18	G01	145	60	30	0	2
N19	G00	145	60	0	0	2
N20	G00	157.5	75	0	0	2
N21	G01	157.5	75	30	0	2
N22	G00	157.5	75	0	0	2
N23	G00	170	60	0	0	2
N24	G01	170	60	30	0	2
N25	G00	170	60	0	0	2

Fig. 8 The assigned pattern and progrmming format used for workpiece milling.

After assembly and installation of equipment together is complated, the next step is to test the performance of the machine. For here is an example of milling the workpiece of the machine that has both linear and circular trajectory path. The example of a milling trajectory on the artificial wood experiments with assigned pattern as shown on Fig. 8. Milling program contains command G00 for rapid positioning (point to point, no-load), G01 for linear interpolation along the axis and angle values, and G03 for circular/helical interpolation counterclockwise. These commands and all parameters form assigned pattern are entered through a front panel of LabVIEW that has been designed in accordance with the G-code format as shown in Fig. 8. The results of the experiment showed that the 3-axis milling machine can manipulate to the various positions and milling as required, the measurement milling trajectory path found that the average error is ±0.5 mm. Fig. 9 shows the results of the experiment.

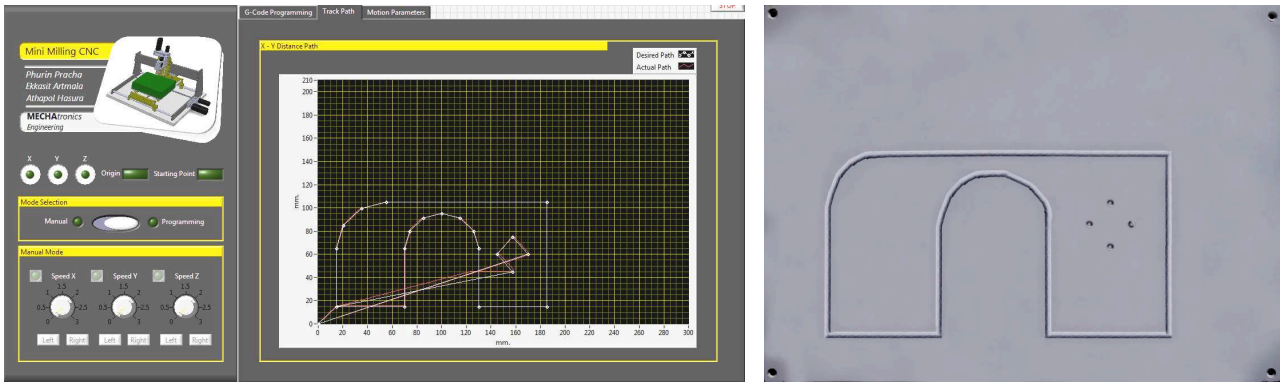

Fig. 9 The results of a milling trajectory path on front panel and artificial wood.

The accuracy of a miniature 3-axis CNC milling machine is not so good mainly due to data transfer between PC and microcontroller (ARM7) using serial comunication has many points that caused the delay which affect the accuracy of the system. Moreover, the results of the experiment show that virtual machine prototype responding slower than real machine prototype because virtaul prototype (3D-CAD) require more processing time. Such problems are solved and improved in the future research, and G-code program will be replace with 3D-CAD.

Summary

This reseach aims to develop a HMI which was applied to a miniature 3-axis milling machine prototyping. For this project will be focus on the combination of SolidWorks with LabVIEW and the NI SoftMotion module that used for virtual and physical prototyping. The development began with the study and design of a milling machine. Then, virtual prototyping, this stage is the integration of aided design, programming design, and simulation design to demonstration the functionality of the virtual machine in a computer environment. After that, the virtual prototype which was verified and optimized to be used a physical prototyping. Finally, links the virtual and physical together. The experimental results show that a performance of proposed HMI in a machine prototyping was safactory.

References

[1] Information on http://en.wikipedia.org/wiki/Milling_(machining)

[2] Wei Qin, Design and analysis of a small-scale cost-effective CNC milling machine, Thesie of graduate college of the university of Illinois at Urbana-Champaign (2013)

[3] Rodrigo Basniak and Marcio Fontana, Design of a PCB milling machine, ABCM Symposium Series in Mechatronics, vol.5, 2012, pp. 1339-1348.

[4] Sasa Zivanovic, Milos Glavonjic, and Zoran Dimic, Methodology for configuring desktop 3-axis parallel kinematic machine, FME Transactions, vol.37. 2009, pp. 107-115.

[5] Kittipong Ekkachai, and others, Design and development of an open architecture CNC controller for milling machine retrofitting, ICROS-SICE International Joint Conference, 2009, pp. 5629-5632.

[6] Engineering Centre, Laboratory manual for engineering skills ECT112, Universiti Malaysia Perlis (2013)

[7] Ryne P. McHugh, Virtual prototyping of mechatronics device, College of technology thesis and projects, Purdue University, (2011)

Applied Mechanics and Materials Vol. 565 (2014) pp 126-132

doi:10.4028/www.scientific.net/AMM.565.126

Long Guide Straightness Error Measurement Based on Laser Interference

Changde Hu[1,a], Yongqiang Li[1], Juan Gao[1], Peng Fu[2], Heping Min[2], Ning Ye[2]

[1]Department of Enlisted Man, the Academy of Equipment , Beijing 102200, China;

[2]The Equipment Department of Tibet Military Area Command，Lasa 850000

[a]hansen1981108@sohu.com

Keyword: Laser interference; Straightness error; Long guide; Contrast experiment

Abstract: A new kind of straightness error measurement system based on laser interference is developed. High stability He-Ne laser beam which is collimated and broadened is cast on wedge-shaped glass plate, on which back and front the light reflects and interfere. The angle of the guide and target would be changed when the motion of the target is along the guide, if there is linearity error existing in the guide. So interference stripes would be moved by the changed angle of the guide and target. In this way the straightness error of the guide is transferred to the displacement of the interference stripes. Then interference stripes are tested by photoelectricity sensor and deviation of the laser beam is acquired. The comparison tests and repeated tests show that the straightness error is 623.103μm when the tested long guide is 50 meters long.

Introduction

With the development of modern technology, it is highly demanded for the measurement accuracy of geometric parameters. Straightness error, as one of the form errors, influences the precision, quality, performance of instrument directly, sometimes it is even the determining factor[1]. In this way, straightness error measurement is one of the most important and basic measurements[2,3]. Long guide straightness error is an important branch of geometric parameters measurement, and with the development of science and technology, the accuracy of long guide is demanded and increased highly[4]. The measurement of long guide straightness error gets harder and harder when becoming longer and longer[5]. A new kind of straightness error measurement system based on laser interference is developed. High stability He-Ne laser beam which is collimated and broadened is cast on wedge-shaped glass plate, on which back and front the light reflects and interfere. The angle of the guide and target would be changed when the motion of the target is along the guide, if there is straightness error existing in the guide. So interference stripes would be moved by the changed angle of the guide and target. In this way the straightness error of the guide is transferred to the displacement of the interference stripes.

The Principle and Elements of the System

Principle of Interference of Parallel Plate

With the laser beam at wedge-shaped plate, interference fringes are produced with the beam reflecting on the upper and lower surfaces. For the wedge angle is minimal, interference of the parallel optical plate could be used as shown in Fig. 1. If the laser beam onto the wedge-shaped beam splitter, the interference fringes are generated with the laser beam reflected on the upper and lower surfaces. Then the variable quantity of the angle of the wedge-shaped splitting plate and the movement of the interference fringes can be derived from Fig. 1. He-Ne laser light is divided into two beam signals[6]. One beam I_2 is reflected by the upper surface, and the other beam I_1 refracted by the glass to the lower surface, then reflected by the lower surface and refracted by the upper surface to air. The beam I_1 from the lower surface and the beam I_2 from the upper surface interfere. Thus optical path

difference Δ could be shown as Eq. 1[7]. Considering the half wave loss of the light reflected from the optically thinner medium to the optically denser medium, the optical path difference Δ could be expressed as the Eq. 2 shown.

$$\Delta = n \times (AB + BC) - CD \qquad CD = AC \times \sin i_1 = 2L \times tgi_2 \sin i_1 \qquad AB = BC = \frac{1}{\cos i_2}. \tag{1}$$

$$\Delta = 2L\sqrt{n^2 - \sin^2 i_1} - \frac{\lambda}{2}. \tag{2}$$

$$\frac{d\Delta}{di_1} = -\frac{L \sin 2i_1}{\sqrt{n^2 - \sin^2 i_1}}. \tag{3}$$

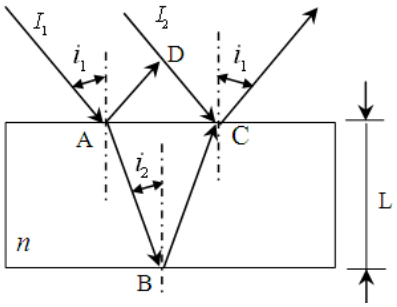

Fig.1 Principle of interference

The Eq. 3 is the transmission ratio of the measurement method, with the change of optical path difference caused by the variation of the angle of incidence, then the movement of the interference fringes could be got. The changes of the angle in the actual measurement is mainly caused by the straightness error of the long guide[8]. When the receiving target moves along the guide, for the straightness errors of the guide, the angle formed by the guide and target bridge is changed. The receiving target inclines and makes the wedge angle change, and interference fringes moved. So the straightness error of the long guide could be tested by detecting the movement of the interference fringes.

Elements of the System

The movement image of the interference fringe caused by the wedge angle changing is received by sensitive element, silicon photocell. With the following processing circuit, and then to the microcontroller, the measurement results are obtained. A specific measurement procedure is as Fig. 2 shown.

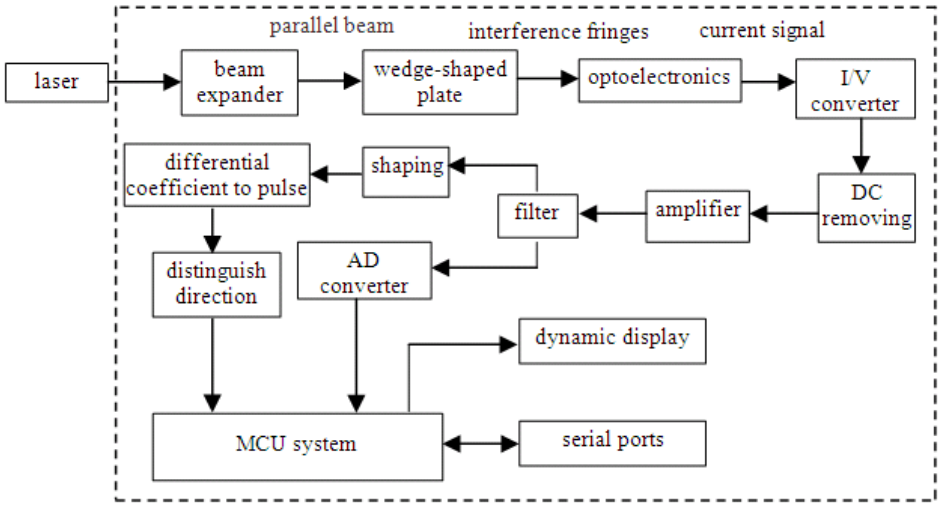

Fig. 2 Elements of the system

As it shown in Fig. 2, the laser beam generated from the He-Ne laser, a parallel light is got with the beam expander system. With the collimation system, the beam is projected onto a glass optical wedge of the receiving target of the long guide. Then reflects on the upper and lower surface of the beam

splitter sequentially, forming two beams, which interfere with each other with the overlapping portion. In this way a set of parallel spaced interference fringes is got by the silicon photocell. When the receiving target moves along the guide, if there is straightness errors of the guide, the angle formed by the guide and the target bridge is changed. In this way the receiving target inclined and makes the wedge angle change, which makes the interference optical path difference changing, and it makes the interference fringes move. The interference fringe image moves in silicon photocell, of which the moving amount converts to the amount of movement of the interference fringes. With the silicon photocell it is converted to the variable quantity of sinusoidal signal. After amplified and with the DC removed, the two sinusoidal signals with phase difference Φ=90° are got. After amplified, the signals are divided into two, one is transferred to square wave signal, differentiating to forward and reverse pulses, making them and the two sinusoidal signals "and", then sending to the MCU to count, in order to distinguish direction and achieve the integral counting of fringe period, the other is sent to the MCU to achieve fraction counting after DA converting. The software of MCU based on software subdivision principle makes integral and fraction a combination, the results could be stored and displayed. It could also be transmitted by serial ports between the MCU and the computer. The experiment equipment is as shown in Fig. 3.

a. precision calibration of experiment equipment b. test picture of the long guide

Fig. 3 Picture of the experiment equipment

Design of the Circuit

The circuit system is the hardware basis of the laser interferometer alignment. This system is mainly used in the measurement of large geometric parameter, such as straightness error, concentricity, parallelism, flatness and other parameters. The elements of the system is as shown in Fig. 4, and the main functions include:

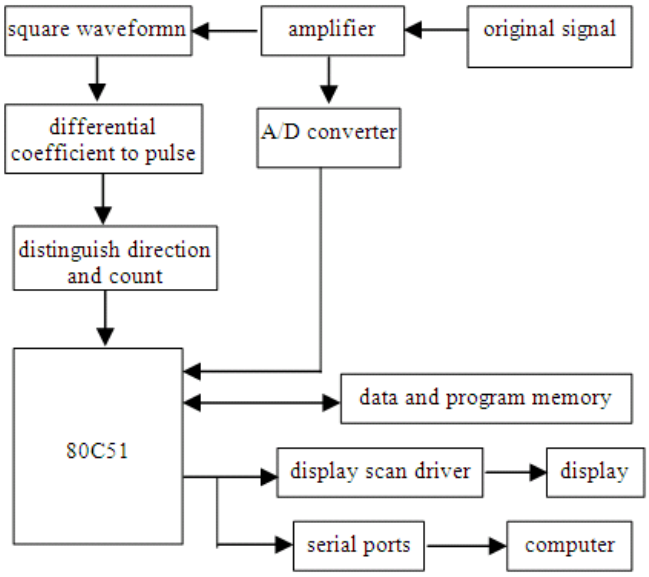

Fig. 4 Elements of the system

1. Real time measurement and display;
2. Strong noise immunity and able to working in the field;
3. Storing data, communicating with the computer and sending the tested data to the computer;
4. Miniaturizing and portable, easy for measurement;
5. Lower the power consumption and prolong service life.

The main functions of the software are interference fringe signal subdivision, measurement data processing, display and communication functions.

Eeperiment

When the straightness error is measured with a level method, height difference of adjacent points in the measurement process is as Eq. 4 [9]:

$$\delta = 0.005acL = 0.005cL\theta . \quad (4)$$

c（″）——division value of the instrument, got from the accuracy comparative experiments;

L（mm）——bridge length;

a（″）——angle of the bridge connection with the reference light, display of the instrument of θ;

In the measurement section, the horizontal coordinate system is established to the horizontal line over the measuring point from the horizontal axis, then the error of the sampling points in the direction of the axis coordinate values could be expressed as Eq. 5:

$$y_i = \sum_i \delta_i = 0.005cL\sum_i a_i = 0.005cL\sum_i \theta_i . \quad (5)$$

The coordinate values in the error direction of each sampling point of the object to be measured could be calculated with Eq. 4 and Eq. 5.

End point connecting method

The end point connecting method is used in evaluating the straightness error of the long guide. The end point connecting method refers to evaluating the straightness error with two ends connection of the surface for the ideal line position. Hi refers to the deviation of the measuring points from the ideal straight, the straightness error is the difference between the maximum deviation and minimum deviation.

As it shown in Fig. 5, the positive maximum deviation of the straightness error is $i_{\max}$, and the negative maximum deviation of the straightness error is $i_{\min}$. The formula with the end point connecting method evaluating the straightness error is as Eq. 6 :

$$\mathrm{y}_{\max} - \frac{i_{\max}}{n} y_n) + \left| y_{\min} - \frac{i_{\min}}{n} y_n \right| . \quad (6)$$

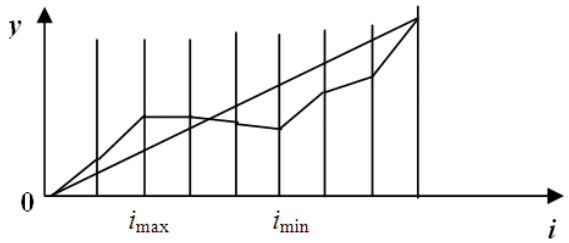

Fig. 5 Sketch map of end point connecting method

Precision Calibration Experiment of the instrument

The precision calibration experiments are done by the axis electronic autocollimator (specification of ELCOMAT 2000) developed by the German. The main performance parameters: any 20 seconds (in absolute measurement mode) error: ± 0.10 ", whole error: ± 0.25", resolution: 0.005 ", repeatability: 0.05."In the experiment, the specification of ELCOMAT 2000 is placed on the damping platform with a mirror on the top and bottom (Y direction) and left (X direction) adjustable pads which are on the damping platform too. The measuring device is placed on these adjustable pads, moving together with the mirror of the Specification of ELCOMAT 2000. So that the turning angle of the mirror is the same

as the measuring device. Then the calibration accuracy of the instrument could be done by the specification of ELCOMAT 2000. When recording data, try to make the Y direction of the electronic autocollimator turn a certain angle, while X direction with no angle change.

Every 10" angle of the Specification of ELCOMAT 2000 turned, then the data of the system is read and recorded with 40 data as a group. Then turn the opposite direction, and have another group measuring of 40 data. And five groups of measuring are done, and the Table 1 is the average of the 5 groups data forward and backward.

Table 1 The average of the 5 groups of data forward and backward

average of each group	1	2	3	4	5
average of the forward /″	11.0	11.1	11.1	11.1	11.0
average of the backward /″	10.9	11.0	10.9	10.8	10.9

The actual change of the instrument is 0.904" with every forward 1", and an actual change 0.904" with every backward 1". Comprehensive the two conditions, the actual change of the instrument is s 0.917" with every 1", and c is 0.904 ".

The Repeated Experiment of the Instrument

In addition, the repeated experiment of the instrument is done to measure the stability of the instrument for testing the standard deviation of the data. The experimental conditions were the same as the experimental conditions for precision calibration. In the Repeated experiments, we read and record the data every 50" angle changing of the Specification of ELCOMAT 2000. For a total of 10 times measured data recorded, the return data for a total of 10 times are recorded. Make the above as the first group, and a total of six groups of data would be measured. The testing data was shown in Table 2 and the fitting line with six groups of data and the current standard deviation is as shown in Fig. 6. It shows that the stability of the instrument is good for the correlation coefficient R^2 is 0.999.

Table 2 Standard error of the 6 groups of data forward and backward

group	1	2	3	4	5	6
forward standard error/″	5	10	14	19	24	28
backward standard error /″	5	10	14	19	24	28

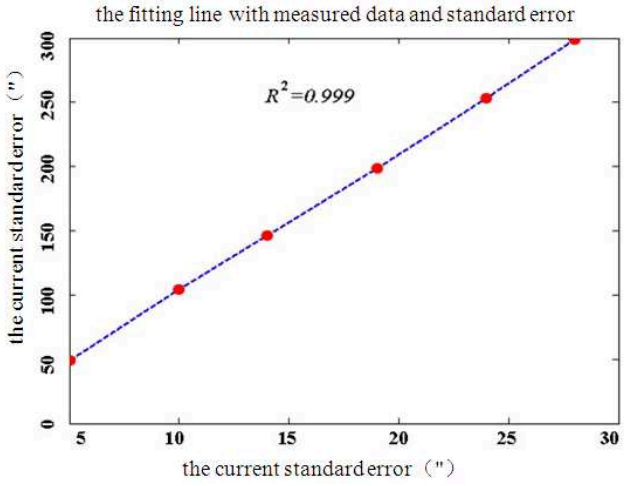

Fig. 6 Correctional line of the tested data and its standard error

Experiment For the Long Guide

The experiment for the long guide is done after the instrument precision calibration experiment done. Measuring location: Ship Model Experiment Center of Tianjin University, the test picture of the long guide shown in Fig. 3 (b). Then the straightness error is measured with the level method. The measuring length is 50m, and with the bridge of 0.5m long, each bridge span for 0.5m. The coordinate system is established with the horizon through the measuring point as horizontal axis. Coordinate value of each sample point in the axis direction can be calculated according to Eq. 5 after a_i is got. The experiment data is as shown in Table 3.

Table 3 The tested data of each section μm）

number of the measuring step	y_1	y_2	y_3	y_4	y_5	y_6	y_7	y_8	y_9	y_{10}
1 10	276.8150	215.7000	278.6125	219.2950	251.6500	212.1050	355.6500	253.4475	147.3950	228.2825
11 20	231.4000	195.2675	393.6525	237.2700	264.2325	122.2300	266.6900	212.1050	194.1300	192.3325
21 30	257.0425	194.1300	357.7025	262.4350	158.1800	171.9000	319.9550	122.2300	215.7000	149.1925
31 40	266.6900	150.9900	372.7425	167.1675	237.2700	125.8250	214.4600	171.9000	154.5850	203.1175
41 50	319.9550	264.2325	462.6175	212.1050	309.1700	213.9025	262.4350	125.8250	127.6225	102.4575
51 60	244.4600	231.8775	490.7175	257.0425	351.1725	191.6725	237.2700	213.9025	244.4600	255.2450
61 70	262.4350	332.5375	424.8700	278.6125	400.8425	243.3675	161.7750	91.6725	154.1075	136.6100
71 80	237.2700	287.6000	404.4375	301.9800	264.2325	129.4200	253.4475	123.3675	260.6375	113.2425
81 90	161.7750	197.7250	287.6000	276.8150	231.8775	161.1150	155.8550	129.4200	215.7000	219.2950
91 100	253.4475	285.6500	373.2200	230.0800	332.5375	120.2500	165.7500	182.7500	194.1300	271.4225

It shows that the maximum positive deviation point $i_{\max}$ is number 53 and $y_{\max} = 490.7175$, the maximum negative deviation point $i_{\min}$ is number 68 $y_{\min} = 91.6725$.

The formula of straightness error according to the end point connecting method is as followings.

$$\Delta = (y_{\max} - \frac{i_{\max}}{n} y_n) + \left| y_{\min} - \frac{i_{\min}}{n} y_n \right|$$

With the number of measurements $n = 100$, $y_n = 271.4225$, then Δ could be got:

$$\Delta = (490.7175 - \frac{53}{100} \times 271.4225) + \left| 91.6725 + \frac{68}{100} \times 271.4225 \right| = 623.103 \quad \mu m$$

So the straightness error is 623.103μm of the 50 meters long guide.

Summary

A new kind of straightness error measurement system based on laser interference is developed. The straightness errors of the long guide could be converted to the amount of movement of interference fringes by clever optical path design. The straightness error of the long guide could be measured by detecting the changes of the interference fringes. The straightness error is 623.103μm when the tested long guide is 50 meters long.The above test results are obtained without any correction, and without any control for laser beam drifting and mechanical vibration. In this way the data 623.103μm is got, it shows that the design of interferometry system is correct and successful. If any control of the measurement conditions is taken, better accuracy could be obtained.

References

[1] ZHANG Gangqiang, CHEN Jiangyuan, LUO Songbao. Technology Researcher of Hydrostatic Length Guideway for Precision Measurement Based on Photoelectric Autocollimator[J]. AVIATION PRECISION MANUFACTURING TECHNOLOGY, 2012, 48(2): 8 ～ 8(in Chinese).

[2] XU Ying, ZHAO Chenglan. Measurement of Slender Guide Straightness[J]. MARINE OPTICS, 2011, 47(3):44～46(in Chinese).

[3] LE Yanfen，SHI Ying，JU Aisong. Design of Heterodyne interferometer signal detectors[J]. LASER TECHNOLOGY, 2012, 36(6):759～762(in Chinese).

[4] PEI Zhongfang. Research on Laser Interference Alignment[D]. Master's degree paper of Tianjin University, 2004(in Chinese).

[5] JIA Lide, ZHENG Ziwen, LI Shengyi. Measurement Method of Straightness Error of a Long Ultra-precise Guideway with a Short Bechmark[J]. CHINESE JOURNAL OF MECHANICAL ENGINEERING, 2008, 44(9):141～146(in Chinese).

[6] ZHANG Tiebi, SUN Shiwei, LI Guang. Design and Study of Elevator Rails Straightness Measurement System[J]. Instrument Technique and Sensor, 2010,329(6)113～114(in Chinese).

[7] CHEN Jihua, ZHANG Jiming, LV Yunpeng. Design of Position Detector for Alignment Laser Line Based on the PSD[J]. MEASUREMENT & CONTRIL TECHNOLOGY, 2012, 31(10)8～11(in Chinese).

[8] GUAN M J, ZHAO D E. Research of the noise based on PIN type photoelectric conversion circuit[J]. ELECTRIC TEST. 2012, 20(2):35～38(in Chinese).

[9] SHA D L, KONG Y X. Design of receive circuit for heterodyne interferometer[J]. CFHI TECHNOLOGY, 2008, 23(6):66～68(in Chinese).

Applied Mechanics and Materials Vol. 565 (2014) pp 133-137

doi:10.4028/www.scientific.net/AMM.565.133

A High Accuracy of Magnetometer by Using Independent Directional Magnetic Field Measurement Technique

Athirot Mano[a] and Wisut Titiroongruang[b]

Department of Electronic Engineering, Faculty of Engineering

King Mongkut's Institute of Technology Ladkrabang

Bangkok 10520, Thailand

[a]manoathirot@yahoo.com, [b]ktwisut@kmitl.ac.th

Keywords: Hall effect sensor, Measurement Technique, Magnetometer

Abstract. In a measurement of magnetic flux density with high accuracy by using Hall effect sensor must be considered position of Hall sensor, that perfect perpendicular with magnetic flux line for measurement. Only one Hall element can cause measuring error. Therefore, this paper presents an application of independent directional magnetic field measurement technique on two dimensions for high accuracy magnetometer. It is presented by using two Hall sensors locate perpendicular to each other and use the relation of the two voltage output signal from both Hall sensors to calculate constant Hall voltage and Magnetic flux density with high accuracy by using trigonometric function with Lab-View programming. And as the result of experiment, this technique can reduce the limitation in term of this angle in the range magnetic flux density can be measured 0-1800 gauss. A calibration curve of this system compare with standard Gauss meter shows the coefficient of determination (R^2) equal to 1 and has the accuracy percentage as less than 0.5%.

Introduction

Due to the current, measurement system need to very high accuracy. Particularly, in magnetic flux density measurement, that can be used to several applications. In the instrument for magnetic flux density measurement such as Vibrating Sample Magnetometer (VSM), Gauss meter etc., importance part for response to magnetic flux density deviation is magnetic sensor. For magnetic sensor, which use widely as Hall effect sensor. It has characteristic to response and change from the magnetic field to voltage output signal is called Hall voltage.

However, the output signal of Hall sensor depends on an angle between magnetic flux line and active area of Hall sensor as sinusoidal function. This limitation is dependent on direction of magnetic field, which must be perpendicular to the sensor. Therefore, using only one Hall sensor can cause an error to measurement of magnetometer system. That is a problem affect to accuracy of the measurement.

"Independent Directional Magnetic Field Measurement Technique" [1,2] is a new technique, which is a choice to reduce the limitation in term of an angle. Therefore, the aim of this research is a high accuracy of magnetic flux density measurement by using independent directional magnetic field measurement technique on two dimensions. We use two semilar commercial Hall sensors, are located perpendicular and use relation of trigonometric function analyze and calculate a high accuracy of flux density value.

Experimental

The magnetic measurement system consist of three main part as magnetic sensors part, micro-controller (PIC-18F252) for controlled rotation of steping motor and convert data from analog Hall voltage signals to digital signals and the last part is flux density computation. The first step, we select to Hall sensor, that have sensitivity be similar to each other. For the first and second Hall has sensitivity 0.00131 and 0.00134 mV/G respectively. That is situated perpendicular to each other shows in Fig. 1. In the experiment, perpendicular Hall is rotated 0-360 degree by 3.6 degree/step in

different magnetic flux density as 0, 450, 900, 1,350 and 1,800 Gauss. Stepping motor is controlled by microcontroller all different steps, analog voltage of two Hall sensors are converted to digital signals by analog to digital converter (ADC 12 bit). The measurement data are transmitted to computer and analyzed Hall voltage constant. All Hall voltage constant are calculated Flux density by Eq.1 [2] in Lab-View programming.

$$k_1 \sin^2\theta + k_2 \cos^2\theta = k_{constant} \quad (1)$$

Finally, calibration of this instrument compare with standard Gauss meter model F.W.BELL5170. In the calibration, we use the five point test method [3] at 0, 25, 50, 75 and 100 percent of magnetic flux range 0-1,800 Gauss for ability testing of the magnetometer system.

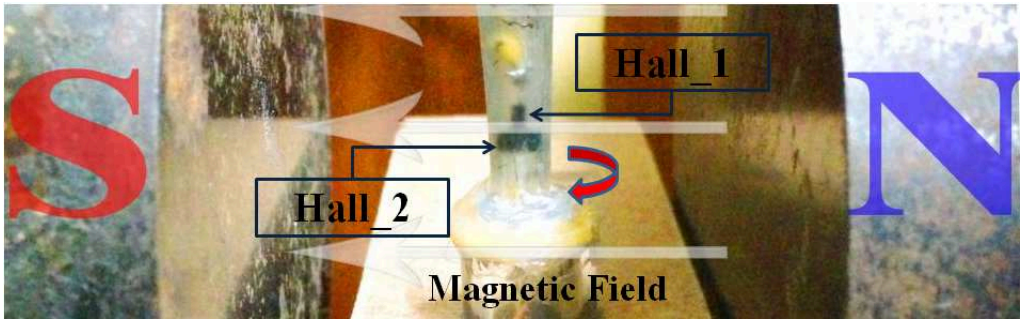

Fig. 1 The part of Magnetic flux density measurement

Result and discussion

The result of this experiment, perpendicular Hall are rotated in circle motion as 0-360 degree in magnetic field 450 G. Fig.2 shows the response of two Hall sensors. For Hall voltage of the first Hall is response to changes an angle corresponds to sinusoidal function. And as the result of second Hall voltage, which is situated perpendicular with the first Hall. Therefore, response of second Hall can be implied as cosine function. Both Hall voltage signals for all angles have phase shift as 90 degrees that shows perpendicular perfectly of two Hall sensors.

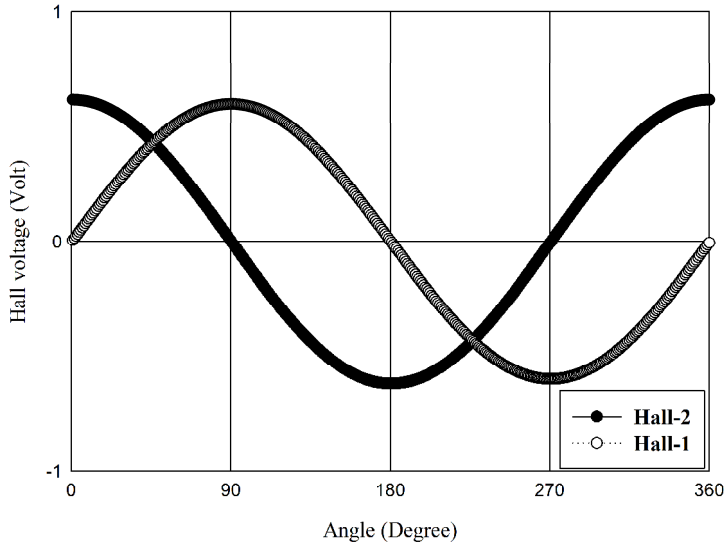

Fig. 2 The response of Hall sensors at angles 0-360 degree (B=450 G)

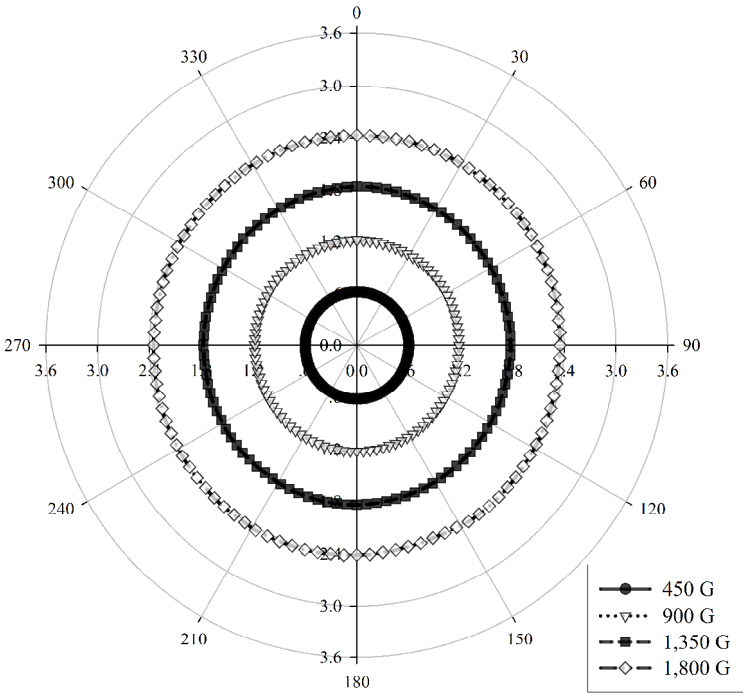

Fig. 3 Polar plot of Constant Hall voltage in flux density 450-1,800 Gauss

The sin and cosine function of two Hall voltage signal correspond to a unit circle of trigonometric equation, which can be calculated for constant Hall voltage independent directional magnetic field by using Eq.1. Fig. 3 shows polar graph of constant Hall voltage at flux density as 450, 900, 1,350 and 1,800 Gauss for all angle 0-360 degree.

The result of average constant Hall voltage as 0.000897, 0.6101, 1.2019, 1.8069 and 2.3867 respectively, that can be plotted linear curve relation versus flux density as shows in Fig.4 and the linear curve presents equation as y=0.00133x+0.00763.

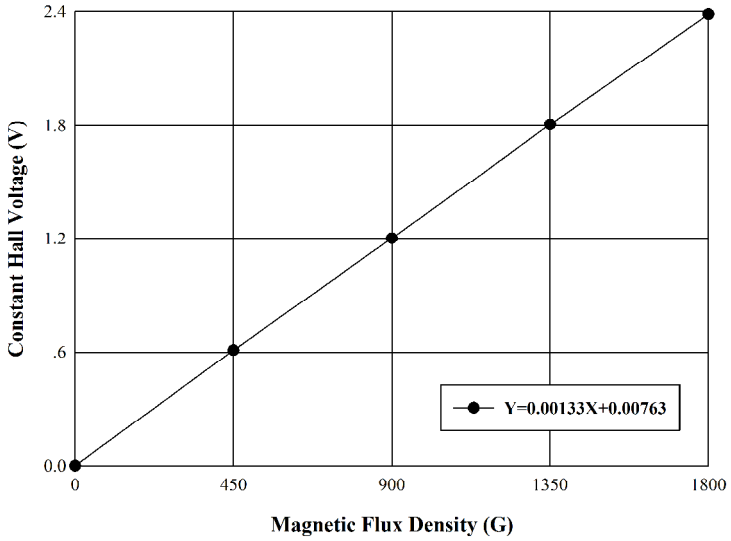

Fig. 4 Linear curve of average constant Hall voltage of the system

Finally, we use linear equation of average constant Hall voltage curve to calculate magnetic flux density by using Lab-View programming at 0, 25, 50, 75 and 100 percent of the magnetic flux density range 0-1800 Gauss. From the result, average magnetic flux density that are measured by using this technique, are compared with the calibration of magnetometer shows in Table 1. All magnetic flux

density value present in Gauss unit. Calibration to compare with F.W.BELL5170 standard Gaussmeter. The calibration curve has shown in Fig.5.

Table 1, The five point test of average magnetic flux density.

	Percentage (%)				
	0	25	50	75	100
Average	0.32	447.12	896.67	1346.22	1797.05
Actual	0	450	900	1,350	1,800
Deviation	0.32	2.88	3.33	3.78	2.95

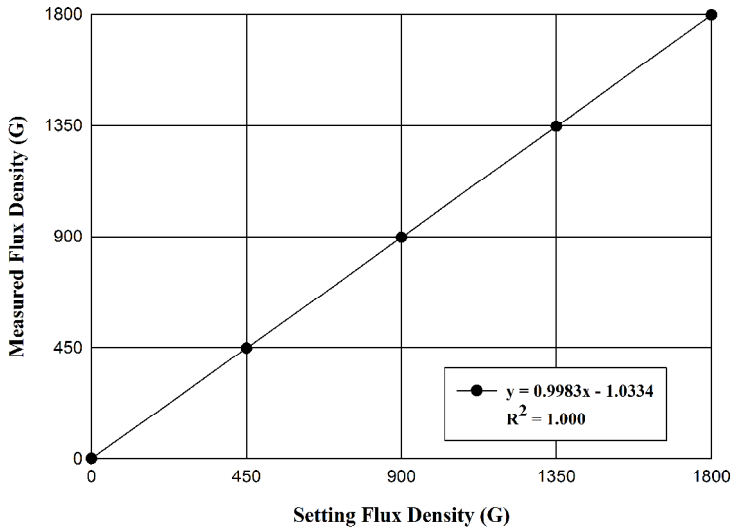

Fig. 5 Calibration curve of the magnetometer.

In Fig.5 presents linear calibration curve that is the relation between flux density measurement value of the magnetometer system and setting flux density value, which can be set by standard magnetometer. The calibration curve shows coefficient of determination (R^2) equal to 1.000.

Conclusions

And as all the result of experiment represent an application of this technique for high accuracy magnetometer that measure magnetic flux density independent angle of magnetic flux line interact with active region Hall element. The accuracy of this system is shown in calibration curve with the coefficient of determination (R^2) equal to 1.000 and has the accuracy percentage less than 0.5% in magnetic measured range 0-1,800 Gauss. Therefore, using this technique, the independent directional magnetic field measurement technique for magnetic flux density measurement can be useful in a high accuracy magnetometer.

Acknowledgment

The authors would like to thank the staffs from Electronic Research Center (ERC) that have been helpful for this research, which was funded by Thailand Graduate Institute of Science and Technology (TGIST)

References

[1] Athirot Mano, Santi Chatruprachewin, Laddawan Supadee, Chaba Suriyaammaranon and Wisut Titiroongruang, Independent Directional Magnetic Field Measurement Technique, Proceeding of the 33rd Electrical Engineering Conference(EECON-33)(2010), (in Thai), pp. 1369-1372, (2010).

[2] Athirot Mano, Narin Atiwongsangthong and Wisut Titiroongruang, Improvement of Independent Directional Magnetic field Measurement Technique with Hall sensors in Journal of Advanced Materials Research, Vol. 811, pp. 347-352, (2013).

[3] Kelly S. Fundamentals of Instrumentation. 2nd ED. Delmar cengage leaning, New York, (2008).

[4] Richard S.Muller and Theodore I.Kamins. Device Electronics for Integrated Circuits, John Wiley&Sons, New York, Inc., (1986).

Applied Mechanics and Materials Vol. 565 (2014) pp 138-141

doi:10.4028/www.scientific.net/AMM.565.138

Radiation Degradation Modeling of Bipolar Operational Amplifier Input Offset Voltage in LTSpice IV

A.S. Bakerenkov[1, a], V.S. Pershenkov[1,b], A.V. Solomatin[1,c], V.V. Belyakov[1,d], V.V. Shurenkov[1,e]

[1]Microelectronic department, National Research Nuclear University MEPhI (NRNU "MEPhI"), Moscow, 115409, Russian Federation

[a]as_bakerenkov@list.ru, [b]vspershenkov@mephi.ru, [c]avsolomatin@list.ru, [d]vvbelyakov@mail.ru, [e]vvshurenkovn@mephi.ru

Keywords: operational amplifiers, input bias current, input offset voltage, space environment, total dose, bipolar transistors, ELDRS.

Abstract. Integrated circuits are used in electronic equipment of spaceships. Therefore, they are impacted by ionizing radiation during space mission. It leads to electronic equipment failures. At present operational amplifiers are base elements of analog electronic devices. Radiation impact leads to degradation of operational amplifiers input stages. Input bias current increasing and input offset voltage drifts are the results of ionizing radiation expose of operational amplifiers. Therefore, space application electronic equipment fails after accumulation of limit dose. It isn't difficult to estimate radiation degradation of input bias currents of bipolar operational amplifiers, but estimation of dose dependence of input offset voltage drift is more complex issue. Schematic modeling technique based on Gummel–Poon transistor model for estimation of input offset voltage drift produced by space radiation impact was experimentally verified for LM324 operational amplifier and presented in this work. Radiation sensitive parameters of Gummel–Poon model were determined using 2N2907 bipolar pnp transistor.

Introduction

There are a set of papers [1-3], in which it is shown that the main radiation-sensitive parameters of operational amplifiers are the input current and voltage offset. In bipolar operational amplifiers input currents are typically base currents of differential input stage bipolar transistors. Because radiation impact results in increasing of bipolar transistor base currents it leads to operational amplifiers input current increase. Radiation degradation of offset voltage is a complex function of total dose and amplifier input stage circuit.

To estimate degradation of the input currents in low dose rate radiation conditions the conversion model [4] can be used. The model determines the dependence of bipolar transistor base current on total dose and irradiation dose rate. Unlike the radiation increase of the input currents, offset voltage degradation can't be described directly by conversion model relationships. This paper presents a circuit simulation method for determining radiation degradation of input offset voltages using defined dependence of input current degradation on total dose. This method allows the radiation input offset voltage shift to be determined by using the conversion model to the input current.

Presented in this work simulation, was performed in LTSpice VI using the Gummel–Poon bipolar transistor model. Using the results of experimental research radiation-sensitive model parameters was estimated. Radiation degradation modeling of the LM324 input currents was performed. Based on the experimental obtained dependence of input current on total dose Gummel–Poon model parameters total dose dependence was extracted. Using this results total dose dependence of input offset voltage was calculated. Modeling results are in good correlation with experimental obtained input offset voltage dependence. It suggests the possibility of using this approach to predict the degradation of offset voltage operational amplifiers in low dose rate radiation environment.

Radiation sensitive parameters of bipolar transistor model

The Gummel–Poon bipolar transistor model for circuit simulation in LTSpice VI was used. This model has many parameters, most of which is used to set the frequency characteristics of the transistor. Because of in this paper static characteristics of bipolar devices are used, the circuit simulation is not required to set frequency parameter values. Part of the model parameters used to describe the transistor in reverse mode. Since, in operational amplifiers transistors are used in the forward mode, the values of these parameters do not affect the simulation results.

Using this assumptions, for base and collector current-voltage characteristics of bipolar transistor it's possible to write relationships:

$$I_c = I_s \exp(U_{eb}/\varphi_T), \quad (1)$$

$$I_b = (I_s/B_f) \exp(U_{eb}/\varphi_T) + I_{se} \exp(U_{eb}/(n_e\varphi_T)), \quad (2)$$

In which I_c – collector current, I_b – base current, U_{eb} – emitter-base voltage, I_s, B_f, I_{se} and n_e – Gummel–Poon model parameters. Since the radiation degradation of the transistor is determined by the increase in the base current at constant collector current, it possible to assume that the parameter I_s does not change at radiation impact. The value of B_f defines pre-exponential multiplier of ideal base current component (proportional $\exp(U_{eb}/\varphi_T)$). This component of the base current is the sum of the currents in the emitter injection and recombination in the active base region. Since in modern transistor size of the active base region are small enough, recombination current in the active base region is much smaller than the current injected into the emitter. Injection current is determined by the emitter forward bias and doesn't dependent on total dose. Thus, the first term in (2) after irradiation remains constant. Because of the I_s value doesn't change, the coefficient B_f shouldn't change too. In this paper assumed that the second term in (2) is surface (interface) recombination current. Thus, the radiation degradation of the base current should be determined by increasing I_{se} parameter.

To confirm this assumption, the irradiation of bipolar pnp transistor 2N2907 was performed. The transistor was exposed to different total dose levels (12 krad (SiO_2), 36 krad (SiO_2), 72 krad (SiO_2)). At each total dose level collector and base voltage-current characteristic measurements were performed at zero collector junction bias. Experimental obtained voltage current characteristics a presented at fig.1a. The static gain dependences for different dose values on emitter-base voltage are shown at fig.1b. Corresponding simulation results in LTSpice VI are presented at fig.1 by solid lines.

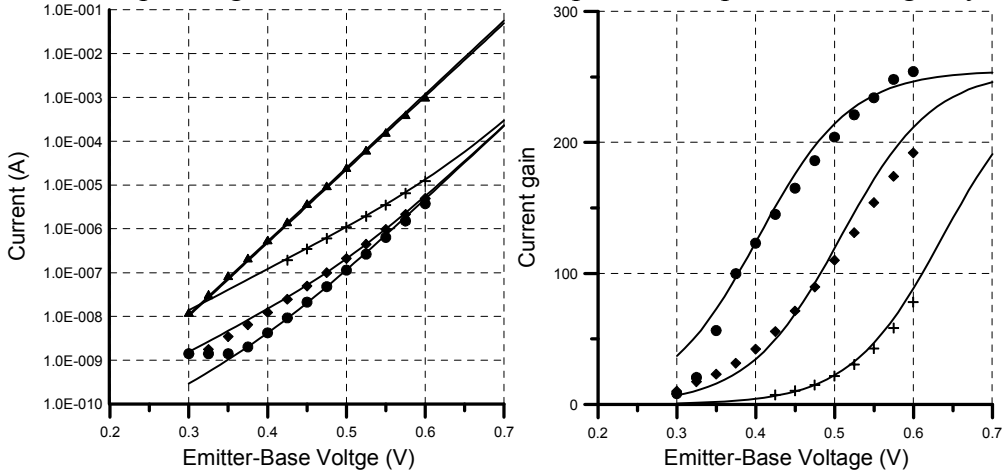

Fig.1. a) Experimental and modeling (solid lines) base current-voltage characteristics for 2N2907 transistor before irradiation (●) and for different dose values (12 krad(Si) – (♦), 72 krad(Si) – (+)); collector current-voltage characteristic before and after irradiation (▲). b) Corresponding dependences of transistor current gain on emitter base voltage.

Using transistor current-voltage characteristics before irradiation initial values of model parameters (I_s, B_f, I_{se} and n_e) were extracted. The results for other total dose values were obtained by changing I_{se} parameter only. The obtained I_{se} dependence on total dose presented at fig.2. The

dependence is close to linear, that is the evidence of linear dependence of surface (interface) recombination current on total dose.

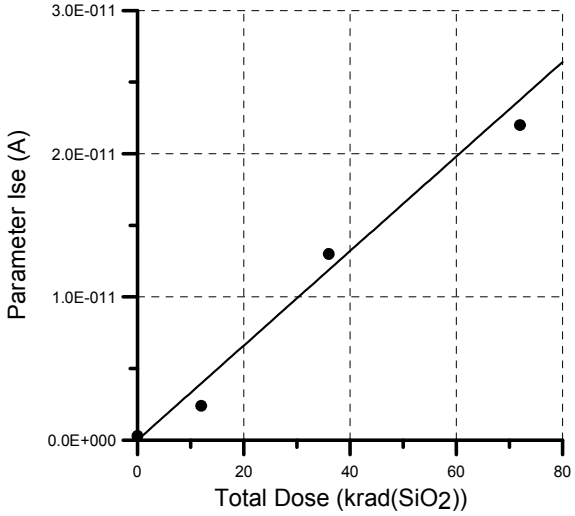

Fig.2. Total dose dependence of I_{se} Gummel–Poon model parameter for 2N2907 transistor

Thus, in Gummel–Poon bipolar transistor model used for circuit simulation, pre-exponential factor I_{se} is the main radiation-sensitive parameter. Other parameters values are total dose independent and must be extracted from current-voltage transistor characteristics before irradiation.

Schematic modeling of input offset voltage radiation degradation in operation amplifiers

Using Gummel–Poon model and schematic modeling enable to calculate input offset voltage degradation using corresponding input current values. For schematic modeling it's necessary to extract Gummel–Poon model parameters of operation amplifier transistors form pre-irradiation values of input currents, input offset voltage and supply current. For defined dose value, using the input current dependence on total dose, it's possible to extract total dose dependence of I_{se} to calculate input offset voltage degradation corresponding defined dose value.

The approach described above was used to calculate input offset voltage radiation degradation for LM324 operational amplifier. The amplifier was irradiated to different total doses. Input currents and offset voltage were measuring during irradiation. Using experimental obtained input current dependence on total dose, corresponding dependence of I_{se} was extracted and radiation degradation of input offset voltage for each dose value was calculated. Experimental and modeling results are presented at fig.3.

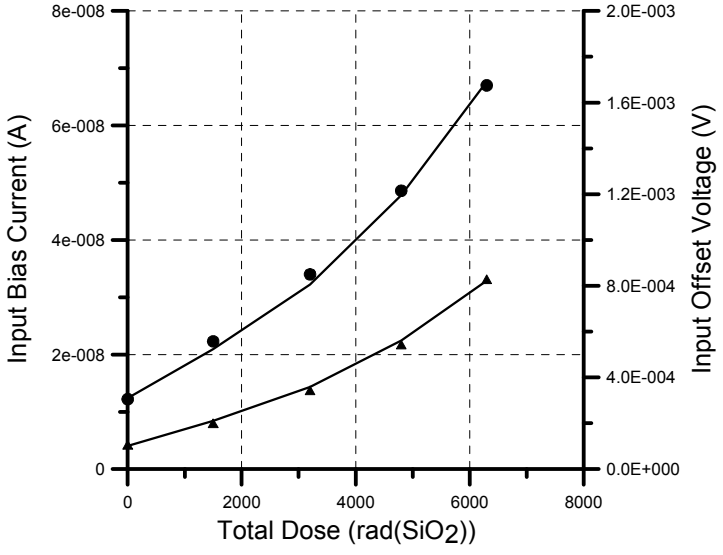

Fig.3. Experimental and modeling (solid lines) total dose dependence of input current (●) and offset voltage (▲) for LM324 operation amplifier

Summary

Input currents on offset voltage are a radiation-sensitive parameters of bipolar operational amplifiers. Radiation impact leads to input offset voltage shift out of specification limit. Depending on operation amplifier circuit design offset voltage parametrical failure may occur before input current malfunction. When predicting performance of operational amplifiers at low dose rate radiation environment a radiation degradation of input offset voltage should be considered. Low dose rate effect conversion model in bipolar devices able to determine only the input current radiation degradation. Simulation technique for prediction radiation degradation of bipolar operation amplifiers input offset voltage, base on circuit simulation in LTSpise VI, was presented and experimentally justified. The method for radiation degradation modeling of bipolar transistors was described and Gummel–Poon model radiation-sensitive parameters were determined. Radiation shift schematic simulation of LM324 input offset voltage was performed. Good correlation of modeling and experimental results provides the evidence of the possibility of using described technique, based on the conversion model, for radiation degradation input offset voltage prediction in low dose rate radiation environment.

References

[1] A.H. Johnston, B.G. Rax, Testing and Qualifying Linear Integrated Circuits for Radiation Degradation in Space. *Proceedings of the European Conference on Radiation and its Effects on Components and Systems, RADECS*, (2005).

[2] R.L. Pease, R.D. Schrimpf, D.M. Fleetwood, ELDRS in bipolar linear circuits: A review. *IEEE Transactions on Nuclear Science, vol. 56(4), pp. 1894-1908*, (2009)

[3] A.H. Johnston, B.G. Rax. Failure Modes and Hardness Assurance for Linear Integrated Circuits in Space Applications. *Proceedings of the European Conference on Radiation and its Effects on Components and Systems, RADECS*, (2009).

[4] V.S. Pershenkov, D.V. Savchenkov, A.S. Bakerenkov, V.N. Ulimov , A.Y. Nikiforov, A.I Chumakov, The conversion model of low dose rate effect in bipolar transistors. *Proceedings of the European Conference on Radiation and its Effects on Components and Systems, RADECS*, (2009).

Applied Mechanics and Materials Vol. 565 (2014) pp 142-146

doi:10.4028/www.scientific.net/AMM.565.142

Mechanism of the Saturation of the Radiation induced Interface Trap Buildup

V.S. Pershenkov[1,a], A.S. Bakerenkov[1, b], A.V. Solomatin[1,c], V.V. Belyakov[1,d], V.V. Shurenkov[1,e]

[1]Microelectronic department, National Research Nuclear University MEPhI (NRNU "MEPhI"), Moscow, 115409, Russian Federation

[a]vspershenkov@mephi.ru, [b]as_bakerenkov@list.ru, [c]avsolomatin@list.ru, [d]vvbelyakov@mail.ru, [e]vvshurenkovn@mephi.ru

Keywords: Interface traps, Ionizing radiation, Integrated circuits, Total dose, Bipolar transistors, ELDRS.

Abstract. Ionizing radiation impact leads to degradation of electrical parameters of microelectronic devices. It is necessary to take this fact to account when dealing with microcircuits for space applications and high energy physics. Main physical reason of radiation-induced failures of spaceship and front end electronic equipment is buidup of interface traps at Si-SiO_2 interface in semiconductor transistor structures. The original mechanism of interface trap annealing based on radiation induced charge neutralization (RICN) effect is presented. It is supposed that the positive charge of trapped holes in oxide is transformed through electron capture into a new defect (the AD center). The AD centers act as interface traps. The appearance of the A^-D^+ state leads to the annihilation of the AD center or annealing of interface trap. The annihilation process can be stimulated by radiation induced or substrate electrons. The competitive between accumulation and annihilation processes leads to saturation of the interface trap buildup. The value of density of interface trap in saturation depends on product of interface trap accumulation rate $(K_{acc})_{it}$ and constant K_{AD} which is function of thermal velocity, capture cross-section of AD center, generation rate and electron yield of radiation induced electrons. The extraction of these parameters allows explaining a known experimental data. The alternative mechanism of the interface trap saturation connected with the exhaustion of initial interface trap precursors is considered.

Introduction

Radiation induced buildup of interface traps N_{it} is a problem that has been known for last 35 years [1,2]. The interface trap density growth on dose was observed to tend toward saturation at high total absorbed doses [3,4]. The detailed analysis of saturation region (in dose range 30 - 50 Mrad (SiO2)) was not fulfilled in early works, because in practice the doses where MOS and bipolar integrated circuits operate, as a rule, much less than saturation doses. Or the study of the saturation region had not got practical sense. But using modern integrated circuits for the front end electronics of High Energy Physics experiments (such as the ATLAS Detector in the Large Hadron Collider at CERN) leads to change the situation [5,6]. The present estimations of the total dose in the ATLAS Upgrade Inner Detector's Middle Region give value near 50 Mrad (SiO2) for the front end electronics operation during 10 years [7]. Authors of [7], investigating a behavior of the silicon-germanium heterojunction bipolar transistors for ATLAS Detector applications, have observed the effect of the anomalous recovery of transistor current gain after total absorbed dose 30 and 50 Mrad (SiO_2). This work stimulated the more careful study of saturation dose region. Moreover the results of works [8,9] at "switched experiments" show that saturation dose for modern bipolar linear microcircuits lay in relatively low dose region 10-50 krad (SiO_2). Even if it is connected with circuits effect [10], in any case the study of the saturation dose region can give new information about physical mechanism of circuit parameter degradation. It means that the investigation of the saturation interface buildup can have practical interest in nearest future.

The goal of this paper is to describe the possible mechanism of the interface buildup saturation. We present the original model of saturation effect.

Mechanism of interface trap buildup in saturation

Background

As a rule the physical mechanism of radiation induced interface state buildup is considered (in huge publications) before interface trap saturation. The most developed model is two-stage "hydrogen" model [1,2,11]. The other model (so called "conversion" model [12]) is based on assumption that generation of interface traps connects with the neutralization of positive charge by the substrate or radiation induced electrons. In this work the radiation induced charge neutralization effect is used for explanation of N_{it} saturation.

The saturation can be explained by two competitive processes: accumulation and annihilation (annealing). At mathematical form it can be written:

$$dN_{it}/dt = G - N_{it} / (\tau \quad (1)$$

Where G is accumulation rate of interface trap; N_{it} is density of interface traps; $(\tau_{ann})_{it}$ is the time constant of interface state annihilation.

In saturation, $dN_{it}/dt = 0$ and N_{it} reaches a saturated value:

$$(N_{it})_{sat} = G \cdot (\tau_{ann})_{it}. \quad (2)$$

The accumulation rate of N_{it} buildup is proportional to the dose rate:

$$G = (K_{acc})_{it} \cdot P, \quad (3)$$

Where $(K_{acc})_{it}$ is a coefficient characterizing interface trap accumulation; P is the dose rate.

Therefore:

$$(N_{it})_{sat} = (K_{acc})_{it} \cdot (\tau_{ann}) \quad (4)$$

The value of $(N_{it})_{sat}$ is proportional the dose rate P if $(K_{acc})_{it}$ and $(\tau_{ann})_{it}$ are constants. But, as follows from experimental data, the value interface trap concentration in saturation $(N_{it})_{sat}$ is very weak function of the dose rate. The changing of the dose rate at more than 4 orders in region from 300 krad (Si)/min to 13 rad (Si)/min leads to very small variation of $(N_{it})_{sat}$ [4]. The same result is obtained in [9,10], where the saturation of N_{it} was observed for the changing of the dose rate from 333 rad (SiO_2) to 5.25 rad (SiO_2).

The coefficient $(K_{acc})_{it}$ is very weak function of the dose rate. It follows from linear dependence of N_{it} buildup at small total doses, that agrees with numerous experimental data reported by [3,4,10]. The value $(N_{it})_{sat}$ is not dependent at the dose rate P if $(\tau_{ann})_{it}$ is inversely proportional P or an annihilation (annealing) of interface traps depend on the dose rate. It is necessary to consider radiation induced charge neutralization (RICN) effect. Usually RICN effect concerns to the annealing of oxide trapped charge. In given work we suppose using RICN effect as basic mechanism of interface trap annealing. The role of interface traps plays co-called AD centers proposed in [13].

Concentration of interface traps in saturation

The model of [13] is based on the assumption that the positive charge of trapped holes in oxide is transformed through electron capture into a new defect (the AD center) with two energy states in forbidden gap of Si. This is point defect, for which the high energy level is acceptor-like and lower energy level is donor-like. The following process of AD center generation and annihilation is proposed. The strained Si-Si bond (oxygen vacancy) serves as precursor for this radiation induced defect. This precursor can be treated as a non-activated donor center D. The radiation induced holes are captured by deep D traps creating a positive charged D^+ center: $D + h = D^+$. Free electron capture

by D^+ center causes its transformation to the two-level AD center: $D^+ + e = A^0D^0$. The AD defect can be found in four different states: A^0D^0, A^-D^0 , A^0D^+ , A^-D^+ . The superscripts after A and D designate charge state of the acceptor and donor levels respectively: A^0D^0 – acceptor level is empty, donor level is occupied; A^-D^0 – acceptor level is occupied, donor level is empty; A^0D^+ – both acceptor and donor levels are empty; A^-D^+ – acceptor level is occupied, donor level is empty. The charge exchange of the A^0D^0 with radiation induced or substrate electrons leads to A^-D^0 and A^0D^+. The charge state A^-D^+ cannot be stable and is assumed to immediately relax back to the D precursor due to energy released during electron transition from higher (A) to lower (D) levels. Therefore, the appearance of the A^-D^+ state leads to the annihilation of the AD center.

The AD center can be formed via E'_γ center (which is responsible for radiation induced positive oxide charge) by following mechanism. Positively charged Si atom in E'_γ center is sp3-hybridized (tetrahedral configuration) [14]. The electron energy level in this defect strongly depend on the distance between Si^+ and SiO atoms [15]. When this distance is large, these levels are located in the oxide close to the Si midgap. When these two atoms are bonded and the distance between them is small, the energy levels of bonding electrons shift to valence and conduction bands. The first electron capture to the E'_γ center changes defect configuration [14,15] which results in the electron energy levels shift from Si midgap towards the Si valence and conduction bands, the distance between Si atoms being of intermediate value. The electrons in this configuration defect are expected to be in the intermediate sp2-sp3 configuration and could form diffusion orbital. This defect configuration may be assumed stable and electron energy levels are proposed to remain unchanged when one of the electrons is removed.

Consider the case when annihilation takes place from A^0D^+ configuration after capture radiation induced electron by A^0 level. The Nit annihilation process can be described by the relationship from recombination theory of Shockly-Read-Hall [16]:

$$(dN_{it}/dt)_{ann} = -\upsilon_{th}\cdot\sigma_t\cdot n\cdot N_{it}, \tag{5}$$

Where υ_{th} is the thermal velocity; σ_t is the capture cross-section of AD center; n is concentration of radiation induced electrons. Concentration of radiation induced electrons equal:

$$n = K_p\cdot K_y\cdot P, \tag{6}$$

Where K_p is generation rate per unit dose rate; K_y is electron yield; P is the dose rate. Result of substituting (6) in equation (5) is

$$(dN_{it}/dt)_{ann} = -\upsilon_{th}\cdot\sigma_t\cdot n\cdot K_p\cdot K_y\cdot P\cdot N_{it} = -P/K_{AD} = -N_{it}/(\tau_{ann})_{it}, \tag{7}$$

Where

$$K_{AD} = 1/\upsilon_{th}\cdot\sigma_t\cdot K_p\cdot K_y. \tag{8}$$

It means that $(\tau_{ann})_{it} = K_{AD}/P$ and

$$(N_{it})_{sat} = (K_{acc})_{it}\cdot K_{AD}. \tag{9}$$

The value of density of interface trap in saturation, as follows from (8), depends on product of interface trap accumulation rate $(K_{acc})_{it}$ and constant K_{AD} which is function of thermal velocity, capture cross-section of AD center, generation rate and electron yield of radiation induced electrons.

Discussion

Consider the analysis of the some results of work [3], using relationship (9). In [3] two vendors (vendor “A” and vendor “B”) of n-channel Metal-Oxide-Semiconductor Field Effect Transistors (MOSFETs) were irradiated with X-ray. The vendors had different initial values of interface trap density and were irradiated at different dose rates, which presented in table 1 with estimated value of $(K_{acc})_{it}$ and K_{AD}. The estimation was performed by using (3) and (9).

Table 1. Experimental conditions and estimation results for transistor venders from [3]

	Dose rate [rad(SiO_2)/s]	Initial N_{it}, [cm^{-2}]	$(K_{acc})_{it}$, [rad(SiO_2)$^{-1}s^{-1}$]	K_{AD}, [rad(SiO_2)]	$(N_{it})_{sat}$, [cm^{-2}]
Vendor "A"	170	$2*10^{10}$	$6.4*10^{4}$	$1.6*10^{7}$	$1*10^{12}$
Vendor "B"	1700	$2*10^{11}$	$1.15*10^{6}$	$1.7*10^{7}$	$2*10^{13}$

The values of K_{AD} are approximately equal for different venders despite different initial Nit, saturation $(N_{it})_{sat}$ values and irradiation dose rate. It means parameter K_{AD} describes the physical characteristics of AD centers. Value of $(K_{acc})_{it}$ is determined by initial Nit buildup rate and depends on parameters of manufacture fabrication procedures.

The alternative mechanism of the interface trap saturation proposed in [4], where most likely possibility for the observed saturation is considered the exhaustion of interface trap precursors N_{prec}. The N_{it} growth rate is proportional to the concentration of non transformed precursors $(N_{prec} - N_{it})$

$$dN_{it}/dt = \lambda \cdot P \cdot (N_{prec} - N_{it}), \quad (10)$$

where λ is the probability that any given precursor will complete the transformation to an interface trap; is the N_{prec} initial precursor concentration; P is the dose rate.

An increasing of interface trap concentration leads to decreasing of growth rate. In saturation level of the interface trap is equal to the initial pre-irradiation precursor concentration:

$$(N_{it})_{sat} = N_{prec}. \quad (11)$$

It is interesting that negative term $(-\lambda \cdot P \cdot N_{it})$ in (10) which can be responsible for interface trap annealing is proportional to the dose rate as we suppose in our described above analysis. The model of the exhaustion of interface trap precursors cannot explain the temporal reducing Nit concentration which takes place at elevated temperature irradiation [17,18]. The mechanism AD center annealing can explain it. Moreover our model can be used for a description of interface concentration annealing without irradiation when P=0. In that case the electron concentration n in equation (5) corresponds to concentration of substrate electrons due to thermal excitation.

Summary

The original mechanism of the radiation induced interface trap buildup in saturation is described. The physical model is based on assumption that the positive charge of trapped holes in oxide is transformed through electron capture into a new defect (the AD center). The AD centers act as interface traps. One of the states $A^{-}D^{+}$ cannot be stable and immediately relaxes backs to the precursor. The appearance of the $A^{-}D^{+}$ state leads to the annihilation of the AD center or annealing of interface trap. The annihilation process can be stimulated by radiation induced or substrate electrons. The competitive between accumulation and annihilation processes leads to saturation of the interface trap buildup. The value of density of interface trap in saturation depends on product of interface trap accumulation rate $(K_{acc})_{it}$ and constant K_{AD} which is function of thermal velocity, capture cross-section of AD center, generation rate and electron yield of radiation induced electrons. The alternative mechanism of the interface trap saturation connected with the exhaustion of initial interface trap precursors is considered.

References

[1] P.S. Winokur, H.E. Boesch, Interface state generation in radiation-hard oxides. *IEEE transactions on Nuclear Science, vol. 27, № 6, pp. 1647-1650*, (1980).

[2] F.B. McLean, A framework for understanding radiation-induced interface state in SiO_2 MOS structures. *IEEE transactions on Nuclear Science, vol. 27, № 6, pp. 1651-1657,* (1980).

[3] J. M. Benedetto, H.E. Boesch, F.B. Mclean, Dose and energy dependence of interface trap formation in Cobalt-60 and X-ray environments. *IEEE transactions on Nuclear Science, vol. 35, № 6, pp. 1260-1264*, (1988).

[4] M.P. Baze, R.E. Plaag, A.H. Johnston, Dose dependence of interface traps in gate oxides at high levels of total dose. *IEEE transactions on Nuclear Science, vol. 36, № 6, pp. 1858-1864*, (1989).

[5] M. Ullán, J. Rice, G. Brooijmans, et al, Evaluation of Silicon-Germanium (SiGe) Bipolar Technologies for Use in an Upgraded ATLAS Detector. *Nuclear Instruments and Methods in Physics Research, A, vol. 604, pp. 668-674*, (2009).

[6] S. Díez, M. Lozano, G. Pellegrini, I. Mandić, D. Knoll, B. Heinemann, M. Ullán, IHP SiGe:C BiCMOS technologies as a suitable backup solution for the ATLAS Upgrade Front-End electronics. *IEEE Trans. on Nuclear Science, vol. 56, pp. 2449-2456*, (2009).

[7] M. Ullan, M. Wilder, H. Spieler , E. Spencer, S. Rescia, F.M. Newcomer, F. Martinez-McKinney, W. Kononenko, A.A. Glillo, S. Diez, Enhanced Low Dose Rate Sensitivity (ELDRS) tests on advanced SiGe bipolar transistors for very high total dose applications. *IEEE Trans. on Nuclear Science, vol. 56, pp. 2449-2456*, (2009).

[8] J. Boch, F. Saigne, S. Ducret, R.D. Schrimpf, D. M. Fleetwood, P. Iacconi, L. Dusseau, Total dose effects on bipolar integrated circuits: characterization of the saturation region. *IEEE transactions on Nuclear Science, vol. 51, № 6, pp. 3225-3230*, (2004).

[9] J. Boch, Y.G. Velo, F. Sainge, N. Roche, R.D. Schrimpf, J. Vaille, L. Dusseau, C. Chatry, E. Lorfevre, R. Ecoffet, A.D. Touboul, The use of dose rate switching technique to characterize bipolar devices. *IEEE transactions on Nuclear Science, vol. 53, №6, pp. 3347-3353*, (2009).

[10] H.J. Barnaby, R.D. Schrimpf, R.L. Pease, P.Cole, T. Turflinger, J.Kreig, J. Titus, D. Emily, M. Gehlhausen, S.C. Witczak, M.C. Maher, D. Van Nort, Identification of degradation mechanisms in bipolar linear voltage comparator through correlation of transistor and circuit response. *IEEE transactions on Nuclear Science, vol. 46, №6, pp. 1666-1673*, (1999).

[11] T. R. Oldham, F.B. McLean, Total ionizing dose effects in MOS oxides and devices. *IEEE transactions on Nuclear Science, vol. 50, №3, pp. 483-499*, (2003).

[12] S.K. Lai, Interface trap generation in silicon dioxide when electrons are captured by trapped holes. *Journal of Applied Physics vol. 54, Issue 5, pp. 2540-2546*, (1983).

[13] V.S. Pershenkov, S.V. Cherepko, A.V. Sogoyan, V.V. Belyakov, V.N. Ulimov, V.V. Abramov, A.V. Shalnov, V.I. Rusanovsky, Proposed two-level acceptor-donor (AD) center and nature of switching traps in irradiated MOS structures. *IEEE transactions on Nuclear Science, vol. 43, №6, pp. 2579-2586*, (1996).

[14] K.L. Yip, W.B. Fowler, Electronic structure of E ′ centers in SiO_2, *Phys. Rev. B, vol. 11(6), pp. 2427-2438*, (1975).

[15] E.P. Reilly, J. Roberston, Theory of defect's in vitrous silicon dioxide. *Phys. Rev. B, vol. 27(6), pp. 3780-3788*, (1981).

[16] S.M. Sze, Physics of semiconductor devices. *New York, Willey*, (1981).

[17] S.C. Witczak, R.D. Schrimpf, K.F. Galloway, D. M. Fleetwood, R.L. Pease, J.M. Puhl, D.M. Schmidt, W.E. Combs, J.S. Suehle, Accelerated tests for simulating low dose rate gain degradation of lateral and substrate pnp bipolar junction transistors. *IEEE transactions on Nuclear Science, vol. 43, №6, pp. 3151-3160*, (1996).

[18] G.I. Zebrev et al, Radiation response of bipolar transistors at various irradiation temperature and electric biases: modeling and experiment. *IEEE transactions on Nuclear Science, vol. 53, №6, pp. 1981-1987*, (2006).

Applied Mechanics and Materials Vol. 565 (2014) pp 147-151

doi:10.4028/www.scientific.net/AMM.565.147

Experimental Study of Wind Driven Scroll Pump

Chanchai Wiroonritichai[1, a], Assist. Prof. Pollakrit Kritmaitree[1,b]

[1]Mechanical Engineering Department, Faculty of Engineering, Kasetsart University, Thailand

[a]chanchai_kaset@hotmail.com, [b]fengpck@ku.ac.th

Keywords: Scroll Pump, Pump Efficiency, Wind, Experimental, Positive Displacement Pump

Abstract. This paper describes the feasibility study of wind driven scroll pump for wind energy application using in Thailand to design, fabricate and test. The testing set was adapted by the Japanese Industrial Standards (JIS B 8301) to define the relationship of pressure and flow rate curve (H-Q Curves), the relatioship of flow rate and pump speed , and the volumetric flow rate. The results presented the pressure and flow rate which showed the inverse variation in linear equations. The speed of the pump and flow rate were direct variation in linear equations. The maximum flow rate was 20.23 liters/minute in the speed of 714 RPM which fully opened valve. The average of volumetric efficiency was 89.55%.

Introduction

The wind turbine is an importance in water pumping for agriculture and irrigation which compensates the electrical power and diesel machine using in the research of Kasetsart University in the past [1]. This study presented the new development of the scroll pump. It is classified to a type of positive displacement pump which use with water and other liquid. Besides, it can be applied for the transmission of the low speed wind turbine pumping. The scroll pump for one set was carried out in this study. The motor is applied to simulate the operation of wind turbine and the transmission which useful for the scroll pump to find the relationship of pressure and flow rate curve (H-Q Curves), the relatioship of flow rate and pump speed , and the volumetric flow rate of the water pumping for agriculture and irrigation. This study is the guideline to improve the effective wind turbine scroll pump in the future.

Objectives:

1. Studying the creation of the scroll pump.
2. Designing and making the tester for find the relationship of pressure and flow rate curve (H-Q Curves), the relatioship of flow rate and pump speed , and the volumetric flow rate.

Methodology

The scroll pump was designed by using MATLAB and SolidsWorks software and machined by CNC as the following steps.

1.The MATLAB software was chosen for designing and creating of the scroll pump to calculate the coordinates of the wrap curves inwhich a scroll coefficient (α)is 1.5 mm ,and discrepancy of starting roll angle (β) is 0.3π radian. The scroll pump was designed by commercial SolidWorks software. Especially, in the forming of the components, such as the fixed wrap and orbiting wrap, the 5-axis CNC machine was used.

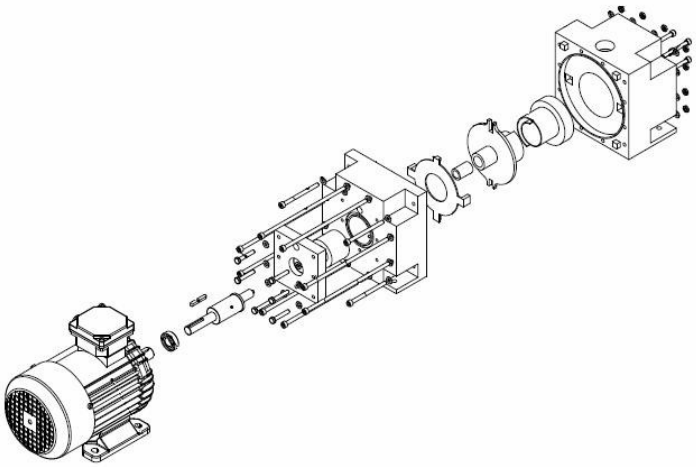

Fig.1: The components of scroll pump

There are two wraps of the scroll pump-a fixed wrap and an orbiting wrap. Those wraps have 2 curves-an inner curve and an outer curve designed by an algebraic spiral scroll equation. The algebraic spiral scroll equation is designed as a x-y coordinate and divided as a spiral scroll equation for a fixed wrap and orbiting wrap which are divided as inner and outer curve equation as shown in Eq.1 to Eq.8 as following adaptation form [2]: Fixed Curve
Inner Curve

$$x = \alpha(\cos\lambda + (\lambda + \pi - \beta)\sin\lambda) \quad (1)$$

$$y = \alpha(\sin\lambda - (\lambda + \pi - \beta)\cos\lambda) \quad (2)$$

When $3\pi \le \lambda \le 6\pi$
Outer Curve

$$x = \alpha(\cos\lambda + (\lambda - \pi)\sin\lambda) \quad (3)$$

$$y = \alpha(\sin\lambda - (\lambda - \pi)\cos\lambda) \quad (4)$$

When $5\pi \le \lambda \le 8\pi$
Orbiting Wrap
Inner Curve

$$x = \alpha(\cos\lambda + (\lambda - \beta)\sin\lambda) + \gamma\cos\theta \quad (5)$$
$$y = \alpha(\sin\lambda - (\lambda - \beta)\cos\lambda) + \gamma\sin\theta \quad (6)$$

When $4\pi \le \lambda \le 7\pi$
Outer Curve

$$x = \alpha(\cos\lambda + \lambda\sin\lambda) + \gamma\cos\theta \quad (7)$$
$$y = \alpha(\sin\lambda - \lambda\cos\lambda) + \gamma\sin\theta \quad (8)$$

When $4\pi \le \lambda \le 7\pi$

As some samples of spiral curves, fixed and orbiting wraps as shown in Fig. 2. There is a scroll coefficient value(α) of 3 mm, and a discrepancy of starting roll angle (β) is 0.3π radian [3].

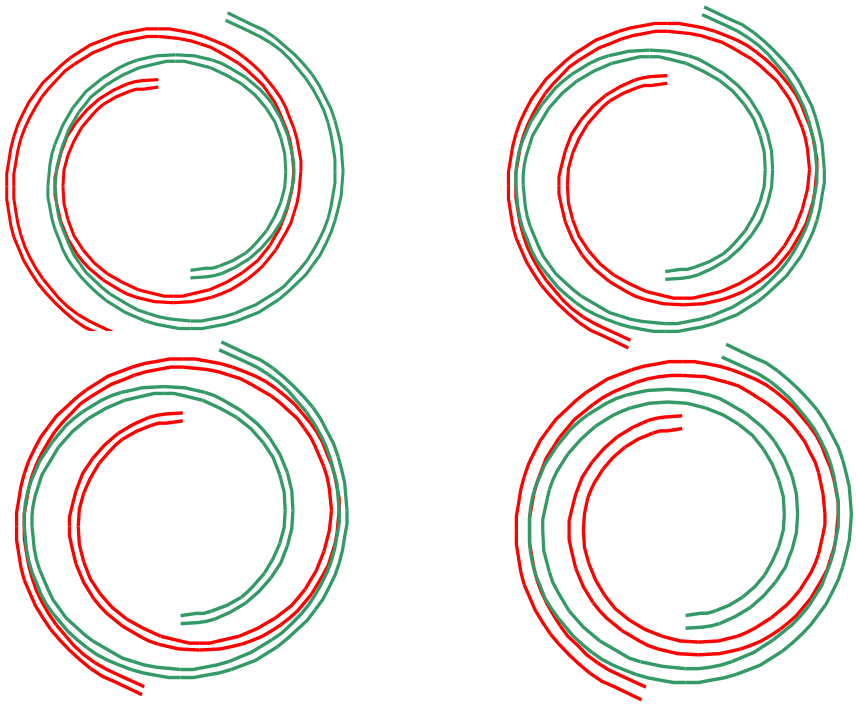

$\theta = 0.3\pi$ radian $\theta = 0.5\pi$ radian

Fig. 2: The spiral curves of the scroll pump α =1.5 mm. β =0.3 π radian

A set of Japanese Industrial Standards (JIS B 8301) [4] is designed for the volumetric and total efficiency of the scroll pump testing which adapt AC motor 3 phases, 380 voltages, and 1 HP for simulate of the low speed wind turbine pump testing. Two sets of the transmission are designed by straight bevel gears which should use with the horizontal shaft of scroll pump.

Fig. 3: Transmission of scroll pump

Fig. 4: Testing equipment for scroll pump

Scroll Pump Test

The test of the scroll pump was performed as the following procedures:**(1)** In this work, the speed of pump was varied at 204, 306, 408, 510, 612 and 714 RPM via the gear transmission units. The first step of study, the water was filled in the container at least 80 liters, where a control valve is fully opened. The speed of pump was adjusted around 204 RPM using the digital tachometer. In the steady flow condition, the pressure, flow rate, and electrical power was measured.

(2) The second step, the speed of pump is adjusted to 306 RPM until steady condition and the pressure, flow rate, and electrical power are collected and added to 408, 510, 612, and 714 RPM at

100%, respectively. The position of the needle valve is reduced to 85.71, 71.43, 57.14, and 42.86%, respectively and the data were collected with the same as 100% of open valve.

(3) Finally, the experiment was repeated by 4 times for enough data to calculate the average values. The relationship of pressure and flow rate curve (H-Q Curves), the relatioship of flow rate and pump speed , and the volumetric flow rate of the pump were presented by graphs.

Results and Discussion.

Based on the testing result and the parameter calculation of Scroll Pump shown in Fig.5, Fig. 6 and Fig.7.

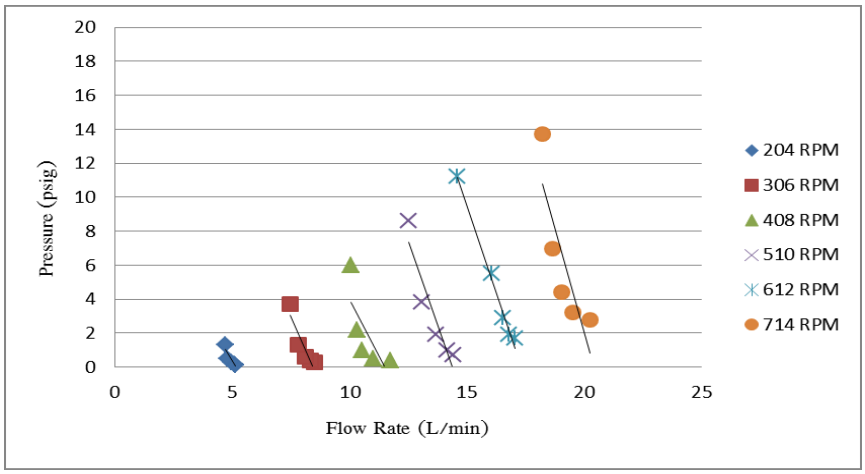

Fig. 5: The relationship of pressure and flow rate (H-Q Curves)

Fig.5 shows the relationship between pressure and flow rate with speed of the pump at 204 -714 RPM and presents the inversely linear equation. The maximum flow rate equals 20.23 Liters/minute detected at 714 RPM of pump speed and 100% of valve opening. The maximum pressure is 13.7 pounds/inches^2 at 714 RPM of pump speed and 42.86% of valve opening.

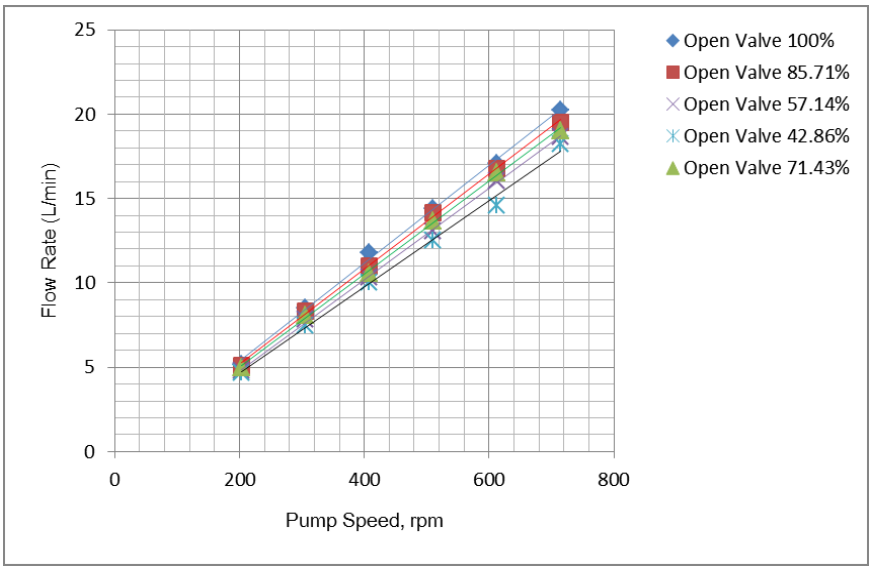

Fig.6: The relationship of flow rate and Pump Speed

Fig.6 shows the correlation of flow rate and motor speed. The data could be designate that the flow rate of scroll pump shows directly variation with motor speed in linear equation at the specific value of valve opening. For example, the increasing of pump speed relates to the increasing of flow rate.

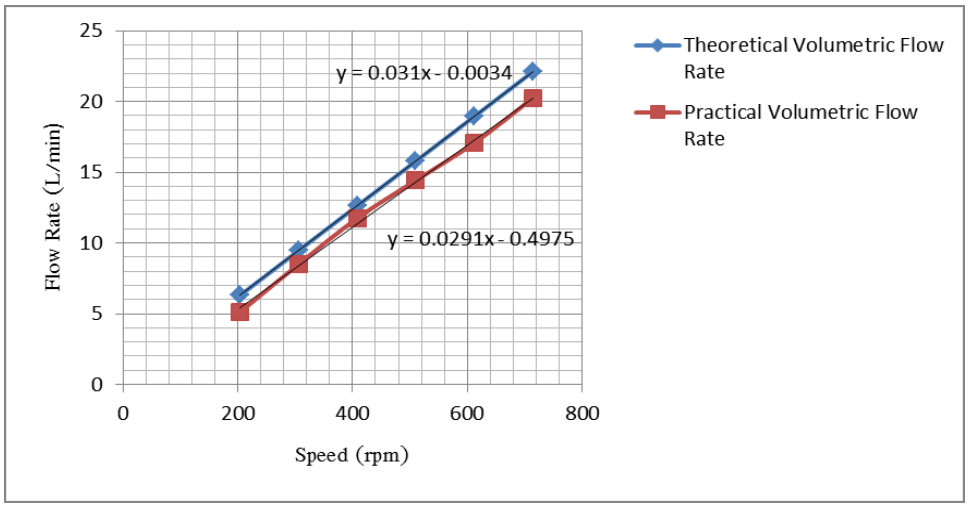

Fig.7: The theoretical volumetric flow rate compared with Practical Volumetric flow rate.

From Fig.7, the volumetric flow rate based on theory is obviously similar to the value from lab-testing with 100% of valve opening. The average of volumetric efficiency from calculation equals 89.55% that means the leakage inside the pump detected to 10.45%.Summary

In this study, the results indicate that the relationship of pressure and flow rate (H-Q Curve) is inversely linear equation with very high slope. The pump speed is directly related to the flow rate as linear equation that generally likes positive displacement pumps. The maximum of flow rate is 20.23 liters/minute, the pump speed is 714 RPM and the valve opening is 100%.

References

[1] Yuttachai Keawsuntia (2004). A Study and Development of Windmill for Water Pumping in Thailand. Master of Engineering Thesis, the Faculty of Engineering, Kasetsart University.

[2] Phichai Kritmaitree (2002). Study of Volumetric Scroll Pump for the Cold Moderator System. Ph.D. Thesis, Utsunomiya University, Japan.

[3] Thana Phuphuekrat (2005). An Analysis of the Wrap of the Scroll Wrap Pump Loss. Master of Engineering Thesis, the Faculty of Engineering, Kasetsart University.

[4] Japan Standard Association (1990). Testing Methods for Centrifugal Pump, Mixed Flow Pump and Axial Flow Pumps. JIS B 8301 Japanese Standards Association: Tokyo, Japan.

Applied Mechanics and Materials Vol. 565 (2014) pp 152-155

doi:10.4028/www.scientific.net/AMM.565.152

The Study of Flaws of High-viscosity Fluids in Interaction with Peripheral Annular Water Flow in Complex Pipelines

Malozemov A.V. [a], Kharlamov S. N. [b]

National Research Tomsk Polytechnic University, Russia

[a]night-00-hunter@rambler.ru, [b]kharsn@mail.ru

Keywords: Modeling, Hydrodynamics, Mixtures

Abstract. In this paper the structure is investigated of three-dimensional flows of rheological complex media (water-oil mixtures) in pipes and channels with long and short sections of constant and variable cross-sections. This is operating units of equipment for the oil and gas industry and power engineering. The steady and unsteady modes flows are modeling of oil-water environments in the internal systems. The ability analyzed of a low-viscosity two-phase structure of the movement to regroup in the peripheral region of the pipe wall with a higher shear stress. We study the pattern of change: coefficient of friction reducing its relatively high viscosity of the nucleus by forming a water ring, local hydrodynamic parameters for complex mixtures flow. The mechanisms are obtained of the influence of flow regimes on the phase boundary. Marked parts modeling of flow profile with immiscible phases within the system full equations of two-phase flow dynamics with allowance for the effects of interfacial interaction. The particular boundary conditions discussed for these flows. The reliability calculation estimated by comparison with the existing data of similar flows (for example, A.Wegmann and P.R. Rohr's results).

Studies of the effects caused by redistribution of energy under merge and/or splitting of premixed and pure viscous flows in branch connections and pipe joints of branched pipeline systems are important for fuel and energy sector. The design of high-reliability connectors needs in thorough analysis of regularities of hydrodynamics and of heat-and-mass transfer either within phases or on the boundaries of fluids interaction. Reduction in expenditure of energy on friction caused by the flow of rheological complex viscous mixture and its interaction with pipe wall leads to control of flow patterns, organization of specific flow conditions (e.g. peripheral input of low viscous flow as a lubricant), which increases product delivery to customers. We need to notice [1,2,3] that during the transportation of heavy hydrocarbon mixtures (e.g. high-viscosity petroleum and oil) in pipeline systems considerable saving of power can be reached due to usage of water, that this mixture contains as a lubricant, in case of divided peripheral feed at the input. In such conditions spatial processes of momentum transfer, heat transfer and mass transfer can be predicted due to involvement usage of multiparametric models and effective numerical methods.

Bibliographic analysis shows [4, 5] that dynamics of the structures of interacting phases in the pipeline is characterized by variety of flow patterns and flow conditions. Water-oil flows are frequently unstable even on the sections of constant cross-section and are complicated by structural transfers because of nonlinear unsteady and convective-diffusion interactions within the phases. It is known that in flows of mixtures the formations of spatial phase patterns are possible. They are characteristic for annular, dispersed, stratified, annular dispersed and intermittent flows.

Annular flow is the subject of interest during the transportation of heavy hydrocarbon mixtures. Therefore, processes and mechanisms of regrouping of low-viscosity structure in two-phase flow to peripherical area of pipe wall with higher shear stress are investigated numerically.

Mathematical modeling of flow profile with immiscible phases are viewed in terms of dynamic system equations of two-phase flow taking into account the effects of interphase interaction [4]. The method is based on fractional function $\boldsymbol{C}$ that determines volume fractions of the phase in final volume. According to this method the motion of phases is described by one and the same hydrodynamic equation while the values of density and viscosity suffer a break at the surface of a section. The system of determining equation for description of hydrodynamics in steady and unsteady motion of two-phase medium is supplemented with boundary conditions (initial and

boundary) for different types of flows and boundary conditions at the surface of phase. The algorithm presupposes ***C*** function evaluation timing each step, with given phase interface at the initial time. Numerical integration of finite-difference equations is carried out on non-uniform meshes using the algorithm SIMPLE [6].

The prediction algorithm conformity of hydrodynamic and diffusion processes in the motion of drop two-phase media in channels were estimated by means of comparison of changes of local and integral parameters with solutions and experimental data made by other authors [5,7]. The experiment shows that this method allows to predict how the changes of physical characteristics of dynamic structure of the mixture entering the pipe in conditions of unstable phase motions influence on flows and mass transfer in wide range of changes of key parameters (Re=50-4000, L/D =700).

Research data of flow local properties.

The data represented on the figures 1-3 describe the results of investigation of dispersed flow and changes of its structure. There are the images of changes of the structure of turbulent flow in dispersed and annular dispersed flows on the figures 1, 2.

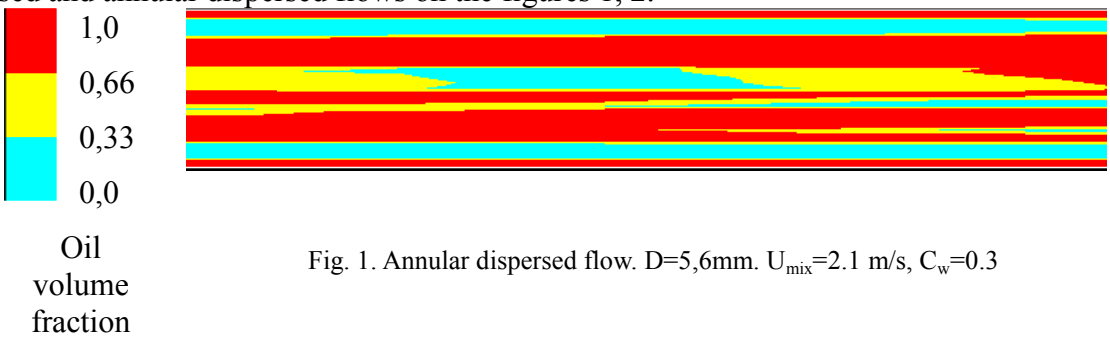

Fig. 1. Annular dispersed flow. D=5,6mm. U_{mix}=2.1 m/s, C_w=0.3

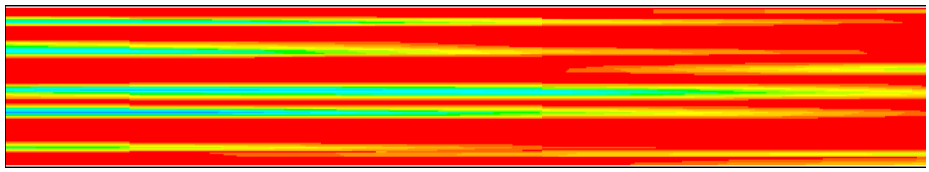

Fig. 2. Dispersed flow. D=5,6mm. U_{mix}=1.94 m/s, C_w=0.1

Results of verification of model and method of analysis are presented on figure 3. Here qualitative and quantitative potential of the method to predict hydrodynamic process and evolution of the flow structure can be regarded. Measurements (fig.3, b) correspond to the data of A.Wegmann, P. R. Rohr[5].

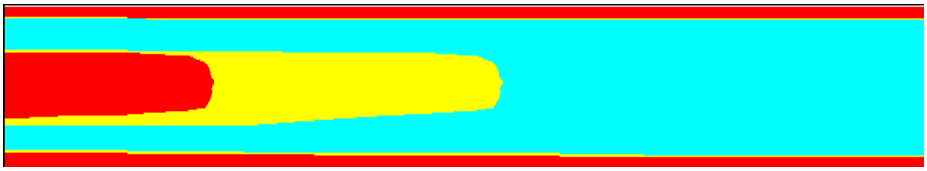

a)

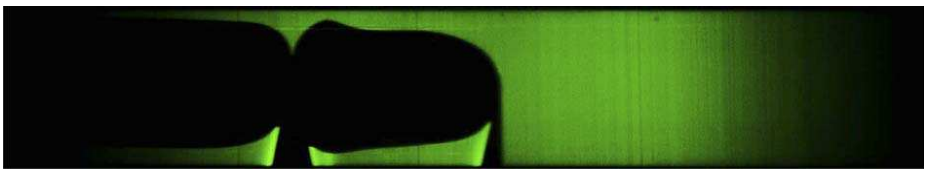

b)

Fig. 3. Piston flow. D=5,6mm. U_{mix}=1.94 m/s, C_w=0.8.

а)-model visualization, б)- experiment.

We can find more information about the influence of velocity field and mass on the flow from the analysis of flow pattern map represented on the figure 4. This information also corresponds to the experimental data [5].

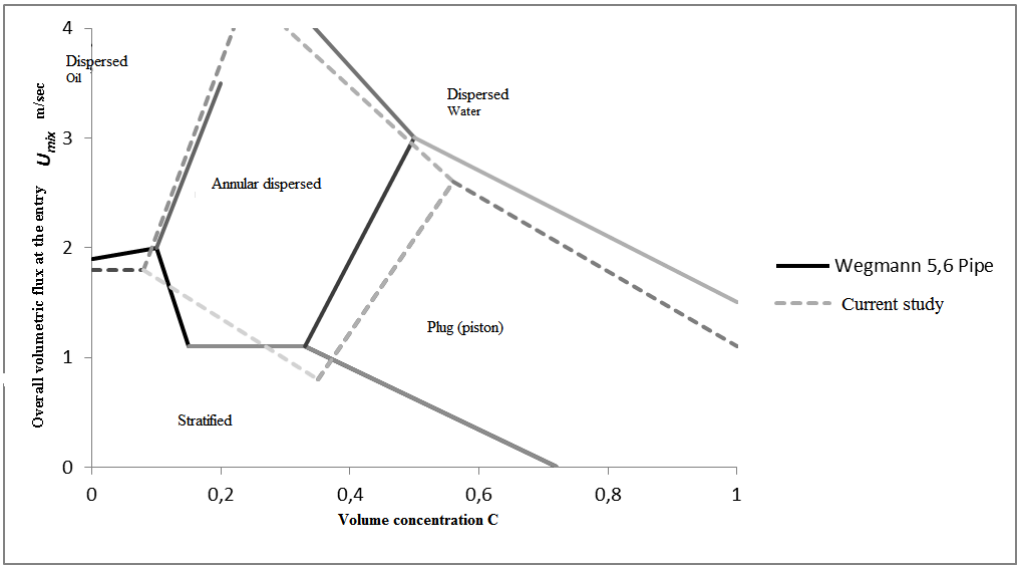

Fig. 4 Flow pattern map

The experiments were made on the plant of Swiss technological university [5]. The principle scheme of the plant is represented in the figure 5.

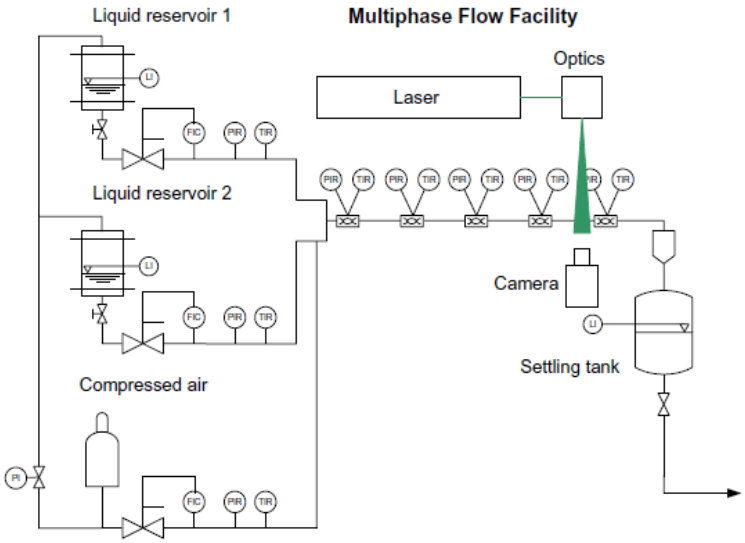

Fig. 5. The scheme of experimental plant.

Integral parameters and their regularities.

This paper was aimed at thorough investigation of basic regularities of changes of integral parameters of the flow and mass exchange in dispersed oil-water systems. On the figure 6 there are represented the data of distribution of wall friction over the pipeline and reduction of wall friction relative to high-viscosity core due to formation of water ring. The local hydrodynamic parameters are represented also for mixture complex flow. The data describe the behavior of friction factor at the condition of steady turbulent flow ($D=5,6mm$. $U_{mix}=2.1$ *m/s*, $C_w=0.3$). It is obvious that in the process of flow motion in the proximal part of the pipeline (x=50 mm) the stable convective and diffusion interactions are formed. They are formed in the processes of momentum transfer and mass transfer which can be predicted by implementation of applied research of friction based on the correlation (ς -x) in the zone x>= 0,05 m.

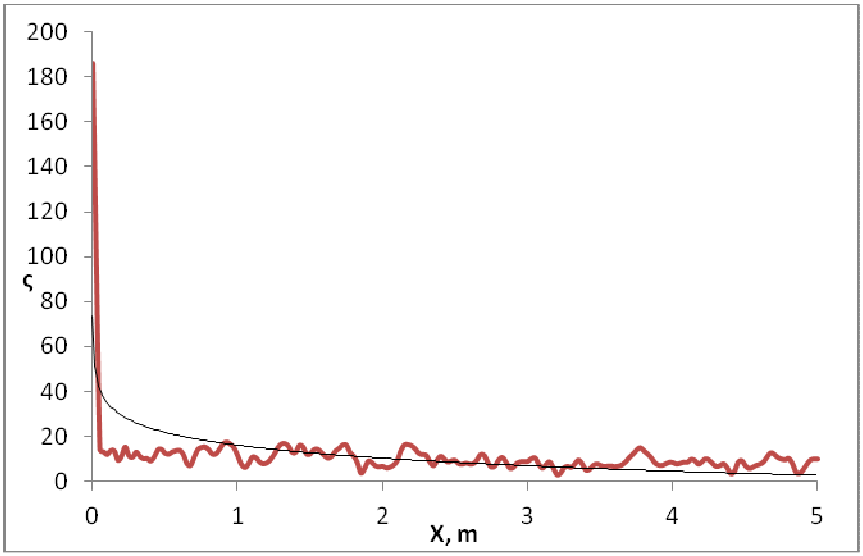

Fig. 6. Distribution of wall friction over the pipeline (D=5,6mm).

U_{mix}=2.1 m/s, C_w=0.3).

Thus, the research helps to predict how the changes of physical characteristics of dynamic structure of the mixture entering the pipe in conditions of unstable phase motions influence on flows and mass exchange. The mechanisms of flow influence on the phase interface are pointed. The generalization of the evaluation of flows of oil-water mixtures are represented as criterion connections for friction factor in wide range of changes of key parameters of phase motions. The reliability of the evaluations was compared with actual data of similar flows made by other authors [5]. The future research is to review flow regimes depending on the structure of the flow at the inlet.

References

[1] Keil OM. 1968. US Patent 3,378,047 (1968)

[2] Neiman et al. 1999. US Patent 5,988,198 (1998)

[3] Ooms G., Poesio P. Stationary core-annular flow through a horizontal pipe: Physics Review. (2003) Ser. E 68, 066301.

[4] R.I. Nigmatulin: Dynamics of Multiphase Media, Part 1, (1987) Nauka

[5] Adrian Wegmann, Philipp Rudolf von Rohr. Two phase liquid–liquid flows in pipes of small diameters: International Journal of Multiphase Flow. Vol. 32, (2006) 1017–1028

[6] S.V. Patankar: Numerical Heat Transfer and Fluid Flow, (1980) CRC Press

[7] Brauner N.C. The prediction of dispersed flows boundaries in liquid–liquid and gas–liquid systems: International Journal of Multiphase Flow. Vol. 27, (2001), p. 886–910.

Applied Mechanics and Materials Vol. 565 (2014) pp 156-163

doi:10.4028/www.scientific.net/AMM.565.156

Numerical Prediction of Erosive Potential of Unsteady Cavitating Flow around Hydrofoil

SEDLÁŘ Milan[1,a], ZIMA Patrik[2,b] and KOMÁREK Martin[1,c]

[1]Centre of Hydraulic Research, s.r.o., J. Sigmunda 79, Lutín, 783 50, Czech Republic

[2]Institute of Thermomechanics ASCR, v.v.i., Dolejškova 5, Praha 8, 182 00, Czech Republic

[a]m.sedlar@sigma.cz, [b]zimap@it.cas.cz, [c]m.komarek@sigma.cz

Keywords: Cavitation Erosion, CFD, Hydraulic Machinery, Bubble Dynamics, NACA 2412

Abstract. The paper attempts to assess the erosive potential of cavitation bubbles in unsteady flow of liquid over a prismatic hydrofoil using two-way coupling of the URANS and the Rayleigh-Plesset equations. The erosive potential of the cavitating flow is evaluated from the energy dissipated during the collapses of imploding cavitation bubbles near the solid surface of the hydrofoil. The bubbles are assumed spherical and the phase slip is neglected. Bubble fission is modelled using a simple break-up model. The interaction between bubbles is considered by superposing the pressure change due to pressure waves generated by collapsing bubbles and propagated in the computational domain over the local pressure in the liquid (external to the bubble). The rate of erosion of the solid material is not studied in this work. The flow is analysed using the in-house three-dimensional solver for unsteady turbulent flow with bubble dynamics. The results are demonstrated on the NACA 2412 hydrofoil with the incidence angle of 8 degrees and the cavitation number 1.37, which corresponds to the regime of oscillating partial cavity with periodic shedding of bubble cloud downstream of the cavity.

Introduction

Erosion of the blade material in hydraulic machines due to cavitation can severely shorten machine useful life, disrupt machine operation and efficiency as a result of altered geometry, and even cause catastrophic structural failures leading to high maintenance costs. The erosive potential of the cavitating flow is carried by violent collapses of vapour structures (bubbles) [1] in the vicinity of the solid surface. It is common and tolerated that, at design conditions (or lower cavitation intensities), these vapour structures are limited to sparsely distributed transient cavitation bubbles travelling with the flow. Such regime is usually steady or near-steady and its analysis does not present substantial numerical difficulties (for example [2]). The erosion under such conditions is caused by the combined effect of the shock waves propagated from the centre of the collapsing bubble and liquid micro-jet formed during non-spherical bubble collapse. At off-design conditions (or higher cavitation intensities), however, other erosive mechanisms can be observed, such as coherent collapses of large vapour structures or bubble clouds. Bubble clouds, which grow and collapse concurrently, are known to be particularly destructive [3].

The mode and strength of the bubble collapse depends on a number of factors, most importantly on the ratio of the maximum bubble size to the distance from the solid surface [4]. After its first collapse, the cavitation bubble either rebounds several times before it dissolves or breaks up into many fragments (this phenomenon is known commonly as bubble fission). In general, the first one or two collapses are usually most violent and therefore have the strongest destructive power.

Modelling the rate of erosion of a given solid material is complex and requires the knowledge of the response of the material, especially its fatigue strength. Recently, an erosion model coupled with the 2-dimensional CFD tool based on the barotropic state law for the liquid flow was examined in [5] for unsteady cavitation with periodic vapour shedding. Enhancement of the single-bubble collapses by the shock wave from the collapsing bubble cloud was identified as the main erosion mechanism. As shown in [6], the impact loads generated by the collapsing bubbles must be measured for the

material in question and different cavitation intensities in order to obtain any reliable prediction on the erosion parameters (such as incubation period or erosion rates). In [7], it has been shown that the erosive potential of the flow can be determined from the pitting tests. This paper does not intend to study the rate of erosion, instead, it aspires to estimate the amount of useful energy submitted to the material surface to cause cavitation erosion.

Because the total erosive potential of the cavitating flow depends on the number and size of the bubbles in the flow, one has to measure the bubble spectrum (nuclei content) in the inlet flow. Besides this, pitting tests must be performed at different time intervals in order to measure the rate of loss of solid material due to erosion. Both these measurements are experimentally expensive and the data are not available at design stage. In our effort, we look for a computationally inexpensive method, which can be used at design stage to quantify the erosive potential of the cavitating flow, without the explicit knowledge of nuclei content and erosion rate. Therefore, in our analysis, we use the bubble spectrum obtained in our previous experiments from the cavitation tunnel in the Centre of Hydraulic Research in Lutín described in [2].

In our model, we must determine the strength of each bubble collapse. For this purpose, bubble dynamics must be taken into account and the bubbles must be tracked along their trajectories. Commercial CFD codes relying on the Euler-Euler approach and the simplified Rayleigh-Plesset equation (one that neglects higher-order terms, and thus cannot predict bubble rebounds) are not suitable for this purpose because such codes are unable to determine the position and collapse energy of the bubbles. In addition, such codes usually do not consider different bubble sizes in the inlet flow, instead, all the bubbles are assumed to have the same initial size.

In contrast, our analysis uses the Euler-Lagrange approach to couple the CFD analysis of the turbulent liquid flow with the analysis of the spherical bubble dynamics using the full Rayleigh-Plesset equation along carefully selected trajectories. The fundamentals of the steady-state model are described in [2]. This paper extends the model to include the effect of flow unsteadiness and bubble-bubble interactions via the effect of bubble collapses on the external bubble pressure. As a result, the steady-state streamlines are replaced by bubble trajectories. The effect of unsteady bubble structures such as bubble clouds is taken into account by superposing the pressure change due to pressure waves generated by collapsing bubbles at different positions in the flow and propagated in the computational domain over the local pressure in the liquid (external to the bubble).

Model of 3D Turbulent Liquid Flow with Bubble Dynamics

The 3D turbulent flow is modelled using the in-house FEM-based solver of unsteady Reynolds-averaged Navier-Stokes equations (URANS) for incompressible flow. Turbulence is modelled using the SAS-SST turbulence model, which has been developed primarily for highly unsteady phenomena. Liquid compressibility is expressed using the generalised form of the penalty formulation to take into account the change of density in the bubbly regions [8]. The dynamics of the cavitation bubbles is described by the Rayleigh-Plesset equation in the following form [9]:

$$R\frac{D^2R}{Dt^2}+\frac{3}{2}\left(\frac{DR}{Dt}\right)^2+\frac{4\nu_e}{R}\frac{DR}{Dt}+\frac{2\sigma}{\rho_l R}\left[1-\left(\frac{R_0}{R}\right)^{3\kappa-1}\right]=$$
$$=\frac{p_v-p_0}{\rho_l}\left[1-\left(\frac{R_0}{R}\right)^{3\kappa}\right]+\frac{p_0-p}{\rho_l}+\frac{R}{\rho_l c_l}\frac{D}{Dt}\left(p_g-p\right), \qquad (1)$$

Where p_0 is the liquid ambient pressure at undisturbed initial condition, p_v is the equilibrium vapour pressure, p_g is the pressure of gas mixture inside the bubble, ρ_l is the liquid density, c_l is the sound velocity of the liquid, σ is the surface tension of the liquid and κ is the polytropic index of the gas mixture inside the bubble. ν_e is called "effective" viscosity. It is usually set as a multiple of the

kinematic viscosity of the liquid to take into account the increased damping due to liquid compressibility and thermal effects. The last term in Eq. 1 expresses the liquid compressibility. For an ideal mixture of non-condensable gases in the bubble interior we can write

$$p_g R^{3\kappa} = p_{g0} R_0^{3\kappa}, p_{g0} = p_0 - p_v + 2\sigma/R_0 , \quad (2)$$

Where p_{g0} is the initial pressure of the gas mixture (for $R = R_0$). We assume that the gas mixture behaves isothermally ($\kappa = 1$).

The coupling of Eq. 1 with the URANS equations is achieved iteratively, using the Euler-Lagrange approach (two-way coupling) described in [8]. First, the bubble trajectories are obtained from the URANS solver. The bubble spectrum is assigned to each trajectory of the computational domain equitably to satisfy the assumption of uniform nuclei population in the inlet cross-section. Eq. 1 is then integrated along all trajectories for each bubble size of the initial nuclei spectrum using the Runge-Kutta fourth-order scheme with adaptive step-size algorithm. Volume fraction is calculated to obtain the density field in the liquid flow. The density field is then used to reiterate the continuity and momentum equations for the flow. Once the iteration process is completed, the trajectories to be examined for bubble collapses are identified. Finally, the points of all bubble collapses on these trajectories are identified and the collapse aggressiveness is evaluated.

Model of Erosive Potential of Bubble Collapse

The main contribution to cavitation erosion arises from the mechanical effects of the violent collapses of bubbles near the solid surface. The mechanical effects can be determined experimentally by measuring the impact forces. In the present model, these effects are modelled by estimating the amount of energy available during the collapse to cause damage to the surface of the solid material. Let us denote the energy dissipated during the *i*-th collapse as ΔE_i. Let us also denote the work done by the pressure inside the bubble p_b against the ambient liquid pressure p to expand the bubble from the minimum radius $R_{min,i}$ to the maximum radius $R_{max,i}$ as $W_{growth.}$ We can estimate ΔE_i by subtracting W_{growth} for the *(i+1)*-th bubble expansion from W_{growth} for the *i*-th bubble expansion. The following holds if the effects of liquid viscosity, compressibility and surface tension are neglected:

$$\Delta E_i = W_{growth}\Big|_{R\min,i}^{R\max,i} - W_{growth}\Big|_{R\min,i+1}^{R\max,i+1}, \text{ where } W_{growth}\Big|_{R\,\min}^{R\,\max} = \int_{R_{min}}^{R_{max}} 4\pi R^2 (p - p_b) dR . \quad (3)$$

We further assume that only a part of the energy ΔE_i presents the erosive potential of the collapse and the remaining part represents thermal effects (evaporation/condensation and heating up the non-condensable gas inside the bubble), viscous effects (turbulent mixing), bubble fragmentation (creation of new surfaces during bubble break-up), and acoustics. The erosive part of ΔE_i is denoted as E_{EP} and can be expressed as $E_{EP} = C\Delta E_i$, where C is a geometric parameter, which depends mainly on the distance of the bubble centre from the solid surface. For bubbles very far from the solid surface C tends to zero. For bubbles very close to the solid surface C must be lower than 0.5 [8]. The value of C is a subject of ongoing research. In this analysis, $C = 0.25$ if the distance of the bubble centre from the solid surface is lower than the maximum radius of the bubble. When the distance is higher, the value of C decreases with the second power of the distance.

The values of E_{EP} must be calculated for each bubble size in the bubble spectrum and for each collapse along the selected trajectories. The effect of bubble breakup is taken into account using the model described in [10], where the linear Rayleigh-Taylor analysis for the stability of the spherical bubble surface is applied with some modifications.

The results of the model of erosive potential have been verified for the regime of steady-state travelling bubble cavitation on a prismatic NACA 0020 hydrofoil (incidence angle of 1° and cavitation number $\sigma = 1.93$) in [11]. The numerical results were compared with the results of experimental pitting tests in the cavitation tunnel of the Centre of Hydraulic Research in Lutín and the results of the numerical prediction were in good agreement with the experimental evidence.

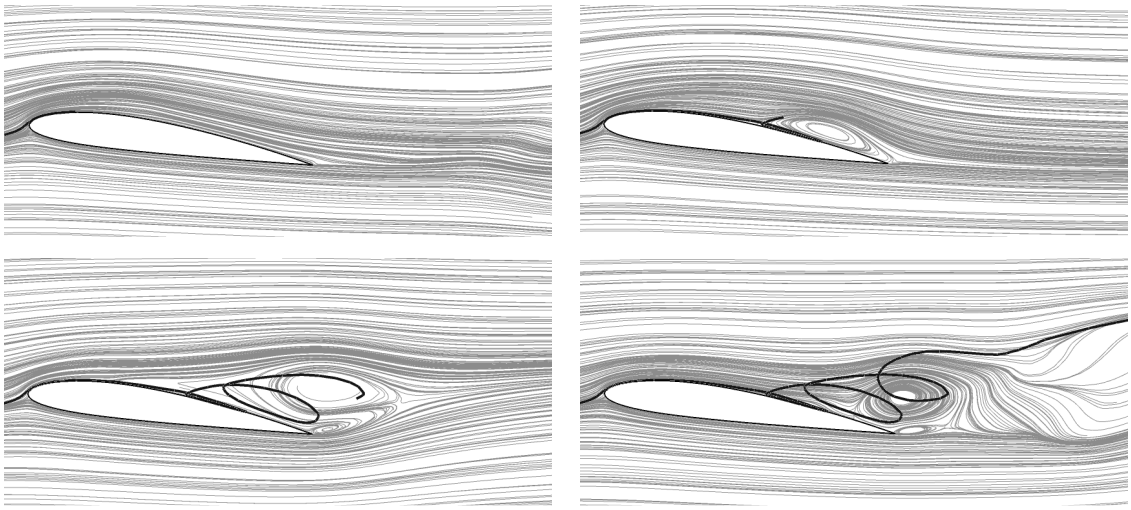

Fig. 1. Development of the trajectory (dark curve) at midspan of NACA 2412 hydrofoil compared to streamlines at different time instants with time interval between images 18 ms.

Determination of Bubble Trajectories

For steady-state cavitating flow, Eq. 1 is solved along the streamlines. To obtain the correct flow field (including the pressure and the streamlines), several iterations of the two-way coupling of macroscopic and microscopic analyses are required. For unsteady flow, however, Eq. 1 must be solved along bubble trajectories, which develop with time (Fig. 1). The trajectories are updated at each global time step of the macroscopic (URANS) analysis. Typically, one or two internal iterations are required to obtain the correct flow field.

Model of Bubble-Bubble Interaction via Shockwave Pressure Induced by Bubble Collapses

In order to model the effect of shock waves induced by the collapsing bubbles on the pressure field in the cavitating flow, we apply the estimation of the pressure pulse from a spherical bubble collapse derived in [12,13]. The estimation can be implemented along the bubble trajectories without increasing the numerical difficulties considerably.

In [12,13], it is assumed that the pressure field in the vicinity of the collapsing bubble can be approximated as the potential flow induced by the spherical motion of the bubble wall. The pressure p_r at the radial position r from the bubble centre during the collapse can be expressed as follows:

$$p_r = \rho_l \left(\frac{f'}{r} + \frac{1}{2} \left(\frac{f^2}{r^4} + \frac{2}{c_l} \frac{ff'}{r^3} + \frac{1}{c_l^2} \frac{Df'^2}{r^2} \right) \right), \tag{4}$$

where the function f is defined by

$$f\left(t - \frac{r-R}{c_l} \right) = -R^2 \frac{DR}{Dt} + \frac{1}{c_l} \left(R^3 \frac{D^2R}{Dt^2} + 2R^2 \left(\frac{DR}{Dt} \right)^2 \right). \tag{5}$$

The prime denotes the derivative with respect to $t - (r - R)/c_l$ and has to be evaluated numerically. The influence of all pressure pulses with large magnitudes and very short times of duration has to be counted up along all flow trajectories at each global time step during the internal iterations of the macroscopic flow analysis.

Cavitating Flow around NACA 2412 Hydrofoil: Experimental Evidence and CFD Analysis

The model described in the previous chapters has been tested for the case of cavitating flow over a NACA 2412 hydrofoil. The NACA 2412 hydrofoil has been chosen as the test case for the experimental research in the water cavitation tunnel in the Centre of Hydraulic Research in Lutín described in [11]. The tunnel has a rectangular test section with the cross section 150 × 150 mm. All the walls of the test section are transparent. The hydrofoil chord length is 120 mm, the incidence angle is 8°, the velocity of the undisturbed flow is 13 m/s and the cavitation number in the test was $\sigma = 1.37$. In this flow regime, periodic shedding of a cloud cavity at the hydrofoil trailing edge is observed. The different stages of the periodic shedding are shown in the upper part of Fig. 2. The first photograph shows the sheet cavity covering the suction side with the cavity closure reaching about one half of the chord length. In the second photograph, the sheet cavity closure becomes unstable, its main part retracts and a smaller cloud cavity is formed. In the last photograph, the cloud cavity is detached from the hydrofoil and is "washed away" towards the hydrofoil trailing edge. The cloud cavity detaches from the sheet cavity with the frequency 15 Hz. The pressure pulses measured at 40% chord length have two dominant frequencies of 15 Hz and 30 Hz, corresponding to the Strouhal number $St = 0.138$ and 0.276 ($St = f L / v$, where f is frequency, L is the hydrofoil chord length, and v is the velocity of the undisturbed flow). This is in good agreement with the results found in [14] for the Clark Y hydrofoil. The lower part of Fig. 2 shows the results of the same regime using the present CFD model. Here the cavitation regions are visualized as the locations where the void fraction (the ratio of the local volumes of vapour and liquid) exceeds 10%.

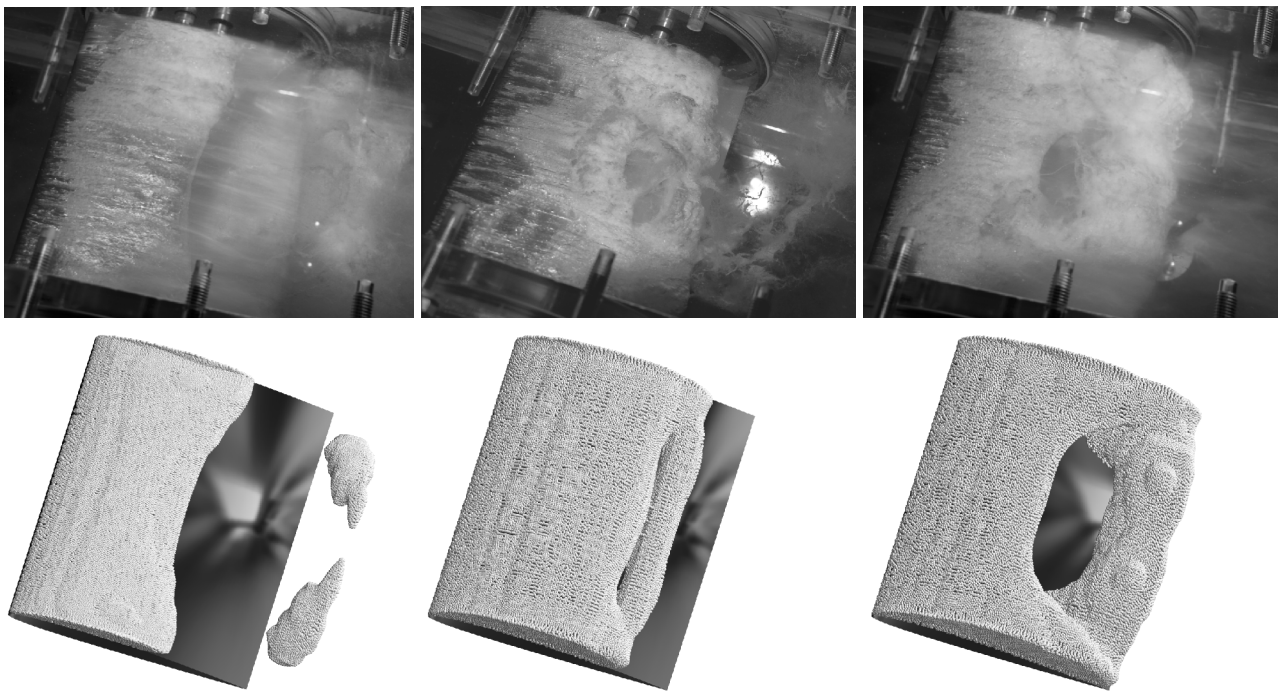

Fig. 2. Cavitation regions on NACA 2412 hydrofoil. Comparison of experimental data (top) and CFD analysis (bottom). Cavitation number σ = 1.37, Strouhal number St = 0.138/0.276.

The flow medium is water at normal temperature. The effective viscosity was set to $\nu_e = 10\nu_l$ (ν_l is the kinematic viscosity of the water at normal temperature). The initial bubble spectrum in the inlet flow used in the numerical analysis was measured in water during previous experiments in the same cavitation tunnel using the acoustic bubble spectrometer (ABS) and can be found in [2]. The bubble spectrum consists of ten bubble sizes between 5 and 105 micrometres and the total number of nuclei in a cubic metre is of the order of 10^7. We consider a uniform distribution of nuclei with a constant distance between them. For the given number of nuclei per volume, the average distance between bubbles is between 1 and 3 millimetres. The quantity r in Eq. 4 can be perceived as a parameter

representing the number density of the bubbles. When the values of r are in the order of millimetres, the first term on the right hand side of Eq. 4 plays the dominant role.

The results of the numerical analysis are shown in Figs. 3-6. The left part of Fig. 3 shows the streamlines at the hydrofoil midspan. The dark curve denotes the trajectory of the bubbles as it develops in time. The right part of Fig. 3 shows the regions where the void fraction exceeds 10%. Three dark circles denote three coherent collapses of cavitation bubbles identified along the trajectory, resulting in three high-pressure pulses (see Figs. 4 and 5 for one bubble size). The magnitude (~10 bars) of the pulses and their duration (~10^{-4} s) agree well with the experimental results obtained in [3]. The results shown in Figs. 4 and 5 were obtained for the average distance between bubbles of 1 mm.

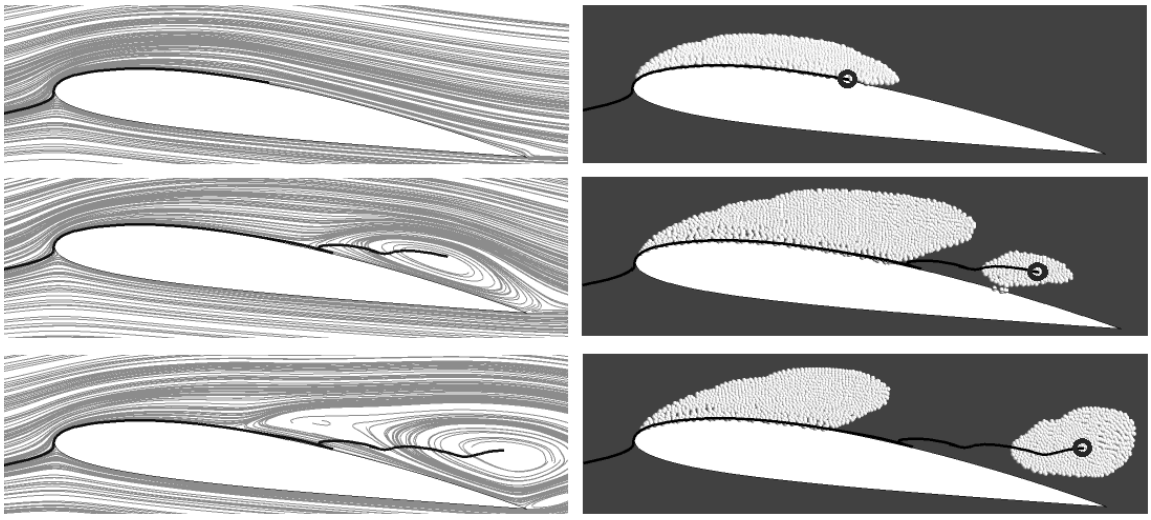

Fig. 3. Development of the trajectory (dark curve, left) at midspan of NACA 2412 hydrofoil passing through separated bubble cloud and positions of coherent bubble collapses (dark rings, right). $\sigma = 1.37$.

Fig. 4 shows the dynamics of the bubble with the initial radius 45 μm for the trajectory from Fig. 3. The figure compares the results obtained with and without considering the interaction between bubbles calculated from Eq. 4. The light curve in Fig. 4 shows the development of the bubble radius along its trajectory from the leading edge towards the trailing edge of the hydrofoil when no bubble-bubble interaction is considered (Eq. 4 is not applied and the bubble does not "feel" the nearby bubbles). The bubble expands slowly to its maximum radius as the liquid pressure decreases downstream of the leading edge. It then reaches the region of higher pressure and collapses violently. The bubble rebounds several times immediately after the first collapse before it reaches the points of further expansions and collapses shown in Fig. 3. The dark curve shows the same bubble, however, with the bubble-bubble interaction considered. Fig. 4 reveals that when the shock wave pressures due to collapse calculated from Eq. 4 are superposed to the liquid pressure, the bubble is forced to collapse earlier.

Fig. 5 shows the magnitudes of the pressure pulses generated by bubble collapses and calculated from Eq. 4 for the trajectory from Fig. 3. The dark curve depicts the pressure calculated for the collapses of the bubbles travelling along the trajectory. The light curve depicts the pressure increase from the bubble collapses on the neighbouring trajectories. The dark and light curves are superposed with the liquid pressure to obtain the pressure p in Eq. 1. The dashed line separates the energetically significant collapses (above the line) and the insignificant collapses (below the line). Figure 5 illustrates how the given bubble "feels" the bubbles on its trajectory and the bubbles on the nearby trajectories.

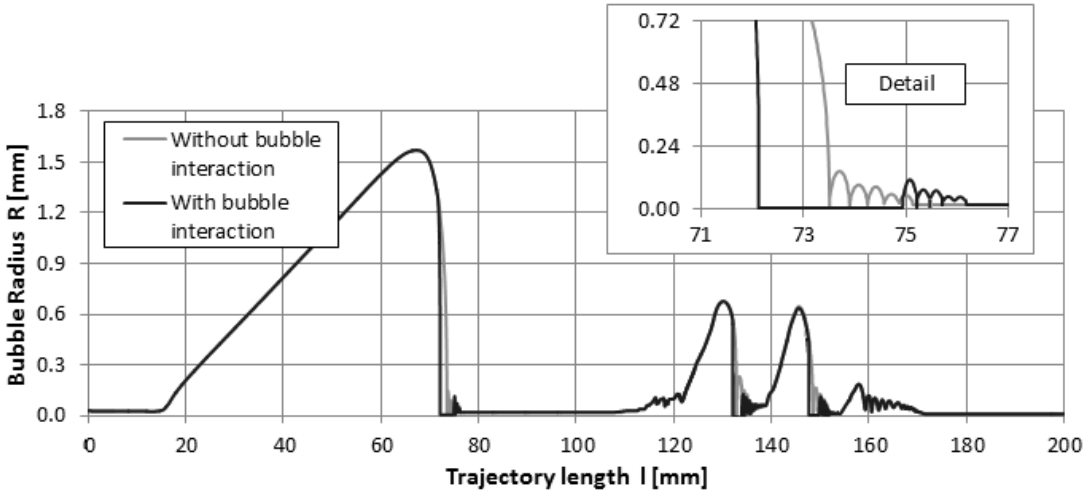

Fig. 4. Dynamics of bubble with initial radius 45 μm. Trajectory from Fig. 3. With bubble breakup.

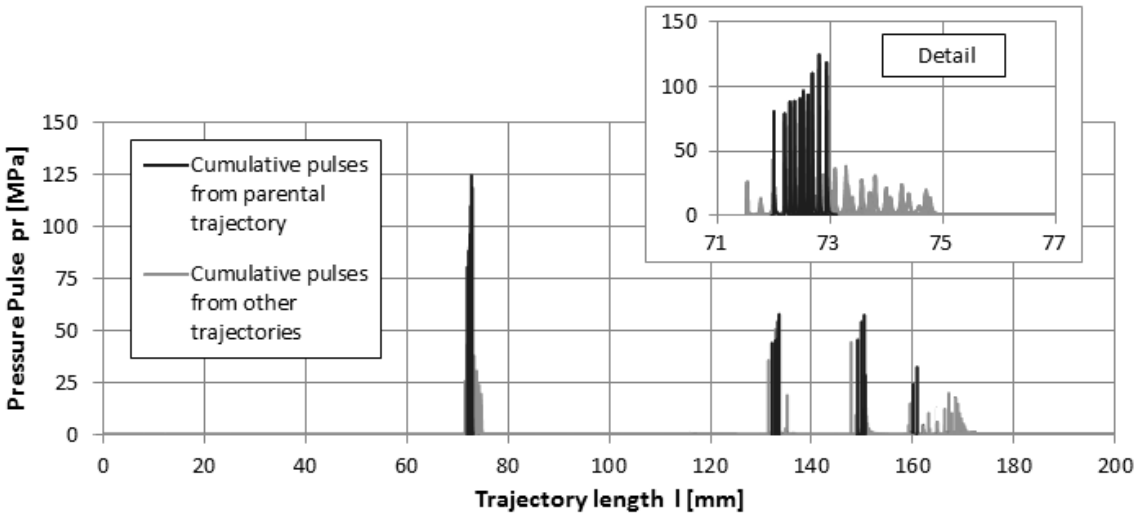

Fig. 5. Pressure pulses generated by bubble collapses. Trajectory from Fig. 3. With bubble breakup.

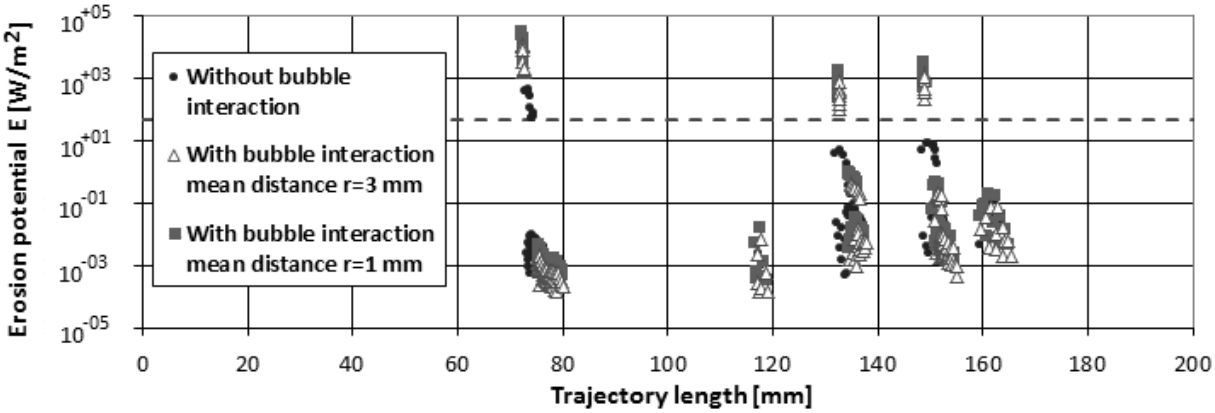

Fig. 6. Position and cumulative erosive potential of bubble collapses for ten different initial bubble sizes. Numerical analysis corresponding to Figs. 3 and 4.

Fig. 6 compares the cumulative erosive potential E_{EP} for three numerical setups: i) dark circles: no bubble-bubble interaction; ii) triangles: weak bubble-bubble interaction (mean distance between bubbles $r = 3$ mm); iii) squares: strong bubble-bubble interaction (mean distance between bubbles $r = 1$ mm). Each point in the figure represents the sum for collapses of all the bubbles of the same size

assigned to the trajectory. The leftmost set of points (trajectory coordinate ~72 mm) represents the first coherent bubble collapses (compare to Figs. 4 and 5). The value of E_{EP} associated with the first collapses is in the range 5×10^2–5×10^4 W/m^2. These collapses are most energetic and dangerous as they occur on the hydrofoil surface (see top right picture in Fig. 3). The subsequent small collapses (trajectory coordinate ~75 mm) are several orders of magnitude weaker that the first ones. Further downstream, the two groups of coherent collapses at trajectory coordinate 133 and 149 mm are also rather strong ($E_{EP} \approx 1$–4×10^3 W/m^2) and the risk of erosion associated with them should be considered.

Summary

The numerical model presented in this paper enables to predict the erosive potential of three-dimensional unsteady turbulent cavitating flow using computationally efficient method. The model is able to determine the fully non-linear dynamics of cavitation bubbles. The dynamics of the bubble collapses includes the effect of bubble breakup and, to a certain extent, the interaction between bubbles via the pressure pulses generated by the collapsing and rebounding bubbles. It makes possible to assess the behaviour of large vapour structures and the locations of coherent collapses of cavitation bubbles. These collapses are associated with increased bubble-bubble interaction, which has been shown to enhance the erosive potential of the collapse. The effect of bubble-bubble interaction decreases with increasing mean distance between the bubbles (i.e. decreasing bubble density). The results for the cavitating flow around the NACA 2412 hydrofoil for the regime of partial cavitation with periodic shedding of cloud cavity agree well with the experimental visualization in the water cavitation tunnel and the results found in the literature.

Currently, extensive experimental study is being carried out to visualize the cavitating flow and measure the pressure impacts on the hydrofoil using the grid of PVDF films with the aim to validate and further develop the presented model of erosive potential for the purpose of hydromachinery design.

Acknowledgements

This work has been supported by Grant no. 101/13/23550S of the Czech Science Foundation.

References

[1] J.P. Franc and J.M. Michel: *Fundamentals of Cavitation* (Kluwer Academic Publishers 2004)

[2] P. Zima and M. Sedlar: Proc. CAV2012, Paper 209, Singapore (2012)

[3] G.E. Reisman and C.E. Brennen: 21st Int. Symp. Shock Waves, Issw21, Paper 1570 (1997)

[4] J. Hujer: Master Thesis, Technical University of Liberec (2013)

[5] M. Dular and O. Coutier-Delgosha: Intl. J. for Num. Meth. Fluids, Wiley InterScience (2009)

[6] S. Hattori, T. Hirose and K. Sugiyama: Journal of Physics: Conf. Series, Vol. 147 (2009)

[7] N. Berchiche, J.P. Franc and J.M. Michel: J. Fluids Engineering, 124 (2002), p. 601

[8] P. Zima, M. Sedlar and F. Marsik, in: Water, Steam and Aqueous Solutions for Electric Power. Advances in Science and Technology, Kyoto, Maruzen Co., Ltd. (2005), p. 232

[9] S. Hilgenfeldt et al: J. Fluid Mech., Vol. 365 (1998), p. 171

[10] C.F. Delale, S. Pasinlioglu and P. Zima: Proc. CAV2012, Paper 192, Singapore (2012)

[11] M. Sedlar et al.: EPJ Web of Conferences 25, 01084 (2012)

[12] N. Ochiai, Y. Iga, M. Nohmi and T. Ikohagi: J. Fluid Sci. and Tech., Vol 5 (2010), p. 416

[13] N. Ochiai, Y. Iga, M. Nohmi and T. Ikohagi: J. Fluids Engng., Vol 135 (2013), p. 011302-1

[14] S. Watanabe et al.: WIMRC 3rd Int. Cav. Forum 2011 (2011)

Applied Mechanics and Materials Vol. 565 (2014) pp 164-169

doi:10.4028/www.scientific.net/AMM.565.164

Study on the Stiffness of Positioning Platform with Large Trip and High Precision under Thermal to Structure Coupling

Weiwei Yang[a], Jizhu Liu[b], Mingqiang Pan, Tao Chen, Liguo Chen, Linsen Chen, Lining Sun

School of Mechanical and Electric Engineering& Collaborative Innovation Center of Suzhou Nano Science and Technology, Soochow University, Suzhou 215006, China

[a]wisty@163.com, [b]liu_jizhu@163.com

Keywords: Coupling stiffness, High precision positioning platform, Finite element, Grey system

Abstract. Thermal influences the stiffness, and then affects dynamic characteristics of the platform. The paper appoints a method to calculate the global stiffness of the positioning platform with large trip and high precision, and find the rule that the platform stiffness changing with the temperature to follow. The rule provides a fundamental basis for establishing vibration model of the platform. The main method to collect analysis data is finite element. Firstly, choose a number of points from the surfaces of the platform. Through the experiment data of thermal stress coupling analysis on the platform and a degree of grey incidence, the degree of correlation between all concerned points and thermal displacement can be solved. The key points are confirmed the one which have large degree of grey incidence which also have large influence on the stiffness, and will be the input value of stiffness model of the platform. Calculate the global stiffness value of positioning platform under different temperature using the finite element method analysis. Establish the stiffness model using BP neural network.

Introduction

High precision positioning platform is widely used in the fields of semiconductor manufacturing, MEMS, biochips, biomedical, etc. Stiffness is the ability to resist deformation of platform. During, high speed operation makes the platform vibrated which affects the accuracy of the platform. Vibration model of platform is introduced in order to effectively eliminate and compensate the vibration of platform. Stiffness affected the frequency and amplitude of vibration. When establishing the vibration model, researchers often consider the stiffness of the platform as a fixed value and ignore the effects of heat. Such establishment of the vibration model of platform is not accurate. In fact, when running at high speed, the linear motor of the platform will produce a lot of heat which would change the stiffness of the platform. To reduce the frequency and amplitude of the vibration more accurately, it's necessary to establish the model of stiffness changing with temperature.

Although, theoretically, all positioning and connection components will affect the overall stiffness of the platform, while key points on the platform which have greater impact on the platform stiffness exist. Therefore, this paper is mainly concerned with the overall stiffness of the platform which is changed with the change of these key points' temperature.

Positioning platform thermal—structure stiffness analysis

High precision positioning platform structure and stiffness.

Positioning platform's stiffness is ability to resist deformation. Static stiffness is characterized the characteristics of machine tools, which show platform's ability to resist deformation under static load. The ability to resist cyclic loading is platform's dynamic stiffness. If the disturbing force changes slowly, the frequency of the disturbing force is far less than the natural frequency of structures, dynamic stiffness and static stiffness are basically the same. An organization's static stiffness calculation formula:

$$K = \frac{P}{\delta}(\mathrm{N/m}) \tag{1}$$

Where P is applied to constant force of the organization, δ is the deformation generated by the force.

When calculate stiffness, the total stiffness of parallel and serial parts could be denoted as [1]:

$$K = 1/\sum_{i=1}^{n}\frac{1}{K_i}\ ; \quad K = \sum_{i=1}^{n} K_i \tag{2}$$

In positioning platform motion system, the drive part is permanent magnet linear synchronous motor, while the carriage of guide rail acts as transmission parts that equal to a series of spring. Platform structure stiffness can be represented as shown in figure 1. By the formula (2), the overall stiffness of positioning platform can be expressed as

$$\mathrm{K}=1/(1/(K1+K2+K3+K4)+1/(K5+K6+K7+K8)) \tag{3}$$

After the platform reaching heat balance, thermal deformation of components of platform would deliver to the workbench and lead to displacement error of platform as a whole. The effect of deformation in different parts of the overall error is different. In these hot deformations, the more impact on the overall error, the more impact to the integral stiffness of positioning platform. In this paper, stiffness would be ranked as the key research point for stiffness model.

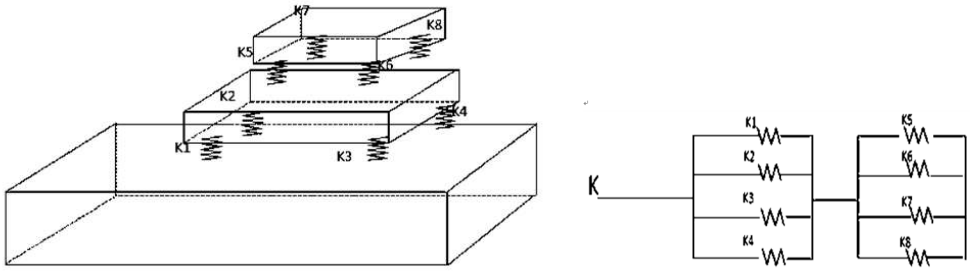

Fig. 1 Stiffness characteristics of platform

Positioning platform thermal – stiffness finite element analysis.

Simulation software used in finite element analysis is ANSYS. Appropriate simplification and equivalent principle is adopted to establish the model of the platform. The equivalent principle makes sure the difference between stiffness of simulation model and real model is small. The object of example is a positioning platform driven by a permanent magnet linear synchronous motor (PMLSM) with the character of two dimension X/Y, large trip and high precision. The size of the platform is 1500x1500mm. The simulation model is shown as Fig. 2. The material of the foundation bed is marble. The other materials are 45 steel. Steel elastic modulus changing with temperature value is shown as Table 1.

For expressing clearly, the coordinate system mentioned below is referred to the coordinate system shown as Fig. 2-the coordinate system of model. There will be no special instructions below.

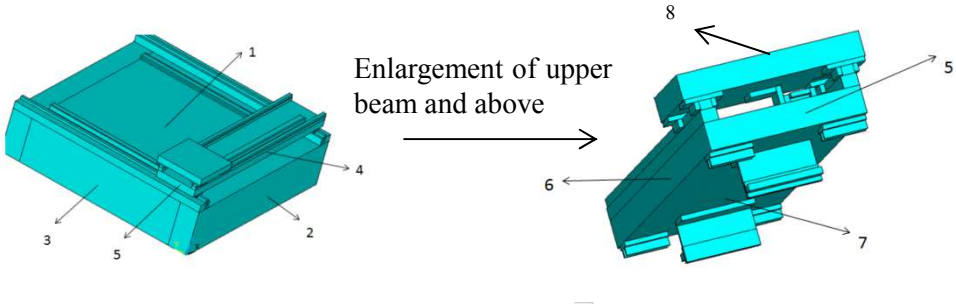

1. Foundation bed's upper surface; 2 foundation bed's front surface; 3. Foundation bed's left surface; 4. Upper beam's front surface; 5. Upper beam's left surface; 6. Upper beam' back surface; 7. of upper beam's bottom surface; 8.work platform

Fig. 2. Surfaces of temperature points

Table 1. Elastic modulus of 45 steel

Temperature[^{0}C]	20	100	200	300	400	500
Elastic modulus [Gpa]	209	207	202	196	186	174

The initial temperature is 20^{o}C. Loading conditions of the platform are the heat produced by working motor and air convention from the outside. Other heat sources, such as light radiation and friction between guide rails, are ignored. When the motor works at different speed and for different time, the heat it produced is also different. The internal thermal distribution of the motor is complicated. Hence the loading heat is supposed to be uniform distribution. loaded temperature $k=1,2,...,6$ means 25^{o}C, 27^{o}C ,29^{o}C , 31^{o}C, 33^{o}C, 35^{o}C , respectively, and different coordinate of the work plane of the platform $i=1,2,...,5$ means work plane different locations (0,0), (0,0.130), (0,0.260), (0,0.390),(0,0.520). Fig. 3 is cloud pictures of temperature distribution when k=2 and i=5. Fig. 4 is cloud pictures of displacement distribution when k=2 and i=5.

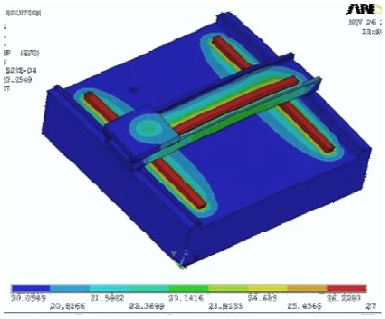

Fig. 3 Temperature distribution

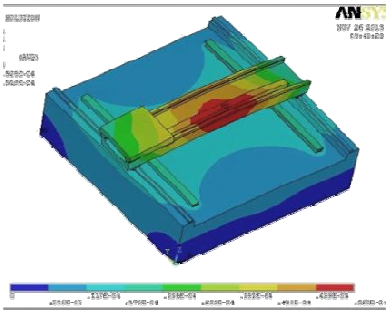

Fig. 4 Displacement distribution

Stiffness of key research based on the grey system theory.

Choosing certain interest points as the object of study in the surface of the positioning platform, the surface number as shown in figure 2, concerned about the point number determination to follow after the first left right, previously after rules. Selection is shown in table 2

Table 2. Each surface care point positioning platform

Number of the platform surfaces	Number of concerned points	The total number
1	53	1-53
2	124	54-177
3	17	178-194
4	31	195-225
5	31	226-256
6	31	257-287
7	155	288-442
8	96	443-538

Grey system analysis is in accordance with the characteristics of the system parameter series similarity between similar degree in mathematical theory of system analysis[2]. To solve the grey correlation degree is divided into the following five steps[3]:

Calculate the initial image of the sequence

Calculate the difference sequence,

Calculate the range

Calculation of correlation coefficient

Degree of grey relation of the sequence 1 ~ 538 and the compared sequence

According to the method of calculating the degree of grey relation, on the platform of the workbench coordinates are in the position i, Read out the workbench displacement variation $x_0(n)$ of the different load condition, $n=1,2,...6$， the 538 concerned points temperature value of the platform $x_m(\mathrm{n})$， $m=1,2,...,538$， $n=1,2,...6$,the displacement change values $x_0(n)$ as grey reference sequence of analysis, $x_m(\mathrm{n})$ as the comparative sequence of grey relation analysis, to solve the grey correlation degree.

Eventually point for the 538, correlation between larger six points in the total number of 4, 211, 305, 324, 305, 478, remember to key points 1 ~ 6, located in positioning platform in the presence of face 1, face 4, face 7, face 7,face 7, face 8. The thermal deformation caused by temperature rise of the six key points on the platform had a greater influence on the overall displacement change, therefore, the key points of the 6 stiffness affects the overall platform for larger stiffness , as the key point of solving stiffness model.

Stiffness model of positioning platform with large trip and high precision.

By the method of grey correlation analysis, the key points which are used to establish the stiffness model are confirmed successful. According to the definition of stiffness, apply a pressure P along the Z axis downward In the work platform surface to make sure P*A=1Newton (P-pressure, A-the superficial area of the work platform). In the finite element model, A=0.35m*0.35m, so P=8.1633N/m2. Then the Z axis displacement value of the platform is got, represented as δ_2. Thus, the stiffness value of the platform is represented as $K=\dfrac{1}{\delta_2-\delta_1}$, where δ_1 is the displacement of the platform under thermal loads. Different stiffness values are calculated in different conditions including different loaded temperature k and different coordinate of the work plane of the platform i. Shown as Table 3.

Table 3. Stiffness in different conditions [N/m]

i/k	1	2	3
1	58.824	62.500	25.000
2	40.000	28.571	17.857
3	31.250	22.222	14.085
4	26.316	18.519	12.048
5	22.727	16.129	10.753
6	20.000	14.085	9.1743

Stiffness model error simulation analysis

BP network is a one-way transmission of multi-layer forward network. The network has the input and output nodes, and also has one layer or layers of hidden layer nodes. There is no coupling among the nodes in the same layer. The input signals from the input layer nodes, pass through the hidden layer nodes, and then pass to the output nodes. The output of the nodes in each layer only affects the output of the next layer node. The transfer function of neurons is usually S type. The output transfer function can be linear or "S" [4].

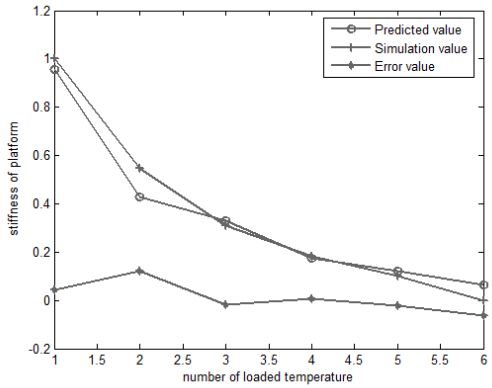

Fig. 5 Stiffness model of the platform

A two-layer BP network is used. Process the table data by normalization for the interval between the [0, 1].

After many tests, the nodes of first hidden layer are 12, and the nodes of second are 42. Function of first layer is tansig, and the second is logsig. The data from row 1 and 2 are used to establish model, and the row 3 are used to test the precision of the model. At last the error MSE= 9.9660e-005. It is found that BP network is fitting for the stiffness modeling. Shown as Fig. 5.

Conclusions

The stiffness of large travel and high precision positioning platform expresses the ability to resist deformation. At the same time, the precision of the positioning platform will be higher. Solving the stiffness of positioning platform in different temperature will provide a measurement to improve analysis platform overall stiffness and provide a fundamental basis for establishing vibration model of the platform in the future. Firstly, choose a number of points from the surfaces of the platform. Through the experiment data of thermal stress coupling analysis on the platform, the temperature of 538 points and displacements of the platform are read out. Then a degree of grey incidence from grey system theory is introduced to identify the degree of correlation between all temperature points and thermal displacements. The key temperature points are confirmed the one which have large degree of grey incidence. The key points also have large influences on the stiffness. Find out the global stiffness value of positioning platform under different temperature using the finite element method analysis. At last, establish the stiffness model using BP neural network successful. Simulation first avoids fixing too much temperature sensors and displacement sensor s in experiments without destination. Workload and cost are decreased at the same time. Grey system theory makes is so convenient that picking up a big amount of points becomes possible and fewer key points would be left out. BP neural network is Convenient and accurate for fitting.

Acknowledgement

The authors would like to thank National Natural Science Foundation of China (No. 51105263) for the support to this work; The National Science Foundation for Post-doctoral Scientists of China (the Grant Number 2012M511316)

Corresponding author: Liu Jizhu; Tel: +86-512-67587217; Fax: +86-512-67587217; E-mail: liu_jizhu@163.com

References

[1] Degang Liu. The effect of Stiffness of feed system on Loss of momentum of NC machine tool[J]. Manufacturing Technology & Machine tool, 1999(11):22-23.

[2] Youxin Luo,Longting Zhang,Min Li. Grey systems theory and application in Mechanic engineering[M]. National University of Defense Technology press, 2001.

[3] Sifeng Liu, etal. Grey systems: Theory and Applicationsthe fifth Edition[M]. Science Press, 2010.

[4] Guoliang Liu, Hongtao Zhang, Hongtao Cao, etal. Study on the application of the neural network theories in the NC machine tool error modeling[J]. Numerical Control Process Technology, 2005(8):20-23.

CHAPTER 3:

Computation Methods and Information Technologies

Applied Mechanics and Materials Vol. 565 (2014) pp 173-178

doi:10.4028/www.scientific.net/AMM.565.173

New Observations from Comparison between the Benner et al. and the Ainley and Mathieson Models for Profile Losses

Zhenwei Yuan[a], Dongshuai Zhu[b], Jun Zhang[c]

School of Chemical Engineering and Energy, Zhengzhou University, Zhengzhou 450001, China

[a]yuanzw@zzu.edu.cn, [b]zhudongs@zzu.edu.cn, [c]zhangjun@zzu.edu.cn

Keywords: comparison and observation; profile losses; prediction models; incidence; incidence correction factor

Abstract. Based on the inspection of the Ainley and Mathieson and the Benner et al. models for profile losses, the two models are compared through numerical simulations. The discrepancies between them are examined and discussed with new observations. It is observed that the stalling incidence predicted by the Benner et al. model is smaller than that predicted by the Ainley and Mathieson model. And also, the Benner et al. model demonstrates that profile losses experience three evidently different regimes, say, insensitive to incidence or the ratio of incidence to stalling incidence from -3.0 to +0.65, sensitive from +0.65 to +2.0, and very sensitive beyond +2.0, but the Ainley and Mathieson model does not. In particular, the third regime had not been covered by the Ainley and Mathieson model. The Benner et al. model is superior to the Ainley and Mathieson model both in preciseness and coverage in that the former is developed through a series of improvements to fit the existing measurements.

Introduction

Aerodynamic loss is a critical factor that influences the performances of a turbine cascade. For a long time, it has been a focus in the research and development of turbomachinery. Since Ainley and Mathieson [1, 2] in 1951 first devised the loss system for turbine cascades, large amount of research work has been done and great achievements have been made so far. Although different researchers investigated this problem in a variety ways and with different measurements, nearly all works boiled down to the same basic loss system as the Ainley and Mathieson's. This basic loss system stated that the total aerodynamic loss from a turbine cascade consists of three parts, say, profile loss, secondary loss and tip-leakage loss. Accordingly, research efforts were poured on these three components. In particular, the profile loss was given much more attentions than the other two components, especially in the early stage, because it is the fundamental or primitive loss and plays an important role in the total aerodynamic loss of a cascade. Ainley and Mathieson first composed a correlation for profile loss. Based on the results obtained from their preliminary investigations on two special blade cases ($\beta_1 = 0$ and $\beta_1 = -\alpha_2$), they devised an interpolation equation for any other cases of combination of angles at zero incidence. Then the profile loss at incidence other than zero incidence was determined by assuming that the ratio of profile loss at any incidence to profile loss at zero incidence is a function of the ratio of incidence to stalling incidence and fitting a curve of the relationship to the measurements. Afterwards, although new loss systems and correlations were proposed in a sequence by Stewart et al. [3], Craig and Cox [4] and Denton [5], the Ainley and Mathieson correlations were the most widely accepted work. Still, the Ainley and Mathieson correlations experienced a series of improvements made by several researchers. Among them, the works of Dunham and Came [6], Kacker and Okapuu [7], Moustapha et al. [8] and Benner et al. [9] are notably worthy of mentioning. On the basis of their insights and measurements, Dunham and Came in 1970 introduced the outlet mean Mach number as a correlating parameter to correct the profile loss correlation of Ainley and Mathieson with great success, forming the so called AMDC design-point correlation. In 1982, Kacker and Okapuu inspected the previous works according to their comprehensive understanding of the problem and the collected experimental dada, leading to a modification to the AMDC correlation. The modified correlation is characterized by the

introduction of a Mach number correction factor and the shock loss term into profile loss correlation, to reflect the advances in turbo aerodynamics in the preceding decade. Nearly a decade later, Moustapha et al. in 1990 devised new correlations for the profile and secondary losses after reviewing the available correlations for profile loss and secondary losses at off-design conditions and comparing them with a range of recent measurements. Drawing on the work of Mukhtarov and Krichakin [10], Moustapha et al. introduced the leading-edge diameter as a correlating parameter. The new off-design correlations were intended for use with the Kacker and Okapuu design-point correlations to form a complete loss system. To verify the Moustapha et al. correlations and to investigate further the influence of leading edge geometry on the off-design behavior of turbine blades, Benner et al. [9] in 1997 initiated an experimental study in a low-speed cascade wind tunnel, leading to a more reliable correlation for profile loss. More recently, after inspecting the previous loss systems and correlations, Benner et al. [11, 12] chose the Kacker and Okapuu design-point correlations and the Moustapha et al. off-design correlations as the best works to base their work on. But they found the deficiencies and made significant improvements to them both for profile and secondary losses. The improvements were highlighted by a new loss breakdown scheme and a penetration depth correlation that is used in the profile loss calculation. At present, the works of Benner et al. [11, 12] are believed to be the newest works reported in the open literature.

The present paper is motivated to compare the primitive Ainley and Mathieson [1, 2] model with the newest Benner et al. [9] model for midspan profile loss and try to get new observations that will be beneficial to the aerodynamic designs of turbine cascades.

The Ainley and Mathieson model for profile losses

Profile loss at zero-incidence. According to Ainley and Mathieson [1, 2], the midspan profile loss at zero incidence, $Y_{p(i=0)}$, is expressed as

$$Y_{p(i=0)} = \left[Y_{p(\beta_1=0)} + \left(\frac{\beta_1}{\alpha_2}\right)^2 \left(Y_{p(\beta_1=-\alpha_2)} - Y_{p(\beta_1=0)}\right)\right]\left(\frac{t_{max}}{0.2C}\right)^{\frac{-\beta_1}{\alpha_2}} \quad (1)$$

where t_{max} is blade maximum thickness, C is chord length of blade, $Y_{p(\beta_1=0)}$ and $Y_{p(\beta_1=-\alpha_2)}$ are two benchmark profile losses corresponding to two special cases of $\beta_1 = 0$ and $\beta_1 = -\alpha_2$ respectively and can be obtained from Ainley and Mathieson [2].

Profile loss at any incidence. As stated in Ainley and Mathieson [2], profile losses at incidences other than zero are then obtained from the assumption that the ratio of profile loss at any incidence to profile loss at zero incidence, $Y_p/Y_{p(i=0)}$, is a function of the ratio of incidence to stalling incidence, i/i_s. This relationship had been obtained from experiments and plotted in Ainley and Mathieson [1]. Here, we simply duplicate the plotted curve as shown in Fig. 1.

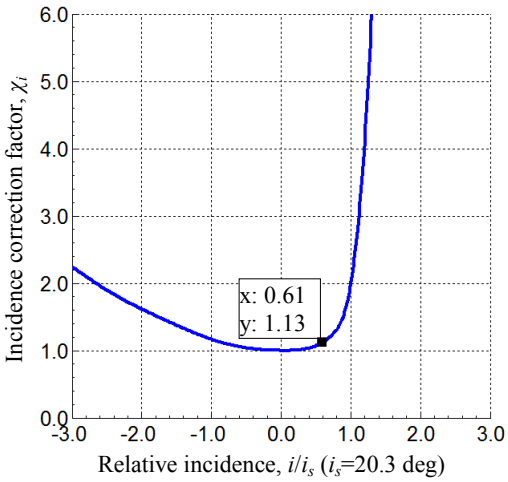

Fig. 1 The Ainley and Mathieson model [1]

The Benner et al. model for profile losses

In the Benner et al. model [9], a new incidence parameter χ was introduced to develop the profile loss correlation at off-design or nonzero incidences. However, the correlation is not for the total profile loss. It just represents the additional loss to the zero-incidence loss. It was expressed as following.

In the first place, the additional profile loss coefficient caused by an off-design incidence was identified as the change to kinetic-energy coefficient $\Delta\Phi^2$, which was given by a fitted polynomial function

$$\Delta\Phi^2 = a_8\chi^8 + a_7\chi^7 + a_6\chi^6 + a_5\chi^5 + a_4\chi^4 + a_3\chi^3 + a_2\chi^2 + a_1\chi, \quad \text{for } \chi \geq 0$$

$$\Delta\Phi^2 = b_2\chi^2 + b_1\chi, \quad \text{for } \chi < 0 \tag{2}$$

where $a_8 = 3.711 \times 10^{-7}$, $a_7 = -5.318 \times 10^{-6}$, $a_6 = 1.106 \times 10^{-5}$, $a_5 = 9.017 \times 10^{-5}$, $a_4 = -1.542 \times 10^{-4}$, $a_3 = -2.506 \times 10^{-4}$, $a_2 = 1.327 \times 10^{-3}$, $a_1 = -6.149 \times 10^{-5}$, $b_2 = 1.358 \times 10^{-4}$, $b_1 = -8.720 \times 10^{-4}$, and χ is a correlated incidence parameter and was defined by the expressions in Benner et al. [9] as

$$\chi = \left(\frac{d}{s}\right)^{-0.05} W_e^{-0.2} \left(\frac{\cos\beta_1}{\cos\beta_2}\right)^{-1.4} (\alpha_1 - \alpha_{1des}) \tag{3}$$

where d is the diameter of leading-edge circle, s is blade pitch, W_e is leading-edge wedge angle (in degrees), α_{1des} is design inlet flow angle, β_1 and β_2 are inlet and outlet blade metal angles measured from the axial direction respectively.

To match the more conventional form for profile losses expressed as pressure loss coefficient, conversion was made according to the following formula, using ΔY_p as the counterpart of $\Delta\Phi^2$.

$$\Delta Y_p = \frac{\left[1 - \frac{\gamma-1}{2} M_2^2 \left(\frac{1}{1-\Delta\Phi^2} - 1\right)\right]^{\frac{-\gamma}{\gamma-1}} - 1}{1 - \left(1 + \frac{\gamma-1}{2} M_2^2\right)^{\frac{\gamma}{\gamma-1}}} \tag{4}$$

where M_2 is the outlet mean Mach number, γ is specific heat ratio of working fluid.

In order to compare with the ratio of profile loss at any incidence to profile loss at zero incidence $Y_p/Y_{p(i=0)}$ as stated in Ainley and Mathieson [2], here we introduce an incidence correction factor, named χ_i, to represent $Y_p/Y_{p(i=0)}$, which is defined according to its connotation by

$$\chi_i = 1 + \frac{\Delta Y_p}{Y_{p(i=0)}} \tag{5}$$

Comparisons and analyses

In order to compare the two models, numerical simulations for the Benner et al. model were performed with MATLAB. The parameters used for the calculations were taken from Benner et al. [9, 11, 12], where d/s=0.151, t_{max}/C=0.196, M_2=0.5, W_e=43.0°, α_1=28.4°, α_{1des}=28.4°, α_2=-57.7°, β_1=25.5°, β_2=-57.5°, γ=1.33. Numerical results are displayed in Fig. 2 and Fig. 3 to compare with Fig.1 that has been duplicated in Sec. 2 from Ainley and Mathieson [1].

Figs. 1-3 are illustrations for the variation of incidence correction factor with relative incidence obtained from the Ainley and Mathieson model [1, 2] and the Benner et al. model [9]. Fig. 1 is simply duplicated from Ainley and Mathieson [1]. Fig. 2 is deduced from the Benner et al. model [9] with the ordinate truncated to match Fig. 1. Fig. 2(a) was drawn with the same stalling incidence as

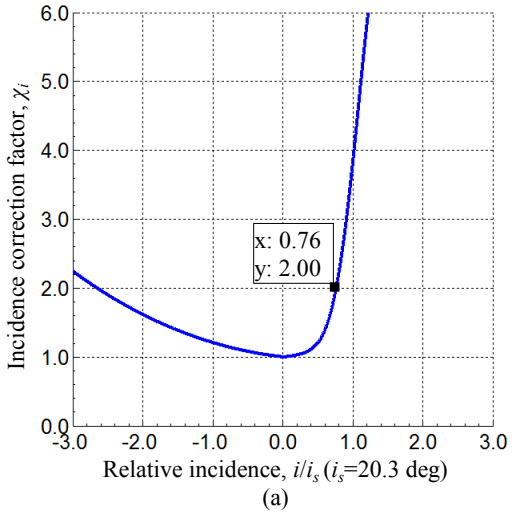

(a)

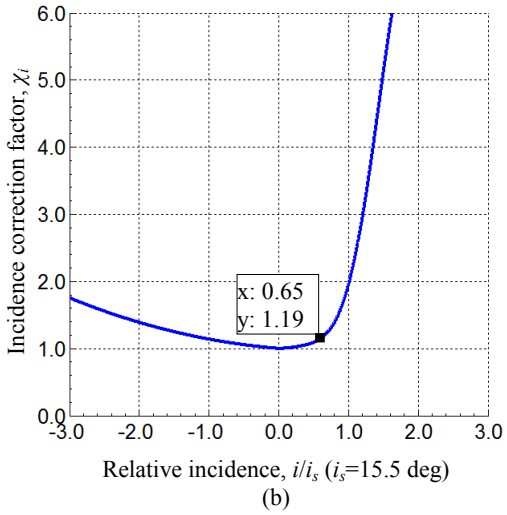

(b)

Fig. 2 The truncated Benner et al. model [9]

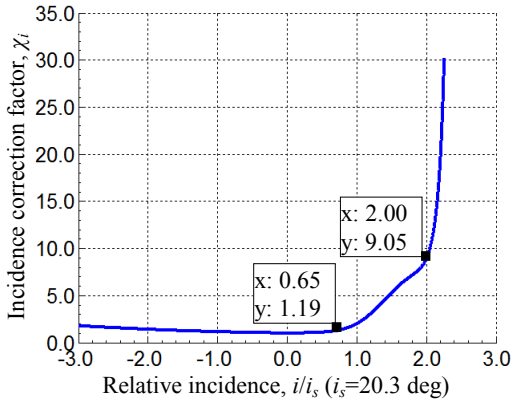

Fig. 3 The full scope Benner et al. model [9]

used in the Ainley and Mathieson model, say 20.3 deg, as a reference incidence, while Fig. 2(b) was drawn with the stalling incidence determined by the Benner et al. model as a reference incidence. Fig. 3 is also deduced from the Benner et al. model [9] but with a full scope of ordinate.

From the figures, it can be seen that apparent discrepancies exist between the two models. By comparing Fig.1 with Fig. 2(a), it is observed that the two models predict very different incidence correction factors at stalling incidence, which is defined as the incidence at which profile loss is twice the loss at zero incidence. The value predicted by the Ainley and Mathieson model is 2.0, which is identical to the definition of stalling incidence. But that predicted by the Benner et al. [9]

model is 3.81, which is obviously against the definition of stalling incidence. This suggests that the 20.3 deg stalling incidence determined by the Ainley and Mathieson model is no longer the stalling incidence for the Benner et al. [9] model. The stalling incidence for the Benner et al. [9] model should be smaller than that for the Ainley and Mathieson model. This is manifested in Fig. 2(a) by the fact that the ratio of incidence to stalling incidence i/i_s=0.76 when the incidence correction factor χ_i =2, corresponding to an incidence of 15.5 deg. Hence, it should be concluded that the Benner et al. [9] model predicts a smaller stalling incidence than the Ainley and Mathieson model. This has not yet been seen reported in the literature.

Compared to Fig. 1, three major changes are observed from Fig. 2(b). One change is that the section of the Benner et al. [9] curve from i/i_s=-3.0 to 0.0 becomes flatter than the counterpart of the Ainley and Mathieson curve. This suggests that the Benner et al. [9] model predicts a lower change rate of incidence correction factor with negative incidences than the Ainley and Mathieson model. In other words, the Benner et al. [9] model predicts that profile loss is not sensitive to negative incidences, whereas the Ainley and Mathieson model does to the contrary. By the Ainley and Mathieson model, the incidence correction factor varies rapidly with the negative incidence. But by the Benner et al. [9] model, the incidence correction factor varies slowly with the negative incidence. It has been proved in the literature [9, 13] that predictions from the Benner et al. [9] model agreed better with the experimental and CFD results than those from Ainley and Mathieson model, owing to the improvements made by Moustapha et al. [8] and Benner et al. [9] to the off-design correlations for profile loss. The second change is that the critical incidence point (point with the biggest curvature) moves forward from (0.61, 1.13) in Fig. 1 to (0.65, 1.19) in Fig. 2(b). This means that the critical incidence predicted by the Benner et al. [9] model, beyond which the variation of incidence correction factor becomes violent, delayed by 0.04 compared to that predicted by the Ainley and Mathieson model. In other words, the Benner et al. [9] model predicts a larger relatively stable regime near the zero incidence point than the Ainley and Mathieson model, in which the profile loss varies slowly with incidence. It has been proved in the literature [9, 13] that the former is more identical to the measurements. The third change is that beyond the critical incidence point, the variation of incidence correction factor with incidence predicted by the Benner et al. [9] model becomes more violent than that predicted by the Ainley and Mathieson model. This indicates that beyond the critical incidence the profile loss predicted by the Benner et al. [9] model increases more rapidly than those predicted by the Ainley and Mathieson model. It has also been proved in the literature [9, 13] that the former is fitted better to the measurements.

Fig. 3 gives the overview of the incidence correction factor predicted by the Benner et al. [9] model. From the figure, it can be seen that the curve has two turn points at (0.65, 1.19) and (2.0, 9.05) where large curvatures occur, corresponding to the two critical points at which the incidence correction factor varies most violently with incidence. These two points divided the curve into three parts, flat part from -3.0 to +0.65, slope part from +0.65 to +2.0, and steep part from +2.0 on. This indicates that profile loss is not sensitive to incidence from -3.0 to +0.65, sensitive from +0.65 to +2.0, and very sensitive beyond +2.0. The third part is what the Ainley and Mathieson model had not revealed.

Conclusions and remarks

On the basis of inspecting the prediction correlations for profile loss derived by Ainley and Mathieson and Benner et al. [9], we compared the two prediction models through numerical simulations. While discrepancies between them being examined, new features were disclosed. Conclusions are reached and remarks are made as follows:

(1) The Benner et al. [9] model is superior to the Ainley and Mathieson model both in preciseness and coverage in that the former is developed through a series of improvements to fit the existing measurements.

(2) Stalling incidence predicted by the Benner et al. [9] model is smaller than that predicted by the Ainley and Mathieson model.

(3) The Benner et al. [9] model demonstrates that profile loss experiences three evidently different regimes, say, insensitive to incidence from -3.0 to +0.65, sensitive from +0.65 to +2.0, and very sensitive beyond +2.0, but the Ainley and Mathieson model does not. In particular, the third regime had not been covered by Ainley and Mathieson model.

Acknowledgments

This paper is supported by the Natural Science Foundation of China (No. 11172270 & No.10972200).

References

[1] D.G. Ainley, and G.C.R. Mathieson. An examination of the flow and pressure losses in blade rows of axial flow turbines. British Aeronautical Research Council, R and M 2891, 1951.

[2] D.G. Ainley, and G.C.R. Mathieson. A method of performance estimation for axial flow turbines. British Aeronautical Research Council, R and M 2974, 1951.

[3] W.L. Stewart, W.J. Whitney, R.Y. Wong. A study of boundary layer characteristics of turbomachine blade rows and their relation to overall blade loss. Transactions of the ASME, 1960, 82: 588-592.

[4] H.R.M. Craig, and H.J.A. Cox. Performance estimation of axial flow turbines. Proceedings Institution of Mechanical Engineers, 1971, 185(32): 407-424.

[5] J.D. Denton. Loss mechanisms in turbomachinery. ASME Journal of Turbomachinery, 1993, 115: 621-656.

[6] J. Dunham, and P.M. Came. Improvements to the Ainley-Mathieson method of turbine performance prediction. ASME Journal of Engineering for Power, 1970, 92: 252-256.

[7] S.C. Kacker, and U. Okapuu. A mean line prediction method for axial flow turbine efficiency. ASME Journal of Engineering for Power, 1982, 104: 111-119.

[8] S.H. Moustapha, S.C. Kacker, and B. Tremblay. An improved incidence losses prediction method for turbine airfoils. ASME Journal of Turbomachinery, 1990, 112: 267-276.

[9] M.W. Benner, S.A.Sjolander, and S.H. Moustapha. Influence of leading-edge geometry on profile losses in turbines at off-design incidence: Experimental results and an improved correlation. ASME Journal of Turbomachinery, 1997, 119: 193-200.

[10] M.K. Mukhtarov, and V.I. Krichakin. Procedure of estimating flow section losses in axial flow turbines when calculating their characteristics. Teploenergetika, 1969, 16(7): 76-79.

[11] M.W. Benner, S.A. Sjolander, and S.H. Moustapha. An empirical prediction method for secondary losses in turbines—Part I: A new loss breakdown scheme and penetration depth correlation. ASME Journal of Turbomachinery, 2006, 128: 273-280.

[12] M.W. Benner, S.A. Sjolander, and S.H. Moustapha. An empirical prediction method for secondary losses in turbines—Part II: A new secondary loss correlation. ASME Journal of Turbomachinery, 2006, 128: 281- 291.

[13] Sun Da-wei, Qiao Wei-yang, Xu Kai-fu, and Li Wei. Influence of different incidences on loss in turbine cascade. Journal of Aerospace Power, 2008, 23 (7): 1232-1239.

Applied Mechanics and Materials Vol. 565 (2014) pp 179-182

doi:10.4028/www.scientific.net/AMM.565.179

Study on TEA Encryption for Public Communication Network Wireless Remoter

Yuetao Ge[a], Xiaoming Liu[b] and Xiaotong Yin[c]

Beijing HIWING Scientific and Technological Information Institute, Beijing, 100074, China.

[a]geyuetao@gmail.com, [b]liuxiaoming_buaa@163.com, [c]yinxiaotongivy@gmail.com

Keywords: Tiny Encryption Algorithm (TEA), Algorithm, communication, remoter

Abstract. In order to realize wireless remoter not only securely but also quickly data transmission in the public communication network, the Tiny Encryption Algorithm (TEA) encryption and decryption algorithm is studied in this paper and the properties of TEA are analyzed. According to communication protocol of remoter, encryption and decryption program process are designed. Because of TEA encryption, remoter transmitter and receiver can communicate strongly in the public communication network.

Introduction

Since the remoter using electromagnetic wave belonging to the wireless communication for data transmission via a public communication network, security of data transmission is very important, thus encrypted data transmission it generally required. The commonly used encryption algorithms are DES, 3DES, MD5, IDEA, RC4, RCS, RC6, TEA, IDEA and so on. Taking into account the characteristics of embedded systems, in addition to considering the security of the encryption algorithm, the encryption and decryption of real-time and ease of implementation is also very important, so it requires a measure to protect the data remote transmission and prevent eavesdropping or destroy some ulterior motives of people.

TEA Properties

Tiny Encryption Algorithm (TEA), which was designed by David Wheeler and Roger Needham of the Cambridge Computer Laboratory in 1994, is a block cipher notable for its simplicity of description and implementation, typically a few lines of code.

TEA operates on two 32-bit unsigned integers (which could be derived from a 64-bit data block) and uses a 128-bit key. It has a Feistel structure with a suggested 64 rounds, typically implemented in pairs termed cycles. It has an extremely simple key schedule, mixing all of the key material in exactly the same way for each cycle. Different multiples of a magic constant are used to prevent simple attacks based on the symmetry of the rounds. The magic constant, 2654435769 or 9E3779B916 is chosen to be 232/φ, where φ is the golden ratio.

But furthermore TEA has a few weaknesses. Each key of the algorithm is equivalent to three others, which means that the effective key size is only 126 bits, so it suffers from equivalent keys. Thus, TEA is not suited to a cryptographic hash function. TEA is also susceptible to a related-key attack which requires 223 chosen plaintexts under a related-key pair, with 232 time complexity. So TEA has followed modified version.

The first published version of TEA was supplemented by a second version that incorporated extensions to make it more secure. Block TEA (sometimes referred to as XTEA) operates on arbitrary-size blocks in place of the 64-bit blocks of the original.

A third version (XXTEA), published in 1998, described further improvements for enhancing the security of the Block TEA algorithm.

But, in this paper, TEA is enough for RF wireless remoter.

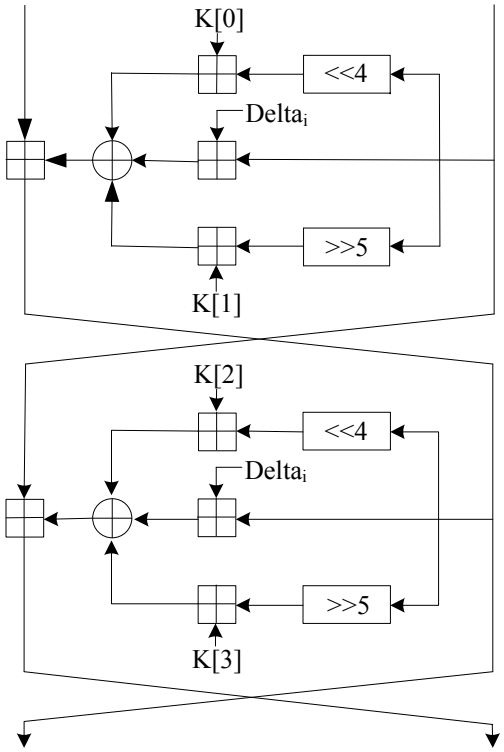

Fig. 1 Two Feistel rounds (one cycle) of TEA

The features of TEA are extremely fast encryption, strong resistance to differential attacks and simple algorithm. Until now, it has not yet been broken. What is more important, the algorithm is simple, efficient and occupy less storage space. It is very suitable for embedded systems. Therefore, the TEA encryption is selected for this radio frequency transmission to protect data communications.

Encryption process

The address, data and CRC checksum of the encryption processing which are shown in table 1 encrypted. If the data bit is less than 4 bytes, the zero will be used to complete 4 bytes. Then, the encryption byte is 8 bytes (64 bits), this is meet encrypted data length 64, the key is 128 bits of data. The algorithm is as follows:

Table 1 RF communication protocol

Data head	Shifting discriminate byte	Address	Data	CRC	End mark
AAAAAAAAH	FFH	XXXXH	XXXXXXXXH	XXXXH	0DH
4 bytes	1 byte	2 bytes	4 bytes	2 bytes	1 byte

The processes of encryption are as follow:

S1: Initialization process

Encryption data is divided into two parts data v (0), v (1), each 32 bits.

y←v(0)，z←v(1)，Sum←0，Delta←0x9e3779b9 (hexadecimal).

128-bit key is divided into four parts k(0), k(1), k(2), k(3), each 32 bits.

a←k(0)，b←k(1)，c←k(2)，d←k(3)，n←32

S2: If n>0 then go to S3, or else go to S4.

S3: Sum←Sum+Delta,

y←y+(z<<4)+a^z+Sum^(z>>5)+b;

z←z+(y<<4)+c^y+Sum^(y>>5)+d;

n←n-1, go to S2.

S4: v(0)←y，v(1)←z，finish.

In the S3, there are the << operator, >> computing, ^ operator, as well as the + operator. Its first order for the << or >>, and then make the ^ operator, and finally the + operator.

Decipherment algorithm is similar to encryption algorithm:

S1，Initialization process

Decrypted data is divided into two parts data v (0), v (1), each 32 bits.

y←(0), z←v(1), Sum←0xc6ef3720 (hexadecimal), Deltra←0x9e3779b9 (hexadecimal).

a←k(0), b←k(1), c←k(2), d←k(3), n←32.

S2，If n>0 then go to S3, or else go to S4.

S3，z←z(y<<4)+c^y+Sum^(y>>5)+d;

y←(z<<4)+c^z+Sum^(z>>5)+b;

Sum←Sum-Deltra;

n←n-1, go to S2.

S4，v(0)←y, v(1)←z, finish.

Specific procedures are as follows:

Encryption data is divided into two parts data m_v[0], m_v[1], each 32 bits, and y= m_v[0], m_v[1], sum=0;

delta＝0x9e3779b9; 128-bits key is divided into four parts, m_k[0], m_k[1], m_k[2], m_k[3],

```
void encipher(void)// Encryption calculation subroutine
{
    unsigned char i;
    unsigned long y, z;
    y=m_v[0]; z=m_v[1]; sum=0;
    for(i=0; i<32; i++)
    {
        sum += delta;
        y += (z<<4)+m_k[0]^z+sum^(z>>5)+m_k[1];
        z += (y<<4)+m_k[2]^y+sum^(y>>5)+m_k[3];
    }
    m_v1[0]=y;
    m_v1[1]=z;
}
//
```

While decrypting data, delta＝0x9e3779b9; sum＝0xc6ef3720.

```
void decipher(void)// Decryption calculation subroutine
{
    unsigned char i;
    unsigned long y, z;
    y=m_v1[0]; z=m_v1[1], sum = 0xc6ef3720;
    for(i=0; i<32; i++)
    {
        z -= (y<<4)+m_k[2]^y+sum^(y>>5)+m_k[3];
        y -= (z<<4)+m_k[0]^z+sum^(z>>5)+m_k[1];
        sum -= delta ;
    }
    m_v2[0]=y;
    m_v2[1]=z;
}
```

Thus, the encryption and decryption process are finished.

Conclusions

We argue that the value of DELTA in this algorithm has little impact on the algorithm, the purpose is just to avoid bad values, the recommended value of DELTA adopt the hexadecimal value 0x9e3779b9, which is after rounding the product of golden section ratio $(\sqrt{5}-2)/2$ and 2^{32}. The iterations of TEA encryption algorithm can be changed, l bit plaintext or key information diffusion up to 32bits need at most six iterations, so 16 iterations may be enough. For example, this algorithm is widely used in QQ data encryption, which used 16 iterations of the TEA encryption algorithm. In this paper, the remoter communication algorithm adopts adequate standard 32 iterations encryption.

With TEA algorithm, the wireless remoter could realize securely and quickly data transmission in the public communication network.

References

[1] Wheeler D J, Needham R M. TEA, a tiny encryption algorithm[C]//Fast Software Encryption. Springer Berlin Heidelberg, 1995: 363-366.

[2] Israsena P. Securing ubiquitous and low-cost RFID using tiny encryption algorithm[C]//Wireless Pervasive Computing, 2006 1st International Symposium on. IEEE, 2006: 4.

[3] Andem V R. A cryptanalysis of the tiny encryption algorithm[D]. The University of Alabama TUSCALOOSA, 2003.

[4] Standaert F X, Piret G, Gershenfeld N, et al. SEA: A scalable encryption algorithm for small embedded applications[M]//Smart Card Research and Advanced Applications. Springer Berlin Heidelberg, 2006: 222-236.

[5] Shepherd S J. The tiny encryption algorithm[J]. Cryptologia, 2007, 31(3): 233-245.

[6] Zafar F, Olano M, Curtis A. GPU random numbers via the tiny encryption algorithm[C]//Proceedings of the Conference on High Performance Graphics. Eurographics Association, 2010: 133-141.

[7] Weis S A, Sarma S E, Rivest R L, et al. Security and privacy aspects of low-cost radio frequency identification systems[M]//Security in pervasive computing. Springer Berlin Heidelberg, 2004: 201-212.

[8] Bogdanov A, Knudsen L R, Leander G, et al. PRESENT: An ultra-lightweight block cipher[M]//Cryptographic Hardware and Embedded Systems-CHES 2007. Springer Berlin Heidelberg, 2007: 450-466.

[9] Staake T, Thiesse F, Fleisch E. Extending the EPC network: the potential of RFID in anti-counterfeiting[C]//Proceedings of the 2005 ACM symposium on Applied computing. ACM, 2005: 1607-1612.

[10] Hu W, Corke P, Shih W C, et al. secfleck: A public key technology platform for wireless sensor networks[M]//Wireless Sensor Networks. Springer Berlin Heidelberg, 2009: 296-311.

[11] Suwartadi E, Gunawan C, Setijadi A, et al. First step toward internet based embedded control system[C]//Control Conference, 2004. 5th Asian. IEEE, 2004, 2: 1226-1231.

[12] Kaps J P. Chai-tea, cryptographic hardware implementations of xtea[M]//Progress in Cryptology-INDOCRYPT 2008. Springer Berlin Heidelberg, 2008: 363-375.

Applied Mechanics and Materials Vol. 565 (2014) pp 183-186

doi:10.4028/www.scientific.net/AMM.565.183

Educational Opportunities via Distance Learning System

Ilya Mimorov[a], Irina Livshits[b] and Vladimir Vasiliev[c]

NRU ITMO - National Research University Information Technologies Mechanics Optics

197101, St. Petersburg, Kronverkskiy Prospect, 49.

[a]I.Mimorov@iods.pro, [b]ecenter-optica10@yandex.ru, [c]Vasiliev@mail.ifmo.ru

Keywords: Distance teaching, Remote learning, I-learning, E-teaching, Webinar, Teaching knowledge base, Software open source, Internet.

Abstract. Distance teaching is an important part of the education process and it is necessary to implement such systems to achieve success at building the new teaching process with modern technology and software. Professors of National Research University of Information Technologies, Mechanics and Optics obtain big experience in specially teaching optical design and other areas of science. Because of growing international links between different universities the distance education becomes an important part of all educational process. Introduction of a system of distance teaching is one of the important projects that will give an opportunity to get students and teachers all around the world. The current publication is devoted to analyze steps to integrate distance teaching system at educational process.

Introduction

Considering positive tendencies of development of an information component and flexibility open source decisions for the organization of initial systems, at present use of systems of remote training is the most perspective development or addition of operating system of training.

Remote training is a principal view of transfer of knowledge for the people trained out of university, or for the teachers, ready to exchange the saved up knowledge or to pass courses of improvement of qualification. For so different tasks specific preparation of teachers for work with the given system is required from the personnel serving system.

Distance teaching

Distance teaching is the system that provides the information exchange and collects all the given information to create a database of knowledge. The first step is to create the process of the teaching, understanding the future results that must be reached. The second one is the internal organization of service. And many other steps that should make the process of distance education much more easily for students, professors and all people who will use.

One of the main problems of the distance teaching is search of necessary training material and professor that will train students. The easiest way is to merge both of these problems and make the initial preparation of professor how to educate over distance teaching system. During these process teacher will understand the principle of work of system, meet with the supporting personal and study the workflow during the whole studying period.

Professor and training material

The whole process of distance teaching is based on the teaching material and the professor that study students or provide the online conference to exchange the experience. According to the students requests it is very hard to find professors who possess a specific knowledge. Our university NRU ITMO(National Research University Information Technologies Mechanics Optics) occupies a leading position in teaching optics, mechanics and etc. that grants us receiving a good material for the remote teaching system. The teaching materials only have to be prepared to special form to use it over the distance teaching.

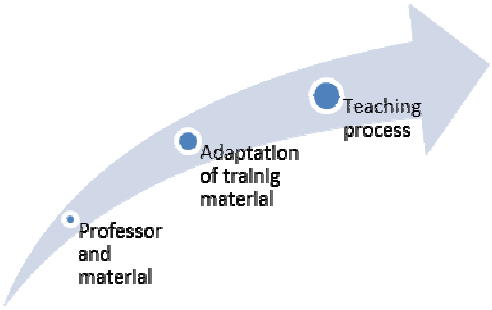

Fig.1 This picture show the main steps of making the database of distance teaching system.

Teaching process

Distance teaching offer the most useful feature – teach anyone from anywhere. Using the new opportunities that arise when combining the standard education process and distance learning system, the universities and the teachers receive unique possibility at teaching students. Before the beginning of academic year the professor can plan teaching of a certain material through system of distance teaching that will allow both to the teacher and students at a certain time receive a freedom of movement without losing the quality of teaching. Free time is formed because of economy on road to university, internal moving's and the resolving of organizational moments.

According to the required system resources for using distance teaching system both of them, internet access and multimedia headset, lectures and practical exercises can be hold at any point of the earth. These functions offer the professor using a combined teaching system at the studying period use a released free time for take a part at the conferences; make an exchange of experience with other professors out of the university without any harm to the teaching process. Students can use free time to level up their skills, make practical exercises and spent time as they wish and loose no information at the same time.

The main target of the construction teaching process is the step by step filling the teaching database with studying material and maximized integration with the system of distance teaching at the same time, that will help to release a lot of free time for students and professors and make the teaching process more flexible and clear for both of them.

Combined type of education

Main functions of the distance teaching system can afford strong planning of whole teaching period according to the time points, use audio and video internet conferencing, and, using the *cloud infrastructure*, suggest an access to specific programs which will be used during the study period. According to the optics specialization of our university it's planned to use programs that allows to make calculation, construction of the specific optics systems. These features will help to resolve one of the biggest problems of the distance teaching – control the studying progress of the students, see the real feedback.

Using the mixed system of education professor has a chance to compare the process of education with lectures at the university and check feedback from students after lectures using distance teaching system. According to the received information professor can correct the education program and change information at the distance teaching system. It's very difficult analytical work to sort the material and make the decision what material should be taught through the distance teaching system and which material at the university's lectures. At the end of the first education period the exhausted information on the arisen questions from students and teachers will be collected and sorted, that will help to simplify as much as possible process of training for all further will be received.

Material control

After the each studying period starts the analyzing period when the professors and the technical personal of the distance teaching system stick in the final information, sort and categorized errors and mistakes and plan the future actualization of the teaching material. It is very important to make the information at the distance teaching system actualized to the modern teach requirements.

Distance teaching and optics

Optics is an important direction of development of a science. It is a big work to prepare courses of lectures and to implement special calculating and modeling optics program at the system of distance teaching. Professors of National Research University of Information Technologies, Mechanics and Optics obtain big experience in teaching optical design and ready to take part in building the distance teaching system that is suitable for usage in optics system. Consolidation of well-qualified technical specialist and professors with big experience will make the system more effective at optics sphere, with actual information and completely filled content.

To teach optics is hard not only for the lecturer but for students too. Lecturer can't give the whole information during the webinar (mixed audio and video conference) and students have to read additional information in a free time and use the new information not only to make homework but to make a practical training independently.

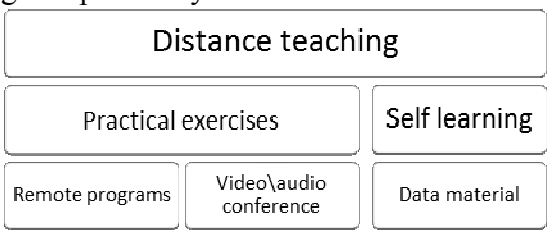

Pic.2 Shows the education process based on distance teaching system

It all will be possible if the listed conditions of implementing distance teaching system will be executed.

Summary

Optics is an important direction of development of a science. It is a big work to prepare courses of lectures and to implement special calculating and modeling optics program at the system of distance teaching. Professors of National Research University of Information Technologies, Mechanics and Optics obtain big experience in teaching optical design and ready to take part in building the distance teaching system that is suitable for usage in optics system. Consolidation of well-qualified technical specialist and professors with big experience will make the system more effective at optics sphere, with actual information and completely filled content.

To teach optics is hard not only for the lecturer but for students too. Lecturer can't give the whole information during the webinar (mixed audio and video conference) and students have to read additional information in a free time and use the new information not only to make homework but to make a practical training independently.

Acknowledgement

Building of the test laboratory, research of the new methods of the distance education and help with filling distance teaching database is supported by NRU ITMO - National Research University Information Technologies Mechanics Optics. This work was partially financially supported by Government of Russian Federation, Grant 074-U01.

References

[1] Ilya Mimorov, Irina Livshits and Vladimir Vasiliev: Applied Mechanics and Materials 457-458(2014) PP. 793 - 796

[2] Mimorov, I., Vasiliev, V., Livshits, I.: Advances in Intelligent and Soft Computing 108(2011) PP. 437 - 444

Applied Mechanics and Materials Vol. 565 (2014) pp 187-193

doi:10.4028/www.scientific.net/AMM.565.187

United Estimation of Time Delay and Frequency Drift In XNAV

Zhenni He[1, a], Baojun Fei[1, b], Guozheng Yao[1, c], Jian Du[1, d]

[1]Department of Fundamental Courses, Academy of Armored Force Engineering, Beijing 100072, China

[a]zhennihe@gmail.com, [b]bjfei@263.net, [c]yaoguozheng@163.com, [d]jiandu2531@163.com

Keywords: XNAV (X-ray Pulsar-based Navigation); pulse profile; parameters estimation; least square method

Abstract. The original navigation information of XNAV is the arrival time series of X-ray photons received by spacecraft. The key issue is to estimate parameters，including time delay, frequency drift and change rate of the observed profile by comparing it with corresponding standard profile in "folding process". This paper illustrates the equation of equiphase point in time series of photons, and gets the initial approximate value of time delay and frequency drift by Larsson cycle folding and coherent function methods. Higher-order approximation is obtained by least square method, and more precise value is calculated by cyclic iteration. Simulation result indicates our method can achieve high precision even without noise eliminating and smoothing process. The proposed method, maybe kind of complicate, it proves the feasibility of XNAV.

In XNAV, the arrival time series of X-ray photons from pulsar, measured by an X-ray detector onboard a spacecraft, are the original navigation information. If we can obtain the "observed profile" of the pulsing signal through the time series, and comparing it with corresponding standard profile, we can estimate its phase difference and frequency drift relative to the "standard profile", and then work out the position and speed of the spacecraft [1,2].

So the primary issue is how to obtain the correct "observed profile" from the time series of photons. However, this is not a simple task, according to present experiment data and navigation theory. The reasons are as follows:

(1) The signal received by detector is quite weak. The flux of most candidate pulsars is about 10^{-2}-10^{-5} ph/cm^2/s (except for Crab, its flux is 1.54 ph/cm^2/s). A sensor with detection area of 1m^2 receives only a few photons in one pulse, no 5mention of the low signal-noise ratio [3]. Here, the arriving time of photons is random, so it is impossible to see the radiation property of the pulsar through a short period observation. To get the observed profile, we must observe the signal for a considerable time (such as 1000s), and then fold the time series of photons according to the equiphase point. Then the accumulated observed profile may show the statistical characteristic of the pulsar.

(2) As the observing time cannot be too short, we need consider the movement of aircraft, including speed, acceleration and its change rate. (When the observed time is very short, the impact of the acceleration and the change rate of acceleration could be neglected.) Because of the Doppler Effect, the cycle of time series of X-ray photon differs not only from its inherent cycle, but also from the instant speed of the aircraft. So during the profile folding process, besides the initial speed of aircraft, parameters such as acceleration and the acceleration changing rate should be knew to get the instant speed. However these parameters are unknown and need to be estimated. This is the obstacle for cycle folding.

(3) The criterion of "correct observed profile" is it's similar to standard profile. However, these two profiles not only have frequency drift mentioned above, but also have the phase difference or time delay, which need to be measured. So the folding process, the time-delay and frequency drift estimation are entangled together.

On conclusion, cycle folding is a key step of XNAV. The observed profile and standard profile share the same statistical characteristic. During this step, we can estimate the phase, frequency and

frequency changing rate of the observed profile with searching or iteration method, which is our major task.

The equiphase point in time series of the photons

Discretization the observed time to $t = t_0, t_1, \cdots, t_k, \cdots, T_{obs}$, the time interval is set to $t_{k+1} - t_k = t_{bin}$. Setting time series of photons received by X-ray detector is $\{z(t_k) | k = 0,1,2,\cdots\}$, where $z(t_k)$ represents photons over the interval ($t_k \sim t_{k+1}$). On the other hand, we can express the time series with phase series $z(\varphi_k)$ $\{z(\varphi_k) | k = 0,1,2,\cdots\}$, where $\varphi_k \equiv \varphi(t_k)$ express the phase at time t_k. As far as the statistical effect, $z(\varphi_k)$ should satisfy cyclic condition:

$$z(\varphi_k + m) = z(\varphi_k) \quad (m = 1,2,\cdots,M). \tag{1}$$

Setting the initial observed time to be zero, $t_0 = 0$. In case t_k is close to t_0, the phase of t_k can be expressed as

$$\varphi(t_k) = \varphi(0) + f t_k + \frac{1}{2}\dot{f} t_k^2 + \frac{1}{6}\ddot{f} t_k^3. \tag{2}$$

Where $f, \dot{f}, \ddot{f}$ are frequency and frequency derivations of the time series at t_0. According to Doppler Effect, the relationship between these parameters and the f_B (the frequency of pulse profile observed at SSB) is given by the expression [1,4]:

$$\begin{cases} f = f_B(1 + \boldsymbol{n}' \cdot \boldsymbol{v}_0 / c) = f_B(1+\beta), \\ \dot{f} = f_B(\boldsymbol{n}' \cdot \boldsymbol{a}_0 / c) = f_B \dot{\beta}, \\ \ddot{f} = f_B(\boldsymbol{n}' \cdot \dot{\boldsymbol{a}}_0 / c) = f_B \ddot{\beta}. \end{cases} \tag{3}$$

where $\boldsymbol{n}' \approx \boldsymbol{n} + \boldsymbol{d}_\perp / D$, $\boldsymbol{n}'$ is the vector of pulsar direction at present time; $\boldsymbol{n}, D$ are the vector direction and the distance of pulsar at reference time; $\boldsymbol{d}_\perp$ is the pulsar's transversal displacement over the interval from reference time to present time; $\beta, \dot{\beta}, \ddot{\beta}$ are ratios of projection of $\boldsymbol{v}_0$, $\boldsymbol{a}_0$, $\dot{\boldsymbol{a}}_0$ in $\boldsymbol{n}'$ direction respective with light speed c, where $\boldsymbol{v}_0, \boldsymbol{a}_0$ and $\dot{\boldsymbol{a}}_0$ are the speed , acceleration and it's change rate of spacecraft related to SSB.

We combined the frequency drift $(f - f_B)/f_B$ and its first-order and second-order derivation into a three dimensional column vector, which is called the vector parameter of frequency drift:

$$\boldsymbol{\zeta} = (\zeta_1, \zeta_2, \zeta_3)^{\mathrm{T}} = \frac{1}{f_B}\left(f - f_B, \dot{f}, \ddot{f}\right)^{\mathrm{T}} = \left(\beta, \ \dot{\beta}, \ \ddot{\beta}\right)^{\mathrm{T}}. \tag{4}$$

According to the above expression, the vector parameter of frequency drift can be regarded as a state vector of three state parameters $(\beta, \dot{\beta}, \ddot{\beta})$.

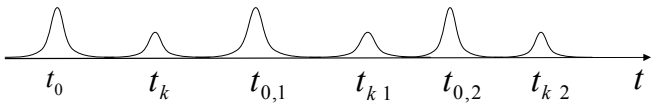

Figure 1 The schema of time series of photons

As showed in figure 1, marking the discrete time in time series with $t_{k,m}$, where the subscript identifies the cycle number. Choosing a giving time t_k in the first cycle, the equiphase points in other cycle can be expressed as:

$$\varphi(t_{k,m}) = \varphi(t_k) + m, (\mathrm{m} = 0,1,\cdots,M), \tag{5}$$

Where $t_{k,0} \equiv t_k$. M is the total number of observed cycles, $t_{k,m}$ can be ascertained by Eqn. (2).

$$(1+\zeta_1)(t_{k,m} - t_k) + \frac{1}{2}\zeta_2(t_{k,m}^2 - t_k^2) + \frac{1}{6}\zeta_3(t_{k,m}^3 - t_k^3) = mT_B. \tag{6}$$

For the spacecraft around the earth, the orders of their three parameters of frequency drift are as follows: $\zeta_1 / \zeta_2 / \zeta_3 = \beta / \dot{\beta} / \ddot{\beta} = 10^{-4} / 10^{-8}\,\mathrm{s}^{-1} / 10^{-12}\,\mathrm{s}^{-2}$. So in case the observed time $T_{obs} < 1000\mathrm{s}$, these parameters can be solved with iteration method. If reserving the first term in the left part of Eqn. (6), we can get zero-level approximate value of $(t_k - t_{k,m})$, then substituting it back to the second and third term of the left part, we can solve out $t_{k,m}$:

$$t_{k,m}(\boldsymbol{\zeta}) = t_k + mT_0\left[1 - \frac{\zeta_2}{2(1+\zeta_1)}(\mathrm{m}T_0 + 2t_k) - \frac{\zeta_3}{6(1+\zeta_1)}\left(m^2T_0^2 + 3mT_0t_k + 3t_k^2\right)\right], \quad (7)$$

Where $T_0 = T_B / (1+\zeta_1)$ is the length of the first cycle (with accuracy in "ns").

For the given pulsar period T_B and parameters (k,m), the right sight of Eqn. (7) is a nonlinear function of frequency drift. However, we can make pre estimation of frequency drift, expressed as $\tilde{\zeta}$, according to initial movement state value $(\beta, \dot{\beta}, \ddot{\beta})$ of spacecraft. Then the equiphase point $t_{k,m}(\tilde{\boldsymbol{\zeta}})$ can be confirmed on basis of above equations. A small change $\delta\boldsymbol{\zeta}$ occurred in frequency drift will lead to changes of equiphase point, the changed equphase point expressed with $\boldsymbol{\zeta} = \tilde{\boldsymbol{\zeta}} + \delta\boldsymbol{\zeta}$ are as follows:

$$t_{k,m}(\boldsymbol{\zeta}) = t_{k,m}(\tilde{\boldsymbol{\zeta}}) + \boldsymbol{A}(k,m)\cdot\delta\boldsymbol{\zeta}, \quad (8)$$

$$\boldsymbol{A} = \nabla_{\boldsymbol{\zeta}} t_{k,m} \approx -mT_B\left[1, \frac{1}{2}(\mathrm{m}T_B + 2t_k), \frac{1}{6}\left((mT_B)^2 + 3mT_Bt_k + 3t_k^2\right)\right]. \quad (9)$$

The 3-dimension row vector "A" is only related with the parameter (k,m), so $t_{k,m}(\boldsymbol{\zeta})$ is linear with $\boldsymbol{\zeta}$ in its neighborhood. Increment of any component of $\boldsymbol{\zeta}$ will decrease the value of $t_{k,m}$, vice versa.

The length of the *m*th cycle in time series of photons is as follows:

$$T_m = t_{0,m} - t_{0,m-1} = T_0\left[1 - \frac{\zeta_2 T_0}{2(1+\zeta_1)}(2\,\mathrm{m}-1) - \frac{\zeta_3 T_0^2}{6(1+\zeta_1)}(3m^2 - 3\,\mathrm{m} + 1)\right]. \quad (10)$$

Generally, the period of the signal cycle in the time series is shifting, and spacecraft's acceleration and acceleration changing lead to inhomogeneous cycle.

Pulsar profile folding and initial estimating of frequency drift and time delay

On the assumption that the pre-estimation of frequency drift is ζ, the equiphase point $t_{k,m}(\zeta)$ can be calculated by Eqn. (7). $z\left(t_{k,m}(\zeta)\right)$ expressing the number of received photons in the interval of $t_{k,m} \sim t_{k,m+1}$, the following expression can be obtained by summing m up.

$$x_k(\boldsymbol{\zeta}) \equiv x(t_k, \boldsymbol{\zeta}) = \sum_{m=0}^{M-1} z\left(t_{k,m}(\boldsymbol{\zeta})\right). \quad (11)$$

This profile has the cycle of T_0. In order to compare it with standard profile, it should be transformed to T_B, which can be easily done by redefine the time t_k as follows:

$$t_k \to t_n = t_k T_B / T_0 = t_k(1+\zeta_1). \quad (12)$$

Now the $\{x(\zeta) | n = 0,1,2,\cdots N-1\}$ makes up the observed pulsar profile with cycle T_B, and its phase is as follows:

$$\varphi(t_n) = \varphi(0) + f_B t_n. \quad (13)$$

If the pre-estimation of frequency drift widely differ from optimal value, the shape of above observed profile will also widely differ from the standard profile. Then ζ can be further estimated by using the method of Larsson [7].

$$\chi^2(\zeta)=\sum_{n=0}^{N-1}\left[\frac{x_n(\zeta)-\bar{x}}{\sqrt{\sigma_{tot}^2 x_n(\zeta)}}\right]^2, \tag{14}$$

Where $\bar{x}$ is the average value of pulsar profile, and σ_{tot} is the standard deviation of photons. The initial estimate value of frequency drift is calculated by using χ^2 hypothesis test to the above equations.

Fitting the standard pulsar profile to a smooth curve [8], setting p(t) as the normalized distribution function and making use of total number of observed photons n_{tot}, the photons distribution of the standard profile is acquired as follows:

$$y_n=n_{tot}\int_{t_n}^{t_{n+1}}p(t)dt\ ,\quad \left(\int_0^{T_B}p(t)dt=1, n_{tot}=\sum_{n=0}^{N-1}x_n\right), \tag{15}$$

Its phase $\varphi_B(t_n)$ is $\varphi_B(t_n)=\varphi_B(0)+f_B t_n$, and its phase difference relative to observed profile depends on their initial phase differences.

$$\varphi_B(t_n)-\varphi(t_n)=\varphi_B(0)-\varphi(0)\equiv f_B\tau, \tag{16}$$

τ is the undetermined time delay parameter. This expression means event $\varphi_n(\zeta)=x(t_n,\zeta)$ in observed profile is equiphase with event $y_n(\tau)=y(t_n-\tau)$ in standard profile.

Using Fourier transform of fundamental frequency to observed and standard profile, the values are as follows:

$$X(\zeta)=\sum_{n=0}^{N-1}x_n(\zeta)e^{i2\pi t_n/T_B}, Y=\sum_{n=0}^{N-1}y_n e^{i2\pi t_n/T_B}\ . \tag{17}$$

Then approximate value of time delay is obtained by using coherent function method [2].

$$\tau=\frac{T_B}{2\pi}\left[\arg\left(X(\zeta)\right)-\arg(Y)\right]. \tag{18}$$

As a result, the initial estimate value of time delay $\tau^{(0)}$ is calculated.

United estimation of time delay and frequency drift

Define a least square statistics of four parameters as:

$$Q(\tau,\zeta)=\sum_{n=0}^{N-1}\left[\frac{x_n(\zeta)-y_n(\tau)}{\sqrt{y_n(\tau)}}\right]^2, \tag{19}$$

Where the four parameters (τ,ζ) depend on the spacecraft's position and its projection of $\boldsymbol{v}_0$, $\boldsymbol{a}_0$ and $\dot{\boldsymbol{a}}_0$ in $\boldsymbol{n}'$ direction, which are independent to each other and can be calculated separately. Their estimation should be relatively satisfied as follows:

$$\partial_\tau Q(\hat{\tau},\zeta)=-\sum_{n=0}^{N-1}\frac{x_n^2(\zeta)}{y_n^2(\hat{\tau})}\dot{y}_n(\hat{\tau})=0, \tag{20}$$

$$\nabla_\zeta Q\left(\tau,\hat{\zeta}\right)=2\sum_{n=0}^{N-1}\frac{x_n\left(\hat{\zeta}\right)}{y_n(\tau)}\nabla_\zeta x_n\left(\hat{\zeta}\right)=0. \tag{21}$$

Above equations are deduced by below formulas:

$$\sum\dot{y}_n(\tau)=\dot{n}_{tot}=0, \sum\nabla_\zeta x_n(\zeta)=\nabla_\zeta n_{tot}=0.$$

Firstly, the estimation of time delay is calculated. Using the segment $\tau^{(0)}$ as the zero-level proximate value, the higher-level similar value is achieved by solving Eqn. (20) with Newton iteration method.

$$\tau^{(i+1)} = \tau^{(i)} + h\left(\tau^{(i)}\right) \quad (i = 0,1,2,\cdots), \tag{22}$$

$$h(\tau) = \frac{1}{2}\left[\sum_{n=0}^{N-1} \frac{x_n^2(\boldsymbol{\zeta})\dot{y}_n^2(\tau)}{y_n^3(\tau)}\right]^{-1} \sum_{n=0}^{N-1} \frac{x_n^2(\boldsymbol{\zeta})\dot{y}_n(\tau)}{y_n^2(\tau)}, \tag{23}$$

$$\dot{y}_n(\tau) = n_{tot}\left[p(t_{n+1}+\tau) - p(t_n+\tau)\right]. \tag{24}$$

For small pre-set time $h_\varepsilon > 0$, the iteration is terminated when the equation $\left|\tau^{(i+1)} - \tau^{(i)}\right| < h_\varepsilon$ is satisfied, and $\tau^{(i+1)} = \hat{\tau}$ is the final estimation of time delay.

And then the estimation of frequency drift is calculated. Using the following segment $\zeta^{(0)}$ as the zero-level approximate value, the following formulas are got by solving Eqn. (21) with Gauss-Newton iteration method.

$$\boldsymbol{\zeta}^{(i+1)} = \boldsymbol{\zeta}^{(i)} + \boldsymbol{H}\left(\boldsymbol{\zeta}^{(i)}\right) \quad (i = 0,1,2,\cdots), \tag{25}$$

$$\boldsymbol{H}(\boldsymbol{\zeta}) = -\left[\sum_{n=0}^{N-1} \frac{\boldsymbol{D}_n(\boldsymbol{\zeta})\boldsymbol{D}_n^{\mathrm{T}}(\boldsymbol{\zeta})}{y_n(\hat{\tau})}\right]^{-1} \sum_{n=0}^{N-1} \frac{x_n(\boldsymbol{\zeta})\boldsymbol{D}_n(\boldsymbol{\zeta})}{y_n(\hat{\tau})}, \tag{26}$$

$$\boldsymbol{D}_n(\boldsymbol{\zeta}) = \left[\partial_{\zeta_1} x_n, \partial_{\zeta_2} x_n, \partial_{\zeta_3} x_n\right]^{\mathrm{T}}(\boldsymbol{\zeta}). \tag{27}$$

The right side of the Eqn. (26) is the multiply result of a 3×3 inverse matrix multiply and a 3-dimensional columns matrix, and summary is done for every elements of the matrix. As the observed profile is not a continuous function, derivation of the Eqn. (27) can be numerically calculated. Similar to time delay estimation, a three columns matrix vector $\boldsymbol{H}_\varepsilon$ is preset, and when $\left|\boldsymbol{\zeta}^{(i+1)} - \boldsymbol{\zeta}^{(i)}\right| < \boldsymbol{H}_\varepsilon$ is satisfied, the iteration is terminated and get $\boldsymbol{\zeta}^{(i=1)} = \hat{\boldsymbol{\zeta}}$ as the final estimation of frequency drift.

Results of preliminary simulation

Take the observed data of Crab provided by RXTE as an instance [3]. Its inherent cycle is $T_B = 33400.0\mu s$ .For simplifying calculating process, and intensifying the impact of spacecraft movement to the pulsar profile, set the virtual value of frequency drift parameters as $\boldsymbol{\zeta}_{real} = (1.0\times10^{-2}, 1.0\times10^{-5}\ \mathrm{s}^{-1}, 1.0\times10^{-8}\ \mathrm{s}^{-2})^{\mathrm{T}}$,So the real cycle of pulsar profile can be solved out as $T_{real} = 33069.29\mu s$.

According to the arrival time distribution of photons from Crab, ten thousand cycles of time series through the Monte-Carlo process are simulated. Overlying one thousand consecutive cycles into one cycle, ten lines of photon arrival time series in ten different timeslot is got as showed in figure 2. The real observed profile line 3 in figure 3 and the peak time are calculated according to the Eqn. (7) and Eqn. (11). $\tau_{real} = 9986.93\mu s$.

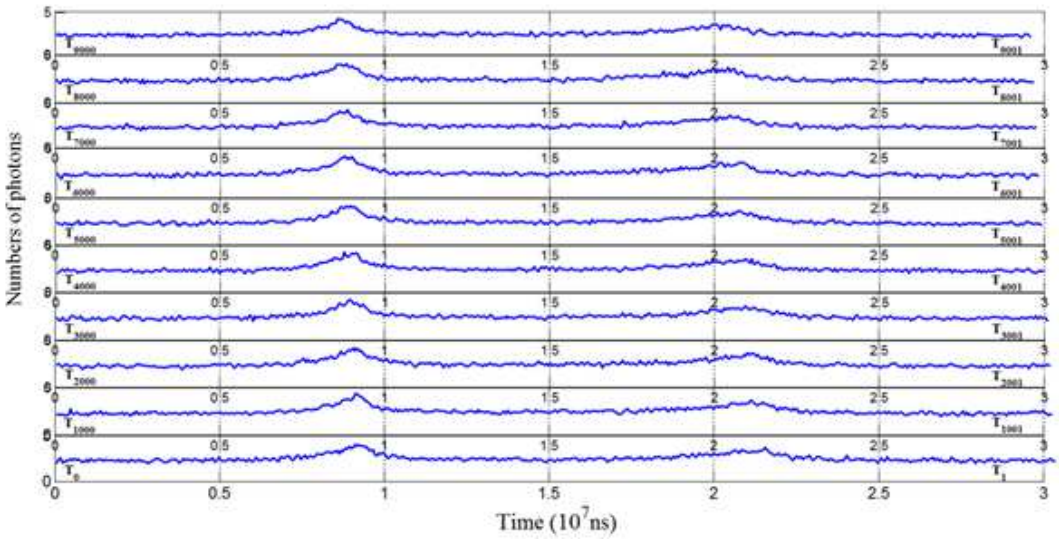

Figure 2 Time series of photons of Crab pulsar separately in ten time cycles.

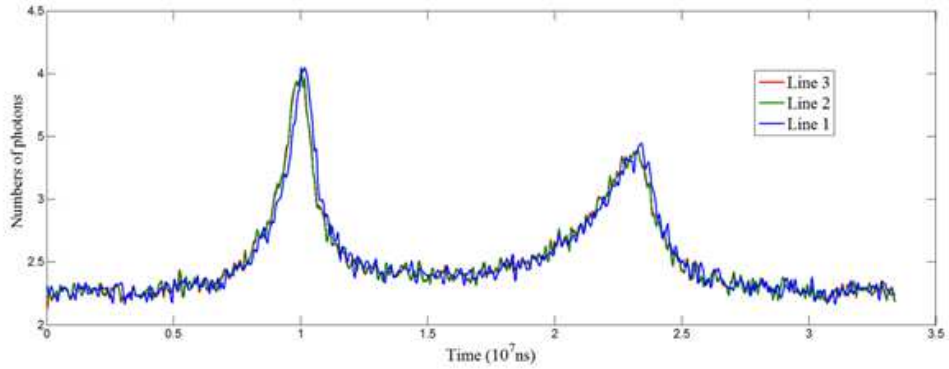

Figure 3 Comparison between the standard profile and the observed profile of Crab.

(Line 1: estimate value ; Line 2: calculate value b; Line 3: real value)

Table 1 Estimate values of time delay and frequency drift parameter

	$\tau/\mu s$	ζ_1	ζ_2 / s^{-1}	ζ_3 / s^{-2}
Real value	9986.93	1.0×10^{-2}	1.0×10^{-5}	1.0×10^{-8}
Estimate value		1.001×10^{-2}	1.001×10^{-5}	1.001×10^{-8}
Calculate value a	9999.21	1.00026×10^{-2}	1.0087×10^{-5}	1.0170×10^{-8}
Calculate value b	9986.96	1.00002×10^{-2}	1.0006×10^{-5}	1.0034×10^{-8}

Pr-set the value of frequency drift as

$\boldsymbol{\zeta} = (1.001\times10^{-2}, 1.001\times10^{-5}\ \mathrm{s}^{-1}, 1.001\times10^{-8}\ \mathrm{s}^{-2})^{\mathrm{T}}$

and the finally iteration step length as

$\boldsymbol{H}_{\varepsilon} = (1\times10^{-6}, 1\times10^{-9}\ \mathrm{s}^{-1}, 1\times10^{-12}\ \mathrm{s}^{-2})^{\mathrm{T}}$, $h_{\varepsilon} = 20ns$.

Applying the methods proposed in section 2 and 3, the estimations of frequency drift and time delay are worked out, and showed as Calculate a in table 1. Reset the finally iterate step length as

$\boldsymbol{H} = (1\times10^{-7}, 1\times10^{-10}\ \mathrm{s}^{-1}, 1\times10^{-13}\ \mathrm{s}^{-2})^{\mathrm{T}}$, $h_{\varepsilon} = 10ns$.

Repeat the calculating, draw the observed profile 2, and work out the estimations of Calculate b in table 1. In figure 3, the observed profile line 2 is essentially coincident with line 3. In table 1, the estimations of frequency drift and time delay are approaching to true value with the decreasing of

the length of the finally iterate step. The absolute error of time delay is within 30ns, which means the error of positing is the order of meter.

Brief summary and discussion

This paper firstly attempt to united estimate four observed parameters of pulsar profile received by spacecraft, which is close to the actual situation of XNAV. In the dynamic measurement of spacecraft, although observe time cannot be too small and spacecraft maybe accelerate, it is possible to estimate the four observed parameters. This shows the feasibility of XNAV. A workable estimating process for XNAV is proposed: obtaining initial estimation during cycle folding process with coherent function methods; making united estimation of four parameters with least square method, together with iteration approach to get higher precise estimations of time delay and frequency drift of observed profile. There are several issues for further discussion:

(1) This method does not eliminate the noise of pulsar profile, but take pulsar signal and noise as a whole, which is proper to data processing of "relative navigation". As previous proved that the calculation error of noise is time invariant [2]. In "relative navigation", although noise was considered during calculating on both standard spacecraft and target spacecraft, its impact can be naturally eliminated in differencing process.

(2) The above calculation used interpolating process, but without smoothing. If the line is smoothed, better precision maybe achieved. This is because the line should be linear in local part when using Gauss-Newton iteration, and a continuous profile obtained from smoothing process can speed up the convergence of iteration.

(3) Although this method can achieve higher accuracy, the calculating process is relative complicated, and we hope to improve it in further work.

References

[1] Fei B J，Yao G Z，Du J，et al．The pulse profile and united measurement equation in XNAV. Sci. Chin(G), 2010, 40(5)：644–650 (in Chinese).

[2] Fei B J, Pan G T, Yao G Z, et al. Arithmetic of frequency drift and time delay between pulse profiles in XNAV. Acta Geodaetica et Cartographica Sinica，2011，41(Sup)：126–132(in Chinese).

[3] Ge M Y, Lu F J, Qu J L, et al. X-ray phase-resolved spectroscopy of PSRs B0531+21, B1509 − 58, and B0540 − 69 with RXTE. Astrophysical Journal Supplement Series, 2012, 199(2):401-420.

[4] Yao G Z, Fei B J, Xiao Y. On the Position Measurement Equation of XNAV. Acta Astronomica Sinica, 2012, 53(2):119-125(in Chinese).

[5] Emadzadeh A, Speyer J. X-ray Pulsar-based Relative Navigation Using Epoch Folding. IEEE Trans on Aerospace and Electronic Systems, 2011, 47(4):2317-2328.

[6] Emadzadeh A, Speyer J. On Modeling and Pulse Phase Estimation of X-ray Pulsars. IEEE Trans on Signal Processing, 2010, 58(9):4484-4495.

[7] Larsson S. Parameter Estimation in Epoch Folding Analysis. Astronomy and Astrophysics Supplement, 1996, 117:197-201.

[8] Xu X B, Wu X J. Mean Pulse Analysis and Spectral Character Study of Pulsar PSR B2111 +46. Science in China Series G: Physics, Mechanics and Astronomy, 2003, 46(1):104-112.

Applied Mechanics and Materials Vol. 565 (2014) pp 194-197

doi:10.4028/www.scientific.net/AMM.565.194

Task-Level Learning from Demonstration and Generation of Action Examples for Hierarchical Control Structure

Anna Gorbenko[1, a]

[1] Ural Federal University, 620083, Ekaterinburg, Russia

[a]gorbenko.aa@gmail.com

Keywords: Task-level robot learning, Learning from demonstration, Control structure, Mobile robot, Actions.

Abstract. We consider the problem of the task-level robot learning from demonstration. In particular, we consider a model that uses the hierarchical control structure. For this model, we propose the problem of selection of action examples. We present a polynomial time algorithm for solution of this problem. Also, we consider some experimental results for task-level learning from demonstration.

Introduction

The task-level robot learning from demonstration paradigm has received great attention recently (see e.g. [1-3]). In particular, learning from demonstration methods are extensively studied for humanoid robots (see e.g. [4-6]). Such methods allow to avoid explicit programming of complex skills, behaviors, and knowledge of humans which is usually considered as a difficult problem.

Note that an ability of humans to select proper sequences of movement templates is based on the syntactic hierarchical control structure [7]. It is natural to use some analog of this structure for learning of humanoid robots. A hierarchical approach to task-level humanoid robot learning from demonstration was proposed in [6].

It is clear that the quality of the hierarchical learning depends critically on the selection of action examples. In this paper, we consider the problem of generation of action examples for hierarchical control structure and propose an approach to solution of the problem.

Problem Definition

It is clear that we can consider single acts as letters of some alphabet. In particular, let

$$\Sigma = \{ a[1], a[2], \ldots , a[m] \}$$

be a fixed alphabet of single acts.

Let S be a sequence of single acts. We can consider S as a string over Σ. We use S[i] to denote the ith single act in string S, and S[i,j] to denote the substring of S consisting of the ith single act through the jth single act. The length of a string S is the number of single acts in it and is denoted as $| S |$. We assume that Σ^+ is the set of all nonempty strings over Σ. The set Σ^+ can be considered as the set of all possible actions.

Let $L \subseteq \Sigma^+$ be a set of learned actions. It is clear that to learn all compound actions the robot needs to learn all single acts. However, in general, it is not sufficient. The robot needs some system of action integration. Also, the robot needs some system for decomposition of compound actions into a sequence of single acts and compound actions. Therefore, we can not assume that L is closed under substrings and string concatenation.

Clearly, the quality of learning is critically dependent on the selection of action examples for demonstrations. First of all, a new compound action should be maximally covered by previous demonstrations. Such approach allows to reduce the learning time and possible failures. Also, it is clear that we need to minimize a number of action examples. Therefore, we need to solve the following problem.

The problem of selection of action examples for hierarchical control structure (PS):
Instance: A set $L \subseteq \Sigma^+$, a compound action $w \in \Sigma^+$, and positive integers N and K.
Question: Is there a sequence

$$0 < i[1] < j[1] < \ldots i[r] < j[r] < | w | + 1$$

such that

- $r < N + 1$;
- $w[i[p],j[p]] \in L$, for all $0 < p < r + 1$;
- $| w | - | w[i[1],j[1]] | - | w[i[2],j[2]] | - \ldots - | w[i[r],j[r]] | < K + 1$?

Strategies of Task-Level Learning

Let w = w[1] w[2] ... w[n] be a compound action over Σ+. In general, we can consider a number of different strategies of task-level learning for such actions.

It is clear that we can use the model of linear learning from demonstrations (LL). In this case, we can consider the set $\Pi \subseteq \Sigma$ such that $u \in \Pi$ if and only if u = w[i] for some i. After this, we can simply demonstrate all single acts from Π.

To provide a better learning repetitive actions, we can consider the model of weighted linear learning from demonstrations (WLL). In this case, we use the sequence of demonstrations w[1], w[2], ..., w[n]. However, such strategy not takes into account a system of action integration.

We can consider simple hierarchical model (SH) where the set of action examples consists from all subwords of w. Also, we can consider proportional hierarchical model (PH) where the set of action examples consists from all subwords u of w such that | u | = 1, 2, 4, 8, ...

It is natural to consider greedy hierarchical model (GH). In this case, we consider the set L of learned actions. Let w = u[1]v[1]u[2]v[2]... where u[i] is a maximal subword such that $u[i] \in L$. We assume that v[1], v[2], ... is a sequence of new examples.

Finally, we can use the problem of selection of action examples for hierarchical control structure. It is easy to see that PS allows us to use parameters N and K to control the speed and quality of learning. In particular, we can use genetic algorithms for prediction proper values of such parameters.

An Algorithm for Solution of PS

To solve PS we can use the following naive algorithm:

```
b[1] := 1; I := 1; r[1] := 0; p[1] := 0;
for i = 1 to i = I
   while b[i] < | w | + 1
   for x ∈ L
      if w[b[i],| x |] = x then
         begin
            b[I+1] := b[i] + | x |;
            r[I+1] := r[i] +1;
            I := I+1;
            p[I] := p[i] + | x |;
         end;
      b[i] := b[i]+1;
```

It is clear that if there is i such that r[i] < N + 1 and | w | - p[i] < K + 1, then there is a sequence of integers 0 < i[1] < j[1] < ... i[r] < j[r] < | w | + 1 such that

- r < N + 1;
- w[i[p],j[p]] ∈ L, for all 0 < p < r + 1;
- | w | - | w[i[1],j[1]] | - | w[i[2],j[2]] | - ... - | w[i[r],j[r]] | < K + 1.

It is easy to see that it is not polynomial time algorithm. However, we can do some better. In particular, if b[i] = b[j], r[i] < r[j] + 1, and p[i] + 1 > p[j], then we can remove j. In this case, we obtane polynomial time algorithm.

Experimental Results

In our experiments, we consider the problem of footstep planning for humanoid robots (see e.g. [8,9]). We have created a data set (SET 1) for this problem for humanoid robot Nao [10].

It is clear that the hierarchical approach to task-level robot learning from demonstration can be applied not only for humanoid robots. Therefore, it is natural to consider such approach for some other robots.

It is well known that visual landmarks are extensively used in simple mobile robot navigation (see e.g. [11-13]). So, we can try to apply the hierarchical approach to task-level robot learning from demonstration to some problem of visual landmark navigation. In this paper, we consider the problem of simple topological robot navigation using visual landmarks. We have created a data set (SET 2) for mobile robot Kuzma-II (see e.g. [14]) and Neato XV-11 [15] with an onboard camera. For data sets SET 1 and SET 2, we assume that SET i (n) denotes the subset of SET i that contains instances with average number of single acts n.

Let T(X,Y) denotes the time of learning for strategy X and data set Y. Let E(X,Y) denotes the number of errors for strategy X and data set Y. It is clear that we can consider T(X,Y) / T(LL,Y) and E(X,Y) / E(LL,Y) as measures of quality of strategy X on data set Y. Selected experimental results are given in Tab. 1 and Tab. 2.

Table 1. The time performance of different strategies of learning.

Strategy	WLL	SH	PH	GH	PS
SET 1 (1 000)	4.722	55.633	32.514	2.116	0.782
SET 1 (10 000)	6.453	283.394	78.213	3.228	1.224
SET 1 (50 000)	7.328	976.115	96.454	3.879	1.266
SET 2 (1 000)	6.412	44.315	27.049	1.869	0.663
SET 2 (10 000)	8.542	156.441	49.307	2.093	0.945
SET 2 (50 000)	11.399	296.785	53.119	2.241	1.108

Table 2. The number of errors for different strategies of learning.

Strategy	WLL	SH	PH	GH	PS
SET 1 (1 000)	0.951	0.027	0.148	0.444	0.032
SET 1 (10 000)	0.972	0.056	0.239	0.797	0.061
SET 1 (50 000)	0.983	0.064	0.268	0.833	0.068
SET 2 (1 000)	0.872	0.012	0.131	0.436	0.014
SET 2 (10 000)	0.884	0.017	0.172	0.753	0.018
SET 2 (50 000)	0.886	0.019	0.194	0.812	0.021

It is easy to see that the strategy that based on PS demonstrates very good time performance. At same time, this strategy allows us to obtain relatively low level of errors.

In Tab. 1 and Tab. 2, we consider the strategy that based on PS after 1 000 generations of genetic algorithms. It is clear that the quality of this strategy essentially depends from the number of generations of genetic algorithms. Selected experimental results are given in Tab. 3.

Table 3. The dependence of the quality of PS from the number of generations.

Number of generations	100	500	5 000	10 000
Time for SET 1 (1 000)	0.992	0.954	0.781	0.779
Time for SET 2 (1 000)	0.973	0.888	0.662	0.661
Errors for SET 1 (1 000)	0.417	0.055	0.032	0.031
Errors for SET 2 (1 000)	0.226	0.019	0.014	0.014

Summary

In this paper, we have considered the problem of the task-level robot learning from demonstration. In particular, we have considered a model that uses the hierarchical control structure. For this model, we have proposed the problem of selection of action examples. We have presented a polynomial time algorithm for solution of the problem. Also, we have considered some experimental results for task-level learning from demonstration. In particular, we have considered the model of linear learning from demonstrations, the model of weighted linear learning from demonstrations, simple hierarchical model, proportional hierarchical model, greedy hierarchical model, and the strategy that based on the problem of selection of action examples for hierarchical control structure. We have shown that the strategy that based on the problem of selection of action examples for hierarchical control structure demonstrates very good time performance. Also, we have shown that the strategy allows us to obtain relatively low level of errors.

Acknowledgement

This research was partially financially supported by Analytical Departmental Program ”Developing the scientific potential of high school”, RFBR, research project No. 13-01-00048 a, and under the Agreement 02.A03.21.0006 of 27.08.2013 between the Ministry of Education and Science of the Russian Federation and Ural Federal University.

References

[1] J. Aleotti, S. Caselli and M. Reggiani: Robot. Auton. Syst. Vol. 47 (2004), p. 153

[2] K. Doya: Neural Netw. Vol. 15 (2002), p. 495

[3] S. Ekvall and D. Kragic: Int. J. Adv. Robotic Sy. Vol. 5 (2008), p. 223

[4] M. Mataric: IEEE Intell. Syst. Vol. 15 (2000), p. 18

[5] M. Muhlig, M. Gienger and J. Steil: Auton. Robot. Vol. 32 (2012), p. 97

[6] Y. Wu and Y. Demiris, in: 11th International Conference on Control Automation Robotics and Vision, IEEE Press, Piscataway (2010), p. 453

[7] E. Koechlin and T. Jubault: Neuron Vol. 50 (2006), p. 963

[8] A. Gorbenko and V. Popov: Appl. Math. Sci. Vol. 6 (2012), p. 6567

[9] A. Gorbenko and V. Popov: Appl. Math. Sci. Vol. 7, (2013), p. 2357

[10] Information on http://www.aldebaran-robotics.com/en/

[11] A. Gorbenko and V. Popov: Appl. Math. Sci. Vol. 7 (2013), p. 1205

[12] A. Gorbenko and V. Popov: Appl. Math. Sci. Vol. 7 (2013), P. 651

[13] V. Popov: Appl. Math. Sci. Vol. 6 (2012), p. 6587

[14] A. Gorbenko, V. Popov and A. Sheka: Engineering Letters vol. 19 (2011), p. 169

[15] Information on http://www.neatorobotics.com/

Applied Mechanics and Materials Vol. 565 (2014) pp 198-204

doi:10.4028/www.scientific.net/AMM.565.198

Single-machine Rescheduling of New Orders with Learning and Deterioration Effects Consideration

Chiamin Pai[1,a], Yuling Liu[2,b] and Choujung Hsu[3,c,*]

[1,3]Department of Industrial Engineering and Management, Nan Kai University of Technology, Nantou 542, Taiwan, R.O.C.

[2]Department of applied foreign languages, Nan Kai University of Technology, Nantou 542, Taiwan, R.O.C.

[a]charming120599@gmail.com, [b]lindaliu@nkut.edu.tw, [c,*]jrsheu@nkut.edu.tw

Keywords: Rescheduling; Single-machine; Learning and deterioration effects; Total completion time

Abstract. This paper explored single-machine rescheduling of new orders with both learning and deterioration effects consideration. According to the literature research, rescheduling means that a set of original jobs has already been scheduled to minimize classical objective, and later a new set of jobs arrives and creates a disruption. Two kinds of constraints, the maximum sequence disruption of the original jobs cannot exceed a fixed number and the maximum time disruption of the original jobs cannot exceed a known value, were examined. The objectives of this paper were to minimize total completion time based on the constraints respectively. We proved that both problems are solved in polynomial time algorithms.

Introduction

In recent years, numerous studies have assessed scheduling problems with simultaneous learning and deterioration (aging) effects because the phenomena can be found in many real-life situations [1]. Examples can be found in financial management, steel production, the car repair or maintenance by a worker, hospital emergency wards, and so on. Lee [2] may be the first researcher who investigated jobs with both deterioration and learning effects on a single-machine. The author proposed two actual processing time models for the jobs. The first actual processing time model of job J_j is $p_{jr} = \alpha_j t r^a$ if it starts at time t and is scheduled in position r in a sequence, where α_j, t and a are the deterioration rate, starting time, and learning rate of job J_j, respectively. The author showed that the optimal schedule can be obtained by the smallest deterioration rate (SDR) principle if the objectives are to minimize makespan, the flow time, and the sum of the lateness, respectively. The second actual processing time model of job J_j is $p_{jr} = \left(p_0 + \alpha_j t\right) r^a$ if it starts at time t and is scheduled in position r in a sequence, where p_0 is the original processing time of each job. The author gave counter examples to explain the SDR principle does not provide the optimal solution for those objectives in the first model. Wang [1] proposed a model of the actual processing time of job J_j is $p_{jr} = \left(\alpha_j + \beta t\right) r^a$ if it starts at time $t \geq 0$ and is scheduled in position r in a sequence, where $a \leq 0$ is the learning index. On the single-machine setting, he showed that the makespan and the total completion time minimization problems can be optimally solved by the well-known rule of SPT, the total weighted completion time minimization problem can be optimally solved by the weighted shortest processing time if jobs have agreeable weights, and the maximum lateness minimization problem can be optimally solved by the earliest due date (EDD) if jobs have agreeable due dates. On the flowshop setting, he showed that several classical objectives minimization problems can be optimally solved in polynomial time under certain conditions. After then, various of the actual processing time model with simultaneous learning and deterioration effects are proposed by Wang and Cheng [3], Wang and Cheng [4],

Cheng et al. [5], Toksar and Guner [6, 7], Yang and Kuo [8, 9], and others. Janiak et al. [10] presented the state of the art of scheduling problems with simultaneous effects of learning and ageing (deterioration). After religious analysis, the authors deemed that the learning and ageing effects are in general long time horizon phenomena observed in repetitive systems. Moreover, scheduling theory concerns either with repetitive short-horizon planning problems or single long-horizon projects. Thus, from real life point of view about applications, there is no sense to consider these scheduling problems, unless an appropriate reasonable practical example is presented.

Since a manufacturing system is stochastic, dynamic, and unexpected events occur, rescheduling is necessary to update a production schedule when the state of the manufacturing system becomes it infeasible or inefficiency. There are various papers concerning rescheduling problems, which have been published before 2003, such as Church and Uzsoy [11], Wu et al. [12], Jain and Elmaraghy [13], Unal et al. [14], and others. Vieira et al. [15] provided an extensive review of rescheduling problems and presented definitions appropriate for most applications of rescheduling manufacturing systems and described a framework for understanding rescheduling strategies, policies, and methods. Hall and Poots [16] explored the problem of rescheduling for new orders on single-machine to minimize the maximum lateness and the total completion time under a limit of the disruption from the original scheduling. Qi et al. [17] gave a formal definition of disruption management for machine scheduling. The authors studied single-machine problem where the shortest processing time rule is optimal for the original problem. Lee et al. [18] studied machine scheduling under disruption with transportation consideration. They discussed several basic problems with different related costs. In each problem, they either provided a polynomial algorithm to solve the problem optimally or showed it is NP-hard. Yuan and Mu [19] examined the rescheduling problem for jobs on a single-machine with release dates to minimize makespan under a limit on the maximum sequence disruption. They show the problem can be solved in polynomial time. Zhao and Tang [20] explored machine scheduling problems with deteriorating jobs under disruption. The objective is to discover weighted sum of total completion time and total tardiness. For the single-machine problems and two parallel machines problems, either a polynomial algorithm or pseudo-polynomial dynamic programming algorithm is provided, respectively. Zhao and Tang [21] investigated two single-machine rescheduling problems with linear deteriorating jobs under disruption. The objective is to minimize the total completion time under a limit of the disruption from the original scheduling. They presented polynomial time algorithms for the problems. Hoogeveen et al. [22] studied single-machine rescheduling for new orders with setup time. They tackled several simple setup time configurations yielding different scheduling problems and proposed optimal polynomial time algorithms or provided NP-hardness proofs.

To the best of our knowledge, there are rare researches on rescheduling problems with both deterioration and learning effects consideration. The scheduling problem studied in this paper was motivated by the manufacturing of the metal processing industry and a distinguished paper of Hall and Poots [16]. In order to study the effects of deterioration and learning simultaneously, we explored the actual processing time model proposed by Yang and kuo [8]. Two polynomial time algorithms are proposed for the problems.

Notations and problem formulation

In this paper we investigated single-machine rescheduling new orders with both learning and deterioration effects consideration. Similar to the notations and problem formulation by Hall and Poots [16] and Zhao and Tang [20], the problem can be stated as follows. Let $J_0 = \{J_1, J_2, ..., J_{n_0}\}$ denote a set of original jobs to be processed non-preemptively on a single-machine. The machine can handle at most one job at a time and cannot stand idle until the last job assigned to it has finished processing. In the model, we assume that the jobs in J_0 have been scheduled optimally to minimize some classical objective and that π^* is an optimal schedule. Let $J_N = \{J_{n_0+1}, J_{n_0+2}, ..., J_{n_0+n_N}\}$ denote a set of new jobs that arrive together at time zero after a schedule for the jobs of J_0 has

been determined, but before processing begins. Let $J = J_0 \cup J_N$ and $n = n_0 + n_N$. Let p_{jr} be the actual processing time of job J_j $(j = 1,2,...,n)$ if it is started at time t and scheduled in position r in a sequence. That is, if J_j is scheduled in position r in a sequence, its actual processing time is

$$p_{jr} = \left(p_j + \alpha t\right) r^a \tag{1}$$

where p_j is the original processing time of J_j, $0 < \alpha < 1$ is a common deterioration rate, t is the starting time of J_j, and $a < 0$ is the learning index. For any schedule σ of the jobs in J, we define the following variables:

$C_j(\sigma)$ = the completion of J_j for $J_j \in J$,

$D_j(\pi^*, \sigma)$ = the sequence disruption of J_j for $J_j \in J_0$,

$\Delta_j(\pi^*, \sigma) = \left|C_j(\sigma) - C_j(\pi^*)\right|$, the time disruption of J_j for $J_j \in J_0$,

where the sequence disruption of J_j in schedule σ is the absolute value of the difference between the positions of that job in σ and π^*. When there is no ambiguity, the above parameters are simplified to C_j, $D_j(\pi^*)$, and $\Delta_j(\pi^*)$, respectively. The following two forms of constraints are considered:

$D_{\max}(\pi^*) \le k$: $\max_{J_j \in J_0}\left\{D_j(\pi^*)\right\} \le k$, the maximum sequence disruption of the jobs cannot exceed k.

$\Delta_{\max}(\pi^*) \le k$: $\max_{J_j \in J_0}\left\{\Delta_j(\pi^*)\right\} \le k$, the maximum time disruption of the jobs cannot exceed k.

In the following, we explored single-machine rescheduling jobs with both learning and deterioration effects to minimize total completion time under a limit on the disruption constraints that were described above respectively. Thus, there are two versions:

$1\left|D_{\max}(\pi^*) \le k,\ p_{jr} = \left(p_j + \alpha t\right) r^a\right| \sum C_j$ and $1\left|\Delta_{\max}(\pi^*) \le k,\ p_{jr} = \left(p_j + \alpha t\right) r^a\right| \sum C_j$.

Optimal solutions

Let $J_{[j]}$, $p_{[j]}$, and $C_{[j]}$ denote the job occupying the *j*-th position in the sequence, the original processing time of *j*-th job, and the completion time of *j*-th job, respectively. For any schedule, applying the results those proposed by Yang and Huo [8], the completion time and the total completion time of $J_{[n]}$ can be calculated respectively by $C_{[n]} = \sum_{r=1}^{n} p_{[r]} z_r$ (2)

and $\sum_{j=1}^{n} C_{[j]} = \sum_{j=1}^{n}\left[\sum_{r=j}^{n}\prod_{i=j+1}^{r}\left(1+\alpha i^a\right)\right] j^a p_{[j]}$ (3)

, where the vector $z_r = r^a \prod_{i=r+1}^{n}\left(1+\alpha i^a\right)$ for $r = 1,2,...,n$, and $\prod_{i=n+1}^{n}\left(1+\alpha i^a\right) = 1$. Since the elements of the vector z_r are already sorted in non-increasing order, by the well-known weight matching approach, hence an optimal schedule for problem $1\left|p_{jr} = \left(p_j + \alpha t\right) r^a\right| \sum C_j$ can be found in which jobs are sequenced in non-decreasing order of basic processing time p_j (i.e. *shortest processing time first rule*, *SPT rule*). Taking advantages of the analysis in the Hall and Poots [16], we proved that the following Property 1 also holds for the proposed problems.

Property 1. For problems $1\left|D_{\max}(\pi^*) \le k,\ p_{jr} = \left(p_j + \alpha t\right) r^a\right| \sum C_j$ and $1\left|\Delta_{\max}(\pi^*) \le k,\ p_{jr} = \left(p_j + \alpha t\right) r^a\right| \sum C_j$, there exists an optimal schedule in which the jobs of J_0 are sequenced in SPT order as in π^*, the jobs of J_N are sequenced in SPT order.

Proof. Consider an optimal schedule σ^* in which the jobs of J_0 are not sequenced in SPT order as in π^*. Let J_i be the job with the smallest index that appears later relative to the other jobs of J_0 in σ^* than in π^* and let $J_j\,(i<j)$ be the last job of J_0 that precedes job J_i in σ^*. Suppose jobs $\tilde{J}_1,\tilde{J}_2,...,\tilde{J}_h$ are processed between J_j and J_i. Let $\tilde{p}_1,\tilde{p}_2,...,\tilde{p}_h$ be the original processing time of jobs $\tilde{J}_1,\tilde{J}_2,...,\tilde{J}_h$, respectively. Let $\tilde{C}_1(\sigma^*),\tilde{C}_2(\sigma^*),...,\tilde{C}_h(\sigma^*)$ be the completion time of jobs $\tilde{J}_1,\tilde{J}_2,...,\tilde{J}_h$ in schedule σ^*, respectively. Let the starting time job J_j be s and be scheduled in the r-th position in σ^*. We have

$C_j(\sigma^*)=s+(p_j+\alpha s)r^a$,

$\tilde{C}_1(\sigma^*)=C_j(\sigma^*)+\left[\tilde{p}_1+\alpha C_j(\sigma^*)\right](r+1)^a$,

$\tilde{C}_2(\sigma^*)=\tilde{C}_1(\sigma^*)+\left[\tilde{p}_2+\alpha\tilde{C}_1(\sigma^*)\right](r+2)^a$,

…

$\tilde{C}_h(\sigma^*)=\tilde{C}_{h-1}(\sigma^*)+\left[\tilde{p}_h+\alpha\tilde{C}_{h-1}(\sigma^*)\right](r+h)^a$, and

$C_i(\sigma^*)=\tilde{C}_h(\sigma^*)+\left[p_i+\alpha\tilde{C}_h(\sigma^*)\right](r+h+1)^a$.

Because π^* is a SPT schedule, $p_i\le p_j$. By interchanging the position of jobs J_j and J_i to get a new schedule $\tilde{\sigma}$, we have

$C_i(\tilde{\sigma})=s+(p_i+\alpha s)r^a$,

$\tilde{C}_1(\tilde{\sigma})=C_i(\tilde{\sigma})+\left[\tilde{p}_1+\alpha C_i(\tilde{\sigma})\right](r+1)^a$,

$\tilde{C}_2(\tilde{\sigma})=\tilde{C}_1(\tilde{\sigma})+\left[\tilde{p}_2+\alpha\tilde{C}_1(\tilde{\sigma})\right](r+2)^a$,

…

$\tilde{C}_h(\tilde{\sigma})=\tilde{C}_{h-1}(\tilde{\sigma})+\left[\tilde{p}_h+\alpha\tilde{C}_{h-1}(\tilde{\sigma})\right](r+h)^a$, and

$C_j(\tilde{\sigma})=\tilde{C}_h(\tilde{\sigma})+\left[p_j+\alpha\tilde{C}_h(\tilde{\sigma})\right](r+h+1)^a$.

Since $C_i(\tilde{\sigma})-C_j(\sigma^*)=(p_i-p_j)r^a\le 0$, we deduce that $C_j(\tilde{\sigma})-C_i(\sigma^*)\le 0$. This means that the value of corresponding objective functions does not increase after the interchange. Since the processed position of jobs J_i and J_j in π^* is i and j, respectively. Assume the processed position of job J_j in $\tilde{\sigma}$ is r_1. If $r_1\ge j$ then $D_j(\pi^*,\tilde{\sigma})=r_1-j$ and $D_i(\pi^*,\sigma^*)=r_1-i$. It implies that $D_j(\pi^*,\tilde{\sigma})<D_i(\pi^*,\sigma^*)$. If $r_1<j$ then $D_j(\pi^*,\tilde{\sigma})=j-r_1$ and $D_j(\pi^*,\sigma^*)=j-(r_1-h)=j-r_1+h$. In either case, because $D_i(\pi^*,\tilde{\sigma})=D_i(\pi^*,\sigma^*)-h$ and $D_j(\pi^*,\tilde{\sigma})\le D_j(\pi^*,\sigma^*)+h$, where h is the difference between the positions of jobs i and j in σ^*, we deduce that $D_{\max}(\pi^*,\tilde{\sigma})\le D_{\max}(\pi^*,\sigma^*)$. Thus, $\tilde{\sigma}$ is feasible and optimal. A finite number of repetitions of this argument shows that there exists an optimal schedule in which the jobs of J_0 are sequenced in SPT order as in π^*. A similar interchange argument establishes that the jobs of J_N can also be sequenced in SPT order. □

Clearly, a schedule for problem $1\left|D_{\max}(\pi^*)\le k,\ p_{jr}=(p_j+\alpha t)r^a\right|\sum C_j$ is feasible if and only if the number of jobs of J_N scheduled before the last job of J_0 is less than or equal to *k*. By the problem formulation, the jobs in J_0 have been scheduled in SPT order as in π^*. Applying the Property 1, problem $1\left|D_{\max}(\pi^*)\le k,\ p_{jr}=(p_j+\alpha t)r^a\right|\sum C_j$ can be solved optimally via the following algorithm.

Algorithm 1.

Step 1: Sequenced each jobs of J_N in SPT order, say π_1.

Step 2: Merging the first k jobs in π_1 with the jobs in π^* to form a new SPT order, say π_2.

Step 3: Placing the last $n_N - k$ jobs of the SPT ordered jobs of J_N at the end of the schedule π_2 accordingly.

The computational complexity of Step 1 requires $O(n_N \log n_N)$ time. Merging two ordered sequences to be a new ordered sequence needs the total number of jobs times $O(1)$, the time complexity. That is, Step 2 needs $O(k+n_0)$ time. The computational complexity of Step 3 is $O(n_N - k)$ time. Thus the overall computational complexity of Algorithm 1 is $O(n+n_N \log n_N)$ time. We concluded that the following Theorem holds.

Theorem 1.

Problem $1\left|D_{\max}(\pi^*) \le k,\ p_{jr} = (p_j + \alpha t) r^a\right| \sum C_j$ ***can be solved in*** $O(n+n_N \log n_N)$ ***time.***

Next, we analyzed problem $1\left|\Delta_{\max}(\pi^*) \le k,\ p_{jr} = (p_j + \alpha t) r^a\right| \sum C_j$. The constraint in the second field can be reduced to $C_j \le C_j(\pi^*) + k$ for $J_j \in J_0$. Therefore, the resulting problem is one of minimizing total completion time, subject to deadline constraints, i.e., problem $1\left| p_{jr} = (p_j + \alpha t) r^a, \tilde{d}_j \right| \sum C_j$, where $\tilde{d}_j = C_j(\pi^*) + k$ for $J_j \in J_0$ and $\tilde{d}_j = \infty$ for $J_j \in J_N$. When $\alpha = 0$ and $a = 0$, Smith [23] shows that this problem is solved by a backward scheduling procedure in which at each iteration a feasible job with largest processing time is sequenced last. Clearly, a schedule σ for problem $1\left|\Delta_{\max}(\pi^*) \le k,\ p_{jr} = (p_j + \alpha t) r^a\right| \sum C_j$ is feasible if and only if $C_j(\sigma) \le C_j(\pi^*) + k$ for $J_j \in J_0$. According to the Property 1, problem $1\left|\Delta_{\max}(\pi^*) \le k,\ p_{jr} = (p_j + \alpha t) r^a\right| \sum C_j$ can be solved optimally via the following algorithm.

Algorithm 2.

Step 1: Sequenced each jobs of J_N in SPT order, say π_1, i.e., $\pi_1 = \{J_{[n_0+1]}, J_{[n_0+2]}, ..., J_{[n]}\}$.

Step 2: Calculate $C_j(\pi^*) + k$ for $J_j \in J_0$ vie equation (2). $\sigma := \pi^*$.

Step 3: For $i = n_0 + 1$ to n

Merging $J_{[i]}$ in π_1 with the jobs in σ to form a new SPT order, say σ.

If $C_j(\sigma) \le C_j(\pi^*) + k$ for $J_j \in J_0$ then $\pi_1 := \pi_1 - \{J_{[i]}\}$ and $i := i + 1$ Else exit.

Next i.

Step 4: Placing the remainder jobs of the SPT ordered in π_1 at the end of the schedule σ accordingly.

Obviously, the computational complexity of Step 1 requires $O(n_N \log n_N)$ time. Step 2-4 can be completed in $O(n)$ time. Therefore, the overall computational complexity of Algorithm 2 is $O(n+n_N \log n_N)$ time. Based on the Property 1, we concluded that the following Theorem holds.

Theorem 2.

Problem $1\left|\Delta_{\max}(\pi^*) \le k,\ p_{jr} = (p_j + \alpha t) r^a\right| \sum C_j$ ***can be solved in*** $O(n+n_N \log n_N)$ ***time.***

Conclusion

In this paper, we explored the single-machine rescheduling of new orders with both learning and deterioration effects consideration. Two forms of constraints were examined. The objectives were to minimize the total completion time according to the constraints, respectively. Results showed that the proposed problems can be solved in polynomial time algorithm. Future research may focus on other scheduling performance measures. It would also be interesting to investigate an extension of the problems to other shop settings.

Acknowledgements

This research was supported in part by the National Science Council of the Republic of China under Grant No. NSC 102-2221-E-252-007.

References

[1] J. B. Wang. Single-machine scheduling problems with the effects of learning and deterioration. Omega Vol. 35 (2007), p. 397-402.

[2] W.C. Lee. A note on deteriorating jobs and learning in single-machine scheduling problems. International Journal of Business and Economics 3 (2004), p. 83-89.

[3] J.B. Wang and T.C E. Cheng. Scheduling problems with the effects of deterioration and learning. Asia-Pacific Journal of Operational Research Vol. 24 (2007a), p. 245-261.

[4] X. Wang and T.C.E. Cheng. Single-machine scheduling with deteriorating jobs and learning effects to minimize the makespan. European Journal of Operational Research Vol. 178 (2007), p. 57-70.

[5] T.C.E. Cheng, C.C. Wu and W.C. Lee. Some scheduling problems with deteriorating jobs and learning effects. Computers & Industrial Engineering Vol. 54 (2008), p. 972-982.

[6] M.D. Toksari and E. Guner. Minimizing the earliness/tardiness costs on parallel machine with learning effects and deteriorating jobs: a mixed nonlinear integer programming approach. The International Journal of Advanced Manufacturing Technology Vol. 38 (2008), p. 801-808.

[7] M.D. Toksari and E. Guner. Parallel machine earliness/tardiness scheduling problem under the effects of position based learning and linear/nonlinear deterioration. Computers & Operations Research Vol. 36 (2009), p. 2394-2417.

[8] D.L. Yang and W.H. Kuo. Single-machine scheduling with both deterioration and learning effects. Annals of Operations Research Vol. 172 (2009), p. 315-327.

[9] D.L. Yang and W.H. Kuo. Some scheduling problems with deteriorating jobs and learning effects. Computers & Industrial Engineering Vol. 58 (2010), p. 25-28.

[10]A. Janiak, T. Krysiak and R. Trela. Scheduling problems with learning and ageing effects: a survey. Decision Making in Manufacturing and Services Vol. 5 (2011), p. 19-36.

[11]L.K. Church and R. Uzsoy. Analysis of periodic and event-driven rescheduling policies in dynamic shops. International Journal of Computer Integrated Manufacturing Vol. 5 (1992), p. 153-163.

[12]S.D. Wu, R.H. Storer and P.-C. Chang. A rescheduling procedure for manufacturing systems under random disruptions. *New Directions for Operations Research in Manufacturing*, Springer-Verlag Berlin Heidelberg, p.292-308 (1992).

[13]A.K. Jain and H.A. Elmaraghy. Production scheduling/rescheduling in flexible manufacturing. International Journal of Production Research Vol.35 (1997), p. 281-309.

[14]A.T. Unal, R. Uzsoy and A.S. Kiran. Rescheduling on a single machine with part-type dependent setup times and deadlines. Annals of Operations Research Vol. 70 (1997), p. 93-113.

[15]G.E. Vieira, J.W. Herrmann and E. Lin. Rescheduling manufacturing systems: a framework of strategies, policies, and methods, Journal of scheduling Vol. 6 (2003), p. 39-62.

[16]N.G. Hall and C.N. Poots. Rescheduling for new orders. Operations Research Vol. 52 (2004), p. 440-453.

[17]X. Qi, J.F. Bard and G. Yu. Disruption management for machine scheduling: The case of SPT schedules. International Journal of Production Economics Vol. 103 (2006), p. 166-184.

[18]C.Y. Lee, J.Y.T. Leung and G. Yu. Two machine scheduling under disruption with transportation considerations. Journal of Scheduling Vol. 9 (2006), p. 35-48.

[19] J.J. Yuan and Y.D. Mu. Rescheduling with release dates to minimize makespan under a limit on the maximum sequence disruption. European Journal of Operational Research Vol. 182 (2007), p. 936-944.

[20]C.L. Zhao and H.Y. Tang. Rescheduling problems with deteriorating jobs under disruptions. Applied Mathematical Modelling Vol. 34 (2010), p. 238-243.

[21]C.L. Zhao and H.Y. Tang. Scheduling deteriorating jobs under disruption. International Journal of Production Economics Vol. 125 (2010), p. 294-299.

[22]H. Hoogeveen, C. Lente and V. Tkindt. Rescheduling for new orders on a single machine with setup times. European Journal of Operational Research, Vol. 223 (2012), p. 40-46.

[23]W.E. Smith. Various optimizers for single-stage production. Naval Research Logistics Quarterly Vol. 3 (1956), p.59-66.

Applied Mechanics and Materials Vol. 565 (2014) pp 205-210

doi:10.4028/www.scientific.net/AMM.565.205

The Output Competition Game between FDI Port Enterprises and Incumbent Port Enterprises

Wenfen Zhang[1, a], Min Tu[2, b] and Wenfeng Sun[3, c]

[1, 2, 3] School of Transportation, Wuhan University of Technology, China

[a]cicizhangwenfen@126.com, [b]tumin0929@sina.com, [c]sunwenfeng2010@163.com

Keywords: Port; FDI; Output competition game; Reaction function

Abstract. With the opening to the outside world, port market entry and exit become relatively free in China. In this context, there will be a game of market entry and anti-entry between foreign direct investment (FDI) port enterprises and incumbent ones. Cournot and Dixit Model were both used to study the output competition game between above two kinds of enterprises. Cournot equilibrium shows that FDI port enterprises' output falls as the its own marginal cost increases but increases as the competitors' marginal cost increases. In Dixit Model, by researching the reaction function based on the production scale, marginal cost and scale cost, the selection conditions of FDI port enterprises' market entry strategy were studied. Results show that enterprises entry strategy selection is relative to the limitation and equilibrium output.

Introduction

Port is the bridge and link to connect the domestic and international market. On April 1, 2002 China cancelled ownership restrictions on port facilities and construction business, in recent years, the foreign investment of port basically showed an increasing trend year by year. With the way of Foreign Investment is becoming more and more diversified, Foreign Investment mainly use Foreign Direct Investment (FDI for short) to enter Chinese port market. In the construction of the Chinese port it plays an important role. It plays an active role at the upgrading concept of technology improving service quality, investment diversification, etc. However, at the same time it is bound to establish competition structure between the host country domestic port enterprises, and occupy a certain market share. There are many ports in our country, in order to attract more supply of goods, "production competition" has become a common strategy of competition between ports of the same area.

The output competition game based on the Cournot model between FDI port enterprises and incumbent port enterprises

Western economics define oligopoly market as market structure that a few companies complete control over an industry. Oligopoly market is considered to be ubiquitous. The limit of the oligopoly market is duopoly market that an industry is controlled by two companies. Augustin Curnot first proposed a mathematical model to examine the so-called duopoly that an industry controlled by two companies. The model was later named Cournot model. Cournot model assumes that oligopoly market with only two manufacturers, provide a particular product; both the companies' total cost and marginal cost is zero (This assumption is not substantial, it also can assume that the two enterprises product in the same cost, and the unit cost is fixed in any involved production range); two companies grasp the market demand, they all face the same linear demand curve; according to the action of opponents, and assumes that opponents continue to behave this way, companies make their own decisions.[1]It suggests that the company's equilibrium output falls as the marginal cost rises, and increases as competition's marginal cost rises. [2]

Now assume that there are only two container port enterprises on the market, the enterprise 1 is port enterprise with foreign investment, enterprise 2 is the incumbent port enterprise, they compete in output, each company regard opponents' outputs as fixed, then select the output to maximize its own

profit. Assume that the output of two ports respectively is q_1 and q_2, market demand function is P (Q) = a - bQ.

P and Q respectively are the port cost (price) of unit TEU and the container throughput, a and b are positive constants, $Q=q_1+q_2$； make P = 0, get Q = a/b. Make d= a/b, obviously d represent the market capacity. And assume that the marginal cost is constant, namely $MC_1 = c_1$, $MC_2 = c_2$, and enterprise cost function is $C(q_i) = c_i q_i (i= 1, 2)$, then the company's profit function is:

$$\pi_1(q_1,q_2)=q_1P(Q)-c_1q_1 \tag{1}$$

$$\pi_2(q_1,q_2)=q_2P(Q)-c_2q_2 \tag{2}$$

The first order conditions of profit maximization are:

$$\frac{\partial \pi_1}{\partial q_1} = P(Q) + q_1 \frac{\partial P(Q)}{\partial q_1} - c_1 = 0 \tag{3}$$

$$\frac{\partial \pi_2}{\partial q_2} = P(Q) + q_2 \frac{\partial P(Q)}{\partial q_2} - c_2 = 0 \tag{4}$$

Due to $Q = q_1+q_2$, and the another port company's production is fix, the first-order condition equations can be written separately $q_1 = R_1 (q_2)$, $q_2 = R_2 (q_1)$. They respectively represent the best output of each company under the premise of regarding opponents' outputs as fixed. In the Cournot model, this kind of function is called reaction function. Stay the known linear demand function $P(Q) = a - b(q_1+q_2)$ and its partial derivative into the first order condition equation, can get the following reaction function respectively:

$$q_1 = R(q_2) = \frac{a - bq_2 - c_1}{2b} \tag{5}$$

$$q_2 = R(q_1) = \frac{a - bq_1 - c_2}{2b} \tag{6}$$

Simultaneous solution of equation (5) and (6) can get the Cournot equilibrium output of two port companies respectively:

$$q_1^* = \frac{a - 2c_1 + c_2}{3b} \tag{7}$$

$$q_2^* = \frac{a - 2c_2 + c_1}{3b} \tag{8}$$

The Cournot equilibrium indicates that the output of port enterprise with foreign investment falls as its marginal cost rises, and increases as competition's marginal cost rises. The reason of the former is intuitive, and the latter is that the higher marginal cost makes the incumbent port enterprise reduce its output. This gives foreign port enterprise larger surplus demand space, thus further encourage foreign ports to expand production. At the same time, because FDI port enterprises have the advantage of technology, capital and management and its large-scale investment in the host country (sunk costs), make the threat of its expansion has credibility and further reduce its marginal cost in the host country. And the incumbent port enterprise in the host country under the competitive threat of FDI port further exposes its disadvantage in capital, technology and management, thus its marginal cost is rising.

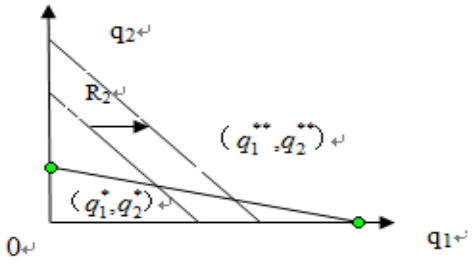

Fig. 1 The exchange of equilibrium point when the FDI investment tends to expand

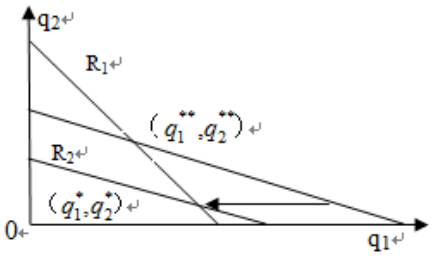

Fig. 2 The exchange of equilibrium point when the host investment tends to expand

Fig. 1 shows that at the beginning of the foreign port enterprises enter the host country, the reaction function of FDI port enterprise and incumbent port enterprise are R_1 and R_2, the market equilibrium output is (q_1^*,q_2^*). High entry barriers make FDI port enterprise marginal cost higher, so at this time the incumbent enterprise is still dominant, performance in figure 1, q_1^* is for far more than q_2^*. With the expanding of FDI port enterprises investing in the host country, scale economy and scope economy make its marginal cost drops rapidly, reaction function translate to the right, the new equilibrium is . As shown in figure 1, $q_1^{**} > q_1^*$, $q_2^{**} < q_2^*$, this means that the FDI port enterprise output levels will increase to occupy more market share, in the case of other condition is constant, the market forces of multinational companies are strengthened. On the other hand, when the marginal cost of FDI port enterprises increase, reaction function of multinational companies translate to the left, its share of the market reduce, market forces relatively weakened.

In the same way, with the given reaction function of the FDI port enterprise, the change of the marginal cost of incumbent enterprise also can produce the same results. Along with the investment of foreign investment port enterprise increasing in the host country, the advantage of the scale economy begins to emerge, make its marginal cost began to drop. While the local enterprises faces the competition pressure of the advanced technology and management experience of multinational corporation, the marginal cost will continue to rise, performance in Fig. 2, the reaction function R2 of the incumbent port enterprise continuously translates to the bottom left, reaching a new equilibrium (q_1^{**},q_2^{**}), $q_1^{**} > q_1^*$, $q_2^{**} < q_2^*$, result the increasing market share of multinational company, the shrinking market share of domestic company. Local company will slow their competitive momentum, reduce their output, release part of his own market, result the improvement of market concentration of our country.

However, for incumbent port enterprises, will have to reduce their output, until the FDI port enterprises to fully occupy the whole market share? This depends on the competition of reducing cost, and on the other hand also depends on the supply elasticity of the entire market. Get the deformation formula of the maximize first-order condition:

$$P(Q) - c_1 = -q_1 \frac{\partial P(Q)}{\partial q_1} \tag{9}$$

Divided by P (Q) on both sides:

$$\frac{P(Q)-c_1}{P(Q)} = -\frac{q_1 \frac{\partial P(Q)}{\partial q_1}}{P(Q)} \tag{10}$$

Reduction to $\frac{P(Q)-c_1}{P(Q)} = -\frac{q_1}{Q}\frac{\frac{\partial P(Q)}{\partial q_1}Q}{P(Q)} = -=-\frac{q_1}{Q}\Big/ e_s \ (e_s = -\frac{\frac{\partial Q}{\partial q_1}}{Q}\Big/\frac{\frac{\partial P(Q)}{\partial q_1}}{P(Q)})$ (11)

The left equation reflects the degree of market equilibrium price deviating from the enterprise marginal cost, it is actually a measure of market concentration index, Lerner index (L), the right side of the equation are the enterprise's market share (q_1/Q) and the market supply elasticity of product (e_s).Show that market concentration is directly proportional to the market share of the product, and has a reverse change relationship of market supply elasticity. [3][4]

The output competition game based on the dixit model between fdi port enterprises and incumbent port enterprises

For eliminating competition and protecting their own interests, the incumbent enterprise always has motivation to deter the entry of the potential enterprise; therefore incumbent enterprises will set entry barriers from output, price and other strategic competition variables on potential enterprises. The essence of Dixit model is to consider the existence of sunk cost of the incumbent enterprise, illustrate the strategy of setting up industry entry barrier for incumbent enterprises. [5]

Industry entry barrier is a major feature variable of market structure, it is the factor to prevent new enterprises to enter when incumbent enterprises earn excess profit in a particular industry. B-S-M limit pricing model made by Bain(1949), Sylos-Labili(1962)and Modigliani(1958), described the prevent measures taken by incumbent enterprises, points out that under the premise of scale economy in production technology, through the selected output and not meeting the requirements of scale economy, making potential vendors cannot survive, so as to achieve the aim of prevent potential vendors to enter.

Whether potential entrants enter, depend on whether it will have positive profits when it enters; when the profits are positive, enter, when the profits are zero or negative, don't enter. The incumbent enterprise output that can make the potential entrants have no profit when they enter called limit output.

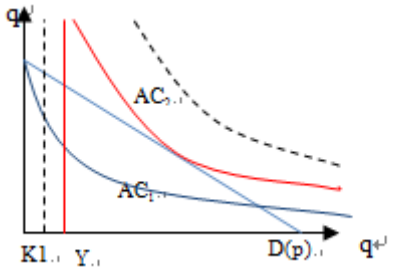

Fig. 3 Average cost curves

Model assumes that:

1) The market demand curve is D (p). The enterprise A exists in the host country market, potential entrance is the FDI port enterprise B. Consumers have no specific preference for any one enterprise.

2) There are two phases; in the first phase enterprise's output is K_1, potential entrance enterprise B can decide whether to enter in the second stage. The two enterprises have the same average cost function.

3) Enterprise B does not consider the change of enterprise A's output, so enterprise B face the demand D (p) - q_1, make Q = K_1 as enterprise B's y coordinate, draw its average cost curve AC_2, the

demand curve of B is part of the market demand curve q = D (p) on the right side of the grid line q = q_1.

Assume that output Y is the limit output, just make B can't get positive profits when it enter the industry, as shown in figure 3, when enterprise A selected output K_1 = Y, the market demand curve and the average cost curve of enterprise B is just tangent, no matter how the output of company B changes, the average cost of production is always higher than the market price, if company B cannot obtain profits, it would not enter. When A selected output K_1 < Y, enterprise B can get positive profits, it will enter the host country market. Conversely, doesn't.

The marginal cost of A and B is fixed constant, the port market is completely competitive. There are two stage T_1 and T_2; the incumbent port enterprises A invest in the phase T_1, the scale of output is K_A; when come to the T_2 stage, potential FDI port enterprises B tries to enter the host country market and has the Cournot competition with enterprise A. [6][7]

Assume that market inverse demand function is P = P (Q), P is the price, $Q = q_A + q_B$ is the total output of industry after the FDI port enterprise B entered the host country market; because of sunk costs, Enterprise A in T_2 stage can only expand output scale and can't reduce, which the marginal cost c1 of enterprise A is fixed within the output scale K_1, if the output scale exceeds K_1 in stage T_2, the exceeded output need to add the corresponding production equipment, σ is the unit investment cost of output scale. C_2 is fixed the marginal cost of enterprise B. Before stage T_2, enterprise B in host countries do not have any means of production investment, the unit output will accompany the σ units cost of investment.

Therefore, the cost functions of enterprise A: $C_A(q_A, K_1) = \begin{cases} c_1 q_A + \sigma K_1, q_A \le K_1 \\ (c_1 + \sigma) q_A, q_A > K_1 \end{cases}$ (12)

The cost function of enterprise B is $C_B(q_B)=(c_2+\sigma)q_B$

According to the equilibrium condition that the marginal cost equals marginal revenue, so the implicit function equation of enterprise A and B are as follows:

$$P(Q) + q_A P'(Q) - \frac{\partial C_A(q_A, K_1)}{\partial q_A} = 0 \quad (13)$$

$$P(Q) + q_B P'(Q) - C_B'(q_B) = 0 \quad (14)$$

Under Cournot competition, the reaction curves of enterprises A and B as shown in figure 4. The cost function of enterprises A is discontinuous in place K_1, when $q_A < K_1$, the marginal cost is c_1, reaction curve is R_A ($q_B \mid c_1$); , when $q_A > K_1$, the marginal cost is $c_1+\sigma$, reaction curve is R_A ($q_B \mid c_1+\sigma$), when $q_A = K_1$, reaction curve is the vertical that connect $R_A(q_B \mid c_1)$ and $R_A(q_B \mid c_1+\sigma)$. The reaction curve of B is R_B ($q_A \mid c_2$). [8]

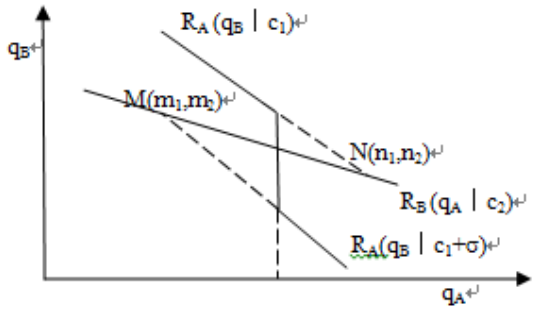

Fig. 4 Enterprises' reaction curve

From Fig. 4 you can see, M and N point are intersection points of enterprise B and A reaction curve, any point between the M and N on the R_B ($q_A \mid c_2$) can be equilibrium point. As long as selected output scale $K_1$of the enterprise A in the T_1 phase is between M and N, its vertical section of reaction curve intersect with reaction curve R_B ($q_A \mid c_2$) of enterprise B, namely exist equilibrium output. Known the level of limit output Y, incumbent enterprises can use tactical settings within a certain range by its own output scale to prevent entry of potential enterprise B.

In figure 4, if $m_1 \leq Y \leq n$, incumbent enterprise just need set the output scale K_1 as $K_1=Y$, can eliminate the possibility of the potential entrance enterprises participating in the competition; if $Y<m_1$, the "natural prevent " happened, the minimum output chosen by incumbent enterprise A is greater than the limit output, B will be unprofitable after enter the market. Due to the investment of enterprise A formed sinking assets in phase T_1, it effectively prevents the entry of enterprise B in the limited range between M and N; if $Y>n$, after incumbent enterprise enter the market, if its high output that maintain the balance of payments is less than the limit output, it's a bad bargain for enterprise A preventing, enterprise B will enter the host country market. [1]

Conclusions and Prospects

In this paper, by using the Cournot and Dixit Model to study the output competition game between FDI port enterprises and incumbent port enterprises, get that FDI port enterprises' output falls as the its own marginal cost increases but increases as the competitors' marginal cost increases. and the entry strategy of FDI port enterprises is related to limitation output and equilibrium output. However, due to the lack of actual data, have not yet applied the conclusion to the actual port economic decision-making, which is the focus of research in the future. This paper uses the game theory to analysis the optimal strategy from the perspective of foreign firms and domestic ports, when foreign capital enters into China's port market. However, the effect of the Chinese government restrictions policy isn't taken into consideration, lacking the analysis of Chinese government policy, so the research still needs to be further improved.

Acknowledgements

The paper is supported by project The regional differentiation of Foreign Direct Investment in China's port and its Influence on the market structure of the port supported by NSFC (41101106).

References

[1] Xiaowo Tang: Journal of University of Electronic Science and Technology of China, Vol.1 (1997), p83-88.In Chinese

[2]Hui Zeng: Journal of Zhejiang Gongshang University, Vol.2 (2008), p60-65 .In Chinese

[3] Jun Xiao: Research and analysis on Cournot competition between random productivity and more enterprises, Hua Zhong University of Science and Technology, Master (2010) .In Chinese

[4] Licheng Qiu,Hong Yong: Contemporary Finance & Economics,Vol.11(2003),p95-99. In Chinese

[5] Hong Zhang: Journal of Shandong University (Philosophy and Social Sciences), Vol.1 (2006), p103-109. In Chinese

[6] Xiao hua Yang, Xia huo song,Luo Yun feng: China Management Science,Vol.3 (2010). In Chinese

[7] Avinash Dixit: The Journal of Political Economy, 97(1989).p. 620-638

[8] He Zhang: Impact on the structure of China's market when multinational companies enter, Tianjin University of Finance and Economics, Master (2009). In Chinese

Applied Mechanics and Materials Vol. 565 (2014) pp 211-216

doi:10.4028/www.scientific.net/AMM.565.211

Research on Parameterized Modeling Technology for the Bolted Joints Structure

Xue Zhai[1, a], Qinggang Zhai[2, b], Jianjun Wang[1, c], Xuguang Fu[3, d]

[1] School of Jet Propulsion, Beihang University, Beijing, 100191, China

[2] Beijing Aeronautical Technology Research Center, Beijing, 100076, China

[3] AVIC Xinxiang Aviation Industries (GROUP) CO. LTD

[a]buaa_zhaixue@163.com, [b]mastercatia@163.com,

[c]wangjianjun@buaa.edu.cn, [d]fuxuguang@163.com

Keywords: Bolted joints structure; Aero-engine; Parameterized modeling; Spring elements; Thin layer elements

Abstract. Bolted joints structures exist in modern mechanical system, it is difficult to simulate the characteristics of the bolted joints accurately and effectively because of their complexity and diversity, which bring a great challenge to the whole structure modeling. Based on theoretical derivation of the bolted joints mechanical characteristics, the parameterized simulation technology and modeling method was used to equivalent simulate the bolted joints and with the example of a certain type of modern turbofan engine to elaborate the application of the parameterized modeling method. The research results have shown that the parameterized modeling method can not only simulate the true characteristics of bolted joints but also can improve calculation efficiency and saving computing cost effectively.

Introduction

Bolted joints are one of important component connections, and hold simple processing, convenient assembly, enduring strong loads, etc. But the looseness, slipping and fracture of bolted joints will directly influence mechanical system security, reliability and dynamic performance [1]. Therefore, the bolted joints structure should be processed and analyzed effectively. However, the performances are different to simulate realistically and accurately, especially for complex mechanical system with a large number of bolted joints because of the obvious nonlinear features of structural stiffness and damping [2]. However, bolted joints play an important role in connecting components, transferring forces and moments, which seriously affect the whole structure vibration characteristics. Thus, how to accurately simulate the true characteristics is a key technology addressed urgently for establishing high-fidelity FE model.

Traditional FE modeling method cannot meet the precision demand and some modeling processes are complex. In order to effectively solve the problem, scholars have done a lot of research work recently [3-6]. The presently modeling methods comprise of non-parametric modeling method and parameterized modeling method. The non-parametric modeling method cannot be applied widely due to the simplification of real structure must be done through experiment; the parameterized modeling method has good versatility, which simulate complex structural characteristics by a simple structure. So this method has been applied in many aspects [7-9]. However, the parameterized modeling method hasn't been employed in the design and analysis of true aero-engine bolted joints structure.

The objective of this paper attempts to build the bolted joints structure FE model accurately with parameterized modeling method. Firstly, based on thin layer elements [10-11] the mechanics characteristics were analyzes and through theoretical derivation the equivalent characteristic parameters have been identified. Then, the parameterized modeling method based on spring elements were researched to equivalent simulates the bolted joints and an example of a certain type of aero-engine was taken to elaborate the application of parameterized modeling method.

The parameterized modeling theory for bolted joints structure

Using parameterized modeling method to simulate actual structure, first of all, it needs to analyze the structure mechanical characteristics and replaces the structure by simplified equivalent parameters, then through parameterized modeling method to simulate the equivalent parameters to achieve the goal of simulating actual structural characteristics equivalently. So firstly the theoretical derivation has carried out on the bolted joints mechanics characteristics based on thin layer elements and the equivalent parameters for simulating different stiffness of the bolted joints were gained, which provide a theory basis for parameterized modeling method.

Parameterized modeling equation

Bolted joints structure has 5 different stiffness, they are the stiffness of tensile, compressive, transverse, bending and torque. The objective of simulating bolted joints properties can be achieved through parameterized modeling method to simulate the 5 stiffness simultaneously. The thin layer elements have a certain thickness; the element stiffness matrix and the element load vector are formed from the node information, and then formed the structure stiffness matrix and load vector. Finally, the statics FE equation can be obtained:

$$\begin{bmatrix} K_{11} & K_{12} & K_{13} & \cdots & K_{1i} & \cdots & K_{1n} \\ & K_{22} & K_{23} & \cdots & K_{2i} & \cdots & K_{2n} \\ & & K_{33} & \cdots & K_{3i} & \cdots & K_{3n} \\ & & & \ddots & \vdots & \vdots & \vdots \\ & & & & K_{ii} & \cdots & K_{in} \\ & & & & & \ddots & \vdots \\ sym & & & & & & K_{nn} \end{bmatrix} \begin{Bmatrix} a_1 \\ a_2 \\ a_3 \\ \vdots \\ a_i \\ \vdots \\ a_n \end{Bmatrix} = \begin{bmatrix} F_1 \\ F_2 \\ F_3 \\ \vdots \\ F_i \\ \vdots \\ F_n \end{bmatrix} \quad (1)$$

In Eq. 1 the structural stiffness matrix K including thin layer elements and other elements.

Bolted joints stiffness analysis

The tension and compression stiffness of bolted joints are as follows:

$$k_N = \frac{F_N}{\Delta l} \quad (2)$$

Based on Eq. 1, the axial stiffness can be simplified to:

$$k_N = \frac{F_N}{x_i} = \boxed{\sum_{m=1}^{k} \oint_{V_m} (A_{11} A_{j1} c'_{11}) dV_m \bullet \frac{x_1}{x_i} + \sum_{m=1}^{k} \oint_{V_m} (A_{21} A_{j1} c'_{11}) dV_m \bullet \frac{x_2}{x_i}} + \ldots + \sum_{m=1}^{k} \oint_{V_m} (A_{i1} A_{j1} c_{11}) dV_m + \ldots + \sum_{m=1}^{k} \oint_{V_m} (A_{n1} A_{j1} c_{11}) dV_m \bullet \frac{x_n}{x_i} \quad (3)$$

Assuming the first two items represent the thin layer elements and the other items represent the non-thin layer elements. It can be seen that for a certain component, the section size and the FE element type are determined, the tension and compressive stiffness are only associated with the axial elastic modulus of the thin layer elements material.

When the bolted joints structure under horizontal load, based on the tension and compression stiffness, the equivalent bending stiffness can be available:

$$k_M = \frac{M}{\theta} = \frac{b^2 k_+ (3 n_{CT} + 1)}{2(n_{CT} + 3)} \quad (4)$$

In Eq. 4, $n_{CT} = k_- / k_+$ is ratio between tension and compression stiffness, b is cylinder diameter. It can be seen that when the section size of the thin layer elements is determined and the nonlinear stiffness is ignored, that is to say the n_{CT} is 1, the bending stiffness k_M can be determined by the axial elastic modulus of the thin layer elements.

The torsional stiffness of bolted joints structure is as follows:

$$k_\theta = \frac{T}{\theta} = \frac{TR}{\Delta l} \quad (5)$$

Based on Eq. 1, the torsional stiffness can be simplified to:

$$k_\theta = \frac{T_{jy}R}{y_i} = \boxed{\sum_{m=1}^{k}\oint_{V_m}(A_{11}A_{j1}c'_{44})dV_m \bullet \frac{y_1 R}{y_i} + \sum_{m=1}^{k}\oint_{V_m}(A_{21}A_{j1}c'_{44})dV_m \bullet \frac{y_2 R}{y_i}} + \ldots + \sum_{m=1}^{k}\oint_{V_m}(A_{i1}A_{j1}c_{44})dV_m \bullet R + \ldots + \sum_{m=1}^{k}\oint_{V_m}(A_{n1}A_{j1}c_{44})dV_m \bullet \frac{y_n R}{y_i} \quad (6)$$

Similarly, when the structure size and the FE element type are determined, the torsional stiffness is only related to the circumferential shear modulus of the thin layer elements material.

The shear stiffness of bolted joints structure is as follows:

$$k_S = \frac{F_S}{\Delta l} \quad (7)$$

Based on Eq. 1, the direction of z and y shear stiffness can be simplified to:

$$k_s = \frac{F_{jz}}{z_i} = \boxed{\sum_{m=1}^{k}\oint_{V_m}(A_{11}A_{j1}c_{66})dV_m \bullet \frac{z_1}{z_i} + \sum_{m=1}^{k}\oint_{V_m}(A_{21}A_{j1}c_{66})dV_m \bullet \frac{z_2}{z_i}} + \ldots + \sum_{m=1}^{k}\oint_{V_m}(A_{i1}A_{j1}c_{66})dV_m + \ldots + \sum_{m=1}^{k}\oint_{V_m}(A_{n1}A_{j1}c_{66})dV_m \bullet \frac{z_n}{z_i} \quad (8)$$

$$k_s = \frac{F_{jy}}{y_i} = \boxed{\sum_{m=1}^{k}\oint_{V_m}(A_{11}A_{j1}c_{44})dV_m \bullet \frac{y_1}{y_i} + \sum_{m=1}^{k}\oint_{V_m}(A_{21}A_{j1}c_{44})dV_m \bullet \frac{y_2}{y_i}} + \ldots + \sum_{m=1}^{k}\oint_{V_m}(A_{i1}A_{j1}c_{44})dV_m \bullet R + \ldots + \sum_{m=1}^{k}\oint_{V_m}(A_{n1}A_{j1}c_{44})dV_m \bullet \frac{y_n}{y_i} \quad (9)$$

Assuming the first two items of Eq. 8 and 9 represent the thin layer elements and the other items represent the non-thin layer elements. For a specific structure component, when the structure size and the FE element type are determined, the shear stiffness is only related to the tangential shear modulus of the thin layer elements material.

Parameterized modeling for bolted joints structure based on spring elements

Using parameterized modeling technology based on thin layer elements to simulate bolted joints structure has the advantages of simple modeling and high computational efficiency. But this kind of modeling method has some disadvantages:

1) Equivalent simulation for bolted joints needs to determine the material attribute values of the thin layer elements based on the test data, which cannot use without test data;
2) For the regular bolted joints, the interface can be easy to add a thin layer element, but for the irregular bolted joints, the interface is difficult to add a thin layer element to simulate.

In order to solve these problems effectively, this paper attempts to use the parameterized modeling method based on spring elements to equivalent simulate the bolted joints structure.

Through the above theoretical derivation, the tension, compression and bending stiffness can be determined by the axial elastic modulus of the thin layer elements, so based on spring elements to add axial spring between bolted joints interface and through adjusting the axial spring stiffness can also simulate the tension, compression and bending stiffness; similarly, adding circumferential spring can simulate the torsional stiffness and adding tangential spring can simulate the shear stiffness. This paper has taken the bolted joints in a certain type of modern turbofan engine as an example to elaborate the practical application of parameterized modeling method.

Parameterized simulation and modeling for bolted joints in a certain type of aero-engine

Structural feature of the bolted joints

The bolted joints structure in the aero-engine rotor system is usually with a centering surface and usually using the non-strict bolts to connect. Some critical joint components need to use the centering surface and strict bolts simultaneously to ensure the connection precision. The centering surface can play a role of positioning and through the tightness connection can increase the radial stiffness. Therefore, the shear load of bolted joints is mainly bear together by the static friction of junction surface and the centering surface, meanwhile, the research results in literature [1] has verified the radial stiffness of this kind of bolted joints is same as the fully coupled structure. As a result, the stiffness changes factor is mainly decided by the axial tension and compression stiffness.

In the bolted joints structure of the aero-engine stator system, due to the existence of tight snap and strict bolts, which make the shear load is mainly withstand by the tight snap and the friction between contact surfaces, so the radial stiffness is also same as the fully coupled structure. As a result, the stiffness changes factor of the bolted joints in stator system is also mainly decided by the axial tension and compression stiffness.

Parameterized simulation and modeling for bolted joints

The bolted joints stiffness factors in the rotor and stator system is mainly determined by the axial tension and compression stiffness. Through the above theoretical derivation, this paper will use the parameterized modeling method of combining with the spring elements and contact nodes constrained to establish the aero-engine FE model.

Parameterized modeling for bolted joints in the rotor system

The bolted joints structure in the high pressure rotor can be shown in Fig. 1. The radial direction of the interface corresponding contact nodes were constrained to simulate the tangential stiffness and the axial springs were added to simulate the axial tension and compression stiffness. In the modeling progress, because the true joint stiffness is determined by the flange and bolts together, so all the 3 row of nodes were selected to add spring elements and the bolted joints parameterized model was established as shown in Fig. 2.

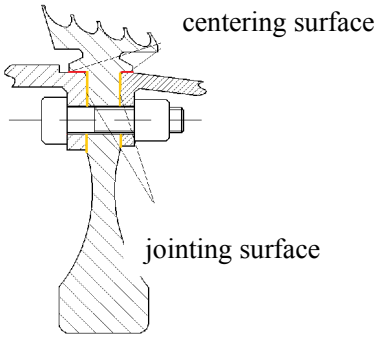

Fig. 1 The bolted joint structure

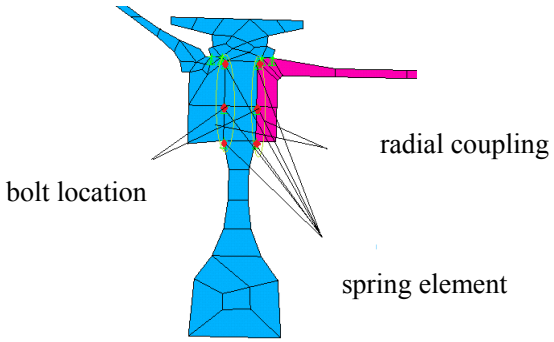

Fig. 2 The bolted joints parameterized model

In order to verify the accuracy of the parameterized modeling method effectively, the contrastive research has carried out between the parameterized model and the fully coupled model. Due to the contact nodes have been added radial constraints for the parameterized model and only the axial direction between contact nodes have been jointed with spring elements, so if the total spring stiffness value in parameterized model reaching a certain level, it will much similar with the fully coupled model. Through the FE modal calculation, the first ten orders natural frequency value of the two kings of model are available as shown in Table 1. The research results show that when the spring stiffness of the parameterized model reach magnitude of 1*10^9N/m, the parameterized model has been much closed with the full coupled model.

Table 1 The natural frequency comparison between fully coupled model and parameterized model [Hz]

Order		1	2	3	4	5	6	7	8	9	10
Natural frequency	Fully coupled	0.000	51.93	51.93	124.10	124.10	205.60	336.60	336.60	357.16	361.11
	Parameterized model	0.000	51.92	51.92	124.00	124.00	205.00	333.28	333.28	357.16	360.95

Through the above modal calculation, it has proved the validity of the parameterized modeling method. However, in the practical application the spring stiffness value need to be set accurately. Table 2 shows the basic parameters data for the typical bolts in the high pressure rotor system, and Φ is the bolt diameter, N is the bolts number, K is the calculated bolted joints stiffness, N_{elem} is the used spring elements number between every contact surface. K_{elem} is the spring elements stiffness value that should be set, and the calculated equation is:

$$K_{elem} = K \times N/N_{elem} \quad (10)$$

The spring parameter can be modified according to Eq. 10. Through calculating, the spring element stiffness should be 2.306 e8 N/m that can simulate the bolted joints in the typical high pressure rotor.

Table 2 The bolted joints parameters and corresponding spring elements parameters

Number	Φ(mm)	N	K(N/m)	N_{elem}	K_{elem}(N/m)
	9.5	38	7.285e8	120	2.306e8

Parameterized modeling for bolted joints in the stator system

The research object of bolted joints in stator system is the connection between low pressure turbine case, combustion chamber rear case and turbine rear bearing case, the structure FE model as shown in Fig. 3. The parameterized model was established shown in Fig. 4.

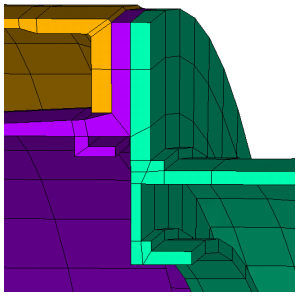

Fig. 3 The bolted joints structure

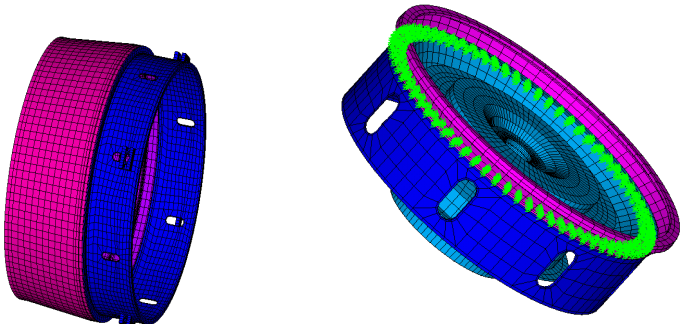

Fig. 4 The bolted joints parameterized model

Through calculating, the first ten order natural frequency value of the fully coupled FE model and the parameterized model are available, as shown in Table 3. By comparison, it can be seen that the natural frequency values between two kinds of model are very close, which proved the validity of the parameterized modeling method and through setting accurate spring stiffness parameter values based on the above spring stiffness calculation method can be equivalent to simulate the bolted joints properties.

Table 3 The comparison between fully coupled model and parameterized model [Hz]

(The first six zero frequency have been passed)

Order		1	2	3	4	5	6	7	8	9	10
Natural frequency	Fully coupled	368.09	368.09	652.31	652.31	997.36	1117.6	1117.6	1172.6	1192.1	1342.8
	Parameterized model	367.60	367.61	651.67	651.67	992.18	1112.1	1112.1	1172.0	1191.4	1335.7

The spring elements parameterized modeling method has a wide range of practical value and strong flexibility. This section has rationally simulated the bolted joints stiffness properties based on the mechanics characteristics of bolted joints structure in aero-engine system. If the research objects have different mechanics characteristics, which need to simulate the tangential stiffness, tension and compression stiffness, bending stiffness and torsional stiffness, it can be added different spring elements between contact nodes and through adjusting these spring stiffness to achieve the purpose of simulating the actual bolted joints stiffness characteristics equivalently.

Conclusion

This paper researched the parameterized modeling technology for bolted joints structure. Firstly, the theoretical derivation has carried out to the mechanical properties of bolted joints based on the thin layer elements, and the equivalent parameters for different stiffness that need to simulate have been identified, which provides theoretical basis for parameterized modeling. And then this paper explored to use the parameterized modeling method based on spring elements to simulate the bolted joints properties. The parameterized modeling method was verified by the modal calculation to a certain

aero-engine. Finally the paper discussed the modeling method that based on the parameterized modeling technology can apply to different bolted joints structure in engineering system, and which has provided effective technical support for the establishment of the FE model and dynamic characteristics analysis of mechanical system.

References

[1] Liu Shuguo,Wang Jun,Hong Jieet al. Dynamics design of the aero-engine rotor joint structures based on experimental and numerical study [M]. ASME Turbo Expo，2010: 49-60.

[2] Morteza Iranzad,Hamid Ahmadian. Identification of nonlinear bolted lap joint models [J]. Computers \& Structures. 2012. 96: 1-8.

[3] J. Kim, J. Yoon, B. Kang. Finite element analysis and modeling of structure with bolted joints [J]. Applied Mathematical Modelling, 2007, 31: 895–911.

[4] J. D. Reid, N. R. Hiser. Detailed modeling of bolted joints with slippage [J]. Finite Elements in Analysis and Design ,2005,41:547–562.

[5] Ming Zhang，Yanyao Jiang，Chu-Hwa Lee。Finite element modeling of self-loosening of bolted joints [J]. Journal of Mechanical Design. 2007, 129:218-226.

[6] M. Jaroslav. Finite element analysis of fastening and joining: a bibliography (1990-2002) .International Journal of Pressure Vessels and Piping.2003, 80: 253-271

[7] M. Yoshimura. Measurement of dynamic rigidity and damping property for simplified joint [J]. Models and Simulation by Computer Annals of the CIRP, 1977, 25(1): 193-198.

[8] M. Yoshimura. Computer-aided design improvement of machine tool structure incorporating joint dynamics data. Annals of the CIRP, 1979, 28(1): 241-246.

[9] W. K. Belivin. Modelling of joints for the dynamic analysis of truss structures. NASA Technical Paper, 1987.

[10] H. Ahmadian,M. Ebrahimi,J. E. Mottersheadet al. Identification of bolted-joint interface models [M]. Proceedings of ISMA，2002: 1741-1748.

[11] H. Ahmadian, John E. Mottershead, Simon Jameset al. Modelling and updating of large surface-to-surface joints in the AWE-MACE structure [J]. Mechanical Systems and Signal Processing, 2006, 20(4) : 868-880.

Applied Mechanics and Materials Vol. 565 (2014) pp 217-222

doi:10.4028/www.scientific.net/AMM.565.217

GNSS RAIM Performance Analysis for World Wide Area

Zilu Wang[1,a], Bin Wu[1,b]

[1]Beijing Aeronautical Science & Technology Research Institute of COMAC, China

[a]wangzilu@comac.cc, [b]binwu@comac.cc

Keywords: GNSS, RAIM, Multi-constellation

Abstract. Multi-constellations provide much better satellite geometrics, thus RAIM algorithms areexpected to achieve greater reliability and integrity performance. This paper mainly discusses different RAIM algorithms and gives simulations of RAIM availability and reliability of standalone GPS and integrated GPS/GLONASS, GPS/BEIDOU and GPS/GLONASS/BEIDOU constellations.The results show that multi-constellation improve RAIM availability and reliability greatly. It is no less than 99.7%for APV I. Also MDB values indicate thatinternal and external reliability of satellite navigation system can be enhanced by multi-constellation.

Introduction

A dramatically improved GNSS(Global NavigationSatellite System) will soon be adapted by civil transportation, satellite based navigation system is becoming more reliable due to better satellite geometries. Thus, in the coming future, more pseudorange measurements will be available than any of us would dreamed of several decades ago.Thus, RAIM (Receiver Autonomous Integrity Monitoring) could be expected to play more and more important role in navigational integrity.

GNSS interoperation studies relate to RAIM on GPS/GLONASS availability over Europe are originate to 1997 by Hein[1]. And then Ryan and Lachapelle[2] studied GPS/GALILEO constellation availability and reliability in 2000. Merino and O'Keefe[3] investigated the integrity, availability and continuity for combined GPS and GALILEO systems separately. Furthermore, Ochieng, Blimenhofer and Lee[4] et gave studies on GPS/GALILEO availability and reliability performance assessmentin 2004 and 2005.

In this paper, to evaluate the performance of GNSS RAIM availability and reliability for worldwide area, two RAIM schemes are used to assess performance levels of standalone GPS and integrated GPS/GLONASS and GPS/GLONASS/BEIDOU systems. One of them is conventional RAIM and another is Advanced RAIM used to handle multi faults which cannot be neglectable in multiple constellations. And comparison, assessment and discussion of simulation results, is also included.

VPL calculation for RAIM

The Linear equation of GNSS measurements is given as[5]

$$y = Hx + \varepsilon \tag{1}$$

Where y is pseudorange mesurements, H presents $n \times 4$ observatory matrix (ie. direction of cosines), we assumes that there are n visible GPS satellites, m GLONASS satellites and k BEIDOU satellites, then[6],

$$H = \begin{bmatrix} a_x^1 & a_y^1 & a_z^1 & 1 & 0 & 0 \\ \vdots & \vdots & \vdots & \vdots & \vdots & \vdots \\ a_x^n & a_y^n & a_z^n & 1 & 0 & 0 \\ a_x^{n+1} & a_y^{n+1} & a_z^{n+1} & 0 & 1 & 0 \\ \vdots & \vdots & \vdots & \vdots & \vdots & \vdots \\ a_x^{n+m} & a_y^{n+m} & a_z^{n+m} & 0 & 1 & 0 \\ a_x^{n+m+1} & a_y^{n+m+1} & a_z^{n+m+1} & 0 & 0 & 1 \\ \vdots & \vdots & \vdots & \vdots & \vdots & \vdots \\ a_x^{n+m+k} & a_y^{n+m+k} & a_z^{n+m+k} & 0 & 0 & 1 \end{bmatrix} \quad (2)$$

And ε is error vector.

Then we can get an optimal solution of X through weighted iterative least squares algorithm:

$$\hat{\mathrm{X}} = (\mathrm{H^T WH})^{-1}\mathrm{H^T W} \quad (3)$$

Here the weight matrix W is the inversion of covariance matrix

$$\Sigma = \mathrm{diag}\{\sigma_1^2, \sigma_2^2, \ldots, \sigma_n^2\} \quad (4)$$

$$\sigma_i^2 = \sigma_{i,URA}^2 + \sigma_{i,iono}^2 + \sigma_{i,tropo}^2 + \sigma_{i,mp}^2 \quad (5)$$

Where, $\sigma_{\mathrm{i,tropo}} = \frac{0.08\times 1.001}{\sqrt{0.002001+sin^2(el)}}$, and $\sigma_{\mathrm{i,mp}} = 0.18 - 0.1 \cdot (el-5)/85$.

The post-fix measurement residuals are needed in the subsequent processing and are given by:

$$\mathrm{r} = \mathrm{S}\varepsilon \quad (6)$$

Where r is the residual vector with one element corresponding to the measurements and S is a residual sensitivity matrix, for a weighted least squares solution is:

$$\mathrm{S} = I - H(H^T \Sigma^{-1} H)^{-1} H^T \Sigma^{-1} \quad (7)$$

The detection of cycle-slips in the carrier-phase measurements will generally be computed in equation above.

$$\sigma = \sqrt{\frac{r^T r}{n-4}} = \sqrt{\frac{SSE}{n-4}} \quad (8)$$

According to statistic distribution theory, SSE/σ_0^2 obey χ^2 distribution, where the degree of freedom is $\mathrm{n}-4$, and the standard deviation is $\frac{SSE}{\sigma_0}$,then we have following assumption,

1) No fault assumption
   $H_0: E(\varepsilon) = 0$, then $\mathrm{SSE}/\sigma_0^2 \sim \chi^2(n-4)$
2) Faulty assumption
   $H_1: E(\varepsilon) \neq 0$, then $\mathrm{SSE}/\sigma_0^2 \sim \chi^2(n-4, \lambda)$
   if false alarm rate is P_{FA}, then we have following statistic equation,

$$P_r\left(\frac{SSE}{\sigma_0^2} < T^2\right) = \int_0^{T^2} f\chi^2_{(n-4)}(x)dx = 1 - P_{FA} \quad (9)$$

Threshold value could be determined by above equation, $\sigma_T = \sigma_0 T/\sqrt{n-4}$. If $\sigma > \sigma_T$, means that a fault is detected. The vertical protection level and horizontal protection level is used for determining the availability of satellite geometry. On the one hand it guarantees the system availability and the other hand it indicates the quality of satellite geometry, the calculation formula is given by:

$$\mathrm{HPL} = \delta_{HDOP} \times \sigma_0 \times \sqrt{\lambda} \quad (10)$$

$$\mathrm{VPL} = \delta_{VDOP} \times \sigma_0 \times \sqrt{\lambda} \quad (11)$$

Where,

$$\delta_{HDOP} = \max\left(\sqrt{(A_{1i}^{*2} + A_{2i}^{*2})/Q_{vii}}\right) = \sqrt{HDOP_i^2 - HDOP^2} \quad (12)$$

$$\delta_{VDOP} = \max\left(\sqrt{A_{3i}^{*2}/Q_{vii}}\right) = \sqrt{VDOP_i^2 - VDOP^2} \quad (13)$$

Where $A^* = (A^T A)^{-1} A^T$, and then RAIM algorithm availability can be calculated through comparing HPL, VPL to HAL, VAL separately.

VPL calculation for ARAIM

ARAIM is proposed to get rid of multiple faults. It is based on the solution separation method. The VPL of the subset for solution separation method is given by[7]

$$VPL_n = D_n + a_n \quad (14)$$

Where k is the serial number of subset, and D_n is the threshold of detection, and a_n is the probability of missed detection.

For ARAIM algorithm,

$$D_n = K_{ffd,n} \times \sigma_{dV,n} + \sum_{i=1}^{N} |\Delta S_n(3,i)| \times B\_max(i) \quad (15)$$

$$K_{ffd,n} = Q^{-1}\left(\frac{P_{ffd}}{2 \times N}\right) \quad (16)$$

Where $K_{ffd,n}$ is false alarm rate, P_{ffd} is the maximum fault tolerance of the system, Q^{-1} is inverse Gaussian function, N is the number of visible satellites. $\sigma_{dV,n}$ is standard deviation of error in vertical direction.

$$S_n = (H^T M_n W_{URA} H)^{-1} H^T M_n W_{URA} \quad (17)$$

Where M_n is a $n \times n$ diagnose matrix, and W_{URA} is weighted diagonal matrix whose diagonal element is $\sigma_{URA,n}^2$.

The fault-free full-set VPL_0 is given as follow,

$$\mathrm{VPL}_0 = K_{md,0} \times \sigma_{v,0} + \sum_{i=1}^{N} |S_0(3,i)| \times B\_max(i) \quad (18)$$

The ARAIM VPL is derived from the fault-free full-set VPL and the faulted subset VPL, is given as

$$\mathrm{VPL} = \max\{VPL_0, VPL_n\} \quad (19)$$

Availability Assessment Model

A.UERE model

In order to calculate GNSS RAIM availability more precisely, we model measurement errors in different satellite constellation separately. In absence of biases, the pseudorange error is composed as User Equivalent Range Error (UERE) which is included the following errors: orbit determination error, ionosphere residual error, multipath residual error, troposphere residual error and receiver noise residual error.

Future GNSS broadcast ranging signals for users on several frequencies, GPS with L1 and L5, Galileo with E1 and E5b, Beidou with B1, B2 and B3, GLONASS with L1 and L2. The frequency diversity will eliminate the effects of ionospheric delay, so ionospheric error is treated to be ignored. Martinean proposed a model to describe tropospheric model and multi-path error as the function of elevation angle. UERE values are listed in Tab. 1 while URA =1m.

Table 1 GNSS UERE Values

Elev.Angle	5°	10°	15°	20°	30°	50°	60°	90°
GPS	1.99	1.51	1.33	1.21	1.02	1.05	1.01	1.03
Galileo	1.87	1.45	1.45	1.13	1.05	1.01	1.01	1.01
GLONASS	2.01	1.53	1.47	1.15	1.09	1.03	1.03	1.03
Beidou	2.03	1.55	1.47	1.17	1.09	1.03	1.01	1.01

B. Constellation and User Grid Model

Satellites orbit is computed by Satellite Tool Kits (STK) and it is assumed that there are 31 GPS satellites, 24 GLONASS satellites, 24 Galileo satellites and 16 Beidou satellites.

In order to analysis the world wide performance, a high resolution grid is defined. Coefficients are configured with a latitude step of 1 degrees and a longitude step of 1 degrees. There are amount of 32400 user locations in total.

Simulation Results

Due to during the process of precision approaches, VPL is more critical than HPL. The time based VPLs of one user are sorted from small to big, we 99.5^{th} percent value of sorted VPLs are calculated for comparing with Vertical Alert Limit (VAL).Thus VPL are evaluated over worldwide grid of points at 5-minute samples over 24-hour for GPS, Galileo and Beidou constellations. In additional, elevation angle is set to 15°. Two different RAIM algorithm simulation results are shown respectively. Furthermore, internal reliability will be evaluated by using multi-constellations.The worldwide VPL results calculated by RAIM using only GPS constellation are shown in Figure 1, it is clear to see the VPL values are extremely large (over 1000) in some location. Smaller VPL values could be expected by using multi-constellations (GPS, GLONASS, Beidou), it is clearly shown in 99.5% VPL for RAIM(GPS) Figure 2 the maximum VPL value in worldwide is no more than 100.

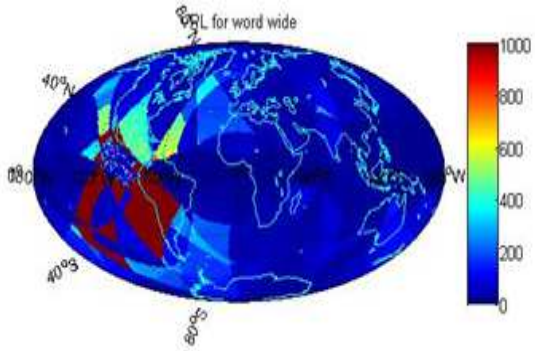

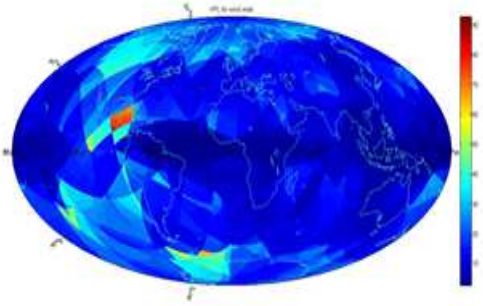

Figure 1 99.5% VPL for RAIM(GPS) Figure 2 99.5% VPL for RAIM(GPS,GLONASS,Beidou)

In order to evaluate the multi-fault RAIM, VPLs of ARAIM are computed in Figure 3, 99.5% VPL for ARAIM(GPS)Figure 4 by using single GPS constellation and GPS, GLONASS, Beidou multi-constellation respectively. From 99.5% VPL for ARAIM(GPS)Figure 4, it is clear that the VPLs are no larger than 17m, much smaller than using standalone GPS navigation system.

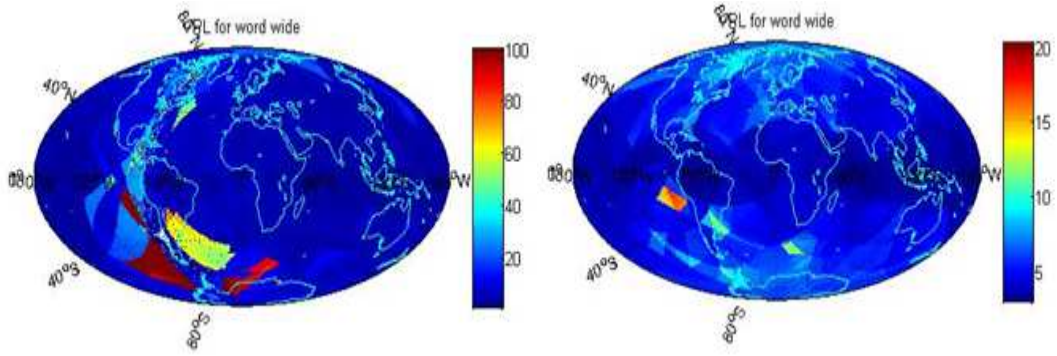

Figure 3 99.5% VPL for ARAIM(GPS)Figure 4 99.5% VPL for ARAIM(GPS,GLONASS,Beidou)

Table 2 Summary of coverage for 99.5% availability for RAIM and ARAIM

	LPV 200	APV I	APV II	CAT I	CAT II	CAT III
RAIM(GPS)	100%	100%	97.99%	16%	0%	0%
RAIM(GPS/GLONASS/Beidou)	100%	100%	100%	97.2%	36.7%	17.3%
ARAIM	100%	100%	98.01%	17.1%	0%	0%
ARAIM(GPS/GLONASS/Beidou)	100%	100%	100%	99.7%	73.2%	37.3%

Table 2 gives the conclusion of RAIM and ARAIM availability for single GPS and multi-constellations,

It is obviously to see GPS/GLONASS/Beidou combined system is far available than standalone GPS.

Summery

VPL computation procedures for conventional RAIM and Advanced RAIM have been described along with the performance measures of reliability. Simulation results show that the GPS/GLONASS/Beidou scenario is much more reliable and available than GPS standalone system. The worldwide. Furthermore, we could get the conclusion from the simulation results that GNSS will provide not only horizontal but also vertical guidance for precision approaches down to APV II without the help of GBAS or SBAS, and with the development of RAIM algorithm, it will enhance the availability and reliability of the GNSS integrity dramatically.

References

[1] Hein G. W., Pielmeier J., Zink T. and Eissfeller B. GPS and GLONASS RAIM Availability

[2] Analysis over Europe, ION GPS-97, Kansas City, Missouri, September 16-19, 465-474

[3] Ryan, S. and G. Lachapelle. Impact of GPS/Galileo Integration on Marine Navigation, IAIN World Congress / ION Annual Meeting, 721-731.

[4] O'Keefe K. Availability and Reliabilty Advantages of GPS/Galileo Integration, ION GPS 2001, Salt Lake City, Utah, September 11-14, 1-10

[5] Lee, H. K., Wang, J., Rizos, C., Barnes, J., Tsujii, T., and Soon, B. K. H., (2002) Analysis of Pseudolite

[6] Augmentation for GPS Airborne Application. ION GPS 2002, Portland, Oregon, September 24-27: 2610-2618.

[7] Ron H, Tenny S, Yunchun Y. A Simple RAIM and Fault Isolation Scheme. Proceedings of ION GPS-2003:802-804.

[8] Zhao C, Ou J and Yuan Y. Positioning Accuracy and Reliability of GALILEO Integrated GPS/GALILEO System Based on Single Positioning Mode. Chinese Science Bulletin, 2005, 50(12): 1252-1260.

[9] Juan B, et al. Prototyping Advanced RAIM for Vertical. 23rd International Technical Meeting of the Satellite Division of the Institute of Navigation, Portland, OR, September 21-24, 2010:285-291.

Applied Mechanics and Materials Vol. 565 (2014) pp 223-227

doi:10.4028/www.scientific.net/AMM.565.223

Emulator of Communication of SATEX-II Satellite with Earth Station

Hector Vargas[1a,] , Jorge Aguilar[1b], Miguel Alonso[2c]

[1] Department of engineering, Universidad Popular Autónoma del Estado de Puebla, UPAEP-CIP,

21 South # 1103, Barrio de Santiago Puebla, Pue. 72410, Mexico,

[a]hectorsimon.varga@upaep.mx,[b]Jorge.Aguilar@upaep.mx,

[2]Centro de Investigación Científica y de Educación Superior de Ensenada Baja Californica CICESE,

Carretera Ensenada-Tijuana No. 3918, Zona Playitas, C.P. 22860, Ensenada, B.C. Mexico. Teléfono: 01(646)175-05-00

[c]aalonso@cicese.edu.mx

Keyword: Emulation, Communication, Sensing satellites, Earth station, Low orbit communication Protocols, Conceptual design.

Abstract. We present a project to encourage students to venture into aerospace engineering projects, mainly in the emulation of communicating with the satellite and the earth station. In this exercise was proposed to use all the features of SATEX-II so they could understand a specific project and thus understand all the elements of the TV and play on to scale their communication with the ground station, with the ultimate to generate a comprehensive understanding. And we present to the conceptual design of the various elements of hardware that will Satex-II Satellite and in the most important aspects to consider in choosing the computer. Space conditions are totally different from terrestrial conditions, so the elements of the satellite's computer should be space technology, which require specific materials and fully redundant architecture for the proper functioning of the satellite, which depends mainly on the assigned mission.

Introduction

Given accelerated growth of the industry Aerospace in Mexico, was created first the Mexican Space Agency and after the Association of this sector and the Mexican Board of aerospace education, with the intention of strengthening this industrial branch. Today more than 150 companies from manufacturing, engineering or maintenance services operating in our country with good results.
The Mexican Aerospace Education Council is the first national network of academic institutions in order to address common issues around the industry.This Council provides for Exchange of teachers, students and programs of study; delve into areas of research, and create networks of collaboration. His ulterior purpose is to refine the answer given to the aerospace industry.The basis of the aerospace industry is human talent: is what the companies have been in our country, today with 38,000 500 employees with competitive salaries.

Behind this talent are educational institutions that make it possible, from the technical levels of high school until technological universities, engineering careers in aeronautics - which today are taught in four schools in our country, to graduates and courses of master's degree offered at some universities.

The UPAEP (Universidad Popular Autónoma del Estado de Puebla), is a private university that encourages the 100% research in different areas of scientific knowledge, one that is growing significantly is the aerospace area. Currently in some courses of Bachelor of engineering Mechatronics and electronics are being developed projects in this area, as the objective of this work, is show an emulation of the satex communication with the ground station.

Emulates communication with SATEX - II satellite and the ground station

Satex-II (Mexican experimental satellites) is a microsatellite in low orbit (LEO-siglas in English) which will be approximately 800 km, its size will be 1 cubic meter, with an extension of 6 mtros (fig. 1).

Fig. 1: View simulated the satex low-orbit (LEO), it also shows the view that it would have with the camera for Earth observation.

He was a model to scale of the satex (fig. 2), and was the emulation of communication with the ground station. This project was installed in the model the following elements: a laptop that emulates a computer Board of the satellite, a camera to emulate the Earth observation sensors of temperature, light sensors, current sensors, gyro control system sensor, actuator system that emulates the inertial wheels of the satellite attitude control, and leds that are controlled from the ground station to display the communication in data transmission.

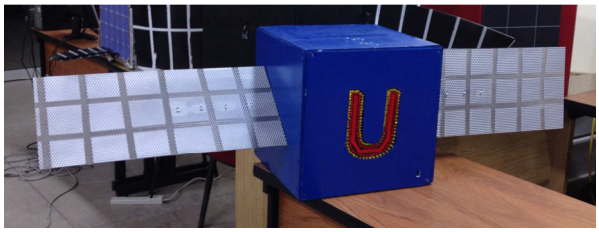

Fig 2: Model of the Satex-II, to show and to emulate the communication with the ground station.

Emulation consisted in making the communication using the TCP/IP protocol between the computer of the ground station and the satellite computer, satellite computer is connected all the above mentioned sensors and sensors data were sent to the ground station. Apply different algorithms to understand images and analysed the times of transmission of these compacted bundles, this in order to send the images to the ground station as quickly as possible.

Requirements for the computer on board the Satex-II satellite

A computer Board (*OBC*) in the SATEX-II satellite must meet several criteria and make an application to the space workable:The computer must provide efficiency of computation for the purpose of the mission, for example, for data processing, control of the vehicle, the handling of data payloads and other functions.It must be mechanically sturdy to withstand the loads induced by the Launcher, with respect to the vibration and shock to the satellite generated by pyrotechnic release devices and the rocket stage separation devices.In orbit, it must support the electromagnetic and thermal conditions. These are especially difficult for missions that have to abandon the belt Van Allen of Earth and even more difficult for missions to the planets near the Sun.

Moreover, the computer must withstand a dose of radiation of high energy particles, and must consider that this dose impacts over the life time of the satellite.The computer must be robust to aggressive chemicals.

The power consumption of the computer is limited by the restrictions imposed system of power generation, it is a difficult challenge for integrated systems as in some cases of historic missions.And finally, the computer should meet the criteria with regard to safety and redundancy.

A. Elements of the computer for the Satex-II

Theelementsthat configure thecomputerforSatex-II are: Microprocessor, Internal SRAM/SDRAM memory, BOOT PROM/EEPROM memory, Memoryprotection, Buses from bus drivers and data, Debugging, services interface interface, Transport interface, Powersupply, Units of reconfiguration, Thermalconditioning and control equipment, Optionallyexternalelements are included: Unit of remote I/O (RIU, its acronym in English), and Mass storage and unit of formatting for scientific data and internal management

B. memory

Each modern *OBC* is equipped with different memory types for different purposes, the OBC for SATEX-II considers the following types of memory:

Memory of boot (Boot):

The OBC of Satex-II will include a storage area of data in non-volatile memory which should persist even after reset the OBC via a power reset. The memory will be implemented as "Memory of only reading programmable" (PROM), or as "PROM erasable electrically" (EEPROM), or how is used in modern systems as "Robust Flash EEPROM to radiation".

Working memory"Random access memory" (RAM), will be used for storage in real time of the executable software, which includes both: control whether software and the operating system itself. In normal operation of the OBC (excluding testing with software of direct load from external sources) the OBSW is copied by the PROM or EEPROM boot loader to RAM and is then initialized.

Memory of security:

This memory will keep the information when turned on and off the system. The OBSW parameters stored in the memory of security is permanently updated with a satellite data configuration key. This report is called "Vector configuration of the satellite" (SCV, acronym in English).

Interconnection of the OBC equipment

To connect the computers in the OBC, there are three types of connections which we mention below:

The first is used to connect computers smart to the OBC, such as simple Thermistors, sensors of Earth and Sun sensors. This is a connection point to point. Oviamente such teams need their separate pair of wires--which complicates the RIU de the OBC, the arneces for the connection of numerous units of the RIU and which increases the total mass of the system.

The next type of connection are the data buses. The OBC of Satex-II for such connections serves the bus driver which is connected to a pair of cables, the bus lines. All the remote computer intelligent, such as the GPS receiver, payloads, the follower of stars, etc., contain their own computers internal or microcontrollers. Thus such edquipos in several cases will provide a data bus interface and can be connected via bus compatible data lines.

MIL-STD-1553B

The military standard MIL-STD-1553B defines the mechanical, electrical and functional characteristics of a serial data bus. It was originally published in 1973 by the US air force and was designed for use in military aircraft, but also has been used in spacecraft "on-board data handling", (OBDH), subsystems.

Decoding of pulse command unit.

There is another reason for the processor CCSDS (Consultative Committee for space data, its acronym in English) is made of pure hardware. As circuit integrated without software (ASICs or FPGAs), provides functionality for emergency commands from the ground where the real flight this OBSW falling, for example due to shock.

This emergency control is achieved through "Command of high priority" (HPC), class over high 1 which is identified by a certain package of commands field, these HPCs codes are identified by the CCSDS processor chip and are routed and called "decoding of pulse command unit", (CPDU). A hardware command comprises 8 bits for channel selection and 8 bits for definition of pulse length.

Units of reconfiguration.
All OBC kernel internal elements as card processors CCSDS, CPU cards, cards of power etc. It will be available with simple redundancy on the satellite. And elements are crossed and coupled which means that N (nominal) CCSDS processor can work with CPU R (redundant) etc. All combinations are possible to provide simple tolerance of failure against any defect of type subcomponent.

Units of reconfiguration which have to activate the selected operational configuration are chip - in most cases ASICS - within the OBC. They control the redundancy of subcomponents OBC between nominal and the redundant switching: either because the command of land; or as reaction of a detected fault (alarm alert-watchdog in English).

Debugging and services interfaces
The CBOs obviously, or in flights or during testing are equipped with a structure of user interface as a keyboard, monitor, drives etc. Therefore as a type of "embedded controller", this pose a challenge for a programmer of OBSW. To enable debugging of code OBSW on the system of modern processors as ERC32, LEON, RS6000 provide interfaces dedicated to debugging as the common tools for standard PCs. For example for ERC32 and LEON the GNU compilers and GDB debuggers are available. However the availability of SW compilers are not sufficient. The system hardware can provide an interface for the exchange of data between the executed code OBSW and debugging tool. Typically the development of cards provides an interface by calling one: unit of debugging support (DSU) or, in circuit debugger (ICD).

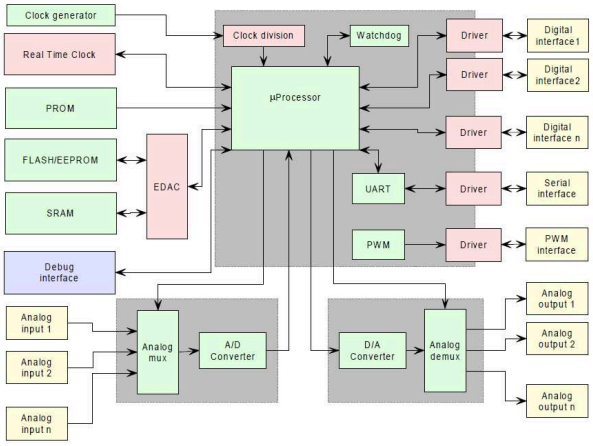

Fig. 3: Conceptual design of the hardware of the computer on-board the Satex-II

Conclusions

The objective of the project is to teach the system of communication between the satellite and the ground station, has it been implemented in courses of engineering in Mechatronics and electronics the UPAEP successfully, has been the enthusiasm of students working in aerospace engineering projects. Therefore, we believe that the UPAEP is committed to the strategies pursued by the Mexican space agency and the Mexican Council of aerospace education to motivate young people in training in this strategic technology area for Mexico.

The conceptual design of the hardware of the computer of the Satex-II, presents a flexibility in terms of the connection of different payloads, and above all which can be visualized as a design modular depending on how many interfaces will have and their interconnections. Therefore, the elements can be placed on the market with affordable prices.

Acknowledgment

The authors thank the support students of Mechatronics Engineering of UPAEP - Andrés Rodríguez, Sara González, Rodolfo García, Carlos Romero, Gerardo Castro, Luis Millán, by making the model and emulation tests.

References

[1] J. R. Martínez Mendoza, "Cabo Tuna" a spatial experience in San Luis Potosí, México: Museum of history of the science of San Luis Potosí, ISBN: 978 - 607-00-2800-7, San Luis Potosí, S. L. P., Mexico, 2010.

[2] A. Pedroza, R. Fournier and D. Vera, "Magnetic torque for attitude control on the SATEX.1 design microsatellite," in Proc. CNES 1995 mécanique Spatiale, Conf. Spaceflight Dynamics., pp. 311-314.

[3] D. Vera, V. Alexandrov, A. Rangel, A. Pedroza, D. Mocencahua and R. Fournier, "Magnetic torque in attitude control of an experimental microsatellite in equatorial orbit", Spaceflight Dynamics 1998 ", Vol. 100 Part II, Advances in the Astronautical Sciences, an American Astronautical Society Publication, 1998, pp.951-954.

[4] Pedroza Meléndez Alejandro, Elsa Chavira Martínez, Héctor Simón Vargas Martínez, Vittorio Zanella Palacios, Alejandro Rojas Lopez, Francisco Javier Mendieta Jiménez and Enrique Pacheco Cabrera, "Project SATEX.2", *in the 1st National Congress of science and aerospace technology, aerospace vehicles, **SOMECYTA**, San Pedro Cholula, Puebla, Mexico, 2011, pp.1-6.*

[5] Pedroza Meléndez Alejandro, Elsa Chavira Martínez and Raúl Fournier Lomas, "*growth of monocrystalline silicon*", science and development, CONACYT, Mexico, no. 70, pp. 25-38, September-October, 1986.

[6] R. Pérez Garcia, "Solar panels", undergraduate thesis, Faculty of engineering chemistry of the University autonomous of Puebla., 1997.

[7] M. C. Beard *et to the*. *Nano Lett*. **10**, 3019 (2010).

[8] E. E. Reber, R. L. Mitchell and C. J. Carter, "Oxygen absorption in the Earth's atmosphere," Aerospace Corp., Los Angeles, CA, Tech. Rep. TR-0200 (4230-46) - 3, Nov. 1968

[9] Celso Gutierrez Martinez, Sergio Vinals Padilla, Saul Santillan Gutiérrez, Francisco Javier Mendieta Jiménez, " "" Design and initial specification microsatellite Mexican SATEX-II", SOMECYTA 2013 ISBN: 978 - 607-95625-2-6.

[10] Tomayko, James: Computers in Spaceflight: The NASA Experience

[11] Tomayko, James : The Apollo guidance computer: Hardware. In: Computers in Spaceflight: The NASA Experience. NASA.

[12] Tomayko, James: Computers in Spaceflight: The NASA Experience,

[13] Hooke, A.J.: In Flight Utilization of the Mariner 10 Spacecraft Computer, J. Br. Interplanetary Society, 29, 277 (April 1976).

[14] Thomas, j. S.: A command and data subsystem for deep space exploration based on the RCA 1802 microprocessor in a distributed configuration Jet Propulsion Laboratory, 1980 Document ID: 19810003139 Accession Number: 81N11647

[15] NASA Office of Logic Design

Applied Mechanics and Materials Vol. 565 (2014) pp 228-232

doi:10.4028/www.scientific.net/AMM.565.228

Errors of Timing Diagram of Automatic Machine

JOMARTOV Assylbek[1, a *]

[1]Kurmagazy street 29, Almaty, Kazakhstan, 050010

[a]legsert@mail.ru

Keywords: automatic machine, timing diagram, error, dimensional chains

Abstract. The paper presents the method of determining of the errors of timing diagram of automatic machine. The timing diagram of automatic machine is represented in a vector form with preservation of the visibility of a linear timing diagram. To determine of the errors of actuation of the mechanisms is used the method of calculating of dimensional chains. The method allows taking into account the errors of operation of mechanisms of automatic machine at design of the timing diagrams.

Introduction

Timing diagram is a sequence of automatic machine operations performed by mechanisms depending on the angular displacement of the main shaft [1-6]. Timing diagram allows determining of the position of each of the executive body at any position of the main shaft (see Fig. 1).

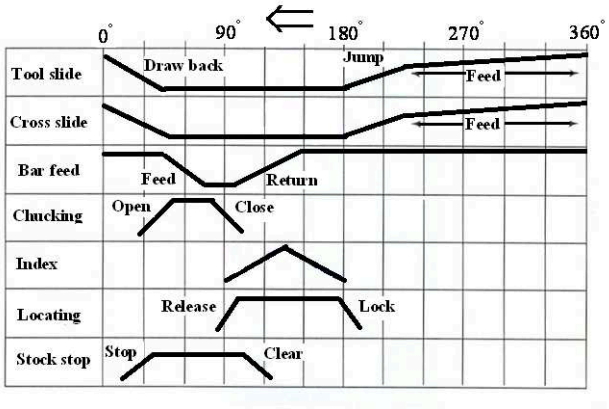

Fig. 1 Linear timing diagram of automatic machine

After the timing diagram of automatic machine is designed are usually, made the prototype and verify sequence operations of the mechanisms in the dynamics. Mechanisms of automatic machine have errors in their work and the timing diagram of a prototype will be different from the designed. We should consider these errors already in the design of timing diagram of automatic machine.

The determination of the errors of timing diagram of automatic machine

Let's consider the determination of the errors of timing diagram of automatic machine for example of the abstract automatic machine has two mechanisms, linear timing diagram is shown in Fig.2.

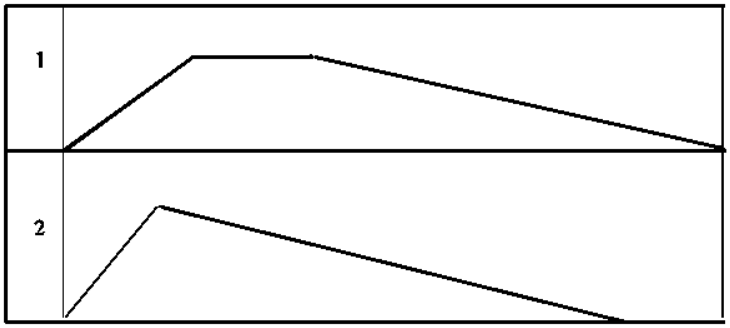

Fig.2. Linear timing diagram of the abstract automatic machine

The first mechanism, for one revolution of the main shaft, executes a motion: open – dwell –close. The second mechanism, for one revolution of the main shaft, executes a motion: open– close - dwell.

We form the vector timing diagram of automatic machine; see Fig. 3 [6].

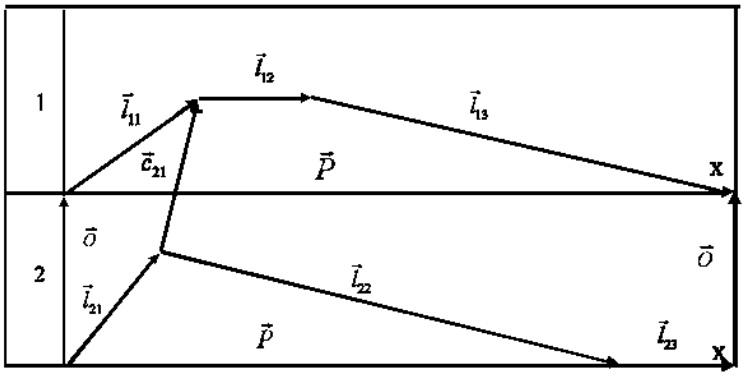

Fig. 3 The vector timing diagram of automatic machine

Timing diagram machines can be represented as vector polygons [6], see Fig 3. We replace the segments linear timing diagram of the vector. Vector directed sequentially from one position to another position of mechanism. We denote the vector of the letter $\vec{\ell}_{ij}$, where n - the number of mechanisms, i - the number of mechanisms, j - the number of position of i - mechanism, m_j - the number of positions of i - mechanism.

The projection of vectors $\vec{\ell}_{ij}$ on the X axis is α_{ij} - phase angles actuation mechanisms. The projection $\vec{\ell}_{ij}$ on the Y axis is the displacement S_{ij} of j - position of i - mechanism.

To explain the parameters α_{ij} and S_{ij} in Fig. 4 shows a diagram of the displacement of mechanism, in the figure denote: α_o - phase angles actuation of mechanism in the position of open, α_d - phase angles actuation of mechanism in the position of dwell, α_c - phase angles actuation of mechanism in the position of close, S_o - the displacement of mechanism in the position of open, S_c - the displacement of mechanism in the position of close.

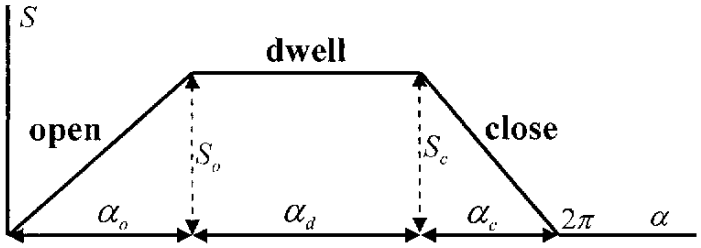

Fig. 4. Diagram of the displacement of mechanism

We introduce the vector $\vec{P}$ connecting the point of beginning and end of the cycle. The projection of the vector $\vec{P}$ on the X axis is 2π on the Y axis is zero. The interaction mechanisms with each other will reflect in the form of vectors of connection $\vec{c}_{ik}$, where $k = 1,...,r_i$, r_i - the number of vectors of connection of i - mechanism.

The projection of vectors of connection to the X-axis is the amount of delay activation mechanism, and the projection on the Y axis is the difference between the displacements of mechanisms.

We impose the timing diagram mechanisms at each other with zero vectors $\vec{O}$, see Fig. 3 connecting the boundary points timing diagram mechanisms for the Y axis.

Set up a system of vector equations describing the works of mechanisms automatic machine, see Fig. 3.

$$\left.\begin{aligned} &\vec{l}_{11} + \vec{l}_{12} + \vec{l}_{13} = \vec{P} \\ &\vec{l}_{21} + \vec{l}_{22} + \vec{l}_{23} = \vec{P} \\ &\vec{c}_{21} = \vec{l}_{11} - \vec{l}_{21} + \vec{O} \end{aligned}\right\} \quad (1)$$

Project the vector equations (1) on the axis X and Y.

$$\left.\begin{aligned} &\alpha_{11} + \alpha_{12} + \alpha_{13} = 2\pi,\ \alpha_{21} + \alpha_{22} + \alpha_{23} = 2\pi \\ &S_{11} + S_{12} + S_{13} = 0,\ S_{21} + S_{22} + S_{23} = 0 \\ &c_{21}^x = \alpha_{11} - \alpha_{21},\ c_{21}^y = S_{11} - S_{21} \end{aligned}\right\} \quad (2)$$

On the phase angles of actuation of mechanisms α_{ij}, and displacements of mechanisms S_{ij} impose constraints

$$\alpha_{ij} \geq \alpha_{ij}^m,\ \mathrm{S}_{ij}^{в} \geq S_{ij} \geq S_{ij}^{н},\ \ i = 1,2;\ \mathrm{j} = 1,2,3 \quad (3)$$

where α_{ij}^m - the minimum allowable phase angles of actuation of mechanisms, $S_{ij}^{в}, \mathrm{S}_{ij}^{н}$ - the upper and lower limits assigned by the designer.

On the projection vectors of connection impose constraints

$$c_{21}^{xв} \geq c_{21}^x \geq c_{21}^{xн},\ c_{21}^{yв} \geq c_{21}^y \geq c_{21}^{yн} \quad (4)$$

where $c_{21}^{xн} = e_{21}^x + \Delta c_{21}^x,\ c_{21}^{yн} = e_{21}^y + \Delta c_{21}^y$, where e_{21}^x, e_{21}^y - the minimum permissible projection vectors of connection, $\Delta c_{21}^x, \Delta c_{21}^y$ - the error of the projections of vectors of connection, $c_{21}^{xв}, c_{21}^{yв}$ - the upper limit imposed by the designer.

Equations (2) and constraints (3, 4) describe the collaboration works of mechanisms (timing diagram) of automatic machine

The projection of vector of connection $\vec{c}_{21}$ on the x-axis determines the sequence actuation of the mechanisms according to timing diagram, see Fig. 3. Let's determine the error of the projection of vector of connection $\vec{c}_{21}$ on the x axis taking into account of the errors of phase angles actuation and displacements of mechanisms.

The errors of phase angles actuation and displacements of mechanisms given in the form:

$$\alpha_{ij}{}^{+\Delta\alpha_{ij}^{B}}_{-\Delta\alpha_{ij}^{H}},\ S_{ij}{}^{+\Delta S_{ij}^{B}}_{+\Delta S_{ij}^{H}},\ \ i=1,2;\ \mathrm{j}=1,2,3,$$

where the errors $+\Delta\alpha_{ij}^{B}$, $-\Delta\alpha_{ij}^{H}$, $+\Delta S_{ij}^{B}$, $-\Delta S_{ij}^{H}$ are determined from experimental data, or by the method proposed in [7].

Module of the vector of connection $\vec{c}_{21}$ is determined by the formula:

$$|\vec{c}_{21}| = |\vec{l}_{11}| \cdot \cos\left(\vec{c}_{21}, \hat{\vec{l}}_{11}\right) - |\vec{l}_{21}| \cdot \cos\left(\vec{c}_{21}, \hat{\vec{l}}_{21}\right),$$

where

$$|\vec{l}_{11}| = \sqrt{\alpha_{11}^2 + S_{11}^2},\ |\vec{l}_{21}| = \sqrt{\alpha_{21}^2 + S_{21}^2},\ c_{21}^x = \alpha_{11} - \alpha_{21},\ c_{21}^y = S_{11} - S_{21},$$

$$\cos\left(\vec{c}_{21}, \hat{\vec{l}}_{11}\right) = \frac{c_{21}^x \cdot \alpha_{11} + c_{21}^y \cdot S_{11}}{|\vec{l}_{11}|\sqrt{(c_{21}^x)^2 + (c_{21}^y)^2}},\ \cos\left(\vec{c}_{21}, \hat{\vec{l}}_{21}\right) = \frac{c_{21}^x \cdot \alpha_{21} + c_{21}^y \cdot S_{21}}{|\vec{l}_{21}|\sqrt{(c_{21}^x)^2 + (c_{21}^y)^2}},$$

We use the method of calculating of dimensional chains [7-11]. Then the vector timing diagram is the dimensional chains, where the vector of connection is the closing link. We have a two dimensional chains, see Fig. 3. Consider the calculation of first dimensional chain, where:

$N_1 = |\vec{l}_{11}|, N_2 = |\vec{l}_{21}|$ - the links, $N_\Sigma = |\vec{c}_{21}|$ - a closing link, $\mathrm{A}_1 = \cos\left(\vec{c}_{21}, \hat{\vec{l}}_{11}\right)$, $\mathrm{A}_2 = \cos\left(\vec{c}_{21}, \hat{\vec{l}}_{21}\right)$ - the transfer functions, δ_t - half of the tolerance, Δ_t - a coordinate of midfield tolerance

$$\delta_t = 0.5 \cdot (\Delta l_{ij}^{B} - \Delta l_{ij}^{H}),\ \Delta_t = 0.5 \cdot (\Delta l_{ij}^{B} + \Delta l_{ij}^{H}),\ i = 1,2;\ j = 1;\ t = 1,2,$$

where

$$\Delta l_{ij}^{B} = \sqrt{(\Delta\alpha_{ij}^{B})^2 + (\Delta S_{ij}^{B})^2},\ \Delta l_{ij}^{H} = \sqrt{(\Delta\alpha_{ij}^{H})^2 + (\Delta S_{ij}^{H})^2}.$$

A closing link is determined by the formula:

$$N_\Sigma = N_1 + N_2$$

The upper and lower deviations of the size of the closing link are determined by formulas [7]:

$$\Delta c_{21}^{B} = \Delta_\Sigma^{'} + \delta_\Sigma^{'};\quad \Delta c_{21}^{H} = \Delta_\Sigma^{'} - \delta_\Sigma^{'}$$

where $\Delta_\Sigma^{'}$ - the coordinate of midfield tolerance of the closing link, $\delta_\Sigma^{'}$ - half of the tolerance of the closing link

$$\Delta_\Sigma^{'} = \sum_{t=1}^{2} A_t(\Delta_i + \beta_t\delta_t) - \beta_\Sigma\delta_\Sigma;\quad \delta_\Sigma^{'} = \frac{1}{K_\Sigma}\sqrt{\sum_{t=1}^{2} A_t^2 K_t^2 \delta_t^2}$$

$$\beta_{\Sigma}=\frac{0.59\cdot\sum_{t=1}^{2}A_t\beta_t\delta_t}{\sum_{t=1}^{2}|A_t|\delta_t};\quad K_{\Sigma}=1+\frac{0.55}{\sum_{t=1}^{2}|A_t|\delta_t}\left(\sqrt{\sum_{t=1}^{2}A_t^2K_t^2\delta_t^2}-\sqrt{\sum_{t=1}^{2}A_t^2\delta_t^2}\right),$$

where K_t, β_t, K_{Σ} are the coefficients are determined for each mechanism according to the method proposed in [7].

Projection vector communication on the x axis shows the delay response of one relative to the other mechanism. The projection of vector of connection $\vec{c}_{21}$ on the x-axis shows the delay of the actuation of the mechanisms. For exclusion an emergency situation we are interested in only the lower deviation of the module of vector of connection Δc_{21}^{H}.

The lower constraint on the projection of vectors of connection on the x-axis is defined by the formula

$$\Delta c_{21}^{x}=\Delta c_{21}^{H}\cdot\cos\left(arctg\frac{S_{21}-S_{11}}{\alpha_{21}-\alpha_{11}}\right)$$

The obtained value of the lower constraint Δc_{21}^{x} should be considered in the synthesis of timing diagram (see Eq. 4.).

Conclusion

The method of determining of the errors of timing diagram of automatic machine allows taking into account the errors of actuation of mechanisms in the synthesis of timing diagram. This will significantly reduce the cost of prototyping machine.

References

[1] J. W. Browne: *The Theory of Machine Tools*, Cassell and Co. Ltd., London, (1965)

[2] D. E. Homer: *Kinematic Design of machines and mechanisms*, McGraw-Hill, New York, (1998)

[3] B. Z. Sandler: *Robotics: designing the mechanisms for automated machinery*, Academic Press, San Diego, (1999)

[4] B. Singh, S. K. Bhattacharya: *Control of machines*, New Age International, New Delhi, (2006)

[5] H. A. Youssef, H. El-Hofy: *Machining technology: machine tools and operations*, Taylor & Francis Group, London, (2008)

[6] A. Jomartov: Vector model of the timing diagram of automatic machine Mech. Sci., 4, 391–396, 2013 (www.mech-sci.net/4/391/2013/ doi:10.5194/ms-4-391-2013)

[7] P. F. Dunaev: *Dimensional Chains* [in Russian], Mashgiz, Moscow (1963)

[8] H. C. Zhang: *Advanced Tolerancing Techniques*, John Wiley & Sons, (1997)

[9] B. R. Fischer: *Mechanical Tolerance Stackup and Analysis,* CRC Press, (2004)

[10] R. C. Dorf, A. Kusiak: *Handbook of design, manufacturing, and automation*, Wiley, (1994)

[11] K.W. Chase: *Multi-dimensional tolerance analysis (automated method).* In: Drake PJR (1999)

Applied Mechanics and Materials Vol. 565 (2014) pp 233-237

doi:10.4028/www.scientific.net/AMM.565.233

Complication Evaluation of Methods of Naval Battlefield Electromagnetic Environment Based on Combat Effectiveness

Xiaofang Shao[1,a], Qi Chen[1, a]

[1]Dept. Information Combat, Dalian Naval Academy, China.

[a]syp793200@163.com

Keywords: Electromagnetic environment, Complication, Operational effectiveness, Index system, Quantitative model

Abstract: Aiming at the lack of unified evaluation criteria and method system to evaluate the naval battlefield electromagnetic environment complication, the methods are raised to work out the problem, such as building methods of index system based on the equipment operational effectiveness, practical evaluation index system ,quantitative index assessment model, evaluation criteria, etc. The methods can satisfy the requirements of naval battlefield electromagnetic environment complication evaluation, and it has reference significance to the navy to operate exercises under complex electromagnetic environment.

Introduction

Complicated electromagnetic environment is a distinct characteristic of naval warfare under the condition of information and constitute the core elements of naval battlefield environment. It restricts the weapon equipment to operate effectively and the troops to improve operation capability, which is not neglectable. Scientific evaluation of naval battle field electromagnetic environment complexity can provide technology and data support for commanders to evaluate the battlefield electromagnetic situation. In this paper, quantitative evaluation methods are raised to evaluate the naval battle field electromagnetic environment complexity, aiming at the characteristics of the naval battle field electromagnetic environment, which can satisfy the requirements and be operated easily.

Evaluation Methods of Electromagnetic Environment Complexity of Naval Battle Field

General technical method for the quantitative evaluation

At present, there are many evaluation methods of the force combat effectiveness, such as index method, the Lanchester equation method, analytic hierarchy process (AHP) and fuzzy comprehensive evaluation method, the computer simulation method, the combination evaluation method [1, 2,3], etc. The evaluation method of the naval battlefield electromagnetic environment complexity based on equipment effectiveness is to locate the equipment in a complicated electromagnetic environment and to observe the performance; the greater the efficiency decline, the more complicated of the electromagnetic environment.

Naval battlefield electromagnetic environment complexity is a "fuzzy" concept [4], the evaluation process are fuzzy, which should be carried out using certain mathematical methods. Efficiency of the equipment should be determined according to the index of the equipment performance, which is a quality of equipment. Actually efficiency evaluation based on the electromagnetic environment complexity is also a kind of multiple attribute decision making problems. As a result, the fuzzy set theory and the evaluation of the multiple attribute decision making method are useful in the evaluation of the naval battlefield electromagnetic environment complexity.

Establishment of hierarchy index system of evaluation

To establish scientific index system is the basis of the complex electromagnetic environment assessment. The efficiency evaluation of electromagnetic environment complexity based on equipment efficiency mainly select the tactical parameters, which are closely related to the equipment operational capability of tactical parameters. Take shipboard radar for example, the hierarchy index system of evaluation is shown in Fig.1.

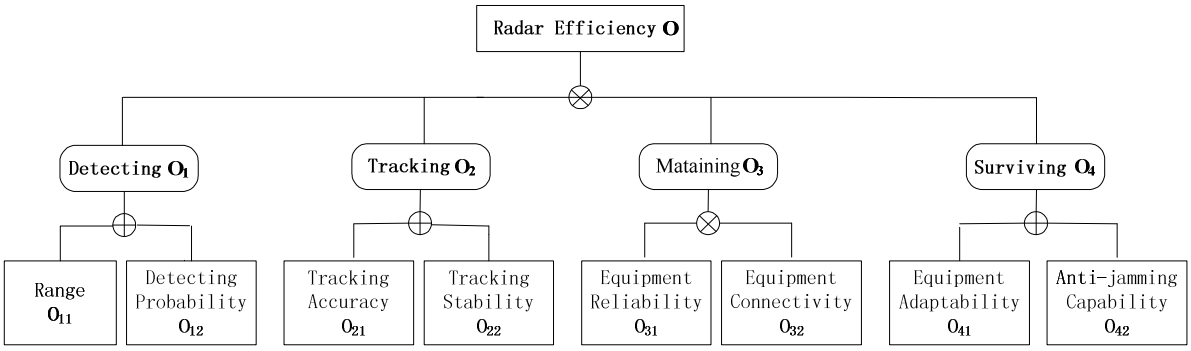

Fig. 1 The evaluation system of shipboard radar

In the index system, "⊕"denotes "the addition of polymerization", indicators in the relatively independent in the analytic hierarchy process (AHP) " ; "⊗" is the strong indicators related to tree, which is used to highlight a short board effect" on the multiplication of polymerization "relationship [5,6,7]. For in addition polymerization model: $y=\sum_{j=1}^{m}\omega_j x_j$ (y is hierarchy index, ω_j weight); Multiplication aggregation model

Method of determining index weight value

Weight concept has obvious fuzzy uncertainty, the determination process should be comprehensive measurement process of a combination of the subjective evaluation and the objective reflect, considering the index (or indicators, factors, etc.) importance in the decision [5-6]. Nowadays, a lot of weight determination methods have been put forward. According to the actual electromagnetic environment complexity evaluation, "the consistency sorting of the weight determining based on the principle of consistency sorting method" has been applied in the paper. The method has many advantages: direct embodiment of the group decision making, isotonic, calculated relatively simple, etc. Specific steps are as follows [7]:

Step 1: any two indicators of same level in three scale are compared by p experts in the same superior subordinate (if O_i is more important than O_k, then $u_{ik}=1,u_{ki}=0$; if O_k is more important than O_i, then $u_{ik}=0,u_{ki}=1$; if O_i and O_k are of the same importance, then $u_{ik}=0.5,u_{ki}=0.5$), constitute p (binary sort qualitative scale matrix).

Step 2: separately examine the necessity and sufficient condition

$$\begin{cases} if u_{ki} > u_{kj}, then u_{ji} > u_{ij} \\ if u_{ki} = u_{kj} = 0.5, then u_{ij} = u_{ji} = 0.5 \\ if u_{ki} < u_{kj}, then u_{ji} < u_{ij} \end{cases}$$

Step 3: if $s_i^l=\sum_{k=1}^{m}u_{ik},i=1,2,\cdots,m$ means the sum of each row, arrange s_i^l in size down, then it is available to get the consistency of the sorting result of each expert. If $\varphi_l(O_i)$ is the number every expert $P_l,l=1,2,\cdots,p$ setting on goal set O according to consistency sorting, then $\varphi(O_i)=\sum_{l=1}^{p}\varphi_l(O_i)$.

Step 4: calculate the weight of indicators $O_i\,(i=1,2,\cdots,m)$to superior hierarchy indicators $\omega_i=\dfrac{\varphi(O_i)}{\sum_{i=1}^{m}\varphi(O_i)}$.

To establish index membership functions

Both membership function analysis method and expert scoring method are applied in the determination of the underlying index in the evaluation index system. The equipment adaptability

index is scored by qualitative and quantitative combined method. The other indicators are calculated by applying the method of membership function analysis.

(1) Detecting range membership function

$$\mu(O_{11}) = \frac{O_{11}}{O_{11}^{'}} = \left(\frac{\mathrm{r}_{\max}}{R_{\max}} \right)^2 \tag{1}$$

Where $r_{\max}$ is the maximum detecting distance of the equipments in battlefield electromagnetic environment; $R_{\max}$ is the theoretical maximum detection distance of the equipment.

(2) Finding probability membership function

$$\mu(O_{12}) = \frac{O_{12}}{O_{12}^{'}} = \begin{cases} \mathrm{n} \Big/ N P_d & \dfrac{\mathrm{n}}{N} \le P_d \\ 1 & \dfrac{\mathrm{n}}{N} > P_d \end{cases} \tag{2}$$

Where n is the total number of objects detected by radar, N is he total number of objects in detection distance, P_d is the theoretical finding probability of radar.

(3) Tracking accuracy membership function

The detection of radar mainly consists of distance accuracy and azimuth accuracy.

Distance accuracy：

$$J_1 = \begin{cases} \dfrac{\Delta D}{|D - D_m|} & |D - D_m| > \Delta D \\ 1 & |D - D_m| \le \Delta D \end{cases} \tag{3}$$

Where D is the radar detecting distance of targets, D_{m} is real radar detecting distance of targets, ΔD is error of the theoretical radar detecting distance of targets.

Azimuth accuracy：

$$J_2 = \begin{cases} \dfrac{\Delta A}{|A - A_m|} & |A - A_m| > \Delta A \\ 1 & |A - A_m| \le \Delta A \end{cases} \tag{4}$$

Where A is the radar detecting azimuth of targets, A_{m} is real radar detecting azimuth of targets, ΔA is error of the theoretical radar detecting azimuth of targets.

We consider that influence of distance accuracy and azimuth accuracy is same, so the tracking accuracy membership function is

$$\mu(O_{21}) = \frac{O_{21}}{O_{21}^{'}} = \frac{J_1 + J_2}{2} \tag{5}$$

(4) Tacking stability membership function

In a complicated electromagnetic environment, the quality of the track decreases due to frequently intermittent loss of shipboard radar target, which affects issued refers or target. The stability of radar tracking target is continuous tracking time of the target between the found point and lost point.

Continuous tracking time：

$$\Delta t = \sum \Delta t_i \, (\Delta t_i \ge t_z) \tag{6}$$

Where Δt_i is the continuous time between the found point and lost point of each tracking of radar, t_z is the shortest time of radar providing target indicating for weapon system, when $\Delta t_i \ge t_z$, the tracking of radar is effective, otherwise, it is of no effect.

Tacking stability membership function is:

$$\mu(O_{22}) = \frac{O_{22}}{O_{22}^{'}} = \frac{\Delta t}{t} \tag{7}$$

Where t is theoretical continuous tracking time of equipments, commonly the time of the whole process from the radar initially finding the target till lose.

(5) Equipment reliability membership function

In operation training, due to the complex electromagnetic environment, the equipment may be system halted or incapable to work, the trustiness descends, it is measured by mean time between failures (MTBF).

The equipment reliability membership function is:

$$\mu(O_{31})=\frac{O_{31}}{O_{31}^{'}}=\begin{cases}\left(1-\dfrac{\sum_i T_i}{T_z}\right)\Big/\dfrac{T_{\mathrm{MTBF}}}{T_{\mathrm{MTTR}}+T_{\mathrm{MTBF}}} & 1-\dfrac{\sum_i T_i}{T_z}\le\dfrac{T_{\mathrm{MTBF}}}{T_{\mathrm{MTTR}}+T_{\mathrm{MTBF}}}\\ 1 & 1-\dfrac{\sum_i T_i}{T_z}>\dfrac{T_{\mathrm{MTBF}}}{T_{\mathrm{MTTR}}+T_{\mathrm{MTBF}}}\end{cases} \tag{8}$$

Where T_i is the continuous time of system halted or breakdown(min), T_z is the total time of system working, T_{MTTR} is the mean time between failure(MTBF).

(6) The equipment anti-jamming membership function

In the circumstance of interference, the performance of radar equipment will be reduced to a certain extent, thus affecting its capability of combat. So according to the interference situation, the equipment anti-jamming are divided into four types of case: the third level of interference (severe), the second level of interference (medium) and first level of interference(light) and no interference.

$$\mu(O_{42})=\begin{cases}0.2 & \text{severe}\\ 0.5 & \text{medium}\\ 0.8 & \text{light}\\ 1 & \text{no anti-jamming}\end{cases} \tag{10}$$

Applications

Calculations of index weight

Adopting the step 1, 2 of part 2.3, the binary qualitative scale matrix of 3 experts can be obtained

$$E^1=\begin{bmatrix}0.5&0&0&1\\1&0.5&1&1\\1&0&0.5&1\\0&0&0&0.5\end{bmatrix},\quad E^2=\begin{bmatrix}0.5&0&1&1\\1&0.5&1&1\\0&0&0.5&0\\0&0&1&0.5\end{bmatrix},\quad E^3=\begin{bmatrix}0.5&0&0&0\\1&0.5&0&1\\1&1&0.5&1\\1&0&0&0.5\end{bmatrix};$$

Adopting the step 3, we can get the result of ordinal consistency: $\varphi(O_1)=8$, $\varphi(O_2)=6$, $\varphi(O_3)=1$, $\varphi(O_4)=3$, so the ordinal consistency of O_1, O_2, O_3 and O_4 is $O_1\succ O_2\succ O_4\succ O_3$.

Adopting the step 4, we can figure out the first level index weight: $\omega_1=0.389$, $\omega_2=0.300$, $\omega_3=0.111$, $\omega_4=0.200$

Similarly, we can figure out the weight of the second level index to the first level:

$\omega_{11}=0.600$, $\omega_{12}=0.400$; $\omega_{21}=0.357$, $\omega_{22}=0.643$; $\omega_{31}=0.524$, $\omega_{32}=0.476$; $\omega_{41}=0.435$, $\omega_{42}=0.565$。

Complexity evaluation

Adopting the method and model introduced of 2.4, we can get the quantitative result of the bottom index.

Table 2 The quantitative value of the bottom index in some environment

O_{11}	O_{12}	O_{21}	O_{22}	O_{31}	O_{32}	O_{41}	O_{42}
0.44	0.83	0.74	0.75	0.93	1	0.7	0.6

According to picture 1, radar effectiveness is $\mu(O)=0.68$.

According to actual naval electromagnetic environment, we define the level of complexity in Tab.3

Table 3 The standard of the level of battle field electromagnetic environment complexity

the level of battle field electromagnetic environment complexity	complexity evaluation
Ⅰ level (simple)	$0.75<\mu(O)\le 1$
Ⅱ level (mild)	$0.5<\mu(O)\le 0.75$
Ⅲ level(moderate)	$0.25<\mu(O)\le 0.5$
Ⅳ level(severe)	$0\le\mu(O)\le 0.25$

The evaluation of the current electromagnetic environment is Ⅱ level (mild complex electromagnetic environment).

Conclusion

According to characteristics of naval battle field electromagnetic environment, the practical application shows that the evaluation method system, with the advantages of maneuverable and scientific, can satisfy requirement for the evaluation of the naval battle field complex electromagnetic environment complexity. The evaluation thought of forces exercise under complicated electromagnetic environment evaluation is of great reference.

References

[1]CHEN Qi, JIANG Ning, CUI Chao. Framework of military exercise based on the combat efficiency[J]. Academic Journal of Dalian Naval Academy, 2011, 34 (5):54-58.

[2]FU Dong, FANG Cheng, WANG Zhenlei. evaluation method of combat capability and efficiency[J]. Military Operations Research and Systems Engineering, 2006.20(4)35-39.

[3]ZHANG Jie, TANG Hong, SU Kai. Study of Methods of Efficiency Evaluation[M].National Defense Industry Press, Beijing, 2009:1-9,23-26.

[4]WU Sanyuan, HOU Zhinan, XIONG Yongkun. Study of Methods of Efficiency Evaluation of Complicated Electronic Environment [J]. Informatization Research, 2010(5):52-54.

[5]LIU Yi, WANG Guoyu, FENG Dejun, etc. Evaluation of Training in Complex Electromagnetic Environment Based on Combat Effectiveness of Equipment [J]. Journal of System Simulation, 2009,21(10):5375-5378.

[6]GUO Yajun. Theory, Methods and application of Multi-Evaluation[M].Science Press, Beijing, 2007:1-28, 79-100, 199-243.

[7]CHEN Qi, JIANG Ning, XU Xianyun. Methods of Navy Exercise Effects Evaluation in Complicated Electronic Environment[J]. Information Countermeasure Journal, 2012.3:67-69.

Applied Mechanics and Materials Vol. 565 (2014) pp 238-242

doi:10.4028/www.scientific.net/AMM.565.238

Research of A New Method to Predict Ocean Wave Spectra

Xinyu Zhang[1, a], Bo Zhou[1, b], Ai-guo Shi[1, c], Meng Liu[1, d]

[1]Dalian Naval Academy, Dalian 116018, China

[a]zhang-xy08@163.com, [b]judyever@sina.com, [c]agshi56@aliyun.com, [d]liumeng9045@163.com

Keywords: Wavelet decomposition; Neural networks; X-band radar; Ocean wave prediction

Abstract: A new method to predict wave spectra is presented in this paper, which is based on X-band radar. Traditional methods to research ocean wave are usually based on the hypothesis that ocean wave is a stationary random process, which is proved to be not right. X-band radar is a remote sensing, ship borne equipment, which can measure wave information in real time conveniently. And the wave spectra measured by this equipment can represent non-stationary of ocean wave. In this paper wavelet decomposition and neural network is combined to predict wave spectra thus the trend how the ocean wave develop can be reflected. The experiment results show that this method is relatively credible.

Introduction

In ocean wave prediction, the predicting objects are usually wave parameters. Relative to these wave parameters like significant wave height, the reflection of ocean wave can be more exact and comprehensive by using wave spectra. Therefore the forecast accuracy could be higher if predicting object was translated into wave spectra.

Up to now, the wave spectra used most continually is statistical spectrum, which is based on the hypothesis that ocean wave is a stationary stochastic process. However, ocean wave is now proved to be non-stationary. So the forecast accuracy cannot be guaranteed if statistical spectrum was used to predict ocean wave. Using real wave spectrum, which is gotten directly by measuring ocean wave, is a better way to improve the forecast accuracy.

However, there is a problem in using real wave spectrum to predict ocean wave. It is very difficult to obtain real wave spectrum in real time. As a new way to observe ocean dynamical environment, X-band wave-measuring radar technique has advantages of low-cost, suitable onboard, convenient for use and high spatiotemporal resolution, which can be a better way to solve this problem.

Real wave spectrum obtainment based on X-band radar

At present, main approach to obtain wave spectrum is on-site observation and direct measurement through various sensors, but these methods cannot be used on warships on voyage, at the same time the requirement for real time data providing cannot be satisfied. Remote sensing technique is another way to obtain wave spectrum which can measure ocean wave spectrum in real time. But in the past the remote sensing equipments were hard to be set onboard and couldn't work well in dark environment or in bad weather [1].

In recent years, X-band wave-measuring radar is proved to be a new powerful tool to monitor ocean wave, which is also a kind of remote sensing technique. It can be set onboard and can provide the data needed in real time.

X-band radar means the high frequency radars the wavelength of which is shorter than 3 centimeters, including fire-control radar and target-track radar.

The surface of the sea is rough. When incidence beam from X-band radar meet the surface and meet the capillary waves whose wavelength are closed to the incidence beam, Bragg scattering occurs. The scattering echo is received by radar receiver and the return is called sea clutter, which contains lots of wave information. In fact, such returns used to be a serious problem in marine navigation because they can interfere echoes from small objects.

In 80's of the 20th century, Hoogemoom[2] and Ziemer[3] et al. developed this theory by digitizing the radar images and finding their two-dimensional Fourier transforms. They found the two-dimensional spectra of the radar images are similar to the spectra from conventional buoy data. So it appears that this radar system can be used to obtain the directional properties of ocean waves. Now there are some mature products emerge like WaMoS II and WAVEX since decades development, which can obtain ocean wave frequency spectrum, directional spectrum and surface currents in real time.

To confirm the reliability of such X-band radar system, researchers in the word carry out lots of comparison experiments. It is generally admitted that dates from buoys is credible, so they use these dates as benchmark. Figure 1 shows the experimental results in Helgoland Germany between significant wave height data from BSH Buoys and WaMoS II.

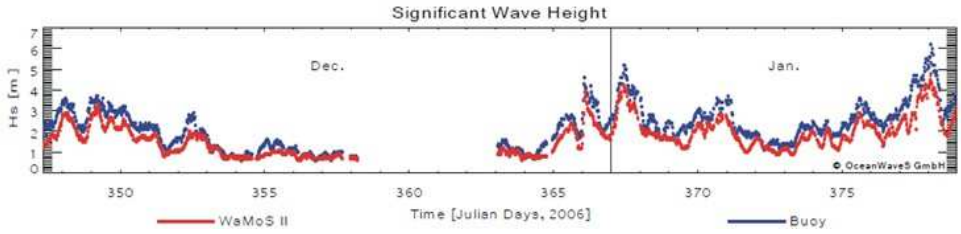

Fig.1 Comparison result of significant wave height

After lots of verification, WAVEX and WaMoS II are proved to have high precision and high reliability. Now the two systems have gotten certificates of approval from DNV and GL Register of shipping.

An X-band wave-measuring radar system contains four parts: X-band radar, A/D converter, PC and corresponding software. In this paper the research is based on data from X-band radar system onboard.

Method of predicting wave spectra based on wavelet analysis

In the progress of ocean wave arising, the condition of stationary stochastic process has been proved to be not real. In nature, ocean wave is a nonlinear stochastic process. Therefore, it is an effective means to draw into nonlinear diagnostic tool in ocean wave prediction using which the forecasting precision can be raised. Artificial neural network (ANN) is one of these nonlinear diagnostic tools, which has the merits of strong adaptability, good self-learning ability, good robustness, and is an important prediction method.

Wavelet analysis is believed to be a breakthrough of traditional Fourier analysis [4]. This theory has a big advantage in processing non-stationary signal as its ability of part signal characteristic in time domain and frequency domain. Conclusions as a result, combination of wavelet analysis and ANN can be used in developing the method of ocean wave spectra prediction.

Up to now there are to ways to combine wavelet analysis and ANN. The first: Applying artificial neural network after data preprocessing using wavelet analysis. The second: Optimizing the learning algorithm of ANN using wavelet analysis. The artificial neural network formed in this way is called wavelet neural networks [5,6] .

Figure 2 shows the data file generated by WaMoS II system, in which frequency spectrum, directional spectrum and surface currents of one short period of time are recorded. Among them frequency spectrum is researched in this paper, in which spectral density is given in 64 different frequencies. WaMoS II system can provide this file every 2 minutes.

```
GAMMA      1.95 CC  Gamma parameter of the JONSWAP spectrum
FMAX      0.350 CC [Hz] < 2* 0.220 Hz Maximum frequency PARA.CFG
DFRE    0.00547 CC [Hz]   Frequency Resolution
IQINT 155 CC                    Qualit Index
EOH    CC ****End of Header****
    0.547E-02    0.000E+00    0.900E+02    0.900E+02
    0.109E-01    0.000E+00    0.900E+02    0.900E+02
    0.164E-01    0.000E+00    0.900E+02    0.900E+02
    0.219E-01    0.000E+00    0.900E+02    0.900E+02
    0.273E-01    0.000E+00    0.900E+02    0.900E+02
    0.328E-01    0.168E-01    0.219E+03    0.441E+02
    0.383E-01    0.466E-01    0.211E+03    0.510E+02
    0.437E-01    0.104E+00    0.209E+03    0.528E+02
    0.492E-01    0.204E+00    0.208E+03    0.532E+02
    0.547E-01    0.360E+00    0.208E+03    0.529E+02
    0.602E-01    0.538E+00    0.208E+03    0.514E+02
    0.656E-01    0.719E+00    0.207E+03    0.501E+02
    0.711E-01    0.854E+00    0.205E+03    0.497E+02
    0.766E-01    0.843E+00    0.206E+03    0.512E+02
    0.820E-01    0.743E+00    0.206E+03    0.539E+02
    0.875E-01    0.632E+00    0.202E+03    0.584E+02
    0.930E-01    0.509E+00    0.193E+03    0.645E+02
    0.984E-01    0.441E+00    0.176E+03    0.678E+02
    0.104E+00    0.432E+00    0.161E+03    0.676E+02
```

Fig.2 Data file provided by WaMoS II

The research in this paper aims at carrying out prediction of ocean wave spectra in 8 hours so that ships can get to know information about ocean environment in advance.

To realize this objective and provide enough accuracy, the substance method is designed as follow.

Step 1: Intercept a period of data long enough(the neural network should be trained long enough) and pre-treat the data.

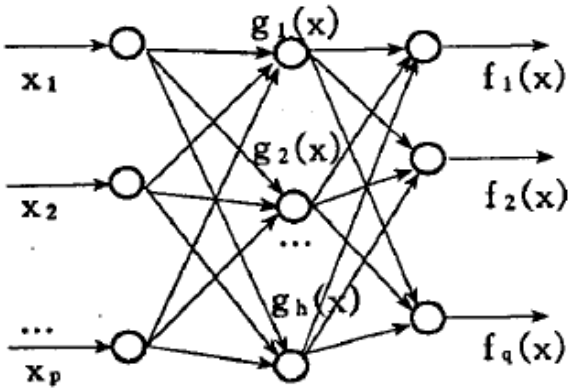

Fig.3 Wavelet neural network structure

Step 2: Combine ANN and wavelet analysis using the second way mentioned above. The wavelet neural network is a feed forward neural network and the number of its hidden layer is one. The network structure is the same with that of RBF network, which is shown in figure 2. And the network is designed to be a multi-input and single-output system.

Activation function of this network is a wavelet function, which is different from RBF network. After experiments, the Morlet function is chosen, which is shown as follow:

$$\psi(t) = \cos(1.75t)\exp(-t^2/2) \tag{1}$$

Step 3: As the forecast object is wave spectrum, the spectrum is processed as an atomic unit. That is to say, inputs and outputs of the system are spectra instead of using spectral density in 64 frequencies respectively. In this way the factors of interaction among different wavelets can be reflected.

Step 4: Divide the data into two parts, the training sample and the testing sample. Suppose the length of data is H hours, then the first H-8 hours is training sample and the rest is testing sample.

Step 5: Input the training sample in the system, compare the output with corresponding measured value and calculate the error function.

Step 6: Correct the weight value of wavelet neural network according to the error function. Repeat this process until the predicted value approximate the expected value(measured value). Then training is completed.

Step 7: Predict the wave spectrum using the trained network, compare the output with the testing sample, and at last evaluate the result.

Prediction result and evaluation

The neural network is used to predict the wave spectrum after well trained, several prediction results are shown in figure 4 and figure 5. In these figures curves formed by circle shows the measured value, and curves formed by plus sign shows the predicted value. It can be clearly seen that the predicted value is fairly near the measured value.

The data of figure 4 is obtained in South China Sea in March 7th, 2012. And the data of figure 5 is obtained in the Indian Ocean in September 19th, 2010. The curves in figure 5 show two single peak, which is the symbol of nonlinear.

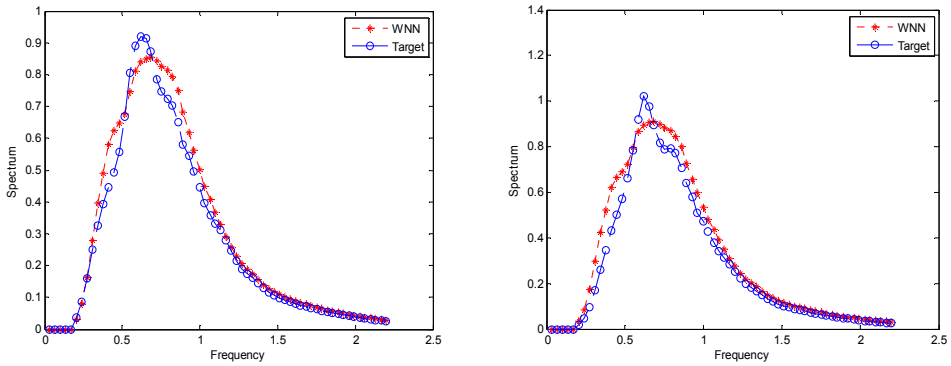

(a) (b)

Fig.4 Prediction results of data in South China Sea in March 7th, 2012

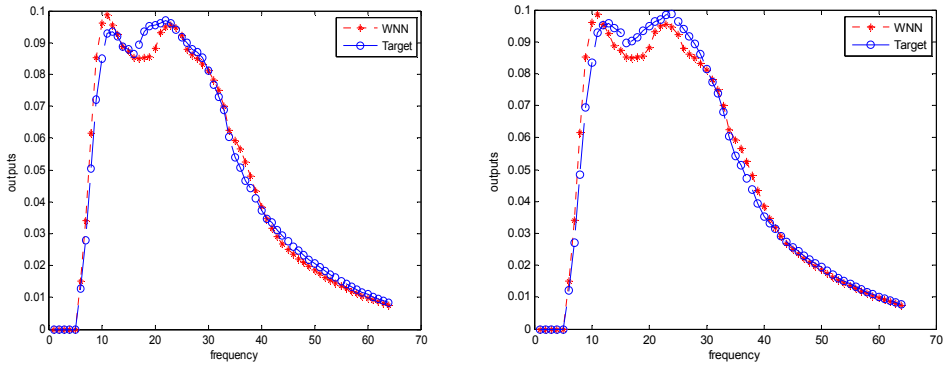

(a) (b)

Fig.5 Prediction results of data in the Indian Ocean in September 19th, 2010

To make the evaluation more general and quantitative, six evaluating indicators are chosen including spectrum peak frequency, spectrum peak value, significant wave height, spectral width, spectral stridency and mean period. Compare the importance of different indicators and endow them different weight in the integrated evaluation index, which is shown as

$$R_x = \sum_{i=1}^{6} K_i \frac{|A_0 - A_i|}{A_0} \tag{2}$$

Where R_x is the integrated evaluation index, K_i is weight coefficient, A_0 is measured value of different indicators and A_i is predicted value in different indicators. Meanwhile, the integrated evaluation value is grated into four criteria. The sum of six weight coefficient is 1. Table 1 shows how the evaluation value is grated.

TABLE 1 .The grating standards of the evaluation value

Value	Grade
$R_x \leq 0.07$	1
$0.07 < R_x \leq 0.15$	2
$0.15 < R_x \leq 0.2$	3
$R_x > 0.2$	4

After testing, the evaluation values in more than 87 percent of the experiments are not worse than grade 2.

Summary and conclusions

In this paper a new method is developed to predict ocean wave spectrum. This proposed method allows us to get information of ocean environment before sailing. The method can improve the accuracy in ocean wave prediction thus it can be used in some situation that high accuracy is required, such as carrier-based aircraft taking off and landing.

References

[1] Wang Shujuan. Ocean wave information extracted from X-band radar images[D].Qingdao: Ocean University of China，2007

[2] Hoogeboom P., W. Rosenthal. Directional wave spectra in radar images[J], International Geoscience and Remote Sensing Symposium, IEEE Geoscience Soc, Munich, June 1-4, 1982

[3] Ziemer F., W. Rosenthal, H. Carlson, Measurements of directional wave spectra by ship radar. IAPSO Symposium, General Assembly Int. Assoc. for Phys. Sci. of the Oceans. Hamburg, Federal Republic of Germany, 1983

[4] Ingrid Daubechies, Li Jianping [translator]. Ten lectures on wavelets [M].Beijing：National Defense Industry Press，2011

[5] Chen Zhe, Feng Tianjin. Research advances on combination of wavelet analysis and neural networks [J].Journal of Electronics, 2000, 20(3): 496-504

[6] Chen Zhe, Feng Tianjin. Research Developments and prospects of wavelet neural networks [J].Journal of Ocean University of Qingdao, 1999, 24(4):663-668

Applied Mechanics and Materials Vol. 565 (2014) pp 243-246

doi:10.4028/www.scientific.net/AMM.565.243

Particle Swarm Optimization Technique for Task-Resource Scheduling for Robotic Clouds

Vladimir Popov[1,a]

[1] Ural Federal University, 620083, Ekaterinburg, Russia

[a] Vladimir.Popov@usu.ru

Keywords: Cloud computing, Robotic cloud, Task-resource scheduling problem, Particle swarm optimization, Runge Kutta neural network.

Abstract. The task-resource scheduling problem is one of the fundamental problems for cloud computing. There are a large number of heuristics based approaches to various scheduling workflow applications. In this paper, we consider the problem for robotic clouds. We propose new method of selection of parameters of a particle swarm optimization algorithm for solution of the task-resource scheduling problem for robotic clouds. In particular, for the prediction of values of the inertia weight we consider genetic algorithms, multilayer perceptron networks with gradient learning algorithm, recurrent neural networks with gradient learning algorithm, and 4-order Runge Kutta neural networks with different learning algorithms. Also, we present experimental results for different intelligent algorithms.

Introduction

Various aspects of cloud computing are among the most rapidly developing areas of computer science (see e.g. [1-3]). In this paper, we consider the task-resource scheduling problem. This is one of the fundamental problems for cloud computing.

It should be noted that the problem is NP-complete [4]. However, there are a large number of heuristics based approaches to scheduling workflow applications (see e.g. [2,5]).

Cloud computing can provide external computing resources to meet the growing computational demands of different applications. In this paper, we consider task-resource scheduling problem for robotic clouds.

A particle swarm optimization algorithm for the task-resource scheduling problem was proposed in [6] (see also [7]). The particle swarm optimization method allows us to optimize a problem by iteratively trying to improve a candidate solution. It is well-known efficient method [8]. It should be noted that the method is extensively used to solve many problems. However, parameters of particle swarm optimization algorithms significantly affect the quality of solutions [8].

An approach to selection of parameters of the particle swarm optimization algorithm for solution of the task-resource scheduling problem was proposed in [2]. In this paper, we consider the task-resource scheduling problem for the robotic cloud and propose new method of selection of parameters of the particle swarm optimization algorithm for solution of the task-resource scheduling problem.

Tasks for the Robotic Cloud

We use enterprise cloud that is intended to solve different robotics problems (see e.g. [9-11]). In our experiments we use different mobile robots. It is assumed that robots have wireless access to resources of the cloud. The robotic cloud allows mobile robots to solve various tasks.

Our mobile robots use a recognition system which consists of a number of separate recognition modules. An intelligent system of selection of recognition modules determines which particular recognition module to be used for solving the current task. In some cases, there are no a recognition module for solution of the current task. In particular, such situation can occur when the current task is

new or the robot is in a new environment. If there are no a recognition module for solution of the current task, then intelligent system of selection of recognition modules formulates the task of generation of a new module. In general, the generation of a new recognition module is a difficult task for the robot. We assume that a generator of recognition modules is used to produce new recognition module. In view of limitations of onboard computing resources of mobile robots, the robot uses only one recognition module at each moment of time. The remaining part of the system is installed on the robotic cloud.

Also, it should be noted that there are a number of robotics tasks that require solutions of NP-hard problems (see e.g. [9,10]). We use SAT-solvers to solve such problems. It is assumed that SAT-solvers are installed on the robotic cloud.

The Particle Swarm Optimization Model

We consider the task-resource scheduling problem as the TRS_HCR problem [2] (see also [5,6,12]). A scheduling heuristic for the TRS_HCR problem was proposed in [5]. This heuristic for dynamically scheduling workflow applications optimizes the cost of task-resource mapping.

The heuristic is based on the solution given by particle swarm optimization technique. The optimization process that proposed in [5] uses two components: the scheduling heuristic (see Algorithm 1 in [5]); the Particle Swarm Optimization steps for task-resource mapping optimization (see Algorithm 2 in [5]). In this paper, we consider only particle swarm optimization part of the heuristic from [5]:

v[i,k+1]=wv[i,k]+c[1]r[1](p[i]-x[i,k])+c[2]r[2](g-x[i,k]),

x[i,k+1]=x[i,k]+v[i,k+1],

Where v[i,k] is the velocity of particle i at iteration k; v[i,k+1] is the velocity of particle i at iteration k + 1; w is the inertia weight; c[j] is an acceleration coefficient, j = 1, 2; r[j] is a random number between 0 and 1, j = 1, 2; x[i,k] is current position of particle i at iteration k; p[i] is the best position of particle i; g is position of the best particle in a population; x[i,k+1] is position of the particle i at iteration k + 1.

Inertia Weight

A method of selection of parameters for the particle swarm optimization for TRS_HCR was proposed in [2]. In particular, a genetic algorithm (CGA) is used for evolving a population of values of c[j]. Another genetic algorithm (RGA) is used for evolving a population of recurrent neural networks that predict values of r[j].

In papers [2,5,6,12], inertia weight w was considered as some constant. However, any clear evidence of such choice was not given. It is clear that we can use some intelligent algorithm for the prediction of the value of w. We consider genetic algorithms (GA), multilayer perceptron networks (MPN) with gradient learning algorithm, recurrent neural networks (RN) with gradient learning algorithm, 4-order Runge Kutta neural networks with the zero-order nonlinear recursive least square learning algorithm (RK[0]) and the first-order nonlinear recursive least square learning algorithm (RK[1]) (see [13]).

Let f(x) be the best fitness value for x iterations and fixed values of w, c[j], and r[j]. Let $f_0(x)$ be the best fitness value for x iterations, fixed values of w, and values of c[j] and r[j] that predicted by CGA and RGA, respectively. Let $f_T(x)$ be the best fitness value for x iterations and values of w, c[j], and r[j] that predicted by T, CGA, and RGA, respectively.

We can consider $f[T,x] = f_T(x) / f(x)$ as a measure of the quality of the convergence of the optimization process with different intelligent algorithms for prediction of values of w, c[j], and r[j]. Selected experimental results for the quality of the convergence of the optimization process with different intelligent algorithms are given in Table 1 and Table 2. In Table 1, we consider only tasks of

generation of recognition modules. In Table 2, we consider tasks of generation of recognition modules and tasks for SAT-solvers.

Table 1. The convergence of the optimization process for tasks of generation of recognition modules.

x	10	20	50	100	200	300	400
F[0,x]	0.752	0.723	0.711	0.704	0.699	0.697	0.696
F[GA,x]	1.241	1.233	1.206	0.724	0.644	0.428	0.092
F[MPN,x]	0.922	0.921	0.920	0.918	0.914	0.911	0.911
F[RN,x]	0.934	0.886	0.841	0.789	0.787	0.786	0.786
F[RK[0],x]	0.942	0.877	0.816	0.754	0.751	0.749	0.748
F[RK[1],x]	0.939	0.864	0.788	0.622	0.615	0.614	0.614

Table 2. The convergence of the optimization process for tasks for SAT-solvers and tasks of generation of recognition modules.

x	10	20	50	100	200	300	400
F[0,x]	0.647	0.598	0.593	0.587	0.581	0.580	0.580
F[GA,x]	1.122	1.118	1.631	0.457	0.111	0.079	0.078
F[MPN,x]	0.971	0.962	0.961	0.959	0.958	0.958	0.958
F[RN,x]	0.993	0.986	0.792	0.789	0.788	0.783	0.781
F[RK[0],x]	0.939	0.871	0.725	0.723	0.721	0.719	0.718
F[RK[1],x]	0.931	0.824	0.573	0.572	0.571	0.571	0.571

It is clear that GA demonstrates low performance for small values of x. However, GA gives us the best performance for large values of x. Also, it should be noted that the performance of neural networks is stabilized for large values of x. In case of SAT-solvers, the performance of neural networks is stabilized faster then for tasks of generation of recognition modules.

It is easy to see that we obtaine the convergence in Table 2 higher then the convergence in Table 1. Therefore, tasks for SAT-solvers are more predictable then tasks of generation of recognition modules.

We can use SAT-solvers to obtain optimal solutions of TRS_HCR (see [2]). It is clear that we can use those optimal solutions as a measure of the quality of solutions that obtained with different intelligent algorithms.

Selected experimental results for the quality of solutions with different intelligent algorithms are given in Table 3 and Table 4. In Table 3, we consider only tasks of generation of recognition modules. In Table 4, we consider tasks of generation of recognition modules and tasks for SAT-solvers.

Table 3. The quality of solutions for tasks of generation of recognition modules.

Algorithms	average	minimum	best
w=const, c[j]=const, r[j]=const	74 %	42 %	88 %
w=const, CGA, RGA	85 %	63 %	97 %
GA, CGA, RGA	91 %	36 %	99 %
MPN, CGA, RGA	86 %	72 %	87 %
RN, CGA, RGA	87 %	83 %	89 %
RK[0], CGA, RGA	89 %	66 %	97 %
RK[1], CGA, RGA	94 %	68 %	97 %

Table 4. The quality of solutions for SAT-solvers and generation of recognition modules.

Algorithms	average	minimum	best
w=const, c[j]=const, r[j]=const	66 %	37 %	72 %
w=const, CGA, RGA	77 %	56 %	81 %
GA, CGA, RGA	78 %	31 %	89 %
MPN, CGA, RGA	89 %	87 %	90 %
RN, CGA, RGA	90 %	89 %	90 %
RK[0], CGA, RGA	92 %	87 %	94 %
RK[1], CGA, RGA	95 %	91 %	96 %

Clearly, Runge Kutta neural networks gives us the best quality of solutions. It should be noted that tasks for SAT-solvers are harder to solve. It is easy to see that neural networks are more predictable.

Summary

In this paper, we have considered the task-resource scheduling problem for robotic clouds. We have proposed a method of selection of parameters of a particle swarm optimization algorithm for solution of the problem. Runge Kutta neural networks gives us the best quality of solutions. However, results of genetic algorithms are also deserved attention. As a future direction of research, we can mention investigation of approaches to improve the predictability of genetic algorithms.

Acknowledgement

This research was partially financially supported by RFBR, research project No. 13-01-00048 a, and under the Agreement 02.A03.21.0006 of 27.08.2013 between the Ministry of Education and Science of the Russian Federation and Ural Federal University.

References

[1] J. Arshad, P. Townend, J. Xu: International Journal of Automation and Computing Vol. 8 (2011), p. 286

[2] A. Gorbenko, V. Popov: International Journal of Automation and Computing Vol. 9 (2012), p. 429

[3] B. Hu, X. Zhang, X. Zhang: JICS Vol. 10 (2013), p. 5945

[4] J.D. Ullman: J. Comput. System Sci. Vol. 10 (1975) p. 384

[5] J. Yu, R. Buyya, K. Ramamohanarao: Studies in Computational Intelligence Vol. 146 (2008), p. 173

[6] S. Pandey, L. Wu, S. M. Guru, R. Buyya, in: Proceedings of the 24th IEEE International Conference on Advanced Information Networking and Applications, IEEE press (2010).

[7] L. Zhang, Y. Chen, R. Sun, S. Jing, B. Yang: IJCIR Vol. 4 (2008), p. 37

[8] A. Jordehi, J. Jasni: J. Exp. Theor. Artif. In. Vol. 25 (2013), p. 527

[9] A. Gorbenko, V. Popov: Advanced Materials Research Vol. 683 (2013), p. 909

[10] V. Popov: AIP Conf. Proc. Vol. 1558 (2013), p. 2083

[11] V. Popov: Applied Mechanics and Materials Vol. 365-366 (2013), p. 946

[12] L. Guo, S. Zhao, S. Shen, C. Jiang: J. Network. Vol. 7 (2012), p. 547

[13] Y.-J. Wang, C.-T. Lin: IEEE T. Neural Networ. Vol. 9 (1998), p. 294

Applied Mechanics and Materials Vol. 565 (2014) pp 247-252

doi:10.4028/www.scientific.net/AMM.565.247

Study on The Grasping Ability and Optimization of Multi-fingered Robot Hands under Different Postures

Haijun Mo[a], Jiajun Zhou[b], Huarong Qiu[c]

School of Mechanical and Automotive Engineering

South China University of Technology

Guangzhou, China; 510640

[a]mohj@scut.edu.cn; [b]Jiajunzhou163@163.com; [c]huayunq@163.com

Keywords: Explosive; Multifingered Hands; Grasping Ability; Grasping Posture

Abstract: A multi-fingered hand has been used in the explosive Disposal Robot to improve the disposal ability of explosive. Grasping ability of the multi-fingered hand is a problem with the change of grasping posture. This paper discusses grasping ability of the multi-fingered robot hand. Screw theory and BP neural network are used to optimize the joint angle of the finger. The most favorite grasping posture is calculated when the multi-fingered robot hand can withstand the largest external wrench. In order to guarantee the explosive not to be exploded under the exceeding grasp force, the weight of the explosive the multi-fingered hand can hold is also discussed in this paper. It is an important theoretical guidance for the multi-fingered robot hand handling of hazardous items.

Introduction

The Explosive Disposal Robot usually works in the place where people are not fit to go. It is also can be used to scout and explore specially[1]. The end part that handles various explosive dangerous articles is an important part for the Explosive Disposal Robot. So far, the majority of the Explosive Disposal Robot equipments are composed of clamps. These clamps are blamed not only for lack of dexterousness because of its' one degree of freedom but also for its' simple clamping method which can only handle limited functions. Additionally, simple clamp is nearly impossible to have an accurate control over the dangerous articles such as explosive. A multi-degree freedom multi-fingered hands robot assembled in the Explosive Disposal Robot will greatly improves the explosive disposal ability.

Aiming at working in the open field and frequently-changed posture of the Explosive Disposal Robot, This paper analysis its' grasping ability and influence factors such as grasping position, finger joint angle as well as the direction of the external spiral force. Grasping ability of the robot with the change of external load direction would also be addressed. Screw theory has been incorporated to establish force spiral balanced equation and mathematics model with the biggest spiral of outside force as optimization objective. To get the most favorite grabbing posture, BP neural network method is used. At the same time, considering the characteristic of easy explosive, excessive contact force may ignite explosive, the grasping force smaller than the explosive limit is also studied which offer theoretical basis for the Explosive Disposal Robot safe operation.

External force wrench balance equation

As shown in Fig 1. when the multi-fingered hand grasps the explosive, wear point contact occurs between finger and the objective which is viewed as projection of contact force exerted by fingers and the external force wrench in reference coordinate[2]. In this paper, sliding movement between finger and the objective is neglected.

$$Gf_{tip} = -F_{ext} \tag{1}$$

F_{ext}： The external force spiral grabbing explosive; G： the grabbing matrix;

f_{tip}： contact force of explosive to finger; $f_{tip} = \begin{bmatrix} f_{x1} & f_{y1} & f_{n1}, f_{x2} & f_{y2} & f_{n2}, \cdots\cdots, f_{xm} & f_{ym} & f_{nm} \end{bmatrix}^T$

f_{xi} f_{yi} : the tangential force between the finger and explosive contact point;

$f_{ni}(i=1,\cdots,m)$: the inner normal component force for the contact point.

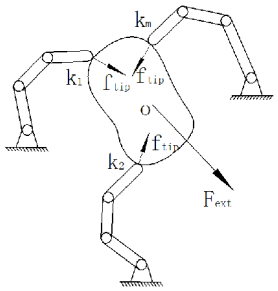

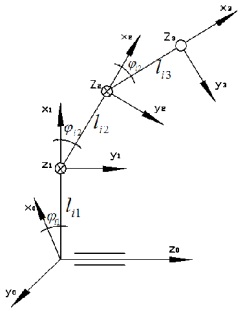

Fig. 1 The model of object grabbed by m fingers. Fig.2 Finger in its' reference coordinate

The optimal grabbing angle of multi-fingered hand

In 1985, Yoshikawa[3]introduced manipulator workable concept, which is defined as the equation (2). This operational indicator constant is related to robot posture. The performance indicator is defined as Equation (2)

$$W=\sqrt{\det(JJ^T)} \qquad (2)$$

J-the Jacobin matrix, related with the length of finger and joint angel.

Based on the Yoshikawa operational indicators and the introduction of force ellipsoid as grasping planning performance metrics, Caihua-Xong[4]get the result that the best position of fetching is the three points evenly distributed in the great circle while three fingers hand grabbing a sphere in hand.

By using of Yoshikawa performance indicators, In the case of fingers and explosives grab position unchanged, the change of finger joint Angle to the grasping ability is analyzed in this section. the best angle is calculated in the end.

As shown in fig. 1, take three fingers multi-finger hand for example, assuming that each of finger has three rotational joints. two parallel axis of rotation in each finger, and another rotation axis which is perpendicular to them. As shown in figure 2 for the fingers and the coordinate system. $l_{ij}(i,j=1,2,3)$ The j joint length of the i finger; $\varphi_{ij}(i,j=1,2,3)$ The j joint angle of the j finger.

According to the Yoshikawa performance indicators, when the size of finger joints is known, the performance indicator serves as a function of finger joint angle. Take one sphere-shaped explosive grabbed by multi-fingered hand for example. According to the most favorite grasping position, three fingers are located in the maximum circle evenly. Considering the structure of multi-finger hand, we can conclude that the second and third finger near palm joints need to be rotated $60°$ respectively. Just as $\varphi_{11}=0,\varphi_{21}=\varphi_{31}=60°$.

As three fingers have the same structure parameters, the second and third joint angel of each finger has the same degree that is $\varphi_{12}=\varphi_{22}=\varphi_{32}=\varphi_2$, $\varphi_{13}=\varphi_{23}=\varphi_{33}=\varphi_3$.

So the Jacobin matrix J is the function of φ_2, φ_3, which can be written as below.

$$J_1=\begin{bmatrix} 0 & -(l_3s(\phi_2+\phi_3)+l_2s\phi_2) & -l_3s(\phi_{12}+\phi_{13}) \\ l_3c(\phi_2+\phi_3)+l_2c\phi_2+l_1 & 0 & 0 \\ 0 & l_3c(\phi_2+\phi_3)+l_2c\phi_2 & l_3c(\phi_{12}+\phi_{13}) \end{bmatrix}$$

$$J_2=\begin{bmatrix} -0.866(l_3c(\phi_2+\phi_3)+l_2c\phi_2+l_1) & -0.5(l_3s(\phi_2+\phi_3)+l_2s\phi_{22}) & -0.5l_3s(\phi_2+\phi_3) \\ 0.5(l_3c(\phi_2+\phi_3)+l_2c\phi_2+l_1) & -0.866(l_3s(\phi_2+\phi_3)+l_2s\phi_{22}) & -0.866l_3s(\phi_2+\phi_3) \\ 0 & l_3c(\phi_2+\phi_3)+l_2c\phi_2 & l_3c(\phi_2+\phi_3) \end{bmatrix}$$

$$J_3=\begin{bmatrix} -0.866(l_3c(\phi_2+\phi_3)+l_2c\phi_2+l_1) & -0.5(l_3s(\phi_2+\phi_3)+l_2s\phi_{32}) & -0.5l_3s(\phi_2+\phi_3) \\ 0.5(l_3c(\phi_2+\phi_3)+l_2c\phi_2+l_1) & -0.866(l_3s(\phi_2+\phi_3)+l_2s\phi_{32}) & -0.866l_3s(\phi_2+\phi_3) \\ 0 & l_3c(\phi_2+\phi_3)+l_2c\phi_2 & l_3c(\phi_2+\phi_3) \end{bmatrix}$$

Then the matrix of multi-finger is got named *J*. Take *J* into Equation (2), we can get the relationship between W and φ, as shown in Fig. 3. The corresponding contour map is shown in fig. 4, from the Fig. 3 and Fig. 4, The maximum performance indicator of the multi-fingered hand falls in two locations. Based on the actual joint angel range, we can conclude the maximum performance indicator is located at $\varphi_2 = 30°$, $\varphi_3 = -75°$.

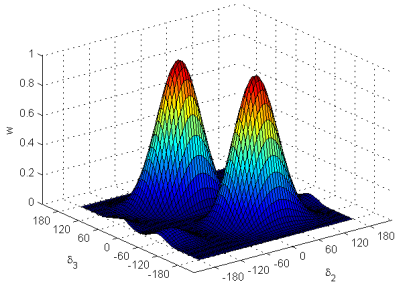

Fig.3. The profile of performance indicator

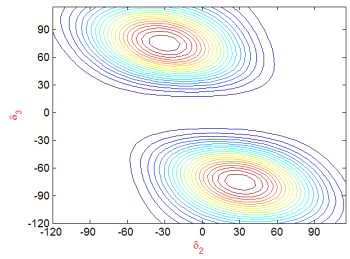

Fig.4. Contour

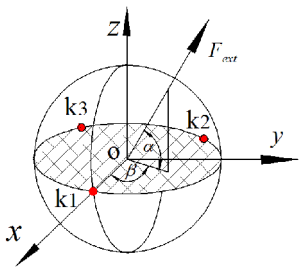

Fig.5. Scheme of grasping force distribution

The optimal grabbing posture of multi-fingered hand

The grasping ability of a multi-fingered is not only related to the grasping location, joint angel but also the external spiral load and its direction. That is, Different posture for different grasping ability. how much explosives a hand can grab or the forces it can resist outside is an important index for the ability of grabbing, also an important basis for the robot design. This section focuses on the grabbing ability of spiral multi-fingered hand for any direction based on the most favorite multi-fingered joint angel. Fig .5 is the scheme of grasping force location and direction k_1、k_2、k_3 are the grasping position. sphere center *O* is the origin of stiffness coordinate.

Based on Equation(1), we can get the spiral force balance equation(3)

$$Gf_{tip} = -\begin{bmatrix} F_{ext}\cos\alpha\cos\beta \\ F_{ext}\cos\alpha\sin\beta \\ F_{ext}\sin\alpha \\ 0 \\ 0 \\ 0 \end{bmatrix} \quad (3)$$

With the greatest external force wrench as optimal objective and considering the following constraints, mathematical optimization model is set up.

Constraints factors

1) For the finger gives the explosive a pressure force instead of pulling, the normal component of the force applied to the object must be positive, see Equation (4).

$$-f_{ni} \le 0 \quad (i = 1,2,3) \quad (4)$$

2) The contact between finger and explosive is frictional point contact. To avoid sliding, f_{ni} must meet the following constraints [5], see Equation (5):

$$\sqrt{f_{xi}^2 + f_{yi}^2} - \mu f_{ni} \le 0 \quad (5)$$

f_{ni} -the normal contact force; μ - the friction coefficient;

3）Constraints of joint moment τ

In multi-finger grasping system, the grasping force of finger top is generated by movement chain which is confined by grasping limit moment. The maximum joint torque constraints must be considered when planning accordingly, The joint moment τ_i can be defined as see Equation (6) [6].

$$\tau_{i\min} \le \tau_i \le \tau_{i\max} \quad (6)$$

The joint moment τ can be described as Equation (7)

$$\tau = J^T f_{tip} \tag{7}$$

J^T -Finger's Jacobi matrix;

So the optimized mathematical modal is written as Equation (8):

$$\begin{cases} \min & -F_{ext} \\ s.t. & Gf_{tip} = -F_{ext} \\ & -f_{ni} \le 0 \\ & \sqrt{f_{xi}^2 + f_{yi}^2} - \mu f_{ni} \le 0 \\ & J^T f_{tip} - \tau_{\max} \le 0 \\ & -J^T f_{tip} + \tau_{\min} \le 0 \end{cases} \tag{8}$$

Neural network optimization

Since optimization model contains the continuous variation α, β, BP neural network optimization simulation is applied. The training samples come from the above-mentioned non-linear programming solution [7]. The training sample data is shown in Table 1.

Table1. The training sample

α \ β	0	15°	30°	45°	60°	75°	90°	105°	120°	135°	150°	165°	180°
-90°	13.8568	13.8568	13.8568	13.8568	13.8568	13.8568	13.8568	13.8568	13.8568	13.8568	13.8568	13.8568	13.8568
-75°	12.8564	12.8702	12.9858	13.1622	13.3599	13.3882	13.219	12.9728	12.8564	12.8703	12.9858	13.1622	13.3599
-60°	11.3105	11.5423	12.0271	12.6203	13.1108	12.5187	11.8507	11.4507	11.3106	11.5424	12.0271	12.6203	13.1107
-45°	10.2005	10.5158	11.3041	12.5086	13.3283	11.9182	10.8305	10.2972	10.2005	10.5158	11.3041	12.5086	13.3283
-30°	9.8992	10.2502	11.1399	12.8364	14.0681	11.852	10.5901	9.9983	9.8991	10.2501	11.1399	12.8365	14.0681
-15°	10.2967	10.6792	11.6851	13.7315	15.5458	12.5459	11.0424	10.3822	10.2966	10.6791	11.685	13.7315	15.5495
0	11.5473	11.7889	12.9416	15.5162	17.0325	14.1133	12.2248	11.4716	11.5471	11.7887	12.9415	15.5161	17.0326
15°	10.2967	10.6792	11.6851	13.7315	14.7302	12.5459	11.0424	10.3822	10.2966	10.6791	11.685	13.7315	15.5495
30°	9.8992	10.2502	11.1399	12.8364	14.0681	11.852	10.5901	9.9983	9.8991	10.2501	11.1399	12.8365	14.0681
45°	10.2005	10.5158	11.3041	12.5086	13.3283	11.9182	10.8305	10.2972	10.2005	10.5158	11.3041	12.5086	13.3283
60°	11.3105	11.5423	12.0271	12.6203	13.1108	12.5187	11.8507	11.4507	11.3106	11.5424	12.0271	12.6203	13.1107
75°	12.8564	12.8702	12.9858	13.1622	13.3599	13.3882	13.219	12.9728	12.8564	12.8703	12.9858	13.1622	13.3599
90°	13.8568	13.8568	13.8568	13.8568	13.8568	13.8568	13.8568	13.8568	13.8568	13.8568	13.8568	13.8568	13.8568

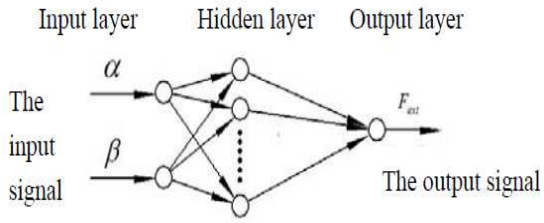

Fig.6. BP neural network

α, β served as input, F_{ext} served as output, the BP neural network modal is shown in Fig. 6.

Setup the BP neural network by Matlab neural network toolbox. And the program code can be written.

After simulating the trained network, the maximum external spiral and contour distribution is pursued as shown in Fig. 7 and Fig. 8. It shows the BP neural network has a good fitness and generalization performance.

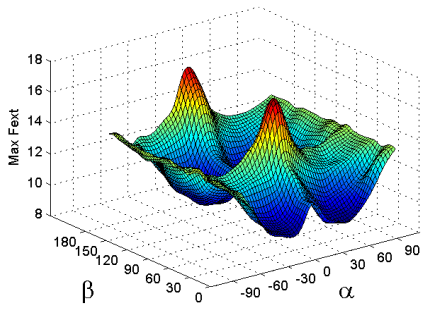

Fig.7. The maximum external spiral

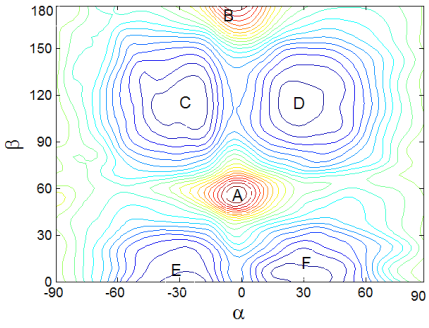

Fig.8. Contour distribution

Analysis of simulation result

From Fig.7. and Fig. 8, the anti-interference ability of multi-fingered hand is related to the direction of external force like α, β.The two maximum external spiral is located at $\alpha = 0°$, $\beta = 60°$ $\alpha = 0°$, $\beta = 180°$ (as shown in fig 9 point A and B).That is, The maximum value is on the XOY plane and falls in the middle of two fingers .The maximum value is 17.03N. In addition, it also can be

seen from the picture, there are four minimum values F_{ext} within the scope of α β ,(as shown in fig 10 point C, D, E and F).

During robot transports the explosive, it has to overcome various obstacles and walk on bumpy road. That means the direction of external force fluctuates with the changing posture. That is, the direction of external force screw is changing. Obviously the external force screw can't get the maximum value when considering the stability of hand in any position. But should take the lowest value of the optimization algorithm maximum value. Only in this way can we ensure the explosive-handling robot that can grabbing explosives in the changing position. This phenomenon also let us know that, When robot grasps the explosive, to be safe, also for resisting the maximum external spiral force. Finger gestures should avoid grabbing explosives when the value is minimum.

The constraints of maximum contact force

From the optimizing result, we know the contact force is proportional to the weight of the explosive. To guarantee the safety of explosive, the maximum normal contact force has to be smaller than the maximum bearing force of the explosive [8][9], which can be written as Equation(9)

$$f_{ni} \le f_{\max} \qquad (9);$$

The mathematical modal is as showed in Equation (10)

$$\begin{cases} \min & -F_{ext} \\ s.t. & Gf_{tip} = -F_{ext} \\ & -f_{ni} \le 0 \\ & f_{ni} \le f_{\max} \\ & \sqrt{f_{xi}^2 + f_{yi}^2} - \mu f_{ni} \le 0 \\ & J^T f_{tip} - \tau_{\max} \le 0 \\ & -J^T f_{tip} + \tau_{\min} \le 0 \end{cases} \qquad (10)$$

Assuming the maximum normal bearing force is 9.8N, the maximum weight of explosive is calculated by using the optimal method and BP neural network. The result is shown in Fig. 9.

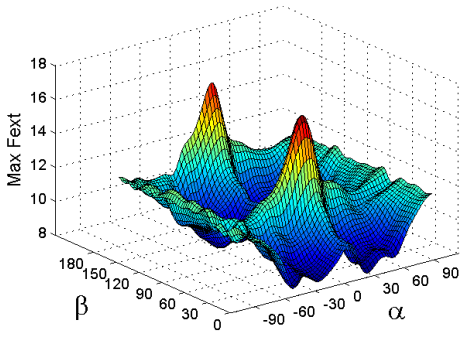

Fig.9. The maximum bearing force distribution

As the constraints of the maximum normal contact force, the maximum weight of explosive the robot can hold is 16.6N. The minimum weight of explosive it can hold in any posture is 8.83 The normal contact forces corresponding to three fingers are shown in the Fig. 10, Fig. 11, Fig. 12.

Obviously, the clamping forces of three fingers do not exceed the maximum normal force 9.8 N it can withstand, which ensure the reliability of operation and the safety of the explosives in some extent.

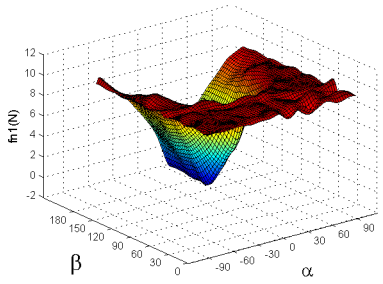

Fig.10. The first finger

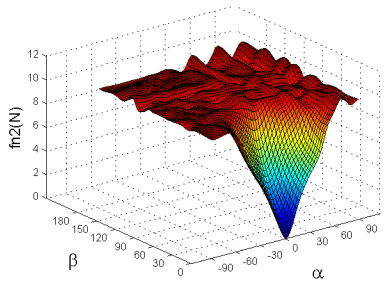

Fig.11. The second finger

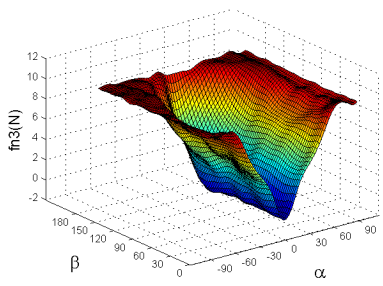

Fig.12. The third finger

Summary

This paper focuses on multi-finger's grasping ability. The most favorite joint angle is calculated, and the influence of the robot posture on the grasping ability. Result shows with the changing posture of explosive Disposal Robot, the maximum explosive weight that the finger can hold is not bigger than 9.89N. The weight of explosive that the multi-finger's can grasp with various posture is 8.83N when the normal force value that the explosive can bear is not bigger than 10N. This paper studies have theoretical guidance meaning for the determination of clamping force when clamping dangerous goods.

References

[1] Moli R.M, Zexiang Li, Introduction to Mathematical Robot Operation [M], Mechanical industry press. 1998

[2] T Yoshikawa, Manipulability of Robotic Mechanisms. The International Journal of Robotics Research[J],1985,4（2）: 3-9

[3] Xionghua Cai, Youlun Xiong, The Layout of The Robot Refers to Grab More Performance Metrics[J], Journal of The Jianghan Petroleum Institute, 1997 19(1)：85-88

[4] Mo Haijun, Hu Qingchun, On The Multifingered Robot Hands Grasping Stability Under Dynamic Load[J], Machine Design & Research, 2008 24(2)：32-35

[5] Mo Haijun, Huang Ping, Planning of Grasping with Multifingered Hands Based on the Maximal External Wrench[J], Journal of Mechanical Engineering, 2009 45(3)：258-262

[6] Akio Namiki ,Masatoshi Ishikawa, The Analysis of High-speed Catching with a Multifingered Robot Hand[C], IEEE International Conference on Robotics and Automation.2005,2666-2671

[7] C Xiong, Y Li, Y Xiong, Grasp Capability Analysis of Multifingered Robot Hands. Robotics and Autonomous Systems [J], 1999 , 27(4):211-224

[8] Nahon, M. Angeles, J. Real-time Force Optimization in Parallel Kinematic Chains Underinequality Constraints. IEEE Transactions on Robotics and Automation[C], 1992,8(4): 439-450

[9] Guanfeng Liu, Zexiang Li, Real-Time Grasping-Force Optimization for Multifingered Manipulation Theory and Experiments[C], IEEE/Asme Transactions on Mechatronics, 2004, 9(1): 65-76

Applied Mechanics and Materials Vol. 565 (2014) pp 253-259

doi:10.4028/www.scientific.net/AMM.565.253

Construction of Point Set Surfaces through Quadric Polynomials

Yu Liu[1, a]

[1] School of Physics and Mechanical & Electrical Engineering, Xiamen University, Xiamen 361005, China

[a]mseliuyu@xmu.edu.cn

Keywords: shape reconstruction, point set surface, quadric polynomials, energy functions.

Abstract. This paper constructs PSSs (Point Set Surfaces) by combining locally fitted quadric polynomials. First, an energy function is defined as the weighted sum of distances from a point to these quadric polynomials. Then, a vector field is constructed by the weighted sum of normal vectors at input points. Finally, points on a PSS are obtained by finding local minima of the energy function along the vector field. Experiments demonstrate that high quality PSSs can be obtained from the method presented for input point clouds sampled from various shapes.

Introduction

PSSs are continuous surfaces defined directly from discrete points. PSSs are able to handle noisy input, easily represent objects of complex topologies, and provide good approximation of the intrinsic properties of the underlying surface such as curvatures directly from a noisy point cloud. Since its inception[1–3], the PSS and its many variants have been widely used in various graphics, visualization, geometric modeling and engineering applications[4–7] .

Levin[1] constructs a PSS by both an MLS (Moving Least Squares) projection procedure and a polynomial fitting procedure. The polynomial fitting procedure should be done after the MLS projection procedure. Amenta and Kil[3] give the function of an implicit surface obtained by a MLS projection procedure which projects points onto local fitted planes iteratively. There is no polynomial fitting procedure in [3]. In the rest of the paper, PSSs introduced in [1] and [3] are denoted by PSS-L and PSS-AK respectively. Different from both PSS-L and PSS-AK, this paper constructs PSSs through a polynomial fitting procedure at each input point first. Points on the presented PSS are local minima of an energy function combining polynomials obtained from the polynomial fitting procedure.

Vector field of PSS-AK is built in and dependent on their energy functions. As examples in [8] and this paper (Fig.1, Fig. 5, and Fig. 6) indicate, points outside a narrow band of the input point cloud cannot be projected correctly using such vector fields. The presented PSS uses a vector field that is independent of its energy function. The vector field and the energy function provide a wide support domain including points near and far away from the input point cloud. Points in such domain can be projected correctly to the presented PSS.

Computational experiments demonstrate that, through the prese

nted PSS, high quality PSSs can be obtained for input points sampled from various shapes. The presented PSS is also compared with PSS-AK, PSS-L, and APSS (algebraic PSS)[9]. The presented PSS has smaller deviations to true surfaces of the input point cloud than PSS-AK, PSS-L, and APSS in our experiments.

The remainder of the paper is organized as follows. Section 2 introduces how to construct a PSS using quadric polynomials, including quadric polynomials fitting, definitions of the energy function and the vector field, the projection procedure, and the implicit surface function of the PSS. Experimental results are given in Section 3. Finally, conclusions are given in Section 4.

Construction of PSSs

Local fitting of quadric polynomials

Given an input point cloud $P = \{\boldsymbol{p}_i, i = 1, \cdots, n\}$, a r-neighborhood centered at point $\boldsymbol{x}$ can be defined as $N_r(\boldsymbol{x}) = \{\boldsymbol{q} | \|\boldsymbol{q} - \boldsymbol{x}\|_2 \leq r, \boldsymbol{q} \in P\}$, where $r > 0$. Assume $\boldsymbol{n}_i$ is the normal vector of the underlying surface at point $\boldsymbol{p}_i$. The $\boldsymbol{n}_i$ is given beforehand or is estimated by the normal vector of a local fitting plane. A local coordinate system centered at point $\boldsymbol{p}_i$ is established by taking $\boldsymbol{n}_i$ as its z axis and two arbitrary orthogonal vectors in the plane passing through point $\boldsymbol{p}_i$ and perpendicular to $\boldsymbol{n}_i$ as its x and y axises. The local coordinate system is denoted by $C(\boldsymbol{p}_i, \boldsymbol{n}_i)$.

Points in $N_r(\boldsymbol{p}_i)$ are fitted by the following quadric surface in the coordinate system $C(\boldsymbol{p}_i, \boldsymbol{n}_i)$:

$$\hat{f}_i(\boldsymbol{x}) = a_{i1}x^2 + a_{i2}y^2 + a_{i3}xy + a_{i4}x + a_{i5}y + a_{i6} - z = \boldsymbol{x}^T A_i \boldsymbol{x} = 0, \tag{1}$$

where $\boldsymbol{x} = [x \quad y \quad z \quad 1]^T$. Now suppose there are m points in $N_r(\boldsymbol{p}_i)$, i.e. $|N_r(\boldsymbol{p}_i)| = m$. $m > 6$ is required for the local quadric polynomial approximation. The elements of A_i in Eq. 1 can be obtained by weighted least square fitting. The weight at a point $\boldsymbol{q}_j \in N_r(\boldsymbol{p}_i), j = 1, \cdots, m$, is given by

$$\omega_j = e^{-\frac{9\|\boldsymbol{q}_j - \boldsymbol{p}_i\|^2}{r^2}} \Big/ \sum_{k=1}^{m} e^{-\frac{9\|\boldsymbol{q}_k - \boldsymbol{p}_i\|^2}{r^2}}. \tag{2}$$

The quadric surface Eq. 1 is converted to the form in the global coordinate system because quadric surfaces at different input points will be blended in the energy function of the presented PSS. Assume the following quadric surface in the global coordinate system represents the same surface as that defined by Eq. 1: $f_i(\boldsymbol{x}) = \boldsymbol{x}^T B_i \boldsymbol{x} = 0$. Then

$$B_i = \begin{bmatrix} R^T & -R^T\boldsymbol{p}_i \\ 0 & 1 \end{bmatrix}^T A_i \begin{bmatrix} R^T & -R^T\boldsymbol{p}_i \\ 0 & 1 \end{bmatrix}, \tag{3}$$

where R is the rotation matrix of the local coordinate system $C(\boldsymbol{p}_i, \boldsymbol{n}_i)$ with respect to the global coordinate system.

Definitions of energy Functions and vector fields

Given the polynomial $f_i(\boldsymbol{x})$ fitted locally at each input point $\boldsymbol{p}_i$, an energy function is defined by

$$e(\boldsymbol{x}) = \sum_i f_i^2(\boldsymbol{x})\theta(\boldsymbol{x}, \boldsymbol{p}_i), \tag{4}$$

where $\theta(\boldsymbol{x}, \boldsymbol{p}_i)$ is a weighting function given by

$$\theta(\boldsymbol{x}, \boldsymbol{p}_i) = e^{\frac{d_{min} - \|\boldsymbol{x} - \boldsymbol{p}_i\|^2}{h^2}} \Big/ \sum_{\boldsymbol{p}_j \in P} e^{\frac{d_{min} - \|\boldsymbol{x} - \boldsymbol{p}_j\|^2}{h^2}}, \tag{5}$$

where $d_{min} = min_{\boldsymbol{p}_j \in P} \|\boldsymbol{x} - \boldsymbol{p}_j\|^2$ is the square of the closest distance from $\boldsymbol{x}$ to points of P and h is the bandwidth of $\theta(\boldsymbol{x}, \boldsymbol{p}_i)$.

Note that Eq. 5 is a normalized weighting function which does not fade out when $\boldsymbol{x}$ is far away from the input points. Different from weighting functions in previous works such as [8], the usage of the d_{min} avoids zero denominator of Eq. 5 when $\boldsymbol{x}$ is far away from the input points.

The following vector field is defined

$$\boldsymbol{n}(\boldsymbol{x}) = \sum_i \boldsymbol{n}_i \theta(\boldsymbol{x}, \boldsymbol{p}_i) / \|\sum_i \boldsymbol{n}_i \theta(\boldsymbol{x}, \boldsymbol{p}_i)\|, \tag{6}$$

where $\boldsymbol{n}_i$ is the normal vector of the underlying surface at point $\boldsymbol{p}_i$, $\theta(\boldsymbol{x}, \boldsymbol{p}_i)$ is the weighting function given by Eq. 5.

The exponential term of $\theta(\boldsymbol{x}, \boldsymbol{p}_i)$ is close to zero if $\|\boldsymbol{x} - \boldsymbol{p}_i\| > 3h$. In order to save the cost of the calculation of Eq. 5 and Eq. 6, only points in $N_{3h}(\boldsymbol{x})$ are considered if $|N_{3h}(\boldsymbol{x})| \geq k$, where k is a constant and is specified by 8 in our experiments. Otherwise, the k nearest neighbors in P from $\boldsymbol{x}$ are used in the calculation. Directions of vectors $\boldsymbol{n}_i$ used in Eq. 6 need to be consistent. Only normal vectors of points in $N_{3h}(\boldsymbol{x})$ or k nearest neighbors of $\boldsymbol{x}$ need to be consistent in the calculation of Eq. 6.

Fig. 1 shows stream lines of the vector field around the point could sampled from a corner, where $h = 5$ in $\theta(\boldsymbol{x}, \boldsymbol{p}_i)$ and the weighting function $\theta(\boldsymbol{x}, \boldsymbol{p}_i)$ is also used in defining the vector field of PSS-AK. As Fig. 1 shows, the vector field of PSS-AK only provides correct directions at points near the input point cloud, while the vector field defined by Eq. 6 has correct directions at points near and far from the input point cloud.

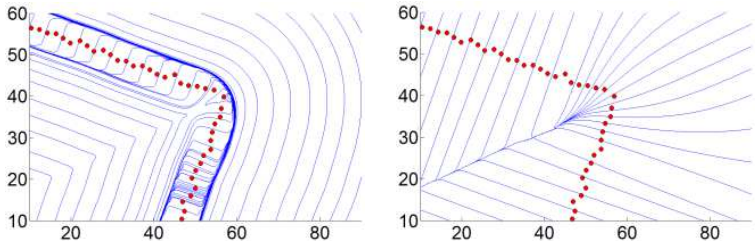

(a) PSS-AK (b) our PSS

Fig. 1. Stream lines of the vector field, where the input point cloud is sampled from a corner

Construction of PSSs

A projection procedure similar with that in [3] can be done for our PSS. According to the definition of the extremal surface in [3], the directional derivative of the energy functional Eq. 4 in direction $\boldsymbol{n}(\boldsymbol{x})$ should be zero at $\boldsymbol{x}$ because a point of the extremal surface is a critical point of the energy functional Eq. 4 on the line $l_{\boldsymbol{x},\boldsymbol{n}(\boldsymbol{x})}$. Then the implicit surface function of our PSS is given by

$$g(\boldsymbol{x}) = \boldsymbol{n}(\boldsymbol{x}) \cdot \nabla_{\boldsymbol{x}} e(\boldsymbol{x}) = 0, \tag{7}$$

where $\cdot$ denotes dot product, $\nabla_{\boldsymbol{x}} e(\boldsymbol{x})$ is the gradient of e as a function of $\boldsymbol{x}$. Submitting Eq. 4 into Eq. 7, we have

$$g(\boldsymbol{x}) = \sum_i \left\{ 2 f_i(\boldsymbol{x}) \frac{\partial f_i(\boldsymbol{x})}{\partial \boldsymbol{x}} \theta(\boldsymbol{x}, \boldsymbol{p}_i) + f_i^2(\boldsymbol{x}) \frac{\partial \theta(\boldsymbol{x}, \boldsymbol{p}_i)}{\partial \boldsymbol{x}} \right\}^T \boldsymbol{n}(\boldsymbol{x}) = 0. \tag{8}$$

Experiments

In this section, we present results of the presented PSS, and compare them with those of PSS-AK, PSS-L, and APSS. The polynomial fitting procedure of PSS-L uses the method introduced in section 2.1. All methods are implemented in Matlab 7. All the experiments are carried out on a computer with an Intel Pentium 3GHz CPU and 2 GB of RAM.

Synthetic shapes are used, including a sphere, a cylinder, a hyperboloid, a torus, and a wavy surface. Points are sampled from these shapes and then random Gaussian noises are added to sample points. Characteristics of these examples are described in Table 1, where n, s_d, μ_0, and σ_0 denote the number of input points, average point space, mean and standard deviation of added noises respectively.

Table 1. Characteristics of synthetic examples

Examples	Equation	n	s_d	μ_0	σ_0
Sphere	$x^2 + y^2 + z^2 = 100$	2606	0.59	0	0.1
Cylinder	$x^2 + y^2 = 100$	5166	0.50	0	0.1
Hyperboloid	$x^2 + y^2 - 0.64z^2 = 0$	10032	0.44	0	0.1
Torus	$(x^2 + y^2 + 200)^2 - 900(x^2 + y^2) = 0$	6227	0.60	0	0.06
Wavy surface	$z = 10\cos(0.12x)\sin(0.09y)$	22500	0.72	0	0.1

PSS-AK, PSS-L, APSS, and the presented PSS are constructed from noisy synthetic data. The radius r in Eq. 2 is specified as three times of the bandwidth h in Eq. 5 for the presented PSS. Since the shape of a PSS is influenced by its bandwidth[10], proper bandwidths are selected for PSSs according to the statistics Z introduced in [11]. Using planes instead of second order polynomials,

PSS-AK always needs smaller bandwidths than the other three PSSs to smooth out noises. Bandwidths selected for PSSs on synthetic examples in the experiments are given in Table 2.

Projection points are obtained by projecting noisy points sampled from a synthetic example to each constructed surface. Differences between a constructed surface and corresponding nominal surface are examined by the deviation between each projection point on the constructed surface and its closest point to the corresponding nominal surface. Table 3 and Table 4 show the differences between PSSs and true surfaces of synthetic examples. Table 3 and Table 4 indicate that the presented PSS has the smallest deviations to corresponding true surfaces in the four PSSs constructed in the experiments.

Table 2. Bandwidths selected for PSSs on synthetic examples

Examples	PSS-AK	PSS-L	APSS	Our PSS
Sphere	2.0	3.0	3.0	3.0
Cylinder	2.0	2.5	2.5	2.5
Hyperboloid	2.5	3.0	3.0	3.0
Torus	1.0	2.5	2.5	2.5
Wavy surface	1.5	3.0	3.0	3.0

Table 3. Mean of differences between PSSs and true surfaces of synthetic examples

Examples	PSS-AK	PSS-L	APSS	Our PSS
Sphere	-0.20	0.018	0.0015	-0.00089
Cylinder	-0.10	0.0026	0.0022	-0.00046
Hyperboloid	-0.086	0.0055	0.0063	-0.00028
Torus	-0.047	0.027	-0.027	0.00057
Wavy surface	-0.00045	0.00038	0.000035	0.000017

Table 4. Standard deviation of differences between PSSs and true surfaces of synthetic examples

Examples	PSS-AK	PSS-L	APSS	Our PSS
Sphere	0.016	0.016	0.015	0.014
Cylinder	0.011	0.014	0.029	0.013
Hyperboloid	0.010	0.011	0.027	0.0095
Torus	0.021	0.012	0.058	0.0091
Wavy surface	0.053	0.019	0.019	0.016

PSS-AK, PSS-L, APSS, and the presented PSS are also constructed from real data. Fig. 2 shows point clouds and rendered plots of a human face and the Stanford bunny[12] used in the experiments. The number and average point space of the point cloud of the face are 10000 and 1.74 respectively, while the number and average point space of the point cloud of the bunny are 35945 and 1.00 respectively.

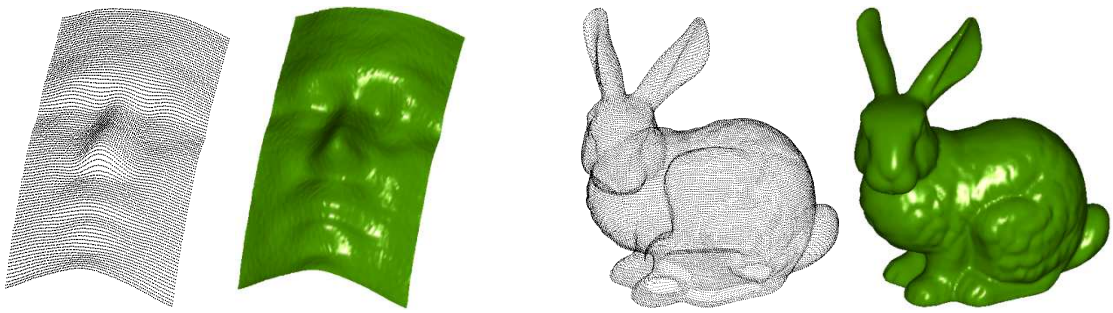

Fig. 2. Point clouds and rendered plots of two real data

Since nominal surfaces of real data are unknown, differences between input data and constructed surfaces are examined. Fig. 3 and Fig. 4 show differences between the input points and constructed

PSSs. As Fig. 3 and Fig. 4 show, PSS-AK has obvious deviations to the input points in regions with high curvatures, while the other three surfaces approximate the examples better.

Fig. 5 and Fig. 6 show iso-contours of energy functions on cross sections of the face and the bunny respectively, where the input point cloud is denoted by small red dots. As Fig. 5 and Fig. 6 indicate, the energy function of PSS-AK is only proportional to squared distances to the underlying surfaces near the input cloud, while the energy functions of our PSS is proportional to distances to the underlying surfaces both near and far from the input point cloud. Then points far from the input point cloud cannot be projected correctly to PSS-AK, while these points can be projected correctly to our PSS. These points also cannot be projected correctly to PSS-L because the projection procedure of PSS-L is similar with that of PSS-AK.

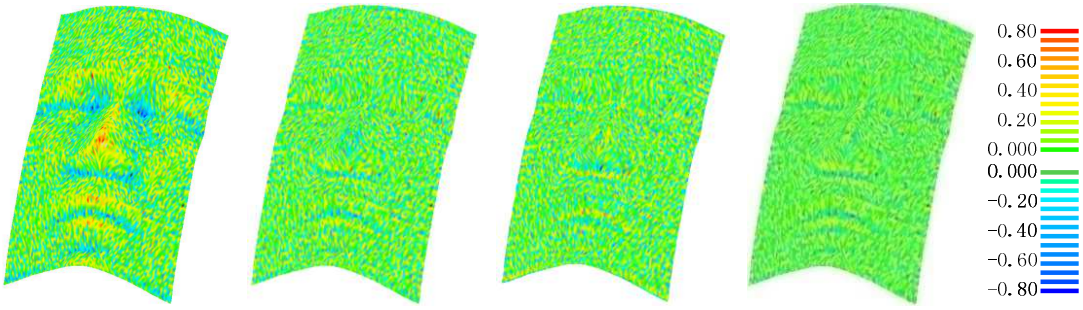

(a) PSS-AK (b) PSS-L (c) APSS (d) Our PSS

Fig. 3. Differences between input point clouds and corresponding PSSs of the face, where the bandwidth is specified by 3 for PSS-AK and 5 for the other three PSSs

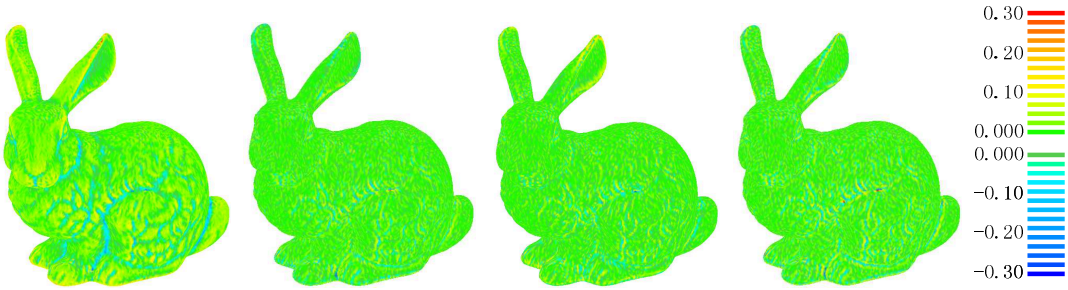

(a) PSS-AK (b) PSS-L (c) APSS (d) Our PSS

Fig. 4. Differences between input point clouds and corresponding PSSs of the bunny, where the bandwidth is specified by 1.0 for PSS-AK and 1.5 for the other three PSSs

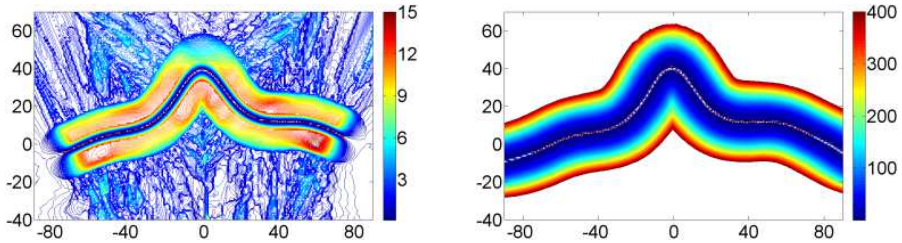

(a) PSS-AK (b) Our PSS

Fig. 5. Iso-contours of an energy function on a cross section of the face, where the bandwidth is 5

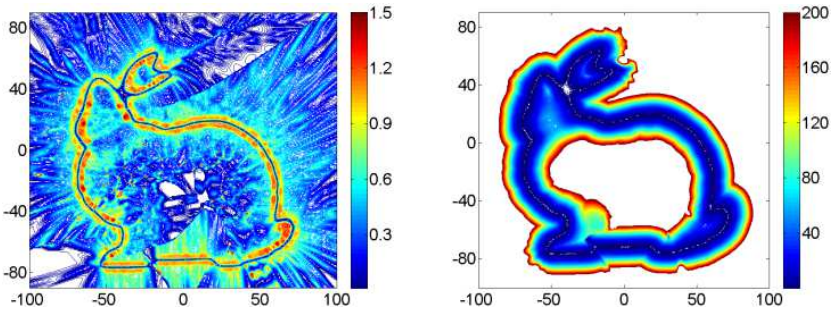

(a) PSS-AK (b) Our PSS

Fig. 6. Iso-contours of an energy function on a cross section of the bunny, where the bandwidth is 1.5

For each example, the total time to projecting all the input points onto the corresponding PSS is recorded. Then the average time of an iteration of the projection procedure is obtained by dividing the total time by the total number of iterations of the projection procedure. The average time of an iteration of the projection procedure of the presented PSS is comparable with those of the other three surfaces. Similar results are also obtained on real examples.

Conclusions

This paper introduces a PSS constructed from quadric polynomials. The quadric polynomials are obtained by fitting neighbors of each input point. Then an energy function is given by combining these quadric polynomials. A vector field is also defined by combining normal vectors at input points. A monotonic weighting function is used in the combining process, which does not fade out when an interested point is far away from the input points. Points near and far away the input points can be projected onto the presented PSS by finding local minima of the energy function along the vector field. The implicit surface function of the presented PSS is also given.

Experimental results on noisy synthetic examples demonstrate that the presented PSS approximates underlying surfaces more accurately than PSS-AK, PSS-L, and APSS. The presented PSS also has more wide support domains than PSS-AK and PSS-L, in which points can be projected correctly onto the corresponding surface. The future work will look into how the presented PSS can be extended to handle sharp features effectively.

Acknowledgements

The author wants to acknowledge the support from the National Natural Science Foundation of China (Grant No. 51205332) and the SRF for the Returned Overseas Chinese Scholars in this work.

References

[1] LEVIN D. Mesh-independent surface interpolation[J]. *Geometric Modeling for Scientific Visualization*, 2003, 3: 37-49.

[2] ALEXA M, BEHR J, COHEN-OR D, Fleishman S, Levin D, Silva C. Computing and rendering point set surfaces[J]. *IEEE Transactions on Visualization and Computer Graphics*, 2003, 9(1): 3-15.

[3] AMENTA N, KIL Y. Defining point-set surfaces[J]. *ACM Transactions on Graphics*, 2004, 23(3): 264-270.

[4] ZWICKER M, PAULY M, KNOLL O, GROSS M. Pointshop 3D: an interactive system for point-based surface editing[C]//*Proceedings of the 29th annual conference on computer graphics and interactive techniques, ACM*, 2002: 322-329.

[5] YANG P H, QIAN X P. Adaptive slicing of moving least squares surfaces: toward direct manufacturing from point cloud data[J]. *ASME Journal of Computing and Information Science in Engineering*, 2008, 8(3): 031003-1-11.

[6] YANG P H, SCHMIDT T, QIAN X P. Direct digital design and manufacturing from massive point-cloud data[J]. *Computer-Aided Design and Applications*, 2009, 6: 685-699.

[7] LIY Y, XIA S T, QIAN X P. Direct numerical control (NC) path generation: from discrete points to continuous spline paths[J]. *ASME Journal of Computing and Information Science in Engineering*, 2012, 12(3): 9-30.

[8] AMENTA N, KIL Y. The domain of a point set surface[C]//*Proceedings of the Eurographics Symposium on Point-Based Graphics*, 2004: 139-147.

[9] GUENNEBAUD G, GROSS M. Algebraic point set surfaces[J]. *ACM Transactions on Graphics*, 2007, 26(3): 23.1-23.9.

[10] WANG H, SCHEIDEGGER C, SILVA C. Optimal bandwidth selection for MLS surfaces[C]//*Proceedings of shape modeling international*, 2008: 111-20.

[11] LIU Y, QIAN X P. Computing point-set surfaces with controlled spatial variation of residuals[J]. *Computer-Aided Design*, 2011, 43(8): 957-970.

[12] http://www.graphics.stanford.edu/data/3Dscanrep/. 2011.

Applied Mechanics and Materials Vol. 565 (2014) pp 260-264

doi:10.4028/www.scientific.net/AMM.565.260

Research on Safe Shipment of the Cargoes Which May Liquefy

Jianwei Xiao

No. 8 Yashen Road, Haihe Education District, Tianjin, 300350, China

Keywords: cargoes which may liquefy, Safe shipment,Ship's Stability,Free Surface

Abstract: This article expounds the transportation situation of cargoes which may liquefy and sea accidents happened in shipping process in recent years; fully studies the various characteristics and harm may existed of cargoes which may liquefy and the main reasons; introduces the principle of determining the water content and Transportable Moisture Limit. And puts forward the requirements for the safe shipment, precautions, emergency measures and attentions should be paid for safe manoeuvring.

Introduction

With the vigorous development of the world shipping, as its strong transportation capability, the low cost, the long distance, not strict time limit and the low freight, the freight volume of maritime transport accounts for more than two-thirds of the current international trade volumes. Large bulk cargo is mainly shipped by maritime transport, the cargoes which may liquefy as one of goods in bulk also mainly adopt the way of maritime transport.

With the development of world economy and demands of the various countries' production and living, maritime transport of cargoes which may liquefy also increase year by year, in order to reduce the possibility of accident in the maritime transport to a maximum, IMO changed the BC Rules (solid bulk cargo safety operation rules) published in 1965 to IMSBC rules (the international maritime solid bulk cargo rules) through four times modified in 1985, 1994, 2008 and 2010, the latest rules will be the newest legal basis for the safety international maritime transport of cargoes which may liquefy.

Transportation status of the cargoes which may liquefy

In recent years, the mining and metallurgy industry in China increase rapidly, the maritime transport of liquefy goods also developed with the development of the foreign trade volume year by year. With the growth of liquefy goods trade, the safety accident rate is also increased. Just in 36 days from October 28, 2010 to December 3, 2010, there are five consecutive catastrophic accidents had taken place in almost the same coastal area in our country caused by loading the same goods. Most of the malignant accidents are due to the unreasonable loading in bad weather conditions or the moisture content is too high, which result in the ship capsize or forming the capsizing condition.

The frequency of safety accidents and severity of liquid goods shipment is of the shock. On October 27, 2010, the panama ship "fusion" carrying 43000 tons of nickel ore, shipped from Indonesia to Shandong port, overturned in the open sea on the way in fujian pingtung goose nose, 25 crew members fell into the water, and 12 people been rescued. On November 10, 2010 morning, the panama ship "Nasco Diamond" of nanjing ocean shipping co., LTD., zhejiang on the way from Indonesia to lianyungang with fully loaded nickel ore, sunk in southern Japanese island of Okinawa, 25 crew on board but only 3 people were rescued.

The perils of sea brought enormous threaten to the safety of life at sea, at the same time caused enormous economic loss. Therefore, after a careful study on cargoes which may liquefy, IMO formulates the relevant rules in order to regulate the maritime transport of cargoes which may liquefy and reduce the amounts of sea accidents.

The characteristics and the threaten of the cargoes which may liquefy

The characteristics of the cargoes which may liquefy

Definition

According to the characteristics of transportation, the IMSBC Code divided the solid bulk cargo into three categories, namely cargoes which may liquefy, goods with chemical and dangerous property, goods may not liquefy and with no chemical dangerous property.

Cargoes which may liquefy (Group A) means the material that is made up of at least part of the mixture of particles and certain content of moisture, if moisture content exceeds a certain proportion, effected by outside forces in the process of maritime transport, the moisture will migrate and gradually form the liquid on the surface of goods then will make the cargo shifting. The liquid refers to the material produces flow trend and possibility under the action of outside factors, it is the most significant and the main features of the cargoes which may liquefy. Such goods may be often dry granular when loading, but may contain considerable moisture, but turns liquefy due to the effect of deposition and vibration during the voyage.

The transportable moisture limit

Transportable moisture limit (HTML) refers to the maximum moisture content for safety transportation of the solid bulk cargoes which may liquefy, which is usually determined by 80-90% of its flow moisture point. Flow moisture point means the minimum moisture content of solid bulk cargoes which may liquefy when flowing.

When the moisture content of the cargoes which may liquefy exceeds the TML, water will separate out gradually on the surface of the goods but not filter through the goods and fall onto the bottom, and the surface of the goods will turn into a state like mud, the turbulence and heavy waves on sea will especially speed up the production of liquid. When the ship tilts to one side, the liquid goods will flow to the same side of the ship, but will not fully back or only a few back when the ship tilts to the other side, which will cause the ship tilt to one side more and more, the greater the ship tilted and rolling, the faster and more the goods flow to one side, finally lead to losing stability and buoyancy of ship, and the ship will capsize instantly. Normally water content below 8% is safe, more than 18% are extremely dangerous.

The Cause and Threaten of the cargoes which may liquefy

Due to the vibration and swing of the ship, the cargoes which may liquefy loaded in a cabin will sink and the pore between particles is reduced, if the water content is high, there may produce excess water. If the water permeability of the goods is good, the excess water and air will exude to the surface to form a free surface; If the goods particle is small and which makes the permeability poor, the full pressure of the cargo sinking will be endured by water between pores firstly, and pore water pressure will produce, this means that the particles cannot very well combine between each other, which will lead the internal friction and cohesive force decrease or loss and the resisting shear strength disappear, resulting the goods flow. Due to the swing, vibration and turbulence, the particles then slowly sink to the middle level in the process of ship sailing, and the moisture will be extruded to surface, and water free surface will form on the surface layers.The large area of free surface in hold will directly affect the stability of the ship, the continuously swing of water free surface will make the particles pushed to one side, the ship will become heeling, if encountered heavy wind and waves, the ship will tilt more severe, eventually lead to sinking.

The liquid does not appear if the following conditions are satisfied:

a. The goods contain very fine particles, particles movement is limited by the viscosity, the water pressure between the space of particles will not increase;

b. The goods consists of large particles and block. Water could go through the space between the particles and will not cause the increase of water pressure, therefore liquid will not form caused by large particles completely;

c. The percentage of air contained in the goods is high, and moisture content is low, which will suppresses the water pressure, and the dry goods may not liquefy.

Determination method of water content for cargoes which may liquefy

The main reason of the accident for cargoes which may liquefy in the process of transportation is due to high water content, therefore, strictly control of the water content is an effective method to reduce accidents, which will require to determine the transportable moisture limit of the goods. The IMSBC Code recommended the laboratory measurement methods, usually includes Flow Table Test , Penetration Test and Proctor/Fagerberg Test. In the absence of test conditions on the ship, simple test can be adopted, which mainly includes:

a. Put the goods into the solid barrel or similar containers for half tank, through it fiercely from about 0.2 m height to hard ground, and repeat 25 times at 1~ 2s intervals, if free water appears or flows on the goods surface, standard water content inspection of goods should be made.

b. Grasp the goods by hand, make it free fall from 1.5 m high to the ground or deck, if it scatters means that the water content is less than 8% and goods can be carried; If it remains conglomeration shows the moisture content exceeds 10%.

c. Grasp the bulk goods clumps by hand, if it can be kneaded scattered by hands shows its moisture content is below 8%, otherwise more than 8%.

d. Put the goods into a flat keel glass or other small container, rocking back and forth for 5 min, if there is obvious liquid floating on the surface of goods, it shows that the moisture content is too high, and formal inspection for water content should be required.

e. Put the goods on a flat plate and press it into a cone, making the flat plate attacking the desktop, if the cone shows fragment or split block and not flow down, it shows the goods is transportable; If it appears collapse pancakes shape, it indicates the moisture content is too high.

f. Step on the goods, if it is soft and flows in a shifting sand shape, it shows that moisture content is too high.

The safe shipment measures for cargoes which may liquefy

The Measures Before Loading

Firstly, before shipment, cargo hold should be cleaned and be watertight; the sewage (Wells) and pipe lines in hold be cleaned up to prevent blockage or damage; Sewage well (trench) should be covered by water permeability dunnage in favor that water could inflow from bilge but not congestion, it can also be used above the sewage one set of "wooden well". Immediately after loading, sewage measurement and pumping test should be made in order to make sure its clear.

Secondly, a certificate of transportable moisture limit and moisture proof should be submit by the shipper to the captain when loading cargo, in which declare that the water content in certificate is the average water content when certificate submitted.

Thirdly, if there is doubt with whether the goods can be safe transport according to the appearance or state by captain, sampling should be made and easy way be taken to test the possibility of flow. If any problem, the cargo owner should be informed immediately to apply for inspection again.

Fourthly, the tally institutions shall take part in comprehensively goods sampling and supervision of loading, so as to control the actual state of the port loading effectively, and reduce the shipping accidents at sea to a minimum.

The Measures in the Process of Loading

a. Impurities should not be mixed in the loading process, especially the combustible material.

b. In addition to otherwise special provisions, loading and unloading work shall not be operated in rainy days.

c. In the process of loading and unloading, close all hatch covers that have completed loading work or prepare to load but not in use.

d. During the voyage, ventilation should not be made to the cargo hold that loading the goods.

e. For the goods easy to oxidation and self-heating tendency, they should be compacted or covered with plastic film to prevent the air into them so as to inhibit oxidation, such goods should be further prevented from ventilation during the voyage.

f. Surface of goods should be regularly checked during the voyage. If the free surface exists or flowing goods discovered, the captain should take appropriate measures to prevent the risk of goods shifting and the ship capsizing, and consider sailing to the nearby port of refuge.

g. During the voyage, measures should be taken to prevent liquid flowing into the cabin of the cargoes which may liquefy. For some goods that will cause a serious accident or corrosion to the hull and machinery when contacting with the water, strict precautions are more important.

The measures after loading

In order to prevent the goods from shifting and reducing the oxidation of the goods, the cabins should be reasonable trimmed after loading regardless of the size of angle of static.

Preventive measures

Rather than remedies afterwards, strengthen prevention is more advisable, the risk factors should be eliminated before loading. The ship should take prevention measures include: improving the quality of the crew, controlling sources of goods, process of loading, reporting in time and taking measures, reasonable arranging the contract of carriage, etc.

Emergency measures

a. Fully understand the nature of the cargoes which may liquefy, once the ship heeling, ballast water must not blindly put into or pumped out.

b. Request guidance, help and assistance in time, do not miss the opportunity to take effective measures.

c. When the vessel heeling, measures to slow down shall promptly be taken so as to reduce ship heeling moment.

d. Do not steering turn round at full speed, which will speed up heeling.

e. When the vessel heeling, do not raise the ship's speed, otherwise it will increase the heeling angle continuously, so that the final capsizing and sinking will be inevitable.

f. The appropriate small rudder angle should be adopted when the ship maneuvering to adjust the ship tilted position, making the low side of the ship by wind.

g. If the ship is sailing along the coast, it can beach timely.

h. When the fire breaking out in the local of cabin, a small amount of water mist should be used to extinguish the fire, do not take the method of sprinkle with a great deal of sea water for cooling, which will make it easily to the fluidization.

Remedies

If the goods are found liquefy and flowing during the voyage, the master should immediately notify the owner, P&I Club for help. If necessary, the master can rely on active beach to save his life.

The area and route should be paid special attention

The course needs to pay special attention is the region that after the rainy season, monsoon and typhoon climate. The main areas are India, Indonesia, the Philippines, New caledonia, and parts of China. Influenced by monsoon, the areas of high-risk accident recently is the New Mangalore of India. Meantime, because a great deal of demand for iron ore recently in China, and the disputes of mining between Chinese and Australian companies, the shipment of mineral from India to China shipping increases greatly, therefore, the course of China-India should be given special attention.

Safe manoeuvring points in sailing

a. During the voyage, making use of good seamanship to adjust the ship course.

b. Taking appropriate and effective measures to slow down.

c. Avoiding turn around significantly in big waves as far as possible.

d. In the process of steering or turning around, it will appear larger heeling in case affected by other factors, the measures to slow down should be promptly adopted, and the rudder angle operated should be gradually reduced, rapidly backing to the rudder must be avoided.

e. During the voyage, if the goods shift causing a heeling, the low side of the ship should be made by wind by correct manoeuvring against further heeling under the action of wind pressure moment produced by wind force.

References

[1] Liu Minyan.The main problem of safety transportation with bulk concentrate ship. Journal of Marine science institute [J]. 2001 (3).

[2] Ding Caiying. Risk analysis of bulk metal ore in shipping. Navigation technology. (6) : 14-18199-0.

[3] IMO. 1974 International Convention for the Safety of Life at sea, 2004.

[4] Xu Bangzhen, Wang Jianping, tian bayijun. Carriage of goods by sea. Dalian: dalian maritime university press, 2001.

[5] Tang Xingqiu. The study of the Characteristic of cargoes which may liquefy and Their Influence on the Transportation. Dalian maritime university. 2000.

[6] Li chen, Jiang Li, Liu Shu, Chen Zonghong. determination of moisture limit of fluorspar power. Chemical world. 11, 2010.

[7] LeiHai. Safe transport of sulfide ore concentrate. Navigation technology. 4, 2006.

Applied Mechanics and Materials Vol. 565 (2014) pp 265-270

doi:10.4028/www.scientific.net/AMM.565.265

The Research on Methods of Complicated Electromagnetic Environment Construction

Xiaofang Shao[1, a], Ning Jiang[1, a]

[1]Dept. Information Combat, Dalian Naval Academy, China.

[a]syp793200@163.com

Keywords: Complicated electromagnetic environment (CEE), Constructing methods, Naval battle field.

Abstract: Aiming at getting the characteristics of electromagnetic environment of naval battle field, the composition of electromagnetic environment is analyzed, including the principles, basis and methods of constructing electromagnetic environment. the different application directions are introduced according to different characteristics of various methods, which is of significance to the construction of complicated electromagnetic environment (CEE).

Introduction

In modern high-tech naval warfare, CEE has become the bottleneck to the weapon equipment operational effectiveness and forces to improve operational ability. Therefore, scientific and reasonable naval battle field electromagnetic environment is required, which can reflect actual combat and provide marine with the CEE for tactical training. The CEE can also improve combat capabilities of the navy to win local naval warfare under high-tech conditions in the future. design basis, principles and methods of electromagnetic environment construction are presented in the paper, according the brief analysis of the characteristics of navy tactical combined training and the basis of naval warfare field electromagnetic environment.

The Basis of Naval Warfare Field Electromagnetic Environment

In the modern local wars on the sea, Marine will faces complicated naval battlefield electromagnetic environment. CEE is mainly composed of background electromagnetic environment and electromagnetic environment with threat. Background electromagnetic environment refers to those the electromagnetic radiation signals influence the participation electronic equipment used in battle area, but mean no direct threats, including natural electromagnetic phenomena and civil electromagnetic environment and interacting with the electromagnetic environment[1][2]. Electromagnetic environment with threat refers to those the electromagnetic radiation signals influence information system and electronic equipment to work normally, caused negative influence on weapons and equipment use and operation in the combat area. Therefore, electromagnetic environment structuring is mainly constructed with threat electromagnetic signal, supplemented by electromagnetic signal in the background. According to potential operations objects and operations style, the electromagnetic threat are mainly composed of the enemy radio jamming signals, radar jamming signal, guided jamming signal, as well as communication signals, radar, guidance signals radioed by the enemy reconnaissance detection system, radio communication system, navigation and positioning system, guided the fire control system, identification system, etc[3,4,5].

The Basis of Electromagnetic Environment Construction

To construct the flexible and controllable electromagnetic environment according to the operational thought

To establish the CEE of naval battlefield is not the chaotic signal accumulation. It is set by the contract tactical training organization team according to the setting and regulation of operational scenarios, including the signal frequency, signal modulation style, appearance time, the radiation

intensity and direction control. That is to say, the CEE of naval battlefield reflects the actual battlefield electromagnetic radiation signals, the relationship between reflect different tactical action of electromagnetic environment characteristics. In different stages of exercise process, the CEE of naval battlefield presents different characteristics. Therefore, the CEE of naval battlefield should be in accordance with the specific participation, training plan and tactical scenarios, the different time interval, using different radiation sources and controlled way, to describe a scenario of naval battle field electromagnetic signal environment. Many should be done to meet these requirements. Firstly, the main radiation source from the technology parameters are controlled, the foundation of all kinds of radiation source parameters database is stored, and can bring up quickly and easily. The second is to establish complicated electromagnetic environment training command and control system, including a number of training scheme of control software package and join the main radiation source control interface. The third is to establish a training evaluation system, data acquisition and result analysis can record the main training links, traces the training process, playback training environment, the evaluation results.

To construct the electromagnetic environment according to the training area

The construction of CEE is a description of a certain naval battle field space, and inevitably closely related with exercise area location elements and electromagnetic radiation. If the training area is in the coastal area, the electromagnetic environment and the tactical training scheme design need to consider electromagnetic environment characteristics formed by air, surface and underwater and shore-based electronic information system and electronic warfare system ; Assuming training sea area is located in the ocean, we need to consider the electromagnetic environment characteristics formed by air, surface and underwater electronic information system and electronic warfare system, especially considering the navy operating independently. In order to meet the requirements, firstly, the CEE needs to be in accordance with the requirements for the naval battlefield, and objectively reflect the electromagnetic environment of real battlefield. Secondly Structuring of the CEE needs be in accordance with complex electromagnetic environment and natural environment of the training area. The CEE should provide commanders and their authority information in order that the commanders can acknowledge the situation and make their determination. In this way, the CEE can be the important elements of the chief determination in the battle plan, command and control.

To construct naval battlefield electromagnetic environment according to the operation targets

Changes and characteristics will appear to different targets of operation in naval battlefield electromagnetic environment, from the training requirements to technical requirements in the CEE construction. Generally, different operational targets and information platforms use different weapons technology system. Otherwise, some weapons platform used by different services are limited to a certain range: the use of the radiation spectrum of electronic information system are with clear division, some focused on radio frequencies, some of the radiation in the microwave and VHF frequencies. Therefore the information characteristics also have different performance. For example, in the attack on the enemy fleet at sea, the CEE focus is shown as: airborne radar signal, the shipboard radar signals, ultra short wave communication, acoustic signals, guidance and electronic jamming signals. Therefore, signals mentioned above will become indispensable CEE factors in the tactical training of attacking the enemy surface fleet. To defeat different operational targets, the troops will be different, the use of electronic information system and electronic warfare system will also be different. To achieve effective training effect, a targeted naval battle field electromagnetic environment should be constructed, according to operational objectives.

To construct practical electromagnetic environment according to the training objectives

Due to different units, different professional troops and equipment covered by different frequency band and the technical system, the demand for electromagnetic environment in training is also different. So according to the different participation objects, the targeted CEE will be constructed in order to satisfy different training objects of reality. Professional training, for example, the construction of CEE for radar troops training, mainly to simulate radar jamming radiation and anti-radiation destroy enemy air. The construction of CEE for communication unit training, efforts will be paid mainly on shortwave radiation ultrashort wave communication interference. The

construction of CEE for the EW forces training are mainly composed of radar system, communication system, the photoelectric system, acoustic system, guidance system.

To construct antagonistic electromagnetic environment according to the actual electromagnetic threaten

In the future, naval battlefield electromagnetic environment, all kinds of radiations may influence our communication system, radar system and photoelectric system. But the maximum factor is EA. Because the target of EA from the enemy is to destroy our communication system, radar system and photoelectric system, etc. EA obviously is not forecast, so its influence is main and serious. Electronic jamming and powerful EMP are the most active and effective electromagnetic radiation sources, it is unaccommodated and passive to the one who is on guard. In other words, electromagnetic radiation of EA is primary factor of CEE. Generally speaking, it is difficult to know the characteristics of enemy electronic jamming radiation, and even harder to know the accurate performance parameter of their electronic equipment. Therefore, the difficult point to construct CEE of battlefield is to radiate EMP according with the enemy radiation of EA. In order to improve the troops' capabilities, such as keeping their electronic equipments working well and accomplishing various missions of operations, the construction of CEE desires theory, technology and method of EW (electronic warfare) to make the CEE to be closed to the war and satisfy the needs of training.

The Principle of Electromagnetic Environment Construction

Pertinence

Pertinence principle refers to that the CEE is constructed according to operational target and the training mission. In the construction of CEE, the most important is to work out the electromagnetic environment, which can reflect electromagnetic action on both sides, especially from enemy weapons and equipment which cause the biggest impact upon the electromagnetic environment. CEE, therefore, the main operational object should take electromagnetic threat as a starting point, combining with the characteristics of specific training course, structuring complex electromagnetic environment.

Verisimilitude

Verisimilitude refers to realistically simulate the electronic information equipment category, scale and tactical use method, etc, which the main operational object may use. Impact of CEE is mainly the using of operations and the equipment. Environmental simulation degree directly determines the training effect, the simulation must be as strict and difficult as the war, showing possible battlefield CEE and improving the effectiveness and adaptability of action and equipment, and finally the actual combat ability of forces.

Antagonism

Antagonism is to simulate electromagnetic attack and defense both sides of the process, meeting the training requirements. In the modern war, in order to achieve a one-way transparent battlefield, both sides will take measures to acquiste the effective information, transmission, meanwhile, effectively preventing competitors from grasping the electromagnetic spectrum is important too. So the struggles in the electromagnetic field gradually reach the unprecedented height. Struggles in the electromagnetic battlefield also lead electromagnetic environment dynamic change in time domain, frequency domain, space and dynamic on power domain. Both parties shall take effective measures timely to cope with the changes of the electromagnetic environment. Therefore, the electromagnetic environment should satisfy confrontational training requirements.

Controllable.

In the informationization battle field, vast space and short process requires forces more mobility and coordination. In order to meet the need of war, both sides of the forces tend to be frequent and dynamic deployment and to gain more active status. In this way, with the development of operational processes, weapons and equipment deployment and application of electronic information system which is bound to be subsequently and change, the main battlefield electromagnetic environment diversity factor. At the same time, in order to make the design of battlefield electromagnetic environment can satisfy the participation of forces and different tactical background and a variety of

personality requirements of different operating patterns, we need to set a variety of tactical thinking and various electromagnetic environment characteristics into the battlefield electromagnetic environment simulate. Inevitably the electromagnetic environments require the ability of controllable and adjustable.

The Construct Methods of Naval Battlefield Electromagnetic Environment

To construct naval battle field CEE, mainly adopts the simulation method and technology to simulate naval battle field electromagnetic environment. At present, the methods to construct CEE of the navy contract tactical training can be used in the actual simulation method, semi real simulation method and digital simulation method. The selection of simulation method depends on the actual situation.

The actual simulation method

The actual simulation method is based on the components of the electromagnetic environment, using the real equipment for field layout method to form a complex electromagnetic environment. The key of the method is to accurately grasp the amount and type of electromagnetic radiation equipment of the enemy, ours and the civil parties. the advantage of the actual simulation method is Verisimilitude. The impact of complex electromagnetic environment can be felt, applicable and dependable.

Actual environment simulations are usually in outdoor field, which are based on the application environment of combat equipment. The simulation environment includes the type of ground, air and sea, etc. Simulation systems are made up of environmental simulation equipments, information warfare equipments, command and control and data processing center and data communication network. The number of information equipments and information warfare equipment those participate in training can be one or more. It depends on the needs of training. It is necessary to establish the precise positioning system, data acquisition and transmission system and equipment and training evaluation system to evaluate the operational effectiveness of equipment and military training effect. In the actual simulation environment, the command and control center controls the whole system through the digital communication network. The whole simulation system must establish unified time standards. It is usual to use training base timing system. And using GPS system is also feasible. The data of each simulation platform can be record in the media real-time, and then the data is send to the processing center. Digital transmission system can transmit data actual-time too. The second method can quickly response situations of the simulation, and it is easy to adjust training deployment and training methods, while the requirements of the digital system is more complicated.

The actual simulation method has been widely applied in exercises. In the training, “red” and “blue” on both sides mobilize the actual force, using actual equipments substitutes the conceived opponent and simulates the battlefield electromagnetic environment and situation. The trainees will be able to feel the real operational environment with actual forces and equipments. The targeted strong antagonism can improve the effect of training. The actual simulation method can simulate specific electromagnetic environment. When it is used to combat training and exercises, the combat and survivability under complicated electromagnetic environment can be improved. It is the most effective way for force to do the combat training and check the calibration of information equipments.

Semi-real simulation method

There is usually a certain limit in the using of the actual simulation method to construct CEE. Firstly, because of the limited number of actual electronic equipment, the high complexity of the electromagnetic environment, that actual simulation demands lots of radiation source type and quantity, advanced technology and actual difficulty of operation, it could be difficult to realistically simulate dense signal environment of the battlefield. Secondly, the cost of training simulation is too high, as a frequent training simulation method. Thirdly, the outdoor experiments are greatly influenced by meteorological and geographical conditions. In comparison, the Semi-real simulation method is appropriate to be a training method, as improvement and supplement to the actual simulation training in outdoor field.

Semi-real simulation constructs CEE by using signal source to simulate the electromagnetic signals. The radiation part of Electromagnetic environment construction adopts actual equipment. Real electromagnetic signals are radiated to the space. The rest of the equipment is implemented by simulation of computers. By using pertinent electromagnetic environment created by simulator, the cost simulation is low, with good effect and easy to handle. When the environments are Detailed constructed, we need to do some reach on electromagnetic situation in certain areas. By using functional analysis or signal analysis, adjusting the frequency of each signal source emission electromagnetic signals, power and signal radiation direction, flexible simulation of electromagnetic environment can be accomplished. The key of this method is to develop signal radiation sources. And it's general composed by the system controller, signal generator, power amplifier and antenna. The signal source can be obtained by using the modification of equipments at services. The signal source also can be manufactured.

At present, Semi-real simulation method is widely applied in the field of military training and equipment inspection. For example, widely used in exercise training and equipment test, microwave dark room, all kinds of radar signal simulation application, communication training application, the anti-ship missile terminal guidance simulation system, etc, are adopting Semi-real simulation to carry out related training and inspect electromagnetic environment. Semi-real simulation method can be carried out out-field, can also infield. Semi-real simulation method can simultaneously simulate moving targets, the echo signals, noises of environment (such as the waves of the sea, could, rain, chaff, etc.), and a lot of signals of radiation sources too.

Digital simulation method

Digital simulation method is an important way to construct CEE. On the basis of mathematical model, the Digital simulation method uses computer and simulation technology to create radiation source and characteristics of signals and target trajectory, without the actual radiation of electromagnetic wave. By using of this method to simulate performance indicators, operational effectiveness, background of the battlefield, the battlefield environment, deployment and combat situation and combat process of the actual combat weapon equipment system, making the training more close to the actual battlefield environment conditions.

Digital simulation method has three characteristics: Firstly, the environment model and equipment model can be assembled conveniently through the block, and environmental simulation and equipment simulation combine together tightly. So the simulation method of training is greatly adaptable, providing cheap and effective means for optimizing design; Secondly, when users want to set up a system, the only thing need to do is assembly, that provides users with flexibility; Thirdly, with a strong ability to expand, it can be easy to add system module that is not modeling yet, but the impact on the original model is little.

Conclusion

To construct realistic battle field electromagnetic environment is the bottom of navy contract tactical training and the key to improve the level of combat training under the conditions of informatization. Actual combat battlefield electromagnetic environment is a dynamic changing environment, along with the operational ideology, operational scale, operation forces, the operational area, operating patterns, force action, tactical using, changes of the number of frequency equipment, characteristics, factors of aspects. So in the actual construction, the method needs to chosen, according to the analysis of the specific operational object and training course.

References

[1] LIU Liming, HUANG Wenliang, SUN Lulu. Construction method of complex electromagnetic environment in sea battlefield[J]. 2010(4)：15-17.

[2] SHOU Baiming. Research of military training in complex electromagnetic environment[J]. Educational Technology Research, 2010(6)：49-51.

[3] RONG Jiangang, WEI Jianning, HUANG Heguo. Building the range of electronic warefare in complex electromagnetic environment[J]. , 2010(1)：5-10.

[4] WU Ruihua. Method of combined tactics training base in complex electromagnetic environment[J]. Educational Technology Research, 2010(6)：51-52.

[5] WU Jie, LIU Xiaogang. Construction of complex electromagnetic environment of battle field[J]. Journal of Changchun University of Science and Technology, 2010(4)：184-185.